

University of Nevada, Reno

INCREASED PROTON ENERGIES –
ABOVE THE ~ 60 MEV EMPIRICAL BARRIER,
FROM HIGH-CONTRAST HIGH-INTENSITY SHORT-PULSE
LASER-INTERACTIONS WITH MICRO-CONE TARGETS

A dissertation submitted in partial fulfillment of
the requirements for the degree of
Ph.D. in Physics

by

Sandrine Anne Gaillard

Dr. Yasuhiko Sentoku / Dissertation Advisor

December 2009



University of Nevada, Reno
Statewide • Worldwide

THE GRADUATE SCHOOL

We recommend that the dissertation
prepared under our supervision by

SANDRINE ANNE GAILLARD

entitled

**Increased Proton Energies - Above the 60 MeV Barrier,
From High-Contrast High-Intensity Short-Pulse
Laser-Interactions with Micro-Cone Targets**

be accepted in partial fulfillment of the
requirements for the degree of

DOCTOR OF PHILOSOPHY

Yasuhiko Sentoku, Ph. D., Advisor

Thomas E. Cowan, Ph. D., Committee Member

Radu Presura, Ph. D., Committee Member

Joseph M. Kindel, Ph. D., Committee Member

Peter Hakel, Ph. D., Committee Member

Aleksey Telyakovskiy, Ph. D., Graduate School Representative

Marsha H. Read, Ph. D., Associate Dean, Graduate School

December, 2009

© by Sandrine A. Gaillard 2009
All rights reserved

ABSTRACT

Ultra-high intensity lasers enable the investigation of extreme states of matter and the study of high energy density physics in the laboratory, as well as the creation of various intense radiation sources, i.e. electrons, X-rays, and ions. Of particular interest to this dissertation is the production of ion beams from solid targets. These ion beams are directly linked to the hot-electron production and transport inside the solid target (as simple as a metal or a plastic foil), which requires that electron heating and transport must be well understood in order to increase ion energies and laser-ion conversion efficiencies. Maximizing the energy and/or the conversion efficiency of these ion beams is of considerable interest for many applications, in particular radiation oncology, and inertial confinement fusion with fast ignition. Several approaches have been proposed to maximize the energy and/or the conversion efficiency of the ion beams: instead of using regular size flat-foil targets (i.e. $\sim 10 \mu\text{m}$ thickness, $\sim 2 \times 2 \text{ mm}^2$ lateral dimensions), one can use ultrathin targets (thickness of the order of the μm or 100s of nm), very small targets, a.k.a. reduced-mass targets (RMTs) (i.e. lateral dimensions of $\sim 100 \times 100 \mu\text{m}^2$), or structured targets (e.g. conical-shape targets). These more elaborate targets can increase the hot-electron temperature and/or the hot-electron density.

In experiments performed in 2006 on the Trident laser at $\sim 20 \text{ J}$, reported in [1], we found that microstructured flat-top cone (FTC) targets (see Figure 5-4), made from Au, yielded an increase in proton energy from 19 MeV to $> 30 \text{ MeV}$, and in laser-proton conversion efficiencies from 0.5 % to 2.5 %, as compared to flat-foil targets. These results were postulated to stem from improved laser guiding toward the cone tip, which would lead to higher laser intensities, increased laser absorption and hotter electrons. Improved electron production and transport were also hypothesized to lead to an increase in the hot-electron

density and hot-electron temperature at the flat-top. Also postulated was the fact that a longer electron confinement time at the flat-top could lead to RMT-like effects such as resistive/confining edge fields and enhanced target (or flat-top) charge up. We also observed experimentally that, when the laser was misaligned and could not reach the cone tip, or from simulations that, when it was absorbed farther from the flat-top due to an excess in preplasma, the proton acceleration was neither as efficient nor as energetic.

After these very promising 2006 results, we endeavored to determine whether this enhancement in proton energy and conversion efficiency would scale for higher laser energies. I participated in the design and the execution of the subsequent experiment, which was performed in 2008, after the Trident laser energy had been upgraded from ~ 20 J to ~ 80 J. This time, surprisingly, we found that the proton energies were in fact lower when FTC targets were used, as opposed to flat-foil targets [2]. To diagnose the laser absorption zone inside the FTC, Cu targets were used (instead of Au) for the purpose of Cu $K\alpha$ 2-D imaging. I had taken part in an experiment on the LULI laser system earlier in 2008 to learn about Cu $K\alpha$ imaging techniques; in this experiment, it was observed that, when a portion of the hot-electron population deposits its energy in the laser absorption zone, the emission of Cu $K\alpha$ X-rays is a direct indication of where the electrons are created, and thus of how much preplasma is filling the cone neck [3]; preplasma is plasma from wall blow-off due to the low level of laser light entering the cone before the main high-intensity pulse, called laser "prepulse". Combining and correlating Cu $K\alpha$ 2-D imaging with proton acceleration was one of my main goals for this dissertation. At an intrinsic 10^{-8} laser contrast, unlike in the 20 J (and $\sim 10^{19}$ W/cm²) case, at 80 J (and $\sim 2 \times 10^{20}$ W/cm²), after the Trident energy enhancement, as well as the addition of a deformable mirror resulting in a spot size decrease from ~ 14 μ m down to ~ 7 μ m FWHM (with 47 % of the energy in the

spot), the amount of plasma prefill (preplasma) prevented the majority of the laser from being efficiently absorbed closer to the cone flat-top or tip [3, 4]. The hot-electron population was thus generated away from the flat-top, as indicated by the Cu $K\alpha$ emission from the cone walls [2], which negatively impacted the proton acceleration, especially in the case of thin FTC necks [1], as the electrons were also not efficiently transported to the flat-top to generate the sheath necessary for ion production. I was also responsible for the electron spectrometer diagnostic; electron spectroscopy confirmed that the temperature of the escaping electrons correlates in a linear fashion with proton energy.

Because of the preplasma issues encountered in 2008 due to an insufficient laser contrast (10^{-8}), I proposed and was the principal investigator of the most recent experiment (2009), which was performed on Trident at ~ 80 J using an enhanced contrast, i.e. this time $> 10^{-10}$. In this case, the proton energies were enhanced to 67.5 MeV [5] from 50 MeV when using FTC Cu targets as opposed to flat-foil targets. These results set a new record in laser-accelerated protons. The previous petawatt laser record was 58 MeV with ~ 400 J [6]. Electron spectroscopy in the enhanced contrast case shows an even better correlation with proton energy, due to a cleaner interaction caused by a lower preplasma level. Besides diagnosing the laser alignment or misalignment, I show in this dissertation via Cu $K\alpha$ imaging, that not only is it crucial to obtain laser absorption at the tip (note that tip heating is dependent on laser contrast and laser intensity [3]), but it is even more important to find the optimum balance [5] between the amount of cone wall emission (CWE) versus top emission (TE) of Cu $K\alpha$ X-rays. Interestingly, at enhanced contrast, the best results for proton acceleration are obtained when the target-laser interaction is asymmetric: i.e. when the laser interacts with the cone-tip and one sidewall more so than the opposing side. These experimental results directly led to simulations of these asymmetric interactions

using a particle-in-cell (PIC) code capable of simulating ultra-intense laser-matter interactions. These simulation results significantly broadened our understanding of this interaction, and explain why the best performing target has a very large neck (i.e. 160 μm), implying that laser light guiding resulting from the cone geometry is not essential, but rather that the grazing of the laser light on as much cone wall surface area as possible (increasing the area where the laser can interact with the wall with a slight angle) is the reason for the observed proton energy enhancement. The knowledge obtained from these series of experiments, supported by the numerical simulations, will help us understand the fundamental laser-cone interaction, and develop new, more efficient targets, hopefully yielding even higher proton energy.

ACKNOWLEDGEMENTS



... It is needless to say that an experimental PhD can come with many difficulties, challenges, and uncertainties... Some rides are bumpier than others, and this one was definitely **very** bumpy! I would like to deeply thank the people who, through encouragement, support and patience, played a decisive role in helping me finish!

To begin, I have a particular thought for one of my high-school physics teachers, who encouraged me *not* to pursue a career in physics – I'm very happy that I did not follow his advice.

I wish to deeply thank all of the members of my committee, for taking the time to read and comment this long dissertation:

- Thomas Cowan (Forschungszentrum Dresden-Rossendorf, FZD, Germany), in particular, for his support and patience throughout all of my graduate school years, as I explored various subjects, and various laboratories; for looking out for me first; for initiating the research on the flat-top cones (FTCs), and giving me such a fruitful and interesting subject; for all the productive scientific explanations and discussions; for being such an open, passionate and enthusiastic scientist; for being demanding; and finally for his responsiveness and involvement in this work, and the thorough comments of the various drafts of this manuscript.

- Yasuhiko Sentoku (NTF – UNR) for his PICLS code, for replacing Tom as my UNR academic advisor, and for the advice he gave me at the EPS conference in Crete in June 2008: “Work hard and graduate!”
- Radu Presura (NTF – UNR): my thanks to him go back to the beginning of graduate school; for answering a variety of questions throughout the years, for being such a model as a scientist: patience, carefulness, incredulity, hard work... and for *finally* being on my committee!
- Joe Kindel (NTF – UNR): for supporting me financially during the transition period, as Tom was taking his new position at FZD.
- Peter Hakel (Physics Department – UNR): for his particularly thorough and careful reading and commenting of this manuscript.
- And Aleksey Telyakovskiy (Mathematics Department – UNR).

I’m absolutely and deeply indebted to the entire Trident laser crew (Randy Johnson, Tom Shimada, Ray Gonzales, Sha-Marie Reid, Fred Archuleta, and Tom Hurry) for being such a hard-working, friendly and customer-oriented team – always ready to chase the various problems. Trident would not be Trident without them! It’s been such a pleasure running experiments with them. I’m looking forward to many more ☺ and I very much apologize for being so intense and demanding, especially during the August 2008 and June 2009 FTC experimental beamtimes...

- Randy and Tom: your laser rocks!!! Thanks for all the information regarding Trident and for all your ideas and useful suggestions during experiments!
- Ray and Sha: thanks for teaching me how to align the laser.
- Fred and Tom: thanks for so carefully checking that everything is fine before each shot!

I would also like to thank Nanolabz (and especially Grant Korgan and Steven Malekos) for their hard work and enthusiasm required in the fabrication of these cool FTC targets! Talking about targets, I am extremely grateful to Julie Baas for so patiently and carefully helping me assemble these horribly delicate targets! Thanks for sharing the pain!

The following people deserve a special mention, and I hope to have a chance to work with them again in the near future:

- Sophie Baton (LULI), for initiating me to Cu K α 2-D imaging and spectroscopy.
- Jonathan Workman (LANL), for lending me his Cu K α 2-D imaging crystal.
- Mariano Lowenstern (CUOS) and Eduardo Mucino (CUOS), for their help and careful work during the August 2008 Trident beamtime.
- Tom Lockard (UNR) and Brady Gall (UMC), for their help and dedication during the June 2009 Trident beamtime.
- Marius Schollmeier (SNL), Frank Nürnberg (TUD), and Knut Harres (TUD), for the RIS Matlab program.
- Dustin Offermann (LANL), for joining the group in time to help me realize that I was at first using the wrong IP files, as well as for sharing his program for analyzing IMG files.
- Michael Bussmann (FZD), and more particularly Thomas Kluge (FZD), for their incredulity and their capacity to make sure we are getting to the root of things, for the extensive number of carefully carried out simulations, for their responsiveness and for their strong and productive involvement in the FTC research.

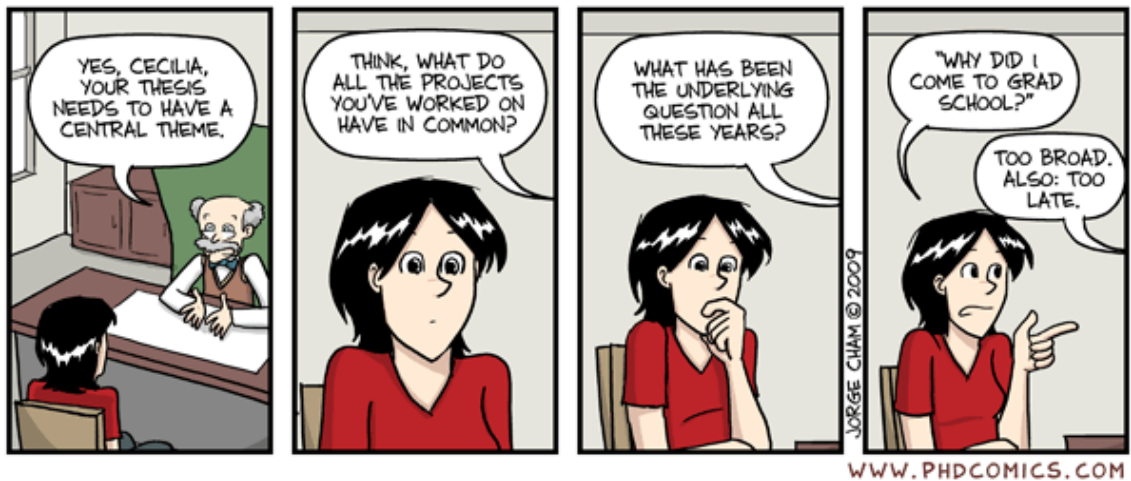
I want to express my deepest gratitude to **all** my friends, for bearing with me during the stressful moments, and believing in me, and I would especially like to mention:

- Jenny Rassuchine: thank you for being such a true kindred spirit and a wonderful friend and scientist; and for being a model of hard work, honesty and integrity!
- John Kline: thank you so very much for encouraging me, pushing me, keeping the pressure up, and checking up often on the progress of my dissertation.

And finally, I would like to thank my in-laws, parents and husband:

- Especially, Hyde and Cheryl Flippo, for welcoming me into their home for 3 months, even though they had never met me, and for making me feel at home. And of course Nana, who just turned 93 years old, for being such a wonderful and admirable role model!

- My parents, André and Madeleine Gaillard, for teaching me early on that, with passion, hard work, honesty and dedication, nothing is impossible; and also that things are only worth being done well, or not at all; for their constant support, encouragement, and for all of the helpful and thoughtful advices, throughout all these years of graduate school, and way before that.
- And last, but not least on this rather long list, I am extremely grateful to my better half, Kirk A. Flippo – who already is “THE” Flippo to me! – for his constant love, patience, moral and intellectual support; for these never ending conversations on how to change the world; for his humor and sarcasm; for his passion and interest in so many things, and in physics in particular; for his righteousness; for his scientific honesty and integrity; and for those long nights spent at the lab helping to prepare for the next day’s experimental run.



To Kirk,
And to anyone who enjoys physics for physics only, and science for science only!
À mes parents,
Et à tous ceux qui, toujours encore, savent s'émerveiller !

TABLE OF CONTENTS

1	INTRODUCTION	1
1.1	MOTIVATION AND POSSIBLE APPLICATIONS	2
1.1.1	Medical applications	3
1.1.1.1	Can laser accelerated protons and heavy ions meet the requirements necessary for therapy?	5
1.1.1.1.1	Ion energy requirements	5
1.1.1.1.2	Dose requirements	8
1.1.1.1.3	Required energy spread $\Delta E/E$	9
1.1.1.1.4	Beam handling and focusing	10
1.1.1.1.5	Shielding requirements	11
1.1.1.1.6	Remaining challenges	11
1.1.2	Fast ignition (FI) overview	12
1.1.2.1	Electron fast ignition (EFI)	12
1.1.2.2	Proton fast ignition (PFI) and ion fast ignition (IFI)	15
1.1.3	Other applications of proton and heavy ion beams	18
1.2	DISSERTATION OUTLINE	19
2	ELECTRON, X-RAY AND PROTON GENERATION FROM SOLID TARGET LASER INTERACTION	22
2.1	ELECTRON GENERATION	25
2.1.1	Thermal electrons and hot electrons	26
2.1.2	Hot-electron temperature scalings as a function of laser intensity and bulk plasma temperature	27
2.1.2.1	Hot-electron generation and propagation measurements	27
2.1.2.2	Long-pulse lasers	28
2.1.2.3	Short-pulse lasers	29
2.1.2.4	Summary of all the scalings, for $I < 10^{18}$ W/cm ² & $I > 10^{18}$ W/cm ²	31
2.2	X-RAY GENERATION	32
2.3	PROTON AND HEAVIER ION GENERATION	36
2.3.1	Front-side acceleration – Ion blow-off	37

2.3.2	Back-side acceleration – target normal sheath acceleration (TNSA)	39
2.3.3	Improving TNSA: target modifications for increasing the proton energy using similar laser conditions	45
2.3.3.1	PIC and PICLS Simulations.....	46
2.3.3.1.1	PIC simulations: generalities	46
2.3.3.1.2	PICLS Code.....	47
2.3.3.2	Cone targets.....	48
2.3.3.3	Hot-electron recirculation and enhanced TNSA (ultrathin targets)	51
2.3.3.4	Reduced-mass targets (RMTs).....	55
2.3.3.5	Summary of the techniques used to make the proton acceleration more 1-D-like (or isothermal-like) to enhance the proton energies.....	58
2.3.4	Summary of the proton acceleration research since 2000	59
2.3.4.1	Proton energy scalings as a function of laser intensity for the Trident laser parameters	59
2.3.4.2	Proton energy measurements so far	61
2.3.4.2.1	Maximum proton energy as a function of laser intensity.....	62
2.3.4.2.2	Maximum proton energy as a function of laser energy	65
3	THE TRIDENT LASER SHORT-PULSE BEAM-LINE.....	67
3.1	BRIEF OVERVIEW OF THE TRIDENT LASER SYSTEM	67
3.2	THE TRIDENT SHORT-PULSE BEAM-LINE: PRE-ENHANCEMENT AND POST-ENHANCEMENT AT INTRINSIC CONTRAST ($\sim 10^{-8}$)	69
3.2.1	The Trident laser system pre-enhancement	72
3.2.2	The Trident laser system post-enhancement.....	75
3.3	IMPROVING THE LASER CONTRAST	77
3.3.1	Prepulses, preplasma, and laser contrast.....	78
3.3.2	Inherent contrast issues to chirped pulse amplification (CPA) laser systems: amplified stimulated emission (ASE).....	80
3.3.3	Optical parametric chirped pulse amplification (OPCPA)	81
3.3.4	Self-pumped optical parametric amplification (SPOPA)	82
3.4	MAJOR LASER BEAM DIAGNOSTICS.....	86
3.4.1	Laser pulse duration	86
3.4.2	Shack-Hartman (SH) wavefront sensor	87

3.4.3 Deformable mirror (DM)	87
3.4.4 Laser spot size at low energy (i.e. CW alignment beam)	87
3.4.5 Target alignment – before the shot	88
3.4.6 Backscatter focal diagnostic (BFD)	89
3.4.6.1 BFD before the shot	89
3.4.6.2 BFD after the shot	89
4 PARTICLE DETECTION AND DIAGNOSTICS.....	91
4.1 CR39 SOLID STATE NUCLEAR TRACK DETECTORS (SSNTDs).....	91
4.2 RADIOCHROMIC FILMS (RCFs) BY GAFCHROMIC®	93
4.2.1 Different types of RCF.....	95
4.2.2 Advantages of using a microdensitometer as opposed to a scanner	97
4.2.3 Aging effect: Scanning using red or white light and a MicroD	99
4.2.4 Calibration curves using a MicroD and white light	100
4.2.4.1 ISP calibrations using a Cobalt 60 source and electrons.....	101
4.2.4.2 RCF calibrations on various particle accelerators.....	102
4.2.4.2.1 Calibration curves for MD-55 scanned using a MicroD and white light	103
4.2.4.2.2 Calibration curves for MD-V2-55	103
4.2.4.2.3 Calibration curves for HS scanned using a MicroD and white light.....	104
4.2.4.2.4 Calibration curves for HD-810 scanned using a MicroD and white light.....	105
4.2.5 RadioChromic film imaging spectroscopy (RIS), or a method to convert the RCF's OD into a proton number or a proton dose	105
4.3 IMAGING PLATES (IPS) BY FUJIFILM.....	114
4.3.1 Different kinds of IPs and advantages over other detectors	117
4.3.2 Calibration of IPs for electrons	118
4.3.3 Effect of time: fading	119
4.4 ELECTRON SPECTROMETER SPECA.....	121
4.5 2-D SPHERICAL CRYSTAL KA X-RAY IMAGER	124
4.5.1.1 Crystal parameters.....	126
4.5.1.2 Experimental set-up	126
4.5.1.3 Magnification	128

4.5.1.4	Effect of target heating.....	128
4.5.1.5	Addition of a pinhole in front of the crystal.....	129
4.5.1.5.1	Field of view.....	129
4.5.1.5.2	Spatial resolution.....	129
4.5.1.5.3	Spectral range.....	130

5 EXPERIMENTS: TARGETS, SET-UPS & RESULTS131

5.1 CONE RESEARCH FOR FAST IGNITION AND OTHER APPLICATIONS131

5.2 TRIDENT, 20 J, $\sim 10^{19}$ W/CM² & INTRINSIC 10^{-8} CONTRAST: MARCH 2006 (SISYPHUS III) & AUGUST 2006 (ALBA) BEAMTIMES 136

5.2.1	Experimental set-up.....	136
5.2.2	Description of the Gold flat-top-cone (Au FTC) targets.....	137
5.2.3	Summary of the results.....	140
5.2.4	Results presented in detail: Comparison in the maximum proton energies for various FTCs, proton spectra and PICLS simulations.....	140
5.2.5	Necessary improvements for future experiments.....	149

5.3 TRIDENT, 80 J, $\sim [1.1-2.3] \times 10^{20}$ W/CM² & INTRINSIC 10^{-8} CONTRAST: AUGUST 2008 & SEPTEMBER 2008 BEAMTIMES150

5.3.1	Experimental set-up.....	151
5.3.1.1	Flat foils.....	151
5.3.1.2	Funnel-cone targets, flat-top-cone targets, and reduced-mass targets.....	152
5.3.2	Description of the targets.....	153
5.3.2.1	Cu, Ni and Al flat-foil targets and Cu reduced-mass targets.....	153
5.3.2.2	Cu (Ti-Cu and Ti-Cu-Ti) funnel cones and Cu flat-top cones.....	153
5.3.3	Summary of the results, 80 J & 10^{-8} contrast.....	155
5.3.3.1	Flat-foil targets and Reduced-mass targets.....	155
5.3.3.2	Funnel cones and flat-top cones.....	156
5.3.4	Results presented in detail (80 J & 10^{-8} contrast): Maximum proton energies and Cu K α emission, organized by target type (i.e. Flats and Cones), for most of the shots of the two 2008 campaigns.....	157
5.3.4.1	Maximum proton energies as a function of target type: summary.....	157
5.3.4.2	Flat-foil targets (Cu, Ni and Al) and reduced-mass targets (Cu, 300 μ m diameter).....	158

5.3.4.3 Cu Snubbed Nose Cones	161
5.3.4.4 Cu funnel and flat-top cones	162
5.3.5 Correlation between electron temperature and proton energy	170
5.4 TRIDENT, 80 J, ~ [1.2–1.9]×10²⁰ W/cm² & ENHANCED > 10⁻¹⁰ CONTRAST: JUNE 2009 BEAMTIME.....	174
5.4.1 Experimental set-up	175
5.4.2 Description of the Targets	177
5.4.2.1 Cu flat-top cones of various top-to-neck ratios	177
5.4.2.2 Funnel cones.....	178
5.4.2.3 Reduced-Mass Targets.....	178
5.4.3 Summary of the results (80 J & 10 ⁻¹⁰ contrast): funnel-cone, flat-top- cone, flat-foil, and reduced-mass targets.....	179
5.4.3.1 Effect of the contrast enhancement on maximum proton energies and conversion efficiencies from flat-foil targets.....	180
5.4.3.2 Effect of the contrast enhancement on the Cu K α emission from cone targets..	181
5.4.3.3 Cu K α emission from the top (TE), from the cone walls (CWE) or/and from the supporting foil (SFE).....	183
5.4.3.4 Proton Energies: Flat-foil targets, RMTs, and FTC targets	185
5.4.4 Correlation between the Cu K α emission and the maximum proton energies – for all shots on FTC targets (80 J & 10 ⁻¹⁰ contrast)	188
5.4.4.1 Case CWE or SFE >> TE and TE ~ 0, where there is much more cone wall emission (CWE) or supporting foil emission (SFE) than top emission (TE), as well as very little TE	188
5.4.4.2 Case TE >> CWE or TE >> SFE, where there is much more top emission (TE) than cone wall emission (CWE) or than supporting foil emission (SFE)	189
5.4.4.3 Case TE >~ CWE, where there is slightly more top emission (TE) than cone wall emission (CWE).....	192
5.4.4.3.1 Best Performers	192
5.4.4.3.2 Understandable exceptions (laser energy, supporting foil size, and supporting foil emission): shots 21169, 21184, and 21192.....	194
5.4.4.4 Behavior of similar small neck size targets.....	196
5.4.5 Correlation between proton energies and supporting foil size.....	197
5.4.6 Correlation between electron temperature and proton energy	198
6 DISCUSSIONS, SIMULATIONS & CONCLUSIONS.....	202

6.1 OVERALL COMPARISON IN TERMS OF PROTON ENERGY AND ELECTRON TEMPERATURE OF ALL RESULTS: 20 J AND 80 J, INTRINSIC AND ENHANCED CONTRAST, FLAT-FOIL, FLAT-TOP-CONE, FUNNEL-CONE, AND REDUCED-MASS TARGETS	202
6.1.1 Proton energies.....	202
6.1.2 Proton conversion efficiencies.....	204
6.1.3 Electron temperatures	205
6.2 DISCUSSIONS, SIMULATIONS, AND CONCLUSIONS	208
6.2.1 Cu $K\alpha$ emission from the top region (TE) compared to emission from the cone region (CWE) and ratio TE / (SFE + CWE + TE): correlations with proton energy.....	208
6.2.1.1 80 J and 10^{-10} contrast	208
6.2.1.2 80 J and 10^{-8} contrast.....	208
6.2.2 Effects of the FTC neck size as well as of the asymmetric laser-FTC interaction	209
6.2.2.1 20 J and 10^{-8} contrast.....	209
6.2.2.2 80 J and 10^{-10} contrast	210
6.2.3 S-polarization vs. P-polarization.....	212
6.2.4 PICLS simulations	214
6.2.4.1 Laser grazing in the throat.....	215
6.2.4.2 PICLS simulations: detailed laser offset scan in the throat.....	216
6.2.5 Validated and unverified hypotheses	226
7 FUTURE WORK.....	233
7.1 LASER.....	233
7.2 DIAGNOSTICS	234
7.3 TARGET DEVELOPMENT	234
7.4 MICRO-STRUCTURED CU FTCS	235
8 VITA AND PUBLICATION LIST	239

9 APPENDIX: LASER-PLASMA INTERACTIONS, AN INTRODUCTION	242
9.1 BASIC PLASMA PHYSICS	242
9.1.1 Definitions	242
9.1.1.1 Plasma: introduction.....	242
9.1.1.2 Plasma and Debye length.....	243
9.1.1.3 Electromagnetism equations	245
9.1.1.4 Equation of motion and continuity equation	245
9.1.1.5 Plasma frequency	246
9.1.2 Electromagnetic waves	247
9.1.2.1 In vacuum.....	247
9.1.2.2 In an unmagnetized plasma.....	248
9.1.2.2.1 Critical density and Characteristic skin depth	249
9.1.2.2.2 Collisionless skin depth and Relativistic induced transparency	250
9.2 LASER INTERACTIONS IN UNDERDENSE AND DENSE PLASMAS	250
9.2.1 Electron motion, quiver velocity, and ponderomotive force	251
9.2.1.1 Definitions.....	251
9.2.1.1.1 Electron quiver velocity.....	251
9.2.1.1.2 Normalized vector potential	251
9.2.1.1.3 Intensity and electric field	252
9.2.1.2 Photon pressure	253
9.2.1.3 Ponderomotive force and Ponderomotive potential	253
9.2.2 Target ionization	254
9.2.2.1 Field ionization potential.....	255
9.2.2.2 Tunneling ionization	255
9.2.2.3 Multi-photon ionization	256
9.2.3 Laser interaction with underdense plasmas	257
9.2.3.1 Ionization-induced defocusing	257
9.2.3.2 Laser self-focusing	258
9.2.3.2.1 Ponderomotive self-focusing	258
9.2.3.2.2 Relativistic self-focusing	259
9.2.3.2.3 Thermal self-focusing	260

9.2.3.2.4	Self-phase modulation	260
9.2.3.2.5	Self-channeling, self-guiding, and sausageing	260
9.2.3.2.6	Filamentation	261
9.2.3.3	Parametric instabilities	261
9.2.3.3.1	Parametric decay instability	261
9.2.3.3.2	Stimulated Brillouin Scattering (SBS)	262
9.2.3.3.3	Stimulated Raman Scattering (SRS)	262
9.2.3.4	Plasma Wake-Field Accelerator	263
9.2.3.4.1	Plasma Wake-Field Acceleration (PWFA)	264
9.2.3.4.2	Plasma Beat-Wave Acceleration (PBWA)	264
9.2.3.4.3	Laser Wake-Field Acceleration (LWFA)	264
9.2.3.4.4	Self-modulated laser Wake-field Acceleration (SMLWFA)	264
9.2.3.4.5	Resonant Laser-Plasma Acceleration (RLPA)	265
9.2.3.5	Density profile steepening	265
9.2.3.6	Laser envelope profile steepening	266
9.2.4	Laser interactions with solids	266
9.2.4.1	Hole boring	267
9.2.4.2	Ion shocks	268
9.2.4.3	Collisional absorption: Helmholtz equations	268
9.2.4.3.1	Case of an <i>S</i> -polarized wave	271
9.2.4.3.2	Case of a <i>P</i> -polarized wave	272
9.2.4.3.3	Solutions of the Helmholtz equations	273
9.2.4.3.4	Inverse Bremsstrahlung absorption	274
9.2.4.3.5	Collisional damping	275
9.2.4.4	Collisionless absorption	275
9.2.4.4.1	<i>P</i> -polarized obliquely incident light wave: Resonance absorption	276
9.2.4.4.2	<i>S</i> -polarized obliquely incident light wave	278
9.2.4.4.3	“Not-so-resonant”, Resonant absorption, Brunel heating or Vacuum heating	279
9.2.4.4.4	Relativistic $J \times B$ (or $v \times B$) heating	284
9.2.4.4.5	Anomalous skin effect and Sheath inverse Bremsstrahlung	286
9.2.4.4.6	Landau damping	288

10 REFERENCES.....289

LIST OF FIGURES

Figure 1-1: Distribution of the relative depth dose [%] in body tissue for various types of radiation [25]: X-rays, γ -rays, neutrons, protons, and carbon ions. Compared to other radiation, protons, and especially ions, have a peaked profile which allows for a greater tumor dose and lower dose into the surrounding healthy tissues, which is an ideal tool for deep-seated tumors. Changing the ion energy simply shifts the position of the energy deposition in depth.....	4
Figure 1-2: System considerations for a laser-based hadron-therapy machine (Diagram by Thomas Cowan).	5
Figure 1-3: Maximum proton energy [MeV] as a function of (a) laser intensity [W/cm^2], (b) laser energy [J] and (c) laser power [TW], for all laser energies, pulse durations, laser intensities, and all targets (CH and metal), showing the best shots for a particular experiment on a given laser. In light blue (horizontal lines) are the low and high levels of the therapeutic window, and in red (diamond), the latest world record of 67.5 MeV obtained on Trident at 80 J using a flat-top cone target.	7
Figure 1-4: Effective dose as a function of tissue equivalent material; to treat a tumor of a few centimeters in size, the deposition should be distributed evenly over a broad depth.....	10
Figure 1-5: Schematic of the Fast Ignition (FI) scenario.....	13
Figure 1-6: Typical EFI target [46].....	14
Figure 1-7: Schematic of the Electron Fast Ignition (EFI) scenario [47].....	14
Figure 1-8: Indirectly driven PFI; (Inset) the rear surface of the laser target is shaped to focus the proton beam into the spark volume [15].....	15
Figure 2-1: Brief overview of the laser-ion acceleration: front-side acceleration and target normal sheath acceleration (TNSA) mechanism (Schematics by Kirk Flippo)....	24
Figure 2-2: Initial stage of the sheath expansion (interpreted from [6(b)]).	25
Figure 2-3: Scalings of the hot-electron temperature [keV] as a function of laser intensity [W/cm^2] for a 1 μm light. Triangles: long (10 of picoseconds) pulse scalings; a bulk temperature of 10 keV is assumed; the scaling only holds up for $I < 10^{18} W/cm^2$. Diamonds: short (100s of femtoseconds) pulse scalings; the Brunel scaling and the Gibbon and Bell scaling hold for $I < 10^{18} W/cm^2$ and the Wilks scaling holds for $I > 10^{18} W/cm^2$. Squares: turquoise border, picosecond pulse, no assumption of the bulk temperature is necessary.	32
Figure 2-4: Stopping power of electrons [$MeV.cm^2/g$] with energies between 1 keV and 10000 MeV (http://physics.nist.gov/cgi-bin/Star/e_table.pl).	34
Figure 2-5: Electron induced K-shell ionization cross-section [barn] for Cu as a function of the electron energy [keV] [109].....	35

Figure 2-6: Transmission [%] as a function of photon energy [keV] through cold solid density Cu obtained from the Henke tables (http://henke.lbl.gov/optical_constants/filter2.html)..... 36

Figure 2-7: Front-side ion acceleration: Mean ion energy (in MeV/AMU) versus laser intensity. The plot is a compilation of data from the Helios CO₂ LANL laser (open circles) and from laboratories throughout the world [66]; the horizontal red line corresponds to the ion energy of 1 MeV. 38

Figure 2-8: Diagram of the TNSA mechanism [11]..... 41

Figure 2-9: Expanding electron sheath at the rear surface of the target, with ions of different energies propagating normal to the sheath, at different divergence angles. 41

Figure 2-10: (left) Hot-electron temperature profile as a function of time; τ_L corresponds to the pulse duration for various cases: isothermal [117] (blue, dashed and dotted line), adiabatic [118] (red, dashed and dotted line) and 2-phase [119] (green, solid line); (right) Sheath expansion phase (interpreted from [6(b)])..... 43

Figure 2-11: Maximum proton energy [MeV] as a function of laser intensity [W/cm²]; the laser energy is varied and the pulse duration (1 ps) and focal spot are kept constant; the targets are Al, 10 μm thick (red dot) and 25 μm thick (blue triangles); the open triangles correspond to laser shots on 25 μm thick Al targets for which the pulse duration and the laser energy are both varied; the green circles are the predictions of the isothermal plasma-expansion model described by Mora [117]; the green squares correspond to results from a revised form of this 1-D model, using two phases for the electron temperature; the green triangles correspond to results using the same model with 3-D effects mimicked; the error bars on the maximum proton energy arise from combining counting statistics with errors in the proton energy measurements; the error bars on the laser intensity are a combination of the measurement uncertainty in laser pulse energy and estimated shot-to-shot fluctuations in pulse duration [119]. 45

Figure 2-12: Concept of the reduced PIC simulation code: electron density (vertical axis) profile as a function of distance x (horizontal axis), where the physics transitions from being purely kinetic (low density) to collisionally dominated (high density) [122]. 48

Figure 2-13: At $t = 16\tau$ (left) Contour plots of the square root of the instantaneous electromagnetic energy in the longitudinal space (a) X-Z and (b) X-Y (polarization plane); plots are normalized by the incident laser E-field, E_0 ; the solid lines indicate the initial target shape; (right) Energy spectra of hot electrons in the laser direction for a conical target (solid line) and for a flat target (dotted line); for these spectra, only the electrons present inside a 1 μm spot in the central region are taken into account [44]. 49

Figure 2-14: At $t = 16\tau$ (left) Contour plot of the quasi-static magnetic field B_z/B_0 ; (right) time-averaged electron energy density $(\gamma-1)n_e/n_0$ [44]. 50

Figure 2-15: Images of the electron circulation inside the target for (I) a thick target and (II) a thin target [124]. 51

- Figure 2-16: Peak proton energy as a function of target thickness. The plots are obtained via 1-D PIC simulations. The back curve shows the empirical scaling, when the target thickness is smaller than the critical thickness [124]. 52
- Figure 2-17: LULI data, 100 TW, Al targets (a1) Maximum proton energy [MeV] as a function of target thickness [μm] and (a2) Laser-to-proton conversion efficiency [%] as a function of target thickness [μm]; (b) LLNL data, Callisto, Al targets, Maximum proton energy [MeV] as a function of target thickness [μm]. 53
- Figure 2-18: Ultrathin and stacked foils (left, from top to bottom) target density as time evolves; (right) Proton spectrum (courtesy of Thomas Kluge). 54
- Figure 2-19: RMTs experiments performed on the 100 TW LULI laser in Palaiseau, France in February 2008 (courtesy of Thomas Cowan and Julien Fuchs). 56
- Figure 2-20: RMT experiments performed on Callisto at the Jupiter facility at LLNL in February 2007; the RCF (green) stack was wrapped around the target (orange), and a hole in the RCF allowed the laser (black arrow) to come in at a 22.5° incident angle (courtesy of Hui Chen and Scott Wilks). 57
- Figure 2-21: Reproduction of Figure 2-11, showing Maximum proton energy [MeV] as a function of laser intensity [W/cm^2] [119] for three models and experimental data; added on the plot are arrows illustrating how various targets allow for increasing the maximum proton energy as a function of laser intensity: RMTs and thin foils (red arrow); hemispherical shell targets, RMTs and larger laser spot sizes (pink arrow) and cones (blue arrow) increase the laser intensity at the tip, resulting in a higher effective intensity. 58
- Figure 2-22: Maximum proton energy [MeV] as a function of laser intensity [W/cm^2] for various empirical (Helios, Beg, CUOS) and theoretical scalings (Fuchs, Schreiber), as well as the “all data” scaling..... 59
- Figure 2-23: Maximum proton energy [MeV] as a function of laser intensity [W/cm^2] for all lasers in the world, grouped by pulse durations, with low contrast (i.e. lower than 10^{-8}). The data plotted is taken from [1, 3-4], and [9] and is represented by \blacklozenge s. It is broken down into pulse duration groups: 30-100 fs (dark blue \blacklozenge s); 101-299 fs (purple \blacklozenge s); 300-400 fs (green \blacklozenge s); 401 -1050 fs (yellow \blacklozenge s). Also plotted are the Trident data at intrinsic contrast (\bullet s) and the Omega EP data (\blacksquare s): Trident data energy scan, for 540-685 fs and constant spot size (orange \bullet s), Trident data spot size scan at 640-1200 fs for constant energy (purple \bullet s) and Omega EP data energy scan for 10000 fs and constant spot size (light blue \blacksquare s). Four fits are shown, one for all the \blacklozenge data in grey (which excludes any of the Trident or Omega EP data), one for the EP data in blue, one for the energy scan on Trident in orange, and one for the spot size scan on Trident in purple. 63
- Figure 2-24: Performance of the 200 TW Trident laser system, in terms of maximum proton energy [MeV] as a function of laser intensity [W/cm^2], compared to three published scaling laws [17]. The October 2007 data (green triangles) and the March 2008 data (blue squares) are from the new Trident 200 TW commissioning runs. The October 2007 values are from shots where the spot size was varied but the energy was relatively constant with an average pulse duration of 1300 fs, without the deformable mirror installed (making the spot

size slightly larger, FWHM of 12 μm , 50 % of encircled energy). The March 2008 data are from shots where the laser energy was varied but the focus was constant, with an average pulse duration of 620 fs. Most reported values above $1 \times 10^{19} \text{ W/cm}^2$ fall below these scalings. A fit to the March 2008 Trident data gives a curve with an exponent of 0.565..... 64

Figure 2-25: Maximum proton energy [MeV] as a function of laser energy [J] for all lasers in the world, grouped by pulse durations, with low contrast (i.e. lower than 10^{-8}). The data plotted is taken from [1, 3-4], and [9] and is represented by \blacklozenge s. It is broken down into pulse duration groups: 30-100 fs (dark blue \blacklozenge s); 101-299 fs (purple \blacklozenge s); 300-400 fs (green \blacklozenge s); 401 -1050 fs (yellow \blacklozenge s). Also plotted are the Trident data at intrinsic contrast (\bullet s) and the Omega EP data (\blacksquare s): Trident data energy scan, for 540-685 fs and constant spot size (orange \bullet s); and Omega EP data energy scan for 10000 fs and constant spot size (light blue \blacksquare s). Three fits are shown, one for all the \blacklozenge data in grey (which excludes any of the Trident or Omega EP data), one for the EP data in blue and one for the energy scan on Trident in orange..... 66

Figure 3-1: Diagram of the Trident pulse lengths [s] and energies [J] (by Robert Gibson)... 68

Figure 3-2: Trident's North Target Area and Chamber..... 69

Figure 3-3: Chirped Pulse Amplification (CPA) scheme. 70

Figure 3-4: Short-pulse laser front-end (version 0), to scale, pre-enhancement, intrinsic contrast (by Randall P. Johnson)..... 70

Figure 3-5: Laser oscillator cavity..... 71

Figure 3-6: Laser *regen* cavity..... 72

Figure 3-7: Block diagram of the Trident CPA laser system, pre-enhancement, intrinsic contrast, with pulse train optics (by Randall P. Johnson)..... 72

Figure 3-8: Gaussian beam: w_0 is the waist, θ the divergence, and Z_R the Rayleigh range..... 74

Figure 3-9: Block diagram of the Trident CPA laser system post-enhancement, intrinsic contrast, with pulse train optics (by Randall P. Johnson)..... 75

Figure 3-10: Trident short-pulse beam-line generating 200 TW after the enhancement, which consisted in the addition of a new front-end, another amplifier, and a vacuum compressor. The optical pulse length is indicated along the beam path. 77

Figure 3-11: Example of a third order cross-correlation trace (laser intensity [W/cm^2] as a function of time [ps] showing the ASE pedestal (10^3 ps corresponds to the front of the pulse, when the pulse starts interacting with the target), a short-pulse prepulse and the main pulse [17]. 78

Figure 3-12: Trident's ASE contrast, as measured from the *regen*, is better than 10^{-7} 0.5 ns prior to the main pulse, and there are two prepulses: one at -220 ps (3×10^{-7}) and one at - 90 ns (9×10^{-8})..... 81

Figure 3-13: Schematic of a low gain OPA temporal pulse cleaning (schematics by Randall P. Johnson). 83

- Figure 3-14: Temporal contrast measurement [147] of both unamplified signal and idler, with calculated cube of signal; Inset shows a larger temporal range; (a): known artifact, (e): etalon reflection, (u): unknown peak, assumed to be an artifact.... 83
- Figure 3-15: Latest auto-correlator measurements (September 2009) of the Trident laser contrast: the intrinsic contrast is shown in red, and the enhanced contrast is shown in dark blue (measurements performed by Randall P. Johnson)..... 84
- Figure 3-16: Short-pulse Front-end, post-enhancement, and including the pulse cleaner, version 1, used during the August 2008 run on 3 shots (diagram by Randall P. Johnson). 85
- Figure 3-17: Short-pulse Front-end, post-enhancement, and including the pulse cleaner, version 2, used during the June 2009 campaign (diagram by Randall P. Johnson). 85
- Figure 3-18: Schematic lay-out of the diagnostic suite used for the short-pulse laser beam (drawing by Tsutomu Shimada)..... 86
- Figure 3-19: (a) Trident encircled energy of the (b) focal spot as a function of encircled radius, a FWHM of $4.7 \mu\text{m}$ in diameter with 49 % of the energy in that radius, and 86 % of the energy within a radius of $14 \mu\text{m}$; (c) the focal spot spatially from the near field, (lower left) $630 \mu\text{m}$ from focus to (upper right) the focus. 88
- Figure 3-20: Backscatter Focusing Diagnostic pictures: (a) 100 nm Al (shot 20548); (b) 800 nm Al (shot 20554); $10 \mu\text{m}$ Cu (shot 20552). 90
- Figure 4-1: Optical scans in transparency mode of the CR39 Tastrak detectors of fluences (horizontally) from $5 \times 10^6 \alpha/\text{cm}^2$ (100 s of exposure time) to $5 \times 10^{10} \alpha/\text{cm}^2$ (10^6 s of exposure time) for etching times (vertically) of $\sim 18'$ to $\sim 78'$; Note the presence of artificial rings after the 5th column..... 92
- Figure 4-2: Proton beam emission from a target (purple arrows), recorded in an RCF stack (blue), protected by a thin Al foil (grey, front of the stack); the stack also contains some thicker Al filters (grey), and a CR39 detector (yellow); note that the most energetic particles penetrate further down the stack, with a more collimated beam divergence than the low energy particles, which have a wider divergence and are stopped early in the stack..... 94
- Figure 4-3: (left) Image of an RCF showing a proton beam profile produced via laser-plasma acceleration experiment, scanned on the MicroD, and exhibiting structures of $100 \mu\text{m}$ and less, with ODs from 1.9 to 5.12, beyond the range of a flat-bed scanner. (right) Scans performed using a MicroD, the Epson V750 (500 and 6400 dpi) and the Epson Expression 1680 (500 dpi) of Wratten Neutral Density Filters (WNUF), using with ODs of 0.08, 0.19, 0.29, 0.62, 0.91, 1.99, 3.01, and 4.14, as measured from the diffuse densitometer (DiffuseD), corresponding to the OD nominal values of 0.1, 0.2, 0.3, 0.6, 0.9, 2, 3 and 4, on two scanners and a MicroD..... 97
- Figure 4-4: (a) Various WNUF size disks with different ODs (different colors) are scanned on an Epson V750 @ 500 dpi (\times) and @ 6400 dpi (\blacklozenge), an Epson Expression 1680 @ 500 dpi (\blacktriangle). (b) Same as (a) but zoomed for $R \sim 1$. (c) Various WNUF size disks with different ODs (different colors) are scanned on a MicroD (\bullet):

regardless of the OD and the size of the disk, the MicroD's resolution is very good, as $R \sim 1$ 98

Figure 4-5: Absorption maxima of the blue-colored dye polymer in RCF at 615 nm and 675 nm [154]..... 99

Figure 4-6: MicroD curve in log-log scale of OD as a function of deposited dose [keV/mm²] for LANL Tandem HD-810 data scanned on a MicroD; immediately after the exposure with red filter (dark blue empty and dark blue full squares) and with white light (turquoise squares) and 1.5 year later with red filter (turquoise squares with red border); the 2007 MicroD scans were performed with an OG 590 red filter, a 3.5× objective and a 20×20 μm² resolution; the 2008 MicroD scans were performed for the White Light case with a 10× objective, a Numerical Aperture (NA) of 0.25 and a 50×50 μm² resolution, and for the Red Filter case with an OG590, a 10× objective, a NA of 0.25 and a 50×50 μm² resolution.....100

Figure 4-7: ISP calibration curves for HD-810, MD-55 and HS: Net density (up to OD ~ 3) as a function of dose [Gy]: the curves show a linear response between density and dose. 101

Figure 4-8: MD-55 (top) Calibration curves giving deposited_dose [keV/mm²] = f(OD); (bottom) Equation of the best fit to the data points. 103

Figure 4-9: HS (top) Calibration curves giving deposited_dose [keV/mm²] = f(OD); (bottom) Equation of the best fit to the data points. 104

Figure 4-10: HD-810 (top) Calibration curves giving deposited_dose [keV/mm²] = f(OD); (bottom) Equation of the best fit to the data points. 105

Figure 4-11: Energy deposited in each single layer of an RCF stack, by a proton of a specific energy (in 0.01 MeV energy steps); the stacks are made of (a) 9 layers of HD, (b) 4 layers of MD and (c) 4 layers of HS..... 107

Figure 4-12: RCF data (Shot 20537) that have been scanned with a MicroD are loaded in the program; (a) RCF spectrum GUI; (b) Image processing GUI. 108

Figure 4-13: Raw data (blue circles), and a simple fit (black dashed line) to the spectrum (#/energy) from the Matlab program assuming an exponential fit to the spectrum for a 10 μm regular Cu flat foil (Shot 20537): Fit C.E. = 1.63 % and the binned raw data C.E. = 1.384 %. This assumes all the particles depositing energy in a layer were of that energy (i.e. "Bragg Peakers"). 110

Figure 4-14: Dose per layer energy from the Matlab program deconvolving the assumed spectrum to fit the dose values. Calculated values (stars) fitting the circles are shown for a 10 μm regular Cu flat foil (Shot 20537), along with another fit based on the Fuchs scaling, which is clearly underestimating the spectrum. The conversion efficiency of the binned data is C.E. = 1.81 %, based on the original layers as energy bins in the previous figure. The dose has a discontinuity when changing from HD to MD at about 15 MeV due to the different construction of the films. 111

Figure 4-15: (left) Proton beam post-analysis, i.e. once the background subtraction and the proton beam selection have been applied; (right) Spectrum from the Matlab program obtained from the deconvolution of the assumed Maxwellian

continuous spectrum (blue circles) for the protons for a 10 μm regular Cu flat foil (Shot 20537): C.E. = 1.60 %.....	112
Figure 4-16: (left) Proton beams post-analysis; (right) Spectra from the Matlab program obtained from the deconvolution of the assumed Maxwellian continuous spectrum (blue circles) of the protons for a 10 μm regular Cu flat foil (Shot 20537); the data is analyzed three times with different background subtraction and beam area selection, as compared to Figure 4-15, yielding different conversion efficiencies: (a) C.E. = 1.82 %; (b) C.E. = 3.06 %; (c) C.E. = 1.59 %.	113
Figure 4-17: (left) Principle of the photostimulation mechanism; (right) A schematic of what happens during the scanning process: the exposed IP is scanned with a focused laser beam, yielding a PSL to be released, which is collected into the photomultiplier (PMT) tube through the light collection guide, and finally converted into electric signals.	116
Figure 4-18: Calibration curve giving PSL/electron as a function of electron energy where the horizontal axis (energy in MeV) is displayed in (a) logarithmic scale and (b) in linear scale.....	119
Figure 4-19: Signal Intensity (SI) in a.u. as a function of time [minutes] after exposition of the IPs, at $t=0$, $SI=1$.	120
Figure 4-20: Example of how the detectors were placed on the magnetic tray during the August 2008 beamtime, and illustration of the bleeding phenomenon (in red).	121
Figure 4-21: Picture of the ion/electron/positron spectrometer attached to the target chamber by a bellow.	121
Figure 4-22: (top) Electron dispersion curves : the purple dispersion curve converts distance on the IP (bottom) to transform a distance on the IP into an electron energy in MeV, and the green curve gives the dE/dx in MeV/cm as a function of distance on the IP.	122
Figure 4-23: Example of an electron spectrum: T_1 is obtained using the red data points and T_2 using the orange data points; the signal past ~ 70 MeV corresponds to noise.	123
Figure 4-24: Spherically bent quartz Bragg crystal: (a) Simple illustration of the set-up of a crystal in the Rowland circle (diameter = $R = 150$ mm); also represented are the laser interacting with the target, the source aperture, the detector slit and the detector. (b) Illustration [180] containing the different variables: the different plans of focus, meridional and sagittal, are displayed; θ is the angle of incidence, p is the object distance and q is the image distance.....	126
Figure 4-25: (a-b) August 2008 experiments: (a) picture of the inside of the target chamber and (b) picture of the crystal and part of the crystal mount; (c) June 2009 experiments: integrated image over a shot.....	127
Figure 4-26: Setup for the transverse 2-D imager: the target is the source, the distance between the crystal and the source is $p \sim 78$ mm, and the distance between the source and the image is $q \sim 799$ mm. The crystal rotation is 1.3° , and the lateral shift is $\Delta y \sim 2$ cm.....	128

- Figure 4-27: Transition energy and wavelength for different ionization states of Cu $K\alpha$ [180]; the neutral state is referred to as cold. In red are the states that can be seen by the Cu $K\alpha$ imager.....129
- Figure 4-28: Spherically bent quartz crystal with pinhole, indicating the angles θ_{\min} and θ_{\max} which determine the spectral range of the crystal: (left) 3-D representation [176] and (right) 2-D representation..... 130
- Figure 5-1: All pictures are to scale (a-c) Cones with 30° opening angle; (a) Au cone, 1 mm long, 5 μm C fiber [45, 178, 179]; (b) Au cone, attached on a 300 μm by 300 μm planar foil [4]; (c) Al Cone with a 1 mm long, 40 μm Cu fiber [177]; (d) Cu Funnel cone (FC) [3, 180, 181]; (e) Au flat-top cone (FTC) [1]; (f) Cu FTC [2, 5].....131
- Figure 5-2: Schematic of PFI/IFI using an FTC as the focusing proton or ion beam target. 135
- Figure 5-3: Set-up of the March 2006 (18554-18584) and August 2006 (18953-19060) Trident beamtimes, where various gold FTCs (with different top and neck diameters) were shot. The proton beam emission is recorded in an RCF stack (blue); the grey layer corresponds to the CR39 detector, and the last layer (light green) to the Lanex regular phosphor screen. Laser parameters: ~ 20 J, ~ 600 fs, ~ 12.6 μm diameter focal spot ($\sim 45\%$), *P*-polarization, $\sim 1 \times 10^{19}$ W/cm². 136
- Figure 5-4: Pictures of Au FTCs: (a) shows a wafer of Au FTCs; (b) shows a side and top view of an FTC. θ_t represents the diameter of the top, and θ_n the outside diameter of the neck. The best performing cone was the one for which $\theta_t = 100$ μm and $\theta_n = 22$ μm , that is a Top/Neck ratio of ~ 4 ; (c) & (d) show color pictures of the FTCs, cut and mounted on a glass post; (e) shows a much larger FTC; (f) has the same characteristics as (e), but the top is only partial. 138
- Figure 5-5: Schematic representation of the profile of a [5 μm ; 10 μm] thick Au or Cu FTC target; (left) with dimensions and (right) showing the Si remains; the blue stands for SiO₂ and the purple for Si₃N₄..... 138
- Figure 5-6: Target holders: (left) Glass stalk, and (right) Ceramic holder..... 139
- Figure 5-7: Shot 18500; Au flat-foil target: 10 μm thick, 2 mm by 15 mm; RCF stack: 12.5 μm Al, 6 HD films, a 25 μm brass absorber spacer, 5 HD films, brass, 2 HD, brass, 2 HD, brass, 2 HD, brass, 2 HD, and 3 MD-55 [1]..... 140
- Figure 5-8: Shot 18582; FTC target: 100 μm top, 25 μm neck, 10 μm thick; laser well aligned laser down the throat; RCF stack: 25 μm Al, 5 HD, 9 MD, 7 HS, a piece of 1100 μm thick CR-39, 2 HS, and a piece of Lanex regular on the back [1]..... 141
- Figure 5-9: RIS beam reconstructions (*Christmas tree*) of (A) a gold 10 μm flat-foil target (shot 18500) and (B) a gold 10 μm FTC target (shot 18582). The number of protons is indicated by the color scale [1]. 142
- Figure 5-10: 3-D reconstruction of the proton beam emitted from the 10 μm gold flat-foil target (shot 18500)..... 142
- Figure 5-11: (top) Shot 19044; FTC target: 117 μm top, 39 μm neck, 10 μm thick; laser not well aligned down the throat; RCF stack: 25 μm Al, 15 HD, 5 MD; the *side beam* (right hand corner) is more energetic than the *top beam* (center); (bottom) To scale, a schematic representation of the experiment showing how the sidewall spray interacted with the RCF [1]..... 143

- Figure 5-12: Proton energy performance as a function of both the top diameter and the neck outside diameter. The proton energy considered here is the *top beam*, and not the *side beam*. The larger the circle is, the greater the proton energy. The yellow and the red circles represent aligned shots from the March and August 2006 campaigns respectively, and the light blue and dark blue circles represent the misaligned shots from the March and August campaign respectively. Inset (A): picture an FTC and a Football top (very close to a large diameter neck funnel).144
- Figure 5-13: For the aligned cases only: maximum proton energy obtained from the RCF stack as a function of the Top-to-Neck ratio of the Au FTC: the yellow squares represent the March data (the crossed yellow squares correspond to the FTCs that were shot at 22.5°) and the red squares the August data.....145
- Figure 5-14: Electron spectra (simulations) of an RMT, a flat-foil target, an aligned (black arrow), and a misaligned (red arrow) FTC target; 1.74×10^8 macroparticles are used in the simulation, and each macroparticle contains 315733 electrons [1].146
- Figure 5-15: Proton spectra of a flat foil (experiment, triangles) and a flat-top cone (2-D PICLS simulations, squares and experiment, circles); the empty triangles and the blue circles correspond to the spectra obtained from the data scanned using a flat-bed scanner, and the filled green triangles and the maroon circles correspond to the spectra obtained from the data scanned using a MicroD.....147
- Figure 5-16: 2-D PICLS Simulations of the total electric fields in the case of (left) the laser propagating on axis, focused on the flat top (offset of 0 μm) and (right) the laser offset by 18.6 μm transversely from the laser axis. The black arrows (left and right) point to the flat top. (right) The orange arrow points to the region of increased electric field amplitude on the cone upper sidewall, due to the increased sheath density [1].....148
- Figure 5-17: Set-up of the August 2008 (Shots 20534-20557) and September 2008 (Shots 20613-20621) Trident beamtimes, where various flat-foil targets (different materials and thicknesses) were shot. Laser parameters: ~ 80 J, ~ 600 fs, 22.5° incidence, ~ 7 μm focal spot (47 %), S-polarization, 1.5×10^{20} W/cm²; SpectroA is the electron spectrometer; (Inset) Integrated picture of a real shot (20551): in the center is the target mounted in a ceramic holder; on the right, the RCF stack and on the left a pinhole camera; from the top left corner, a tantalum shine-shield protecting the (Cu K α) IP from direct exposure. Photo credit: Joe Cowan & Kirk Flippo.151
- Figure 5-18: Set-up of the August 2008 (Shots 20509 – 20533) Trident beamtime, where various geometries of cone targets were shot (Snubbed nose, funnel, and flat-top cones). Laser parameters: ~ 80 J, ~ 600 fs, normal incidence (0°), ~ 7 μm focal spot (47 %), S-polarization, 1.5×10^{20} W/cm²; SpectroA is the electron spectrometer; (Inset) Integrated picture of a real shot (20530): in the center is the target mounted on a glass stalk; on the right, the RCF stack and on the left a pinhole camera; from the top left corner, a tantalum shine-shield protecting the (Cu K α) IP from direct exposure. Photo credit: Joe Cowan & Kirk Flippo.152

Figure 5-19: All targets are represented on the same scale; (a-c) Funnel cones: Side views; (d) flat-top cone; (d-1) Side view; (d-2) Top view.....154

Figure 5-20: Maximum proton energy (MeV) for all the targets shot during the August 2008 beamtime; all targets were $\sim 10 \mu\text{m}$ thick, with the exception of the flat foils: the Cu flats ranged from $1 \mu\text{m}$ to $150 \mu\text{m}$, and the Ni flat was $0.5 \mu\text{m}$; the Ti-Cu-Ti F/Flat target (pink square, blue border) corresponds to a funnel cone which was shot away from the cone neck, similar to a flat foil; the Ti-Cu-Ti F/Hole target (blue diamond) corresponds to a funnel cone whose tip was missing.....157

Figure 5-21: (left, top) Proton energy (MeV) (right, top) Conversion Efficiency (%) as a function of target thickness (μm) in the intrinsic contrast case; (red diamonds and blue triangles) respectively flat-foil targets and RMTs shot in August 2008 using a clean OAP; (yellow diamonds) flat foils shot in September 2008 using a damaged OAP. The horizontal dashed green line shows the maximum proton energy of 58 MeV obtained with 450 J on the Nova PW laser; (bottom) Reproduction of Figure 5-22 (LULI and Callisto data), for comparison with the Trident data.158

Figure 5-23: RCF stacks for Cu flat-foil targets: (a) Shot 20534, $10 \mu\text{m}$ thick; (b) Shot 20549, $1 \mu\text{m}$ thick.159

Figure 5-24: RCF stacks for Cu flat-foil targets: (a) Shot 20613, $2 \mu\text{m}$ thick; (b) Shot 20615, $1 \mu\text{m}$ thick.160

Figure 5-25: Shot 20552: RMT Cu, $300 \mu\text{m}$ diameter; maximum proton energy of 32.2 MeV; the Cu $K\alpha$ 2-D transverse image (at $\sim 22.5^\circ$) shows the emission from the entire target.....161

Figure 5-26: Snubbed noses: (left) Shot 20526, maximum proton energy of 28.1 MeV; (right) Shot 20528, maximum proton energy of 41.7 MeV.....162

Figure 5-27: Shots 20518 (laser well aligned down the throat) and 20521 (laser misaligned and shooting to the side), funnel cones: pictures of the targets, Cu $K\alpha$ images and RCF stacks.....163

Figure 5-28: Shot 20515, funnel cone, laser misaligned, $E_{\text{max}_p+}(\text{side}) > E_{\text{max}_p+}(\text{normal})$, with what would appear to be a monoenergetic feature between RCF layer 8 and layer 9 (since the central beam in detector 8 is much weaker than the side beam, while the central beam of detector 9 is as strong as the side beam); note that the second square corresponds to the first detector, while the first square corresponds to the Aluminum foil protecting the stack.....164

Figure 5-29: Shot 20512, funnel cone, laser aligned, neck so small (i.e. $\sim 16 \mu\text{m}$), and/or so long, that there is no *top beam* emission, and only *side beam* emission.....165

Figure 5-30: Shot 20513, funnel cone, laser aligned, top proton beam with maximum energy $\sim 47 \text{ MeV}$166

Figure 5-31: Shot 20509, funnel cone, laser aligned, largest neck available (i.e. $\sim 39 \mu\text{m}$).166

Figure 5-32: (left) Funnel Cones and (right) Flat-Top Cones; in red the aligned cases, in blue the misaligned cases. From 0.1 to 3 on the vertical axis: Ratio of $E_{\text{max}_p+}(\text{top beam})/E_{\text{max}_p+}(\text{side beam})$ as a function of neck outer diameter [μm]. From 5

to 100 on the vertical axis: Maximum proton energy [MeV] of the <i>top beam</i> as a function of neck outer diameter [μm].....	167
Figure 5-33: Shots 20530 and 20532, laser well aligned down the throat, flat-top cones: pictures of the targets, Cu $K\alpha$ images and RCF stacks.....	168
Figure 5-34: Shot 20516, funnel cone, laser apparently aligned, absence of top proton beam in layers 5-8, and inversion of the proton emission between layer 8 and layer 9.	169
Figure 5-35: Shot 20528, snubbed nose cone, laser well aligned, inversion of the proton emission between layer 15 and layer 16.....	169
Figure 5-36: Shot 20520, FTC, laser well aligned, inversion of the proton beam emission from layer 7 to layer 8.	170
Figure 5-37: Funnel-cone, flat-top-cone and reduced-mass targets: Electron temperature as a function of the proton energy, with trendlines; (left) Lower electron temperature T_1 ; (right) Average of the lower and higher temperatures $(T_1+T_2)/2$	172
Figure 5-38: Flat-foil targets and reduced-mass targets: Electron temperature as a function of proton energy; (left) Lower electron temperature T_1 ; (right) Average of the lower and higher temperatures $(T_1+T_2)/2$. The trendlines do not include the RMT shot because its temperature T_1 is very different than the other temperatures at similar proton energies: RMTs are supposed to behave differently than regular large flat-foil targets, and to have a higher electron temperature.....	172
Figure 5-39: (left) Funnel-cone, flat-top-cone and reduced-mass targets, (right) Flat-foil and reduced-mass targets. As a function of laser intensity [W/cm^2], (top) lower electron temperature T_1 , (bottom) average of the lower and higher temperatures $(T_1+T_2)/2$	173
Figure 5-40: (left) Funnel-cone, flat-top-cone and reduced-mass targets, (right) Flat-foil and reduced-mass targets: Proton energy [MeV] as a function of laser intensity [W/cm^2].....	174
Figure 5-41: Set-up of the June 2009 beamtime (Shots 21145-21197), where Cu FTC targets (with different top and neck diameters), Cu funnel-cone targets, as well as small flat-foil targets and RMTs, were shot. Laser parameters: ~ 80 J, ~ 600 fs, normal incidence, ~ 7 μm focal spot (33 %), S-polarization, $\sim 1.5 \times 10^{20}$ W/cm^2	175
Figure 5-42: Integrated picture of a real shot (21180): in the center is the target mounted on a glass stalk; on the right, the RCF stack; on the bottom a pinhole camera; from the left corner, a large aluminum shine-shield protecting the (Cu $K\alpha$) IP from direct exposure. Photo credit: Joe Cowan & Kirk Flippo.....	177
Figure 5-43: Set of different Cu FTC targets, of different top and neck sizes (to scale).....	177
Figure 5-44: To-scale microscope pictures of RMTs, which are the tops of the FTCs: these targets show the Si side and the Cu side – the diameter of the Si area corresponds to the inner neck diameter of the FTC, whose top broke off: (a) 230 μm diameter, shot 21166, 77.8 J; (b) 270 μm diameter, shot 21156, 96.5 J; (c) 400 μm diameter, shot 21168, 76.3 J; (d) 190 μm diameter, shot 21148, 78 J,	

structured top broken off from the new generation of FTCs described in Section 7.4.....179

Figure 5-45: (left) Proton energy [MeV] (right) Conversion Efficiency [%] as a function of target thickness (μm) of regular flat foils; Red diamonds: August 2008, intrinsic contrast; Green diamonds, August 2008, enhanced contrast; Blue diamonds (note that in the conversion efficiency case, the single diamond represents both cases), June 2009, enhanced contrast..... 181

Figure 5-46: Comparison of the funnel cones (shots 20518 and 21194) and the flat-top cones (shots 20530 and 21184) at intrinsic contrast (shots 20518 and 20530) and enhanced contrast (21194 and 21184); during the experiments at intrinsic contrast, the spatial resolution was $\sim 5 \mu\text{m}$, while during the experiments at enhanced contrast, it was less, i.e. $\sim 10 \mu\text{m}$ 182

Figure 5-47: Integrated averaged lineouts taken around a similar funnel-cone target area for both the intrinsic contrast case (shot 20518) and the enhanced contrast case (shot 21194): PSL value as a function of distance in μm across the funnel cone. 183

Figure 5-48: Definition of the various Cu $K\alpha$ emission zones; (a) Picture of an FTC target – the red arrow shows where the laser is focusing; (b) Cu $K\alpha$ image; since all the targets have different sizes, the height of the box is chosen to be 0.25 times larger than the top diameter (green arrow); (c) Integrated and averaged lineout across the Cu $K\alpha$ image, showing 3 distinctive bumps, referred to as top emission (TE) bump, cone wall emission (CWE) bump, and supporting foil emission (SFE) bump..... 185

Figure 5-49: Maximum proton energy as a function of Cu $K\alpha$ yield fraction in the top versus in the cone walls and in the supporting foil; for each group (i.e. Cu $K\alpha$ (top) ~ 0.25 , ~ 0.5 and ~ 0.75), the averaged value is represented (grey diamond) as well as the maximum and minimum values (grey error bars); in the case where some shots should have performed better, but did not for an understandable reason (i.e. green, blue and orange diamonds), they are isolated within the larger group, and their average as well as maximum and minimum values are also given (light blue error bars); note that the shot indicated by the red diamond (whose performance is low for a less obvious reason than the shots represented by the orange, blue and green diamonds) is included in the group of best performers, bringing the maximum proton energy average down. The horizontal black line at $\sim 50 \text{ MeV}$ represents the average of the flat-foil target results, while that at 58 MeV represents the previous Nova PW record [6]. 187

Figure 5-50: CWE \gg TE or SFE \gg TE and TE ~ 0 ; Shots 21182 and 21208; Cu $K\alpha$ images and integrated averaged lineouts. 189

Figure 5-51: TE \gg CWE or TE \gg SFE and TE ~ 0 ; Shots 21164, 21165, 21187, 21207, and 21208; Cu $K\alpha$ images and integrated averaged lineouts..... 190

Figure 5-52: TE \sim CWE; Shots 21170, 21171, 21180, 21181, 21195, and 21174; Cu $K\alpha$ images and integrated averaged lineouts..... 192

Figure 5-53: TE \sim CWE; Shots that did not perform so well for understandable reasons: 21169, 21184, and 21192; Cu $K\alpha$ images and integrated averaged lineouts..... 194

Figure 5-54: Comparison between shot 21171 and shot 21192; Cu K α images and integrated averaged lineouts.196

Figure 5-55: PSL value as a function of distance for all the shots with the smallest necks: 21182 (12 μ m), 21169 (11 μ m), 21164 (15 μ m), and 21208 (15 μ m).196

Figure 5-56: Correlation between proton energies and RMT area: Maximum proton energy as a function of (left) target area and (right) target volume for the best performing RMTs (black squares) and regular flat-foil targets (white squares).198

Figure 5-57: Correlation between proton energies and supporting foil size of an FTC target: Maximum proton energy as a function of (left) target area and (right) target volume for the best performing FTC targets (diamonds), i.e. for the case where TE \gg CWE; the blue diamond corresponds to shot 21192 (small supporting foil); the red diamond corresponds to shot 21174 (slightly smaller CWE/TE than the others); the green diamond corresponds to shot 21169 (presence of SFE); and the orange diamond corresponds to shot 21184 (low laser energy).198

Figure 5-58: Funnel-cone targets, flat-top-cone targets, and reduced-mass targets: Electron temperatures at enhanced contrast as a function of the proton energy; (left) Lower electron temperature T₁; (right) Average of the lower and higher temperatures (T₁+T₂)/2; The trendline does not include the purple data point (shot 21171).200

Figure 5-59: Flat-foil targets and reduced-mass targets: Electron temperatures at enhanced contrast as a function of the proton energy; (left) Lower electron temperature T₁; (right) Average of the lower and higher temperatures (T₁+T₂)/2. The 3 OPCPA shots obtained in 2008 at enhanced contrast are included. Only 2 shots out of 3 have a T₂, due to bleeding in the last case.201

Figure 5-60: Reproduction of Figure 5-59; added to the data are the cases of the FTCs for which almost no CWE was seen, but a lot of TE (TE \gg CWE). This data seems to fit well with that of the flat-foil targets and reduced-mass targets.201

Figure 6-1: Flat-foil targets and RMTs: summary of the electron temperatures as a function of the proton energy, with trendlines for the intrinsic contrast case (left) and the enhanced contrast case (right); (top) Lower electron temperature T₁; (bottom) Average of the lower and higher temperatures (T₁+T₂)/2.206

Figure 6-2: Cone targets (flat-top cones, funnel cones and snubbed-nose cones): summary of the electron temperatures as a function of the proton energy, with trendlines for the intrinsic contrast case (left) and the enhanced contrast case (right); (top) Lower electron temperature T₁; (bottom) Average of the lower and higher temperatures (T₁+T₂)/2.207

Figure 6-3: Reproduction of Figure 5-12: Proton energy performance as a function of both the top diameter and the neck outside diameter. The larger the circle is, the greater the proton energy. The yellow and the red circles represent aligned shots from the March and August 2006 campaigns respectively, and the light blue and dark blue circles represent the misaligned shots from the March and August campaign respectively. Inset (A): picture an FTC and a Football top (very close to a large diameter neck funnel cone).209

Figure 6-4: Shot 21170, Proton energy: 66.7 MeV, Conversion efficiency: 1.87 %; (top) Cu K α image and RCF stack (the last row of RCFs is contrast-enhanced to see the end of the beam more clearly); (bottom) Proton spectrum.210

Figure 6-5: Shot 21180, Proton energy: 67.5 MeV, Conversion efficiency: 2.06 %; (top) Cu K α image and RCF stack (the last row of RCFs is contrast-enhanced to see the end of the beam more clearly); (bottom) Proton spectrum.211

Figure 6-6: Asymmetric laser-FTC interaction for the case where (left) $TE \gg CWE$ and the case where (right) $TE \sim CWE$212

Figure 6-7: Comparison between the case of a *P*-polarized and an *S*-polarized laser, as it interacts with an FTC (mounted on a stalk) at normal and a slight angle (in the plane of the page) of incidence. In both cases, i.e. the *P*-polarization, 20 J case and in the *S*-polarization 80 J case, the *k* vector is always collinear to the plane of the ground. The picture on the left hand-side of each case corresponds to the nominal case where the stalk is perpendicular to the ground plane and to the *k* vector. The picture on the right-hand side of each case represents, in the frame of the target, the case where the stalk and the target are tilted with respect to the ground plane and to the *k* vector, in such a way that the laser is at an angle with respect to the flat top of the target, creating a case that is similar to a combination of both a *P*-polarization and an *S*-polarization. This mixture of polarizations only matters for small inner-neck diameters, while it does not for the wide necks, because for wide necks, the E-field vector cannot reach the upper portion of the neck.213

Figure 6-8: PICLS simulation: Comparison between the case where the laser is incident at an angle (orange) and horizontally (blue), but always makes it to the top. The electron and proton spectra obtained 213 and 640 fs after the peak of the interaction, and the electron and proton densities obtained 320 fs after the peak of the interaction are given.216

Figure 6-9: PICLS simulations of a cone target for different offsets for the time-step 11; (left) electron energy density; (right) electric field amplitude $(E_x^2 + E_y^2)^{1/2}$219

Figure 6-10: PICLS simulations of a flat target, i.e. of the flat-top of an FTC target, without the cone; electric field amplitude $(E_x^2 + E_y^2)^{1/2}$220

Figure 6-11: As a function of laser offset in the throat [μm] ~ 1.1 ps after the laser hits the targets, (a) Maximum proton (blue) and C^{6+} energy (green); (b) Laser-Proton (blue, left vertical axis) and Laser-Electron (purple, right vertical axis) conversion efficiencies; for (a) and (b), the horizontal lines represent the RMT comparison, i.e. the flat-top of the FTC without the cone.221

Figure 6-12: Field strengths as a function of offset in the throat [μm]: G_{mns} (red) is the electron energy density, E_y (light green) is the electric field in the vertical direction, E (turquoise) is the electric field amplitude $(E_x^2 + E_y^2)^{1/2}$ and B_z (orange) is the magnetic field perpendicular to the simulation plane; G_{mns} , E_y , E and B_z are normalized and compared to the normalized laser potential a_L (grey horizontal line); (a) at time-step 8 and (b) at time step 11; the data given to the left of the vertical axis (corresponds to the flat-top case, without cone (i.e. RMT).222

Figure 6-13: Electron spectra (left) of the RMT (diamonds), and (right) of the FTC target with 15 μm offset (squares), for different time-steps: time-step 8, dark blue; time-step 9, green; time-step 10, orange; time-step 11, red.223

Figure 6-14: Electron spectra at t_8 of the RMT (black), the 30 μm neck FTC target without offset (green) and with 15 μm offset (red), and the 1 μm FTC (without offset, blue).224

Figure 6-15: PICLS simulation, 140 fs after the laser hits the flat top (t_6) for the 15 μm offset case (the laser is grazing the cone wall horizontally), showing (top) B_z , (middle) E and (bottom) current density (color scale is in log-scale).225

Figure 7-1: (left) Schematics of the foil-induced micro-focusing of the laser (red) accelerated proton beam (blue). The foil's grooved rear surface and the proton acceleration induced by the TNSA mechanism cause the micro-focusing of the protons when the acceleration starts. The separation of the beamlets can be seen in the RCF detectors as density modulations of the proton distribution. (right) Example of an interferometry image of the rear side of a micro-structured gold foil: sine structure with a $\sim 10 \mu\text{m}$ period and $\sim 1 \mu\text{m}$ amplitude.237

Figure 7-2: Mold of structured tops FTC targets.238

Figure 7-3: Cu targets made from the Si mold; FTC target g3, shot 21185.238

Figure 9-1: (left) Diagram showing the different states of matter (solid, liquid, gas, and plasma) when the enthalpy of the system goes up; (middle) Illustration of the different states of matter for the example of water; (right) Diagram of the different kinds of plasmas as a function of temperature (in K) and number density (in #charged particles per m^3).243

Figure 9-2: Picture of tunneling or barrier-suppression by a strong external electric field [187, page 21].256

Figure 9-3: Relativistic self-focusing [200].259

Figure 9-4: Phase matching conditions for Stimulated Raman Forward Scattering and Stimulated Raman Backward Scattering [187, page 86].262

Figure 9-5: Schematic of the plasma-based accelerators [216] – the pulses are moving to the right: (a) LWFA (or PWFA) in which a short $L \sim \lambda_p$ laser pulse (or electron beam) drives a plasma wave (dashed curve); (b) PBWA in which two long pulse ($L > \lambda_p$) lasers with frequencies $\omega_1 - \omega_2 \sim \omega_p$ resonantly drive a plasma wave; (c) RLPA in which a train of short laser pulses resonantly drives a plasma wave; (d) SMLWFA in which an initially long pulse (dashed curve) breaks up into a series of short pulses and resonantly drives a plasma wave.263

Figure 9-6: Schematic of a temporal profile steepening of the laser envelope [200].266

Figure 9-7: Geometry of a plane-wave, incident on a plasma density profile for both P -polarized (i.e. the E -field is in the plane of ∇n_e) and S -polarized light (i.e. the E -field is in the vertical (z) direction). When the plane wave is S -polarized, no resonance happens [187, page 135].271

Figure 9-8: Angular absorption dependence for *S*-polarized and *P*-polarized light and for various density scale-lengths: $L/\lambda=1$ (continuous line), $L/\lambda=0.1$ (dashed line), and $L/\lambda=0.01$ (dotted line) [187, page 138].273

Figure 9-9: Diagram of the resonant absorption process: a *P*-polarized laser wave propagating at oblique incidence into a monotonically increasing inhomogeneous plasma, showing that the effective critical surface is reduced by a factor $\cos^2\theta$; the E_x field can tunnel to n_c [11].276

Figure 9-10: Brunel absorption process; the incident laser field E_L corresponds to E_{xy} . [11].281

Figure 9-11: Percentage of absorption as a function of laser intensity for the Brunel heating case (left) for $\theta = 45^\circ$ [187, Figure 5-14, pages 161-162] (right) for $\theta = 30^\circ, 45^\circ$, and 60° [229].283

Figure 9-12: $J \times B$ heating mechanism [11].285

LIST OF TABLES

Table 1: Proton beam and laser requirements for PFI: (1 st column) An estimation of the requirements for an ideal (narrow energy range) proton beam, to ignite the fuel that compresses to a density of 400 g/cm ³ , is given in [15]: 7-10 kJ of 15-23 MeV protons (the required number of protons is therefore $n_p \sim [2-4] \times 10^{15}$), reaching the fuel in a 15-20 ps pulse and focused onto a 15 μm spot. Since then, there have been many more studies on proton beam requirements for fast ignition. (2 nd column) In [16], it is shown that, to relax the ignition requirements on the proton beam, the distance D between the proton source and the compressed fuel should be decreased (requiring some important target design and improvements): simulations show that, while keeping the gain constant, one can go from 26 kJ, 3 MeV, D = 4 mm down to 12 kJ, 5 MeV and D = 500 μm . (3 rd column) In a newer study [48], two proton beams are used with two targets, one at 500 μm , and one further away (at ~ 2 mm). The first beam, a Gaussian profile at 12 MeV with a FWHM of 1 MeV, deposits ~ 1 kJ of energy, expanding the volume it entered, thereby creating a density channel for the second beam of similar energy and spread to propagate into the fuel and depositing 6 kJ of energy, sparking ignition. This scheme reduces the overall energy needed for PFI to 7 kJ of protons.....	16
Table 2: Summary of the intrinsic and enhanced contrast levels on Trident, pre- and post-enhancement.....	79
Table 3: Composition of the various RCF layers.....	95
Table 4: Structure, thicknesses, and tolerances of various RCFs (HS, DM1260, HD810, MD55-1, MD55-2, MD55, and MD55-V2).....	96
Table 5: Structure of the BAS-MS, BAS-SR, and BAS-TR IPs: different layers, layer material, densities, and thicknesses. The density is given within ± 1 % and thickness within ± 6 %.....	118
Table 6: Au FTC and flat foil comparison: Maximum proton energy, conversion efficiency obtained from a scanner and from a MicroD (white light).	140
Table 7: CWE \gg TE or SFE \gg TE and TE ~ 0 ; Shots 21182 and 21208; Values of proton energy, laser energy, laser pulse duration, top, cone wall, and supporting foil emission values (TE, CWE and SFE), ratio Maximum(SFE,CWE)/TE, and ratio TE/(SFE+CWE+TE).....	189
Table 8: TE \gg CWE or TE \gg SFE and TE ~ 0 ; Shots 21164, 21165, 21187, 21207, and 21208; Values of proton energy, laser energy, laser pulse duration, top, cone wall and supporting foil emission values (TE, CWE and SFE), ratio Maximum(SFE,CWE)/TE, and ratio TE/(SFE+CWE+TE).....	190
Table 9: Comparison between shot 21165 and shot 21207: L1 and L2 are the dimensions of the supporting foil, A the area of the supporting foil, V the volume of the supporting foil, T the FTC top diameter, N the FTC outer neck diameter, T/N the top-to-neck ratio, H the FTC height, p+ the maximum proton energy, TE and CWE the amount of top and cone wall emission (respectively), CWE/TE the ratio	

between CWE and TE, Area the area selected around the FTC, Mean the mean PSL value in that area, Min and Max the minimum and maximum PSL values in that area, Int. Density = Area \times Mean PSL value, and Background = Area \times Min PSL value.....191

Table 10: TE \sim CWE; Shots 21170, 21171, 21180, 21181, 21195, and 21174; Values of proton energy, laser energy, laser pulse duration, top, cone wall, and supporting foil emission values (TE, CWE and SFE), ratio Maximum(SFE,CWE)/TE, and ratio TE/(SFE+CWE+TE).....193

Table 11: Comparison between shot 21170 and shot 21174: L1 and L2 are the dimensions of the supporting foil, A the area of the supporting foil, V the volume of the supporting foil, T the FTC top diameter, N the FTC outer neck diameter, T/N the top-to-neck ratio, H the FTC height, p+ the maximum proton energy, TE and CWE the amount of top and cone wall emission (respectively), CWE/TE the ratio between CWE and TE, Area the area selected around the FTC, Mean the mean PSL value in that area, Min and Max the minimum and maximum PSL values in that area, Int. Density = Area \times Mean PSL value, and Background = Area \times Min PSL value.....194

Table 12: TE \sim CWE; Shots that did not perform so well for understandable reasons: 21169, 21184, and 21192; Values of proton energy, laser energy, laser pulse duration, top, cone wall and supporting foil emission values (TE, CWE and SFE), ratio Maximum(SFE,CWE)/TE, and ratio TE/(SFE+CWE+TE).....194

Table 13: Comparison between shot 21171 and shot 21192: L1 and L2 are the dimensions of the supporting foil, A the area of the supporting foil, V the volume of the supporting foil, T the FTC top diameter, N the FTC outer neck diameter, T/N the top-to-neck ratio, H the FTC height, p+ the maximum proton energy, TE and CWE the amount of top and cone wall emission (respectively), CWE/TE the ratio between CWE and TE, Area the area selected around the FTC, Mean the mean PSL value in that area, Min and Max the minimum and maximum PSL values in that area, Int. Density = Area \times Mean PSL value, and Background = Area \times Min PSL value.....195

Table 14: Summary for the best targets ($\sim 10 \mu\text{m}$ thick), represented to scale, of the maximum proton energies obtained for the 3 FTC campaigns on Trident: 2006, 2nd column; 2008, 3rd column; 2009, 4th and 5th columns.....203

Table 15: Summary for the best targets ($\sim 10 \mu\text{m}$ thick), represented to scale, of the laser-to-proton conversion efficiencies for the best targets obtained for the 3 FTC campaigns on Trident: 2006, 2nd column; 2008, 3rd column; 2009, 4th and 5th columns.....204

Table 16: Flat-foil targets and RMTs, enhanced and intrinsic contrast; trendline equations giving $T_1 = f(E_P)$, $(T_1+T_2)/2 = f(E_P)$, $E_P = f(T_1)$, $E_P = f((T_1+T_2)/2)$206

Table 17: Various cones (i.e. Funnel cones, FTCs, Snubbed noses), enhanced and intrinsic contrast; trendline equations giving $T_1 = f(E_P)$, $(T_1+T_2)/2 = f(E_P)$, $E_P = f(T_1)$, $E_P = f((T_1+T_2)/2)$207

Table 18: Summary of the total proton energy, conversion efficiency and maximum proton energy from PICLS simulations for the 1 μm neck FTC (no offset), for the 30 μm neck FTC with 15 μm offset and no offset, and for the RMT.....226

1 INTRODUCTION

Since the first short-pulse, high-energy laser-proton acceleration experiments in the 1999-2000 time frame [6, 7, 8], the maximum proton energy of ~ 58 MeV obtained at LLNL on the Nova PW laser with 450 J [6] had never been surpassed [9]. This dissertation reports on a new record in proton acceleration yielding up to 67.5 MeV, using the Los Alamos National Laboratory Trident laser system with merely 80 J, and cone-shaped targets [5]. This corresponds to a proton energy increase of ~ 116 % as compared to the Nova PW results, but more importantly, to a more efficient proton acceleration, since the laser-energy-to-maximum-proton-energy ratio of ~ 0.85 MeV/J is obtained with 5 times less laser energy, compared to ~ 0.13 MeV/J for the Nova PW results. Both the Trident result and the Nova PW result are comparable since they were both obtained using a similar laser technology (i.e. single shot glass lasers), at similar laser pulse durations (~ 500 fs) and intensities (i.e. $\sim 1.3 \times 10^{20}$ W/cm² and $\sim 2.6 \times 10^{20}$ W/cm² respectively).

MeV protons and ions can be accelerated via charge displacement (ambipolar fields) generated on the target by the ultra-high short-pulse laser. They are accelerated from both sides of the target [10, 11] in similar fashions, but the highest energy results obtained in [6, 7, 8] stem from the so-called Target Normal Sheath Acceleration (TNSA) mechanism [12] from the rear-side of the target. A positive characteristic of these laser-accelerated ion beams is that they are virtually charge neutral, which results in a very low emittance [13, 14]; however, prior to using charge neutral beam, the electrons would need to be stripped. Because these MeV ions (including protons) present a new compact ion source for many existing and novel exciting applications for physics research, medical purposes and ion fast ignition, the field of laser-ion acceleration has been very active.

For potential applications, the energy of the ion beam is important, but just as important is the laser-to-ion energy conversion efficiency. The initial short-pulse laser experiments observed mainly protons leaving the rear surface of flat-foil targets as a collimated beam [7, 8] with efficiencies greater than 1 %. In the case of the Nova PW, the reported efficiency is ~ 12 % [6]. This was never reproduced, and conflicting reports from the same group exist, claiming only 5 % [15, 16]. The Nova PW laser was disassembled shortly thereafter. Compared to the ~ 20 MeV protons obtained with the Trident laser pre-enhancement at 20 J, the enhanced Trident 200 TW laser at ~ 95 J showed an increase of 2.5 times to 50 MeV [17]. This value fits the predicted value based on a power-law extrapolated fit of the intensity for the Trident laser (see Figure 2-24 in Section 2.3.4.2.1, i.e. $E_{\max_p+} \propto I^{0.56492}$). However, the laser-to-proton conversion efficiency was improved to around 4.5 % from less than 1 % [17].

The medical applications and requirements, as well as some background on fast ignition, and other potential uses, are presented in more detail in Section 1.1. This is followed by a general outline of the dissertation in Section 1.2.

1.1 Motivation and possible applications

The proton beam requirements are dependent on the application: in this section, medical applications [1.1.1] and fast ignition [1.1.2] using protons and heavier ions are discussed. For medical applications, the important parameter is the maximum proton cut-off energy, which has to be made as high as possible; conversion efficiency is not as crucial. On the other hand, for proton fast ignition, the main requirement is the laser-to-proton conversion efficiency, while a very high proton energy is not required.

1.1.1 Medical applications

This section discusses the advantages of hadron-therapy compared to x-ray radiation therapy, as well as the feasibility of using laser-accelerated ion beams instead of conventional accelerators (see [18], [19], and [20]).

Hadron-therapy is a collective term used to describe oncological radiotherapy which utilizes fast non-elementary particles made of quarks. Protons, neutrons, and the nuclei they comprise are the hadrons used to locally control many types of tumors. Proton therapy is an effective treatment against cancers located in areas which are inaccessible to the surgeon's instruments, or which are hard to treat by current gamma or electron radiotherapy. This is the case for brain tumors, and for areas close to the spinal cord, or inside the eye. In 1946, Robert Wilson published [21] the physical advantages of ion beams for therapy. While at that time, the medical community showed no particular enthusiasm, today proton- and carbon- tumor therapy centers are becoming more and more common, with 5 proton therapy centers in use in North America, and 8 under construction; in Europe, 7 and 5 respectively; and in Asia, 8 and 3 respectively. Currently, more than 450 patients have been treated with carbon ions at GSI, Germany [22], 2000 at NIRS, Japan [23] and 10000 with protons at the Loma Linda University Medical Center in the US [24].

As illustrated in Figure 1-1 [25], the main difference between X-rays and ions is their different depth-dose distribution, yielding a different biological action. For X-rays, the dose decreases exponentially for larger penetration depths. Therefore, deep-seated tumors need to be irradiated from many directions in order to distribute the non-wanted dose in front of the tumor over a large volume, so that the healthy tissues are not exposed to a lot of radiation, possibly inducing secondary tumors when delivering a lethal dose to the primary tumor. In contrast to X-rays, hadron beams [26, 27] have little scattering (diffusion) when

penetrating into bodily tissues and deliver the highest dose near the end of their range (Bragg peak); this way, severe damage to the cancerous cells can be caused, while sparing the traversed healthy tissues, as well as deeper tissues, since they receive very little dose. Since these ion beams are charged (unlike X-rays, gammas, and neutrons), and are heavy (compared to electrons), they allow for higher accuracy (2-3 mm for deep-seated tumors) because they can easily be formed as narrowly focused and scanned pencil beams of variable penetration depth. Carbon ions, compared to protons, have a higher atomic number, and therefore, a much smaller lateral and range scattering. One of the major advantages of heavy-ion tumor therapy over proton therapy is the increase in relative biological effectiveness (dose) of particle beams, in particular at the end of their penetration depth, i.e. in the tumor volume. In general, ions are better for radio-resistant tumors, while protons minimize the risk of appearance of secondary tumors.

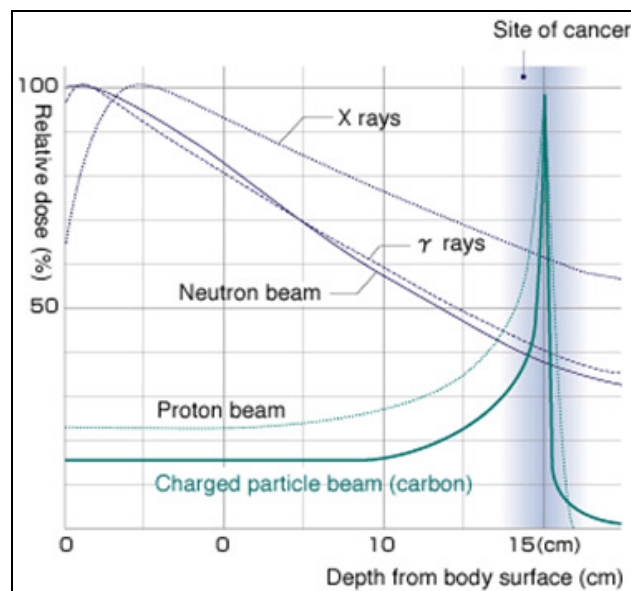


Figure 1-1: Distribution of the relative depth dose [%] in body tissue for various types of radiation [25]: X-rays, γ -rays, neutrons, protons, and carbon ions. Compared to other radiation, protons, and especially ions, have a peaked profile which allows for a greater tumor dose and lower dose into the surrounding healthy tissues, which is an ideal tool for deep-seated tumors. Changing the ion energy simply shifts the position of the energy deposition in depth.

1.1.1.1 Can laser accelerated protons and heavy ions meet the requirements necessary for therapy?

It has been suggested that laser-accelerated ion beams could potentially be utilized in hadron-therapy [20, 28, 29, 30, 31]. The laser technology will be able to replace conventional accelerators as an effective tool in ion beam therapy (IBT) when the beam-delivery systems meet the requirements of the present day IBT configurations. Shown in Figure 1-2 are the different blocks required in a laser-driven hadron-therapy system. The main and most important issue is to be able to maximize the proton energy [1.1.1.1.1]. The dose [1.1.1.1.2], the energy spread [1.1.1.1.3], and the beam focusing and separation [1.1.1.1.4] only require more development.

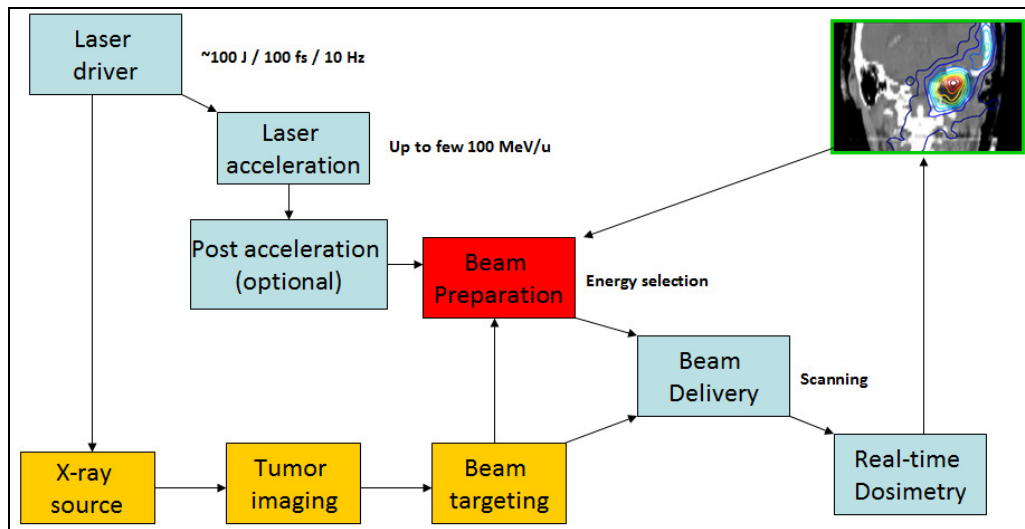


Figure 1-2: System considerations for a laser-based hadron-therapy machine (Diagram by Thomas Cowan).

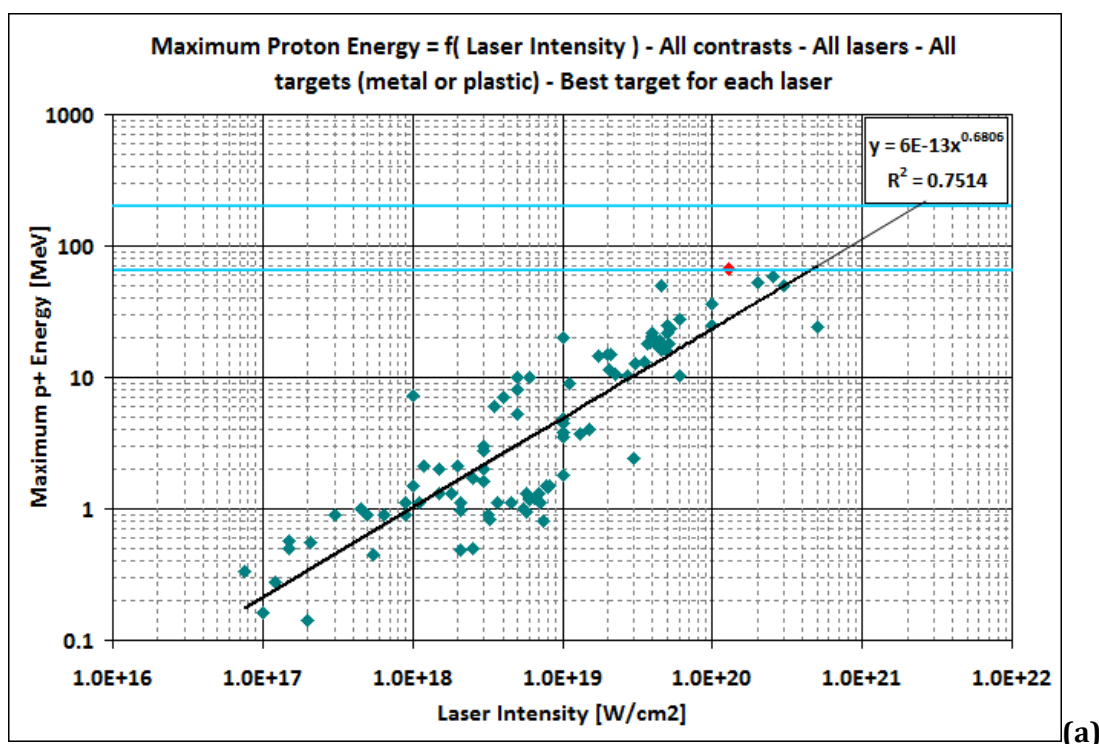
1.1.1.1.1 Ion energy requirements

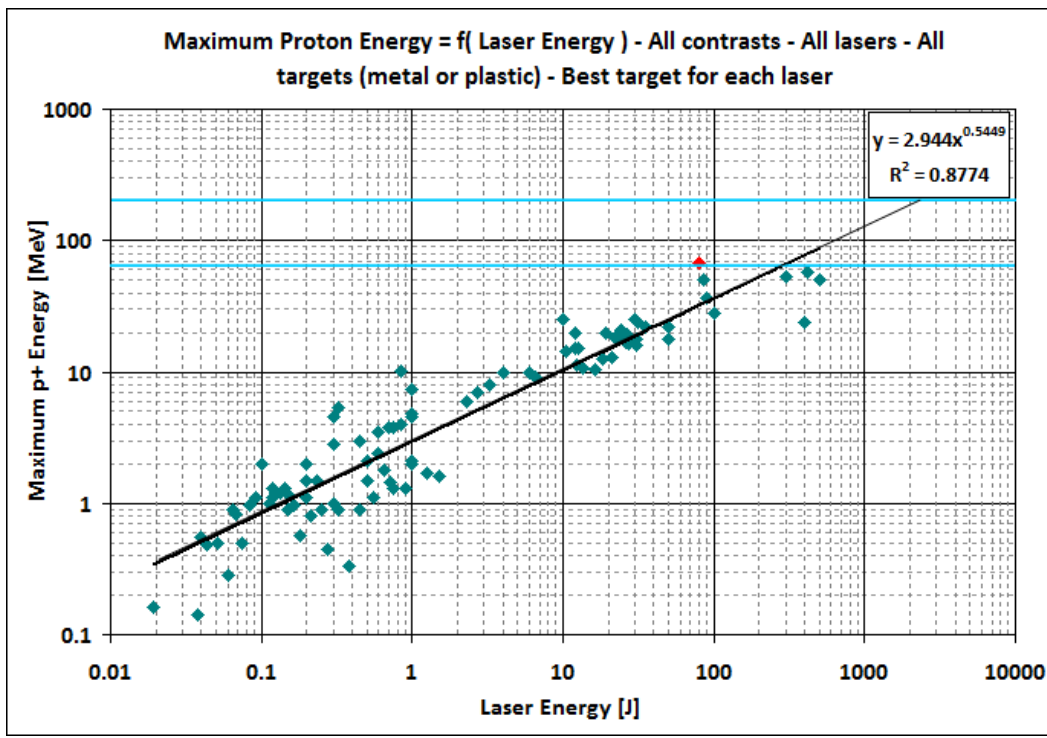
The key issue to a laser-based hadron-therapy system is the maximum proton or ion energy. The goal of the work presented in this dissertation is to find ways to increase the maximum proton energy, which had been stuck for almost a decade at 58 MeV. In this dissertation, it

is shown that using a particular type of target (i.e. a flat-top cone, or FTC target), the energy of the proton beam can indeed be enhanced.

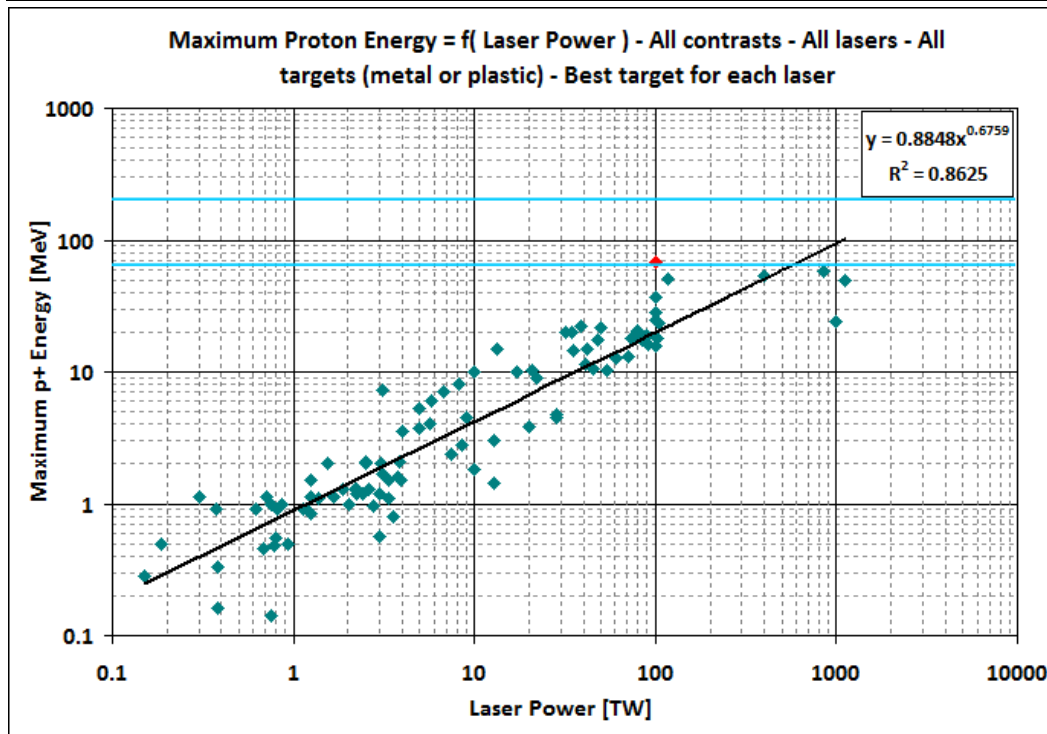
In order to reach soft tissues more than 25 cm deep – necessary to treat *deep-seated tumors* – proton and carbon ion beams must have an initial energy greater than ~ 200 MeV and ~ 4,500 MeV respectively (i.e. ~ 375 MeV/nucleon).

For ocular melanoma, as well as for the treatment of macular degeneration, protons of energies in the range 60–70 MeV are enough.





(b)



(c)

Figure 1-3: Maximum proton energy [MeV] as a function of (a) laser intensity [W/cm²], (b) laser energy [J] and (c) laser power [TW], for all laser energies, pulse durations, laser intensities, and all targets (CH and metal), showing the best shots for a particular experiment on a given laser. In light blue (horizontal lines) are the low and high levels of the therapeutic window, and in red (diamond), the latest world record of 67.5 MeV obtained on Trident at 80 J using a flat-top cone target.

With the new record of laser-proton acceleration near 70 MeV (Figure 1-3, red dot) obtained within the realm of this dissertation with a laser energy of ~ 80 J, a laser power of ~ 100 TW and a laser intensity of $\sim 1.3 \times 10^{20}$ W/cm², medical applications using protons seem much less out of reach, as we begin to enter the therapeutic window (60 – 200 MeV). From Figure 1-3, it seems that the laser characteristics (energy, intensity and power) required for medical treatment are closer to being realized, now that we know that the 60 MeV empirical barrier [9] can be broken at “modest” laser intensities. The equations for the fits of Figure 1-3, giving the maximum proton energy as a function of laser energy, power and intensity, as well as the R^2 factor, are given by:

$$\left\{ \begin{array}{l} E_{\max_p+} = 2.944 \times E_L^{0.5449} \\ E_{\max_p+} = 0.8848 \times P^{0.6759} \\ E_{\max_p+} = 6 \times 10^{-13} \times I^{0.6806} \end{array} \right. \text{ and } \left\{ \begin{array}{l} R^2 = 0.8774 \\ R^2 = 0.8625 \\ R^2 = 0.7514 \end{array} \right.$$

Note that the laser energy or the laser power correlate better with proton energy than laser intensity does. Later in this dissertation (see Section 2.3.4) the reason why that is true is discussed, as well as more (to be published) proton energy scalings for the Trident laser.

1.1.1.1.2 Dose requirements

A typical treatment session consists of delivering 2-2.5 *Gray* (Gy) to the tumor target, while delivering less than 1-1.2 Gy to any of the organs at risk, where 1 Gy = 1 J/kg (the SI unit of absorbed dose). A typical treatment plan lasts about 30 sessions, over 6 weeks, and the total dose delivered to the tumor target is 60-75 Gy. To do so, one would need 10^9 – 10^{10} ions per session, delivered in a few minutes. For laser-produced proton beams, a typical Maxwellian proton spectrum (as shown in Figure 4-15, Figure 4-16, Figure 6-4 and Figure 6-5) contains $\sim 10^{13}$ protons in average (over all energies), which is enough. To further increase the proton number, one can always use a repetition-rated laser system at 10 Hz.

But what is critical is to be able to achieve the high proton energies described in Section 1.1.1.1.1 at a high enough pulse repetition rate for a therapy application (at least greater than several pulses per second), in contrast to the once-per-hour shot rate of the current state-of-the-art Petawatt lasers.

1.1.1.1.3 Required energy spread $\Delta E/E$

While for certain cancer therapies, a small energy spread ($\sim 1-5\%$) would be beneficial, other cancer therapies do not require such a small energy spread. In the latter case, the desired radiation dose should have a broad, flat peak, where the flat section corresponds to the extent of the tumor being treated (see Figure 1-4).

Normally, the radiation is naturally deposited in narrow Bragg peak (see Figure 1-1). To deliver the dosage in a broad, flat distribution, i.e. to shape the proton spectrum, one needs to use the spread-out Bragg peak technique (SOBP). The SOPB can be generated by adding the Bragg peak of successively lower energies and intensities. This technique is also called *passive spreading* technique, or technique of *double scattering*: the protons are diffused by the first *scatterer* and their energy is adapted to the distal form of the tumor by using appropriate absorbers; the transverse form of the irradiation field is defined by collimators [32]. In that case, the requirements for laser-accelerated ion reproducibility and energy resolution are significantly relaxed, and such a technique is well adapted to the TNSA properties.

Ideally, however, the dose should only be deposited inside the target volume. To minimize the dose burden outside the target, and to increase the dose given to the target, one should use the *active spreading* technique, which is based on beam energy and beam intensity variation within the treatment time [32]. In this technique, the proton beam is applied to the patient from many directions using a proton rotating gantry. During the treatment, one

changes the energy of the beam and, with magnets placed upstream, its direction, all at the same time. Two strategies of active magnetic beam scanning are used: the raster scan and the spot scan.

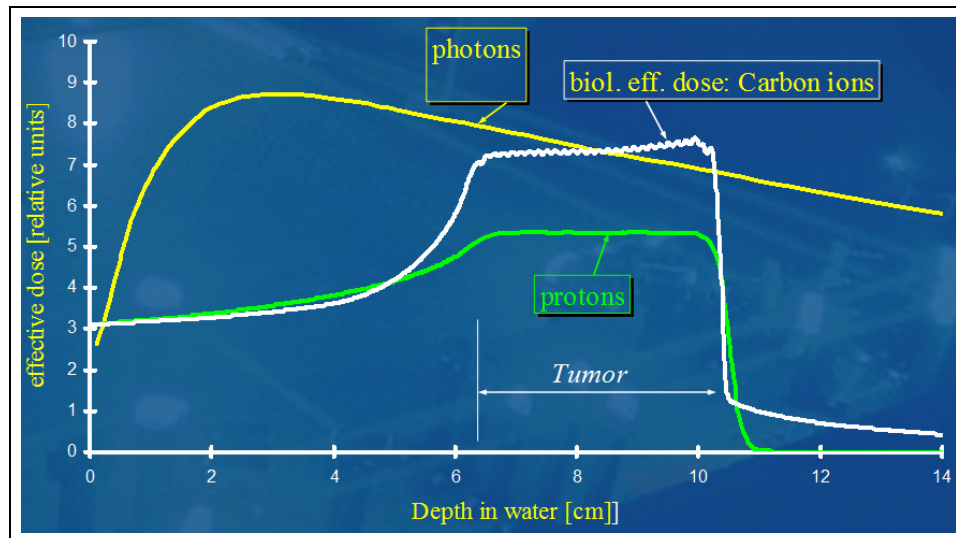


Figure 1-4: Effective dose as a function of tissue equivalent material; to treat a tumor of a few centimeters in size, the deposition should be distributed evenly over a broad depth.

1.1.1.1.4 Beam handling and focusing

Ion beam handling and focusing is still expensive and difficult. In conventional accelerators, very large and expensive structures made up of heavy magnets for beam deflection, weighing from 100 to 200 tons, with diameters from 4 to 10 meters, which would hardly fit within a hospital, are used to transport proton beams from the final section of the accelerator to the patient's tumor.

Petawatt-class lasers are not necessarily much smaller, but since getting photons to the targets (which are just a few millimeters in size) used for proton acceleration is simple, as only optics are required for laser beam transport, compared to heavy and costly magnets, it has been suggested that placing the target as close as possible to the patient could reduce the size and cost of such a facility by a large margin. However, one needs to eliminate all the

other particles and deliver only the protons to the patient. With the current state of laser-ion acceleration being what it is, particle selection and focusing systems [33] will be necessary after the target. Successful short-pulse laser ion focusing experiments have been carried out using ballistic focusing [60], electrostatic micro-focusing [34], and permanent magnet micro-focusing [35], but focusing these beams over a few cm has yet to be demonstrated.

1.1.1.1.5 Shielding requirements

Unlike for an accelerator, which is often tens of meters away from the patient, and therefore requires that the hadron path be highly radio-protected with thick concrete walls (due to radiation from stray particles, and radiation from turning the ion beam), lasers would help reducing the overall shielding cost by reducing the ion transport beam-lines.

1.1.1.1.6 Remaining challenges

The short-pulse laser-solid matter interaction community has still to solve the following issues:

- verify the scaling laws for proton energy with laser power (across pulse durations),
- improve the shot-to-shot reproducibility to the few-percent level,
- develop suitable dose monitoring devices,
- develop techniques for accurate dose control and cutoff,
- address the quality-assurance and the patient-safety aspects;

and be able to develop an entirely new technology for effective beam delivery and dose conformation [20].

1.1.2 Fast ignition (FI) overview

Another use of the ions (and electrons) is related to energy production and Inertial Confinement Fusion (ICF), which will be coming of age in the next decade with the completion of the National Ignition Facility (NIF) at Lawrence Livermore National Laboratory (LLNL). At the NIF, to achieve *thermonuclear ignition and burn*, the point design scenario is called the *central hot spot* scenario, via the *indirect drive* method [36], which relies on simultaneous *compression* and *central hot spot ignition* of a spherical capsule in an implosion (i.e. analogous to the self-ignition of a diesel engine): the lasers heat the inner walls of a gold cavity called a *hohlraum*, creating a super-hot plasma which radiates a uniform *bath* of soft X-rays, which surrounds a deuterium-tritium (DT) pellet. The X-rays rapidly heat the outer surface of the fuel pellet, causing a high-speed ablation, or *blow-off*, of the surface material, and imploding the fuel capsule in the same way as if it had been hit with the lasers directly (*direct drive*). Symmetrically compressing the capsule with radiation forms a central *hot spot*, where fusion processes can begin – the plasma ignites and the compressed fuel burns before it can disassemble.

1.1.2.1 Electron fast ignition (EFI)

Although the *hot spot* approach has a high probability for success, *Electron Fast Ignition* (EFI) [37] is one of the alternative methods currently being extensively explored to achieve ignition while saving on laser driver energy (which will make use of lasers like the NIF Advanced Radiography Concept (ARC), a planned kJ short-pulse laser on NIF, or Omega EP on the Omega laser at LLE). EFI is an approach in which the *compression* phase is separated from the *ignition* phase. EFI uses a similar approach as the central hot spot approach. However, the laser-compression driver energy can be reduced and a high-intensity, ultra-

short-pulse laser is added as the *spark* that achieves ignition. As illustrated in Figure 1-5, a DT target is first compressed to a high density by long-pulse lasers, without increasing its temperature (isothermal compression). Then, the short-pulse laser beam delivers energy to ignite the compressed core (i.e. analogous to a sparkplug in an internal combustion engine) [38].

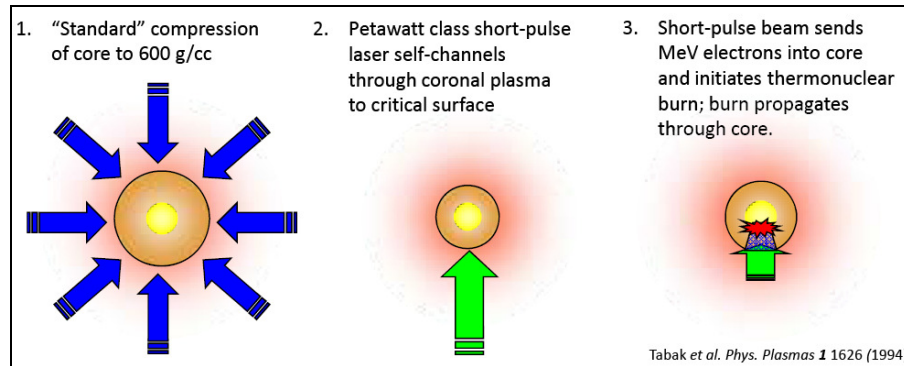


Figure 1-5: Schematic of the Fast Ignition (FI) scenario.

With respect to EFI, various target geometries have been suggested to confine energetic electrons to a small target volume to improve heating uniformity [39, 40, 41, 42, 43]. The cone geometry has also shown promising results. The cone precludes the ablation plasma from entering the path of the ignition beam, allowing the laser energy to be deposited very close to the compressed fuel [44]. Experiments on cone guiding of short-pulse laser light to a compressed core [45] show an important increase in the yield of thermal fusion neutrons: a plasma fiber added on a hollow-cone target (see Figure 5-1 (a)) is shown to guide and collimate an increased density of electrons.

As illustrated in Figure 1-6 [46], a typical EFI target consists of a fuel capsule mounted on, and imploded around, a re-entrant cone – the cone is situated very close to the core. The hot electrons produced when the short-pulse ignition laser interacts with cone tip might be able to heat the fuel efficiently.

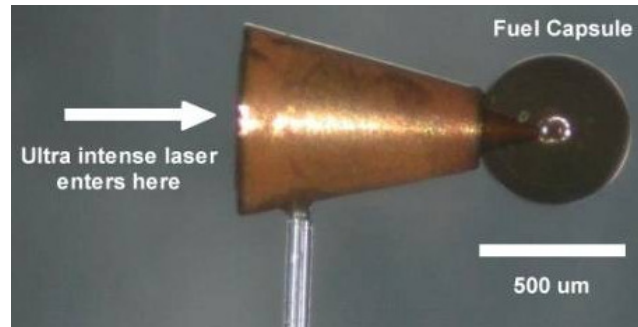


Figure 1-6: Typical EFI target [46].

The four principal steps of EFI are illustrated in Figure 1-7 [47]:

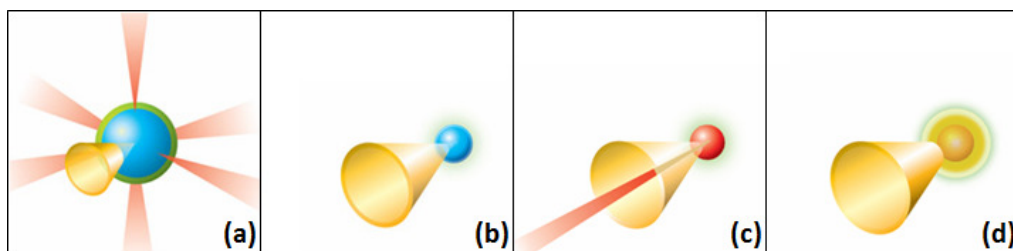


Figure 1-7: Schematic of the Electron Fast Ignition (EFI) scenario [47].

In Figure 1-7 (a), many powerful long-pulse (ns) laser beams irradiate a capsule of DT fuel. The lasers are arranged symmetrically around the capsule and heat a thin layer of the capsule causing it to expand rapidly. This forces the rest of the material in the opposite direction.

In Figure 1-7 (b), the material converges around the tip of a gold cone. The density of the DT is now hundreds of times the density of solid material.

In Figure 1-7 (c), an ultra-intense short-pulse (ps) laser is fired into the gold cone. When the laser interacts with the tip of the gold cone, a large number of energetic electrons is produced.

In Figure 1-7 (d), the energetic electrons travel into the dense DT fuel and deposit their energy. This raises the fuel temperature to 100 million degrees Celsius, which is hot enough to initiate the fusion reactions. However, it is difficult to control the electrons' energy

deposition: if they are too energetic, they might just leave the core, without being able to efficiently deposit their energy where needed.

In general, FI requires heating a small volume ($< 30^3 \mu\text{m}^3$) of a dense capsule (300 g/cm^3), although less dense than a traditional hot-spot capsule, to very high temperatures ($\sim 10 \text{ keV}$) in a very short time ($\sim 20 \text{ ps}$) [15, 16]. Because FI does not rely on converging shocks driven by the compression lasers to light the fusion burn, as done in conventional ignition, FI relaxes the requirements for compression (i.e. density and symmetry), and significantly reduces the overall energy needed to achieve energy breakeven. The energy can be deposited into the core by electrons, but also by protons, or ions.

1.1.2.2 Proton fast ignition (PFI) and ion fast ignition (IFI)

FI using protons or ions is also a heavily research field. Because of the large lateral and longitudinal straggling of the electrons, PFI was first proposed in 2001 [15] as an effective alternative way to deposit energy in the capsule (using the Bragg peak effect). There, the proposed scheme consisted of a standard ICF hohlraum, in which a DT capsule would be ablatively compressed by thermal radiation, as well as a proton source placed just outside the hohlraum, as illustrated in Figure 1-8.

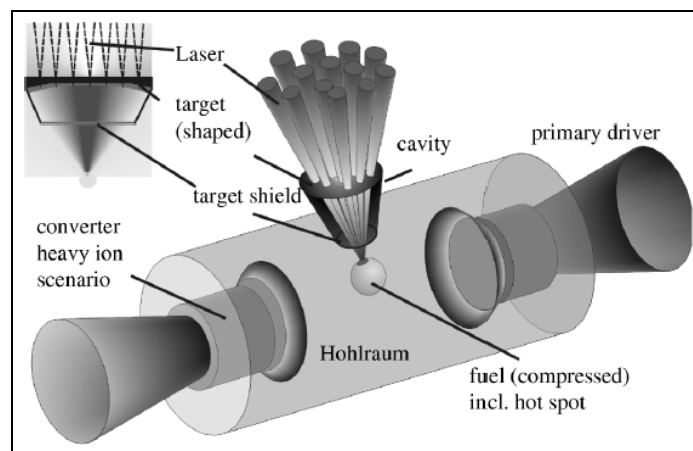


Figure 1-8: Indirectly driven PFI; (Inset) the rear surface of the laser target is shaped to focus the proton beam into the spark volume [15].

At a time close to the fusion fuel's maximum compression, short-pulse (~ picosecond) lasers focused on the proton target would emit, in the direction of the compressed fuel, a burst of protons.

Table 1 summarizes the requirements for PFI on the proton beam number and energy.

PFI references	Ref. [15]	Ref. [16]	Ref. [48] – two proton beams	
Number	$n_p \sim [2-4] \times 10^{15}$	$n_p \sim 1.5 \times 10^{16}$	$n_p \sim 3 \times 10^{14}$	$n_p \sim 5 \times 10^{15}$
Energy	7-10 kJ, 15-23 MeV	12 kJ, 5 MeV	1 kJ, 12 MeV	6 kJ, 12 MeV
Laser energy for a 10 % conversion efficiency	70-100 kJ	120 kJ	10 kJ	60 kJ
Laser energy for a 5 % conversion efficiency	140-200 kJ	240 kJ	20 kJ	120 kJ

Table 1: Proton beam and laser requirements for PFI: (1st column) An estimation of the requirements for an ideal (narrow energy range) proton beam, to ignite the fuel that compresses to a density of 400 g/cm³, is given in [15]: 7-10 kJ of 15-23 MeV protons (the required number of protons is therefore $n_p \sim [2-4] \times 10^{15}$), reaching the fuel in a 15-20 ps pulse and focused onto a 15 μm spot. Since then, there have been many more studies on proton beam requirements for fast ignition. (2nd column) In [16], it is shown that, to relax the ignition requirements on the proton beam, the distance D between the proton source and the compressed fuel should be decreased (requiring some important target design and improvements): simulations show that, while keeping the gain constant, one can go from 26 kJ, 3 MeV, D = 4 mm down to 12 kJ, 5 MeV and D = 500 μm. (3rd column) In a newer study [48], two proton beams are used with two targets, one at 500 μm, and one further away (at ~ 2 mm). The first beam, a Gaussian profile at 12 MeV with a FWHM of 1 MeV, deposits ~ 1 kJ of energy, expanding the volume it entered, thereby creating a density channel for the second beam of similar energy and spread to propagate into the fuel and depositing 6 kJ of energy, sparking ignition. This scheme reduces the overall energy needed for PFI to 7 kJ of protons.

Two of the biggest limitations to the practical implementation of PFI are:

- 1) the laser-to-proton energy conversion efficiency: the conversion efficiencies obtained so far are still relatively low at low intensities and energies, presently on the order of 0.5 % for a flat foil, at laser intensities of $\sim 1 \times 10^{19}$ W/cm² and laser energies of tens of Joules [1], although higher conversion efficiencies have been

obtained, i.e. $\sim 2.5\%$ [1] and $\sim 5\%$ [17]; considering the fact that tens of kilojoules may be required for FI, the laser-to-proton conversion efficiency is an important criterion since it dictates the FI laser energy requirements (i.e. cost and size), and should therefore be $> 10\%$ (and of course as large as possible).

- 2) the proton focusing to a rather tight spot: the focus spot size needs to be $\sim 20\text{-}30\ \mu\text{m}$ in diameter, a few centimeters away from the ion source. As we have already seen for medical applications [1.1.1.1.4], successful short-pulse laser proton focusing experiments have been carried out, using ballistic focusing, electrostatic micro-focusing, and permanent magnet micro-focusing. Here again, however, the focusing technique over a few centimeters has yet to be demonstrated.

In summary, the difficulty in the implementation of PFI will be in balancing the laser intensity required (i.e. $\sim 2 \times 10^{19}\ \text{W}/\text{cm}^2$ for 10 MeV) for the needed proton energy range with the required proton numbers and laser-to-proton conversion efficiencies, which are known to increase with increasing intensity, and which therefore are in conflict with the required laser intensity.

However, protons *may not be* the most ideal ion for the FI “spark”; the most ideal ion still remains to be determined. Ref. [49] shows that fusion gain of a fuel capsule is independent of the ion species used for FI. Mono-energetic carbon beams [50] were produced a few years ago at LANL, using Trident’s short-pulse arm (pre-enhancement). Mono-energetic carbon beams (as well as carbon in general) *may be* a more efficient light-ion “spark”, for the same reason that carbon ions are better than protons for medical applications, i.e. the dE/dx of carbon ions is much higher than that of protons in their Bragg peak and each ion carries more energy than a lighter ion. Therefore, fewer ions need to be generated to deposit the same amount of energy, simplifying target fabrication requirements, as some

calculations (see Table 1) have shown that the number of protons needed would be in the range of 10^{15} – 10^{16} . This could be a difficult number to produce from one or two monolayers that are only tens of microns in diameter. However, the downside is that, for the same reasons these ions are better, they also require higher energies to penetrate the fuel. Generating laser-accelerated ions with 10s of MeV per nucleon has only recently been reported [51, 52]. Several mechanisms have been proposed to achieve these high ion energies: the laser piston acceleration (LPA) mechanism [53], the radiation pressure acceleration (RPA) mechanism [54, 55], and the breakout afterburner (BOA) mechanism [56, 57]. These mechanisms are too far away for a credible attempt at IFI in the near future, as the available lasers in the next 5-10 years will only be those already being built at fusion facilities (like NIF ARC); however, future concepts like the European HiPER project may be able to take advantage of these schemes if they prove viable.

1.1.3 Other applications of proton and heavy ion beams

Discussed above in detail were two applications, hadron therapy and FI (i.e. PFI and IFI). However, these proton and heavier ion beams have many other uses in a multitude of fields that will not be covered in detail, but only mentioned shortly:

- In the field of energy, besides *Ion Fast Ignition Inertial Confinement Fusion*, these beams can be used as sources for nuclear waste transmutation via a (p,n) reaction to produce short-lived isotopes and energy from nuclear waste, similarly to what has been shown in [58].
- For homeland security applications, these beams may, one day, be radiation sources for scanning cargo containers for nuclear material at ports, or sources for standoff nuclear material detection (electrons, X-rays, protons, neutrons, deuterons, or even muons).

- In medicine, laser-driven ion sources may be used as table-top on demand radio-isotope and radio-pharmaceutical machines (i.e. rare isotope production [59]) as well as the aforementioned hadron cancer therapy treatments directly available in every hospital.
- In materials and basic science, these sources open up the possibility of table-top nuclear particle physics [59], and of creating exotic states of matter for materials studies in a university setting and for advanced ion microscopy; isochoric heating (i.e. heating at constant volume) [60, 61]; and radiography sources for probing materials and dense plasmas (i.e. proton imaging and radiography [13, 62, 63, 64]).

All of these applications will be enabled with the maturation of this technology, and will allow for these types of sources and applications to be deployed in multiple settings inexpensively, and especially in locations where large particle accelerators could not typically be employed.

1.2 Dissertation outline

In Section 1.1, the various applications of laser-accelerated protons were described, with more detail given to proton (and ion) beams used for cancer therapy and for fast ignition (FI). For FI, the laser-to-proton (or laser-to-ion) conversion efficiency is a crucial parameter; while for medical applications, the crucial parameter is the proton cutoff energy. Finding ways to maximize the proton energy and scaling this enhancement to higher laser energies is the main goal of the work presented in this dissertation.

Section 2 starts with a brief description of the Target Normal Sheath Acceleration (TNSA) mechanism, which is the theorized mechanism for the acceleration of the ions from the non-laser-irradiated side of the solid target. Besides ions, the interaction of a short-pulse laser with a solid target also yields the generation of hot and thermal electrons and X-rays, which

can be used to diagnose the interaction. Section 9 (Appendix at the end of this dissertation) covers some basics of plasma physics and of laser-plasma interactions, describes the interaction of a laser with both an underdense and an overdense (solid) plasma (i.e. target), and explains the various absorption mechanisms in some detail. In Section 2, some target modifications carried out to increase the proton energies and efficiencies are discussed. The particle in cell (PIC) code, PICLS, used to model laser-plasma interaction experiments is introduced. Section 2 also presents an overview of most of the laser-accelerated proton experiments carried out over the last decade, as a function of various laser parameters, such as energy, intensity, focal spot, pulse duration and contrast.

In Section 3, the Trident laser system is described chronologically (from 2006 to 2009), starting with the Trident pre-enhancement system at 20 J and intrinsic contrast ($\sim 10^{-8}$), then describing some of the changes made for the energy enhancement to ~ 80 J (still at the intrinsic contrast), and finishing with the laser contrast enhancement (to $\sim 10^{-10}$), making Trident the only laser so far capable of shooting at 1ω ($1.054 \mu\text{m}$) and full energy (~ 80 J) on ultrathin targets (down to the nm scale) and thereby realizing very controlled experiments that should be easier to model. Some of the laser beam diagnostics are also described.

In Section 4, the detectors and diagnostics are described: CR39 solid state nuclear detectors, RadioChromic Films, Imaging Plates, the electron spectrometer and the Cu $K\alpha$ imager.

In Section 5, the three experimental beamtimes using the three variations of the Trident short-pulse beam, as described in Section 3, where gold and copper FTC targets were shot (along with flat-foil targets and RMTs for comparison) are presented chronologically and in a comprehensive manner. We start with the experimental set-up, followed by a description of the various targets. Then, for clarity, the major results are discussed briefly at the

beginning of each section. After which, all the results are exposed in detail, combining any two of the following variables: proton energy, laser-to-proton conversion efficiencies, laser characteristics, electron temperature, Cu $K\alpha$ yield, target type, target thickness, RMT diameter, FTC characteristics, etc.

Section 6 consists of a comparison and discussion of the main and most important results. The various PIC simulations, trying to capture the main reasons for the observed enhanced proton energy results, which generally agree with our experimental data, are presented along with them. The disproven and still-to-be-tested hypotheses are exposed.

In Section 7, future work, concerning target, laser, and diagnostics development, is discussed.

2 ELECTRON, X-RAY AND PROTON GENERATION FROM SOLID TARGET LASER INTERACTION

The main laser pulse, after having made its way through some amount of underdense plasma, which directly depends on the laser contrast, finally reaches the critical surface of the solid target, or close to where the original target surface was, unless the preplasma is sufficiently large, producing a hot solid density plasma via collisional and collisionless absorption and various heating mechanisms. The laser absorption mechanisms are described in detail in the Appendix (see Section 9). As this laser pulse interacts with the critical surface up to the skin depth, it couples into electrostatic and/or scattered light waves via both classical (e.g. resonance absorption [9.2.4.4.1] and inverse Bremsstrahlung [9.2.4.3.4]) and relativistic (e.g. vacuum heating [9.2.4.4.3] and $\vec{J} \times \vec{B}$ heating [9.2.4.4.4]) absorption processes. In this dissertation, the laser intensity is $> 10^{18}$ W/cm², therefore the relativistic effects, such as the relativistic Brunel heating and the $\vec{J} \times \vec{B}$ heating mechanisms, are dominant.

All of these laser absorption mechanisms produce thermal and hot electrons, X-rays, and ions. These ions can be generated from both sides of a solid flat target: we call *front side* the laser-irradiated side of the target, and the *back side* the side that is not irradiated by the laser. These ions stem from the contaminants present on the target, such as for example hydrogen, carbon, and oxygen. These contaminants have been observed as early as 1968 [65] in laser-produced plasmas. The contaminant layer has been observed to be ~ 20 Å in thickness, as mentioned in [66, 67]. To remove these contaminants, many techniques have been developed, and to cite only a few: laser-ablation [68], Ohmic heating [69] (in which case a current is passed through the target), laser (Verdi) absorption heating [50, 67],

sputter etching [70], desorption, UV light, etc. However, the cleaned targets do not stay clean for very long, and they would need to either be shot instantaneously or be kept in an ultra-high vacuum.

This dissertation studies the proton acceleration from a solid micro-cone target via the target normal sheath acceleration (TNSA) mechanism. The electrons and X-rays produced during the laser-target interaction are used to diagnose and understand the proton beam emission.

Figure 2-1 shows, in three steps, a sketch of ion acceleration via laser short-pulse laser interaction on a solid target, including both the front-side and the back-side acceleration, which are described in Sections 2.3.1 and 2.3.2 respectively in more detail.

Figure 2-1 (1): The short-pulse laser (solid red) impinges on the target at an angle. However, a few ns before the intense short-pulse reaches the target, depending on the laser, amplified spontaneous emission (ASE) of the laser produces a small ($\sim 10 \mu\text{m}$) scale-length preplasma at the target surface.

Figure 2-1 (2): The intense short-pulse interacts with the preplasma, accelerating electrons into the target via ponderomotive acceleration [9.2.1.3], resonant absorption [9.2.4.4.1], Brunel heating [9.2.4.4.3], $\vec{J} \times \vec{B}$ heating [9.2.4.4.4], and other mechanisms such as stochastic heating, not discussed here [71]. This electron acceleration produces a charge separation and an ambipolar field on the front surface. The electrons (blue) are accelerated into and through the target, emerging on the rear surface to form a sheath. In highly conductive targets, a cold return current (grey arrows) stabilizes the beam propagation, by cancelling a portion of the induced magnetic field, allowing for currents above the Alfvén current limit [72]. The Alfvén current is given in a vacuum by $J_A = \beta\gamma \frac{mc^3}{e} \approx 17\beta\gamma \text{ kA}$

(where β and γ are defined in [9.2.1.1.2]); for the propagation of relativistic beams, when the current becomes greater than J_A , the self-induced magnetic field becomes so strong that the particles actually turn back. Depending on the initial target properties, the electron beam can suffer from many propagation instabilities inside the target that can affect the uniformity of the sheath.

Figure 2-1 (3): On the front of the target, the ions (the protons in this case shown in green) undergo a Coulomb explosion and an additional ambipolar acceleration. On the rear, the ions are field-ionized and accelerated by the large MeV/ μm sheath potential.

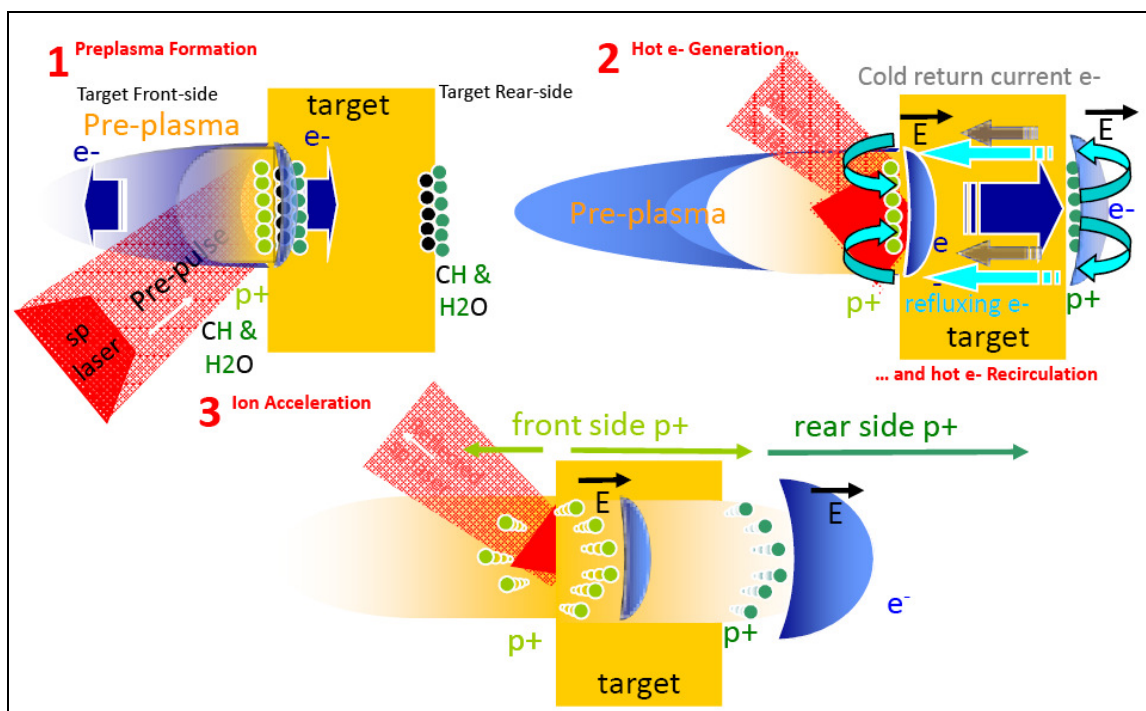


Figure 2-1: Brief overview of the laser-ion acceleration: front-side acceleration and target normal sheath acceleration (TNSA) mechanism (Schematics by Kirk Flippo).

The initial conditions on the sheath electric field, length and density of the hot electrons are summarized in Figure 2-2.

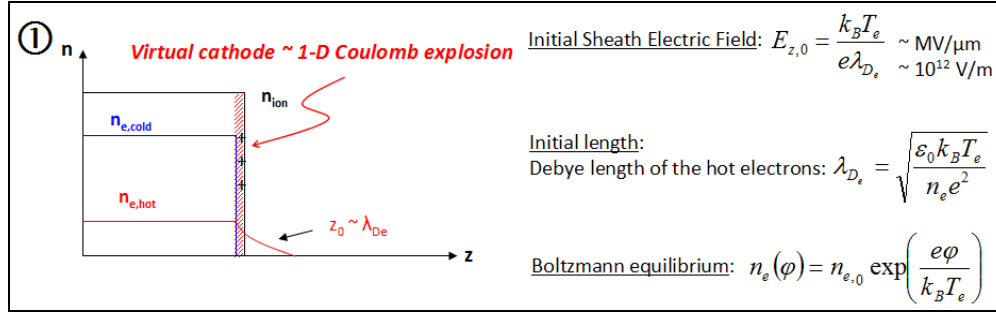


Figure 2-2: Initial stage of the sheath expansion (interpreted from [6(b)]).

2.1 Electron generation

When an electron at rest is irradiated by a relativistic intense laser field, it is quickly

accelerated, up to relativistic energies. The electron quiver velocity $v_e = \frac{eE_L}{m\omega}$ [9.2.1.1.1],

corresponds to the velocity of the electron just after ionization. The ion quiver motion

similarly writes as $v_i = \frac{ZeE_L}{M\omega}$ and in a laser field, it is negligible compared to that of the

electrons, due to the ions' much larger mass. The normalized vector potential [9.2.1.1.2]

can be expressed as $a_0 = \frac{eE_L}{mc\omega}$ or as $a_0 = 0.85\lambda_0 [\mu\text{m}] \sqrt{I \left[10^{18} \frac{\text{W}}{\text{cm}^2} \right]}$ [9.2.1.1.3]. Therefore,

we find that $\frac{v_i}{c} = \frac{Zm}{M} a_0$. To accelerate the ions to relativistic velocities directly via the

laser field, we would need $\frac{v_i}{c} = 1$, which transcribes into $a_0 = 2000$, or a laser intensity of

$\sim 10^{24} \text{ W/cm}^2$. However, MeV range ions have clearly been observed in experiments at

much lower intensities, starting at $\sim 10^{18} \text{ W/cm}^2$. This can be explained as follows: in a

plasma, the laser mainly accelerates the electrons at the absorption point; charge separation

fields are excited locally as well as at the target-vacuum interface. The ions gain energy

through the electrons.

2.1.1 Thermal electrons and hot electrons

It is the plasma waves described in Section 9.1.2 that can be responsible for the acceleration of electrons, which in turn, results in the heating of the target. Most of the laser energy is directly transferred to both *thermal* (also called *cold*) electrons, i.e. $10 \text{ keV} < T_e < 100 \text{ keV}$, and *fast* (also called *hot*) electrons, i.e. $100 \text{ keV} < T_h < \text{several } 10s \text{ of MeV}$; the latest can be accelerated close to the speed of light. In fact, the fast electrons (T_{hot}) transfer their energy to the bulk or thermal electrons (T_e). It is the collective heating mechanisms which account for T_{hot} , while it is collisional heating which leads to an increase in T_e . Therefore, due to the collisionless mechanisms described in Section 9.2.4.4, some fraction of the electrons present in the plasma are heated (or *superheated*) to much higher energies than the initial bulk plasma temperature T_e of the cold electrons. Very often, this supra-thermal electron component has a Maxwellian distribution, with a characteristic temperature $T_h \gg T_e$, which is obtained because of the following. The particle acceleration mechanism leads to strong cycle-to-cycle fluctuations in the trajectories and in the energies acquired by the electrons [73]. When taking the average of these single-part distributions over time, a Maxwellian distribution is obtained. The hot electrons are accelerated by a coherent electric field, from inside the plasma, or from the laser.

Target heating is a result of the lower energy portion of a bi-Maxwellian distribution of energetic electrons (not accounting for the refluxing of the hot electrons or resistive heating via the hot-electron current). However, the rapid lateral transport of the hot electrons can reduce the efficiency of the heating.

2.1.2 Hot-electron temperature scalings as a function of laser intensity and bulk plasma temperature

2.1.2.1 Hot-electron generation and propagation measurements

Hot-electron generation and propagation in matter have been studied extensively for many years both experimentally and theoretically. Laser-matter interactions [74] and electron transport dynamics [75, 76] have been studied both numerically and analytically, including the influence of different plasma density scale-lengths (i.e. depending on the laser contrast, see Section 3.3, and especially Section 3.3.1) on the laser absorption and fast electron temperature [77] and the effects of self-generated magnetic and electric fields on the transport dynamics [78, 79, 80, 81, 82], and in particular, the effect of the target material resistivity [83, 84]. Besides laser contrast and target material, other parameters, such as laser energy, pulse duration, spot size and target shape all also influence the hot-electron temperature. The effect of any single parameter is extremely hard to isolate in experiments. Experimentally, mostly x-ray measurements were employed as diagnostic techniques to look for hot electrons [2.2]. However, direct measurements of the forward escaping electrons [85, 86], shadowgraphy [87, 88] and optical emission from the rear surface [89, 90] have also been used to localize the hot electrons.

The study of fast-electron transport phenomena is important for the development of ultrafast x-ray sources (see Section 2.2) and proton sources (see Section 2.3), as well as for the study of matter in extreme conditions, such as measurements of the equation of state and the opacity of high pressure material relevant to astrophysics [91]. Most applications require the highest possible laser-to-hot-electrons conversion efficiencies, and especially at a specific energy. So far, laser-to-hot-electron coupling efficiencies with regular solid flat-

foil targets have been empirically estimated to be $\sim 10\%$ [42] to $40\% - 50\%$ [95] and by $K\alpha$ emission fluence, $20\% - 30\%$ [92].

The detailed knowledge of the fast electron generation and transport mechanisms is, of course, also of fundamental importance for the electron fast ignition (EFI). As was already discussed in Section 1.1.2.1, in the EFI scheme, an ultra-high current of relativistic electrons has to propagate through an outer low- Z plasma layer in order to deposit the energy of the electrons in the core of the fusion pellet, creating a hot spot and thus igniting the fuel [37, 93].

2.1.2.2 Long-pulse lasers

Since the laser pulse is rather long (i.e. 10s of picoseconds, or more), equilibrium can be assumed. One can therefore also assume the laser and the plasma to be in pressure balance,

which simply writes as $P_e = n_e k_B T_e = \frac{I_0}{c}$, or $T_e = \frac{I_0}{c n_e k_B}$. As long as $n_h < n_c \ll n_e$, the hot

electrons determine the energy balance, while the cold bulk electrons are responsible for momentum and pressure balance, until the hot-electron density becomes of the order of the critical density.

- In [223], the Forslund, Kindel and Lee hot-electron temperature scaling is given by

$$T_h^{FKL} \sim 14 \times (I_{16} \cdot \lambda_\mu^2 \cdot T_e)^{1/3} \text{ keV, assuming pressure balance, and using PIC simulations.}$$

- In [94], a resonant absorption analysis yields to the two very similar Estabrook and Kruer hot-electron temperature scalings:

$$T_h^{EK1} \sim 20 \times (T_e)^{0.25} (I_{16} \cdot \lambda_\mu^2)^{0.39} \text{ keV and } T_h^{EK2} \sim T_e + 21 \times (T_e)^{0.04} (I_{16} \cdot \lambda_\mu^2)^{0.42} \text{ keV.}$$

2.1.2.3 Short-pulse lasers

For much shorter pulses (femtosecond regime), the pressure balance assumption that was made for longer pulses (picosecond regime) cannot be used anymore, due to the lack of equilibrium on femtosecond time-scales, and to the much sharper density and field profiles.

- In [95], the empirical Beg scaling for hot-electron temperature is presented, in the 700 fs – 4 ps regime, with no dependence on the bulk plasma temperature T_e , but only on the laser intensity: $T_h^{Beg} \sim 100 \times (I_{17})^{1/3}$ keV.

- In the Brunel model, using two incident laser beams incident at $\pm 45^\circ$ on a solid target, where surface currents do not cancel [96], the electrons are directly accelerated by the laser field, incident on a step-like density profile. The Brunel hot-electron temperature scaling is given by [187, page 175]: $T_h^B \sim 3.7 \times (I_{16} \cdot \lambda_\mu^2)$ keV.

- Now, using only a single, obliquely incident laser onto a steep but finite ($L/\lambda \leq 0.1$) density gradient, assuming fixed ions, and an electromagnetic field, the Gibbon and Bell hot-electron temperature scaling is found to be [97]: $T_h^{GB} \sim 7 \times (I_{16} \cdot \lambda_\mu^2)^{1/3}$ keV.

- At relativistic intensities, i.e. for $I > 10^{18}$ W/cm², the Wilks scalings [98] and [12] predict a hot-electron temperature scaling derived from the electron momentum in the laser field, and the corresponding kinetic energy for the quiver motion, i.e. $T_h \sim mc^2(\gamma - 1)$, where

$\gamma = \sqrt{1 + \frac{p^2}{m^2 c^2}}$ [9.2.1.1.2]. This scaling assumes mobile ions, and a step-like density profile.

Because the laser interacts with such a profile, only the $\vec{J} \times \vec{B}$ and the Brunel mechanisms are the significant heating mechanisms. However, both scalings differ slightly, and ③ attempts to explain how these two scalings are derived.

① In [98], $T_h^{W1992} \sim mc^2(\gamma-1) = mc^2\left(\sqrt{1+\frac{P_{osc}^2}{m^2c^2}}-1\right)$, which can be rewritten as

$$T_h^{W1992} \sim 511 \times \left(\sqrt{1 + \frac{I \cdot \lambda_\mu^2}{1.37 \times 10^{18}}} - 1 \right) \text{ keV, i.e. } T_h^{W1992} \sim 511 \times \left(\sqrt{1 + 0.73 \times (I_{18} \cdot \lambda_\mu^2)} - 1 \right) \text{ keV.}$$

② In [12], $T_h^{W2001} \sim mc^2 \sqrt{1 + \frac{2U_p}{mc^2}}$, which scales with the ponderomotive potential [99]

$$U_p = 9.33 \times (10^{-17} \cdot I \cdot \lambda_\mu^2) \text{ keV. This yields to } T_h^{W2001} \sim 511 \times \sqrt{1 + 0.365 \times (I_{18} \cdot \lambda_\mu^2)} \text{ keV.}$$

③ [100] From $m\ddot{x} = eE_0 \cos(\omega t)$, we see that $\dot{x} = \frac{eE_0}{m\omega} \cos(\omega t)$. Also, recalling that

$\sqrt{\langle \dot{x}^2 \rangle} = \frac{\dot{x}}{\sqrt{2}}$, we can compute both the maximum ponderomotive potential

$$U_{\max} = \frac{m}{2} \dot{x}^2 = \frac{m}{2} \left(\frac{eE_0}{m\omega} \right)^2 = \frac{e^2 E_0^2}{2m\omega^2}, \text{ as well as the averaged ponderomotive potential}$$

$$U_{osc} = \langle U \rangle = \frac{m}{2} \langle \dot{x}^2 \rangle = \frac{e^2 E_0^2}{4m\omega^2}, \text{ and } U_{\max} = 2U_{osc}. \text{ Since } a_0 = \frac{eE_0}{m\omega c} \text{ and } a_0^2 = \frac{2 \langle p^2 \rangle}{m^2 c^2},$$

$$U_{osc} = \frac{a_0^2 mc^2}{4} = \frac{\langle p^2 \rangle}{2m}. \text{ Also, } \langle E_{total}^2 \rangle = m_0^2 c^4 + \langle p^2 \rangle c^2 = \langle \gamma^2 \rangle m_0^2 c^4, \text{ which leads to}$$

$$\langle \gamma^2 \rangle = 1 + \frac{\langle p^2 \rangle}{m_0^2 c^2}, \text{ i.e. } \langle \gamma \rangle = \sqrt{1 + \frac{\langle p^2 \rangle}{m_0^2 c^2}} = \sqrt{1 + \frac{a_0^2}{2}}, \text{ where } a_0^2 = \frac{I \cdot \lambda_\mu^2}{1.37 \times 10^{18}}, \text{ and}$$

$$T_h^{osc} \sim 511 \times \left(\sqrt{1 + \frac{a_0^2}{2}} - 1 \right) \text{ keV.}$$

$$\text{Also, } \gamma_{\max} = \sqrt{1 + \frac{p_{\max}^2}{m^2 c^2}} = \sqrt{1 + a_0^2}, \text{ and } T_h^{\max} \sim 511 \times \left(\sqrt{1 + a_0^2} - 1 \right) \text{ keV.}$$

Therefore, $T_h^{W1992} \sim 511 \times \left(\sqrt{1 + \frac{I \cdot \lambda_\mu^2}{1.37 \times 10^{18}}} - 1 \right) = 511 \times \left(\sqrt{1 + a_0^2} - 1 \right) = T_h^{\max}$.

T_h^{W2001} , on the other hand, corresponds to $T_h^{osc} \sim 511 \times \left(\sqrt{1 + \frac{a_0^2}{2}} - 1 \right)$, but is missing the

“- 1” term in the parenthesis.

Note that in ① [98], ② [12], and ③, the scaling derivations are not perfectly correct for relativistic cases, as the derivation starts with the equation $m\ddot{x} = eE_0 \cos(\omega t)$ for which the mass is the non-relativistic mass. One should really start with $m\gamma\ddot{x} = eE_0 \cos(\omega t)$, but since $\gamma = \gamma(t)$, the problem would then require solving a system of partial differential equations computationally, as opposed to analytically. Also note that for the case $T_h^{W1992} = T_h^{\max}$, the hot-electron temperature is overestimated by some amount (still to be determined).

2.1.2.4 Summary of all the scalings, for $I < 10^{18}$ W/cm² & $I > 10^{18}$ W/cm²

Figure 2-3 displays all the previously described hot-electron temperature scalings (see Sections 2.1.2.2 and 2.1.2.3).

At a laser intensity of 1.6×10^{20} W/cm², the electron temperatures experimentally measured on Trident are close to both Wilks scalings: $T_{\text{hot}}(W2001)$ [black ♦s] ~ 4 MeV, and $T_{\text{hot}}(W1992)$ [grey ♦s] ~ 5.1 MeV.

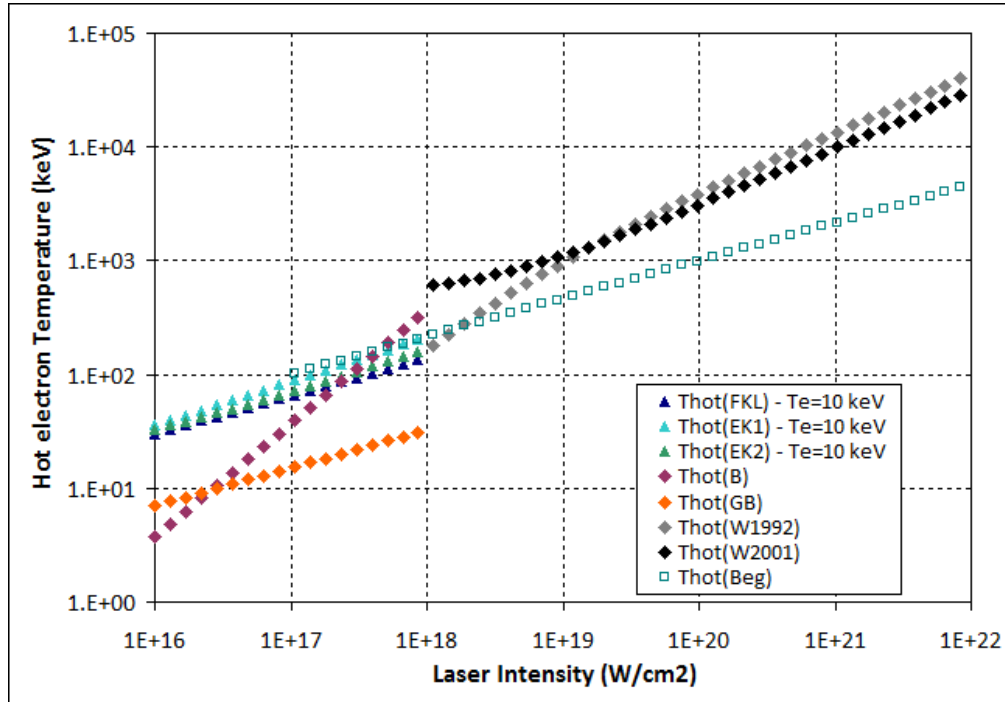


Figure 2-3: Scalings of the hot-electron temperature [keV] as a function of laser intensity [W/cm²] for a 1 μm light. Triangles: long (10 of picoseconds) pulse scalings; a bulk temperature of 10 keV is assumed; the scaling only holds up for $I < 10^{18}$ W/cm². Diamonds: short (100s of femtoseconds) pulse scalings; the Brunel scaling and the Gibbon and Bell scaling hold for $I < 10^{18}$ W/cm² and the Wilks scaling holds for $I > 10^{18}$ W/cm². Squares: turquoise border, picosecond pulse, no assumption of the bulk temperature is necessary.

2.2 X-ray generation

In the previous section [2.1], the electron production scalings in short-pulse high intensity laser-produced plasmas were discussed. The hot electrons produced in the vicinity of the focal spot, when striking the nearby material, produce X-rays – each with the characteristic signature of the native atom. In this dissertation, Cu as a target material is of particular interest (for Cu $K\alpha$ 2-D imaging purposes). These hot electrons are responsible for both direct (Bremsstrahlung, line emission) and indirect (plasma heating) x-ray emission. “Bremsstrahlung appears as a continuum anywhere in the 0.1 keV to MeV range depending on the laser intensity and plasma parameters [101, 102, 103] whereas inner-shell line

emission can be in the 1-100 keV range depending on the atomic number of the target material [104, 105, 106]" [187, page 250].

When a fast electron (with energies above the respective ionization potential), which has a long mean free path, and which penetrates a *cold* region of the target, is slowed down via elastic collisions with ions or the nucleus of an atom, Bremsstrahlung radiation is emitted.

The hot electrons, and the resulting Bremsstrahlung emission, tend to hit everything in the target chamber, especially the chamber walls, causing a lot of background noise. At the lower intrinsic contrast, one expects much more noise than at the higher enhanced contrast: this stems from the fact that, in a longer scale preplasma, the hot-electron coupling to the laser light is important, due to resonance absorption. However, when the contrast is enhanced, one expects much less laser coupling with the hot (supra-thermal) electrons.

When a fast electron, which has a long mean free path, and which penetrates a *cold* region of the target, undergoes inelastic collisions with bound inner-shell electrons of an ion or a neutral atom (i.e. 1s electron shell), it causes an electron from a higher shell (i.e. 2p) to fill this vacancy; the recombination process leads to the production of a $K\alpha$ line emission ($2p \rightarrow 1s$ transitions).

The target material used in the 2008 and 2009 experiments was Cu (which has a density of 8.96 g/cm³). The Cu $K\alpha$ x-ray experimental transition energies (wavelengths) [107] are 8.0278416 keV (1.54442740 Å) for $K\alpha_2$ and 8.0478227 keV (1.54059290 Å) for $K\alpha_1$. Copper targets were used primarily for Cu $K\alpha$ x-ray imaging purposes.

$K\alpha$ radiation can be used as a compact source [108], and also as a diagnostic tool: to determine the energy of the hot electrons, to determine where these electrons are going (electron transport through the target), and to gauge the plasma temperature. In this dissertation, Cu $K\alpha$ radiation is used as an electron transport diagnostic. Using a 2-D

imaging crystal, which only images a narrow energy range (a few 10s of eV at most) around the (cold) $K\alpha$ line, the electron transport can be spatially resolved, making it possible to gauge the amount of preplasma created, the alignment and penetration of the laser beam, e.g. the electron transport in conical targets. This technique has been employed successfully for flat-foils [109, 132] and for cone targets (i.e. for fairly large cone targets [4, 110] and for small funnel-cone targets [3]).

However, the plasmas produced at laser intensities of 10^{20} W/cm² are very hot, and as the target becomes hotter, the ions are no longer neutral, i.e. ionization starts occurring, and the $K\alpha$ line emission shifts and broadens to different wavelengths, as shown in Figure 4-27 in Section 4.5.1.4. The heating of funnel-cone targets has been studied in [3, 180]. Note that the imaging crystal cannot image the very hot Cu $K\alpha$ states (see Section 4.5.1.4).

Figure 2-4 shows the stopping power of electrons in solid density copper. Electrons with energies up to ~ 1 MeV can scatter in the material and deposit their energy. For electron energies greater than 1 MeV, the electrons' mean free path increases with electron energy such that they escape from the target more easily, and do not deposit their energy inside the target, and thereby do not heat it, until radiative dominated stopping takes over.

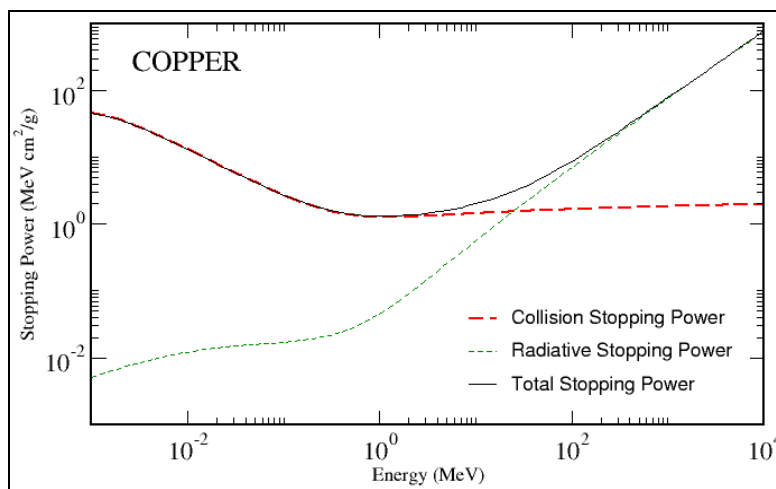


Figure 2-4: Stopping power of electrons [MeV.cm²/g] with energies between 1 keV and 10000 MeV (http://physics.nist.gov/cgi-bin/Star/e_table.pl).

Ref. [111] concludes that the data from electron-induced K-shell ionization can be described very well by the formula $\sigma = (828 \pm 12) \cdot 10^{-16} \frac{R}{U \cdot I^2} \ln U \text{ cm}^2 \cdot \text{eV}^2$, where U is the ratio of

bombarding energy E to the ionization potential I . R is the relativistic correction factor [112], and writes as $R = \left(\frac{2+I}{2+E} \right) \cdot \left(\frac{1+E}{1+I} \right)^2 \cdot \left(\frac{(I+E) \cdot (2+E) \cdot (1+I)^2}{E \cdot (2+E) \cdot (1+I)^2 + I \cdot (2+I)} \right)^{3/2}$.

Figure 2-5 [109] shows the Cu K α cross-section (in barns) – or the electron impact probability, for solid density copper, as a function of the electron impact ionization energy (in keV). The theoretical curve is obtained using the formula presented in [111] and just above. The experimental data points are taken from [113]. The peak cross-section appears at the approximate electron energy of 30-40 keV, which is consistent with values from [114]. In the end, the actual temperature, as well as the K α yield, will end up being a function of the cross-section, as well as of the target characteristics (i.e. thickness) and therefore temperature, which determines the self-absorption.

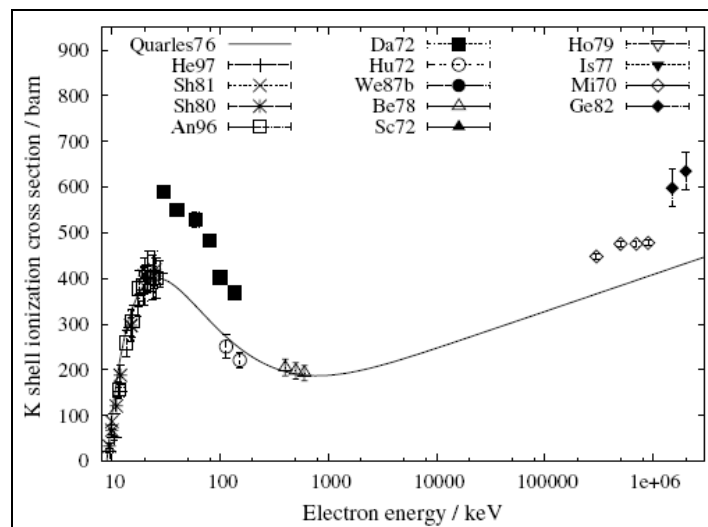


Figure 2-5: Electron induced K-shell ionization cross-section [barn] for Cu as a function of the electron energy [keV] [109].

Figure 2-6 shows the transmission (i.e. self-absorption) of cold solid density copper. The sharp drop corresponds to the K-edge. This plot is useful for example to see how much the target itself might attenuate the $K\alpha$ signal, or to see how much a filter placed in front of the detector will attenuate the signal.

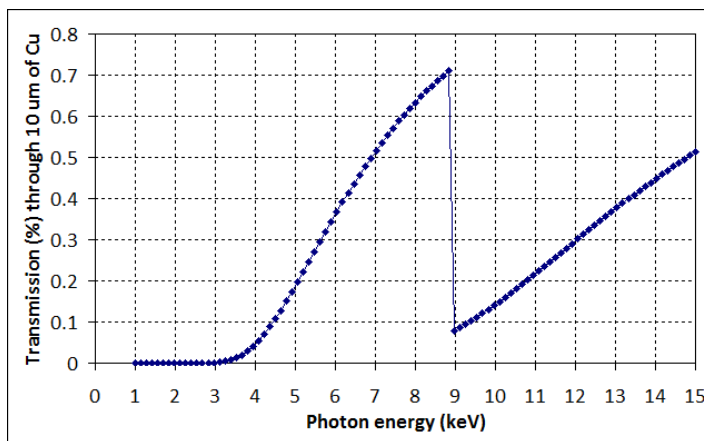


Figure 2-6: Transmission [%] as a function of photon energy [keV] through cold solid density Cu obtained from the Henke tables (http://henke.lbl.gov/optical_constants/filter2.html).

2.3 Proton and heavier ion generation

Besides the production of X-rays, the hot electrons are also responsible for generating the fields responsible for the proton and heavier ion acceleration. In most of the derivations (see Section 9), the ions are always assumed to remain immobile on the sub-picosecond time-scale, therefore providing a neutralizing background to the electron density fluctuations caused by the laser. At sufficiently high intensities ($I > 10^{18}$ W/cm²), this situation alters drastically due to the presence of very large electric fields, typically of the order of GV/m, which originate from the rapid displacement of the electrons from their initial positions. As a result, a portion of the ions can be accelerated to energies of many MeVs.

2.3.1 Front-side acceleration – Ion blow-off

The front surface ion acceleration can simply be based on charge separation arguments. While the laser beam is propagating in the preplasma, before even hitting the solid target, the collective electric field pushes away the electrons present in the preplasma. Since the ions are heavier, they remain. A column of ions extending through the preplasma is therefore created. This column becomes more and more positively charged. The electrons try to move back inside the beam, but they are pushed away by the laser light. This is how a gradient of charge is created inside the beam, leading to a static transverse electric field. At the front solid interface, the laser pressure pushes the electrons away, as long as the pulse lasts, while the ions do not move as fast. This leads to a charge separation, and therefore to the formation of an electrostatic Debye sheath. Intuitively, the photon pressure should be equal to the field at the charge separation. This is how the electrons are swept from the interaction region, inducing ion front surface acceleration away, into and through the target. So in short, the ponderomotive force (i.e. the photon pressure) at the front surface of the target acts on the particles to push them forward, in a non-laminar way, and with a large divergence angle.

The mean ion energy is therefore directly related to the electrostatic sheath potential, and the potential is proportional to the hot-electron temperature. This leads to $E_{ion-front} \propto k_B T_h$. In [66], it is shown that there is a strong experimental correlation between the fast ion bulk energy per atomic mass unit and the hot-electron temperature determined by the x-ray yield. This correlation is described to be due to target surface impurities at the higher temperatures (higher laser intensities) and to the expansion of bulk

target material at the lower temperatures (lower laser intensities), as represented in Figure 2-7.

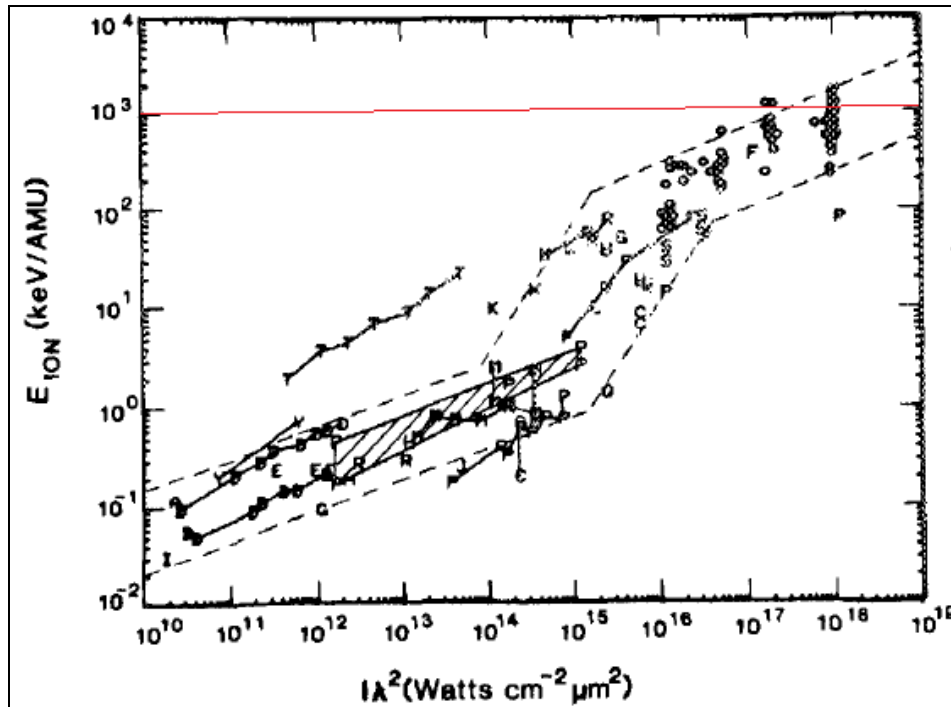


Figure 2-7: Front-side ion acceleration: Mean ion energy (in MeV/AMU) versus laser intensity. The plot is a compilation of data from the Helios CO₂ LANL laser (open circles) and from laboratories throughout the world [66]; the horizontal red line corresponds to the ion energy of 1 MeV.

If we assume [187, page 181] that 1) the energetic particles are significantly hotter than the other less energetic particles, so that $T_h \gg T_e$ and that 2) the bulk of the ions remains fixed on a short (100s of fs) time-scale, the hot electrons will form a cloud in front of the step-like target, resulting in the following induced electric field

$$n_h e E = -\frac{\partial P_h}{\partial x} = -k_B T_h \frac{\partial n_h}{\partial x},$$

where

$$P_h = k_B T_h n_h$$

is the hot-electron pressure. The field is therefore $E \sim \frac{T_h}{L_h}$, with

$$L_h^{-1} \equiv \frac{1}{n_h} \frac{\partial n_h}{\partial x}$$

being the characteristic density scale-length of the hot electrons. This field

is felt by the ions which are in the vicinity of the target surface. These ions are assumed to

obey the usual continuity and momentum equations, i.e. $\frac{\partial n_i}{\partial t} + \frac{\partial(n_i v_i)}{\partial x} = 0$ and

$$\frac{\partial v_i}{\partial t} + v_i \frac{\partial v_i}{\partial x} = \frac{Ze}{M} E. \text{ Using } E = \frac{-k_B T_h}{n_h e} \frac{\partial n_h}{\partial x}, \text{ and the quasi-neutrality condition between}$$

the ions and the hot electrons, i.e. $n_h \approx Z n_i$, the momentum equation rewrites as

$$\frac{\partial v_i}{\partial t} + v_i \frac{\partial v_i}{\partial x} = -C_h^2 \frac{1}{n_i} \frac{\partial n_i}{\partial x}, \text{ where } C_h = \sqrt{\frac{Z k_B T_h}{M}} \text{ is the hot ion sound speed. The}$$

momentum equation has the following solutions: $v_i = C_h + \frac{x}{t}$ and $n_i = n_0 \exp\left(-\frac{x}{C_h t}\right)$

[189]. The maximum ion energy scales as $E_{ion-front-MAX} \sim \frac{1}{2} M v_{max}^2 \sim \frac{1}{2} M C_h^2 \sim Z T_h$ [187,

page 183].

2.3.2 Back-side acceleration – target normal sheath acceleration (TNSA)

The target normal sheath acceleration or TNSA mechanism was first proposed by Wilks *et al.* [115] to explain the results obtained on the Nova PW laser and described in [6]: regardless of the laser incidence angle onto the target's front surface, 45° or normal (0°), the proton beam emission was always emitted normal to the target. The model by Denavit described in [116] was modified, replacing resonance absorption by the ponderomotive scaling.

Figure 2-8 [11] illustrates the TNSA mechanism. The electrons (red arrows) are accelerated from the front side of the target, and propagate through the target via multiple heating mechanisms. Only a few of the hottest electrons can escape from the back surface of the target into the vacuum before the target charges up and before the target capacitance retards further electrons from leaving. The target capacitance refers to the potential to

which the target charges up: as an example, for a 10 μm sphere, 10^{10} , 1 MeV electrons leave the target with a charge of 1 nC, and the capacitance of $\sim 10^{-15}$ F. The remaining hot electrons bounce back and forth and in and out of the target; as they do so, they ionize the target atoms. They quickly fill the target volume and form a thin Debye sheath at the surfaces. The cold target electrons pull inward, exposing a thin layer of ions, and protons (p^+ , green dots), which confine the hot sheath electrons (yellow dots, e^-). This electrostatic sheath can accelerate the exposed ions into the vacuum. If the laser pulse duration is sufficiently long, such that hot electrons returning to the target from the sheath on the rear side can penetrate back to the front-side surface, then these hot electrons can be re-accelerated by the laser field. This is termed refluxing (recirculation) and is shown on the bottom electron trajectory (lavender arrow). It is described in more detail in Section 2.3.3.3.

As soon as these fast electrons reach the rear surface of the target and enter the vacuum region, a charge difference between the plasma region and the outside region is induced again. This creates a highly intense electrostatic potential at the interface between the target and the electron cloud, also referred to as the Coulomb imbalance. Some electrons tend to go back into the target, which is now more positively charged, but on average, all these hot electrons create a dense cloud in equilibrium around the target. This cloud propagates in time as a sheath. The most energetic electrons are able to propagate faster and further, whereas the less energetic (and i.e. slower) ones will stay much closer to the target. The intense potential gradient ionizes the atoms, and accelerates the ions present (as contaminants) on the back surface of the target.

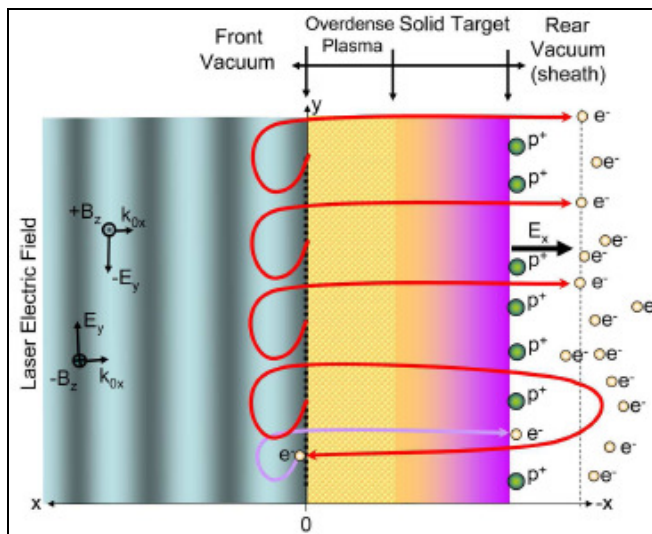


Figure 2-8: Diagram of the TNSA mechanism [11].

As represented in Figure 2-9, the ions propagate perpendicularly to the sheath of electrons. In the region where the electric field is the highest (at the center of the sheath), the ions are accelerated to the highest energies. The highly energetic ions (represented in light blue) propagate further and faster, in a very laminar way, with a very small divergence angle [13]. The divergence angle becomes bigger for decreasing proton energies. However, the lowest energy ions (represented in dark blue) stay very close to the target and also propagate with a small divergence angle, because the electron sheath at this position is almost parallel to the target.

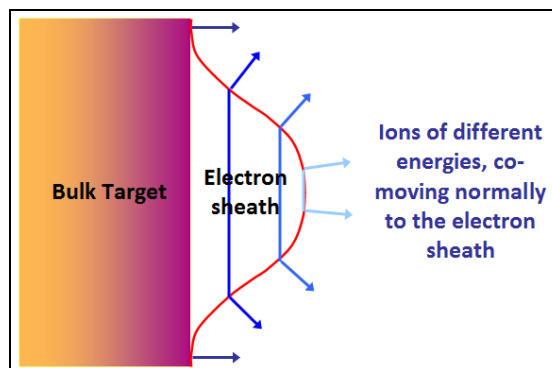


Figure 2-9: Expanding electron sheath at the rear surface of the target, with ions of different energies propagating normal to the sheath, at different divergence angles.

For a freely expanding (Figure 2-10 (right)) isothermal equilibrated plasma (blue curve, Figure 2-10 (left)), the same reasoning as in the case of the ion blow-off [2.3.1] applies. We

can use the solutions for the momentum equation, i.e. $v_i = C_h + \frac{x}{t}$ and

$n_i = n_0 \exp\left(-\frac{x}{C_h t}\right)$. The electric field at the sheath is again given by $n_h e E = -\frac{\partial P_h}{\partial x}$, i.e.

$E = -\frac{1}{n_h e} \frac{\partial(k_B T_h n_h)}{\partial x}$, which yields to $E = \frac{k_B T_h}{e C_h t}$. Using the fact that the plasma scale-

length is $L_n = C_h t$, the electric field writes as $E = \frac{k_B T_h}{e L_n}$. This solution for the electric field

is not valid at the very beginning of the expansion, since $L_n \rightarrow 0$, $E \rightarrow \infty$.

From [187, page 185], we obtain a slightly modified formulation for the electric field, i.e.

$e E_{ion-back-MAX} = \frac{T_h}{\max(L_i, \lambda_{Dh})}$, where L_i is the ion scale-length at the rear, and λ_{Dh} is the

hot-electron Debye length. For a hot-electron temperature of 6 MeV and an ion scale-length of 3 μm , the field is $\sim 2 \text{ MeV}/\mu\text{m}$.

In [117], results are derived concerning the structure of the ion front, the resulting ion energy spectrum, as well as the maximum ion energy, in the case of an isothermal 1-D self-similar plasma expansion (blue curve, Figure 2-10 (left)). The plasma is collisionless, and expands into a vacuum. A Lagrangian code solves the following four equations:

- the electron density [9.1.1.2]: $n_e(\varphi) = n_{e,0} \exp\left(\frac{e\varphi}{k_B T_e}\right)$;
- the Poisson equation for electrons and ions: $\epsilon_0 \frac{\partial^2 \varphi}{\partial x^2} = e(n_e - Z n_i)$;

- the equation of continuity [2.3.1]: $\frac{\partial n_i}{\partial t} + \frac{\partial(n_i v_i)}{\partial x} = 0$;
- the equation of motion [2.3.1]: $\frac{\partial v_i}{\partial t} + v_i \frac{\partial v_i}{\partial x} = \frac{Ze}{M} E$, where $-\frac{\partial \phi}{\partial x} = E$.

The electric field at the ion front, valid at any time, is given by $E_{front} \sim \frac{2E_0}{\sqrt{2e + (\omega_{pi}t)^2}}$,

where $\omega_{pi} = \sqrt{\frac{n_{e,0} Ze^2}{M \epsilon_0}}$ is the ion plasma frequency. For $\tau = \frac{\omega_{pi}t}{\sqrt{2e}}$ and $C_s = \sqrt{\frac{Zk_B T_e}{M}}$ (ion

sound speed), one obtains the ion front velocity $v_{front} \sim 2C_s \ln(\tau + \sqrt{\tau^2 + 1})$ as well as the

ion front position $x_{front} \sim 2\sqrt{2e} \lambda_{D,0} (\tau \ln(\tau + \sqrt{\tau^2 + 1}) - \sqrt{\tau^2 + 1} + 1)$ as a function of time. In

the asymptotic limit $\omega_{pi}t \gg 1$, $v_{front, \omega_{pi}t \gg 1} \sim C_s (2 \ln(\omega_{pi}t) + \ln 2 - 1)$ and

$x_{front, \omega_{pi}t \gg 1} \sim C_s t (2 \ln(\omega_{pi}t) + \ln 2 - 3)$. The cutoff energy is deduced from the equation for

$v_{front} (\omega_{pi}t \gg 1)$: $E_{max} (1D, isothermal) = 2E_0 (\ln(2\tau))^2$ where $E_0 = Zk_B T_e$. For protons, the

cutoff energy is simply $E_{max_{p+}} (1D, isothermal) = 2k_B T_e (\ln(2\tau))^2$. Therefore, the maximum

ion energy is linearly proportional to the electron temperature, limited by a non-dimensional expansion time.

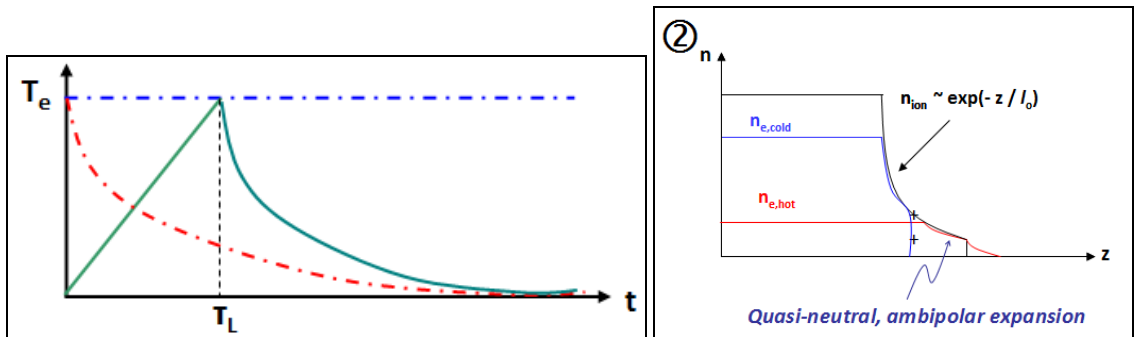


Figure 2-10: (left) Hot-electron temperature profile as a function of time; τ_L corresponds to the pulse duration for various cases: isothermal [117] (blue, dashed and dotted line), adiabatic [118] (red, dashed and dotted line) and 2-phase [119] (green, solid line); (right) Sheath expansion phase (interpreted from [6(b)]).

In [118], the collisionless expansion is assumed to be adiabatic (red curve, Figure 2-10 (left)). The thin foil expands into a vacuum, and has an initial width L . The maximum

proton energy is given by $E_{\max_p+}(\text{1D, adiabatic}) = 4m_p C_s^2 \left(\ln \left(0.32 \frac{L}{\lambda_{D_e}} + 4.2 \right) \right)^2$ from the

fit to the model.

In [119], a 2-phase model is used, which assumes a linearly increasing hot-electron temperature for the duration of the laser pulse, i.e. $T_e(0 < t < \tau_L) \propto t$, and an adiabatic expansion when the laser pulse is turned off to take into account the energy transfer to the ions, i.e. $T_e(t > \tau_L) \propto t^{-2}$ (green curve, Figure 2-10 (left)). In the 2-phase model, 3-D effects

can be added, in order to take into account the hot-electron divergence of the expanding plasma which causes a drop in the hot-electron density. The fit to the data gathered during the experiments in [119] goes as $E_{\max_p+}(\text{Robson, experiments}) \propto I^b$, where $b = 0.5 \pm 0.1$.

These three scaling laws (i.e. 1-D isothermal from [117], 2-phase model [119], 2-phase model with 3-D effects [119]), which give maximum proton energies in MeV as a function of laser intensity in W/cm^2 , are summarized in Figure 2-11. Also shown are experimental data points obtained for various laser energies but for a pulse duration of 1 ps (red dots and blue triangles), as well as data points for which both the laser energy and the pulse duration are varied. At an intensity of $2 \times 10^{20} \text{ W}/\text{cm}^2$, the isothermal model predicts 95 MeV, which is clearly too high; the 2-phase model predicts 60 MeV and the 2-phase model including 3-D effects predicts 40 MeV. Both predictions from the 2-phase model are in the range of proton energies from flat-foil targets obtained on Trident.

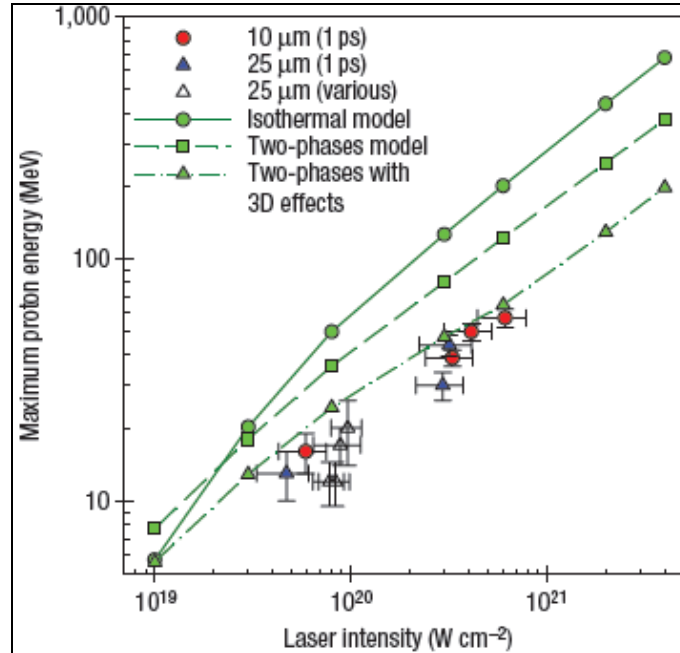


Figure 2-11: Maximum proton energy [MeV] as a function of laser intensity [W/cm^2]; the laser energy is varied and the pulse duration (1 ps) and focal spot are kept constant; the targets are Al, 10 μm thick (red dot) and 25 μm thick (blue triangles); the open triangles correspond to laser shots on 25 μm thick Al targets for which the pulse duration and the laser energy are both varied; the green circles are the predictions of the isothermal plasma-expansion model described by Mora [117]; the green squares correspond to results from a revised form of this 1-D model, using two phases for the electron temperature; the green triangles correspond to results using the same model with 3-D effects mimicked; the error bars on the maximum proton energy arise from combining counting statistics with errors in the proton energy measurements; the error bars on the laser intensity are a combination of the measurement uncertainty in laser pulse energy and estimated shot-to-shot fluctuations in pulse duration [119].

2.3.3 Improving TNSA: target modifications for increasing the proton energy using similar laser conditions

According to our current understanding of the TNSA mechanism, the easiest way to increase the proton energy is to increase the hot-electron temperature T_{hot} ; another way would be to increase the potential of the accelerating sheath, which could be done by increasing the number of electrons at a given T_{hot} , i.e. increase the conversion efficiency. This can certainly be done by using more energetic lasers. One can also vary the laser contrast and add short-pulse prepulses to enhance absorption. But, for a given laser, i.e. for

a given energy and intensity, a few target modifications can be made to increase the maximum proton energy: one can use a conical target geometry [2.3.3.2], thinner flat targets, to make use of the enhanced TNSA [2.3.3.3] and reduced mass targets (RMTs) [2.3.3.4]. Before these target modifications as well as their resulting enhancement in proton energy are described, the PIC technique and the PICLS simulation code are introduced [2.3.3.1].

2.3.3.1 PIC and PICLS Simulations

2.3.3.1.1 PIC simulations: generalities

The Particle-in-Cell (PIC) technique is used to solve a particular class of partial differential equations. The individual particles, or fluid elements, in a Lagrangian frame are tracked in continuous phase-space, while the moments of the distribution such as densities and currents are computed simultaneously on stationary Eulerian mesh points.

In plasma physics applications, such as laser plasma interactions, the PIC method consists of following the trajectories (described by the equation of motion) of the charged and relativistic particles in self-consistent electromagnetic (or electrostatic) fields (described by Maxwell's equations) computed on a fixed mesh [120].

The method typically includes the following procedures:

- Integration of the equations of motion
- Interpolation of charge and current source terms to the field mesh
- Computation of the fields on mesh points
- Interpolation of the fields from the mesh to the particle locations

Since the early days of PIC, it has been shown that the PIC method is susceptible to error from so-called *discrete particle noise* [121]. This error is statistical in nature, and still today,

remains less-well understood than for traditional fixed-grid methods, such as Eulerian or semi-Lagrangian schemes, and prevents PIC codes from being used to treat problems needing low noise.

2.3.3.1.2 PICLS Code

In order to properly computationally model high energy density laboratory plasmas (HEDLP) and laser plasma interactions, PICLS has been designed to solve the following issues:

- to resolve extremely large plasma density ranges, i.e. $\sim 10^{19}$ to 10^{26} cm⁻³ for laser plasma interaction and transport in fast ignition;
- to simulate Coulomb collisions, because these are required to properly simulate energy transport and heating in HEDLP, i.e. to take into account the resistive effects, scattering, etc. Indeed, collisions represent an important heating mechanism in solid density plasmas, which is why an accurate model from the non-relativistic regime to the ultra-relativistic regime is necessary;
- to add dynamic ionization processes, because the plasma electron density and the resistivity depend on the charge state inside the target, as in the case of an ultra-fast heated thin metal target in laser plasma interactions;
- to have strict energy conservation to avoid numerical heating and numerical ionization in HEDLP.

PICLS features binary collisions (fully relativistic) among charged particles, as well as ionization processes [122]. In [122], a “reduced PIC” technique able to reduce the computational cost drastically was proposed to perform simulations on very large density scale plasmas. This concept is based upon collisional damping of kinetic effects in dense

plasmas [123], illustrated in Figure 2-12. Up to a certain density n_{PIC} , the kinetic physics is fully resolved and includes collisional processes. Above n_{PIC} , the kinetic physics becomes less important because of collisional damping, and the simulation becomes more like a Monte-Carlo calculation as the plasma density increases. Below n_{PIC} , kinetic physics is damped at $\sim n_{damp} = 10^{23} \text{ cm}^{-3}$ in hydrogen plasmas and at thermal temperatures under 1 keV [123]. Above n_{damp} , plasma waves are damped and the physics is dominated by collisional processes; it is therefore not necessary to resolve a small scale of the kinetic physics in that case. By setting $n_{PIC} > n_{damp}$, all of the important kinetic physics can be taken into account in the simulation.

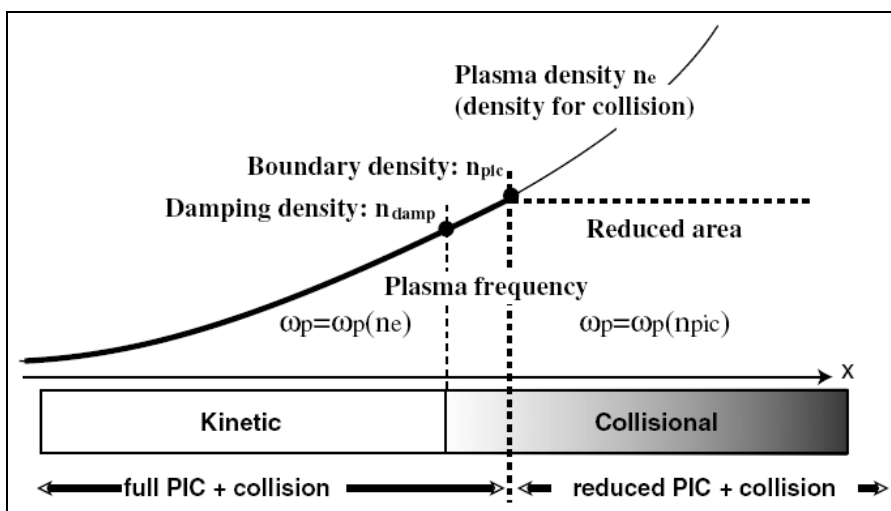


Figure 2-12: Concept of the reduced PIC simulation code: electron density (vertical axis) profile as a function of distance x (horizontal axis), where the physics transitions from being purely kinetic (low density) to collisionally dominated (high density) [122].

2.3.3.2 Cone targets

In Section 5.1, we look in detail at the various cone geometries that have been used so far in cone research, for the generation of electrons, X-rays and protons. Here, we are mentioning some pioneering 3-D PIC simulations performed by Sentoku *et al.* [44] showing how the

cone geometry enhances the electron density: compared to a simple flat-foil target, the laser light is optically guided inside a conical target and concentrated at the tip of the cone, resulting in a large increase (many 10s) in the intensity, in a spot of a few μm (see Figure 2-13 (left)). While the highest energy electrons are driven into the cone wall, the lower energy electrons are accelerated along the target surface and converge to the tip of the cone, enhancing the electron number (see Figure 2-13 (right)). Also, the laser energy can be transferred more effectively to the target electrons with a cone target than with a flat-foil target.

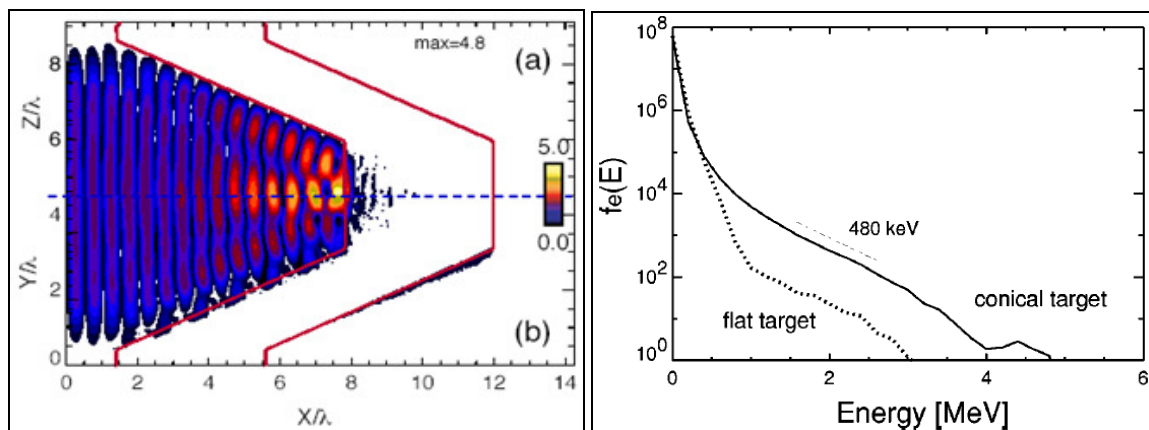


Figure 2-13: At $t = 16\tau$ (left) Contour plots of the square root of the instantaneous electromagnetic energy in the longitudinal space (a) X-Z and (b) X-Y (polarization plane); plots are normalized by the incident laser E-field, E_0 ; the solid lines indicate the initial target shape; (right) Energy spectra of hot electrons in the laser direction for a conical target (solid line) and for a flat target (dotted line); for these spectra, only the electrons present inside a $1 \mu\text{m}$ spot in the central region are taken into account [44].

The hot-electron density at the cone tip is 10 times higher than in a flat-foil target case, due to the convergence of the electron flow guided by the balance between the self-generated quasi-static magnetic fields (the $J \times B$ force pushes the electrons toward the vacuum) and electrostatic sheath fields (which cancels the $J \times B$ force) for relativistic electrons (see Figure 2-14).

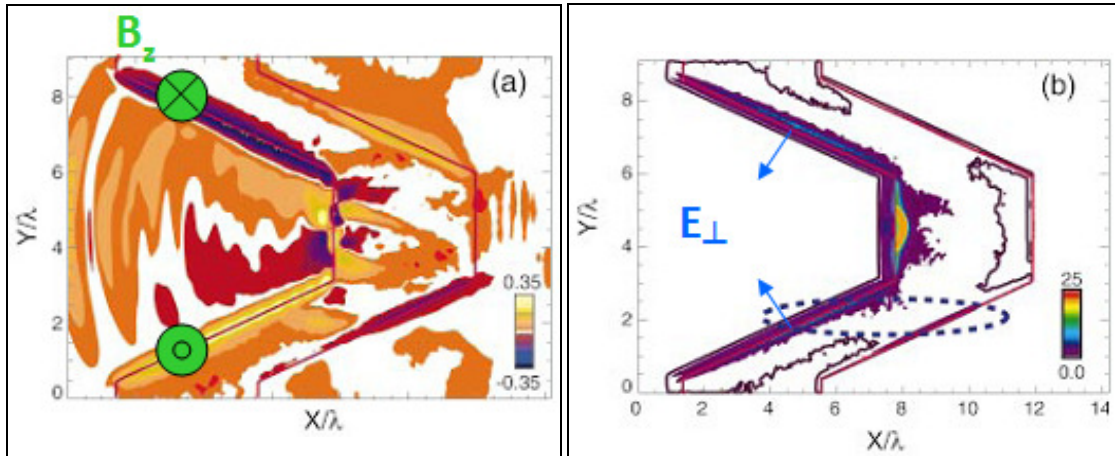


Figure 2-14: At $t = 16\tau$ (left) Contour plot of the quasi-static magnetic field B_z/B_0 ; (right) time-averaged electron energy density $(\gamma-1)n_e/n_0$ [44].

In short, the cone seems to improve laser-target coupling efficiencies and allows for better guiding of the laser light and for hot-electron convergence toward the cone tip. Such an enhancement of the hot-electron population at the cone tip could allow for a more efficient proton acceleration, similarly to what happens in the reduced-mass target case (see Section 2.3.3.4), where the electron density is higher due to the reduced mass of the target, and believed to increase the proton energies. By carefully choosing a target shape, one can control both the electron energy range and the electron directionality.

Note that these PIC simulations were performed at a laser intensity of $\sim 4 \times 10^{18} \text{ W/cm}^2$, which is much lower than the intensity on Trident (post- and even pre-enhancement). Also, the intensity is almost uniform throughout the entire focal spot, as the laser pulse propagates as a parallel beam to the cone tip, with a $6 \mu\text{m}$ spot and a super-Gaussian profile. Because the final size of the cone tip is $3 \mu\text{m}$, the pulse intensity ($I = \mathbf{E}^2$) would increase geometrically by a factor $(6/3)^2$, but since the incoming light and the reflected light overlap, in the perfect reflection case, the ideal focused amplitude is $(6/3) \times 2^{0.5} \approx 2.8$. Due to the resulting concentration of optically reflected light near the central region, the laser is focused to a much smaller spot, $\sim 1 \mu\text{m}$; therefore the maximum value in Figure 2-13 (left)

exceeds the factor 2.8, but is still less than the geometrically expected value of 8.4 ($= (6/1) \times 2^{0.5}$) by the absorption (and hence less than complete reflection).

2.3.3.3 Hot-electron recirculation and enhanced TNSA (ultrathin targets)

The recirculation of the hot electrons has to be taken into consideration even more when the laser pulse duration is sufficiently long (or the target sufficiently thin) for the hot electrons present in the rear-side's sheath to return back to the front-side surface due to target charge-up; in that case, the hot electrons can be re-accelerated by the laser field once they return to the front-side. Figure 2-15 shows schematics taken from [124] of a case where recirculation cannot take place (i.e. when the target thickness L is greater than half the pulse length L_p assuming the electrons travel at about c), and one where recirculation happens, i.e. when the target thickness is smaller than half the pulse length.

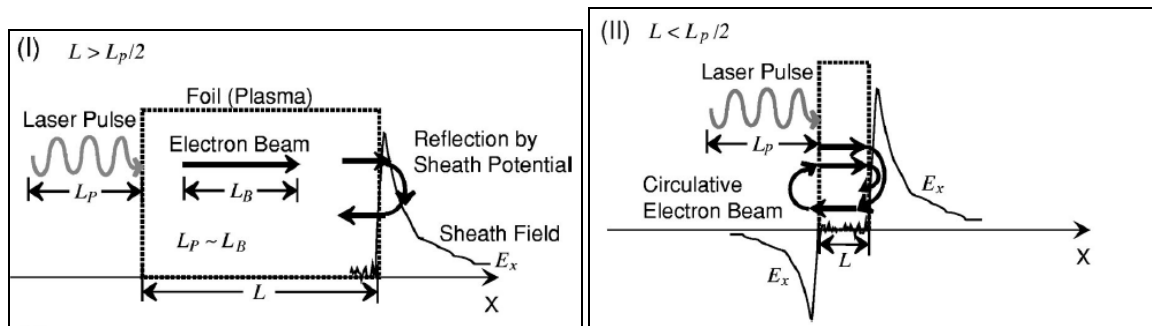


Figure 2-15: Images of the electron circulation inside the target for (I) a thick target and (II) a thin target [124].

Ref. [125] experimentally shows that hot-electron recirculation enhances the sheath acceleration. As illustrated in Figure 2-16, PICLS simulations (see Section 2.3.3.1) from [124] show that, as the target thickness decreases, the proton energy increases. Note that the proton energy increase could also be due to the fact that the electron density is higher because the source size is smaller.

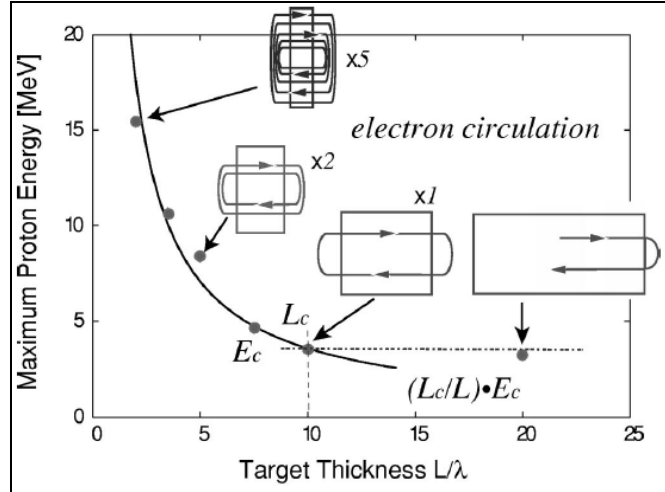


Figure 2-16: Peak proton energy as a function of target thickness. The plots are obtained via 1-D PIC simulations. The back curve shows the empirical scaling, when the target thickness is smaller than the critical thickness [124].

An empirical scaling law for the maximum ion energy, which is valid as long as the target thickness L is smaller than the critical thickness L_c (where $L_c = 2 L_p$), and which remains valid until $L = L_c$ if the electron energy loss is small enough, is also given:

$$E_{ion-back-Sentoku} = \frac{L_c}{L} E_C \sim \frac{L_c}{L} E_{e-max} .$$

The enhanced TNSA [56, 57] corresponds to the best performing TNSA case, which is obtained for an optimized target thickness. This result has been demonstrated for the 100 TW LULI laser ([126], 20 J, 330 fs and 10^6 contrast) and the Callisto laser at LLNL ([125], 10 J, 100 fs and 10^{10} contrast). The best target thickness depends on laser energy, pulse duration, and contrast, as well as hot-electron density. For results obtained on Trident, see Section 5.3.3.1.

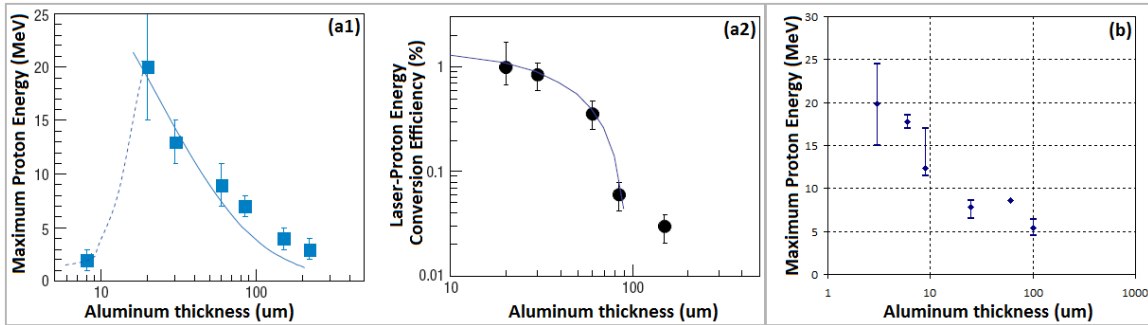


Figure 2-17: LULI data, 100 TW, Al targets (a1) Maximum proton energy [MeV] as a function of target thickness [μm] and (a2) Laser-to-proton conversion efficiency [%] as a function of target thickness [μm]; (b) LLNL data, Callisto, Al targets, Maximum proton energy [MeV] as a function of target thickness [μm].

Ref. [127] shows that a perturbation (caused by a shock) of the rear side of target yields to a degradation of the proton beam; this is exactly what the ASE prepulse does. As the contrast increases, thinner targets can be shot, and higher proton energies can be obtained, most probably due to the recirculation effect. Therefore, it is clear that the target thickness for which the best proton acceleration can be obtained is a gauge of the quality of the contrast: 20 μm (Al) at LULI, 3 μm (Al) at LLNL, 1 μm (Cu) on Trident at intrinsic contrast and 100 nm (Al) and even 5 nm (diamond-like carbon) on Trident at enhanced contrast. There would still be a finite optimum thickness for an infinitely high contrast. Although strong ASE prepulses ruin the proton acceleration, it has been shown [128] that adding some short prepulses before the main pulse arrives to add a little bit of preplasma seems to help the proton acceleration. The key to an efficient ion acceleration is therefore to know which level of preplasma is optimum to enhance laser absorption. The short-pulse fs prepulses are also not as destructive to the target as the longer ASE, since short-pulse ablation is known [129, 130, 131] not to damage any surrounding material, but only a nice area inside the focal spot. Assuming low energy, the shock from a short-pulse is also dissipated in the target quickly as there is no laser “pressure” continuing to push on the target as in the ASE case, which leads to a large shock, able to disrupt the rear-side of the target before the main

pulse arrives. Thus, if low levels of prepulses are used on very thin targets, the targets can survive and still have an electron enhancing preplasma.

Another complementary approach (to be published by T. Kluge) to increase the ion energy is to use ultrathin stacked targets, as shown in Figure 2-18.

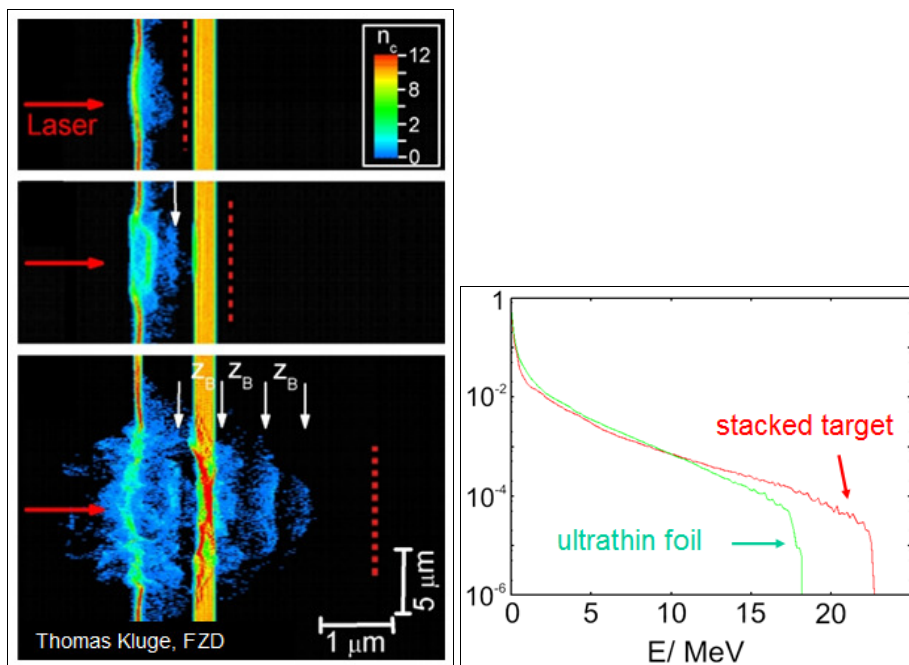


Figure 2-18: Ultrathin and stacked foils (left, from top to bottom) target density as time evolves; (right) Proton spectrum (courtesy of Thomas Kluge).

The first target serves two purposes, assuming it is thin enough: it shapes the laser for the next foil stage, creating a sharp laser temporal profile (instant-on) which can interact very efficiently with the next target; and provides a source of electrons and ions for boosting in the second stage, when spacing is properly chosen. Experiments have not yet been carried out, but PICLS simulations show that stacked foils can yield a 25 % energy difference increase (see Figure 2-18) or a 125 % energy increase.

2.3.3.4 Reduced-mass targets (RMTs)

RMTs are based on a simple idea: for a given laser energy E_L , the target can become hotter if its size is reduced, i.e. if a relatively small number of ions are contained in the target. As an example, a $100 \times 100 \times 100 \text{ } \mu\text{m}^3$ Cu target is $\sim 10^{-5}$ g and contains $\sim 5 \times 10^{18}$ particles, and a $10 \times 10 \times 10 \text{ } \mu\text{m}^3$ Cu target is $\sim 10^{-8}$ g and contains $\sim 5 \times 10^{15}$ particles. The target can be instantaneously ionized (note that for the NIF ARC laser, i.e. 10 kJ in 10 ps, the bulk electron temperature is estimated to be ~ 1 keV).

From the analysis of the $K\alpha$ emission, compared to regular (i.e. many mm^2) flat-foil targets, RMTs have been shown in [132], using the LULI 100 TW laser, i.e. ~ 10 J in ~ 400 fs, to effectively confine the fast electrons inside the target by the induced space charge, i.e. the target quickly charges to several MeVs, confining the remaining electrons. The fast electrons, being electrostatically confined within charge-insulated targets, will deposit their energy over smaller volumes, hence yielding higher temperatures. In the case of [132], the targets are charge-insulated, mass-limited targets, with a total mass of the order of 10^{-5} g; bulk temperatures of 10s eV have been estimated.

RMTs are often mentioned in the realm of the work presented in this dissertation because they are a good comparison to part of the target geometry studied, i.e. the flat top of the flat-top cone (FTC) target, which consists of both a funnel-type cone on top of which an RMT is attached.

As far as proton acceleration is concerned, the assumption, based on x-ray work, is that because the hot-electron temperature is increased (due to the reduced mass of the target), the sheath responsible for the TNSA protons is able to accelerate these protons to higher energies. Unfortunately, besides work using microdroplets [133] and microspheres [134], there is not yet any published data proving that RMTs are indeed enhancing proton

energies, although experiments have been or are being carried out. The following results are preliminary, and have not yet been published.

Experiments on the 100 TW LULI laser at 2ω (10 J and 400 fs) show an enhancement of twice the proton energy using a $80 \times 50 \times 2 \mu\text{m}^3$ RMT compared to that a large flat-foil target, as shown in Figure 2-19 (to be published).

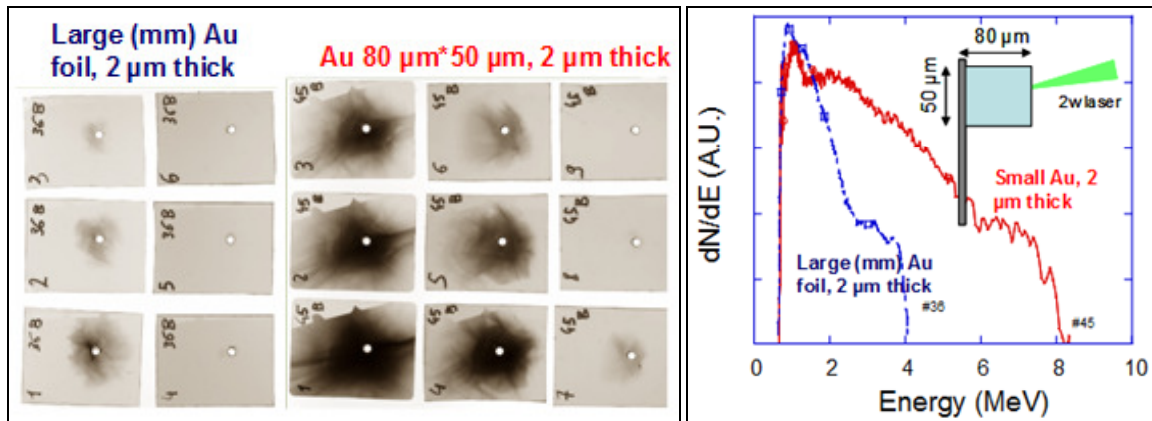


Figure 2-19: RMTs experiments performed on the 100 TW LULI laser in Palaiseau, France in February 2008 (courtesy of Thomas Cowan and Julien Fuchs).

Work on Trident at 80 J and at the intrinsic contrast 10^{-8} , 300 μm diameter and 10 μm thick Cu RMTs show no proton energy enhancement (see Section 5.3.2.1 for the target description and Section 5.3.4.2 for the proton data), and even a poorer proton energy performance by about 5 MeV. At 80 J and at the enhanced contrast 10^{-10} , however, $\sim 250 \mu\text{m}$ diameter and $\sim 10 \mu\text{m}$ thick Cu RMTs seem to improve the proton acceleration (see Section 5.4.2.3 for the target description and Section 5.4.3.4 for the proton data) by about 10 MeV compared to a flat-foil target. However, a major drawback, discovered on Trident, is that the proton beams from RMTs are of poor quality (i.e. less round and less uniform) compared those from flat-foil targets. When the target is small (100 μm on Trident), the strong fields on the target result in a proton emission which is neither round nor uniform. This shows that RMTs can probably enhance the energies of the proton beams assuming a high to very high contrast, if

the proton beam quality can be improved. Of course, an entire campaign should be dedicated to the study of RMTs for target diameters ranging from 50 μm to 500 μm , to determine the optimum RMT size.

This is confirmed by experiments performed on Callisto by Hui Chen *et al.*, and summarized in Figure 2-20.

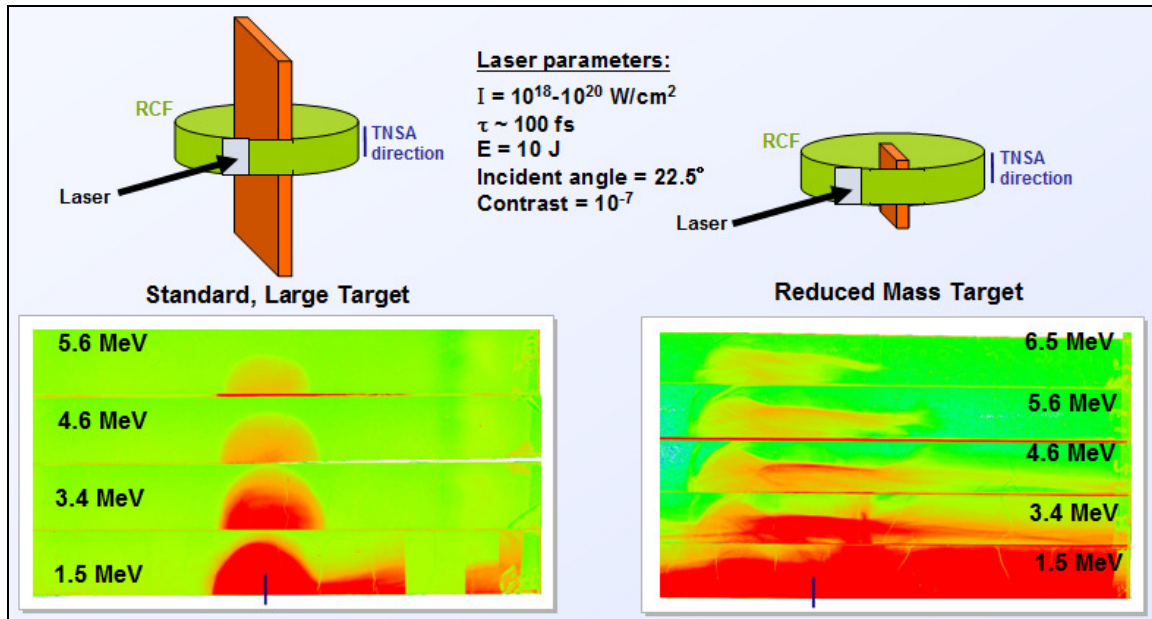


Figure 2-20: RMT experiments performed on Callisto at the Jupiter facility at LLNL in February 2007; the RCF (green) stack was wrapped around the target (orange), and a hole in the RCF allowed the laser (black arrow) to come in at a 22.5° incident angle (courtesy of Hui Chen and Scott Wilks).

At a laser contrast of 10^{-7} (value given by the facility), compared to the proton beam from a regular-size target (i.e. 3-4 mm \times 6-7 mm), the proton emission from a 200 \times 200 μm^2 RMT is slightly higher in energy but non-directional and non-uniform, as shown in Figure 2-20 (bottom). This could be well due to the fact that the laser contrast (i.e. 10^{-7}) is insufficient, causing a large amount of preplasma to wrap around the target and therefore allowing currents and fields to encompass the entire target, destroying the TNSA sheath quality on the rear side.

2.3.3.5 Summary of the techniques used to make the proton acceleration more 1-D-like (or isothermal-like) to enhance the proton energies

Proton acceleration models show that if the acceleration can be made more 1-D or isothermal like, higher proton energies can be obtained at lower laser intensities [119].

As shown in Figure 2-21 with the red arrow, RMTs [2.3.3.4] and thin-foil targets [2.3.3.3] result in an increase of the electron density, and therefore the acceleration becomes more 1-D (2-phase) –like; the 3-D effects act to lower the hot-electron density due to divergence. As shown in Figure 2-21 with the pink arrow, hemispherical-shell targets, RMTs as well as using larger laser spot sizes, yield an acceleration that is more 1-D isothermal like. Finally, as shown in Figure 2-21 with the blue arrow, cone targets [2.3.3.2] yield an increase of the laser intensity at the tip, resulting in a higher effective intensity for a given laser intensity, and therefore a higher proton energy, i.e. for the actual intensity, resulting in a more idealized 1-D acceleration.

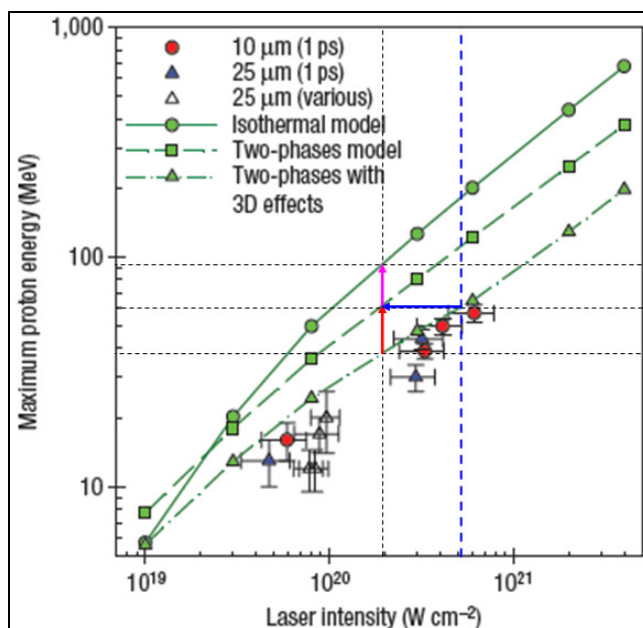


Figure 2-21: Reproduction of Figure 2-11, showing Maximum proton energy [MeV] as a function of laser intensity [W/cm^2] [119] for three models and experimental data; added on the plot are arrows illustrating how various targets allow for increasing the maximum

proton energy as a function of laser intensity: RMTs and thin foils (red arrow); hemispherical shell targets, RMTs and larger laser spot sizes (pink arrow) and cones (blue arrow) increase the laser intensity at the tip, resulting in a higher effective intensity.

2.3.4 Summary of the proton acceleration research since 2000

2.3.4.1 Proton energy scalings as a function of laser intensity for the Trident laser parameters

Figure 2-22 displays, for the Trident parameters (i.e. variable energy, 500 fs and 7 μm diameter focal spot), the maximum proton energy in MeV as a function of laser intensity in W/cm².

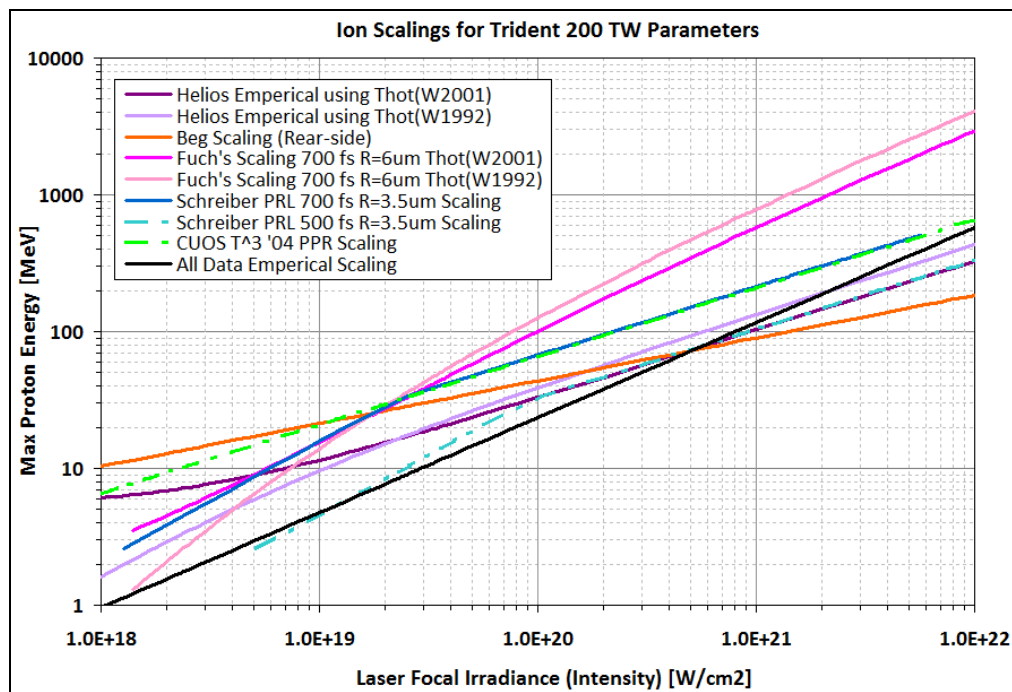


Figure 2-22: Maximum proton energy [MeV] as a function of laser intensity [W/cm²] for various empirical (Helios, Beg, CUOS) and theoretical scalings (Fuchs, Schreiber), as well as the “all data” scaling.

The maximum proton energy is given using the following scalings:

- the scaling from all compiled data (see Figure 1-3), $E_{\max_p+}(\text{All data}) = 6 \times 10^{-13} \times I^{0.6806}$;

- the scaling from the Helios laser data [66], $E_{\max_p+}(\text{Helios}) = [2 - 12.5] \times T_h$, and in Figure 2-22, the scalings $E_{\max_p+}(\text{Helios}) = 10 \times T_h^{W2001}$ as well as $E_{\max_p+}(\text{Helios}) = 10 \times T_h^{W1992}$ are used;

- the Beg scaling [95], i.e. $E_{\max_p+}(\text{Beg scaling, Front side}) = 1.2 \times 10^{-5} \times I^{0.313}$, with a correction (i.e. a factor of 2), based on the results indicating that the front-side accelerated protons are about half the energy of the TNSA accelerated protons [8];

- the CUOS T³ scaling [8], $E_{\max_p+}(\text{CUOS T}^3) = 6.3 \times \lambda \times I_{18}^{0.5}$.

- the Fuchs scaling [126], which is based on a 1-D isothermal expansion [117] (see Section 2.3.2) and which also takes into account the divergence angle of the hot electrons inside the target, the hot-electron temperature, the hot-electron conversion efficiency, the target thickness, the laser spot size and the laser energy E_L : $E_{\max_p+} = 2T_e \left(\ln \left(\tau + \sqrt{\tau^2 + 1} \right) \right)^2$ [117],

where $\tau = \frac{\omega_{pi} t_{acc}}{\sqrt{2e}}$ is the normalized acceleration time and $\omega_{pi} = \sqrt{\frac{n_{e,0} Z e^2}{M \epsilon_0}}$ the ion plasma

frequency; T_e and $n_{e,0}$ are the temperature and density of the hot electrons driving the rear-surface expansion; $T_e = T_h^{W1992}$ (although $T_e = T_h^{W2001}$ should be used) and

$n_{e,0} = \frac{N_e}{c \tau_L S_{sheath}} = \frac{\eta E_L}{c \tau_L S_{sheath} T_h}$, where $t_{acc} = 1.3 \tau_L$, $\eta = 1.2 \times 10^{-15} \times I^{0.74}$ (conversion

efficiency into hot electrons) and $S_{sheath} = \pi (r_0 + d \tan \theta)^2$ (surface of the sheath over which

the hot electrons spread); for lasers with a wavelength of $\sim 1 \mu\text{m}$, $\eta = 1.2 \times 10^{-15} \times I^{0.74}$ and

the maximum conversion efficiency $\eta = 0.5$ is reached for $I = 3.1 \times 10^{19} \text{ W/cm}^2$; S_{sheath}

depends on the half-angle divergence of the hot electrons inside the target θ , the target

thickness d and the initial radius r_0 of the zone over which the electrons are accelerated at the target front surface, i.e. the laser spot size.

- the Schreiber scaling [135], which uses an analytical model based on a radially confined surface charge set up by laser accelerated electrons on the target rear side; the only input parameters are the properties of the laser pulse and the target thickness: using the fact that the laser energy $E_L = P_L \tau_L$ is converted with an efficiency η into hot-electron energy,

$$N_e k_B T_e = \eta E_L, \quad E_{\max_p^+}(\text{Schreiber}) = 2mc^2 \sqrt{\frac{\eta P_L}{P_R}}, \quad \text{where } P_R = \frac{mc^3}{r_e} = 8.71 \text{ GW is the}$$

relativistic power unit and r_e the classical electron radius.

As we can see from Figure 2-22, at the Trident (80 J) laser intensity of $\sim 2 \times 10^{20}$ W/cm², the scalings estimate the maximum proton energy to be in the range of ~ 38 MeV (All data, empirical scaling) to 225 MeV and (Fuchs scaling), the latter being clearly too high. The scaling the closest to results obtained on Trident at 80 J (intrinsic or enhanced contrast) using flat-foil targets is the Schreiber scaling which estimates ~ 60 MeV.

2.3.4.2 Proton energy measurements so far

The following trends (see Figure 2-23, Figure 2-24 and Figure 2-25) stem from data points (I) collected from most published papers in the literature concerning laser-accelerated protons via the TNSA mechanism (i.e. accelerated from the rear surface)[6, 7, 8, 17, 119, 136] (◆s), as well as data collected on the Trident laser system (●s) and on the Omega EP laser (■s), to understand global trends in proton acceleration. A 60 MeV empirical barrier [9] is clearly noticeable (dashed dark red horizontal line in Figure 2-23 and Figure 2-25). This barrier has not been surpassed in the previous 10 years using flat-foils targets, although some of the data has been acquired with a significant amount of laser energy and intensity:

~ 500 J ($\sim 3 \times 10^{20}$ W/cm²) and ~ 1000 J ($\sim 5 \times 10^{18}$ W/cm²). This empirical barrier exists due to limitations in the laser technology: e.g. limitation in laser energy for very short pulse durations and limitation in spot size and focusability for very high laser energies. It could well be that at intensities of $\sim 10^{23}$ W/cm², the proton energies would be much higher than ~ 60 MeV, but at this point in time, for intensities as high as 5×10^{20} W/cm², ~ 60 MeV from flat-foil targets is the maximum energy obtained for the past decade. This dissertation presents data that has reproducibly broken this barrier for the first time, using novel cone targets (see Section 5.4) at a laser energy of 80 J and a laser intensity of 1.3×10^{20} W/cm².

2.3.4.2.1 Maximum proton energy as a function of laser intensity

Figure 2-23 shows data from the above references all together on a plot of laser intensity versus maximum proton energy. Plotted along with the pulse duration groupings (\blacklozenge s), i.e. are two sets of Trident data from flat-foils (\bullet s), both at the intrinsic contrast, and both intensity scalings: one (orange \bullet s) is an energy scan, keeping the spot size constant; and the other (purple \bullet s) a spot size scaling, keeping the energy constant (with slight variation in pulse duration due to an uncooperative stretcher). It is interesting to note that the energy scan falls along the grouping, and the spot size scaling is up and to the left of those points along with the Omega EP (10000 fs, light blue \blacksquare s) kJ data.

The fits yield the following:

$$E_{\max_p+}(\text{All data}) \approx 6 \times 10^{-13} \times I^{0.6796},$$

$$E_{\max_p+}(\text{Trident, Constant spot and pulse duration}) \approx 9 \times 10^{-10} \times I^{0.5318},$$

$$E_{\max_p+}(\text{Trident, Constant energy}) \approx 1 \times 10^{-4} \times I^{0.2829},$$

$$E_{\max_p+}(\text{Omega EP, Constant spot and pulse duration}) \approx 3 \times 10^{-7} \times I^{0.4355}.$$

This shows that for Trident, varying the spot size or the laser pulse duration does not affect the maximum proton energy as much as varying the energy; although it could also mean that the real intensity value is not correctly estimated for larger spot sizes.

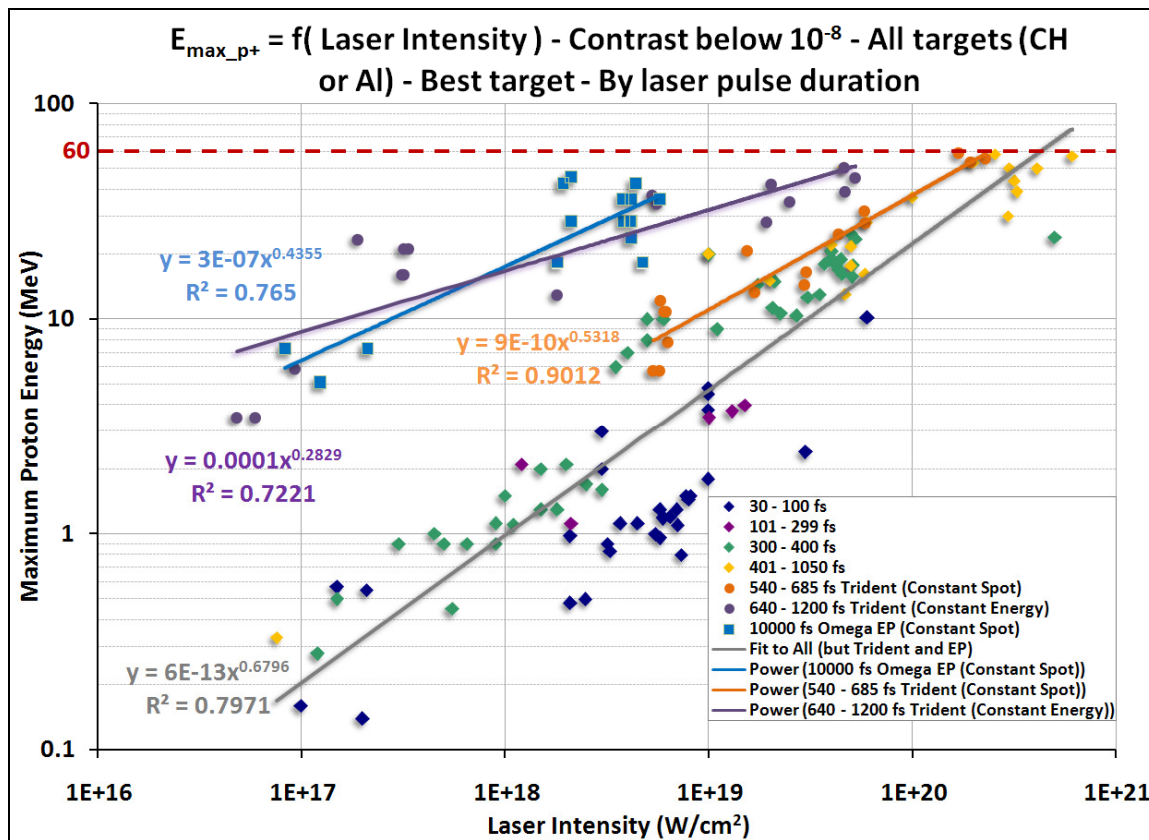


Figure 2-23: Maximum proton energy [MeV] as a function of laser intensity [W/cm²] for all lasers in the world, grouped by pulse durations, with low contrast (i.e. lower than 10⁻⁸). The data plotted is taken from [1, 3-4], and [9] and is represented by ♦s. It is broken down into pulse duration groups: 30-100 fs (dark blue ♦s); 101-299 fs (purple ♦s); 300-400 fs (green ♦s); 401-1050 fs (yellow ♦s). Also plotted are the Trident data at intrinsic contrast (●s) and the Omega EP data (■s): Trident data energy scan, for 540-685 fs and constant spot size (orange ●s), Trident data spot size scan at 640-1200 fs for constant energy (purple ●s) and Omega EP data energy scan for 10000 fs and constant spot size (light blue ■s). Four fits are shown, one for all the ♦ data in grey (which excludes any of the Trident or Omega EP data), one for the EP data in blue, one for the energy scan on Trident in orange, and one for the spot size scan on Trident in purple.

Figure 2-24 [17] shows the performance of the newly commissioned 200 TW Trident laser system in terms of maximum proton energy [MeV] as a function of laser intensity [W/cm²], compared to three published scaling laws, the Fuchs scaling at 700 fs and 580 fs [126], the

Mora scaling [117] and the Schreiber scaling at 600 fs [135]. The October 2007 values (green triangles) are from shots where the spot size was varied but the energy was relatively constant with an average pulse duration of 1300 fs, without the deformable mirror installed (making the smallest spot size slightly larger, FWHM of 12 μm , 50 % of encircled energy). The March 2008 data (blue squares) are from shots where the laser energy was varied but the focus was kept constant, with an average pulse duration of 620 fs. Most values reported in the literature above $1 \times 10^{19} \text{ W/cm}^2$ fall below these scalings. A fit to the March 2008 Trident data was performed, and the following power law equation was obtained: $E_{\text{max}_p+}(\text{Trident, 200 TW, March 08}) \approx 2.8347 \times 10^{-10} \times I^{0.565}$.

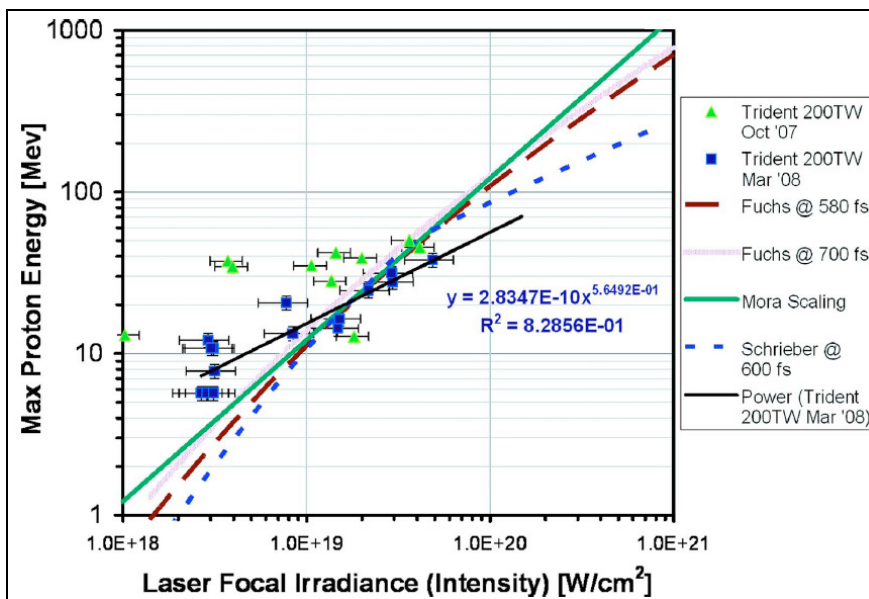


Figure 2-24: Performance of the 200 TW Trident laser system, in terms of maximum proton energy [MeV] as a function of laser intensity [W/cm²], compared to three published scaling laws [17]. The October 2007 data (green triangles) and the March 2008 data (blue squares) are from the new Trident 200 TW commissioning runs. The October 2007 values are from shots where the spot size was varied but the energy was relatively constant with an average pulse duration of 1300 fs, without the deformable mirror installed (making the spot size slightly larger, FWHM of 12 μm , 50 % of encircled energy). The March 2008 data are from shots where the laser energy was varied but the focus was constant, with an average pulse duration of 620 fs. Most reported values above $1 \times 10^{19} \text{ W/cm}^2$ fall below these scalings. A fit to the March 2008 Trident data gives a curve with an exponent of 0.565.

2.3.4.2.2 Maximum proton energy as a function of laser energy

Figure 2-25 assembles again the same data from the literature into a plot of laser energy versus maximum proton energy (all \blacklozenge s), as well as some Trident data (orange \bullet s) and some Omega EP data (blue \blacksquare s). Here, one can see that the data actually groups much better in terms of their deviation from the fit, which basically follows the ponderomotive potential of $\sim I^{0.5}$ and thus $\sim E^{0.5}$, when not accounting for pulse duration. This plot is extremely important, and it should not be understated that the energy is much more important for producing high energy ions than is purely the intensity; alternatively, the spot size and pulse duration. These quantities are folded into the intensity calculation, adding degrees of error and complication. From Figure 2-23, we know from the Trident spot size scan that the spot size affects the maximum ion energy to a lesser extent ($\sim I^{0.28}$ compared to $\sim I^{0.53}$ for Trident) for the same effective intensity change, than the energy does. The data in Figure 2-25 clearly shows that pulse duration is not very important (with the possible exception of the EP data). Also, as each of these points was generally focused to as close to the diffraction limit as possible (again with the notable exception of the Omega EP data, which is many 10s of times the diffraction limit), and thus achieving the maximum intensity for that given energy and pulse duration, it is reasonable to assume that this is the important factor affecting the coupling of laser energy into the electrons. The Trident data only begins to deviate significantly from the group at very small energies, i.e. when dropping below the relativistic limit. The outlying Omega EP data illustrates what a large spot size can do, as it is very large compared to the diffraction limit of the EP optics, though the pulse duration is relatively long (~ 10 times the longest pulse of the other data), both of which could compromise the laser's coupling into the hot electrons: the larger spot size reduces the intensity, and thus hot-electron generation, and also spreads the sheath field out over a

much larger initial area on the back surface; and the long pulse duration may move the acceleration mechanism into a different regime, as the majority of acceleration is over in about 1 ps according to most PIC simulations. The problem with 10 ps is that simulations take too long to run in this regime, so it is as yet poorly studied.

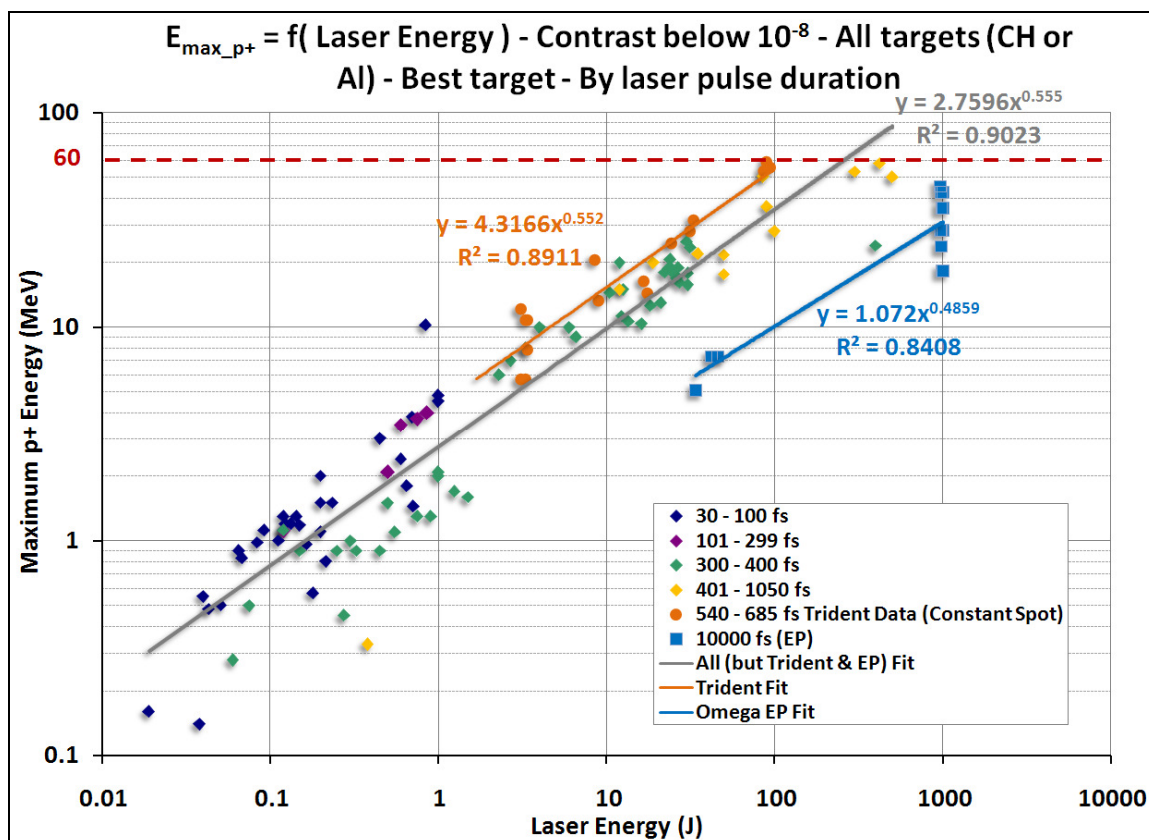


Figure 2-25: Maximum proton energy [MeV] as a function of laser energy [J] for all lasers in the world, grouped by pulse durations, with low contrast (i.e. lower than 10^{-8}). The data plotted is taken from [1, 3-4], and [9] and is represented by \blacklozenge . It is broken down into pulse duration groups: 30-100 fs (dark blue \blacklozenge s); 101-299 fs (purple \blacklozenge s); 300-400 fs (green \blacklozenge s); 401-1050 fs (yellow \blacklozenge s). Also plotted are the Trident data at intrinsic contrast (\bullet s) and the Omega EP data (\blacksquare s): Trident data energy scan, for 540-685 fs and constant spot size (orange \bullet s); and Omega EP data energy scan for 10000 fs and constant spot size (light blue \blacksquare s). Three fits are shown, one for all the \blacklozenge data in grey (which excludes any of the Trident or Omega EP data), one for the EP data in blue and one for the energy scan on Trident in orange.

3 THE TRIDENT LASER SHORT-PULSE BEAM-LINE

3.1 Brief overview of the Trident laser system

The Trident laser [137, 138] is a neodymium-glass laser system, operating at the fundamental wavelength of 1054 nm. As suggested by its name, Trident consists of three high-energy beams: two long-pulse beams, with a final amplifier aperture of 14 cm, and one short-pulse beam, with final aperture of 10 cm. These three beams can be delivered separately or all simultaneously into two independent target experimental areas. The shot cycle is ~ 45 minutes, and the facility performs ~ 1000 shots a year. A new 4th probe beam is also available at 50 mJ and 500 fs.

Multiple oscillators are available to drive these beam-lines with pulse lengths ranging from 0.5 ps – 10 μ s at 1054 nm. Figure 3-1 shows the range of energy and pulse durations available at the Trident laser facility. The maximum output energy of each beam is determined by the beam size and the pulse length. At 1054 nm, the long-pulse beam-lines are capable of producing up to 500 J per beam at 10 μ s (the red dotted line in Figure 3-1 indicates that an output of > 1000 J is possible, but that capability for the μ s beam has never been used in experiments), 500 J at 1054 nm and 250 J at 527 nm in 5-10 ns, and approximately 100 J at 1054 nm and 70 J at 527 nm in 100 ps. Since the Trident upgrade, which took place in 2007, the 1054 nm short-pulse beam is capable of producing up to 100 J (depending on pulse duration limited by the damage threshold of the dielectric gratings, and 95 % transmissive turning mirror), and is configured with a vacuum dielectric grating compressor for chirped-pulse compression as part of the chirped-pulse amplification scheme (see Section 3.3.2) to produce pulses as short as 500-600 fs with up to 200 TW of

power, in a $\sim 7 \mu\text{m}$ diameter FWHM focal spot (containing approximately 50 % of laser the energy), leading to intensities on target $> 10^{20} \text{ W/cm}^2$.

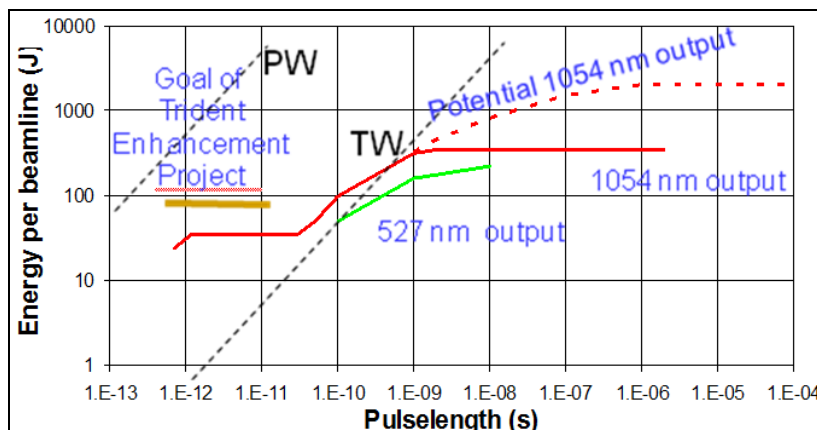


Figure 3-1: Diagram of the Trident pulse lengths [s] and energies [J] (by Robert Gibson).

Nonlinear crystals are available to produce harmonics of the fundamental laser frequency in the long-pulse A and B beam-lines. Experiments performed with pulses in the nanosecond range often use the second harmonic of the laser frequency at 527 nm to reduce unintended electron heating, called pre-heat, due to preplasma (see Section 3.3.1). Up to 250 J of light at 527 nm is available in each beam in pulses of a 5 - 10 ns. The short-pulse C beam-line can be modified to produce a diagnostic beam of high optical quality which, at lower energies and longer pulse durations (a few ps), has been used to produce 2nd, 3rd, and 4th harmonics of the fundamental depending on the experiment.

The Trident Facility has two working target chambers, the South Target Area, and the North Target Area (see Figure 3-2), with a third being built, the West Target Area; allowing two simultaneous experiments to be performed or allowing one experiment to be set up while the other is being performed. Both the South Target Chamber and the North Target Chamber can be used for ns and μs pulse experiments. A large array of optical and x-ray diagnostics is available on both chambers. The spherical North Target Chamber is also used

for sub-ps ultra-high intensity experiments. This is where the experiments described in this dissertation took place.

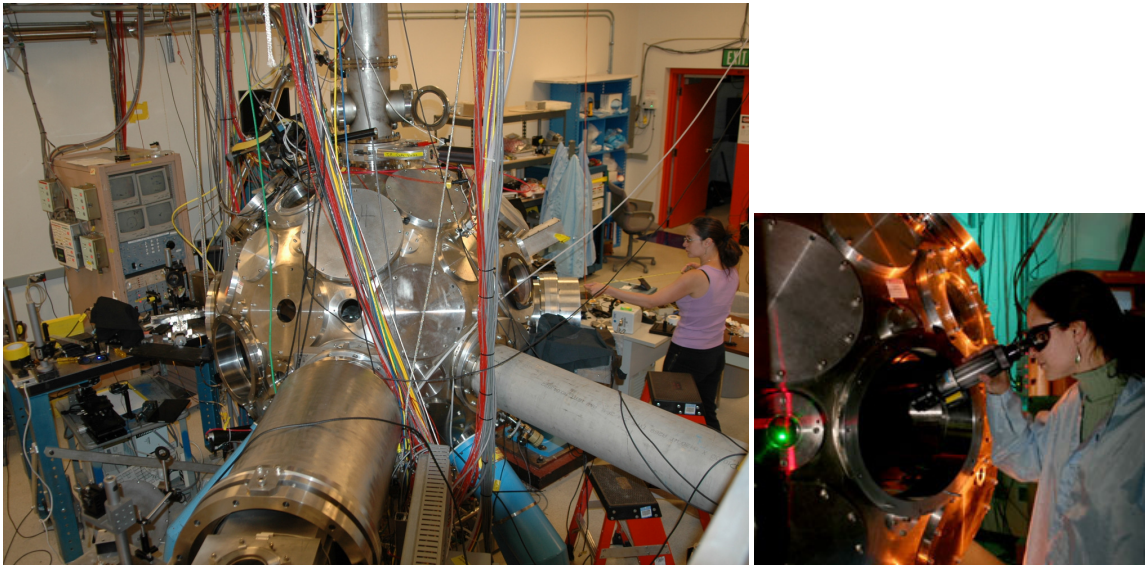


Figure 3-2: Trident's North Target Area and Chamber.

3.2 The Trident short-pulse beam-line: pre-enhancement and post-enhancement at intrinsic contrast ($\sim 10^{-8}$)

The CPA technique was developed for lasers ~ 25 years ago, by D. Strickland and G. Mourou [139]. As illustrated in Figure 3-3, the initial short pulse is stretched, amplified, and finally recompressed, to achieve high energy and short pulse duration. This section describes the entire laser chain, and the differences between the pre- and the post-enhancement laser system.

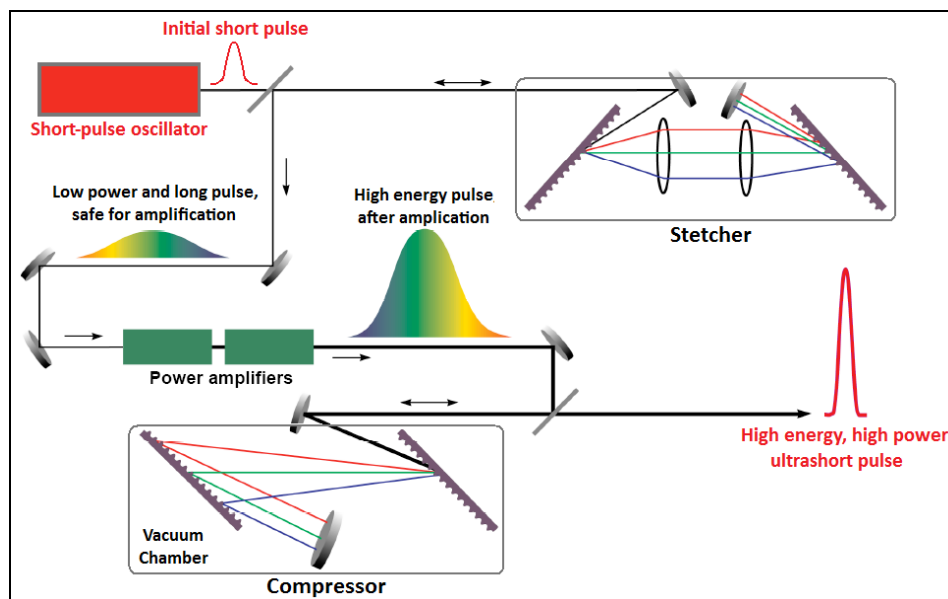


Figure 3-3: Chirped Pulse Amplification (CPA) scheme.

Figure 3-4 shows, to scale, the front-end of the short-pulse laser in the original intrinsic contrast configured for CPA. The laser contrast is defined as the intensity of the main pulse divided by the intensity of the amplified stimulated emission (ASE) pedestal or prepulses. The modifications made to the front-end to improve the laser contrast are presented in Section 3.3.1.

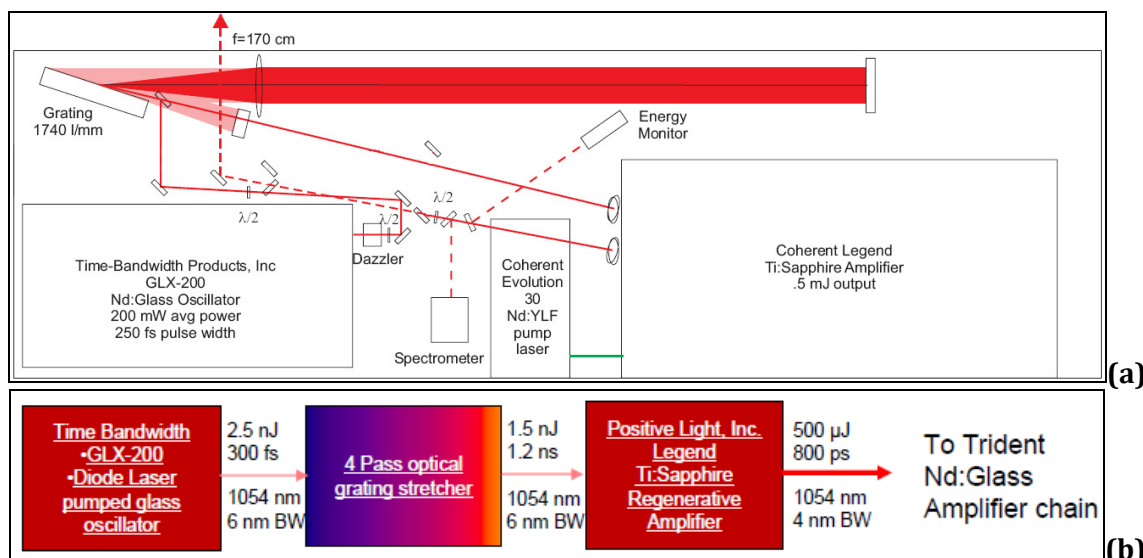


Figure 3-4: Short-pulse laser front-end (version 0), to scale, pre-enhancement, intrinsic contrast (by Randall P. Johnson).

The front-end oscillator is a CLX-200 Nd:Glass laser diode pumped oscillator, from Time Bandwidth Products. It is pumped by 2 W of 800 nm light and outputs 0.2 W in ~ 200 fs pulses. The pump laser excites a Nd:Glass crystal in the oscillator cavity (see Figure 3-5), which lases in a mode-locked configuration at $1.054 \mu\text{m}$ and 76 MHz. This was first installed in 2005 and is the second oscillator.

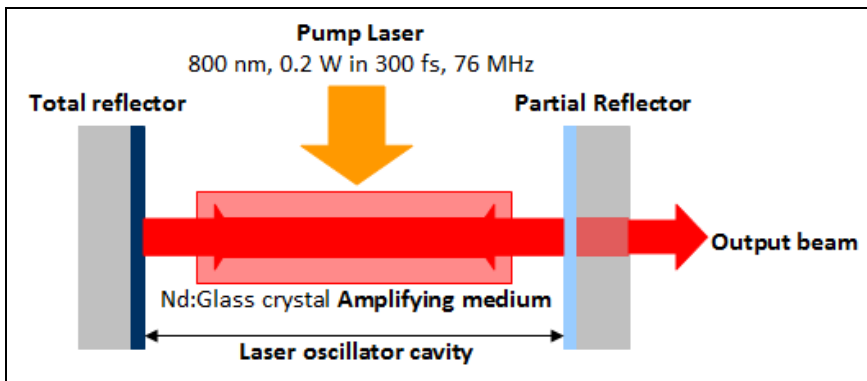


Figure 3-5: Laser oscillator cavity.

This pulse train is sent from the oscillator to the stretcher (one grating and one $f=170$ cm lens), where it is stretched out temporally by 4 passes on a single 1740 lines per mm grating (post-enhancement) to match the dielectric compressor gratings to approximately 800 ps (pre-enhancement: 1480 lines per mm to match the gold compressor gratings). The stretched pulses are then down-selected from 76 MHz to 150 Hz via a Pockels cell and amplified in a Ti:Sapphire regenerative amplifier, also called a *regen* (see Figure 3-6), after which it is down-selected again to 10 Hz for injection into the OPA. The 10 Hz pulse train from the stretcher is then amplified in a Positive Light Legend Ti:Sapph *regen*, to a level of 1 mJ at $1.054 \mu\text{m}$. The *regen* is pumped at 150 Hz by a 15 mJ pump laser at 527 nm, the Coherent Evolution 30, using a Nd:YLF crystal.

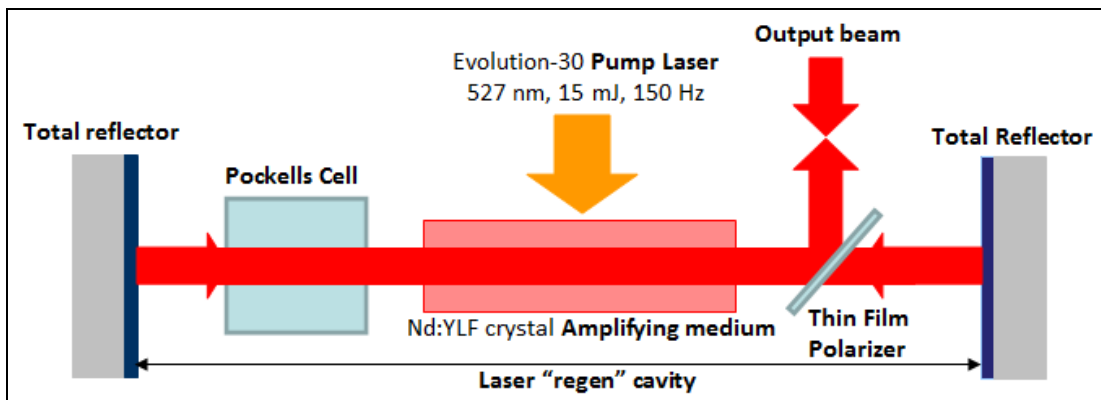


Figure 3-6: Laser *regen* cavity.

3.2.1 The Trident laser system pre-enhancement

Figure 3-7 shows the complete diagram of the three Trident laser system beam-lines, pre-enhancement. After the *regen*, the pulse train is down selected for either 10 Hz or single shot. The 10 Hz simply propagates through the system as an alignment beam, but a single shot is propagated through the system after the rods and disks have been pumped by the flash lamps.

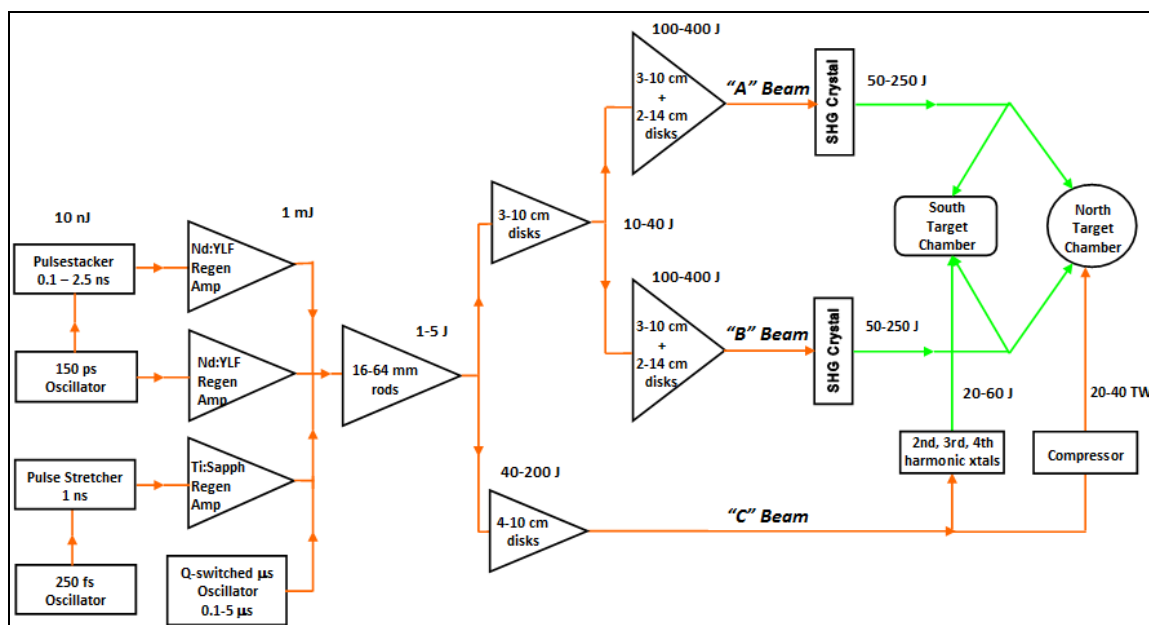


Figure 3-7: Block diagram of the Trident CPA laser system, pre-enhancement, intrinsic contrast, with pulse train optics (by Randall P. Johnson).

As illustrated in Figure 3-7, the *regen* output is coupled into the amplification chain, where it is amplified in 4 neodymium doped glass rods (Nd:Glass) with diameters 16, 25, 45, and 64 mm, up to 5 Joules. Next, the pulse is split in the switch yard to the C beam line and is amplified to 40 J. The amplified pulse then enters the air compressor, located in the North Target Area. The compressor uses a pair of 40 cm in diameter gold gratings, with 1480 lines per mm, to recompress the pulse to $\sim 500\text{-}600$ fs full width at half maximum (FWHM). It has an energy damage threshold of 0.1 J/cm^2 . This process is lossy, and has an energy through-put of $\sim 50 \%$, leaving a compressed pulse of about 20 J.

At 20 J and 500 fs, the power is $\frac{20 \text{ J}}{500 \text{ fs}} = 4 \times 10^{13} \text{ W}$, the unfocused beam has a diameter of

$\sim 14 \text{ cm}$, and the unfocused intensity is $\frac{20 \text{ J}}{500 \text{ fs} \times \pi \times (7)^2 \text{ cm}^2} = 2.6 \times 10^{11} \text{ W/cm}^2$. The

compressor is coupled via a vacuum spool with a CaF window to the North Target Chamber. The laser is sent through that CaF window into vacuum to minimize nonlinear index of refraction effects in air, which could lead to filamentation, self-phase modulation, and phase front distortion (B-integral), which happen for laser beam powers greater than or equal to a few GW [140 and 141, pages 380-382].

Two steering mirrors deliver the $\sim 14 \text{ cm}$ diameter laser beam to the $f^{\#} 3$ off-axis parabola in a diving configuration to save space, resulting in a compound angle (up-down and side-to-side) onto the target. The spot is $\sim 14 \mu\text{m}$ in diameter with $\sim 50 \%$ of the energy in it. It is ~ 2.1 times diffraction limited; however, using the spot value of $\sim 40 \mu\text{m}$ in diameter with $\sim 86 \%$ of the energy in it, it is ~ 5.2 times diffraction limited. This is due to the fact that the real beam is not a true Gaussian.

In a vacuum, the diffraction limit of a Gaussian beam is given by $d_0(86\%) \sim 2.44 f^\# \lambda$ [141, pages 675-676 and 142], where the f number, i.e. $f^\#$, of the focusing optics (i.e. parabola) is given by $f^\# = \frac{f}{D}$. The focal length of the focusing optic is f and D is the size of the beam on

the focusing optics. Also, $d_0(FWHM) \sim \frac{2.44}{\sqrt{2 \ln 2}} f^\# \lambda$, i.e. $d_0(FWHM) \sim 2.07 f^\# \lambda$. So, for

the Trident parameters, we have $d_0(86\%) \sim 7.71 \mu\text{m}$ and $d_0(FWHM) \sim 6.55 \mu\text{m}$.

The Gaussian beam divergence is given by $\Theta = 2\theta = 2 \frac{w_0}{Z_R}$, where w_0 is the waist (radius)

of the laser beam and Z_R is the Rayleigh length or range $Z_R = \frac{\pi w_0^2}{\lambda}$, which corresponds to

the distance from the beam waist, in the propagation direction, where the beam radius is increased by $\sqrt{2}$ (see Figure 3-8 [141 page 669, 142]). In the case of Trident, for a $7 \mu\text{m}$

diameter focal spot, the Rayleigh range of the laser is $Z_R(R = 3.5) = \frac{\pi w_0^2}{\lambda} \sim 36 \mu\text{m}$. For a

$14 \mu\text{m}$ diameter focal spot, it becomes $Z_R(R = 7) = \frac{\pi w_0^2}{\lambda} \sim 146 \mu\text{m}$.

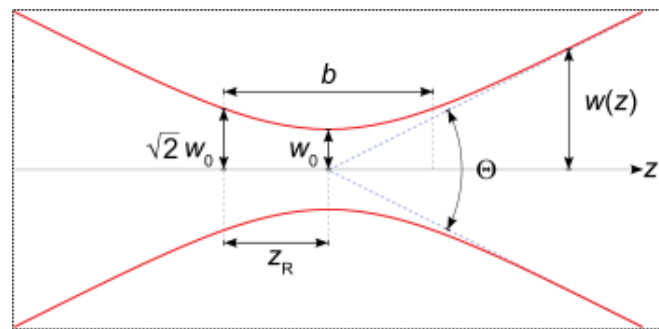


Figure 3-8: Gaussian beam: w_0 is the waist, Θ the divergence, and Z_R the Rayleigh range.

3.2.2 The Trident laser system post-enhancement

Figure 3-9 shows the complete diagram of the three Trident laser system beam-lines, post-enhancement. The main drivers behind the enhancement were the acquisition of dielectric gratings that could support more laser power, and with that, the need for a vacuum compressor. The change from gold gratings to dielectric ones also necessitated a change in the laser polarization from *P*-polarization to *S*-polarization respectively.

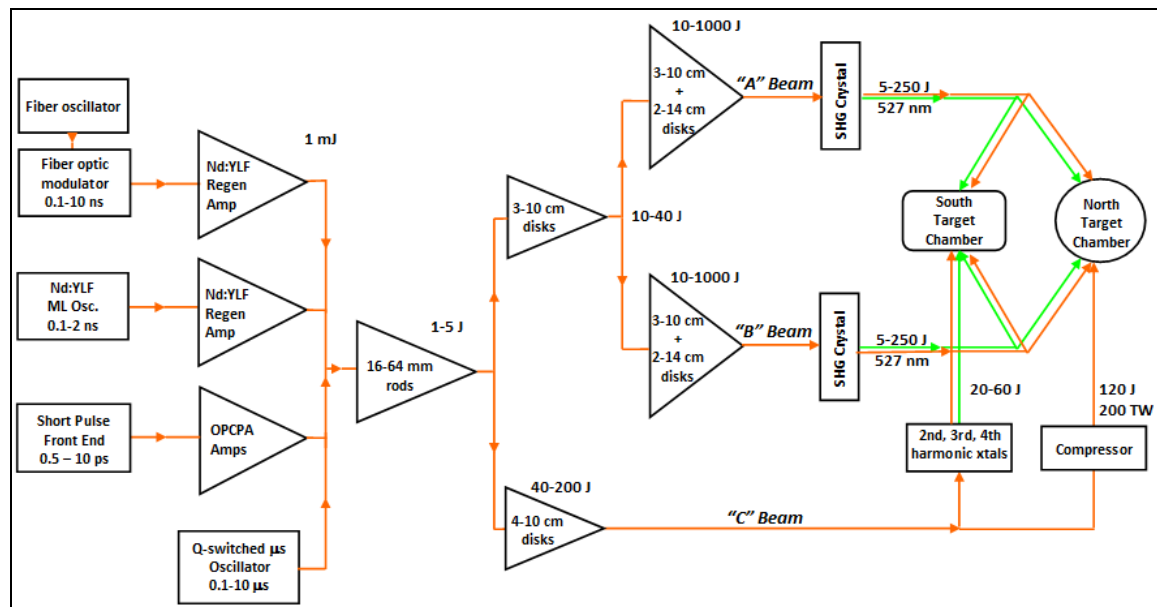


Figure 3-9: Block diagram of the Trident CPA laser system post-enhancement, intrinsic contrast, with pulse train optics (by Randall P. Johnson).

Between the end of 2005 and the end of 2007, the Trident short-pulse beam facility was upgraded in energy to produce ~ 100 J in ~ 500 fs, leading to powers of ~ 200 TW.

As illustrated in Figure 3-9, the *regen* output is coupled into the amplification chain, where it is amplified in four neodymium doped glass rods (Nd:Glass) with diameters 16, 25, 45, and 64 mm, up to 5 Joules. An additional 10-cm-diameter disk amplifier was added to the existing three to increase the energy available in the laser pulse to over 150 J.

An elevated optical transport system was installed between the conversion table and the new vacuum compressor to allow easy access to all components in the laser and target bays. The amplified laser beam is brought back to the ground level through an optical periscope and enters the 1.5×1.5×3 m³ compressor vacuum chamber, located in the North Target Area. The vacuum compressor uses a pair of 40×80 cm² dielectric gratings (1740 lines/mm) to recompress the pulse to ~ 500 fs full width at half maximum (FWHM), as measured by the second order auto-correlator technique [143]. The vacuum compressor is attached to the North Target Chamber with a vacuum tube. At 80–100 J and 500 fs, the

power is $\frac{[80-100]\text{J}}{500\text{ fs}} = [1.6-2]\times 10^{14}\text{ W}$, the unfocused beam has a diameter of ~ 20 cm,

and the unfocused intensity is $\frac{[80-100]\text{J}}{500\text{ fs}\times\pi\times(10)^2\text{ cm}^2} = [5-6.3]\times 10^{11}\text{ W/cm}^2$. The pulse

has to be under vacuum at the compression stage to avoid air break-down, which happens for $I > 6\times 10^{11}\text{ W/cm}^2$ at atmospheric pressure, i.e. 760 torr [144]; and to minimize nonlinear index of refraction effects in air, which, as we already saw in the last section [3.2.1], could lead to filamentation, self-phase modulation, and phase front distortion (B-integral), which happen for laser beam powers greater than or equal to a few GW.

Two steering mirrors (one in the compressor and one in the target chamber) deliver the 20 cm diameter laser beam to the $f^{\#} 3$ off-axis parabola. The beam propagates to the target at either normal incidence (0°) or at a 22.5°. To obtain a small focus spot, a deformable mirror (see Section 3.4.5) was added to the system, in late 2007, in the amplification chain to correct for distortions in the beam path caused by thermal heating of the amplifiers. The resulting spot is shown in Figure 3-19. The spot is ~ 7-9 μm in diameter with ~ 50 % of the energy in it, and therefore ~ 1.25 times diffraction limited; however,

using the spot value of $\sim 28 \mu\text{m}$ in diameter with $\sim 86 \%$ of the energy in it, it is ~ 3.6 times diffraction limited. Again, this is due to the fact that the real beam is not a true Gaussian.

Figure 3-10 shows the updated components in the laser system.

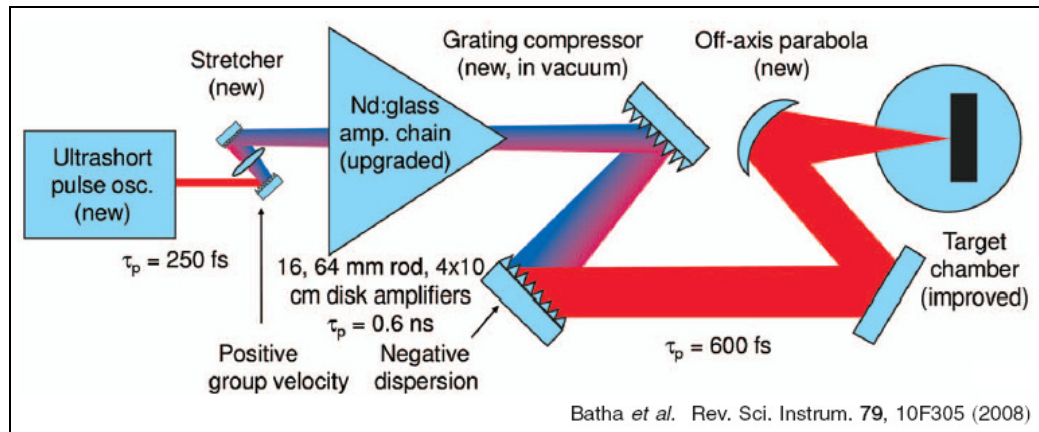


Figure 3-10: Trident short-pulse beam-line generating 200 TW after the enhancement, which consisted in the addition of a new front-end, another amplifier, and a vacuum compressor. The optical pulse length is indicated along the beam path.

3.3 Improving the laser contrast

As described in Section 3.3.1, target preionization can occur if the prepulse intensity is high enough, i.e. for $I_{prepulse} > 10^{10} \text{ W/cm}^2$, so improving the laser contrast is useful and even necessary for allowing one to shoot certain types of targets (e.g. ultrathin targets and cone targets), and to help the modeling of the experiments, by reducing or eliminating almost all of the preformed plasma (also called preplasma), so that the laser can interact with a target that is as clean as possible (similar to an ideal simulation). It is during the *regen* amplification stage of a CPA laser beam, due to the large amount of gain ($\sim \text{nJ}$ to 1 mJ), that most of the pedestal and laser prepulses originate. For the Trident laser and the experiments reported in this dissertation, main pulses are of the order of 10^{19} W/cm^2 (20 J, no deformable mirror) or $2 \times 10^{20} \text{ W/cm}^2$ (80 J, with deformable mirror). This means that the laser contrast has to be better than 10^{-9} or 2×10^{-10} respectively to avoid preionization of

the target (see Section 9.2.2) before the main pulse arrives. Some experiments [186] have even shown that a prepulse as small as $I_{prepulse} \sim 10^8 \text{ W/cm}^2$ can significantly affect and increase the absorption of laser light, and increase desorption of neutral gas, which would then be ionized by the foot of the main pulse. Therefore, even for an ultra-high contrast laser system (unless better than 10^{-12} for a main pulse intensity of $2 \times 10^{20} \text{ W/cm}^2$), this phenomenon can be present, creating a very short scale-length preplasma.

3.3.1 Prepulses, preplasma, and laser contrast

There are two types of prepulse occurring in laser systems using Chirped Pulse Amplification (CPA) (see Section 3.3.2 and Figure 3-11):

- the prepulse pedestal, or amplified stimulated emission (ASE) prepulse, caused by the self-lasing in the crystal (typically the *regen*), which is, in most laser systems, of the order of 10^{-6} of the main pulse;
- the short pulse prepulses, which are caused by imperfect pulse compression, and post-pulses from reflections in the system, which through a non-linear process, can become prepulses [145].

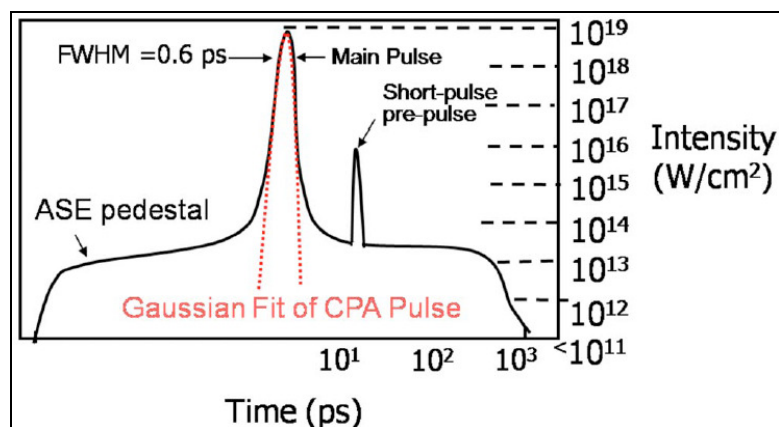


Figure 3-11: Example of a third order cross-correlation trace (laser intensity [W/cm^2] as a function of time [ps] showing the ASE pedestal (10^3 ps corresponds to the front of the pulse, when the pulse starts interacting with the target), a short-pulse prepulse and the main pulse [17].

If the intensity of the prepulses (or of the pedestal) is above the plasma formation threshold ($\sim 10^{10}$ W/cm²), target heating, target ionization, plasma formation and plasma expansion can occur before the main pulse arrives. This expanded plasma is also referred to as preplasma. When the main pulse arrives, it ends up interacting with this preplasma and the plasma critical surface, and not only with an overdense cold solid target. Laser absorption is affected by this preplasma.

For performing well-controlled experiments, it is important to know how much prepulse – therefore how much preplasma – the laser is interacting with. It is also useful to lower the pedestal level, i.e. to improve the contrast of the laser. The laser contrast is defined as the ratio between the level of the main pulse to the pedestal or prepulse created by the ASE.

The plasma scale-length defines the amount of preplasma present in front of a target, and higher contrast laser systems imply sharper density gradients. One definition of the preplasma scale-length is given by the characteristic density scale-length of the hot

electrons derived in Section 2.3.1, i.e. $L_h \equiv \frac{1}{n_h \frac{\partial n_h}{\partial x}}$.

The work presented in this dissertation has been performed on Trident laser at 20 J and at 80 J, at intrinsic and enhanced contrast (see Table 2). At the levels shown, i.e. 10^{10} W/cm² to 10^{12} W/cm², preionization of the target can easily occur (see Section 9.2.2).

	Main pulse intensity at 20 J, 600 fs and 13 μm focal spot (FWHM): 10^{19} W/cm²	Main pulse intensity at 80 J, 600 fs and 7 μm focal spot (FWHM): 2×10^{20} W/cm²
Intrinsic contrast (10^{-8})	10^{11} W/cm ²	10^{12} W/cm ²
Enhanced contrast EC ($> 10^{-10}$)		$< 10^{10}$ W/cm ²

Table 2: Summary of the intrinsic and enhanced contrast levels on Trident, pre- and post-enhancement.

3.3.2 Inherent contrast issues to chirped pulse amplification (CPA) laser systems: amplified stimulated emission (ASE)

The seed pulse is at the nJ level when exiting the oscillator. It needs to be amplified to the mJ level. The laser is let inside of the *regen* laser cavity (see Figure 3-6) by a Pockels cell, which changes the polarization of the pulse. The pulse is amplified inside the cavity by doing ~ 20 round trips through the Ti:Sapph crystal. The cavity is a few ns long (~ 40 cm). While the pulse is bouncing between the reflectors, the crystal can lase without a seed pulse. This is referred to as amplified stimulated emission (ASE). Once the seed pulse has been amplified to the right level (i.e. to the mJ level), it is dumped out of the cavity using the Pockels cell. The ASE, which can fill the cavity completely, leaves with the amplified pulse. This ASE light is not compressible by the gratings and thus results in a poor laser contrast. Also, the Pockels cell does not have a 100 % extinction rate, which is why a portion of the seed pulse can leak out every time the seed pulse bounces off the reflectors inside the cavity, leading to system prepulses at the round trip time of the cavity (a few ns). Other prepulses can come about from postpulses (common from unwanted reflections): due to the nonlinearities of the stretched pulse in the nonlinear or saturated gain media, which would be present when the system is fired at full power, the post-pulses can become prepulses. Most high power short-pulse lasers' ASE pedestals are $\sim 10^{-6}$. Trident 200 TW's intrinsic ASE contrast is better than 10^{-7} (up to 10^{-8}), reducing the amount of preplasma formation on target prior to the main short-pulse's arrival without any added contrast cleaning technique. Figure 3-12 shows a 3rd auto-correlator trace taken at the end of the entire system using the 1 mJ *regen* pulse, showing the ASE prepulse, the short-pulse prepulses and the post-pulses. The contrast is better than 10^{-7} 0.5 ns prior to the main pulse, and there are

also two prepulses prior to the main pulse: one at -220 ps (at 3×10^{-7}) and one at -90 ns (at 9×10^{-8}). Unfortunately, no such measurement is available at the full power level.

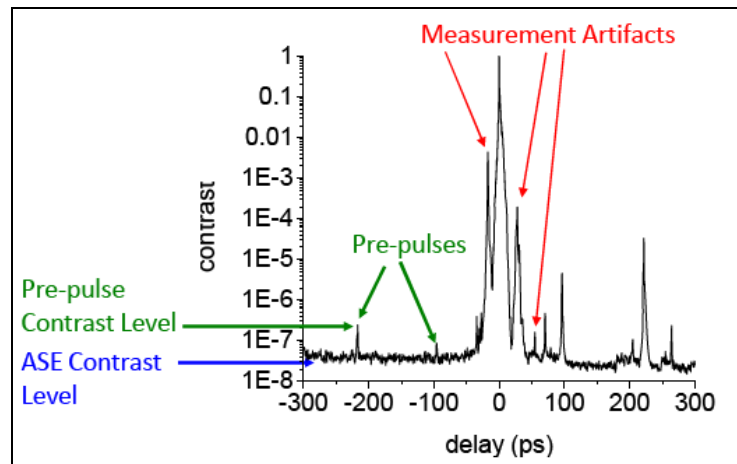


Figure 3-12: Trident's ASE contrast, as measured from the *regen*, is better than 10^{-7} 0.5 ns prior to the main pulse, and there are two prepulses: one at -220 ps (3×10^{-7}) and one at -90 ns (9×10^{-8}).

3.3.3 Optical parametric chirped pulse amplification (OPCPA)

One well known method to improve the laser contrast is to combine the Chirped Pulse Amplification (CPA) method with an Optical Parametric Amplification (OPCPA) method [146].

Unlike the previous section [3.3.2], the pump laser pulse (typically a few ns) is overlapped with the seed pulse which comes clean from an oscillator, and the overlapped resulting pulse makes a single pass into a non-linear crystal, in which there is no population inversion, i.e. no energy is stored in the crystal, and therefore no ASE is produced. The energy is transferred from the pumped pulse to the seed pulse, and into a third pulse, the idler. The idler is slightly shifted in frequency, compared to the seed pulse, unless a second non-linear crystal is used to prevent this frequency walk-off, in which case the idler of the 1st crystal is used as the seed pulse for the 2nd crystal.

However, there is an analog of ASE called spontaneous fluorescence, typically a few orders of magnitude lower than the ASE from a *regen*.

3.3.4 Self-pumped optical parametric amplification (SPOPA)

In addition to the OPCPA scheme, a totally novel cleaning scheme based on Optical Parametric Amplification (OPA) was developed for the Trident laser by R. P. Johnson and built by a postdoc (R. C. Shah). It was commissioned in August 2008. The mechanism yielding a higher contrast, termed SPOPA, is explained in [147].

The laser pulse is cleaned from the intrinsic 10^{-8} contrast from the *regen*, and is sent into a new OPCPA system for pre-amplification before being sent through the main amplifier chain. Figure 3-13 shows the short-pulse cleaning system, which takes the 1 mJ *regen* output and splits it into two chains (90:10) and doubles the frequency of the more energetic chain to 527 nm. This $\sim 40 \mu\text{J}$ level green pulse is then used in a non-linear crystal as the pump pulse for an OPCPA scheme, using the lower energy arm as the seed pulse in a degenerate mode to produce an idler pulse at the same frequency as the seed (1054 nm), but with the clean characteristics of the green frequency doubled pump pulse.

Fundamentally, in any OPA system, energy and momentum have to be conserved, so one pump photon that is being used must be split between the signal and the idler beams, and the relative energy between the two is dictated by the frequency of the beams. In the case of Trident, for the main OPAs, the pump is 532 nm, the signal is 1054 nm, and the idler is 1073 nm. The signal and the idler are close enough in frequency that the energy is nearly split equally between them. Also, the gain of these OPAs can be quite high. The first stage (single crystal), pumped by 120 mJ of green has a small signal gain of about 500; however, due to saturation at a level of a few mJ, the actual gain is about 300 – about $10 \mu\text{J}$ in and

about 3 mJ out. This would mean 3 mJ in the signal beam and 3 mJ minus 10 μ J in the idler, and 120 mJ minus 6 mJ left in the pump.

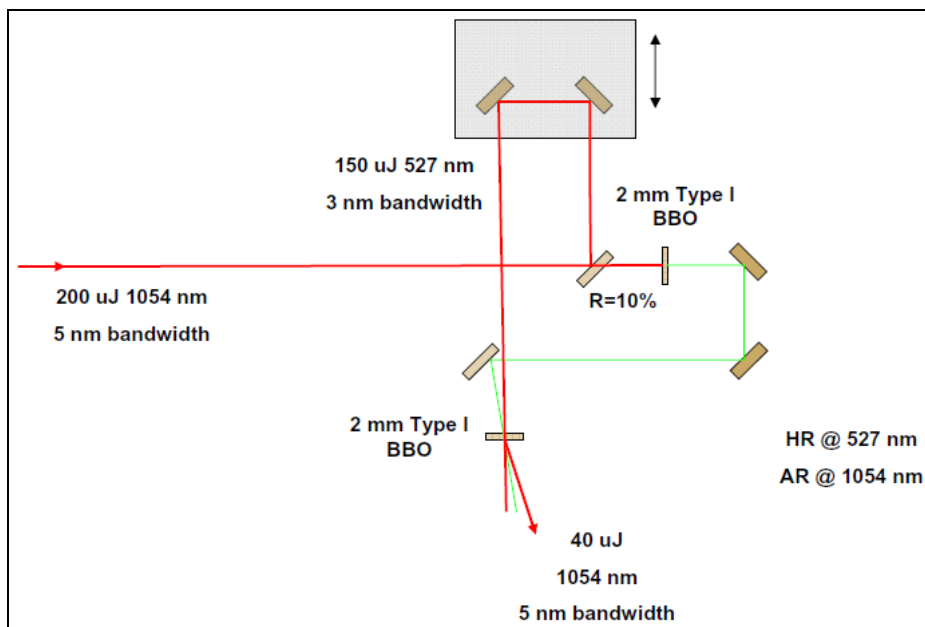


Figure 3-13: Schematic of a low gain OPA temporal pulse cleaning (schematics by Randall P. Johnson).

The resulting clean pulse from that system is shown in red in Figure 3-14.

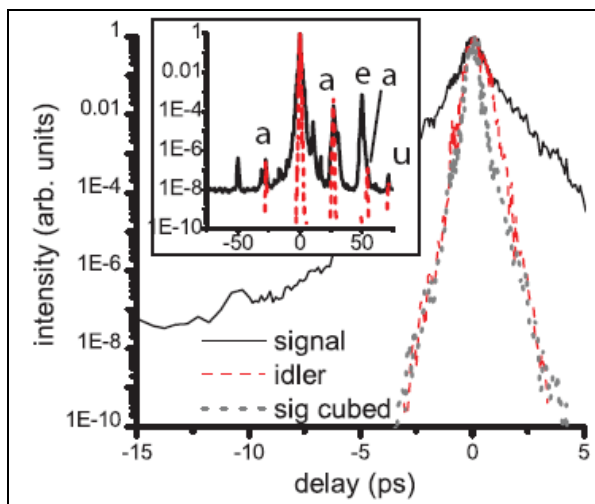


Figure 3-14: Temporal contrast measurement [147] of both unamplified signal and idler, with calculated cube of signal; Inset shows a larger temporal range; (a): known artifact, (e): etalon reflection, (u): unknown peak, assumed to be an artifact.

The original seed pulse is shown in solid black, the calculated pump pulse in dashed black, and the cleaned idler in dashed red. The inset shows a 3rd order cross-correlation out to 75 ps, showing the seed (solid black) and the new clean pulse (dashed red), which is cleaned beyond the detection limit of the cross-correlator.

Figure 3-15 shows the latest auto-correlator measurements of the Trident intrinsic and enhanced contrasts.

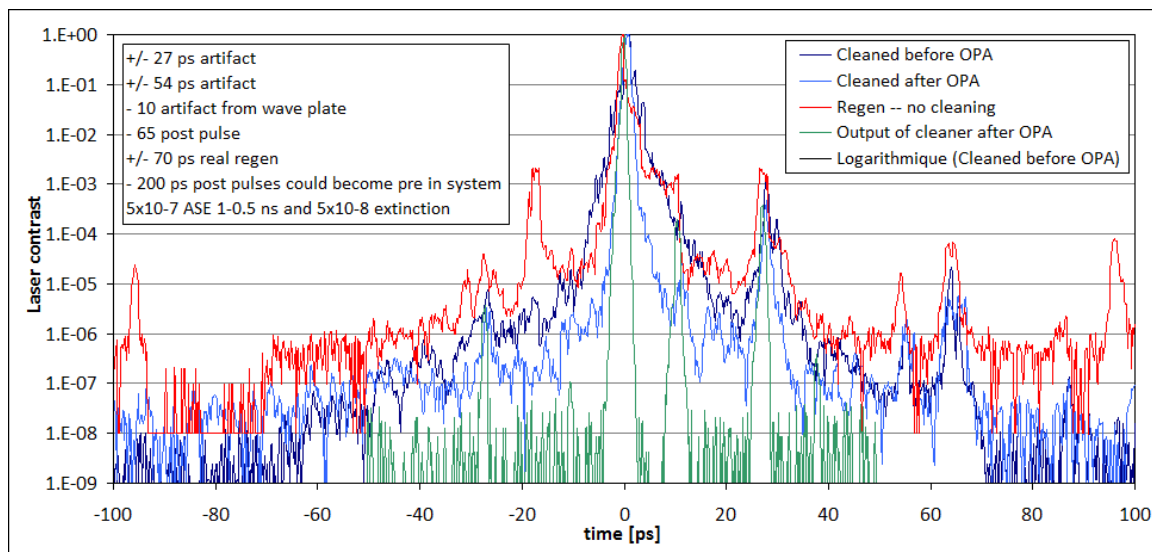


Figure 3-15: Latest auto-correlator measurements (September 2009) of the Trident laser contrast: the intrinsic contrast is shown in red, and the enhanced contrast is shown in dark blue (measurements performed by Randall P. Johnson).

Figure 3-4 in Section 3.2 shows the short-pulse laser front-end before the contrast enhancement (version 0). Figure 3-16 and Figure 3-17 show the front-end post-enhancement, which of course includes the pulse cleaner (version 1 and version 2 respectively).

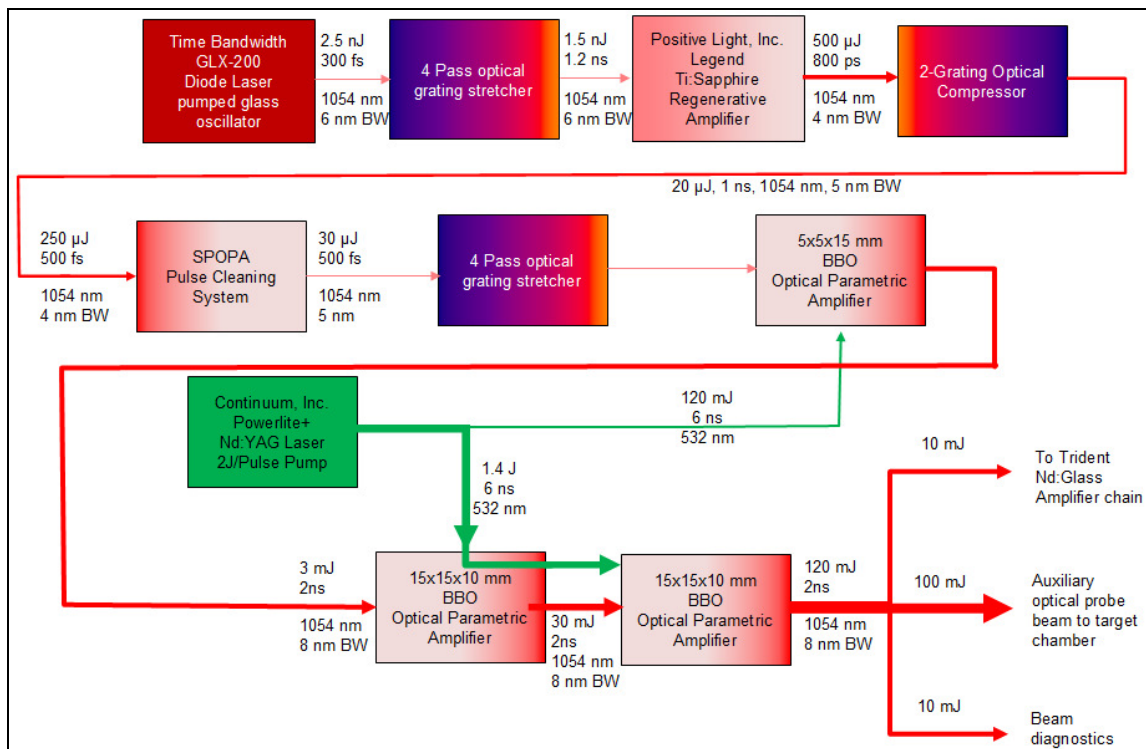


Figure 3-16: Short-pulse Front-end, post-enhancement, and including the pulse cleaner, version 1, used during the August 2008 run on 3 shots (diagram by Randall P. Johnson).

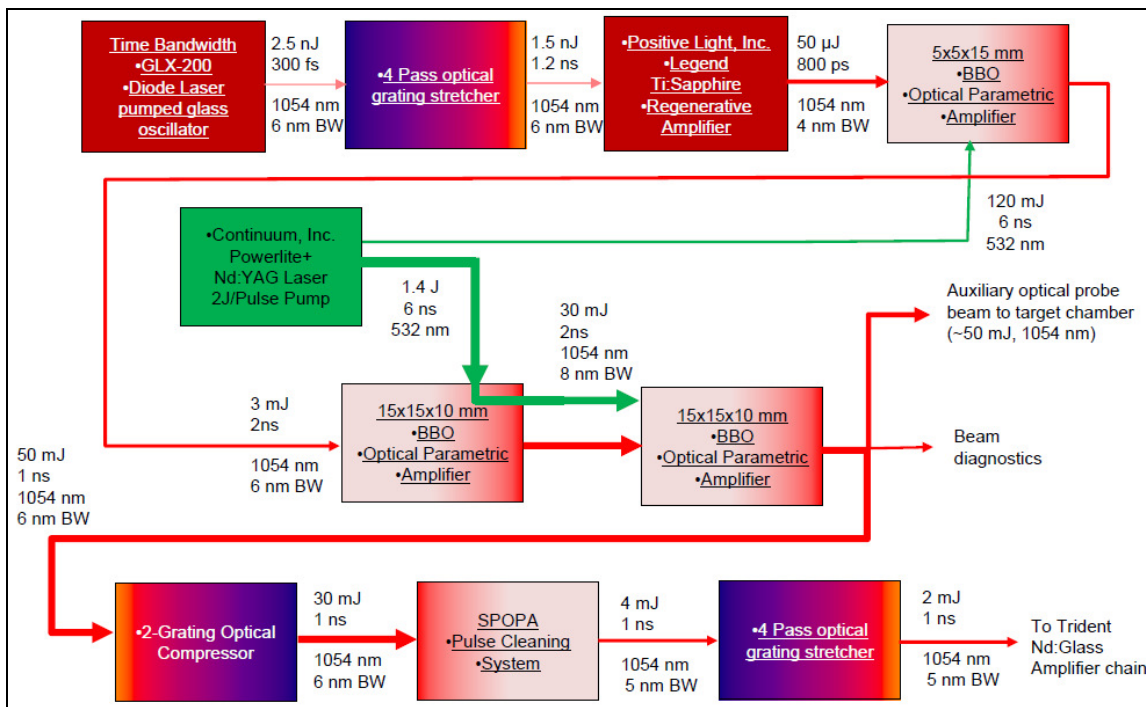


Figure 3-17: Short-pulse Front-end, post-enhancement, and including the pulse cleaner, version 2, used during the June 2009 campaign (diagram by Randall P. Johnson).

3.4 Major laser beam diagnostics

During our experiments, we have used the full suite of laser diagnostics available in the North Target Area. Pulse length, prepulse contrast, focal spot quality, pulse spectrum, and near-field beam quality are measured on each shot. A lay-out of this diagnostic package is shown in Figure 3-18.

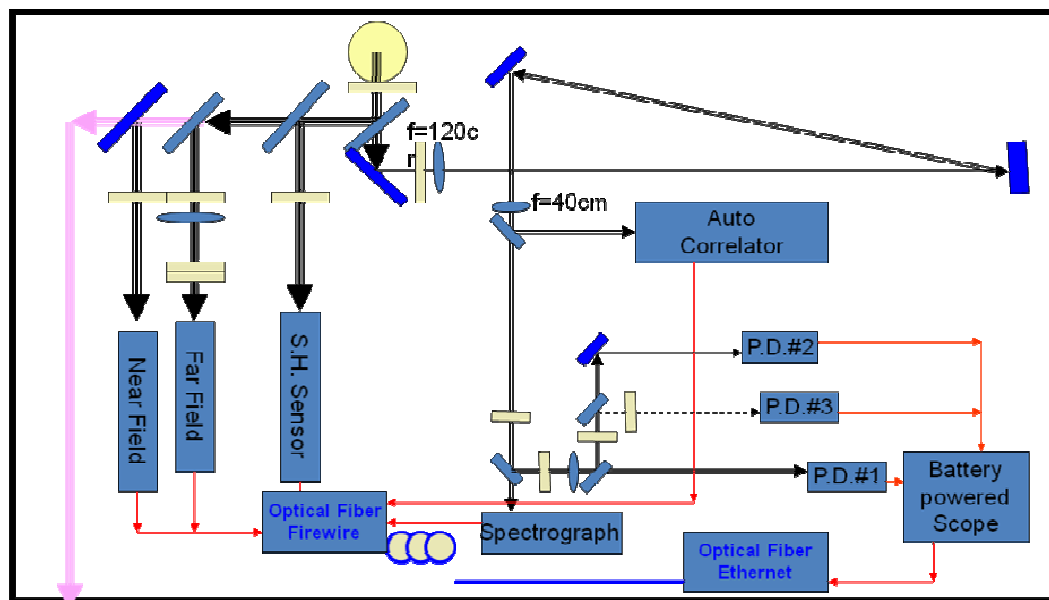


Figure 3-18: Schematic lay-out of the diagnostic suite used for the short-pulse laser beam (drawing by Tsutomu Shimada).

3.4.1 Laser pulse duration

A standard second order auto-correlator is used to determine the laser pulse duration on every shot. This system consists of a doubling crystal and a CCD. The beam interacts with itself in the crystal, producing a beam of second harmonic light, which is directly related to the beam's temporal profile, and can be analyzed from the CCD image captured. A computer algorithm fits many points across the height of the trace and outputs the averaged pulse duration based on a fit to a Gaussian function.

3.4.2 Shack-Hartman (SH) wavefront sensor

The SH wavefront sensor [148] measures the laser wavefront to correct for static and dynamic phase aberrations in the wave front. This sensor is used to obtain the correction file for the deformable mirror. It is not used on all shots, but rather at the beginning of a campaign to correct for the current laser conditions (every 1-4 weeks).

3.4.3 Deformable mirror (DM)

The DM was added to the system in late 2007/early 2008, and improved the focal spot diameter by about a factor of 2. The DM is used to pre-correct the phase fronts of the laser beam for the static aberrations downstream of the mirror caused by the thermal stresses in the large glass disk amplifiers.

3.4.4 Laser spot size at low energy (i.e. CW alignment beam)

Trident uses two orthogonal backlit target viewing cameras to align the target to target chamber center (TCC). TCC is defined using a sharp pointer (the rocket) specially designed to point within 100 μm of true TCC from any of the 12 inch flanges on the North Target Chamber. The viewing system resolution is $\sim 20\text{-}30 \mu\text{m}$.

A wire placed at TCC (defined by the rocket and the viewing systems) is imaged by a high magnification imaging system (30-60 \times) coupled to a 12-bit CCD. Then, the focal spot is aligned to the wire. The Trident CW alignment beam is finally adjusted to reach the smallest and most symmetric spot. This is how best focus is obtained at TCC.

As shown in Figure 3-19 (a) and (b) [17], the combination of the DM and a high quality focusing off-axis parabolic mirror produces a 2 \times diffraction limited spot on target that is about 7 μm in diameter with $\sim 60\%$ encircled energy. Pulses as short as 495 fs have been

produced as well as pulses amplified to 100 J. The peak laser power produced has been ~ 200 TW, with peak intensity on target near 2×10^{20} W/cm².

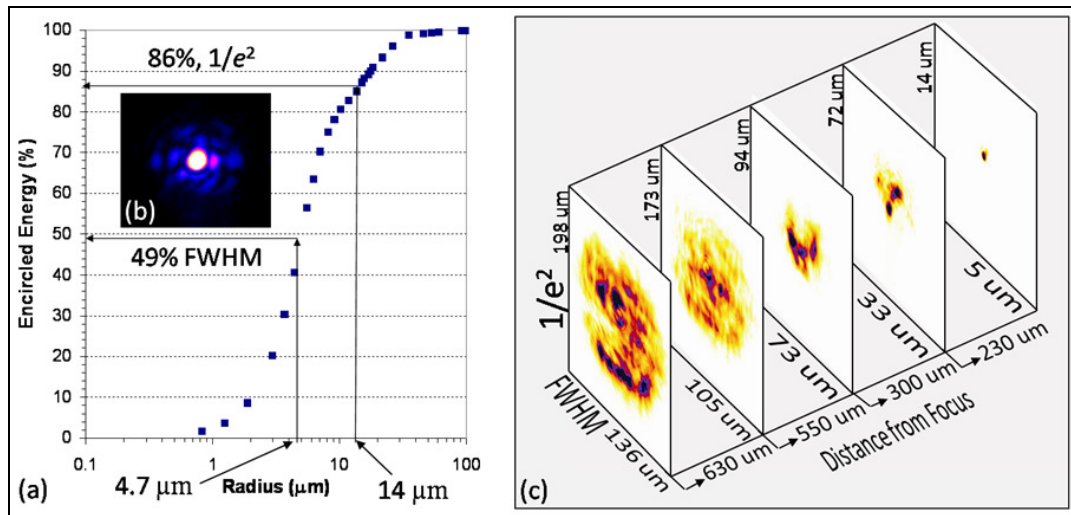


Figure 3-19: (a) Trident encircled energy of the (b) focal spot as a function of encircled radius, a FWHM of 4.7 μm in diameter with 49 % of the energy in that radius, and 86 % of the energy within a radius of 14 μm; (c) the focal spot spatially from the near field, (lower left) 630 μm from focus to (upper right) the focus.

3.4.5 Target alignment – before the shot

The targets are usually positioned using “dead-reckoning” with the viewing system reticles used as fiducials. A laser interferometer has been used successfully on Trident in the past to position targets and an in situ-CCD sensor for vacuum laser alignment. The laser Rayleigh range can be anywhere between 35 μm and 100 μm (see Section 3.2.1), which is well within the accuracy of the positioning system. A new positioning system is under development to improve positioning for thin targets and for absolute motion. These systems must be very robust, because the large levels of electromagnetic interference (EMI) cause many devices to fail during 200 TW shots, including digital cameras, motor controllers, motor encoders, and computers.

Another diagnostic useful in target alignment (focal centering) is the Back-Scatter Focal Diagnostic (BFD) [149], discussed in the following section.

3.4.6 Backscatter focal diagnostic (BFD)

The BFD system directly observes the focal spot for both the off-axis parabola (OAP) alignment and the on-target full power focal spot (also called “as-shot focus”), the latter allowing one to assess the size of the spot and the quality of the target as the main laser pulse arrives.

3.4.6.1 BFD before the shot

The characterization of the focal spot is typically done prior to the shot with the low-power alignment beam, using equivalent plane imaging techniques. In addition, the back reflection from the front side (i.e. laser irradiated side) of the target down the BFD beam-path can be very helpful when aligning FTC and FC targets. The reflection changes as the target is moved and as different zones are struck by the alignment beam light: with practice, one can distinguish the supporting foil (the brightest) from the edge of the cone (still fairly bright), from the entrance hole of the cone (light scatters off opposite rim), and from down the hole to the tip (typically the roundest and possibly the brightest depending on target). Once both rims of the entrance hole of the cone have been recognized, in the vertical and horizontal (screen-wise, showing the “down-the-neck” view) directions, the target is positioned at the center reflection point.

3.4.6.2 BFD after the shot

Because of thermal and B -integral effects, the focal spot cannot be measured at full laser intensity. The only available measurement is that from the low power CW alignment beam. So, in order to find out how the spot must have looked like during the shot, as well as the quality of the target as the main pulse interacted with it, the BFD was implemented. This

allows for the actual full-power, on-target, as-shot focal spot, to be imaged. This diagnostic uses the final focusing optic itself as the collection optic for the backscattered light from the target during the shot.

Figure 3-20 displays three pictures taken with the BFD: (a) the 100 nm Al foil target shot at intrinsic contrast shows a distinct hole, confirming that the pedestal of the laser pulse drilled a hole in the target, ensuring that the main pulse of the target had to have interacted with only a preplasma and no solid target; (b) the 800 nm Al foil target, on the other hand was still intact even after the prepulse; (c) and the same is true of the 10 μm thick Cu foil target.

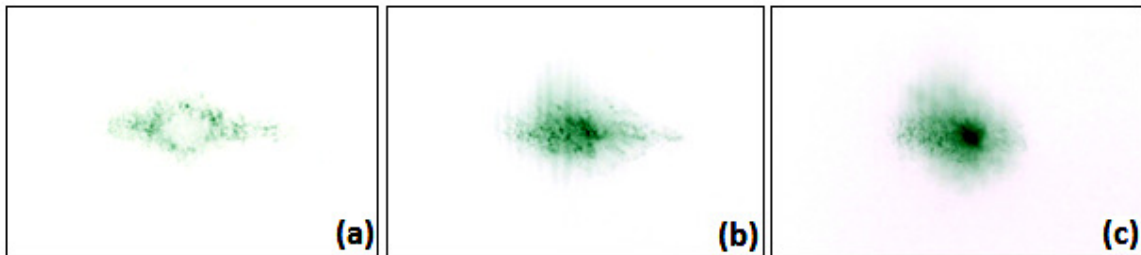


Figure 3-20: Backscatter Focusing Diagnostic pictures: (a) 100 nm Al (shot 20548); (b) 800 nm Al (shot 20554); 10 μm Cu (shot 20552).

4 PARTICLE DETECTION AND DIAGNOSTICS

“The type of damage produced by irradiation of solids depends not only on the nature of the ionizing radiation but also on the nature of the solid itself. [150]” Heavy particles mostly deposit their energy through a great amount of *inelastic collisions with bound electrons*. The greatest amount of energy is deposited at the very end of the particle’s trajectory (Bragg peak). Electrons can be *elastically scattered* (the probability of scattering is higher for a high-Z material), but they lose their energy through *inelastic collisions with the nuclei* (leading to Bremsstrahlung), as well as with the electrons bound to the nucleus. The interaction between photons and matter mainly results in the production of electrons. This section describes the various diagnostics and particle detectors used in the experiments presented in the next section [5].

Sections 4.1–4.3 describe how the particle detectors used in laser-plasma interaction experiments work: CR39 detects protons and heavier ions, and requires developing [4.1], while RadioChromic Film (RCF) [4.2] and Imaging Plates (IPs) [4.3] detect all radiations; RCF self-develops, and IPs require the use of a *scanner*. In most cases, RCF is used as stack to obtain proton beam information as a function of energy (spectrum, divergence, beam quality, etc.). Section 4.4 describes the electron spectrometer, in which the particles are recorded by an IP, and Section 4.5 describes the Cu K α imager which is used in combination with an IP.

4.1 CR39 solid state nuclear track detectors (SSNTDs)

CR39 detectors [151, and references therein] have been widely used as ion detectors in laser-plasma produced ion beams, because they are very accurate, as each pit corresponds to a single ion. However, they require extensive post-processing (etching and counting each

pit under a microscope, manually or by using sophisticated robotically controlled hardware). They also have the downside of becoming saturated [152, 153] at the fluences of ions (protons and heavier ions) reached in laser-plasma experiments, and exhibiting ring-like and bull’s-eye-like structures, as illustrated in Figure 4-1. Because of these various issues, CR39 has only been used on a few occasions in the experiments described in Section 5.2.

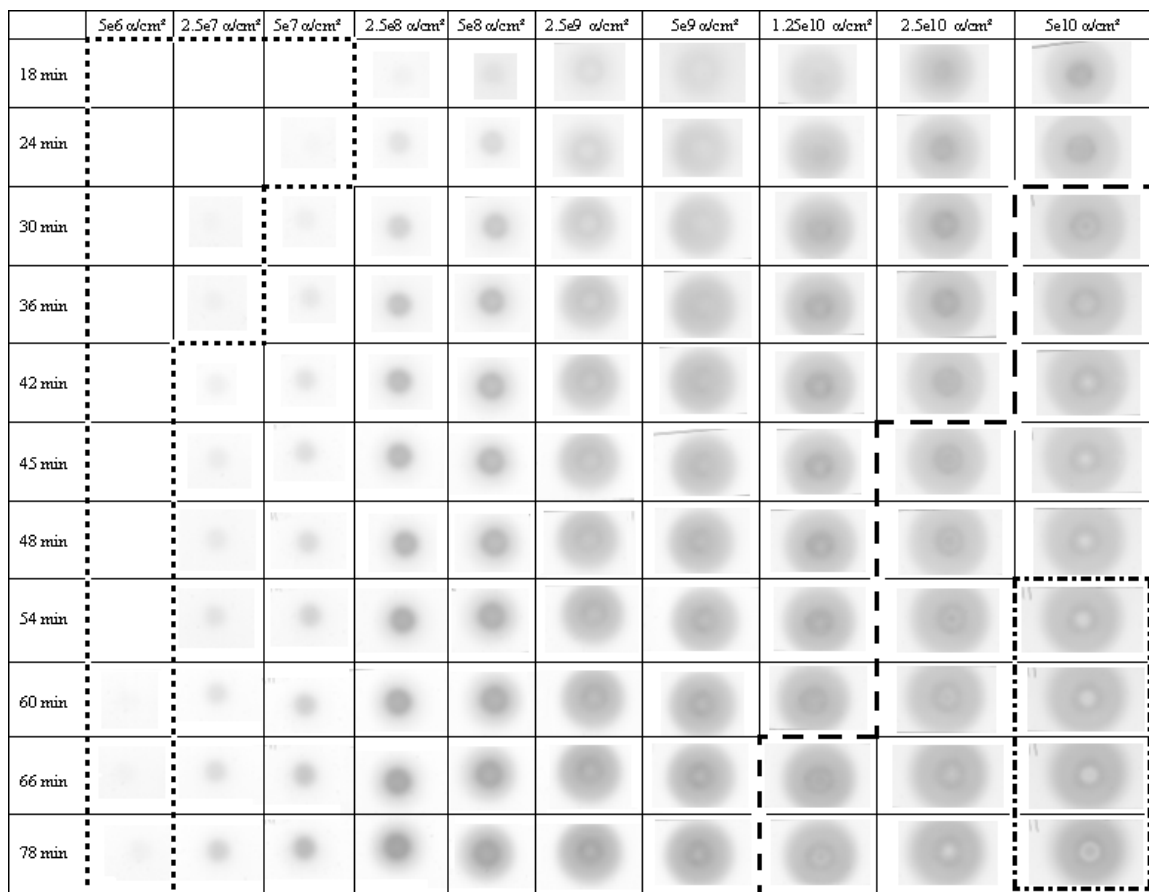


Figure 4-1: Optical scans in transparency mode of the CR39 Tastrak detectors of fluences (horizontally) from $5 \times 10^6 \alpha/cm^2$ (100 s of exposure time) to $5 \times 10^{10} \alpha/cm^2$ (10^6 s of exposure time) for etching times (vertically) of ~ 18' to ~ 78'; Note the presence of artificial rings after the 5th column.

Even though the etching time step is very short (~ 6'), the detectors look a lot different from one etching step to the next. As the etching time is increased, more data is revealed: the

diameter of the α -particle impact zone increases, revealing more of the pits left by the α -particles which have traveled a longer distance in the air. However, the data is not erased yet since the final etching time is short (78 minutes, versus the 25 hours of etching (at a 1.21 $\mu\text{m}/\text{hour}$ rate) which would be necessary to erase all sign of tracks - the normally incident 5.5 MeV α -particles penetrate $\sim 30 \mu\text{m}$ deep).

The region with the dotted contour corresponds to the zone where the detector is not saturated. This is why the detector is transparent to the eye. The scanner is not able to detect the particle signal either, which is why some of the boxes seem blank. The region with the dashed contour corresponds to an extremely saturated zone, in which the bull's eye structures appear. The region limited by a dash-dotted contour corresponds to a region in which a clumping pattern appears in the whiter zone (central region) of the detector. Between these two regions, the detector is moderately-to-highly saturated: ring features start appearing, and the pits cannot be distinguished anymore under a microscope. Note: A detector with enough particle signal for the scanner to detect is already entering saturation. In laser experiments, one needs to remember that the detector is saturated as soon as signal on the detector can be distinguished by the eye.

4.2 RadioChromic Films (RCFs) by GafChromic®

RCFs, produced by International Specialty Products (ISP [154]), are routinely used as proton diagnostics in high-intensity short-pulse laser-matter interaction experiments, to record qualitative information of the proton beams, i.e. profile and divergence, but also quantitative information in terms of proton fluence, deduced from the optical density (OD) of the film.

The active layer in an RCF is comprised of sub-micron sized crystals of a radiation-sensitive monomer; it is a self-developing film of a light blue color, and darkens upon exposure to X-rays, protons, heavy ions and electrons. Ref. [155] states that “the RadioChromic reaction is a solid-state polymerization, whereby the films turn deep blue proportionately to radiation dose, due to progressive 1,4-*trans* additions which lead to colored poly-conjugated, ladder-like polymer chains”.

When the detectors are placed in a stack, as shown in Figure 4-2, they allow one to obtain energy dependent information (each layer corresponds to an energy bin), such as beam divergence and proton number for example. The protons with the lowest energies are stopped in the earlier layers, whereas the protons with the highest energies penetrate farther through the stack and are stopped in the last films of the stack.

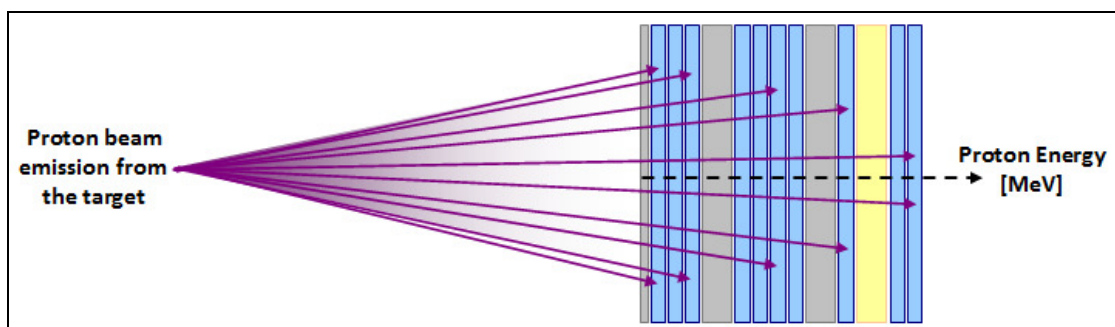


Figure 4-2: Proton beam emission from a target (purple arrows), recorded in an RCF stack (blue), protected by a thin Al foil (grey, front of the stack); the stack also contains some thicker Al filters (grey), and a CR39 detector (yellow); note that the most energetic particles penetrate further down the stack, with a more collimated beam divergence than the low energy particles, which have a wider divergence and are stopped early in the stack.

In experiments, RCF is covered by a thin layer of Al foil (see Figure 4-2) for example to avoid darkening due to laser light, and stray light. Protons can be easily distinguished from electrons or X-rays as they deposit energy differently into the active layer of the film. Protons have a pronounced Bragg peak compared to electrons and X-rays, and leave well-defined sharp-bounded profiles in the RCF, much darker than the surrounding background

of electrons and X-rays, which tends to be diffuse and ill-defined in nature. This background is subtracted from the signal and the proton number, and energy can be extracted: this is called RadioChromic Film Imaging Spectroscopy (RIS) [156, 14]. The proton dose and the proton fluence are deduced from the OD of the film.

Knowing the calibration issues for RCF, i.e. the energy dependence, dose vs. dose rate (fluence vs. flux) dependence, aging, etc., and knowing how these films are analyzed is critical to obtaining well-characterized RCF, which is necessary to understand the laser-to-proton conversion efficiencies of laser-matter ion acceleration experiments.

4.2.1 Different types of RCF

Three different types of RCFs can be used during experiments: **MD-55** (now replaced by **MD-55-V2**), **HD-810**, **HS**, and to a lesser extent **EBT** (not discussed here). They all have different thicknesses and are made to have different sensitivities to ionizing radiation (see Section 4.2.4.1). Table 3 [155] shows the different elements constituting each layer of a film.

Material	Element	Atom %
Polyester base	Carbon	45
	Hydrogen	36
	Oxygen	19
Sensitive layer	Carbon	31
	Hydrogen	56
	Nitrogen	5
	Oxygen	8
Adhesive layer	Carbon	33
	Hydrogen	50
	Oxygen	17
Conductive layer	Indium Tin Oxide	

Table 3: Composition of the various RCF layers.

Table 4 was obtained using both ref. [155] and new information from ISP. It shows the history of the various RCFs that have been sold since before 1994.

Type	Material	Thickness (µm)	Tolerance (µm)
HS			
	Clear polyester	96.5	2.5
	Active layer	40	2
	Clear polyester	96.5	2.5
	TOTAL	233	7 (3 %)
DM1260 (old HD810)			
	Sensitive layer	7	1
	Adhesive layer	1.5	N.A.
	Conductive layer	0.05	N.A.
	Polyester base	99	N.A.
	TOTAL	107.55	N.A.
HD810			
	Surface layer	0.75	0.75
	Active layer	6.5	1 to 2
	Clear polyester	3.8 x 25.4 = 96.52	2.5
	TOTAL	103.77	3.6 – 4.6 (3.4 – 4.4 %)
MD55-1			
Before 1994	Sensitive layer	15	1
	Polyester base	67	N.A.
	TOTAL	82	
MD55-2			
From 1994 to ????	Polyester base	67	N.A.
	Sensitive layer	15	1
	Adhesive layer	44.5	N.A.
	Polyester base	25	N.A.
	Adhesive layer	44.5	N.A.
	Sensitive layer	15	1
	Polyester base	67	N.A.
	TOTAL	278	N.A.
MD55			
From ???? to 2008	Clear polyester	2.6 x 25.4 = 66.04	2.5
	Active layer	16	2
	Adhesive	1 x 25.4	2.5
	Clear polyester	1 x 25.4	2.5
	Adhesive	1 x 25.4	2.5
	Active layer	16	2
	Clear polyester	2.6 x 25.4 = 66.04	2.5
	TOTAL	240.28	16.5 (6.86 %)
MD55-V2			
From 2008 to NOW	Clear polyester	3.8 x 25.4 = 96.52	2.5
	Active layer	17.5	2
	Gelatin	0.75	0.1
	Adhesive	1.25 x 25.4 = 31.75	2.5
	Clear polyester	1 x 25.4	2.5
	Adhesive	1.25 x 25.4 = 31.75	2.5
	Gelatin	0.75	0.1
	Active layer	17.5	2
	Clear polyester	3.8 x 25.4 = 96.52	2.5
	TOTAL	318.44	16.7 (5.24 %)

Table 4: Structure, thicknesses, and tolerances of various RCFs (HS, DM1260, HD810, MD55-1, MD55-2, MD55, and MD55-V2).

4.2.2 Advantages of using a microdensitometer as opposed to a scanner

A detailed study concerning the advantages of using a microdensitometer (e.g. MicroD, Elmer Perkins, PDS) rather than a flat-bed scanner has been published in [157]. Proton beams obtained in laser-plasma experiments often exhibit 100 μm or less type structures (Figure 4-3 (left)), and when the film is scanned with a regular flat-bed scanner, these are washed out. The scanned OD in some regions can exceed a value of ~ 5 , which flat-bed scanners are incapable of detecting.

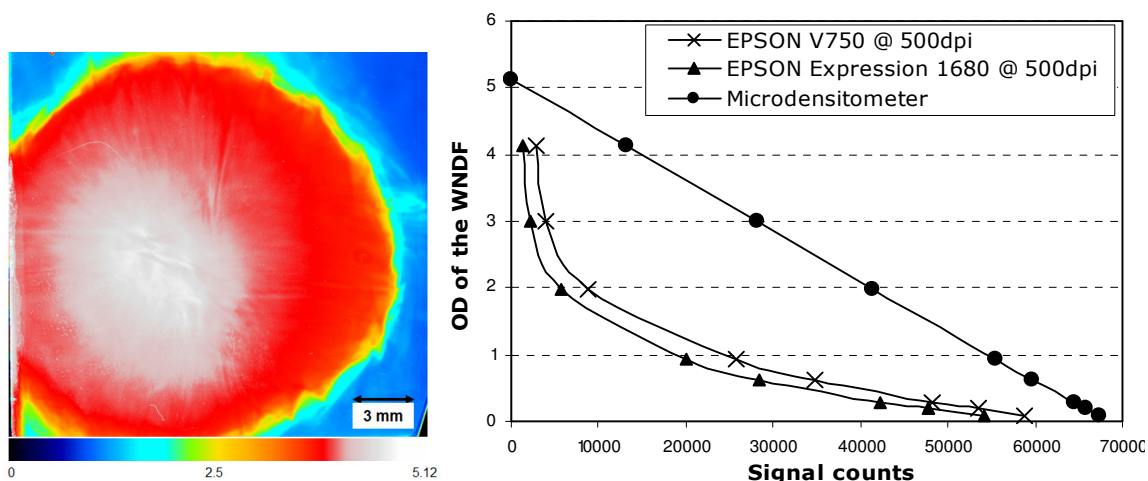


Figure 4-3: (left) Image of an RCF showing a proton beam profile produced via laser-plasma acceleration experiment, scanned on the MicroD, and exhibiting structures of 100 μm and less, with ODs from 1.9 to 5.12, beyond the range of a flat-bed scanner. (right) Scans performed using a MicroD, the Epson V750 (500 and 6400 dpi) and the Epson Expression 1680 (500 dpi) of Wratten Neutral Density Filters (WDF), using with ODs of 0.08, 0.19, 0.29, 0.62, 0.91, 1.99, 3.01, and 4.14, as measured from the diffused densitometer (Diffused), corresponding to the OD nominal values of 0.1, 0.2, 0.3, 0.6, 0.9, 2, 3 and 4, on two scanners and a MicroD.

Even though scanning RCFs on a MicroD is quite time intensive, it is much more accurate than using a flat-bed scanner, because of a greater OD range (> 5), lack of pixel cross-talk (i.e. bleeding), better scan fidelity and resolution (pixel size) of $20 \times 20 \mu\text{m}^2$. However, RCF is scanned by almost all groups using flat-bed scanners because they are easy to use, fast, cheap, and even recommended by the manufacturer (ISP). Not only do flat-bed scanners saturate around an OD of 3, below the limit of RCF ($>$ than an OD of 5), and have a very non

linear response past an OD of 2, as shown in Figure 4-3 (right), but they also lose fidelity with small features size and abrupt gradients in OD, resulting in wrong OD values. Because of scattered light, small size structures become lighter at higher ODs than the dose would indicate. Also, fast transitions from low OD to high OD can be washed out on flat-bed scanners. The data collected on a flat-bed scanner can become unreliable, even when the OD is slightly greater than ~ 1 , as illustrated in Figure 4-4. Note that in the figure, R corresponds to the ratio of the average number of counts in the central area of the large sheet of WNDF (used as a control at the nominal OD) to the average number of counts in the small disk (i.e. 1.5, 2.5, 3, 4, 5, 5.5, 6, and 8 mm in diameter).

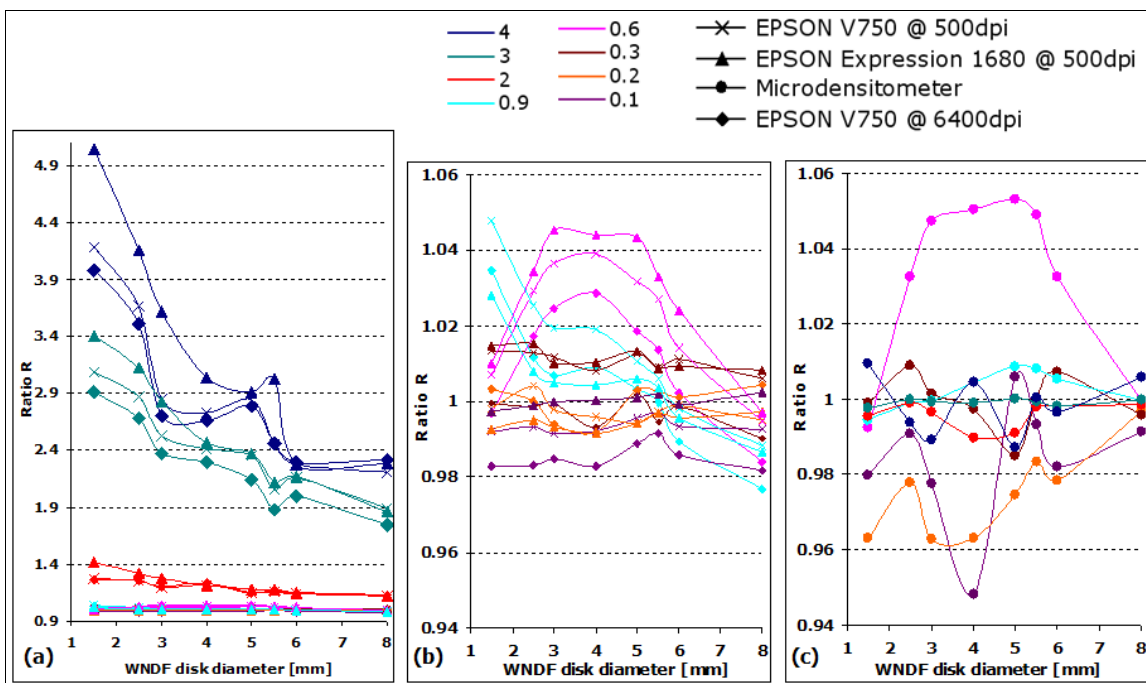


Figure 4-4: (a) Various WNDF size disks with different ODs (different colors) are scanned on an Epson V750 @ 500 dpi (x) and @ 6400 dpi (diamond), an Epson Expression 1680 @ 500 dpi (triangle). (b) Same as (a) but zoomed for $R \sim 1$. (c) Various WNDF size disks with different ODs (different colors) are scanned on a MicroD (circle): regardless of the OD and the size of the disk, the MicroD's resolution is very good, as $R \sim 1$.

4.2.3 Aging effect: Scanning using red or white light and a MicroD

According to ISP [154], the absorption peaks of the RCF are at ~ 615 nm and ~ 675 nm (see Figure 4-5), thus the response of the dosimetry film media can be enhanced by a factor of ~ 3 when performing the measurement with red light, i.e. using a red light source or a red filter at the 660 nm wavelength (close to the major peak absorbance in the spectrum of the photopolymer), compared to black-and-white measurements.

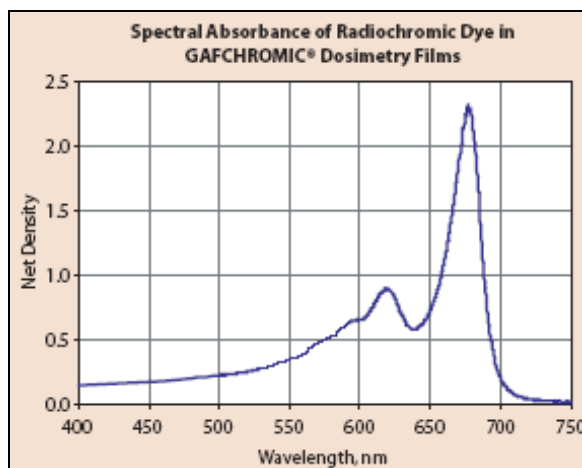


Figure 4-5: Absorption maxima of the blue-colored dye polymer in RCF at 615 nm and 675 nm [154].

As a function of deposited dose in keV/mm², the OD response of a MicroD is linear (see Figure 4-6, dark blue filled and unfilled squares, *MicroD, Red Filter, 2007*). The films were originally exposed in 2007. However, when scanning them one year later using a red filter, the film has not only darkened (which was expected) but the response is no longer linear on a log-log scale (see Figure 4-6, red squares filled with turquoise, *MicroD, Red Filter, 2008*). Such a behavior makes it much harder and much less accurate to obtain a dose from an OD using red light.

In 2008, after realizing the lack of linearity using the red filter, we decided to only perform MicroD scans using white light. To verify whether the same non-linear effect happens with

white light, the turquoise curve was obtained, which, a year after exposure still showed a linear trend, with a slight change in slope. As it ages, the film darkens but the response stays linear (when using white light).

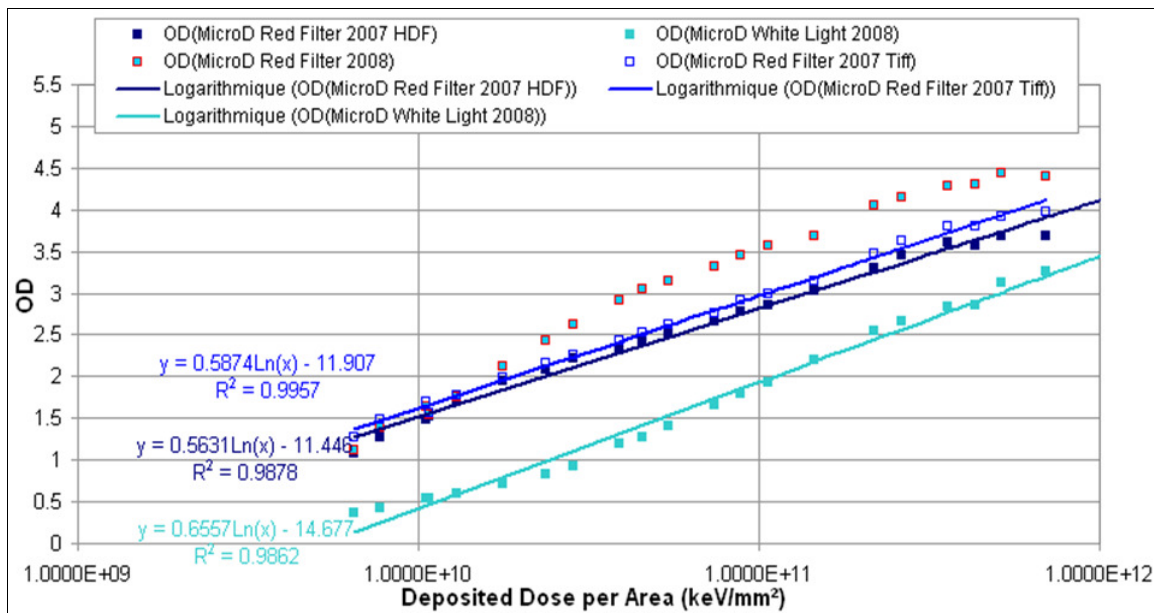


Figure 4-6: MicroD curve in log-log scale of OD as a function of deposited dose [keV/mm²] for LANL Tandem HD-810 data scanned on a MicroD; immediately after the exposure with red filter (dark blue empty and dark blue full squares) and with white light (turquoise squares) and 1.5 year later with red filter (turquoise squares with red border); the 2007 MicroD scans were performed with an OG 590 red filter, a 3.5× objective and a 20×20 μm² resolution; the 2008 MicroD scans were performed for the White Light case with a 10× objective, a Numerical Aperture (NA) of 0.25 and a 50×50 μm² resolution, and for the Red Filter case with an OG590, a 10× objective, a NA of 0.25 and a 50×50 μm² resolution.

4.2.4 Calibration curves using a MicroD and white light

The following RCF calibration curves presented in this section are used in the RIS Matlab program, which converts the OD in each layer of the RCF stack into the proton dose and proton number, thereby creating a proton spectrum, and which is described in more detail in Section 4.2.5. They have been obtained using MicroD scans and white light for the three types of RCF, i.e. HD-810, MD-55 and HS. These curves give the OD of the film as a function of deposited dose, or particle fluence.

Note that each film batch is different: the thickness of the active layer may vary slightly from batch-to-batch in order to provide the product, used primarily for medical imaging, with a reproducible x-ray sensitometric response; and for liability reasons, ISP refuses to give a calibration for each batch sold.

4.2.4.1 ISP calibrations using a Cobalt 60 source and electrons

ISP calibrates RCF using electron and x-ray sources, but never using ions. For a particular batch calibration, HD-810 (batch H1032H810) and MD-55 (batch J1426-MD55) have been exposed to Co60 (β : 0.31 MeV; γ : 1.17 MeV and γ : 1.33 MeV), and HS (batch 30263) has been exposed to X-rays (6 and 18 MeV) and electrons (6 and 18 MeV).

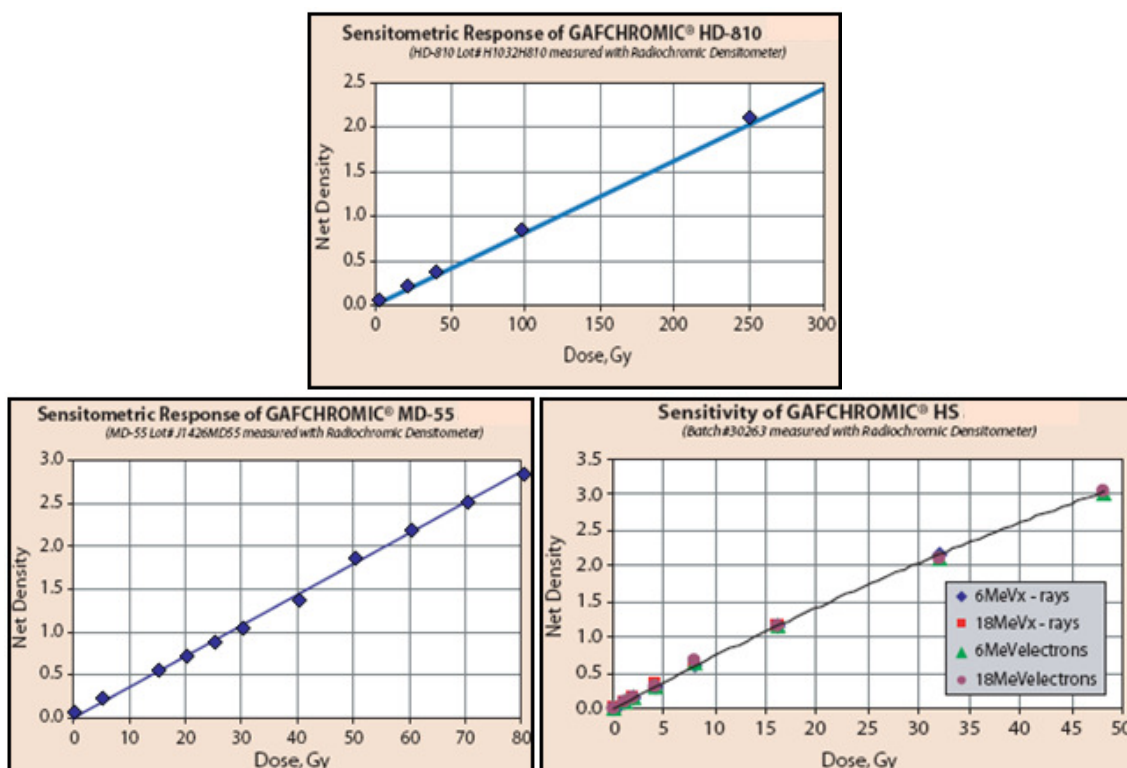


Figure 4-7: ISP calibration curves for HD-810, MD-55 and HS: Net density (up to OD ~ 3) as a function of dose [Gy]: the curves show a linear response between density and dose.

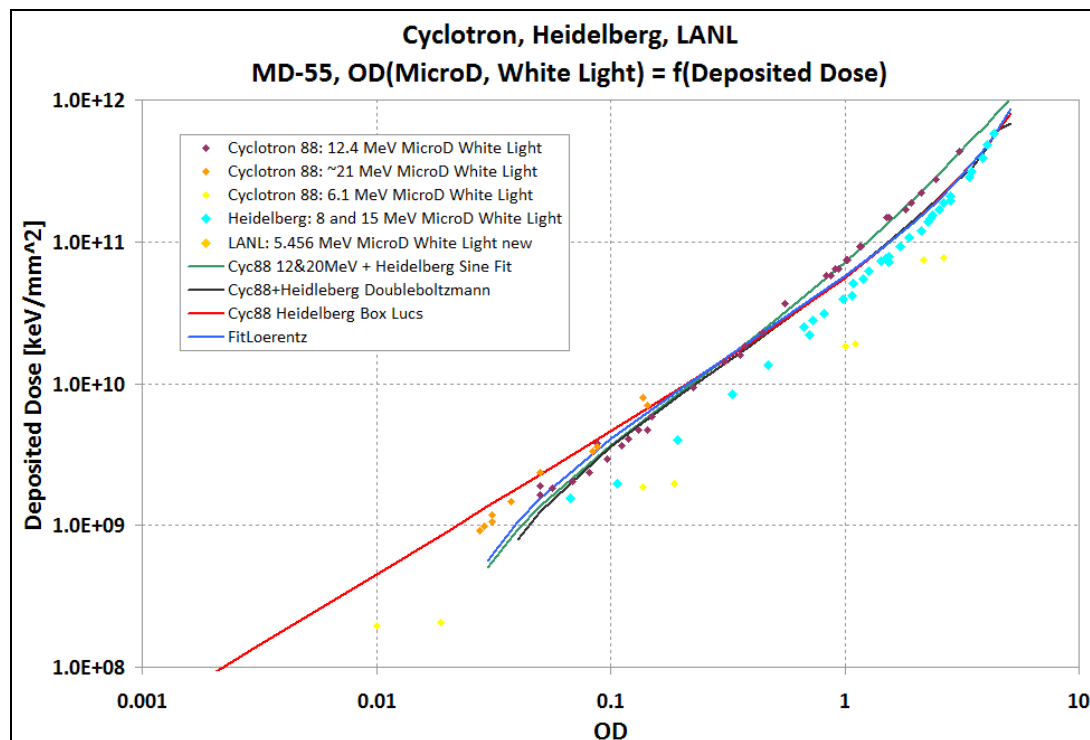
The response of HD-810 (MD-55) when measured with a densitometer is essentially linear with dose up to 250 (50) Gy. It has been shown that the response of HD-810 is independent of energy when exposed with Co60 and 10 MeV electrons [158] and decreases by ~ 30 % when the effective electron {x-ray} energy decreases from 1710 keV {4 MeV} to 28 keV {60 keV and 2 mm Al filtration} [159].

For our purposes, these calibrations are not sufficiently accurate since the RCFs are not used to measure X-rays or electrons, but are used to measure protons and determine proton fluxes as well as laser-proton conversion efficiencies. Although the RCF response in OD to a dose of X-rays and electrons is linear, it is not the same for protons, as described in the next sections [4.2.4.2.1 through 4.2.4.2.4].

4.2.4.2 RCF calibrations on various particle accelerators

To be able to perform RIS, many calibration runs of RCF type MD-55, HD-810 and HS have been performed at the Heidelberg Tandem, at the LANL Tandem and at the LBL 88" Cyclotron, for proton energies of ~ 5 MeV to 20 MeV, for a combination of fluxes and exposure times. It would take too long to describe each of these calibration runs in detail, so for more information, refer to [160]. RCFs were scanned with a MicroD and white light. The final fitted calibration curves used for data analysis are the ones that seem to fit more of the data points for the various calibration runs, never over-estimating the deposited dose as a function of OD, compared to the calibration data.

4.2.4.2.1 Calibration curves for MD-55 scanned using a MicroD and white light



Heidelberg 8 & 12 MeV MD-55 Energy Deposition		
Model	BoxLucas1	
Equation	$y = a*(1 - \exp(-b*x))$	
Reduced Chi-Square	9.07E+20	
Adj. R-Square	0.93631	
	Value	Standard Error
	a	-1.07861000E+11 1.79721000E+10
	b	-0.41703 0.03718

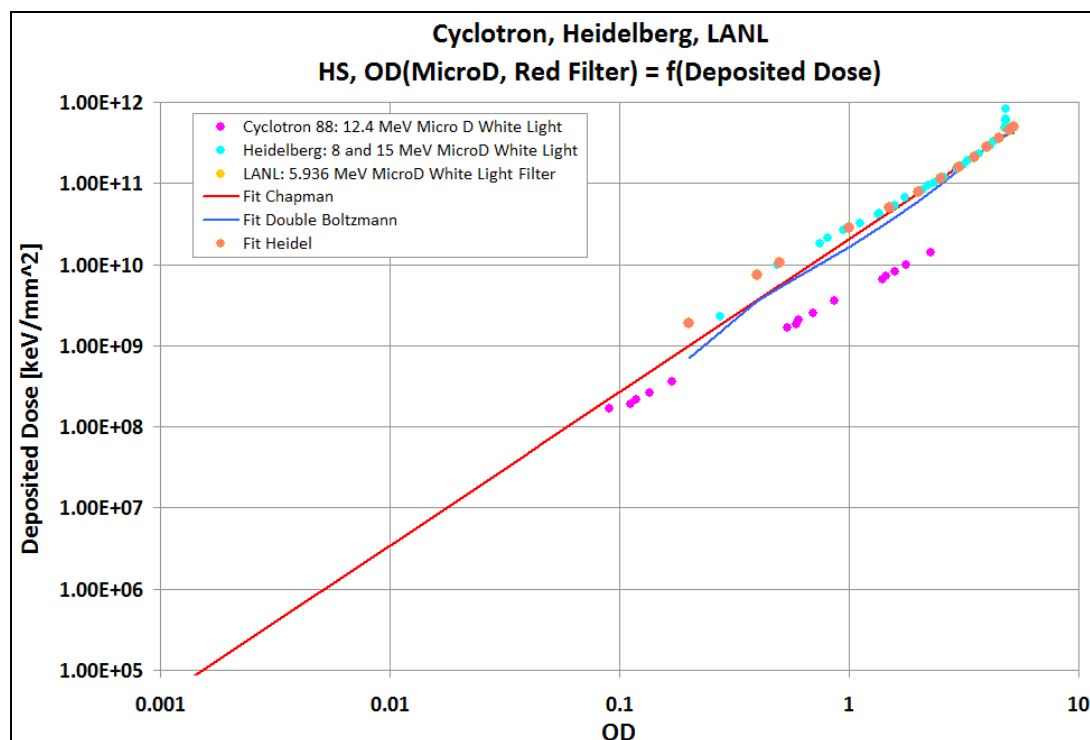
Figure 4-8: MD-55 (top) Calibration curves giving deposited_dose [keV/mm²] = f(OD); (bottom) Equation of the best fit to the data points.

4.2.4.2.2 Calibration curves for MD-V2-55

Except for the target thickness scan of August 2008, the RCF type MD that was used was the MD-V2-55, rather than MD-55 because ISP stopped producing MD-55. So both cone runs (2008 and 2009) used MD-V2-55. No calibration curve is available for MD-V2-55, but the behavior is the same as MD-55. The only important difference is the fact that MD-V2-55 is

thicker than MD-55. Also, MD-55 and MD-V2-55 have been cross-calibrated by M. Geissel and M. Schollmeier [161] at Sandia National Laboratory. It was found that MD-55 is more sensitive than MD-55-V2, and that there is a simple shift of the calibration curve by a factor of 0.72. i.e. $\text{deposited_dose}(\text{MD-V2-55}) = 0.72 \times \text{deposited_dose}(\text{MD-55})$, which is equivalent to $\text{OD}(\text{MD-V2-55}) = 0.72 \times \text{OD}(\text{MD-55})$.

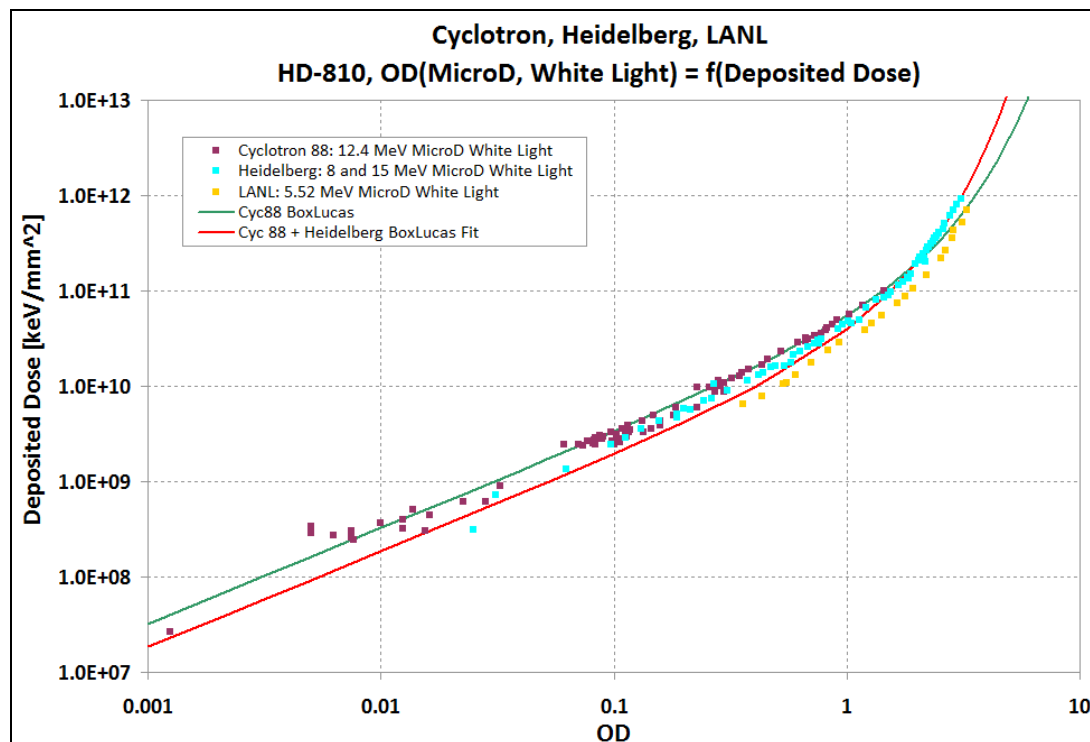
4.2.4.2.3 Calibration curves for HS scanned using a MicroD and white light



Cyc88 and Heidelberg HS Energy Deposition			
<u>Model</u>	Chapman		
<u>Equation</u>	$y = a * (1 - \exp(-b * x))^c$		
<u>Reduced Chi-Square</u>	3.21E+19		
<u>Adj. R-Square</u>	0.99722		
		<u>Value</u>	<u>Standard Error</u>
	a	5.43E+15	4.48E+17
	b	0.00133	0.05905
	c	1.88534	0.17428

Figure 4-9: HS (top) Calibration curves giving $\text{deposited_dose} [\text{keV}/\text{mm}^2] = f(\text{OD})$; (bottom) Equation of the best fit to the data points.

4.2.4.2.4 Calibration curves for HD-810 scanned using a MicroD and white light



Cyc 88 and Heidelberg HD-810 Energy Deposition		
<u>Model</u>	BoxLucas1Mod	
<u>Equation</u>	$y = a*(1 - b^x)$	
<u>Reduced Chi-Square</u>	6.60E+19	
<u>Adj. R-Square</u>		
	Value	Standard Error
	a	-1.3298700E+10 4.01E+08
	b	4.0000200E+00 0.04375

Figure 4-10: HD-810 (top) Calibration curves giving deposited_dose [keV/mm²] = f(OD); (bottom) Equation of the best fit to the data points.

4.2.5 RadioChromic film imaging spectroscopy (RIS), or a method to convert the RCF's OD into a proton number or a proton dose

As we saw in Sections 4.2.2 and 4.2.3, MicroDs (and a white light filter) should be used rather than flat-bed scanners. For the experiments described in this thesis, after exposure to radiation, almost all RCFs from a stack were scanned on a MicroD.

After scanning the film on a MicroD, the OD can be easily obtained from the HDF4 file format, by dividing the value associated with each pixel by simply 800: **OD = Counts(MicroD)/800.**

Note that for flat-bed scanners, the number of counts is obtained from the greyscale image file. This number of counts can be transformed into OD via a calibration curve of the particular scanner used, which is obtained using known ODs, giving **OD = f(number of counts for that scanner).**

Next, the dose or energy deposition (keV/mm²) in each layer of a film stack is computed for the given set of known proton energy, flux and exposure time (“flux multiplied by time” yields “fluence for a given flux”).

Dose is computed throughout the detectors in the stack (see Figure 4-12) by a Matlab program (developed by GSI/LANL [14]) making use of interpolated SRIM (Stopping Range In Materials) data. The tolerances of RCFs are large enough, especially in the case of MD-55 and HS, and need to be taken into account when computing the deposited dose since they result in an important difference in the stack thickness, especially when stacks are large. This process needs a very good calibration of any RCF (MD-55, HD-810 and HS) at many energies and fluxes.

When protons penetrate through RCF, they lose kinetic energy in the film material; charge transfer and scattering of the protons also occur in the film. The differential linear energy loss equation dE_{prot}/dx describes this phenomenon.

- For the film HD-810, which has a single active layer, the deposited energy per proton in the active layer is plotted in Figure 4-11 (a). The energy of the maximum of this curve corresponds to the energy of the protons that are totally stopped in the active layer (i.e. the Bragg peak takes place in the active layer).

- In the case of HS, MD-55 and MD-V2-55 films, the active layers are thicker, which leads to the fact that the maxima of the energy deposition are higher (see Figure 4-11 (b) and (c)) than in the case of HD-810 (see Figure 4-11 (a)).
- For the MD-55 and MD-V2-55 films, which have 2 active layers, the resulting energy deposition curve is an overlap of two shifted curves, and therefore, the energy deposition curve has two maxima (see Figure 4-11 (b)).

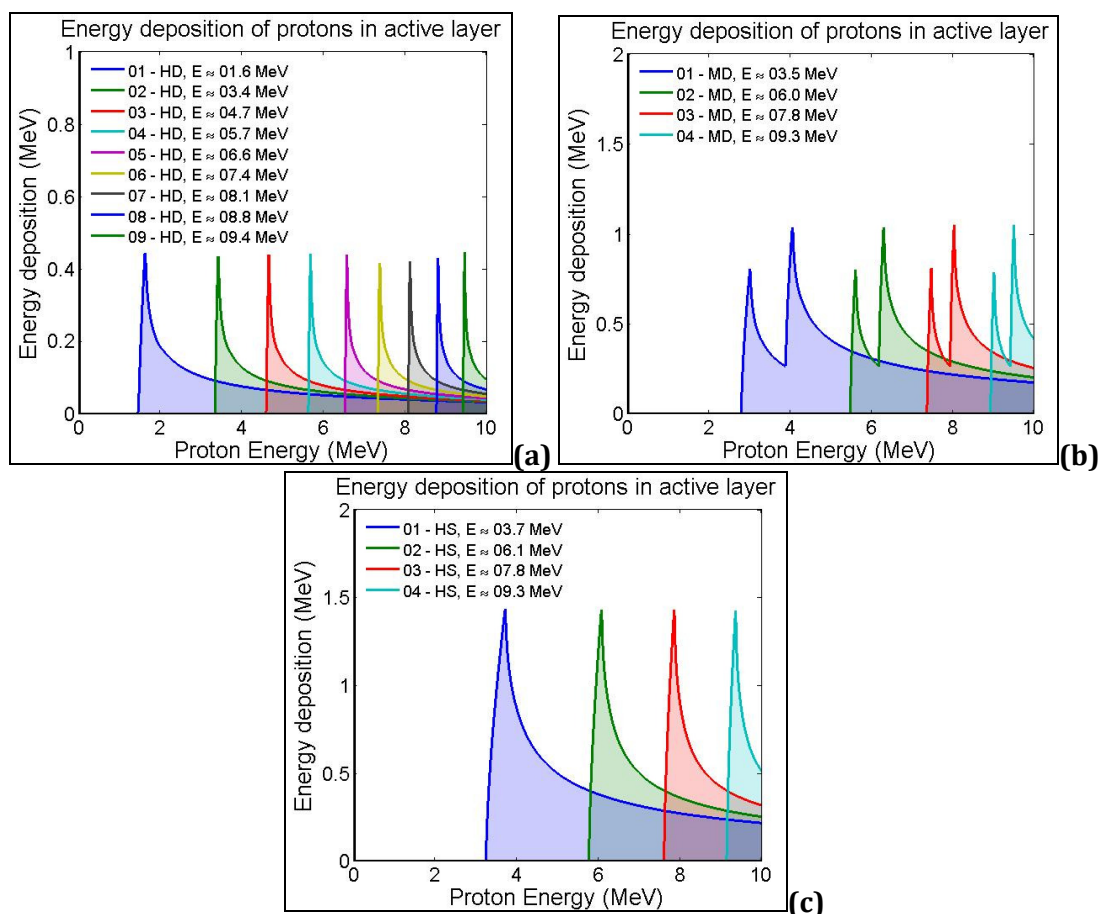


Figure 4-11: Energy deposited in each single layer of an RCF stack, by a proton of a specific energy (in 0.01 MeV energy steps); the stacks are made of (a) 9 layers of HD, (b) 4 layers of MD and (c) 4 layers of HS.

Figure 4-12 shows the Matlab program's GUI for loading the RCF stack after it has been scanned with a MicroD, and for processing the image (i.e. remove background, dust, ...). The

proton beam energy and particle number can be extracted from the dose for the whole stack to give a spectrum.

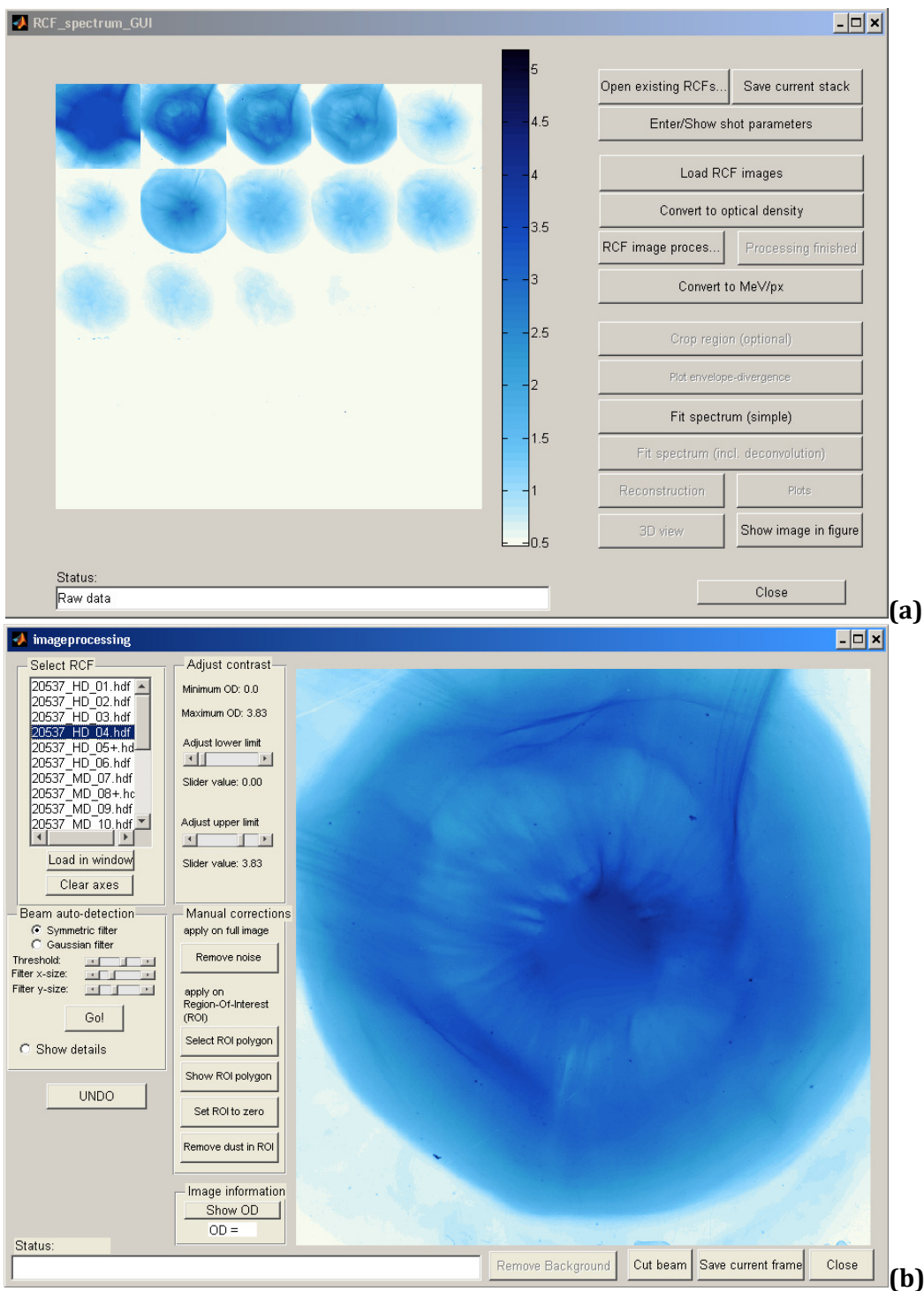


Figure 4-12: RCF data (Shot 20537) that have been scanned with a MicroD are loaded in the program; (a) RCF spectrum GUI; (b) Image processing GUI.

Before stopping in a particular layer, protons deposit a fraction of their energy in all of the previous layers (see Figure 4-11). (This fraction is, however, much smaller compared to the Bragg peak deposition.) Therefore, the measured total deposited energy E_{total} in a specific RCF layer corresponds to a convolution between the spectrum and the response function of the RCF, i.e. $E_{total} = \int \frac{dN(\xi)}{d\xi} E_{loss}(\xi) d\xi$, where $\frac{dN(\xi)}{d\xi}$ is the spectrum of proton number per unit energy and E_{loss} is the calculated energy loss of a proton with energy E in the given layer. The Matlab program assumes a convolution with *an assumed function (i.e. exponential type) for the proton spectrum*, and recursively fits this function to the data. A few possibilities for this exponential function are the following:

- a simple exponential decay as a Boltzmann distribution $\frac{dN(E)}{dE} = \frac{N_0}{E} \exp\left(-\frac{E}{k_B T}\right)$ for a thermal plasma expansion;
- a modified exponential by [126], $\frac{dN(E)}{dE} = \frac{N_0}{\sqrt{2Ek_B T}} \exp\left(-\sqrt{\frac{2E}{k_B T}}\right)$, as a result of an isothermal, quasi-neutral adiabatic plasma expansion [118];
- a Gaussian $\frac{dN(E)}{dE} = \frac{N_0}{E} \exp\left(-\left(\frac{E}{k_B T}\right)^2\right)$ which includes an adiabatic plasma expansion [162];

In the Matlab program, any of these three functions can be used, but for our purposes in this dissertation, we assume a simple exponential, which fits the recorded spectra well.

With the function for the proton spectrum and the E_{loss} values given by SRIM a theoretical total deposited energy is calculated for each RCF layer in the stack. The integral in

$E_{total} = \int \frac{dN(\xi)}{d\xi} E_{loss}(\xi) d\xi$ is solved using Simpson's rule for numerical integration. The

calculated energy values of the RCFs are compared to the experiment. By minimization of the RMS deviation, the parameters N_0 and $k_B T$ are iteratively determined.

Figure 4-13 gives the proton spectrum obtained assuming that a single proton, which deposits its energy in a layer, Bragg-peaked in that layer, while leaving an insignificant amount of energy in the other layers.

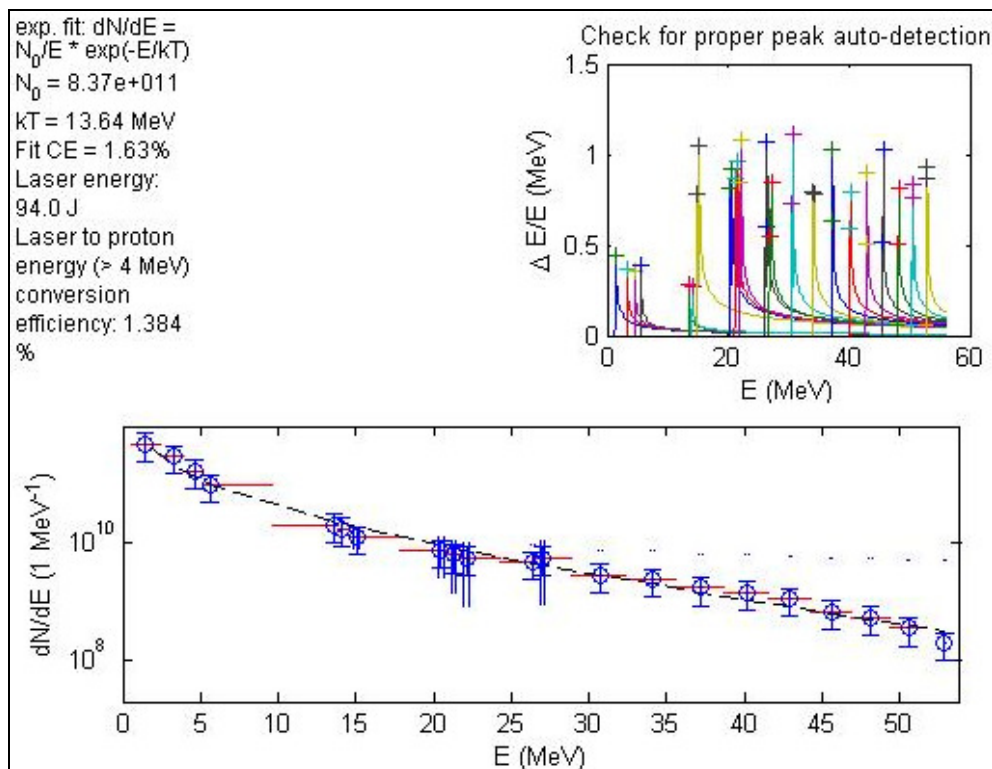


Figure 4-13: Raw data (blue circles), and a simple fit (black dashed line) to the spectrum (#/energy) from the Matlab program assuming an exponential fit to the spectrum for a 10 μm regular Cu flat foil (Shot 20537): Fit C.E. = 1.63 % and the binned raw data C.E. = 1.384 %. This assumes all the particles depositing energy in a layer were of that energy (i.e. "Bragg Peakers").

On the other hand, Figure 4-14 and Figure 4-15 are obtained assuming that each proton actually had an effect on all layers. Figure 4-14 shows the dose as a function of proton energy: the circles correspond to the total dose deposited in each layer; and the stars, to the fitted dose assuming an exponential function for each layer. Figure 4-15 shows the final proton spectrum. Using the fitted dose data (stars from Figure 4-14), the circles in Figure

4-15 correspond to the fitted spectrum, and the stars in Figure 4-15 represent the fitted dose data (stars from Figure 4-14) multiplied by the Bragg-peak energy loss for a given layer. Also shown in Figure 4-14 and Figure 4-15 in green are the predicted dose and proton number from the Fuchs scaling.

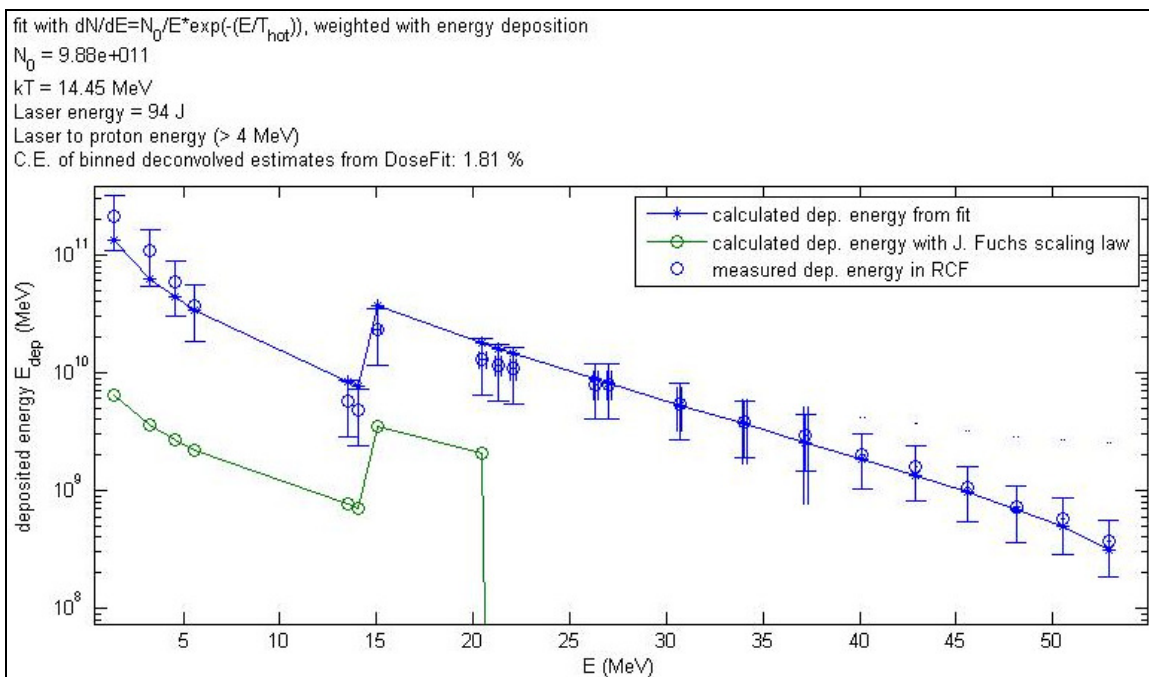


Figure 4-14: Dose per layer energy from the Matlab program deconvolving the assumed spectrum to fit the dose values. Calculated values (stars) fitting the circles are shown for a 10 μ m regular Cu flat foil (Shot 20537), along with another fit based on the Fuchs scaling, which is clearly underestimating the spectrum. The conversion efficiency of the binned data is C.E. = 1.81 %, based on the original layers as energy bins in the previous figure. The dose has a discontinuity when changing from HD to MD at about 15 MeV due to the different construction of the films.

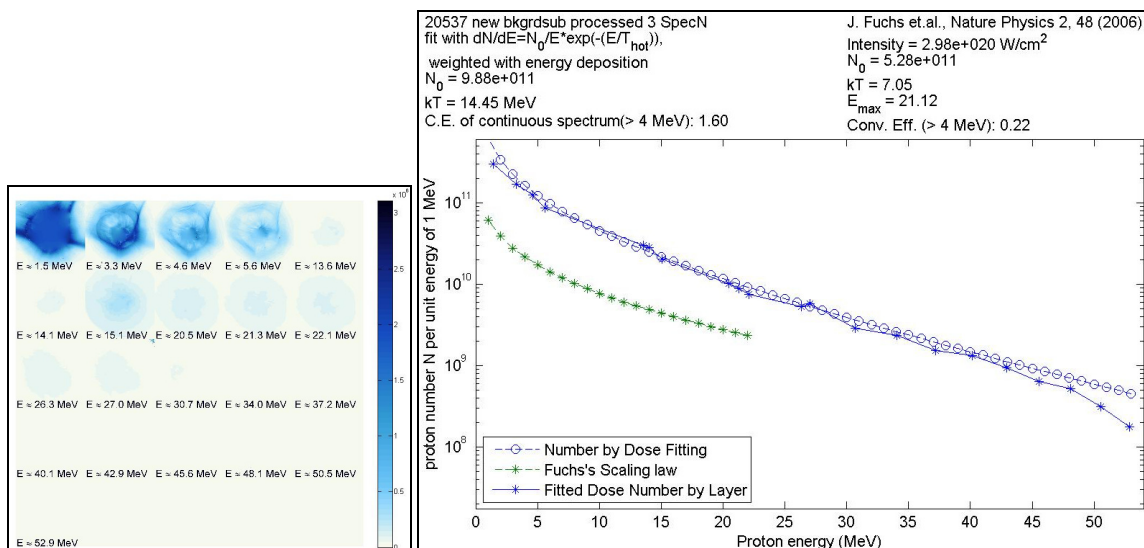


Figure 4-15: (left) Proton beam post-analysis, i.e. once the background subtraction and the proton beam selection have been applied; (right) Spectrum from the Matlab program obtained from the deconvolution of the assumed Maxwellian continuous spectrum (blue circles) for the protons for a 10 μ m regular Cu flat foil (Shot 20537): C.E. = 1.60 %.

Note that there is some level of uncertainty in the analysis of the laser-to-proton conversion efficiency due to beam treatment and the resulting fit temperature. Indeed, Figure 4-15 shows a C.E. = 1.60 %, while Figure 4-16 shows (a) C.E. = 1.82 %, (b) C.E. = 3.06 %, and (c) C.E. = 1.59 %. The initial data in Figure 4-15 and Figure 4-16 is the same, but it is analyzed differently: the variation in the C.E. comes from a difference in the background radiation dose subtraction and the proton beam area selection. The proton beams post-analysis are shown in Figure 4-15 (left) and Figure 4-16 (left). Between the minimum and the maximum values of the conversion efficiency, there is a variation of $(3.06-1.59)/2.325 = 63$ % in the result. The highest value 3.06 % results in a beam temperature of 48 MeV, which seems unrealistic, and is much higher than the other cases, so it can probably be rejected. Therefore kT can be used to verify that the data processing, as an incorrect (too high) background subtraction in the first layers (HD) can lead to a flatter spectrum, and thus result in a much higher kT .

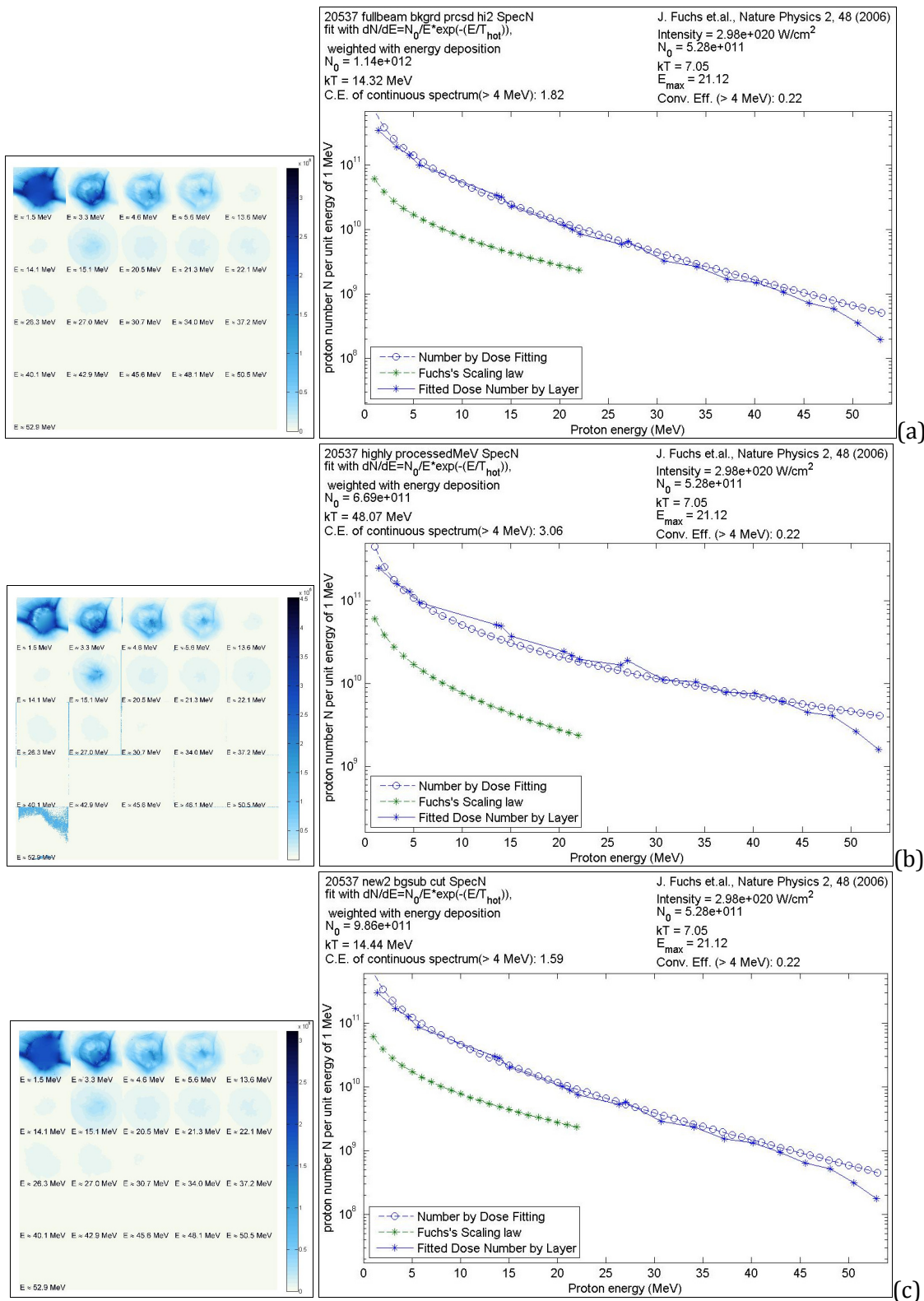


Figure 4-16: (left) Proton beams post-analysis; (right) Spectra from the Matlab program obtained from the deconvolution of the assumed Maxwellian continuous spectrum (blue circles) of the protons for a 10 μ m regular Cu flat foil (Shot 20537);

**the data is analyzed three times with different background subtraction and beam area selection, as compared to Figure 4-15, yielding different conversion efficiencies:
(a) C.E. = 1.82 %; (b) C.E. = 3.06 %; (c) C.E. = 1.59 %.**

In this dissertation, we choose to use the C.E. given by the continuous fitted spectrum (blue circles in Figure 4-15), to compare spectra for protons above 4 MeV using the most conservative number. In rare cases, some spectra do not fit a Maxwellian well, so a different fit must be assumed, or the raw data used. The spectra discussed in this dissertation fit the assumed Maxwellian. It must be noted that the C.E. can be affected by the analysis of the RCF using the program, specifically by how, and how much background signal is subtracted from each film, and by which method (MicroD, or flatbed scanner) the RCF was scanned and calibrated, with the MicroD erring on the side of caution (yielding lower C.E.s than the same data analyzed on a flat-bed, by up to a factor of 2). There is also a $\sim 2\%$ uncertainty in the energy of each layer due to energy straggling of the protons in the active layer.

4.3 Imaging plates (IPs) by FujiFilm

An IP is a flexible image sensor, which consists of a protective layer, a photo-stimulable phosphor layer, uniformly coated on a polyester support layer. The phosphor layer consists of bunches of very small crystals (grain size: $\sim 5\ \mu\text{m}$) of photo-stimulable phosphor of barium fluorobromide, and containing a trace amount of bivalent europium which acts as a luminescence center. It is formulated as BaFBr:Eu^{2+} . IPs are used in scientific imaging such as radioisotope detection and electron detection. In our experiments, we used FujiFilm IPs [163].

When stimulated by radiation, a phosphor emits light. The light disappears instantaneously when the stimulation ceases. This phenomenon is called *fluorescence*. However, some phosphors continue emitting light for a while after the stimulation stops; this is called

phosphorescence. Fluorescence and phosphorescence are both varieties of *luminescence*, which is simply "*cold light*" which can be emitted at normal and lower temperatures.

Photostimulated luminescence (PSL) is the release of stored energy within a phosphor by stimulation with visible light to produce luminescent signal. The IP stores the first radiation information and releases that information as light (i.e. 400 nm) when irradiated by a different wavelength (i.e. 650 nm). After exposition, the IP has to be scanned (Figure 4-17 (right)) for the information to be released as luminescence.

The photo-stimulable phosphor substance of the IP is made out of the BaFBr:Eu²⁺ crystal, which is an ionic crystal of tetragonal structure. Europium is a divalent cation, which replaces barium to create a solid solution. As illustrated in Figure 4-17 (left), when hit by ionizing radiation (e.g. X-rays), Eu²⁺ ions lose an additional electron and become Eu³⁺ ions. These electrons are released into the conduction band of the crystal, becoming trapped in the bromine ion empty lattice of the crystal (lattice defects are inherently present in the crystal); color centers of the metastable state are formed. This metastable state is higher in energy than the original condition; so a lower-frequency light source (i.e. 650 nm, see Figure 4-17 (left)), which would be insufficient in energy to create more Eu³⁺ ions, can return the trapped electrons to the conduction band. As these mobilized electrons encounter Eu³⁺ ions, they release luminescence (i.e. 400 nm). This light is produced in proportion to the number of trapped electrons, and thus in proportion to the original x-ray signal. This light (or luminescence) is collected by a photomultiplier tube (see Figure 4-17 (right)), in which it is converted to analog electric signals, in chronological order. Subsequently, these electric signals are converted to digital signals of 8 to 16 bits. The IP is reusable after *erasing* (exposing it to visible light) the residual latent image on the IP.

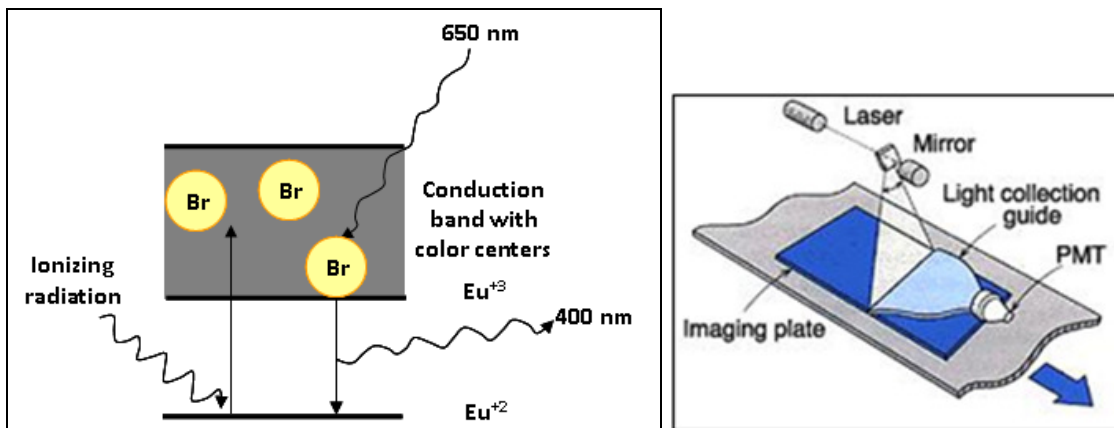


Figure 4-17: (left) Principle of the photostimulation mechanism; (right) A schematic of what happens during the scanning process: the exposed IP is scanned with a focused laser beam, yielding a PSL to be released, which is collected into the photomultiplier (PMT) tube through the light collection guide, and finally converted into electric signals.

The scanner produces 3 files:

- a picture *.TIF* file, which has been rescaled and should not be used for data analysis
- an information *.INF* file, which contains the scanning settings:
 - S: the sensitivity (1000, 4000 or 10000);
 - R: the pixel size, also referred to as the resolution R (25, 50, 100, 200);
 - the size of the image;
 - L: the latitude (4 or 5), which corresponds to the orders of magnitude of analog data values digitized into the 16-bit image.
- a 16 bit raw data file *.IMG*, containing the quantum levels. The quantum levels have a logarithmic response to the intensity of stimulated photoemission. They are related to the photoluminescence signal (PSL) by the following formula:

$$PSL = \begin{cases} \frac{4000}{S} \left(\frac{R}{100} \right)^2 10^{L \left(\frac{QL}{65535} - \frac{1}{2} \right)} & \text{if } QL > 0 \\ 0 & \text{if } QL < 0 \end{cases}$$

The PSL value ranges from a minimum value of $PSL_{\min}(10000,25,4) = 0.025 \cdot 10^4 \left(\frac{QL}{65535} - \frac{1}{2} \right)$ to

a maximum value of $PSL_{\max}(1000,200,5) = 16 \cdot 10^5 \left(\frac{QL}{65535} - \frac{1}{2} \right)$.

To increase the image quality, FujiFilm recommends:

- increasing the exposure time of the IP (not possible during experiments);
- increasing R (to obtain a better S/N ratio), which decreases the spatial resolution.

4.3.1 Different kinds of IPs and advantages over other detectors

There are various types of IPs. Of those, we are only citing the ones which have been commonly used in laser-plasma experiments to detect all types of radiation emitted from the target: protons, electrons and X-rays. The Multi-purpose Standard IP is the BAS-MS type (white). In the BAS-SR type, a blue pigment was added to the MS formula to increase resolution. In the BAS-TR type, the protective layer was excluded from the BAS-SR type to be able to detect ^3H .

Compared to other detectors, IPs can be processed quickly and easily, and they have:

- an ultrahigh sensitivity (10 – 1000 times more sensitive than film);
- a wider dynamic range ($10^4 - 10^5$ compared to 10^2 for film);
- a superior linearity (the fluorescence emission is proportional to the dose in the entire range);
- a higher spatial resolution.

Table 5 [164, 165] gives the specifications of these particular three IPs.

Layer	Surface layer / Protective layer	Phosphor layer	Back layer / Undercoat	Base layer	Ferrite layer	Back protective layer
Material	Polyethylene-teraphtalate	Phosphor*:urethane = 25:1	Plastic	Polyethylene-teraphtalate	MnO, ZnO, Fe2O3 + plastic	Polyethylene-teraphtalate
		* Ba:F:Br:I atom number ratio: 1:1:0.85:0.15				
Density (g/cm ³)	1.4	Variable	1.4	1.4	3.0	1.4
MS (white)	9 μm	115 μm	12 μm	190 μm	80 μm	25 μm
		3.18 g/cm ³ Barium weight: 19 %				
TR (blue)	0 μm	52 μm	11 μm	247 μm	80 μm	25 μm
		3.07 g/cm ³ Barium weight: 16 %				
		* Ba:F:Br atom number ratio: 1:1:1				
SR (blue)	7 μm	121 μm	12 μm	190 μm	80 μm	25 μm
		3.07 g/cm ³ Barium weight: 20 %				

Table 5: Structure of the BAS-MS, BAS-SR, and BAS-TR IPs: different layers, layer material, densities, and thicknesses. The density is given within ± 1 % and thickness within ± 6 %.

4.3.2 Calibration of IPs for electrons

In [166], the BAS-SR2025 IP scanned using the BAS-1800 scanner was calibrated for different electron energies (11.5, 30, and 100 MeV). The rest of the curve shown in logarithmic scale in Figure 4-18 (a) was based on prior data. Figure 4-18 (b) displays the same graph in a linear scale. It shows that, for the electron range that we are interested in,

i.e. a few MeV – 100 MeV, the PSL/#electron ratio is almost constant. Note that these calibrations have been performed using the scanner BAS-1000, while in our experiments, the scanner FLA-7000 was used. For our purposes, we assumed that the PSL/#electron ratio would remain fairly constant regardless of the scanner, instead of performing a strict calibration.

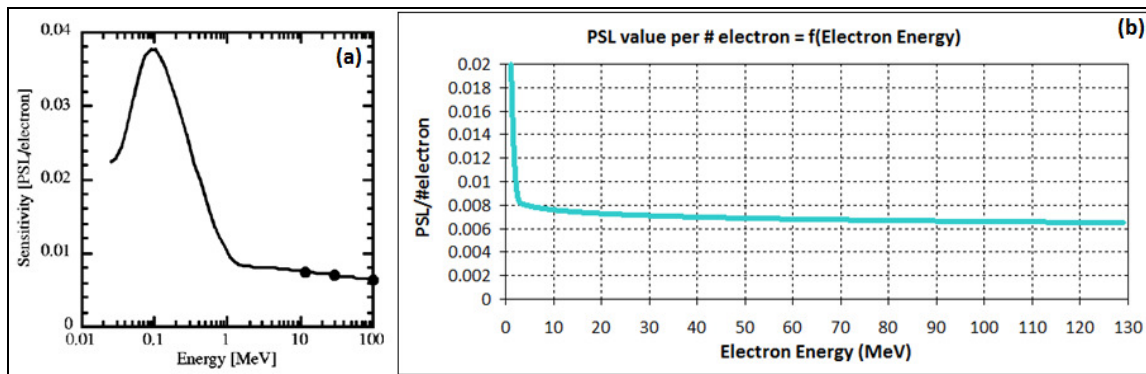


Figure 4-18: Calibration curve giving PSL/electron as a function of electron energy where the horizontal axis (energy in MeV) is displayed in (a) logarithmic scale and (b) in linear scale.

4.3.3 Effect of time: fading

In [166], the curve displayed in Figure 4-19 is obtained, and shows that the intensity of the signal decreases naturally as time goes by after exposure: some electrons which are in a meta-stable state lose energy due for example to thermal influence, thereby causing the fading phenomenon (the higher the ambient temperature, the greater the fading). The decrease in signal is the most important in the first 20 minutes (30 %), after which, between 20 minutes and 120 minutes, the fading effect is slow (less than 10 %).

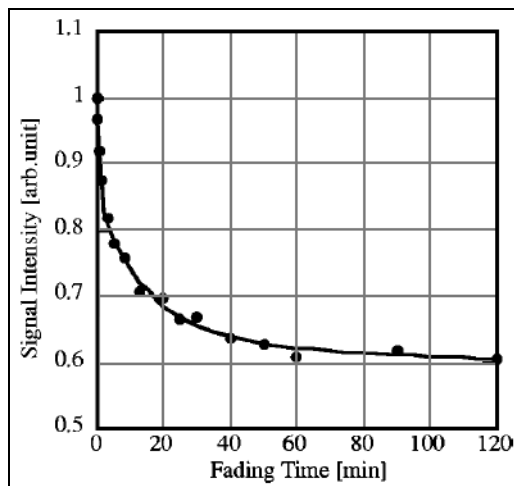


Figure 4-19: Signal Intensity (SI) in a.u. as a function of time [minutes] after exposition of the IPs, at t=0, SI=1.

In fact, FujiFilm recommends starting the scan 10 minutes after exposure, and also keeping the IP in a refrigerated shield-box, or in an environment at 14 °C. Only then can they assure that the PSL value will be proportional to exposure time (i.e. if 10 PSL are recorded in 1 hour, 100 PSL will be recorded in 10 hours).

During the August 2008 beamtime, we scanned the spectrometer’s IPs ~ 15 (\pm 5) minutes after the shot (because we were short on IPs and had to reload the cassette before pumping for the next shot). Also, we encountered some bleeding issues from one IP to the other, as illustrated in Figure 4-20: the detectors with a lot of signal (b) ends up bleeding onto the detectors placed below it, i.e. (c) all the way to (d). This is why some of the electron spectra sometimes have some zones along the spectrum lacking information.

During the June 2009 beamtime, to avoid bleeding, we made sure to scan only 1 line of detectors at the same time: we scanned the Cu K α imager’s IP as well as the shuttle spectrometer’s IP ~ 10 (\pm 2) minutes after the shot, the positron and proton IPs ~ 20 (\pm 2) minutes after the shot, and the electron’s IP ~ 30 (\pm 2) minutes after the shot.

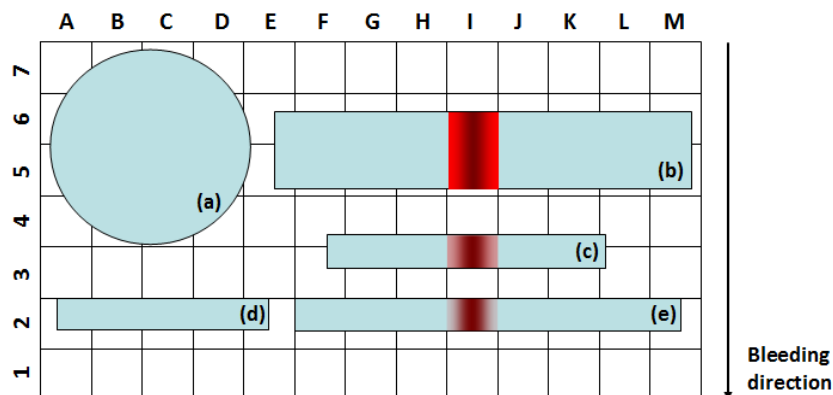


Figure 4-20: Example of how the detectors were placed on the magnetic tray during the August 2008 beamtime, and illustration of the bleeding phenomenon (in red).

4.4 Electron spectrometer SpecA

The electron spectrometer used in the experiments described in this dissertation has been used on the Nova PW experiments in 2000 [167]. It is designed to also record protons and positrons, as shown in Figure 4-21.

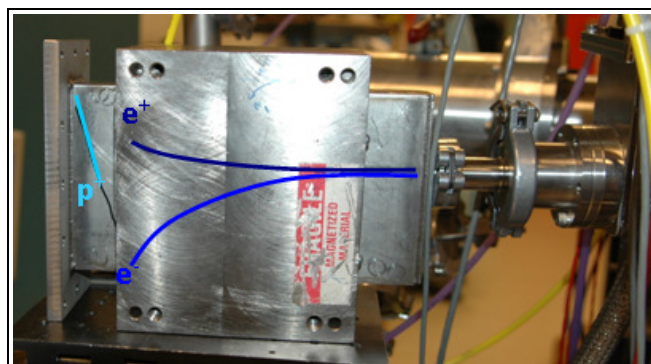


Figure 4-21: Picture of the ion/electron/positron spectrometer attached to the target chamber by a bellow.

As illustrated in Figure 4-21, the electron spectrometer can also be used for protons and positrons. The positron data has yet to be analyzed. As far as the proton spectra, they show modulations due to the generation of other ions, and in the end, they accumulate a lot of uncertainty in shape and number. This is why the proton spectra presented in this dissertation stem from the RCF stacks.

Using the electron energy deflection curve (purple curve in Figure 4-22) and the dE/dx curve (green curve in Figure 4-22), one can obtain an electron spectrum (see Figure 4-23) over the whole energy range from the data recorded on the IP (bottom of Figure 4-22).

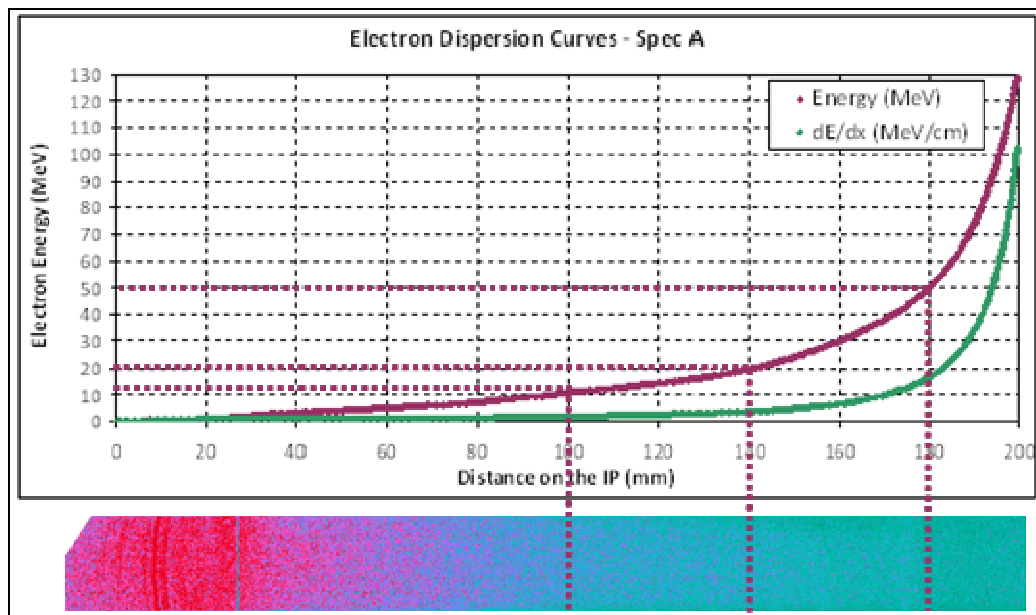


Figure 4-22: (top) Electron dispersion curves : the purple dispersion curve converts distance on the IP (bottom) to transform a distance on the IP into an electron energy in MeV, and the green curve gives the dE/dx in MeV/cm as a function of distance on the IP.

The zero of the electron spectrometer is defined on the IP at the extreme edge on the electron high energy side (i.e. 130 MeV). In the cassette storing the three IPs during the shot, the slot designed to receive the electron IP is such that, to fit, the IP has to be longer by about 1 cm on the low electron energy side.

From the electron energy deflection curve, one can see that the 1 – 50 MeV energy range occupies most of the length of the IP, i.e. 18 cm, while the 50 – 130 MeV energy range occupies only 2 cm on the IP. This means that the spectrometer is much more accurate for the energies between 5 and 50 MeV than at the highest energies. In most of the cases anyway, past 50 MeV, mostly noise is recorded.

The following shows the different steps needed to retrieve an electron spectrum such as the one displayed in Figure 4-23:

1) To obtain $\frac{N(E)_{PSL}}{dx} = f(mm)$, use an integrated and averaged lineout (of the .img file of the scanned IP) across the whole length of the detector.

2) To obtain $\frac{N(E)_{PSL}}{dx} = f(E)$, apply the purple curve shown in Figure 4-22.

3) To obtain $\frac{\frac{N(E)_{PSL}}{dx}}{\frac{dE}{dx}} = f(E) = \frac{N(E)_{PSL}}{dE}$, divide by the green curve shown in Figure 4-22.

4) To obtain $\frac{\frac{N(E)_{PSL}}{dE}}{\frac{PSL}{\#e}} = \frac{N(E)_{\#electron}}{dE} = f(E)$, divide by the turquoise curve shown in

Figure 4-18 (b).

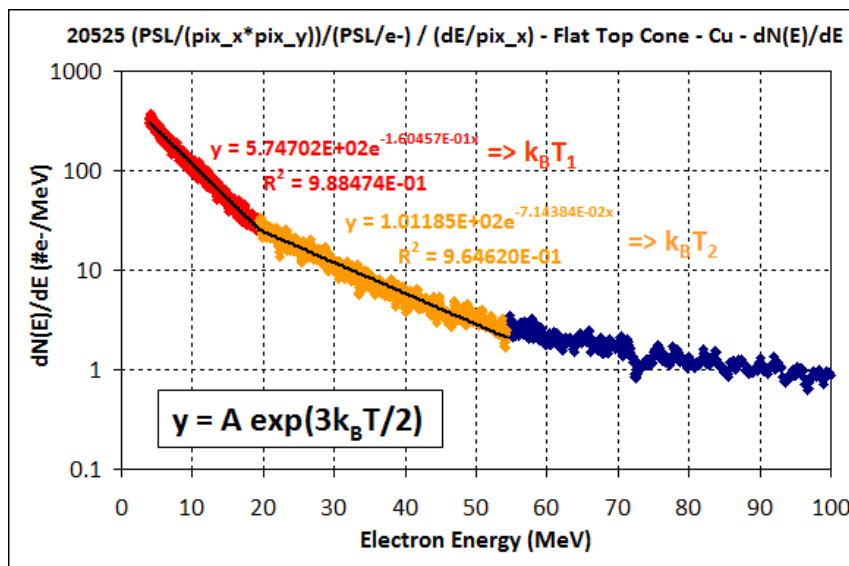


Figure 4-23: Example of an electron spectrum: T_1 is obtained using the red data points and T_2 using the orange data points; the signal past ~ 70 MeV corresponds to noise.

Note that there is some significant amount of error in the electron temperature measurement, due to the fact that the hole in the RCF, which allows the electrons to reach the spectrometer unperturbed, and which is set to coincide with the entrance slit of the spectrometer, does not necessarily coincide with the center of the proton beam and/or the most energetic portion of the electron beam. The beam shown in Figure 5-23 (a) is perfectly aligned with the hole, while it is not true of the beams shown in Figure 5-23 (b) and Figure 5-33 for example. Moreover, the solid angle sampled by the spectrometer is rather small (for energy resolution purposes), which does not allow for significant spatial sampling of the electron population. The electron divergence is difficult to characterize for each shot. Also, the electron spectrum does not always follow a Maxwellian distribution. However, all of the shots analyzed for the purpose of this dissertation exhibited a distribution very similar or close to a Maxwellian distribution, except for the case of shot 21171, which is therefore excluded from the trendlines in Figure 5-58.

4.5 2-D spherical crystal $K\alpha$ X-ray imager

As discussed previously, $K\alpha$ x-ray emission can be indicative, in dense matter, of fast electron transport: electrons which have sufficient energy above the ionization potential can create K-shell 1s vacancies allowing for $2p \rightarrow 1s$ transitions. In a cone target, 2-D $K\alpha$ x-ray emission helps diagnose the amount of preplasma filling, as well as the laser alignment.

The narrow x-ray emission range (around the Cu $K\alpha$ lines, in energy: 8.02784 keV and 8.04782 keV, or in wavelength 1.54442 Å and 1.54059 Å) from the laser-irradiated target is time integrated and spatially resolved using a spherically-bent Bragg quartz crystal imager

[168, 169, 170]. Indeed, two-dimensionally bent Bragg imaging crystals are commonly used to image multi-keV plasma x-ray emission [171, 172, 173, 174, 175].

Quartz crystals have been used extensively for x-ray imaging. The imaging properties of spherically-bent crystals are analogous to those of spherical mirrors, and can be described via simple geometric optics. Although through destructive interference the x-ray waves cancel one another out in most directions from the crystal, they add constructively in a few specific directions, determined by Bragg's law $2d \sin \theta = n\lambda$, where d is the spacing between the diffracting planes, θ is the incident angle also known as Bragg angle, n is the diffraction order, and λ is the wavelength of the beam. The wavelength λ of the X-rays is typically the same order of magnitude (1-100 Å) as the spacing d between planes in the crystal.

Spherically-bent quartz crystals can be used to image at many different x-ray energies. This is due to the fact that quartz crystals contain numerous planes with different inter-planar spacings suitable for Bragg diffraction, thanks to the structural properties of framework silicates. When the crystal structure itself is nearly perfect, high-quality x-ray images can be obtained.

In order to minimize astigmatism, the angle of incidence θ has to be within several degrees of normal, allowing spherically bent crystals to provide high spatial resolution over large fields of view. This restriction on θ , along with the fixed inter-planar spacing $2d$ of the crystal itself, restricts the operating wavelength λ for a particular crystal to a narrow range to the short-wavelength side of $\lambda = 2d$.

To broaden the range of suitable imaging wavelengths, instead of using spherically-bent crystals, one can use either toroidally-bent crystals, or a completely different type of crystal. Toroidally-bent crystals use different sagittal and meridional radii of curvature to eliminate

astigmatism for incident angles far from normal; however, high-quality toroidal surfaces are much more complex to fabricate, and the resulting imaging optic is difficult to align due to constraints on all six degrees of positioning freedom [168].

4.5.1.1 Crystal parameters

Because of the curvature of the crystal, there is a meridional focus defined as

$$q_m = \frac{pR \sin \theta}{2p - R \sin \theta} \text{ and a sagittal focus defined as } q_s = \frac{pR}{2p \sin \theta - R} .$$

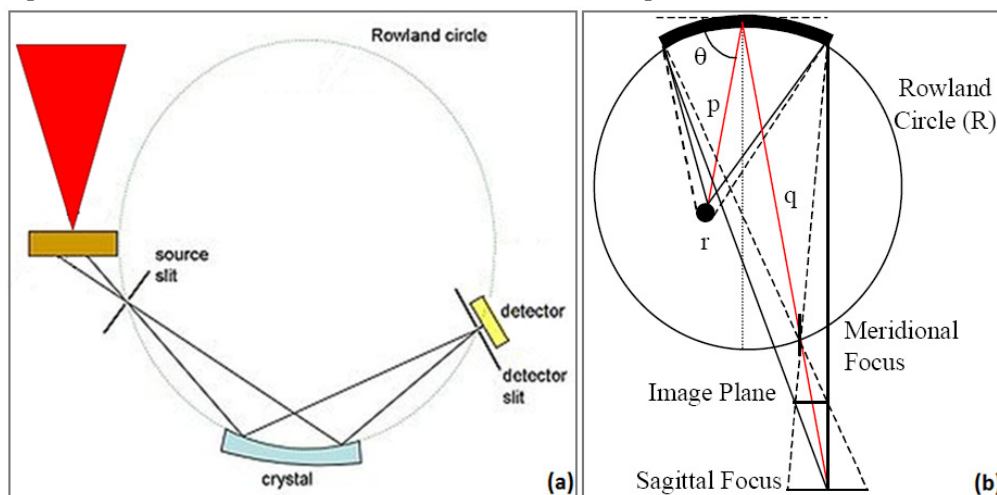


Figure 4-24: Spherically bent quartz Bragg crystal: (a) Simple illustration of the set-up of a crystal in the Rowland circle (diameter = $R = 150$ mm); also represented are the laser interacting with the target, the source aperture, the detector slit and the detector. (b) Illustration [180] containing the different variables: the different plans of focus, meridional and sagittal, are displayed; θ is the angle of incidence, p is the object distance and q is the image distance.

4.5.1.2 Experimental set-up

As discussed in the previous section, the energy of the viewing window depends on both the Bragg angle (which must be small to reduce linear dispersion) and on the $2d$ lattice spacing of the crystal.

In the experiments described in this dissertation, the quartz used is 2131, which has a $2d$ separation of 3.084 \AA and a Bragg angle of 88.7° . The crystal is rotated by 1.3° to observe the Cu $K\alpha_1$ line in the 2nd order diffraction (i.e. $n = 2$). As illustrated in Figure 4-24, the

crystal is placed in a Rowland circle whose diameter equals the radius of curvature of the bent crystal, i.e. $R = 150$ mm, as indicated on the crystal.

The object distance is $p = 78.5$ mm and the image distance is $q = 798.8$ mm.

As shown in Figure 4-25, the crystal was set 22.5° below the equatorial plane and the transverse view of the target was therefore imaged behind a flange with a Kapton window, 22.5° above the equatorial plane in order to minimize the background. Indeed, when positioned in the equatorial plane, the background is much stronger. The crystal was coupled to an IP protected by Al foil and a Cu or Ni filter.

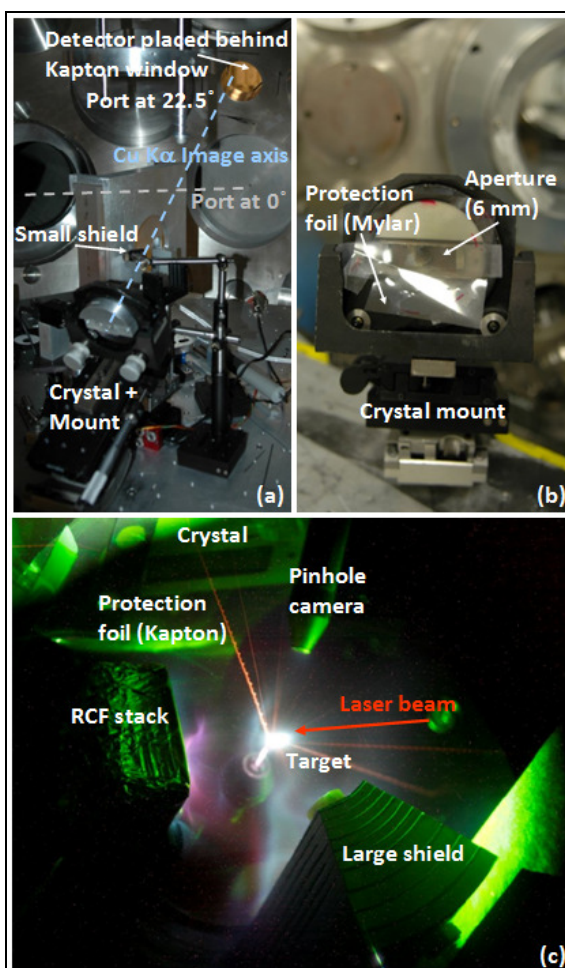


Figure 4-25: (a-b) August 2008 experiments: (a) picture of the inside of the target chamber and (b) picture of the crystal and part of the crystal mount; (c) June 2009 experiments: integrated image over a shot.

4.5.1.3 Magnification

As shown in Figure 4-26, $p = 78.5$ mm and $q = 798.8$ mm, which yields a magnification

$$M = \frac{q}{p} = 10.2.$$

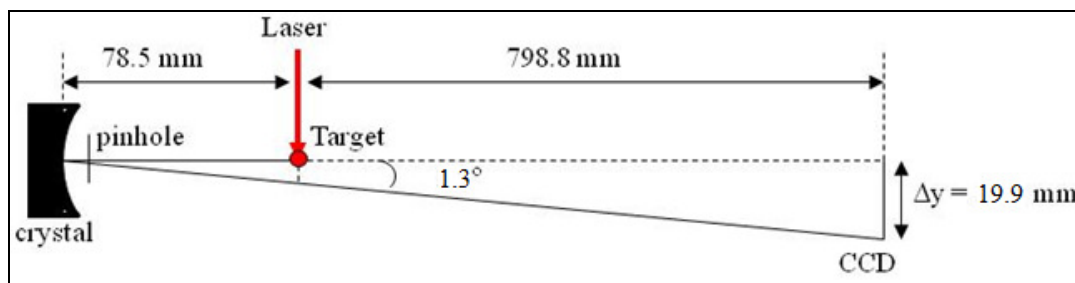


Figure 4-26: Setup for the transverse 2-D imager: the target is the source, the distance between the crystal and the source is $p \sim 78$ mm, and the distance between the source and the image is $q \sim 799$ mm. The crystal rotation is 1.3° , and the lateral shift is $\Delta y \sim 2$ cm.

4.5.1.4 Effect of target heating

At laser intensities of $\sim 10^{20}$ W/cm², as a Cu target is heated, a shift in the ionization balance to higher Cu charge states takes place, which results in a broadening and blue-shift (shorter wavelength) of the $K\alpha$ emission. This causes, for narrow-band crystal imagers, a reduction of the detection efficiency [176]. The imager has a spectral range of at most ~ 10 eV, which means that it is able to detect from 8047.7 eV up to ~ 8057 eV.

Figure 4-27 shows the transition energy and wavelength for different ionization states of Cu $K\alpha$ [180]; the neutral state is referred to as cold. Note that a 2 eV spectral range correspond to 14 ionization states and that the corresponding temperature for Cu¹⁴⁺ is 435 eV and for Cu¹⁵⁺ is 484 eV. Therefore, the imager is still able to see fairly hot states.

Ionization State of Cu	Energy (eV)	Wavelength (Å)	
0	Neutral	8047.77	1.5414
14+	P-like	8049.97	1.5410
15+	Si-like	8055.19	1.5400
16+	Al-like	8060.43	1.5390
17+	Mg-like	8065.67	1.5380
18+	Na-like	8070.92	1.5370
19+	Ne-like	8076.17	1.5360
20+	F-like	8095.14	1.5324
21+	O-like	8132.83	1.5253
22+	N-like	8171.94	1.5180
23+	C-like	8212.40	1.5105
24+	B-like	8254.32	1.5029
25+	Be-like	8297.66	1.4950
26+	Li-like	8337.10	1.4879
27+	He-like	8377.51	1.4808

Figure 4-27: Transition energy and wavelength for different ionization states of Cu K α [180]; the neutral state is referred to as cold. In red are the states that can be seen by the Cu K α imager.

4.5.1.5 Addition of a pinhole in front of the crystal

Adding a pinhole in front of the crystal decreases the field of view, the spectral range and the energy fluence, but increases the spatial resolution.

4.5.1.5.1 Field of view

When using a pinhole, the field of view (fov) of the imager is defined as $fov = \frac{D}{2} \left(1 - \frac{1}{M} \right)$,

where D is the pinhole diameter. For any 1x1 mm² target to be imaged, a pinhole of 2 mm or larger needs to be used. Using the values $D = 6$ mm and $M = 10.2$, the fov is found to be 2.7 mm, which is much larger than what's necessary to image most targets used.

4.5.1.5.2 Spatial resolution

The effective spatial resolution depends on the combination of the incidence Bragg angle, the crystal quality, the (finite) source size (dependent on magnification and pinhole size), and the imaging plate detector. However, what degrades the image resolution the most is

the astigmatism (linked to the Bragg angle). The predicted astigmatism-limited object

$$\text{spatial resolution is given by } \sigma = \frac{D(M + 1)}{M} (1 - \sin \theta).$$

For $D = 6 \text{ mm}$, $M = 10.2$ and $\theta = 88.7$, $\sigma = 1.7 \text{ }\mu\text{m}$.

For $D = 8.8 \text{ mm}$, $\sigma = 2.5 \text{ }\mu\text{m}$. The resolution of the IP is $25 \times 25 \text{ }\mu\text{m}^2$. The image forms on the IP with a factor 10 in magnification. An image which would be $25 \times 25 \text{ }\mu\text{m}^2$ on the IP should therefore stem from an emitting zone in the target of $2.5 \times 2.5 \text{ }\mu\text{m}^2$. This means that any pinhole smaller than 8.8 mm would not improve the image resolution as it cannot be better than $2.5 \text{ }\mu\text{m}$ (due to the IP and magnification constraints).

For $D = 35 \text{ mm}$, $\sigma = 10 \text{ }\mu\text{m}$: this basically describes the case where no pinhole is used.

4.5.1.5.3 Spectral range

A pinhole placed on the crystal increases the spatial resolution but it reduces the spectral range [176], as illustrated in Figure 4-28.

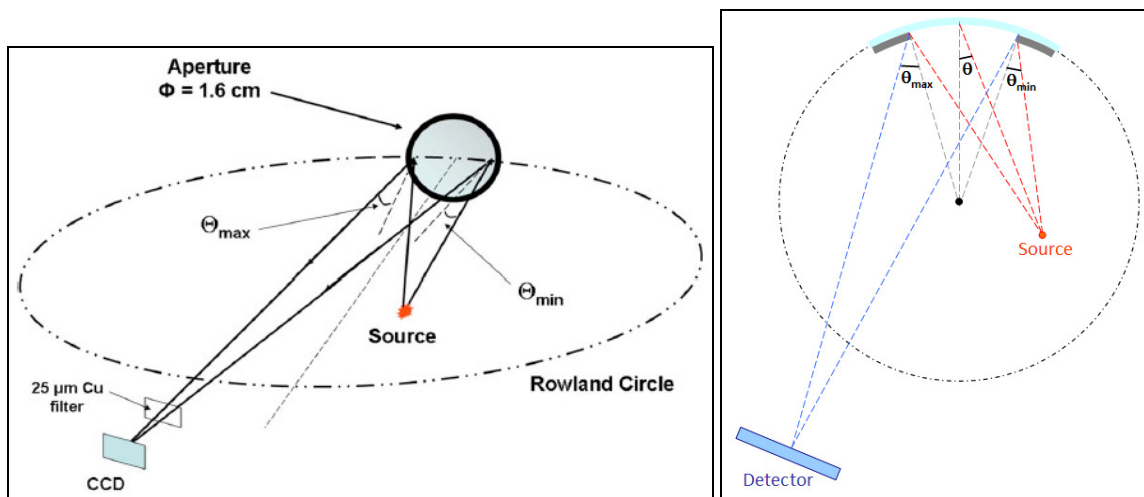


Figure 4-28: Spherically bent quartz crystal with pinhole, indicating the angles θ_{min} and θ_{max} which determine the spectral range of the crystal: (left) 3-D representation [176] and (right) 2-D representation.

5 EXPERIMENTS: TARGETS, SET-UPS & RESULTS

The experiments described in this dissertation have taken place over the past 4 years and consisted of 4 beamtimes on the short pulse arm of the Trident laser system described in Section 3. A lot of data has been acquired, and it is being presented chronologically in a comprehensive fashion in this section. Section 5.2 describes the experiments at 20 J and intrinsic contrast, Section 5.3 describes the experiments at 80 J and intrinsic contrast, and Section 5.4 describes the experiments at 80 J and enhanced contrast. For each experimental campaign, we present the targets, the set-up or set-ups, and the proton, x-ray and electron results. But first, Section 5.1 gives an introduction on the laser-cone interaction research.

5.1 Cone research for Fast Ignition and other applications

Figure 5-1 shows, using the same scale for all images, the various types of targets that have been used so far in laser-cone interaction research. These cones are required by some fast ignition schemes to keep the propagation path for the ignitor laser clear of plasma, to guide the incoming laser, to protect the target generating the electrons or ions, and to enhance the performance of the said target.

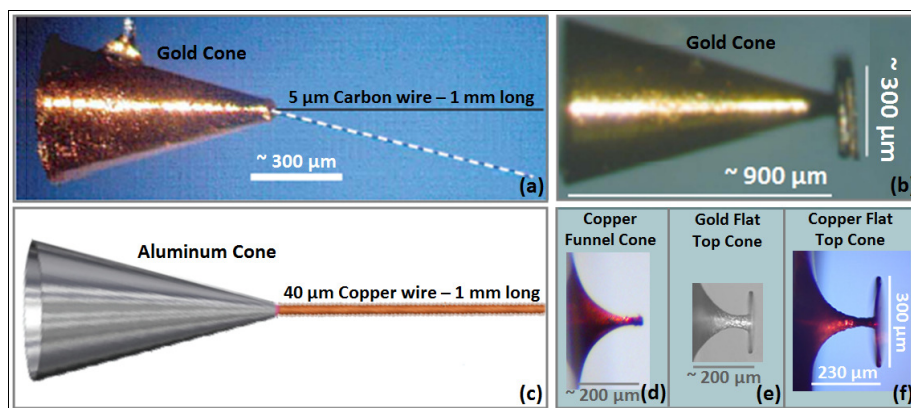


Figure 5-1: All pictures are to scale (a-c) Cones with 30° opening angle; (a) Au cone, 1 mm long, 5 μm C fiber [45, 178, 179]; (b) Au cone, attached on a 300 μm by 300 μm planar foil [4]; (c) Al Cone with a 1 mm long, 40 μm Cu fiber [177]; (d) Cu Funnel cone (FC) [3, 180, 181]; (e) Au flat-top cone (FTC) [1]; (f) Cu FTC [2, 5].

In order to increase the ion energies and conversion efficiencies, following on work by Kodama *et al.* [45], which used hollow gold cones (see Figure 5-1 (a)) to convert ~ 40 % of the laser energy into the hot-electrons and enhance the hot-electron density by an order of magnitude, Y. Sentoku *et al.* [44] carried out 3-D PIC simulations showing how the cone enhances the electron density: compared to a simple flat-foil target, the laser light is optically guided inside a conical target and concentrated at the tip of the cone, resulting in a large increase (many 10s) in the intensity. The hot-electron density at the cone tip is 10 times higher than for a regular flat-foil target, due to the convergence of the electron flow guided by the balance between the self-generated quasi-static magnetic fields (the $J \times B$ force pushes the electrons toward the surface) and the electrostatic sheath fields (which cancels the $J \times B$ force) for relativistic electrons. The cone seems to improve laser-target coupling efficiencies and allows for better guiding of the laser light and for hot-electron convergence toward the cone tip. This simulation work led to some exploratory work by T.E. Cowan *et al.* and the company NanoLabz to produce gold flat-top cone (FTC) targets of the type shown in Figure 5-1 (e). These micro-cone targets were shot on Trident, at 20 J and at the intrinsic 10^{-8} contrast level, first in the 03-2006 Sisyphus III campaign, and then in the 08-2006 Alba campaign, producing some very exciting results [1]. The proton energy was boosted from the nominal 19 MeV (and 0.75 % conversion efficiency) observed from a 10 μm Au flat-foil target to more than 30 MeV (and 2.5 % conversion efficiency) observed from the Au FTC target. Simulations performed by Y. Sentoku and E. d'Humières showed that it was possibly boosted as high as 40 MeV. Unfortunately at the time, the detector stack was limited to an upper range of 30 MeV, due to holder constraints. More simulations also showed that the electron temperature is higher in cones (compared to a planar target or to a reduced-mass target (RMT)) even if the laser is misaligned.

However, in order to efficiently accelerate protons, it is important (and even crucial) that the electrons reach the tip. To take advantage of the cone geometry, the amplified spontaneous emission (ASE) prior to the main pulse has to be decreased to an amount such that the preplasma produced does not prevent the laser from propagating down the tip. Baton *et al.* [4, 110] demonstrated, using the targets shown in Figure 5-1 (b) and Cu K α imaging, that the ASE preformed plasma fills the cone and degrades the respective coupling efficiencies.

Cu K α imaging was also used by T. Ma *et al.* [177] to image the electron propagation down a copper wire attached to an aluminum cone (as illustrated in Figure 5-1 (c)). The cones illustrated in Figure 5-1 (a) and (c) have similar size, shape and an opening angle of 30°. It was shown that the coupling efficiency of the laser into electrons, in the tip of the cone and beyond, is dependent on the laser prepulse and on the cone wall thickness: the coupling decreases by a factor of ~ 3 when the wall thickness increases (from 12 μm to 200 μm), or when the prepulse increases (by a factor of 65).

In [178], Nakatsutsumi *et al.* showed that the slope temperature of fast electrons is strongly dependent on the opening angle of the cone, and is maximum for a cone opening angle of 25°. Ray-tracing calculations were performed to estimate the enhancement of the light intensity and of the energy concentration at the tip of the cone. These calculations confirmed optical guiding and suggested that the optimum opening angle is related to the $f^\#$ of the laser focusing optics.

In [179], Nakatsutsumi *et al.* showed that the hot electrons are able to reflux many times along the wire, depositing more energy; in fact, compared to two types of flat-foil targets (i.e. wide and narrow), the cone/wire geometry (see Figure 5-1 (a)) allowed for increased energy deposition due to longitudinal refluxing, while reducing the electron beam

divergence from 30°-40° (in the flat foil cases) down to 5° in the cone/wire geometry due to lateral refluxing.

The cones illustrated in Figure 5-1 (d-f) are different from the straight cones illustrated in Figure 5-1 (a-c) in that their cone wall angle varies all the way to the tip, allowing for a constant chance to match the laser optics at some point.

In a different conical geometry as that of [4] (i.e. Figure 5-1 (b)), using funnel cones illustrated in Figure 5-1 (d), which are similar to an FTC, but without the flat top, J. Rassuchine *et al.* [180, 3, 181] also showed, always using Cu K α imaging, that at low contrast (1ω , 1064 nm, 20 J), the electrons cannot penetrate deep in the funnel and reach the tip, while at high contrast (2ω , 532 nm, 10 J), there is enhanced laser absorption leading to an enhanced electron density toward the cone tip. In the high contrast case, peak temperatures of ~ 200 eV were observed, revealing similar hot-electron localization and material heating to RMTs, despite having a significantly larger mass (i.e. 900 times larger). Y. Sentoku's collisional PIC simulations attribute the observed enhancement to self-generated resistive magnetic fields (~ 10 MG), forming within the curvature of the funnel-cone wall, which confine energetic electrons to heat a reduced volume at the tip: in the funnel-cone target case, the electron confinement mechanism is magnetic, while in the RMT case, the confinement is caused by the electrostatic sheath.

Funnel-cone targets act like RMTs, allowing the laser to heat a much larger fraction of the electrons to high temperatures, enhancing the hot-electron density and limiting the expansion of the sheath to the area of the flat-top [1], confining the hot-electrons to a denser, more uniform sheath, thus significantly boosting the uniformity, efficiency and energy of the ions accelerated via the TNSA [12] mechanism.

New experiments performed on Trident using copper targets of the geometry illustrated in Figure 5-1 (e) and (f) are described in detail in this dissertation. In these experiments, Cu $K\alpha$ imaging was used to diagnose the laser-target interaction and study the electron propagation and transport, and laser absorption in the cone and to the flat top. The first experimental run was performed in 08-2008 at ~ 80 J and the intrinsic 10^{-8} contrast level [2], and showed that the preplasma prefill inside the cone prevented any efficient proton acceleration: the proton energy was much lower than that of a flat foil of similar thickness. The second experimental run was performed in 06-2009 at ~ 80 J as well, but using the enhanced contrast level of 10^{-10} at the same wavelength (i.e. 1054 nm) [5], and showed enhanced proton energies up to the record energy of 67.5 MeV; however, to our surprise, the proton conversion efficiency using these FTCs was not enhanced to more than that of a flat foil, even though we were expecting an ~ 5 -fold increase, as in [1].

The efficiency of the proton acceleration should be a function of the cone geometry (neck and flat-top) as well as laser conditions (energy, pulse duration, prepulse levels, and alignment) as simulations have shown. More experiments will be performed in a near future (06-2010) to systematically explore the effect of the target geometry and of the laser characteristics on the conversion efficiency. If the efficiency were to exceed 10 %, since the laser-to-proton (or laser-to-ion) conversion efficiency directly translates into a higher fusion gain and/or lower costs, then a geometry such as that illustrated in Figure 5-2, where the flat top would focus the proton beam, could be of great interest for IFI.

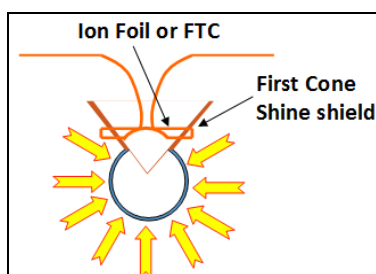


Figure 5-2: Schematic of PFI/IFI using an FTC as the focusing proton or ion beam target.

5.2 Trident, 20 J, $\sim 10^{19}$ W/cm² & intrinsic 10^{-8} contrast: March 2006 (Sisyphus III) & August 2006 (Alba) beamtimes

5.2.1 Experimental set-up

In these two sets of experiments, performed in the North Target Area, the short-pulse of Trident pre-enhancement (3.2.1) was used (*P*-polarized), at intrinsic contrast (10^{-8}). The deformable mirror was not yet installed. As illustrated in Figure 5-3, the set-up of the experiment consisted in a RadioChromic Film stack placed ~ 2.5 cm behind the target and the *P*-polarized laser was normally incident into the FTCs (after, and including shot 18567), while the laser was incident on the flat foils at a compound angle of 18.5° in elevation and 22.5° azimuthally. Although we intended to shoot these FTC targets normal to the laser, the exact angle of laser incidence was hard to determine exactly, because the targets had to be pre-mounted to the stalk in such a way as to correct for the elevation portion of the compound angle, and then rotated 22.5° during the alignment process. So there was undoubtedly some amount of misalignment to the laser beam in all cases. Also note that a few cones (the first few shots) were not rotated i.e. shot with the 22.5° incidence angle.

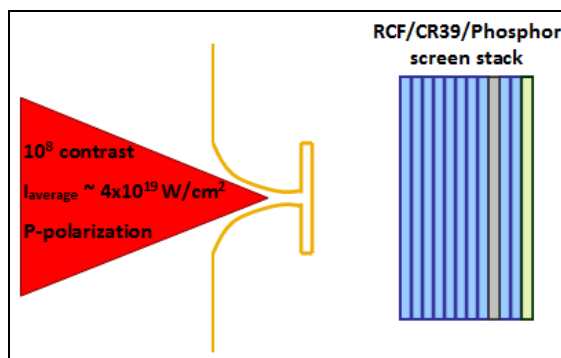


Figure 5-3: Set-up of the March 2006 (18554-18584) and August 2006 (18953-19060) Trident beamtimes, where various gold FTCs (with different top and neck diameters) were shot. The proton beam emission is recorded in an RCF stack (blue); the grey layer corresponds to the CR39 detector, and the last layer (light green) to the Lanex regular phosphor screen. Laser parameters: ~ 20 J, ~ 600 fs, ~ 12.6 μm diameter focal spot ($\sim 45\%$), *P*-polarization, $\sim 1 \times 10^{19}$ W/cm².

5.2.2 Description of the Gold flat-top-cone (Au FTC) targets

These Au FTCs come on a wafer of several hundred. Only a few in a row are displayed in Figure 5-4 (a). They are produced by a nanofabrication lithographic layer process on Si wafer, made initially of silicon nitride Si_3N_4 ($\leq 2 \mu\text{m}$) and silicon oxide SiO_2 ($\leq 4 \mu\text{m}$) thin films. Some unknown amount of Si_3N_4 and SiO_2 is lost in the fabrication process, and the Si_3N_4 layer may not even survive, so in actuality it could even be something like $0 \mu\text{m}$ of Si_3N_4 and SiO_2 of $2 \mu\text{m}$. This thin film is then encased via sputtering deposition by a $5\text{-}10 \mu\text{m}$ layer of ultra-high purity (99.9 %) gold or copper (depending on the desired target material), with a 500 nm adhesion layer of titanium. The sputtering process results in a very uniform deposition, without any preferential deposition axis, i.e. the thickness of the target should be the same everywhere except for the top (which should be slightly thicker, i.e. $10\text{-}15 \mu\text{m}$). After this metallization stage, the silicon mold is etched away (see Figure 5-5), to only leave Au or Cu FTC targets. Note that the top still contains some amount of silicon.

A forest of targets is produced, in rows separated by $\sim 200 \mu\text{m}$ and with separation within a row of $\sim 50 \mu\text{m}$. The small separation distances make it difficult to isolate a single target. Each cut can damage the top (by slightly bending the supporting foil), which also often then fell off.

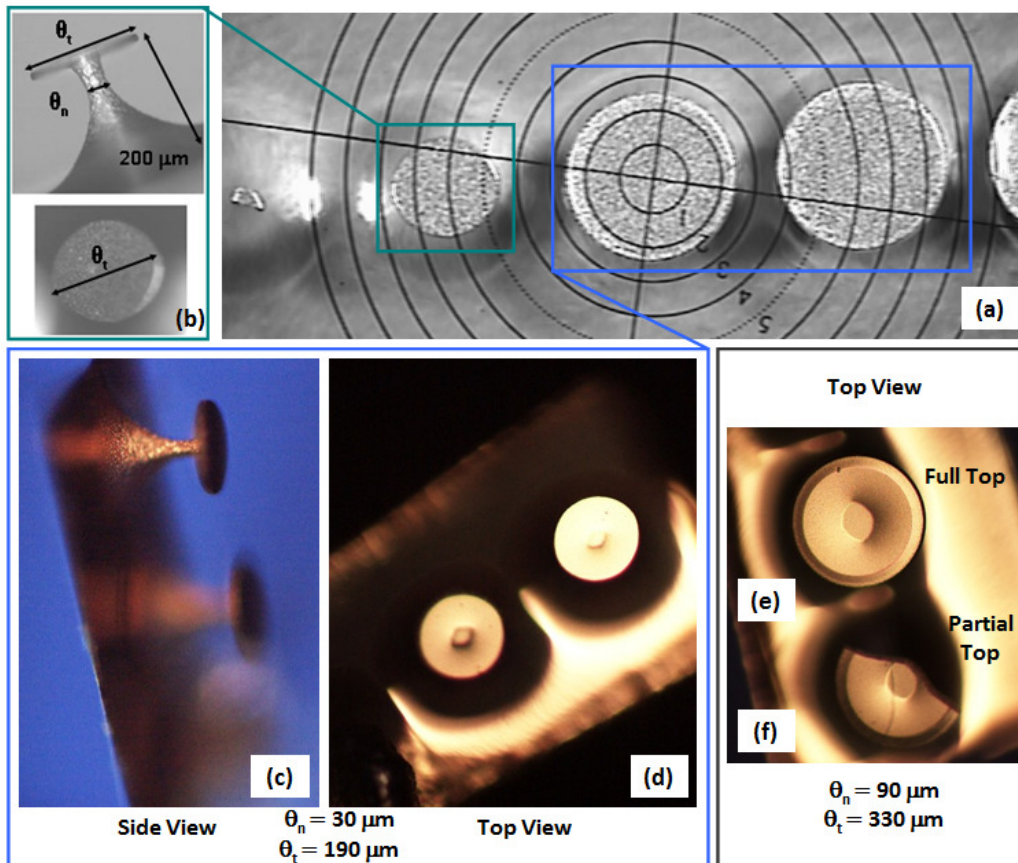


Figure 5-4: Pictures of Au FTCs: (a) shows a wafer of Au FTCs; (b) shows a side and top view of an FTC. θ_t represents the diameter of the top, and θ_n the outside diameter of the neck.

The best performing cone was the one for which $\theta_t = 100 \mu\text{m}$ and $\theta_n = 22 \mu\text{m}$, that is a Top/Neck ratio of ~ 4 ; (c) & (d) show color pictures of the FTCs, cut and mounted on a glass post; (e) shows a much larger FTC; (f) has the same characteristics as (e), but the top is only partial.

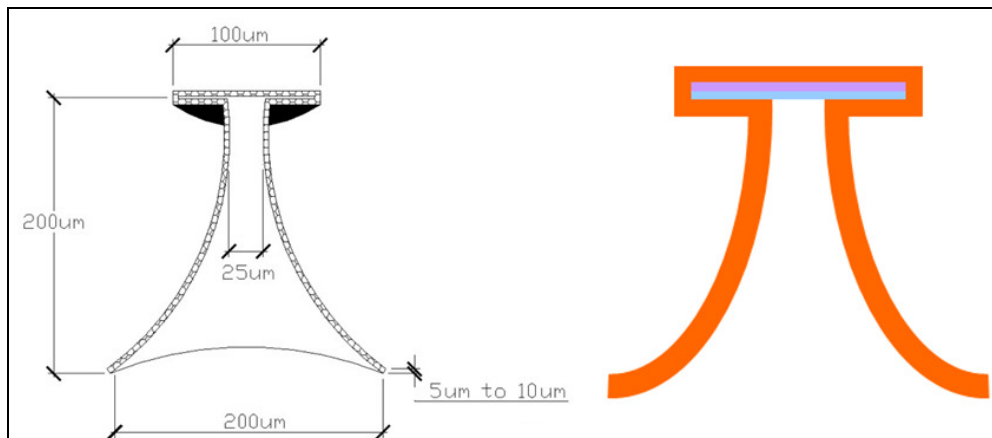


Figure 5-5: Schematic representation of the profile of a [5 μm ; 10 μm] thick Au or Cu FTC target; (left) with dimensions and (right) showing the Si remains; the blue stands for SiO_2 and the purple for Si_3N_4 .

During the March 2006 campaign, a few targets were mounted by the LANL precision target fabrication laboratory. Each target consisted of a single FTC target, glued on a boron fiber which was glued inside of a hollow glass stalk.

During the August 2006 campaign, due to a limited access to the LANL target fabrication laboratory, the targets were cut and mounted in house. In order to make sure that one FTC would survive in the cutting process, 3 at a time were cut out, thereby increasing the size of the supporting foil and the total mass of the target.

Cone targets, RMTs and small flat-foil targets were always glued either directly on glass stalks, pulled to a few 10s of μm thin tips, using a pipette puller, or on a 100 μm diameter boron fiber (sturdier) glued to a glass stalk (Figure 5-6 (left)). The glass stalks were inserted in the target holder inside the chamber. Larger targets (i.e. $2 \times 7 \text{ mm}^2$ flat foils) were held tight in a ceramic holder with a kinematic base (Figure 5-6 (right)). In all cases, the targets were mounted on non-metallic, low conductivity material to minimize the electron flow between the target and the target holder and therefore ensure electrostatic confinement of the fast electrons inside the target [132].

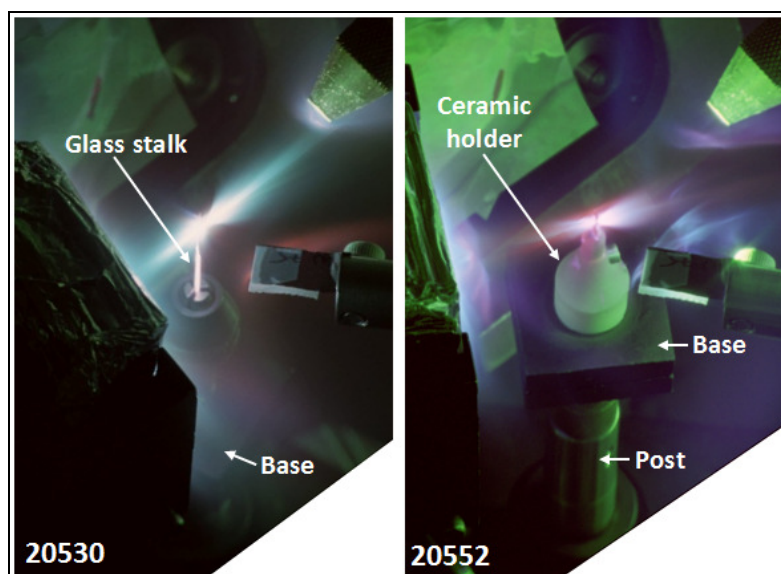


Figure 5-6: Target holders: (left) Glass stalk, and (right) Ceramic holder.

5.2.3 Summary of the results

In short, we found that at 19 J and at the intrinsic 10^{-8} contrast, the maximum proton energy and the laser-to-proton conversion efficiency obtained from a 10 μm Au FCT target were > 30 MeV and 2.5 % respectively, compared to 19 MeV and 0.5 % from a 10 μm Au flat-foil target [1].

However, these conversion efficiencies were obtained using RCFs scanned with a scanner (Epson) and the calibration curves for that scanner (i.e. prone to scanner error). Since then, we obtained calibration curves for a MicroD, and scanned with a MicroD in white light. The results are summarized in Table 6.

	Maximum Proton Energy	Conversion efficiency (scanner)	Conversion efficiency (MicroD)
Au Flat Foil (10 μm)	19 MeV	0.5 %	0.15 %
Au FTC (10 μm thick, best performer)	> 30 MeV	2.5 %	1.1 %

Table 6: Au FTC and flat foil comparison: Maximum proton energy, conversion efficiency obtained from a scanner and from a MicroD (white light).

5.2.4 Results presented in detail: Comparison in the maximum proton energies for various FTCs, proton spectra and PICLS simulations

Figure 5-7 shows the RCF stack obtained from a shot on a 10 μm thick Au flat foil, which produced a proton beam with a maximum proton energy cut-off of 19 ± 1 MeV.

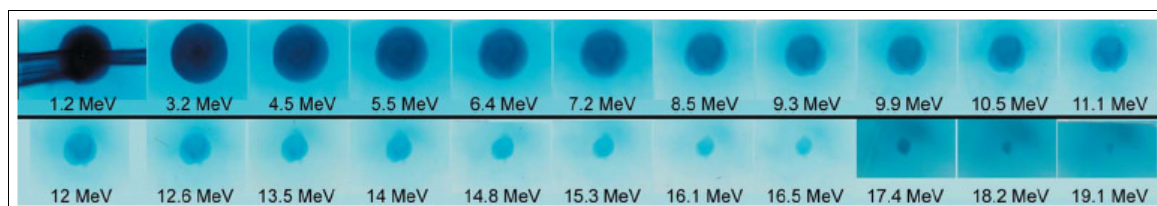


Figure 5-7: Shot 18500; Au flat-foil target: 10 μm thick, 2 mm by 15 mm; RCF stack: 12.5 μm Al, 6 HD films, a 25 μm brass absorber spacer, 5 HD films, brass, 2 HD, brass, 2 HD, brass, 2 HD, brass, 2 HD, and 3 MD-55 [1].

Figure 5-8 shows the RCF stack obtained from a shot on a Au FTC (100 μm top, 25 μm neck, 10 μm thick), which produced a proton beam whose maximum energy was not recorded, because the stack was unfortunately not thick enough, due to holder constraints. The last piece of the stack, a Lanex phosphor screen, corresponded to a proton energy of ~ 30 MeV.

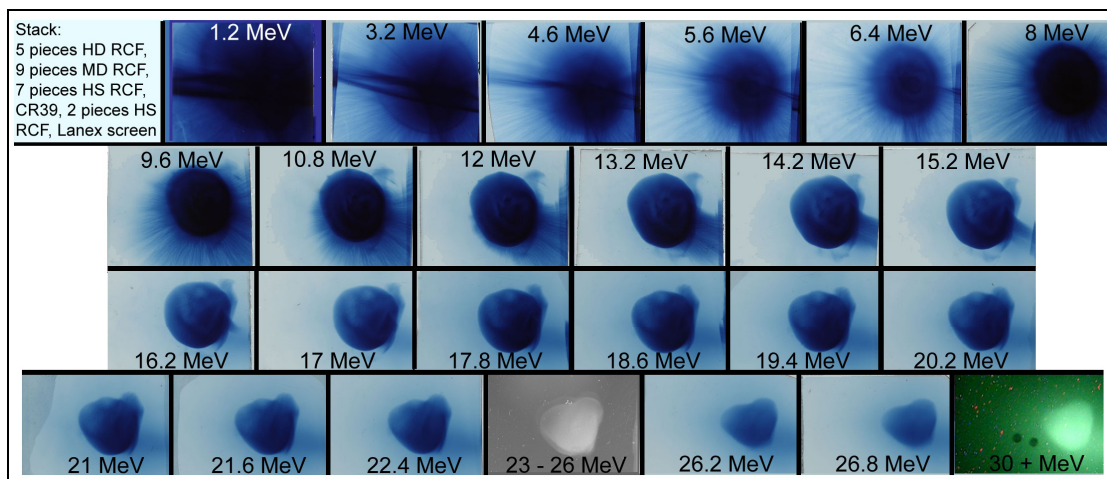


Figure 5-8: Shot 18582; FTC target: 100 μm top, 25 μm neck, 10 μm thick; laser well aligned laser down the throat; RCF stack: 25 μm Al, 5 HD, 9 MD, 7 HS, a piece of 1100 μm thick CR-39, 2 HS, and a piece of Lanex regular on the back [1].

In Figure 5-8, one can also see that the size of the beam is still very large at ~ 30 MeV (compared to the Au flat-foil beam), and we estimated, using the beam reconstruction from the RIS method, as displayed in Figure 5-9, that the beam could have potentially been as energetic as ~ 44 MeV.

In Figure 5-9, the horizontal axis represents the divergence angle θ of the proton beam emitted from the target (rear side), and the vertical axis is the scaled proton energy ratio $E_{\text{proton}}/E_{\text{max}}$, for (A) E_{max} is 19 MeV, and for (B) E_{max} is chosen to be ~ 40 MeV (as suggested by the simulations). Superimposed over each of the reconstructions are similar isosceles triangles with an apex angle ϕ of 49° , indicating that the deposition angle of the beams is similar in both the flat foil and the flat-top cone cases, even though (B) starts out at a much larger initial divergence. At the top of each triangle is a line at the cut-off of (A) and where

this cut-off (assuming the typical cut-off of 5° divergence) should be for (B), indicating that the beam was potentially around 44 MeV.

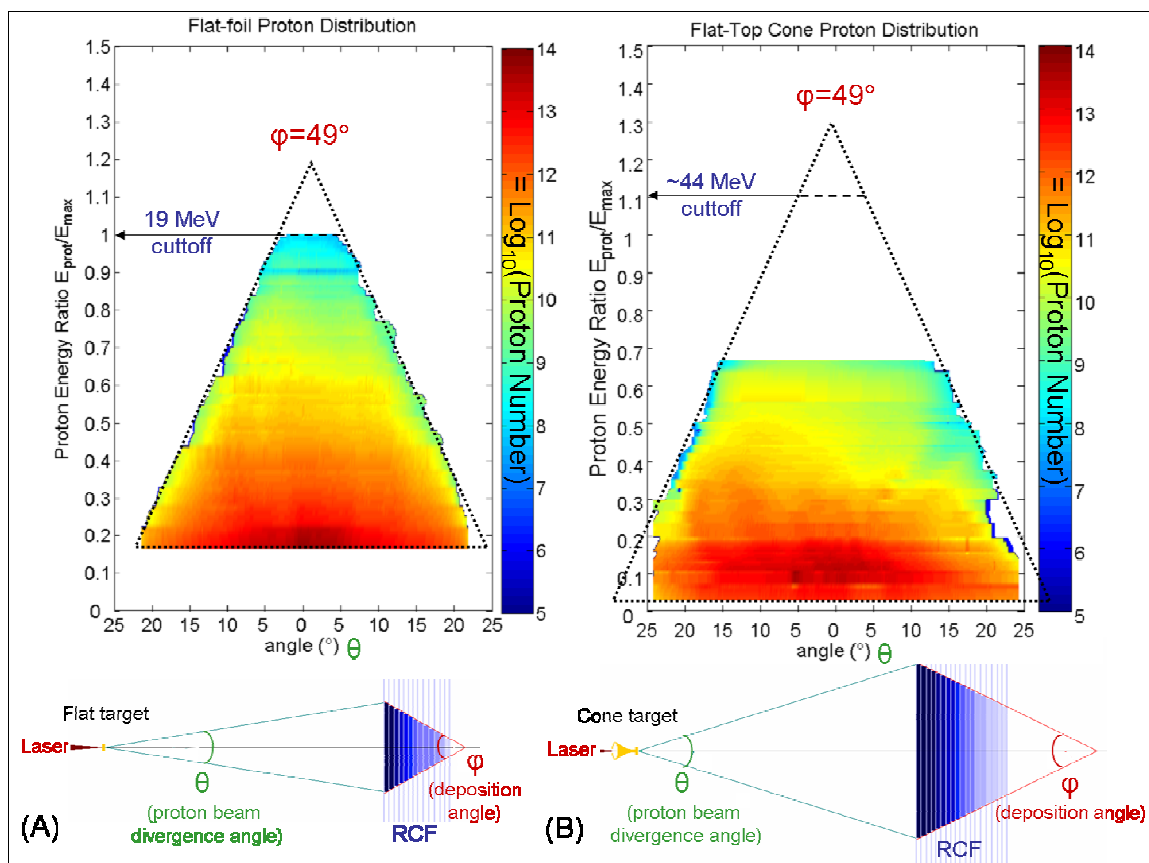


Figure 5-9: RIS beam reconstructions (*Christmas tree*) of (A) a gold 10 μm flat-foil target (shot 18500) and (B) a gold 10 μm FTC target (shot 18582). The number of protons is indicated by the color scale [1].

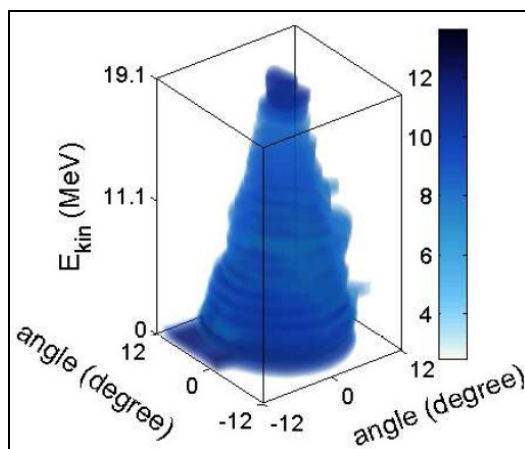


Figure 5-10: 3-D reconstruction of the proton beam emitted from the 10 μm gold flat-foil target (shot 18500).

Figure 5-11 shows an RCF stack obtained from a shot on a Au FTC (Shot 19044, 117 μm top, 39 μm neck, 10 μm thick), where the laser did not hit the flat top aligned down the throat. This is easy to see from the RCF as the proton beam emitted from the flat top (i.e. *top beam*), and which is recorded on the center of each detector, is not quite as energetic (12.8 MeV) as the proton beam or spray coming of the cone side wall (i.e. *side beam*), and which is recorded on the right hand corner of each detector (18 MeV).

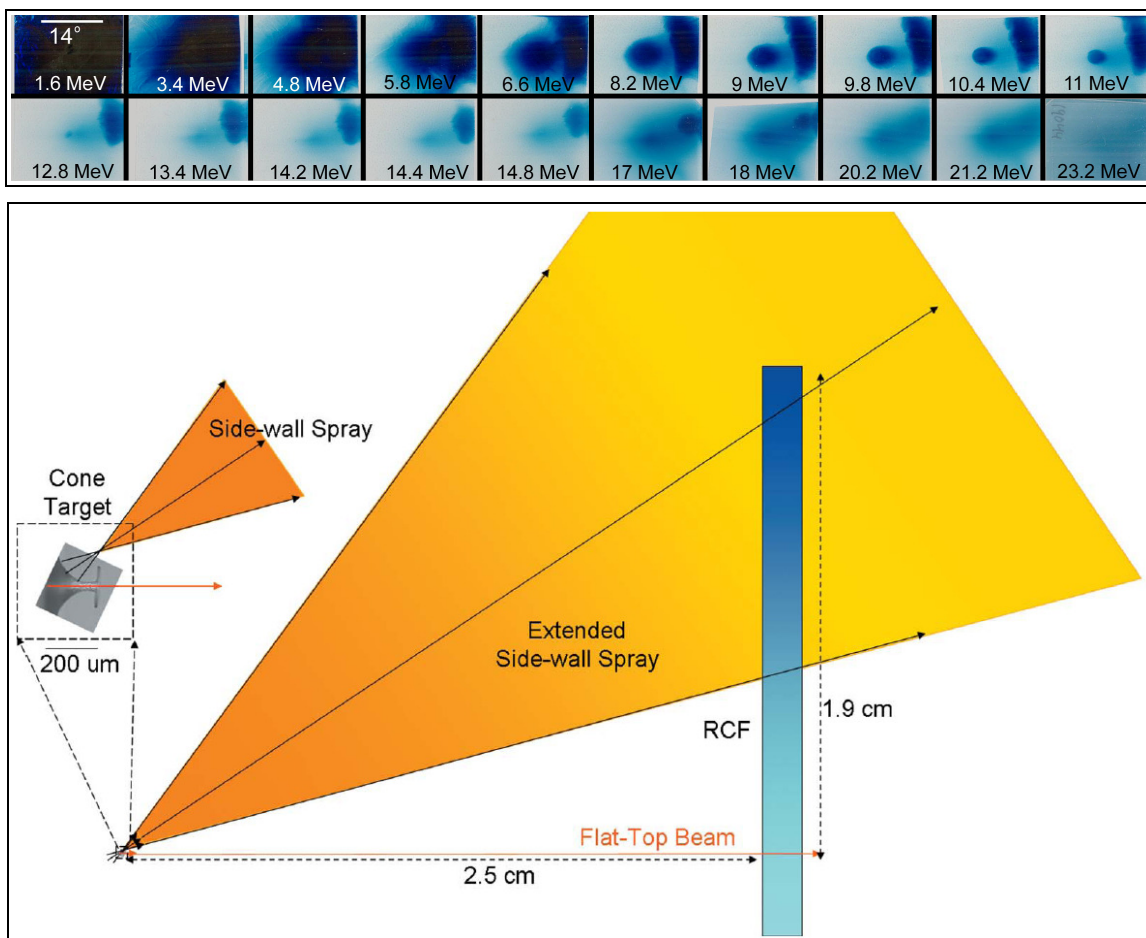


Figure 5-11: (top) Shot 19044; FTC target: 117 μm top, 39 μm neck, 10 μm thick; laser not well aligned down the throat; RCF stack: 25 μm Al, 15 HD, 5 MD; the *side beam* (right hand corner) is more energetic than the *top beam* (center); (bottom) To scale, a schematic representation of the experiment showing how the sidewall spray interacted with the RCF [1].

To test the initial guiding hypothesis, we made use of the range of top and neck sizes which were available to us at the time of the experiments. Figure 5-12 shows how each FTC performed, maximum-proton-energy-wise, as a function of both the top size and the neck size, in the *aligned* cases (red dots) and the *misaligned* cases (blue dots) as determined after the shot by the signal on the RCF (see Figure 5-11). By *aligned*, we understand that the laser made it down the cone neck. But we cannot diagnose precisely how the laser interacted along the neck or where the light was absorbed. The laser could still have come in at a small angle and produced a round proton beam from the flat-top, thereby qualifying as an *aligned* case, although technically not being *perfectly aligned*. By *misaligned*, we mean to say that the laser hit the cone wall and never made it through the cone to the flat-top, as illustrated in the inset of Figure 5-14 (right); the beam emission of a *misaligned* FTC is shown in Figure 5-11.

One can see that there is a large amount of scatter in the data presented in Figure 5-12.

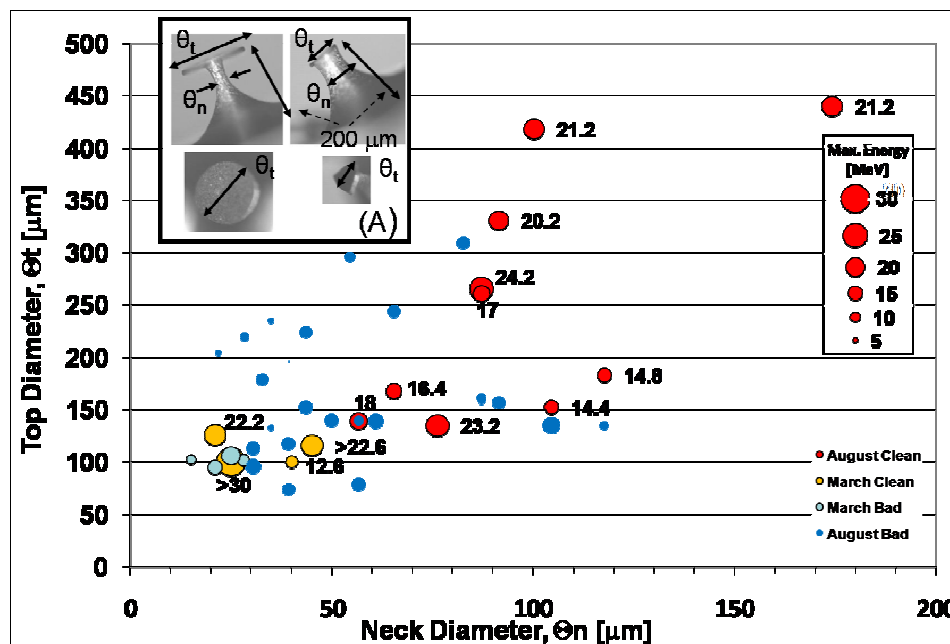


Figure 5-12: Proton energy performance as a function of both the top diameter and the neck outside diameter. The proton energy considered here is the *top beam*, and not the *side beam*. The larger the circle is, the greater the proton energy. The yellow and the red circles represent aligned shots from the March and August 2006 campaigns respectively,

and the light blue and dark blue circles represent the misaligned shots from the March and August campaign respectively. Inset (A): picture an FTC and a Football top (very close to a large diameter neck funnel).

This scatter is hard to interpret as the only particle diagnostic used in these experiments was RCF. Many FTCs of various neck and top sizes performed well, i.e. better than a flat foil did, but the best FTC performer had a small neck (i.e. 22 μm outside neck) and a small top (i.e. 100 μm), which was in good agreement with the hypothesis of laser light guiding (down the neck of the cone). Because of this scatter, in an attempt to identify a correlation between target geometry and proton energy, we looked at the Top/Neck outer diameters ratio, as illustrated in Figure 5-13. There, considering all the aligned cases (diagnosed via the proton beam emission into the RCF), it could be believable that the proton energy is enhanced as the T/N ratio increases, and that the best T/N ratio is 4. Surprisingly, even when shot at an angle, two (out of the three) FTCs performed quite well (crossed yellow squares).

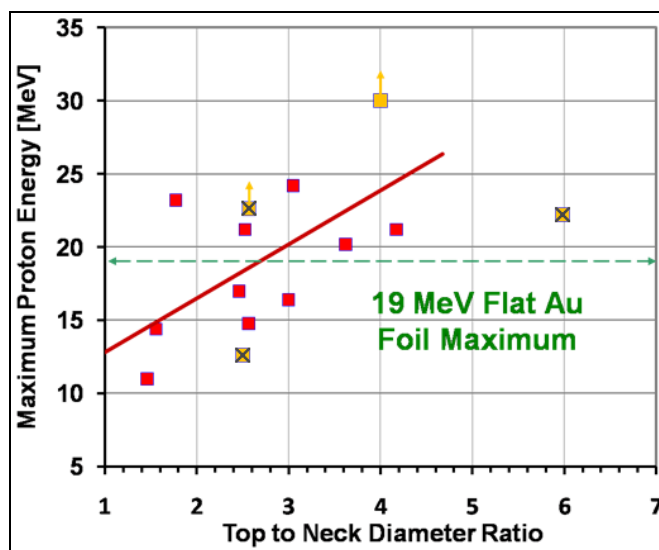


Figure 5-13: For the aligned cases only: maximum proton energy obtained from the RCF stack as a function of the Top-to-Neck ratio of the Au FTC: the yellow squares represent the March data (the crossed yellow squares correspond to the FTCs that were shot at 22.5°) and the red squares the August data.

As a result of the scattered measurements presented in Figure 5-12 and Figure 5-13, we realized the importance of laser alignment in the cone, which may or may not have been the reason for this scatter, and the necessity for added diagnostics to help characterize the laser/cone interaction better (see Section 5.2.5).

Figure 5-14 shows the 2-D PICLS simulation results for the electron spectrum of an aligned FTC target (black), a misaligned FTC target (red), a flat-foil target (blue), and an RMT (grey). The inset shows an FTC target, in the aligned (black) and misaligned (red) cases. Electrons are boosted to higher energies, in both the FTC aligned and misaligned cases, compared to the flat-foil target and even the RMT case: however, if misaligned, the highest electron energy is not as high, but the overall number is quite similar. Therefore more and hotter electrons are available to accelerate the protons from the flat-top of the FTC target to higher energies.

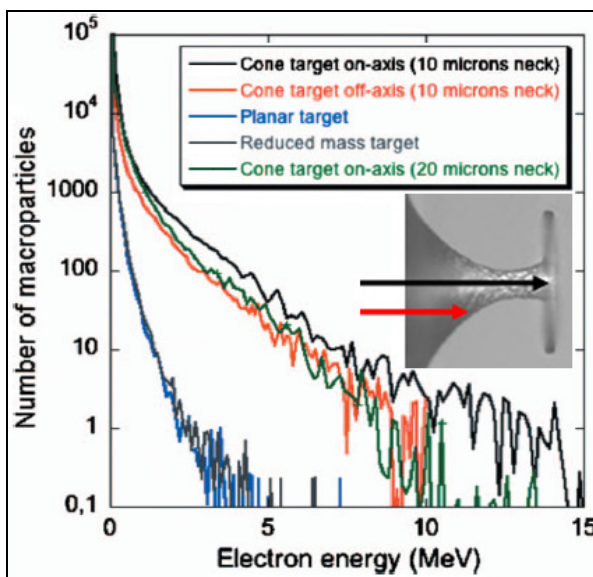


Figure 5-14: Electron spectra (simulations) of an RMT, a flat-foil target, an aligned (black arrow), and a misaligned (red arrow) FTC target; 1.74×10^8 macroparticles are used in the simulation, and each macroparticle contains 315733 electrons [1].

Figure 5-15 shows experimental proton spectra obtained from the RCF, scanned using a flat-bed scanner and a MicroD: in triangles, the experimental data for the flat foil (the empty

green triangles correspond to the scanner case, and the filled green triangles to the MicroD case); in circles, the experimental data for the FTC (the blue circles correspond to the scanner case, and the maroon circles to the MicroD case); and in squares (red, empty) the simulation for the FTC seeing protons with energies up to ~ 40 MeV.

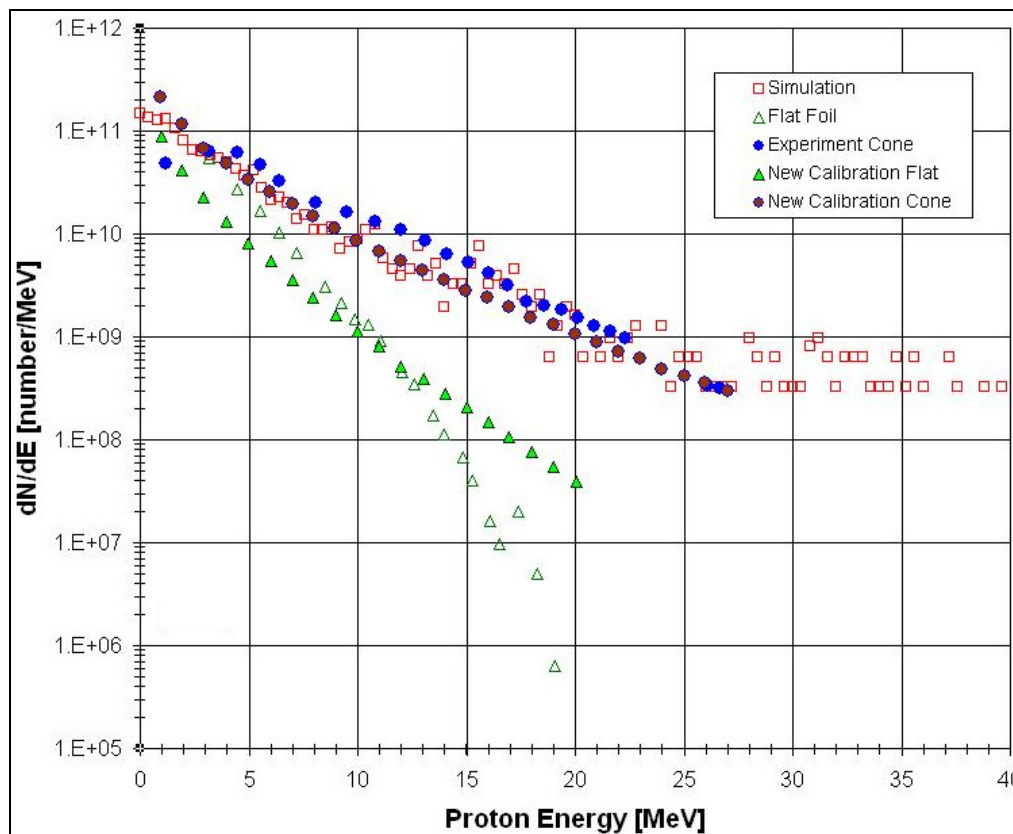


Figure 5-15: Proton spectra of a flat foil (experiment, triangles) and a flat-top cone (2-D PICLS simulations, squares and experiment, circles); the empty triangles and the blue circles correspond to the spectra obtained from the data scanned using a flat-bed scanner, and the filled green triangles and the maroon circles correspond to the spectra obtained from the data scanned using a MicroD.

Figure 5-16 shows 2-D PICLS simulations of the total electric fields (electric field amplitude) for two different cases: (left) for the case where the laser propagated on-axis and (right) for the case where the laser was offset 18.6 μm transversely (upward) from the cone's axis (as shown in the inset of Figure 5-14). The black arrows in both images (left and right) point to the cone flat-top, (left) where a very strong sheath forms when the laser is aligned along the

cone axis and (right) where a barely existent field forms on the flat-top when the laser is shifted. The orange arrow (right) points to the enhanced electric field on the cone sidewalls, caused by the misdirected transport of the hot electrons. When this sheath forms on the sidewall, it can lead to a significant sidewall proton beam spray, observed on the RCF and displayed in Figure 5-11.

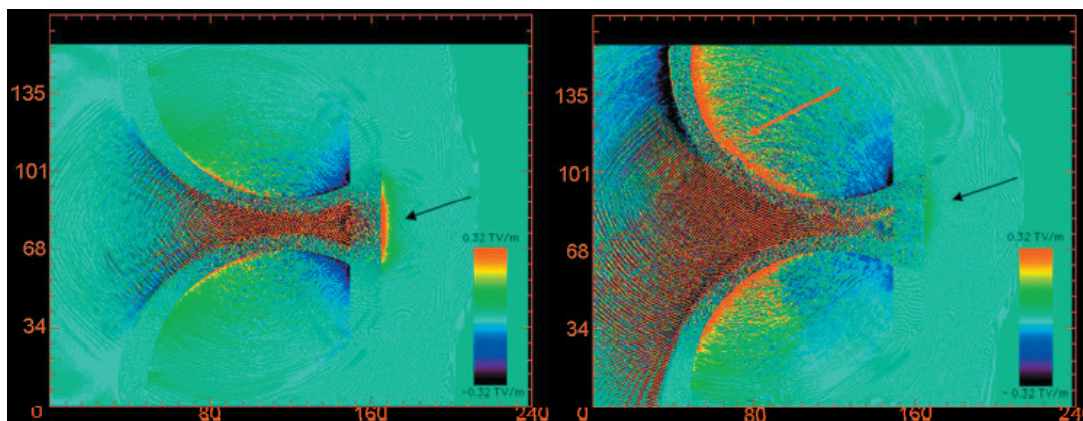


Figure 5-16: 2-D PICLS Simulations of the total electric fields in the case of (left) the laser propagating on axis, focused on the flat top (offset of 0 μm) and (right) the laser offset by 18.6 μm transversely from the laser axis. The black arrows (left and right) point to the flat top. (right) The orange arrow points to the region of increased electric field amplitude on the cone upper sidewall, due to the increased sheath density [1].

So, in summary, the enhanced proton acceleration exhibited with FTC targets compared to flat-foil targets, as deduced by PICLS simulations could be due, in principle, to a combination of multiple effects (note that there could well be other reasons):

- Increased laser absorption in the cone;
- Better coupling efficiency to the responsible electron population;
- Enhanced hot-electron confinement on the flat-top region due to edge fields;
- Hotter electron temperature at the top of the FTC:
 - o due to optical guiding via the cone geometry;
 - o due to a partial plasma prefill in the cone (better underdense coupling);
- Higher electron sheath density at the top of the FTC:

- due to surface electron guiding via the cone geometry;
- due to concentration of more electrons in the flat-top region;
- due to optical collection of laser light from the cone (i.e. an increased effective intensity leads to an increased laser-to-electron conversion efficiency).

Based on the simulations available after the experiment, our understanding was that the most likely hypothesis was an enhancement of the laser absorption and an increase in the hot-electron temperature, caused by laser guiding and/or a small-scale preformed plasma confined within the cone neck.

5.2.5 Necessary improvements for future experiments

Along with the regular RCF stack for diagnosing protons, the next series of experiments described in the next sections [5.3 and 5.4] made use of an electron transport/confinement diagnostic (i.e. a 2-D Cu $K\alpha$ imaging crystal) and an electron temperature diagnostic (i.e. electron spectrometer with MeV energy range) in order to gain better insight into the laser-cone interaction and the hot-electron dynamics.

Indeed, the only use of an RCF stack makes it extremely difficult to diagnose the laser/target interaction and coupling. It is clear from the RCF whether there is beam emission from the side walls of the cone (*misaligned* case), but when the beam is perfectly round, it is hard to prove that it really came from the top as opposed to from the flat foil, with only the cone wall spray as evidence; or to prove that the laser was slightly offset (horizontally or with some small angle of incidence) or perfectly centered down the throat (0 μm offset). One can only assume that the increase in energy that was observed was indeed due to the cone effect, i.e. production of a higher number and more energetic electrons transported and

guided to the flat top as proton energies in that range had never been seen from any target during 4 years of experiments (between 2002 and 2006).

The 2-D Cu $K\alpha$ imaging crystal measures the spatial distribution of the hot electrons in the cone, and diagnoses the laser absorption point, thereby testing the interaction physics and the alignment hypotheses. The target material was switched from gold to copper to use a material whose $K\alpha$ emission could easily be imaged. The 2-D Cu $K\alpha$ side view of the FTC or FC target allows one to see how much the laser is misaligned, how much interaction there is, as well as where the interaction takes place, avoiding any doubt regarding the effect of the cone geometry for proton acceleration.

The electron spectrometer measures the MeV-class hot-electron temperature, to test the hotter electron temperature hypothesis, and to explore in more detail the MeV electron generation and its influence on the proton acceleration in cone geometries, since the effect of the cones on MeV-class electrons is so far largely unexplored. These hot electrons are the electrons most relevant to proton or ion acceleration, and potentially to the Fast Ignitor application.

Finally, the last hypothesis tested in these next experiments is the contrast effect on the laser absorption and the proton acceleration, for two contrast levels, i.e. the intrinsic laser contrast of 10^{-8} [5.3] and the enhanced laser contrast of 10^{-10} [5.4].

5.3 Trident, 80 J, $\sim [1.1-2.3]\times 10^{20}$ W/cm² & intrinsic 10^{-8} contrast: August 2008 & September 2008 beamtimes

The goal of this experiment was to test whether the energy enhancement observed using FTC targets at 20 J would scale with laser energy, i.e. 80 J, and to compare FTC targets to flat-foil targets (of different thicknesses), as well as funnel-cone targets and RMTs.

5.3.1 Experimental set-up

In this experimental run, performed in the North Target Area, the short-pulse arm of Trident post-enhancement (3.2.2) was used (*S*-polarized), at intrinsic contrast (10^{-8}). The deformable mirror was installed and used during the 2008 and 2009 experiments. The experimental set-ups are illustrated in Figure 5-17 for the large flat foil shots (22.5° incidence), and in Figure 5-18 for the cone shots (0° incidence). The important distances were the following: target to slit of the electron spectrometer: 82 cm; target to beginning of the electron spectrometer: 90 cm; target to RCF stack: 2-2.5 cm; target to crystal: 7.85 cm; crystal aperture: 6 mm; crystal magnification: $10\times$.

5.3.1.1 Flat foils

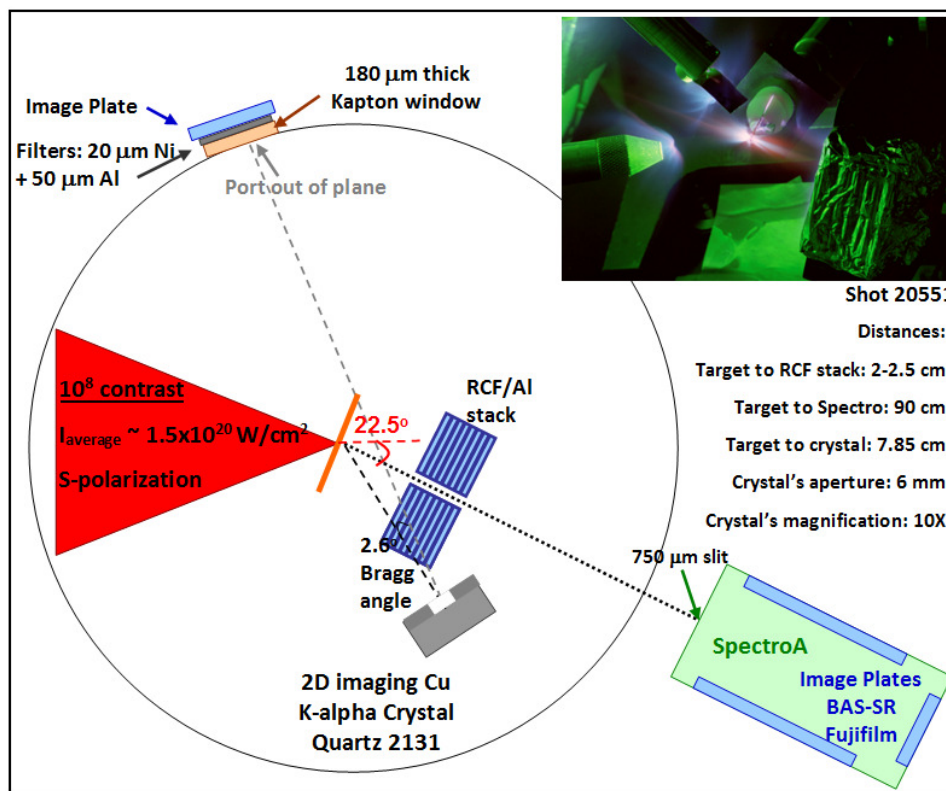


Figure 5-17: Set-up of the August 2008 (Shots 20534-20557) and September 2008 (Shots 20613-20621) Trident beamtimes, where various flat-foil targets (different materials and thicknesses) were shot. Laser parameters: ~ 80 J, ~ 600 fs, 22.5° incidence, ~ 7 μm focal

spot (47 %), S-polarization, 1.5×10^{20} W/cm²; SpectroA is the electron spectrometer; (Inset) Integrated picture of a real shot (20551): in the center is the target mounted in a ceramic holder; on the right, the RCF stack and on the left a pinhole camera; from the top left corner, a tantalum shine-shield protecting the (Cu K α) IP from direct exposure. Photo credit: Joe Cowan & Kirk Flippo.

5.3.1.2 Funnel-cone targets, flat-top-cone targets, and reduced-mass targets

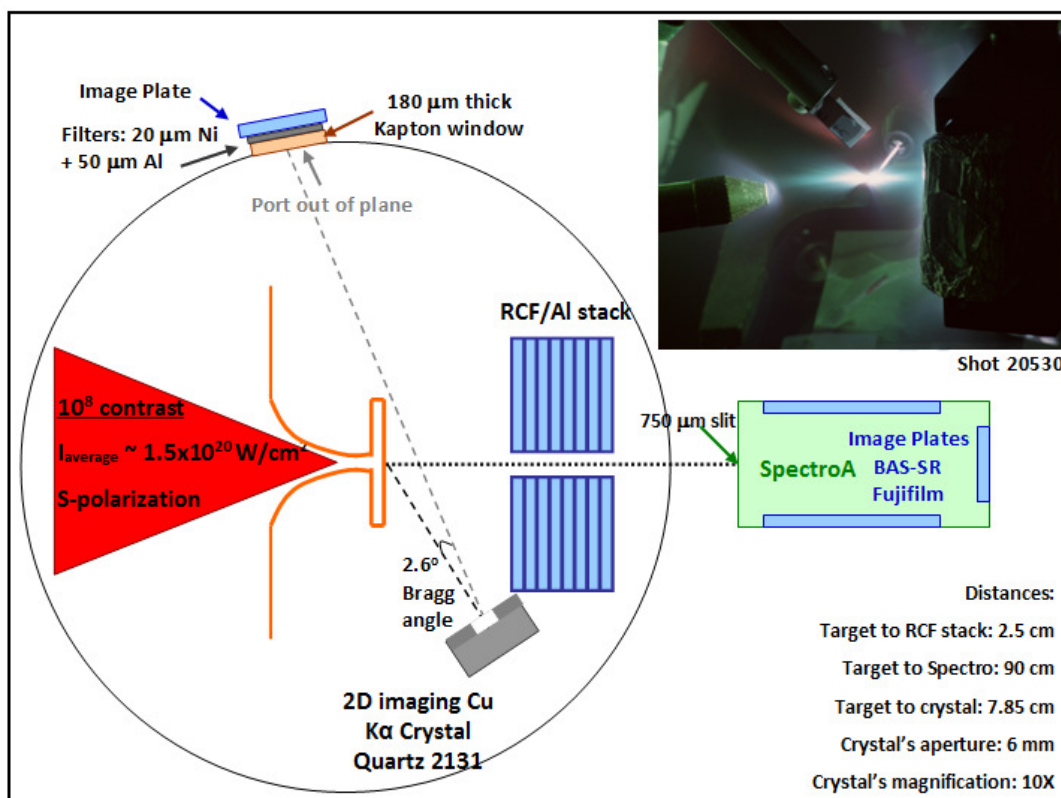


Figure 5-18: Set-up of the August 2008 (Shots 20509 – 20533) Trident beamtime, where various geometries of cone targets were shot (Snubbed nose, funnel, and flat-top cones).

Laser parameters: ~ 80 J, ~ 600 fs, normal incidence (0°), ~ 7 μm focal spot (47 %), S-polarization, 1.5×10^{20} W/cm²; SpectroA is the electron spectrometer; (Inset) Integrated picture of a real shot (20530): in the center is the target mounted on a glass stalk; on the right, the RCF stack and on the left a pinhole camera; from the top left corner, a tantalum shine-shield protecting the (Cu K α) IP from direct exposure. Photo credit: Joe Cowan & Kirk Flippo.

5.3.2 Description of the targets

5.3.2.1 Cu, Ni and Al flat-foil targets and Cu reduced-mass targets

The Cu flat foils were simple laser-cut 2 mm by 7 mm rectangles of Goodfellow supplied material of different thicknesses (5 μm , 10 μm , 20 μm , 50 μm , 100 μm , 150 μm). The 1 μm thick Cu foil was much smaller (due to the fact that such thin Cu rolls over itself), i.e. 1 mm by 1 mm square. At the time of the experiment, we did not have 500 nm of Cu, so we used Ni instead, which has similar density, charge, and electrical properties as Cu.

The RMTs were the 300 μm diameter tops from the FTCs (see Figure 5-19 (d2)) that fell off while cutting out the targets. Note that these RMTs are about 10 (to at most 15) μm thick, and are a sandwich of Cu-SiO₂-Si₃N₄-Cu since they stem from the SiO₂-Si₃N₄ cap used to make the FTCs on the Si wafers; the quantity of SiO₂-Si₃N₄ left after etching was not determined (see Section 5.2.2 and Figure 5-5).

We also had some 100 nm Al available, from Lebow Company, which was mounted on a large 5 cm ring. A few targets mounted on washers were prepared to test ultrathin targets. The 100 nm thick Al is very weak (100 nm is extremely thin, and Al is not as sturdy as Cu or Ni), and basically, the laser burned through that thickness, yielding a few MeV protons, but a beautifully collimated ~ 10 MeV electron beam. These exciting results are not presented in this dissertation but they are described in [182].

5.3.2.2 Cu (Ti-Cu and Ti-Cu-Ti) funnel cones and Cu flat-top cones

As mentioned before, the cone targets are now all made out of Cu, so that via Cu K α 2-D side imaging, it is possible to determine where the laser absorption and electron heating take place.

Figure 5-19 shows pictures of funnel cones (a, b and c) and of a flat-top cone (d), which have a rather rough surface. The motivation for using the 500 nm Ti coating on the top or both on top and bottom was to determine whether the heating was bulk heating or surface heating. The FTCs (Figure 5-19 (d)) were the only ones that were made available to us for that particular campaign. The size specifications of the FTCs were not quite that of the previous successful Au cone run. Compared to the Au FTCs, the Cu FTCs' heights and tops were larger, i.e. respectively $\sim 250 \mu\text{m}$ and always $\sim 300 \mu\text{m}$, compared to $\sim 200 \mu\text{m}$ and $\sim [100-200] \mu\text{m}$. The maximum neck outer diameter of the Cu FTCs that was shot was $\sim 45 \mu\text{m}$. These targets stemmed from a different Si mold structure than that used in the Au forests of FTCs, and were spaced a few millimeters from each other to facilitate cutting and handling.

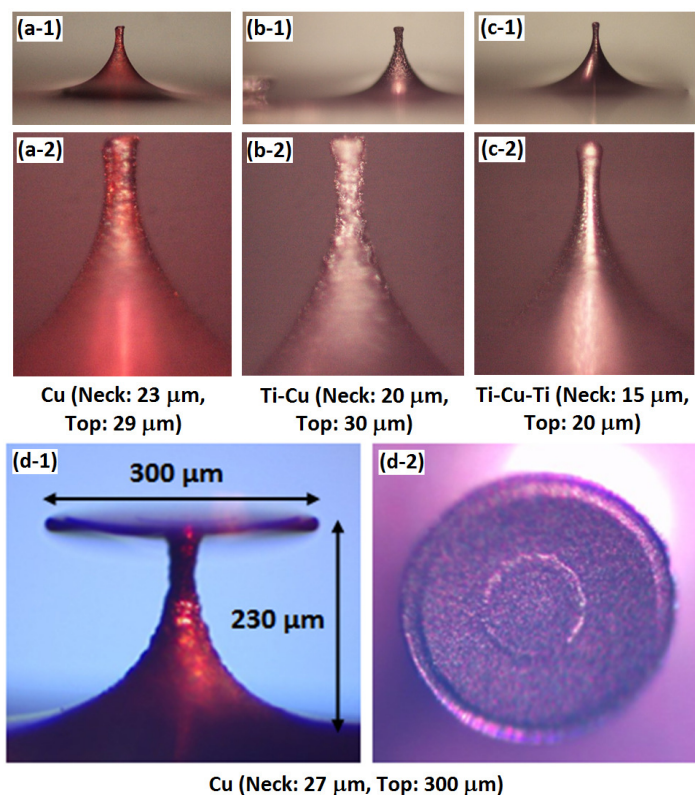


Figure 5-19: All targets are represented on the same scale; (a-c) Funnel cones: Side views; (d) flat-top cone; (d-1) Side view; (d-2) Top view.

With the laser energy increase of the Trident short pulse beam arm by a factor of 4 (from ~ 20 J to ~ 80 J), and the spot size decrease due to the addition of the deformable mirror (from $14 \mu\text{m}$ down to $7 \mu\text{m}$), leading to an increase in intensity from $\sim 10^{19}$ W/cm² to $\sim 2 \times 10^{20}$ W/cm², it was foreseeable (although it still needed to be tested) that the level of preplasma in the FTC would also increase by an order of magnitude and could become significant, such that the hot electrons driving the TNSA protons would be born far upstream in the neck and not be able to reach the flat-top for the thinnest necks, given the 10^{-8} contrast, making the ion-acceleration inefficient, and thus making larger neck FTCs more desirable, which unfortunately were not unavailable to us for that experimental beamtime.

5.3.3 Summary of the results, 80 J & 10^{-8} contrast

This section presents a summary of the results obtained at 80 J and 10^{-8} contrast for flat-foil targets, RMTs and micro-cone targets, i.e. FTCs, FCs, and snubbed noses.

5.3.3.1 Flat-foil targets and Reduced-mass targets

We performed a target thickness scan, summarized in Figure 5-21, for proton energy and conversion efficiency. The S-polarized laser hit the foils at an incident angle of 22.5° , and the RMTs at normal incidence. As shown by the red diamonds in Figure 5-21, the maximum energy and conversion efficiency were obtained for the $1 \mu\text{m}$ thick Cu target: 58.5 MeV and 3.73 %. Being able to shoot such a thin target at this intensity means that Trident's intrinsic contrast is quite high, compared to other lasers (see Section 2.3.3 and especially Figure 2-17). This 58.5 MeV result was already matching the Nova PW record (Figure 5-21, green dashed line). As was already pointed out earlier, it is fair to compare the Trident laser to

the Nova PW laser since they are both single shot glass lasers, and they have similar intensities and pulse durations:

- Nova, PW, 450 J, 2.6×10^{20} W/cm², 500 fs, 58 MeV => **0.13 MeV/J**

- Trident (10^{-8} contrast), 130 TW, 89.6 J, 1.7×10^{20} W/cm², 690 fs, 58.5 MeV => **0.65 MeV/J**

Only two 300 μm diameter Cu RMTs were shot (see Figure 5-21, blue triangles); both of which did not perform as well as the 10 μm (or even 20 μm) thick flat-foil targets: 32.2 MeV and 44.3 MeV compared to ~ 52 MeV, although RMTs were expected to perform better than flat-foil targets due to a theoretical and empirically measured increase in hot electrons [132]. A few possible reasons that could explain the lack of better performance are for example the fact that the diameter was not optimum relative to pulse duration; or that there was too much preplasma, wrapping around the target, distorting the rear-side sheath, thereby decreasing the energy and efficiency of the proton acceleration.

5.3.3.2 Funnel cones and flat-top cones

In [2], we show that at the intrinsic contrast (10^{-8}) and 80 J (normal laser incidence), only a small portion of the hot electrons is able to propagate to the top of both the FTC and the funnel cone, as indicated by the Cu $K\alpha$ emission at the tip (i.e. top emission or TE), while most of the emission comes from the cone walls (i.e. cone wall emission or CWE). A large amount of preplasma is filling the cone, preventing the laser from being efficiently absorbed closer to the cone tip. This limited laser penetration in the FTCs results in no improvement in maximum proton energies, compared to simple flat foils. If the low energy end of the hot-electron population is stopped somewhere in the FTC neck, and does not make it to the flat-top, it is a direct indication of preplasma filling the cone, which has been shown in simulations to negatively impact the proton acceleration, and will also be an indicator of

how to optimize the cones. In that case, the Cu K α emission happens at the cone walls (CWE), while little top emission (TE) is observed.

5.3.4 Results presented in detail (80 J & 10⁻⁸ contrast): Maximum proton energies and Cu K α emission, organized by target type (i.e. Flats and Cones), for most of the shots of the two 2008 campaigns

5.3.4.1 Maximum proton energies as a function of target type: summary

Figure 5-20 presents a summary of the maximum proton energies obtained from all the targets shot during the August and September 2008 beamtimes. The targets were Cu RMTs (Cu, August, 10⁻⁸), flat foils (Cu, Ni; August, 10⁻⁸; September, 10⁻⁸), funnel cones (Cu, Ti-Cu, Ti-Cu-Ti; August, 10⁻⁸), snubbed noses (Cu, August, 10⁻⁸) and FTCs (Cu, August, 10⁻⁸). Note that the “Ti-Cu-Ti F/Hole” represents a shot where the tip of the funnel cone was missing; and that the “Ti-Cu-Ti F/Flat” represents a funnel-cone target but the laser hit too low (or too high), missing the neck of the cone, hitting the supporting foil instead, and therefore producing a beam identical to that of a flat foil.

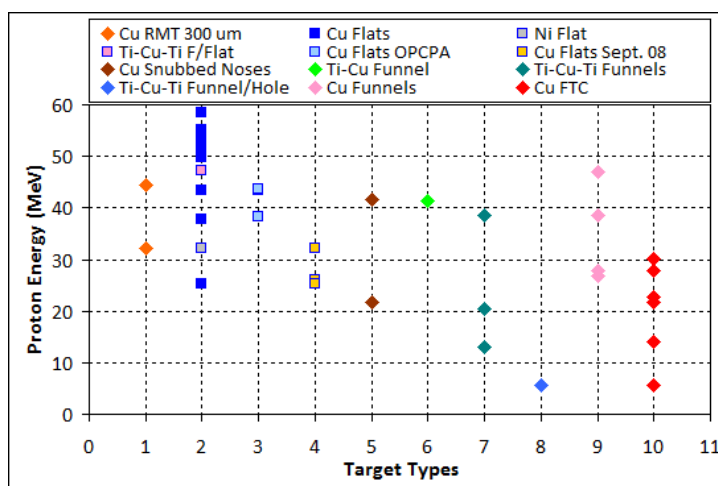


Figure 5-20: Maximum proton energy (MeV) for all the targets shot during the August 2008 beamtime; all targets were ~ 10 μ m thick, with the exception of the flat foils: the Cu flats ranged from 1 μ m to 150 μ m, and the Ni flat was 0.5 μ m; the Ti-Cu-Ti F/Flat target (pink

square, blue border) corresponds to a funnel cone which was shot away from the cone neck, similar to a flat foil; the Ti-Cu-Ti F/Hole target (blue diamond) corresponds to a funnel cone whose tip was missing.

Also note that this graph displays the maximum proton energy of the normal proton beam (i.e. emitted from the top of the cone, or from the tip of the funnel cone, also called *normal beam*). In the cases where the laser was misaligned, and a proton beam of higher energy was emitted from the side walls of the cone (i.e. cone wall spray emission, also called *side beam*), that proton beam energy was not taken into account in Figure 5-20.

5.3.4.2 Flat-foil targets (Cu, Ni and Al) and reduced-mass targets (Cu, 300 μm diameter)

As shown by the red diamonds in Figure 5-21, the maximum energy and conversion efficiency were obtained for the 1 μm thick Cu target: 58.5 MeV and 3.73 % respectively.

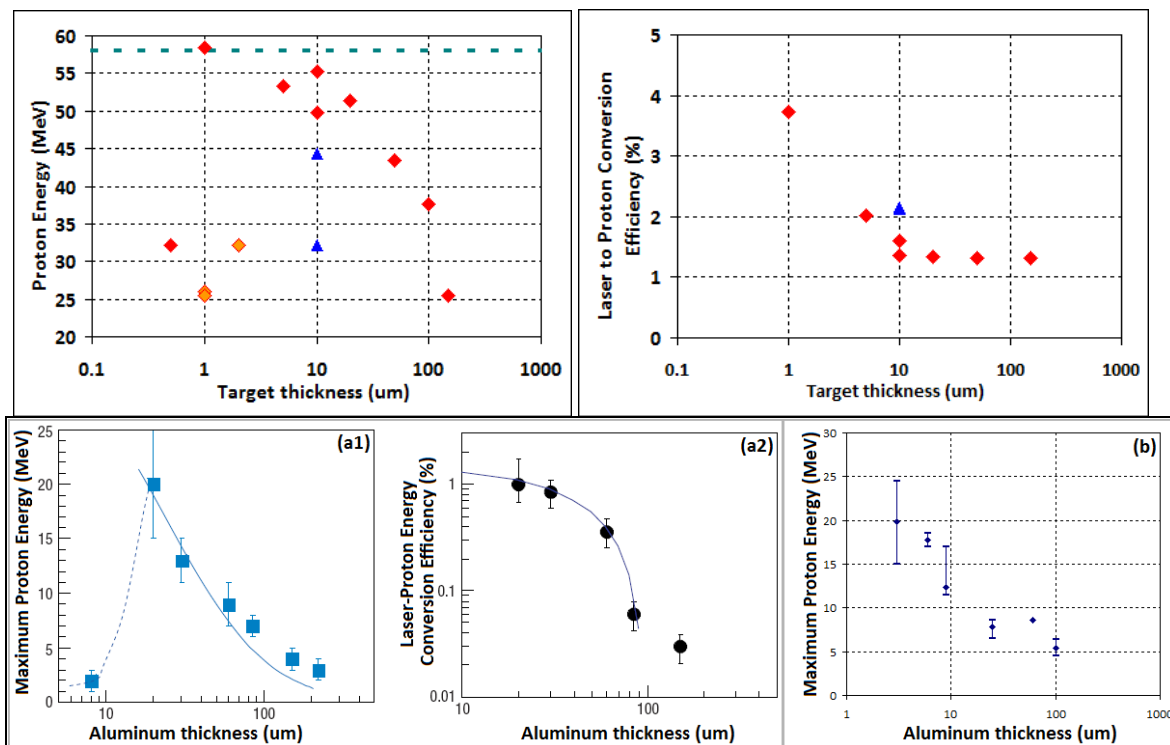


Figure 5-21: (left, top) Proton energy (MeV) (right, top) Conversion Efficiency (%) as a function of target thickness (μm) in the intrinsic contrast case; (red diamonds and blue triangles) respectively flat-foil targets and RMTs shot in August 2008 using a clean OAP;

(yellow diamonds) flat foils shot in September 2008 using a damaged OAP. The horizontal dashed green line shows the maximum proton energy of 58 MeV obtained with 450 J on the Nova PW laser; (bottom) Reproduction of Figure 5-22 (LULI and Callisto data), for comparison with the Trident data.

However, note that the quality of the proton beam decreases with target thickness, as illustrated by the RCF stacks shown in Figure 5-23 (a) and (b).

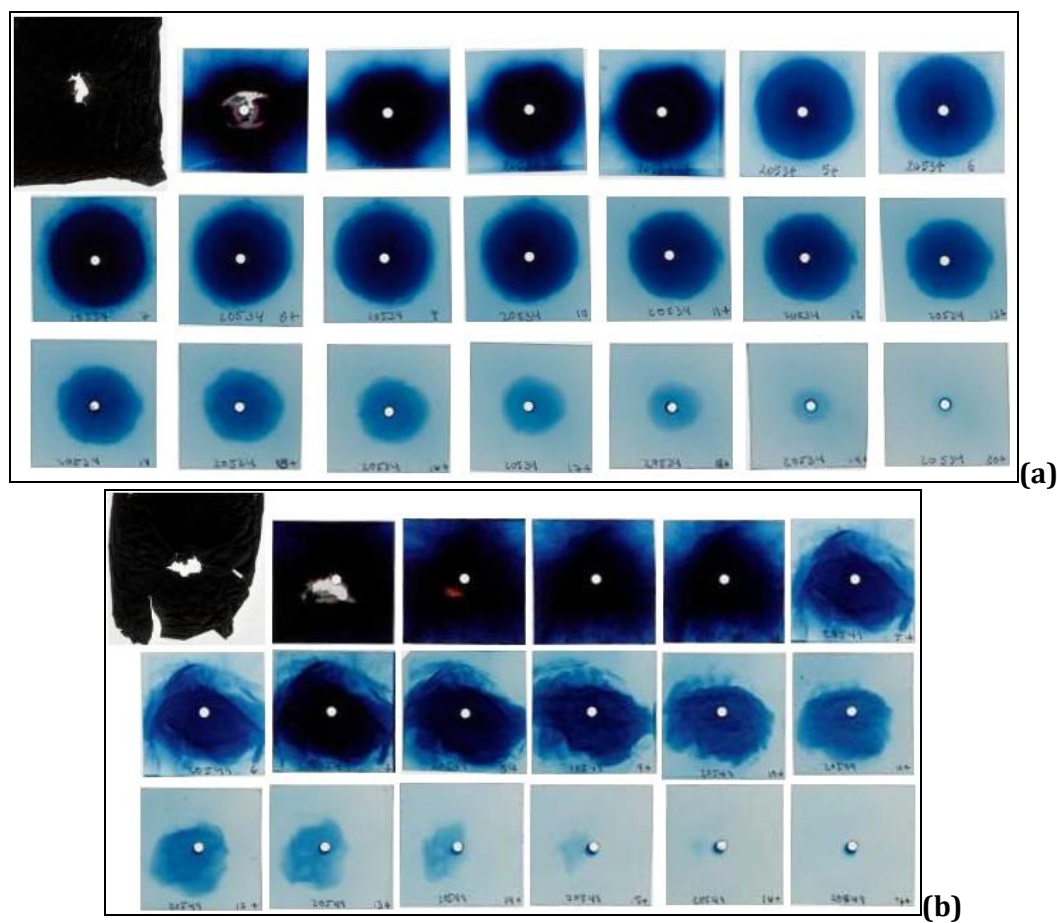


Figure 5-23: RCF stacks for Cu flat-foil targets: (a) Shot 20534, 10 μm thick; (b) Shot 20549, 1 μm thick.

In Figure 5-21 are also shown a set of 3 points (yellow diamonds) from a few shots obtained in September 2008, where we attempted to complete the target thickness scan obtained one month earlier (August 2008, Figure 5-21, red diamonds), adding a 2 μm Cu target (shot 20613) and repeating the best case with 1 μm Cu targets (shots 20615 and 20620).

However, the proton beams were very non-uniform (see Figure 5-24 (a) and (b)), and the proton energies were much lower: the reason for this degradation was the damage (caused by metal debris) of the off-axis focusing parabola, which was not able anymore to focus the focal spot to as tight a spot size as in August 2008. The September 2008 spot size contained a lot more energy in the wings, and did not look as round as before. This shows this importance of a good focus and of a clean focusing optics.

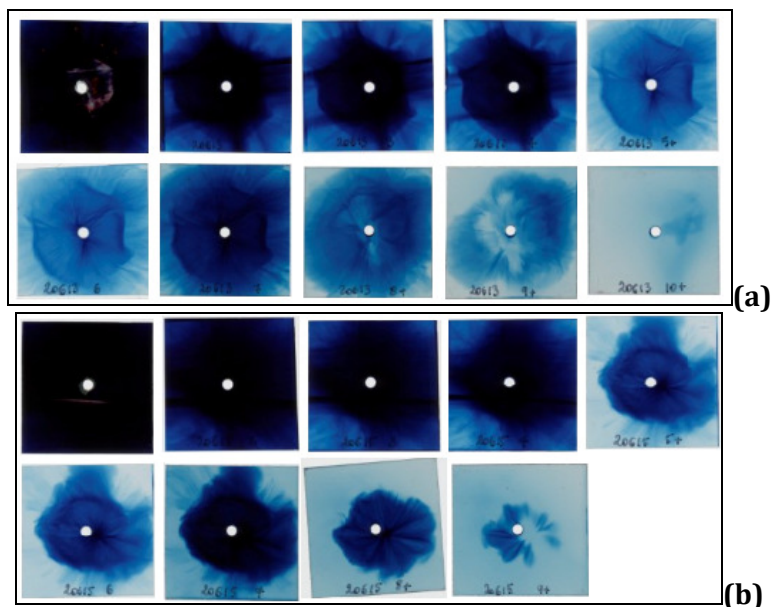


Figure 5-24: RCF stacks for Cu flat-foil targets: (a) Shot 20613, 2 μm thick; (b) Shot 20615, 1 μm thick.

Two 300 μm diameter RMTs were shot at maximum intensity ($\sim 2 \times 10^{20}$ W/cm²):

- Shot 20508 (82 J, 620 fs) yielded a maximum proton energy of ~ 43 MeV, while the Cu K α crystal was not yet working;
- Shot 20552 (88 J, 558 fs), illustrated in Figure 5-25, yielded a maximum proton energy of ~ 32 MeV, and the Cu K α image shows Cu K α emission of the entire 300 μm diameter RMT, with a much brighter Cu K α emission region, which undoubtedly corresponds to the zone where the laser interacted.

There is therefore a large fluctuation in the proton beam energy, which could be due to how and where the laser interacted with the target, but since no Cu K α image is available for shot 20508, it remains difficult to tell. However, the C.E.s for both shots are very similar, i.e. $\sim 2.1\%$. In the RCF stack in Figure 5-25, one can see two horizontal lines across the RCFs in the first four detectors, while only one horizontal line remains in the next three detectors; they are believed to be field enhancements due to wrap around of the front side plasma, but determining the exact mechanism would require 3-D simulations.

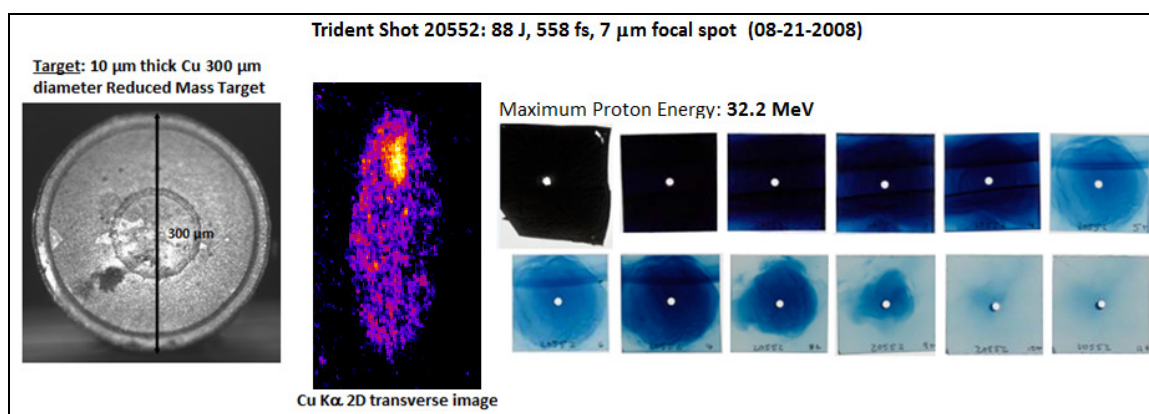


Figure 5-25: Shot 20552: RMT Cu, 300 μm diameter; maximum proton energy of 32.2 MeV; the Cu K α 2-D transverse image (at $\sim 22.5^\circ$) shows the emission from the entire target.

5.3.4.3 Cu Snubbed Nose Cones

Two $\sim 10\ \mu\text{m}$ thick Snubbed Nosed cones were shot at maximum intensity, illustrated in Figure 5-26:

- Shot 20528 (88.3 J, 503 fs), yielding $\sim 42\ \text{MeV}$;
- Shot 20526 (77.5 J, 620 fs), yielding $\sim 28\ \text{MeV}$.

In both cases, the laser had no difficulty making it to the tip: the neck of the target was wide enough ($\sim 50\ \mu\text{m}$) and the height (length) small enough ($\sim 70\ \mu\text{m}$) – a height which is similar to the height of the targets used in the June 2009 experiments [5.4.2]. There is both cone wall interaction and top interaction in those cases, as well as preplasma filling the

snubbed nose, with even a little asymmetry (or even misalignment) in the case of shot 20526, which yielded the least amount of proton energy. However, it would be hard to correlate the asymmetry to less proton energy since the laser energy was also 10 J lower than in the other case (shot 20528).

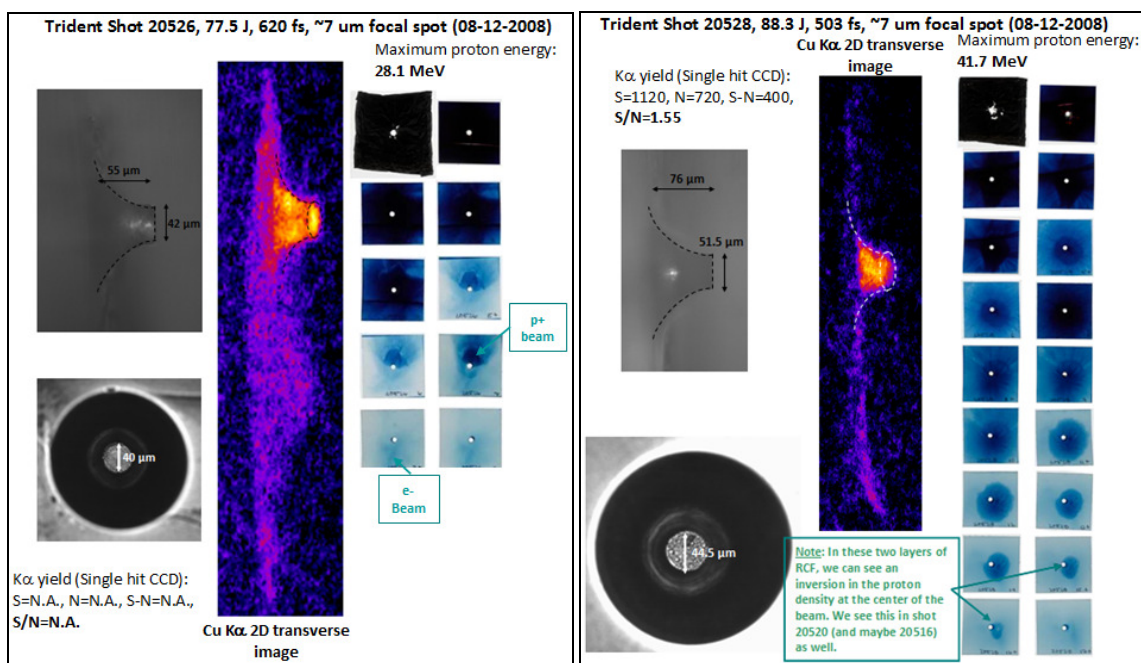


Figure 5-26: Snubbed noses: (left) Shot 20526, maximum proton energy of 28.1 MeV; (right) Shot 20528, maximum proton energy of 41.7 MeV.

5.3.4.4 Cu funnel and flat-top cones

As we shortly mentioned earlier in the summary [5.3.3.2], the amount and balance between cone wall Cu K α emission (CWE) and top emission (TE) is particularly important. In the intrinsic contrast case, there is too much CWE and not enough TE, i.e. CWE \gg TE. This is correlated with the fact that the proton energies produced from either funnel cones or FTCs are never higher than that produced from a flat foil, whether the cone is aligned or misaligned:

- flat foil, 10 μm => ~ 50 to ~ 55 MeV and 20 μm => ~ 51 MeV;
- funnel cone, 10 μm => ~ 12 MeV to ~ 47 MeV;

- FTC, $10\ \mu\text{m} \Rightarrow \sim 5\ \text{MeV}$ to $\sim 30\ \text{MeV}$.

The proton energies taken into account here are the proton energies of the *top beam* (beam normal to top of the FTC or to the tip of the funnel cone), since the *top beam* is the one emitted as a nice round uniform beam, and is co-linear with the spectrometer; the *side beam* is ignored, which tends to only be emitted as an annular non-uniform spray. It is worth noting that even when misaligned, in all cases, the proton energy of the side beam was never greater than that of a flat foil (i.e. $> 47.2\ \text{MeV}$ compared to $55\ \text{MeV}$).

Figure 5-27 compares both the Cu $K\alpha$ images and the RCFs stacks of shot 20518 (*aligned*) and shot 20521 (*misaligned*).

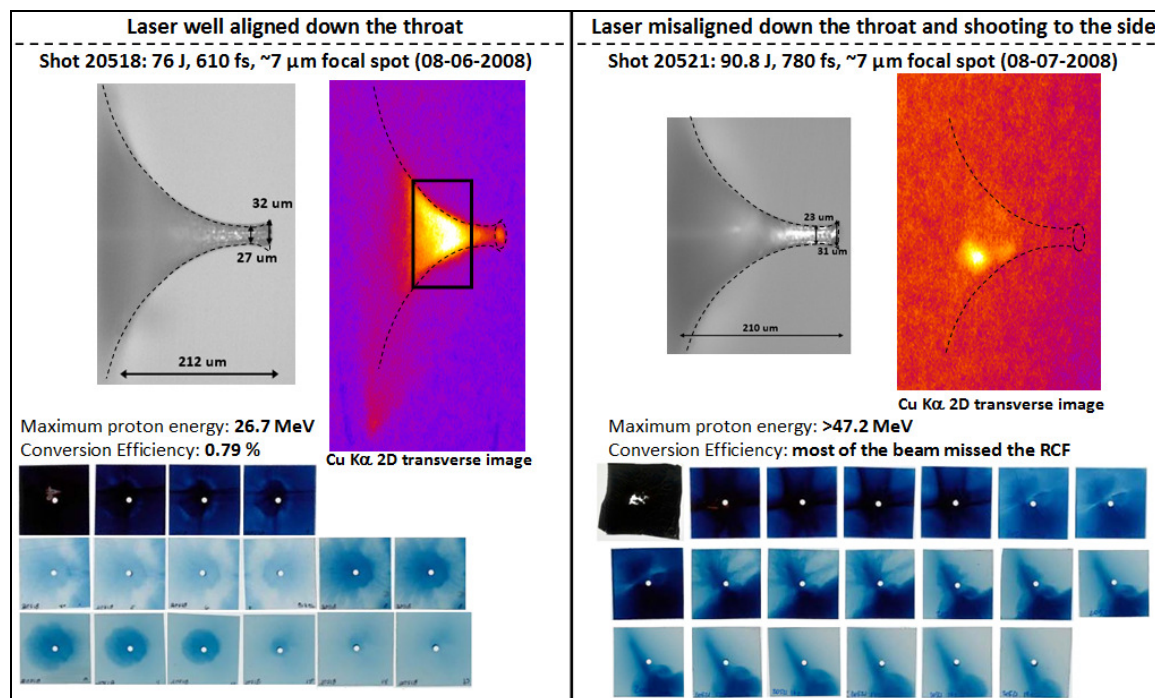


Figure 5-27: Shots 20518 (laser well aligned down the throat) and 20521 (laser misaligned and shooting to the side), funnel cones: pictures of the targets, Cu $K\alpha$ images and RCF stacks.

The *top beam* from shot 20518 shown in Figure 5-27 (left) is particularly round and uniform, but not particularly energetic, and the conversion efficiency is pretty low (i.e. 0.79 %). The Cu $K\alpha$ image shows a lot of CWE, and only a little TE, which again means there

is a lot of preplasma filling in the cone, and the interaction is such that only modest energy protons are accelerated from the tip. Note that in that case, the electron beam is very weak, and hard to distinguish.

The *top beam* from shot 20521 shown in Figure 5-27 (right) is hard to distinguish (second to last detector on the second row of RCFs) and has a low energy (27.8 MeV), while the *side beam* emitted from the side walls is very energetic (i.e. > 47.2 MeV – the stack was too short and the end of the beam was not caught). This is a case of a truly *misaligned* beam, as can be seen clearly from the Cu K α image. The beam was about as energetic as that of a flat foil (10 μ m), i.e. the laser did not have to traverse a significant amount of preplasma in the neck. Also very interesting is the very energetic oblique (upper left to lower right) beam present on almost all detectors, which seems to be comprised of mostly energetic electrons, which, one could imagine, are due to a sheath extending part way up the side wall of the funnel cone, emitting in a cylindrical pattern, caught here by the flat RCF.

Usually, when the laser is misaligned, the side wall emission (*side beam*) is more or much more energetic than the emission from the tip (normal emission). This is illustrated in Figure 5-28.

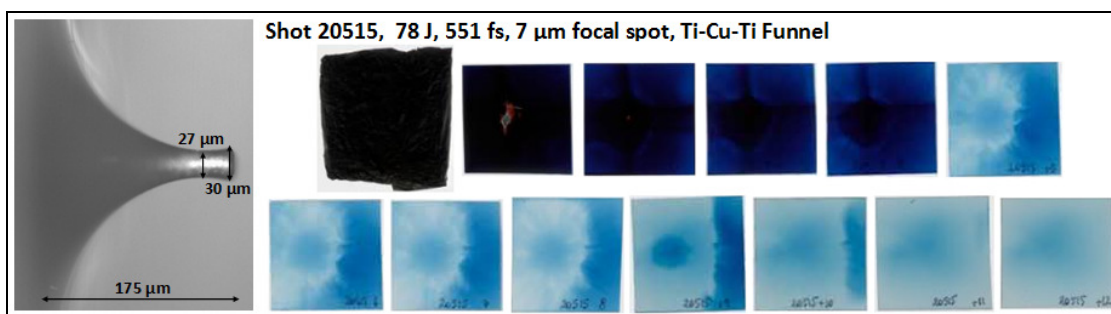


Figure 5-28: Shot 20515, funnel cone, laser misaligned, $E_{max_p+}(side) > E_{max_p+}(normal)$, with what would appear to be a monoenergetic feature between RCF layer 8 and layer 9 (since the central beam in detector 8 is much weaker than the side beam, while the central beam of detector 9 is as strong as the side beam); note that the second square corresponds to the first detector, while the first square corresponds to the Aluminum foil protecting the stack.

This last statement is always true, unless the neck diameter is so small, and/or the neck is so long, that even when the laser is well aligned, no proton beam can form off the tip, and all the emission comes from the walls, as illustrated in Figure 5-29, displaying a 16 μm outer diameter neck, and the complete absence of a *top beam*.

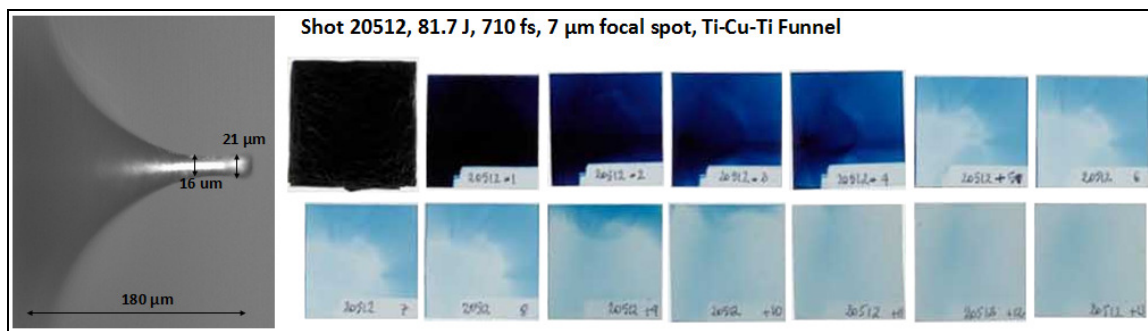


Figure 5-29: Shot 20512, funnel cone, laser aligned, neck so small (i.e. $\sim 16 \mu\text{m}$), and/or so long, that there is no *top beam* emission, and only *side beam* emission.

As illustrated in Figure 5-30, when the neck diameter is increased to 25 μm , the aligned laser penetrates well enough to produce a *top beam* with energy $\sim 46.9 \text{ MeV}$ (shot 20513). Note the presence of a strong electron beam on the last few layers of RCF. This high energy proton beam emission is fairly surprising since it differs a lot from shots 20512 (i.e. Figure 5-29), 20515 (i.e. Figure 5-28) and 20518 (Figure 5-27 (left, bottom)). In fact, a lower proton energy would indeed make more sense due to preplasma filling of the cone preventing the laser from efficiently reaching the tip. However, in the case of shot 20513, there is no Cu $K\alpha$ image which would be able to diagnose the amount of cone wall emission/interaction versus top emission/interaction for a good comparison.

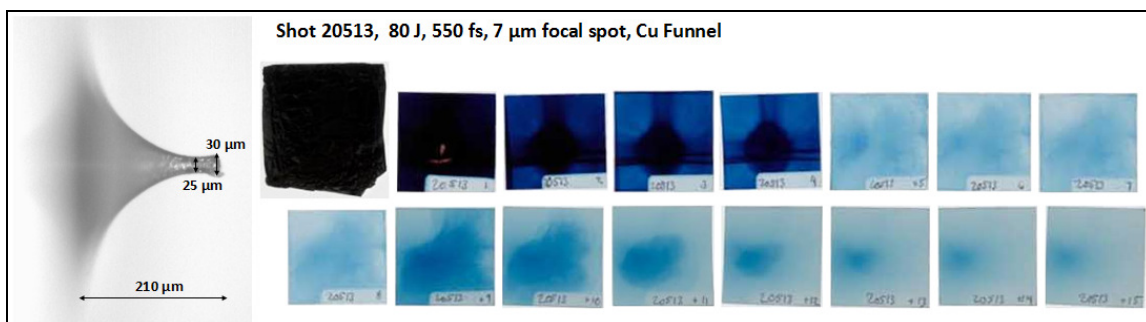


Figure 5-30: Shot 20513, funnel cone, laser aligned, top proton beam with maximum energy ~ 47 MeV.

Shown in Figure 5-31, the largest neck available, ~ 39 μm, which yielded a maximum proton energy of ~ 30 MeV for the *top beam*, while the *side beam* yielded ~ 14 MeV.

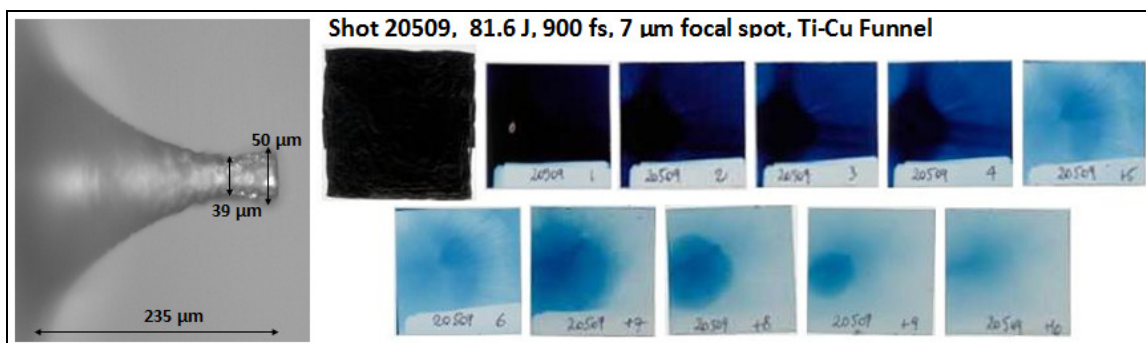


Figure 5-31: Shot 20509, funnel cone, laser aligned, largest neck available (i.e. ~ 39 μm).

In summary, and as illustrated in Figure 5-32 (left), when the neck is too thin, no proton acceleration occurs from the tip, but only from the side walls. When the neck is larger, beams are formed on the tip, the maximum proton energy goes up and the ratio *Maximum proton energy (top beam) / Maximum proton energy (side beam)* increases. When the neck diameter increases even more, the proton energy seems to go back down, although this conclusion is drawn from only one shot. From Figure 5-32 (right), illustrating what happens with the FTCs, there is very little evidence of a trend, because only 4 out of the 8 shots were well aligned. Note that these FTCs were very rough, which made them very hard to align perfectly with certainty, due to the method of alignment of these cones, which used

the back-scattered alignment beam [3.4.6.1], unlike the funnel cones, which were much smoother and therefore were easier to align (i.e. 8 shots aligned out of 11).

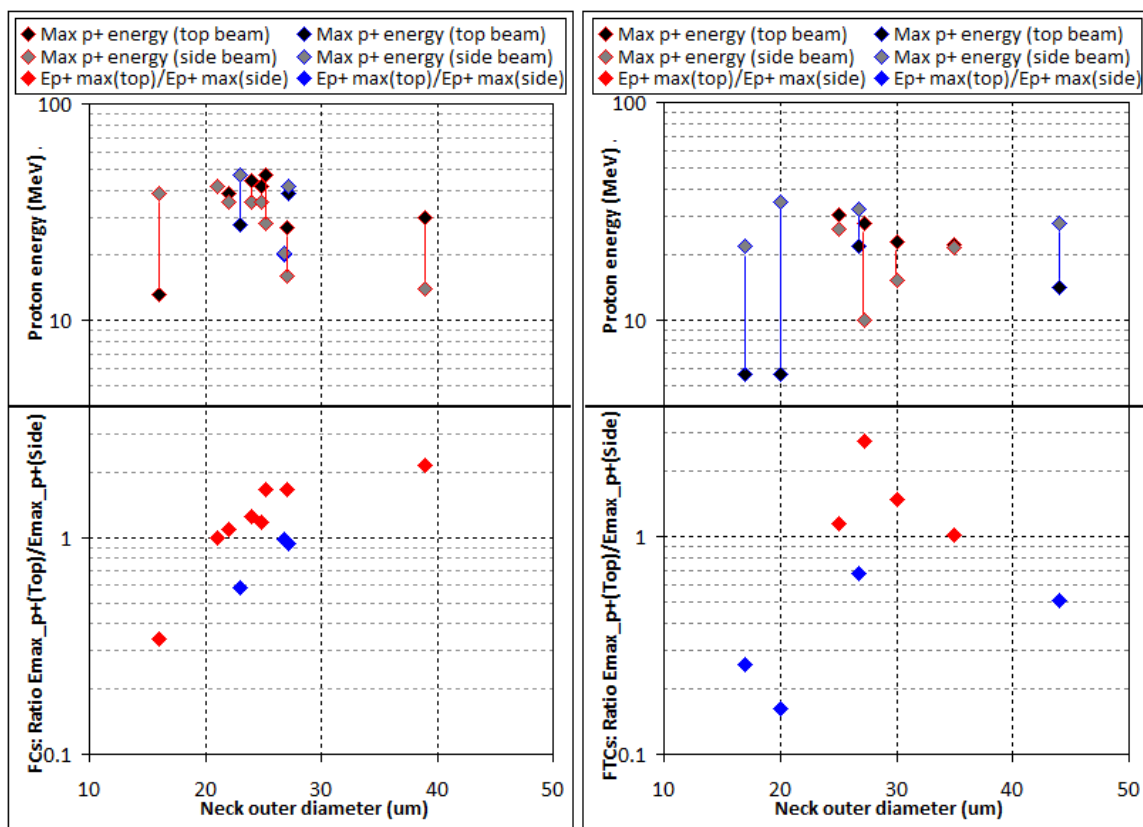


Figure 5-32: (left) Funnel Cones and (right) Flat-Top Cones; in red the aligned cases, in blue the misaligned cases. From 0.1 to 3 on the vertical axis: Ratio of $E_{max_p+}(top\ beam)/E_{max_p+}(side\ beam)$ as a function of neck outer diameter [μm]. From 5 to 100 on the vertical axis: Maximum proton energy [MeV] of the *top beam* as a function of neck outer diameter [μm].

Just as in the funnel cone case (shot 20518), the preplasma fills the cone of the FTC, leading to little flat-top interaction, and thereby yielding no maximum proton energy increase in shots 20530 and 20532, as illustrated in Figure 5-33. Note that here also, there is a fairly strong electron beam emitted from the flat top, especially in the case of shot 20532. The laser-to-proton conversion efficiency of shot 20532 is 1.62 %. This is higher than that obtained with the well aligned funnel cone (i.e. 0.79 %, shot 20518) by a factor of 2: this increase in conversion efficiency could well be due to the fact that in the case of an FTC, a

larger area is available for protons to be accelerated from (i.e. 300 μm diameter top versus a 30 μm diameter tip). The stack used in shot 20530 only has a few RCFs because it was placed in the target chamber the wrong side forward, lacking all the early layers of HD: the stack was as thick as in the case of shot 20532 but with less RCFs and more Al filters in the beginning of the stack. Because only 4 RCF layers are available, the conversion efficiency cannot be obtained with accuracy.

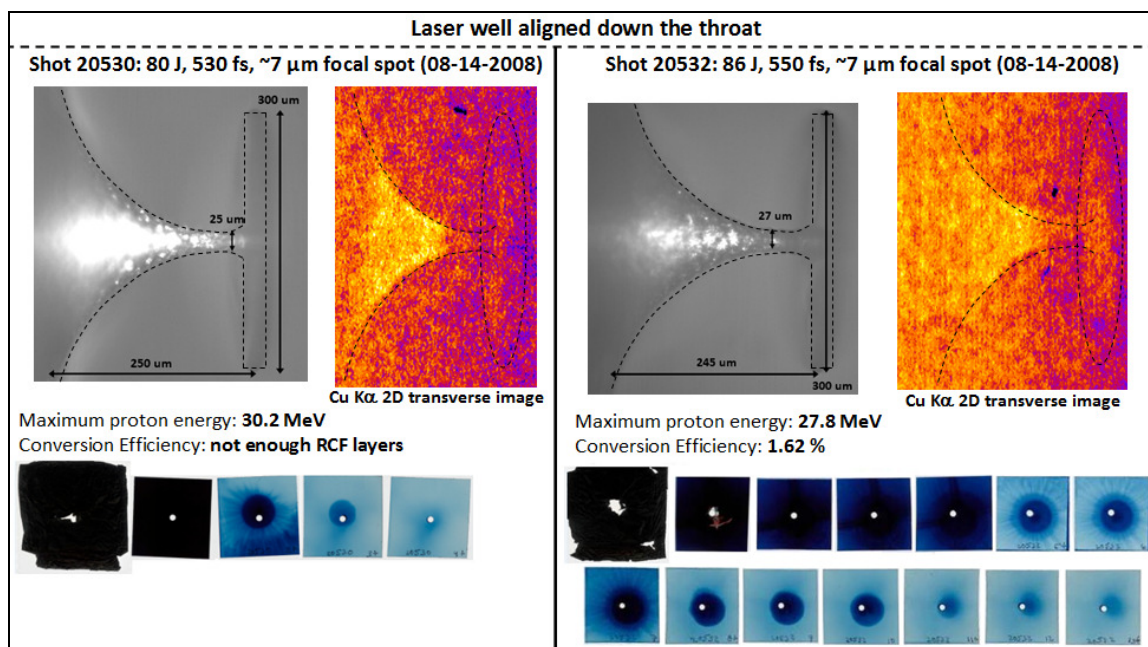


Figure 5-33: Shots 20530 and 20532, laser well aligned down the throat, flat-top cones: pictures of the targets, Cu K α images and RCF stacks.

The following three examples show RCF stacks from laser shots with each cone geometry which exhibit some interesting monoenergetic features: funnel cone (Shot 20516, Figure 5-34), snubbed nose cone (Shot 20528, Figure 5-35), and flat-top cone (Shot 20520, Figure 5-36). Another shot which was presented earlier (Shot 20515, Figure 5-28) also exhibited some monoenergetic features.

The RCF stack shown in Figure 5-34 exhibits a very strange proton beam. The proton beam is depleted in detectors 5, 6, 7 and 8. This is similar to the case where the neck diameter is

very small, or the neck is very long (i.e. Shot 20512, Figure 5-29), preventing a proton beam from being produced. However, in this case, a proton beam accelerated from the top *is* produced. In fact, from detectors 8 to 9, an inversion of the proton density takes place, i.e. in detector 8 the density evolves through the detector from the center as “little signal, less/no signal, signal” and in detector 9, as “signal, less signal, even less signal”. This indicates that the beam had more particles in the more energetic portion!

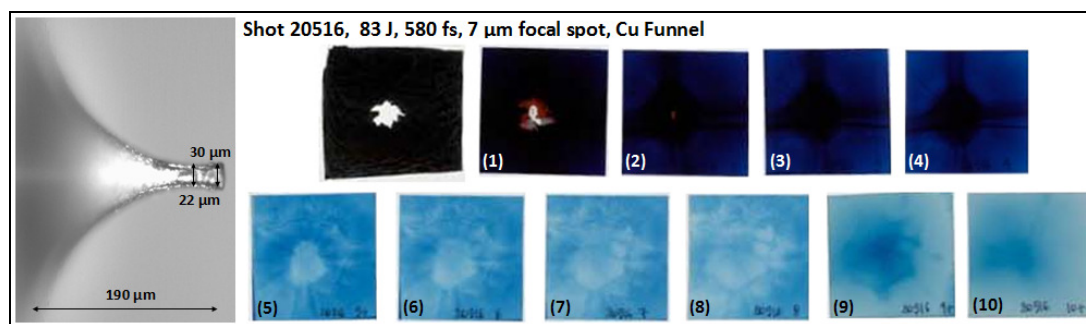


Figure 5-34: Shot 20516, funnel cone, laser apparently aligned, absence of top proton beam in layers 5-8, and inversion of the proton emission between layer 8 and layer 9.

The RCF stack shown in Figure 5-35 also exhibits an inversion of the proton density from detector 15 to detector 16 at the very center of the proton beam, just below the hole of the RCF.

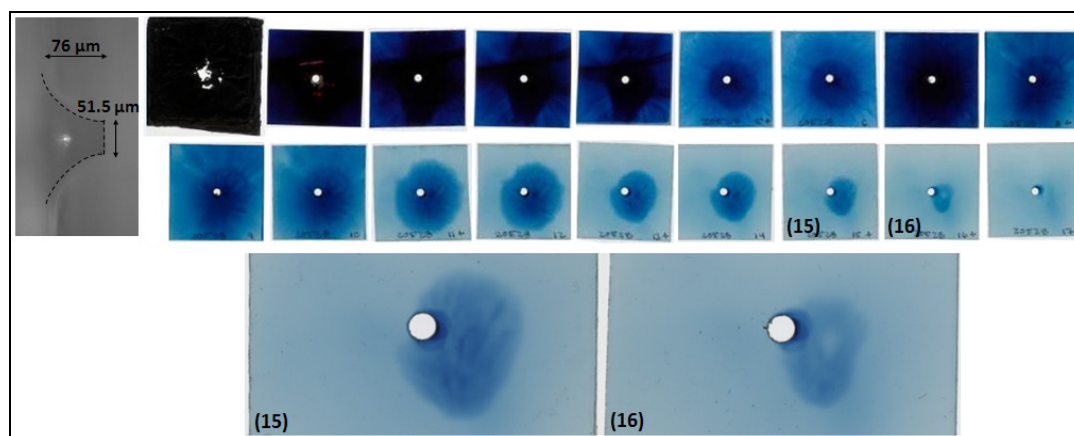


Figure 5-35: Shot 20528, snubbed nose cone, laser well aligned, inversion of the proton emission between layer 15 and layer 16.

The RCF stack shown in Figure 5-36 exhibits also an inversion of the proton density from detector 7 to detector 8 in the very center of the proton beam, just above the RCF hole.

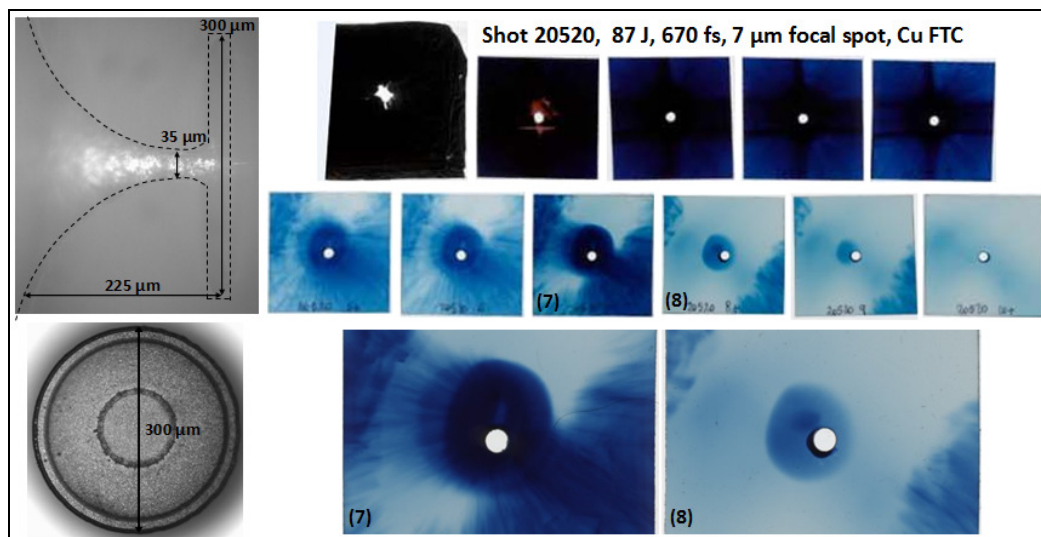


Figure 5-36: Shot 20520, FTC, laser well aligned, inversion of the proton beam emission from layer 7 to layer 8.

These results are extremely interesting and are introduced here even though no complete explanation is available as to why this is happening – more work needs to be done on these particular cases. Possible reasons for these features could be proton layer depletion, enhanced sheath fields capable of accelerating all protons from the surface to the same energies, or fields which disperse the lower energy ions leaving only higher energy ions to see the higher field. Some indication of very complex fields is visible in detectors 7 and 8 of Figure 5-34.

5.3.5 Correlation between electron temperature and proton energy

Figure 5-37 and Figure 5-38 show the electron temperatures T_1 and $(T_1+T_2)/2$ as a function of proton energy for cone targets (see Figure 5-37), as well as for flat-foil targets and RMTs (see Figure 5-38). The lower electron temperature T_1 is taken between 4 and 20 MeV, and the higher electron temperature T_2 between 20 and 50 MeV (see Figure 4-23). The meaning

of $(T_1+T_2)/2$ might not be as significant as that of T_1 alone; indeed, one should probably consider a temperature average weighted by the number of electrons for each energy, requiring more data analysis. Again, the proton energies taken into account here might not necessarily be the highest, but are always the ones corresponding to the proton beam emitted from the top of the FTC or from the tip of the funnel cone, i.e. the *top beam*, which is the beam co-linear with the electron spectrometer.

Three trendlines of the type $T_{e^-} = \alpha E_{\max_p^+}$, $T_{e^-} = \alpha E_{\max_p^+} + \beta$, and $T_{e^-} = \alpha E_{\max_p^+}^\gamma$ are added to each set of electron temperatures. Physically, the hot-electron temperature and the maximum proton energy should be linked by a simple linear relation, i.e. $T_{e^-} = \alpha E_{\max_p^+}$, which requires that when $T_{e^-} = 0$, $E_{\max_p^+} = 0$. This relation is the one presented in [98]. However, the data shown in Figure 5-37 indicates that there is a better correlation between proton energy and electron temperature if an equation of the type $T_{e^-} = \alpha E_{\max_p^+} + \beta$ is used. This may well be due to the fact that for the TNSA protons to be accelerated, a certain sheath field has to exist, i.e. a certain sheath electron temperature and sheath electron density, and if those conditions are not met, the acceleration cannot turn on, and this could well be due to the fact that the TNSA mechanism is not simply an ion blow off process like what occurs on the front-side. Similarly, an equation of the type $T_{e^-} = \alpha E_{\max_p^+}^\gamma$ also would indicate a certain threshold above which the TNSA ions can be accelerated, and below which they cannot. Note that in the case of the cone targets, the average $(T_1+T_2)/2$ of these temperatures yields a much better correlation with proton energy than T_1 alone (using $T_{e^-} = \alpha E_{\max_p^+} + \beta$).

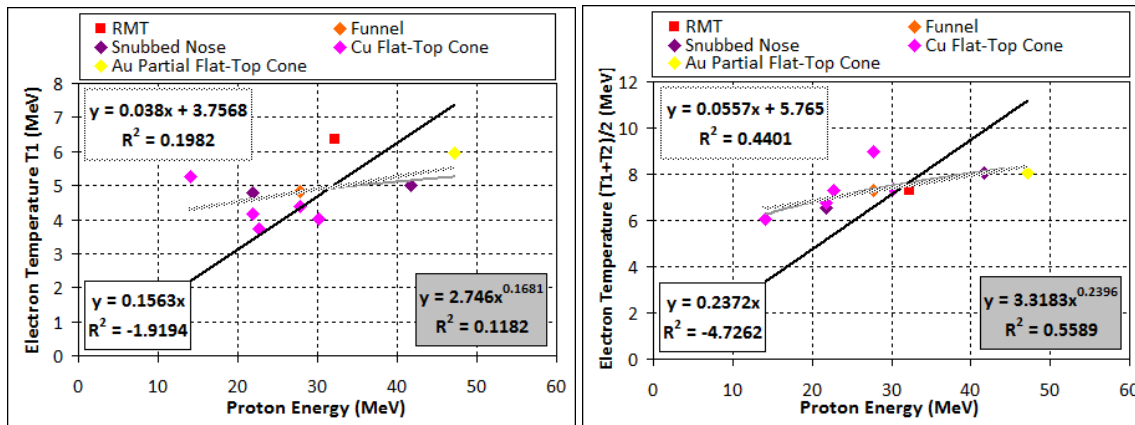


Figure 5-37: Funnel-cone, flat-top-cone and reduced-mass targets: Electron temperature as a function of the proton energy, with trendlines; (left) Lower electron temperature T₁; (right) Average of the lower and higher temperatures (T₁+T₂)/2.

In the case of flat-foil targets (note that the RMT case is not used to obtain the trendlines), whether one uses $T_{e-} = \alpha E_{\max_p+}$, $T_{e-} = \alpha E_{\max_p+} + \beta$ or $T_{e-} = \alpha E_{\max_p+}^\gamma$, the correlation between electron temperature and proton energy is poor (see Figure 5-38). The most obvious reason is the fact that the flat-foil targets presented here all have different thicknesses, as this data was acquired during a target thickness scan to look at maximum proton energy.

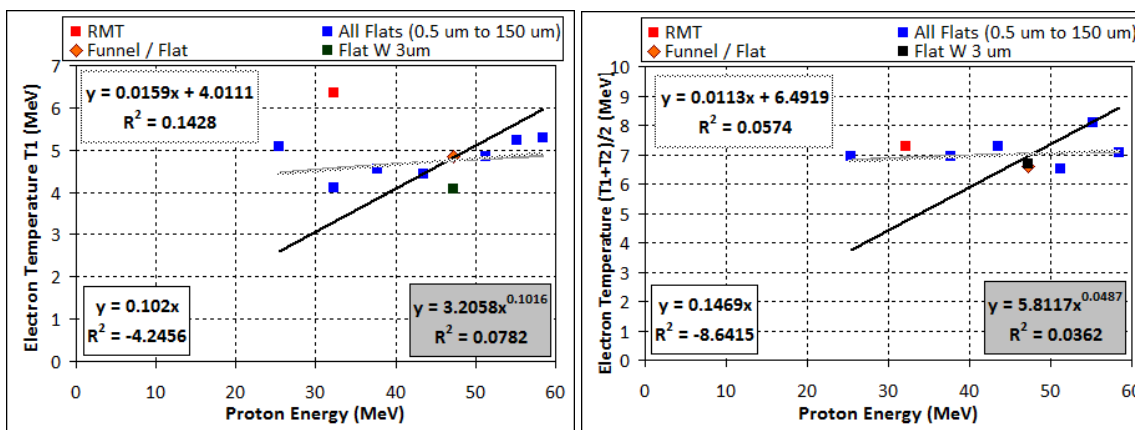


Figure 5-38: Flat-foil targets and reduced-mass targets: Electron temperature as a function of proton energy; (left) Lower electron temperature T₁; (right) Average of the lower and higher temperatures (T₁+T₂)/2. The trendlines do not include the RMT shot because its temperature T₁ is very different than the other temperatures at similar proton energies: RMTs are supposed to behave differently than regular large flat-foil targets, and to have a higher electron temperature.

The laser intensity was not perfectly constant: for flat-foil targets and RMTs, the intensity range was $[1.5\text{--}2.3]\times 10^{20}$ W/cm² and for cone targets, it was $[1.1\text{--}2.3]\times 10^{20}$ W/cm². The hot-electron temperature should scale as $T_{e-} \propto I^{0.5}$, but the data does not show that (see Figure 5-39). However, the very small intensity range over which the targets were shot does not allow for a proper data analysis. The goal was to keep the intensity constant. Determining the intensity accurately is very difficult: a small error in the focal spot (i.e. target position) yields a relatively large error in the intensity; and in the case of the cones, since the laser did not interact with the target directly but with a large amount of preplasma, the actual intensity seen by the target is hard to determine, and different than in the flat foil cases.

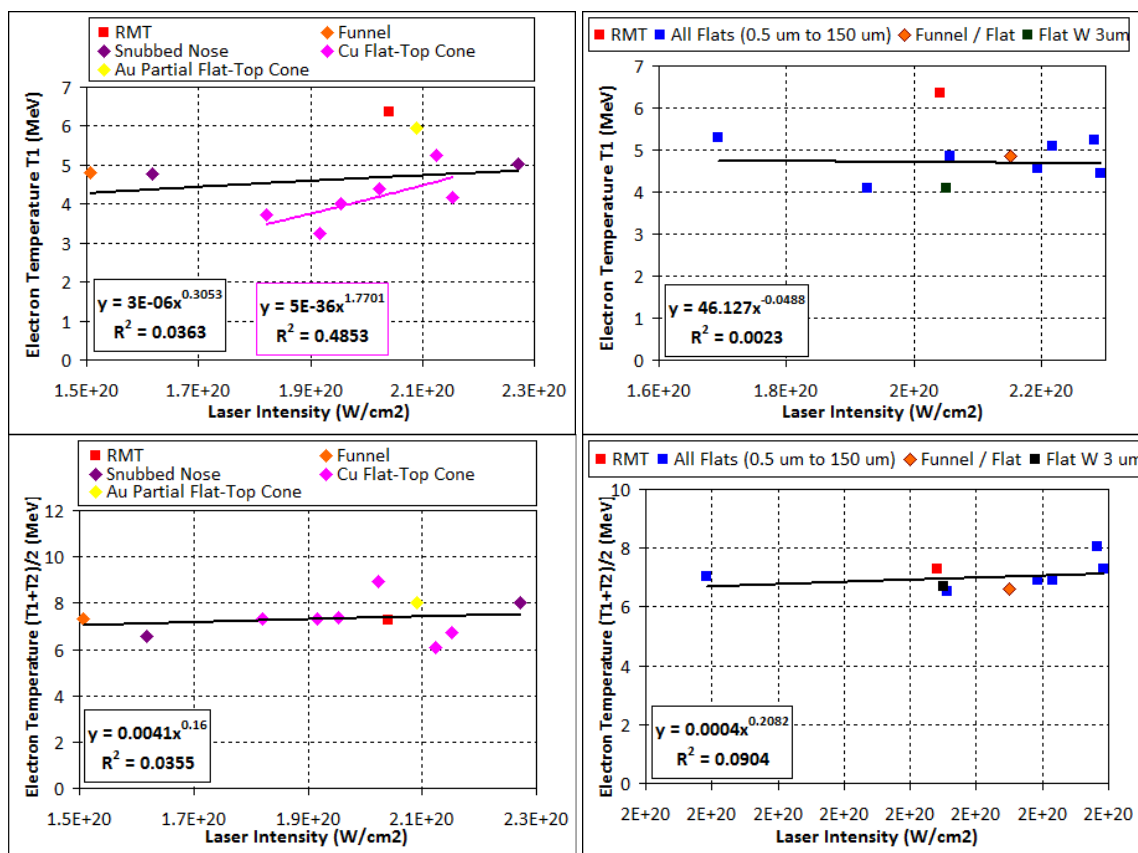


Figure 5-39: (left) Funnel-cone, flat-top-cone and reduced-mass targets, (right) Flat-foil and reduced-mass targets. As a function of laser intensity [W/cm²], (top) lower electron temperature T_1 , (bottom) average of the lower and higher temperatures $(T_1+T_2)/2$.

The proton energy should also scale as $E_{\max_p+} \propto I^{0.5}$. The data shows it in the case of the cones (see Figure 5-39 (left)), but does not in the case of the flat foils, which all had different thicknesses (see Figure 5-39 (right)).

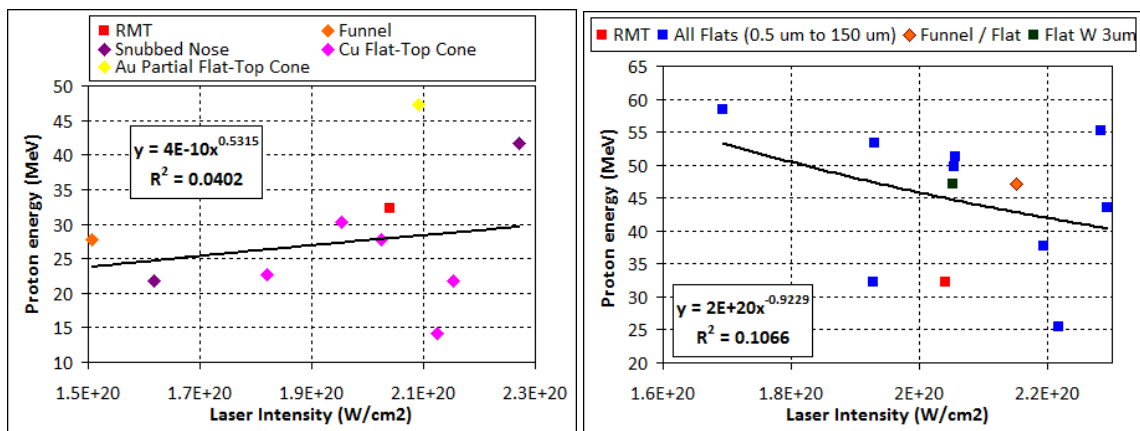


Figure 5-40: (left) Funnel-cone, flat-top-cone and reduced-mass targets, (right) Flat-foil and reduced-mass targets: Proton energy [MeV] as a function of laser intensity [W/cm²].

5.4 Trident, 80 J, $\sim [1.2-1.9] \times 10^{20}$ W/cm² & enhanced $> 10^{-10}$ contrast: June 2009 beamtime

After understanding the negative impact of preplasma filling of the cone on proton acceleration in the August 2008 experiments, where no proton energy enhancement was observed using FTC targets compared to simple flat-foil targets, the goal of this experiment was the same as in August 2008: i.e. to verify whether the energy enhancement observed using FTC targets at 20 J would scale with a laser energy of 80 J, but this time, using a much higher laser contrast, i.e. $> 10^{-10}$. RMTs and funnel-cone targets were also used for comparison, the latter especially for comparison with the data obtained at LULI in December 2006 [3, 180, 181].

5.4.1 Experimental set-up

In this experimental run, performed in the North Target Area, the short-pulse of Trident post-enhancement [3.2.2] was used (*S*-polarized), at enhanced contrast (10^{-10}) [3.3.4]. The experimental set-up is illustrated in Figure 5-41 for all targets, i.e. RMTs, cone targets and small flat-foil targets. The important distances were the following: target to slit of the electron spectrometer slit: 82 cm; target to beginning of the electron spectrometer: 90 cm; target to RCF stack: 2.5 cm; target to crystal: 7.2 cm; crystal magnification: 10 \times .

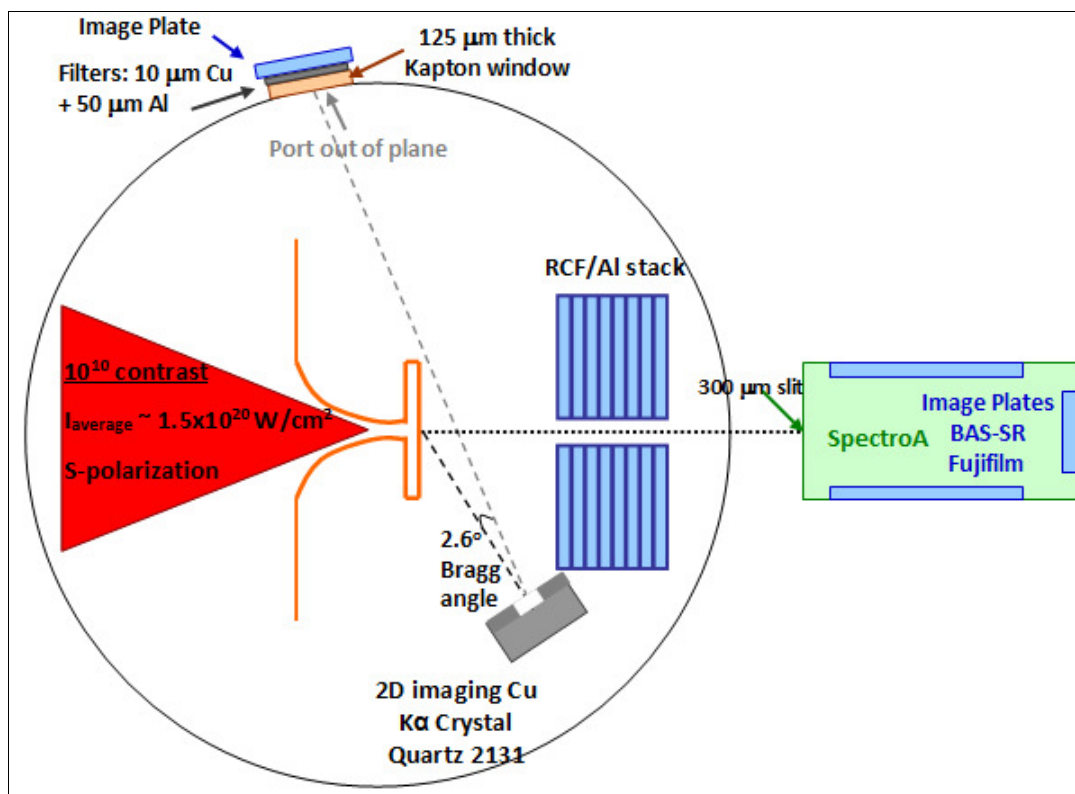


Figure 5-41: Set-up of the June 2009 beamtime (Shots 21145-21197), where Cu FTC targets (with different top and neck diameters), Cu funnel-cone targets, as well as small flat-foil targets and RMTs, were shot. Laser parameters: $\sim 80 \text{ J}$, $\sim 600 \text{ fs}$, normal incidence, $\sim 7 \mu\text{m}$ focal spot (33 %), *S*-polarization, $\sim 1.5 \times 10^{20} \text{ W/cm}^2$.

As far as the June 2009 experimental set-up illustrated in Figure 5-41 is concerned, it is very similar to the one used during the August 2008 beamtime (Figure 5-18), except for the following changes (improvements or unexpected problems):

- The shielding (shine-shield) blocking some amount of background radiation was increased (see Figure 5-42), thereby reducing the amount of noise on the Cu $K\alpha$ imager IP (see Figure 5-46).
- The electron slit was smaller in both directions (300 μm by 5 mm compared to 700 μm by 6 mm).
- A layer of 90 μm thick Kapton was to the usual 25 μm aluminum layer wrapping the RCF stack to bring the OD of the 1st layer of RCF down.
- The single hit CCD did not work as it had during the August 2008 beamtime, although nothing obvious had happened to it – making us doubt the previous Single hit CCD results, which have not been presented in this dissertation for that reason.
- Preliminary analysis indicates that there was less energy in the focal spot (i.e. 33 %), probably due to the off-axis focusing parabola not being brand new, compared to the August 2008 beamtime (i.e. 47 %).
- No aperture was placed on the Cu $K\alpha$ crystal, which worsened the resolution (by a factor of ~ 2 , see Figure 5-46).

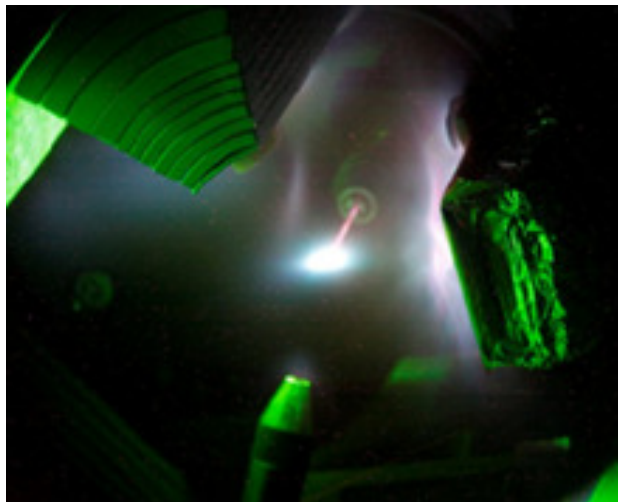


Figure 5-42: Integrated picture of a real shot (21180): in the center is the target mounted on a glass stalk; on the right, the RCF stack; on the bottom a pinhole camera; from the left corner, a large aluminum shine-shield protecting the (Cu K α) IP from direct exposure. Photo credit: Joe Cowan & Kirk Flippo.

5.4.2 Description of the Targets

5.4.2.1 Cu flat-top cones of various top-to-neck ratios

The Cu FTC targets used in this experimental run and illustrated in Figure 5-43 stemmed from a new batch, fairly similar to the batch which yielded the Au forest of FTCs: the targets had the same approximate characteristics (i.e. neck and top diameter size), but their height was in general much smaller. The thickness of the supporting foil and of the cone wall was $\sim 5\text{-}10\ \mu\text{m}$, while the top thickness was $\sim 10\text{-}15\ \mu\text{m}$, as described in Section 5.3.2.2. For a given top and neck outside diameter, i.e. $110\ \mu\text{m}$ and $22\ \mu\text{m}$ respectively, the height was $\sim 65\ \mu\text{m}$ for the Cu batch, when for the Au batch, the height was closer to $\sim 200\ \mu\text{m}$.

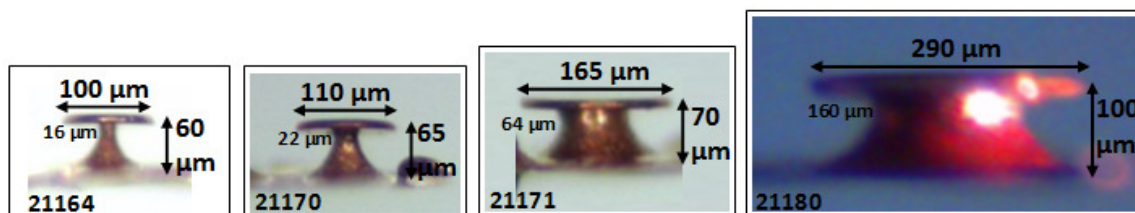


Figure 5-43: Set of different Cu FTC targets, of different top and neck sizes (to scale).

Each FTC was cut out separately from the batch. The size of the supporting foil was not necessarily kept the same at first – as the experiment went on, we made sure to carefully record the exact size, and cut out the FTC on a particular supporting foil size. It turns out there seemed to be a correlation between the supporting foil size and the maximum proton energy (see Section 5.4.5); however, we did not gather enough data to support that statement with absolute certainty. But this adds another variable that needs to be tested again to the FTCs, i.e. top diameter, neck diameter, height, and supporting foil size.

We also used the only remaining mounted Cu tall FTC target (whose top had not fallen off) from the August 2008 experiment (see Figure 5-19 (c)).

5.4.2.2 Funnel cones

Three funnel-cone targets, illustrated in Figure 5-19 (a), were shot during this campaign. They stemmed from the same batch as those used in the August 2008 experiment.

5.4.2.3 Reduced-Mass Targets

As described in detail in Section 5.2.2, the tops from the FTCs still contain some amount of Si. These tops are a sandwich of Cu-Si-Cu around the rim, and in the center a sandwich of only Si-Cu. The Si layer could be either a layer of SiO₂ or a bilayer of SiO₂-Si₃N₄. This is known from the fabrication process, and verified by looking at the target under a microscope (see Figure 5-44), comparing the dull region of the target (i.e. the Si layer) to the shiny region (i.e. the Cu layer). Note that the size of the Si area is the same as the neck inner diameter of the FTC from which the top fell of.

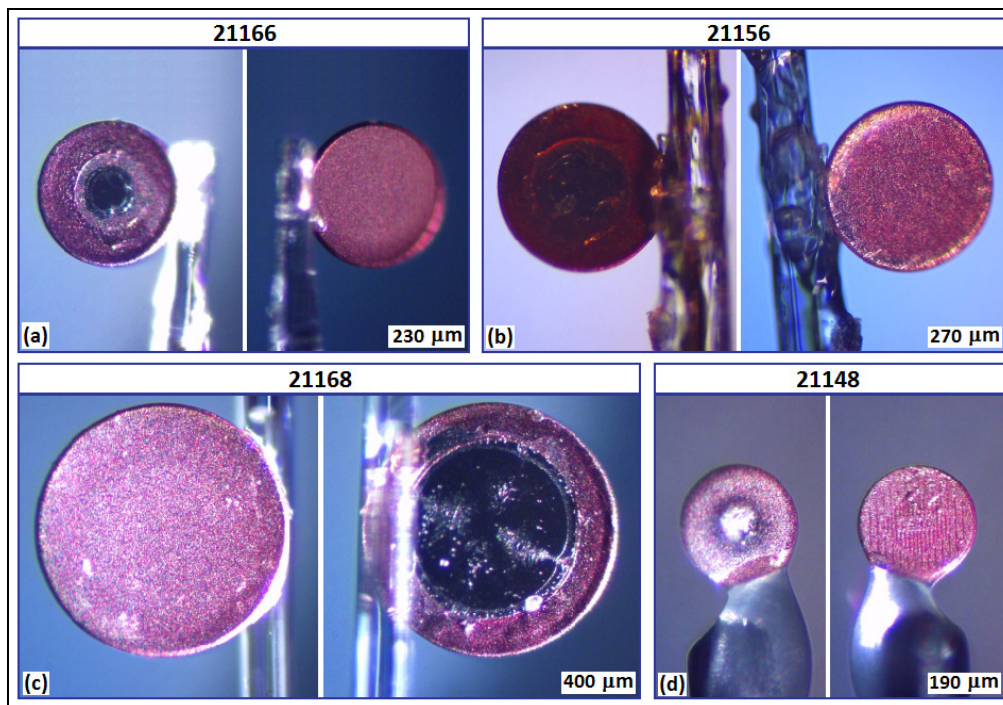


Figure 5-44: To-scale microscope pictures of RMTs, which are the tops of the FTCs: these targets show the Si side and the Cu side – the diameter of the Si area corresponds to the inner neck diameter of the FTC, whose top broke off: (a) 230 μm diameter, shot 21166, 77.8 J; (b) 270 μm diameter, shot 21156, 96.5 J; (c) 400 μm diameter, shot 21168, 76.3 J; (d) 190 μm diameter, shot 21148, 78 J, structured top broken off from the new generation of FTCs described in Section 7.4.

5.4.3 Summary of the results (80 J & 10^{-10} contrast): funnel-cone, flat-top-cone, flat-foil, and reduced-mass targets

As we look closely at what happens when the contrast is enhanced, it is important to note that, if we know that a better contrast yields less preplasma, we do not necessarily know how the contrast value scales with the preplasma density profile in front of a flat foil, or inside a cone, i.e. whether the amount of preplasma goes up linearly when the contrast goes down; this can be simulated if one has the laser profile, which is not exactly known at full power, but only assumed from low power data.

It is also important to realize that these June 2009 cone experiments are the first cone experiments performed at such a high contrast (10^{-10}), without any loss of laser energy

(~ 80 J) that might occur with plasma mirrors or by frequency doubling the laser beam, and therefore with an intensity similar to that of the prior August 2008 experiments at the intrinsic contrast ($\sim 2 \times 10^{20}$ W/cm²). In fact, up to now, to reach such a high contrast level, one needed to either switch from 1ω to 2ω , thereby losing a factor of ~ 2 in laser energy, or implement a set-up making use of plasma mirrors, thereby losing a factor of ~ 2 to 3 in laser energy, while possibly destroying the focusability of the laser beam, and having no idea what the focus actually looked like, yielding laser beam characteristics very hard to diagnose.

5.4.3.1 Effect of the contrast enhancement on maximum proton energies and conversion efficiencies from flat-foil targets

At the end of the August 2008 beamtime, the contrast enhancement on Trident was commissioned. The first few shots on Cu flat foils, i.e. $10 \mu\text{m}$ thick and $2 \times 7 \text{ mm}^2$, $5 \mu\text{m}$ thick and $2 \times 7 \text{ mm}^2$, and $1 \mu\text{m}$ thick and $1 \times 1 \text{ mm}^2$, were obtained, using the same experimental set-up as the one shown in Figure 5-17 (i.e. 22.5° laser incidence). During the June 2009 beamtime, whose set-up is shown in Figure 5-41, $10 \mu\text{m}$ thick, $1 \times 1 \text{ mm}^2$ Cu flat-foil targets were shot at normal incidence (0°). Figure 5-45 shows comparisons (in a few cases only) between the maximum proton energies (left) and the conversion efficiencies (right) in the enhanced contrast case (green and blue, 10^{-10}) to the intrinsic contrast case (red, 10^{-8}). The enhanced contrast allows for shooting thinner targets, but it does not seem to boost the maximum proton energy, not even for targets thinner than $1 \mu\text{m}$. However, the conversion efficiency is slightly higher at enhanced contrast than at intrinsic contrast. The $10 \mu\text{m}$ thick, $1 \times 1 \text{ mm}^2$ Cu flat-foil targets shot at normal incidence and enhanced contrast in June 2009 yielded higher energies than the ones obtained at enhanced contrast in August 2008, and

similar proton energy performances to the 10 μm thick, $2 \times 7 \text{ mm}^2$ Cu flat foils shot at 22.5° and intrinsic contrast.

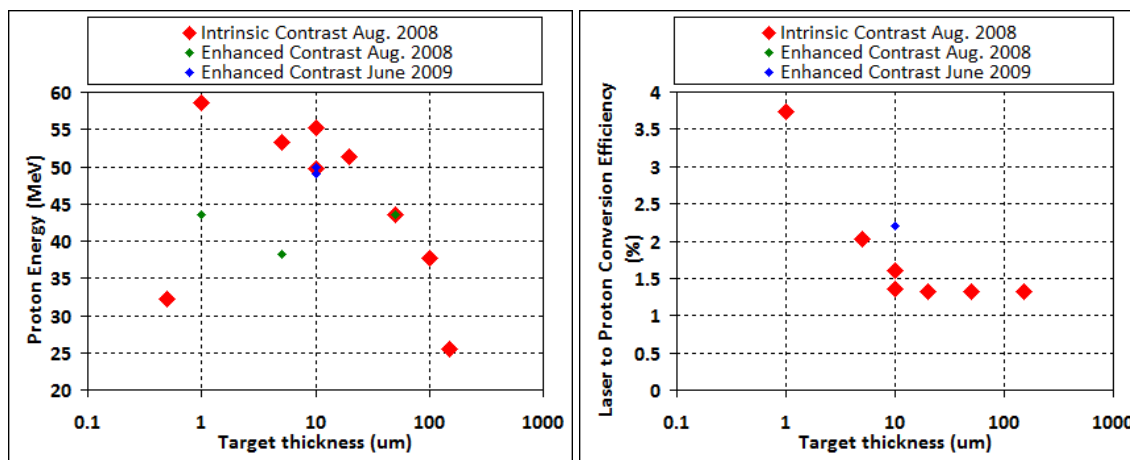


Figure 5-45: (left) Proton energy [MeV] (right) Conversion Efficiency [%] as a function of target thickness (μm) of regular flat foils; Red diamonds: August 2008, intrinsic contrast; Green diamonds, August 2008, enhanced contrast; Blue diamonds (note that in the conversion efficiency case, the single diamond represents both cases), June 2009, enhanced contrast.

5.4.3.2 Effect of the contrast enhancement on the Cu $K\alpha$ emission from cone targets

With the 10^{-10} enhanced contrast, Cu $K\alpha$ imaging of the funnel-cone targets and of the flat-top-cone targets shows deep penetration of the laser light into the funnel and bright emission from the tip of the funnel cone and the flat top of the FTC (see Figure 5-46). This resembles what was observed in [180, 3, 181], i.e. there is much more laser penetration at high contrast (2ω , 10 J) than at low contrast (1ω , 20 J). The signal-to-noise ratio is much better at enhanced contrast than it is at intrinsic contrast. The amount of background noise is significantly reduced from the intrinsic contrast case for two reasons. First, at enhanced contrast, we used much more shielding to protect the Cu $K\alpha$ image plate. And second, the hot electrons, and the resulting Bremsstrahlung emission, tend to hit everything in the target chamber, especially the chamber walls, causing a lot of background noise. At intrinsic

contrast, one expects much more noise than at enhanced contrast: this stems from the fact that, in a longer scale preplasma, the hot-electron coupling to the laser light is greater, due to resonance absorption. However, when the contrast is enhanced, one expects much less laser coupling with the hot (supra-thermal) electrons.

Note that, in Figure 5-46, the Cu K α image of an FTC at enhanced contrast and 54 J is displayed, for lack of the 80 J case due to laser fluctuations, and also for lack of another similar FTC to repeat the shot at 80 J. However, the penetration in the funnel at 80 J is very deep, which means that there is no reason why the same penetration would not have been observed for the FTC at 80 J.

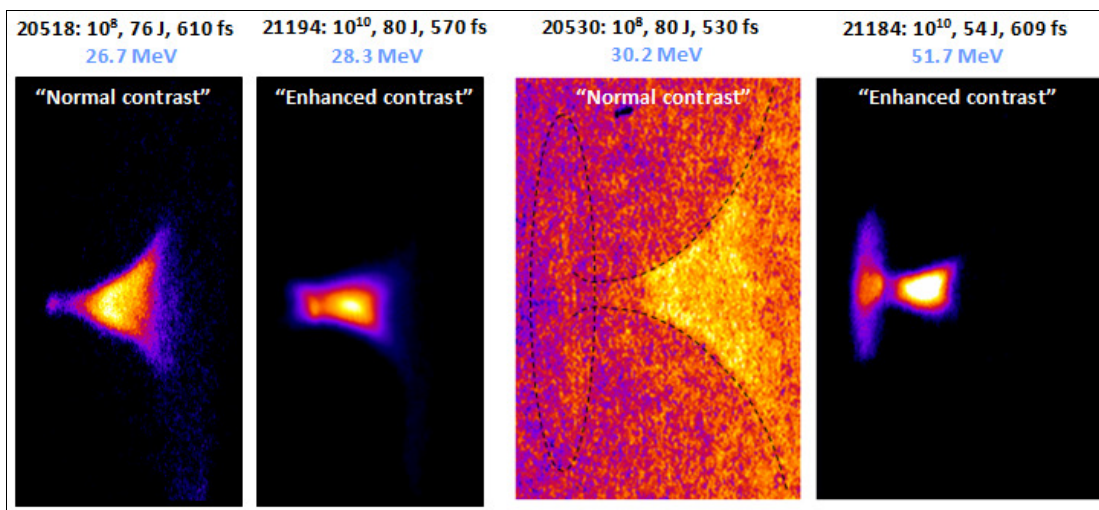


Figure 5-46: Comparison of the funnel cones (shots 20518 and 21194) and the flat-top cones (shots 20530 and 21184) at intrinsic contrast (shots 20518 and 20530) and enhanced contrast (21194 and 21184); during the experiments at intrinsic contrast, the spatial resolution was $\sim 5 \mu\text{m}$, while during the experiments at enhanced contrast, it was less, i.e. $\sim 10 \mu\text{m}$.

Also note the bright limb in the Cu K α cone wall emission of shot 20530 at intrinsic contrast (Figure 5-46). It is indicative of a cylindrically symmetric emission. At high contrast, the emission is not predominantly on the edges because the interaction is not perfectly symmetric.

When the contrast goes up, the noise is reduced, the Cu K α *signal-to-noise* ratio increases and the signal itself (Cu K α yield) increases, as illustrated in Figure 5-47, which shows integrated averaged lineouts taken around a similar area for both the intrinsic contrast case (shot 20518) and the enhanced contrast case (shot 21194).

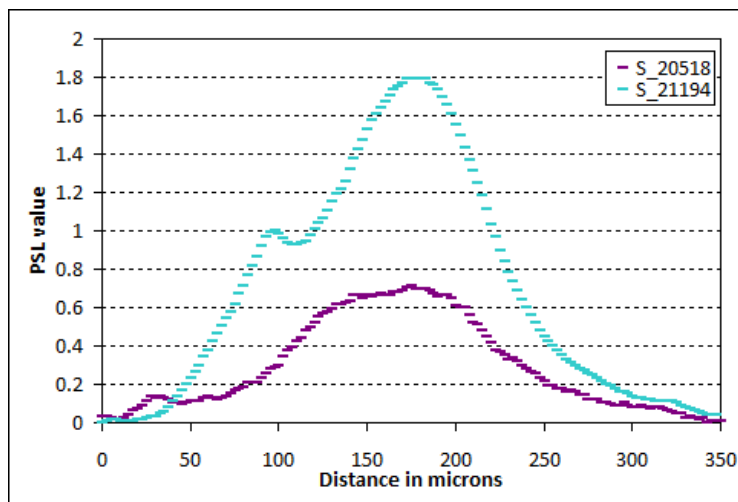


Figure 5-47: Integrated averaged lineouts taken around a similar funnel-cone target area for both the intrinsic contrast case (shot 20518) and the enhanced contrast case (shot 21194): PSL value as a function of distance in μm across the funnel cone.

5.4.3.3 Cu K α emission from the top (TE), from the cone walls (CWE) or/and from the supporting foil (SFE)

Figure 5-48 (b-c) shows the three different regions of the cone target, illustrated in Figure 5-48 (a) which can emit Cu K α : the top, the cone walls, and the supporting foil. When a bump is seen in the integrated averaged lineout of the Cu K α image (Figure 5-48 (c)) in the region where cone walls are, it is labeled as cone wall emission (CWE); when the bump is seen where the flat top is, it is labeled top emission (TE); and when the bump is seen where the supporting foil is, it is labeled supporting foil emission (SFE). The terminology of CWE and TE was already discussed several times, and especially in Section 5.3.3.2.

For maximizing the proton energy, what seems to matter is not only to absorb at the tip, but to also have the right amount of laser light absorbed in the cone wall *and* the tip, i.e. a balance has to be found between the amount of cone wall emission (CWE) and of top emission (TE), as determined in the 2009 experiments (see Section 5.4.3.4). In the intrinsic contrast case however, there is clearly too much CWE and not enough TE (see Section 5.3.4.4).

The Cu K α emission from a region of the target (e.g. neck, top, cone walls...) can in some cases be directly correlated to the laser interaction with that particular target region, especially when bright, as shown in Figure 5-25 in the case of the RMT, although not necessarily. Just as in the case of the RMT, if the laser were misaligned and hit the supporting foil, then a bright spot would exist, indicating a direct interaction, versus an indirect interaction, with secondary electrons and return current resulting in a glow (not as bright as the bright spot mentioned above). However, when there is bright emission from the cone walls, the main laser pulse did not necessarily interact with the cone walls directly, but rather interacted with the preplasma in the cone, and the hot electrons reached the cone walls, resulting in Cu K α emission. In the aligned cases, where there is mostly TE, some CWE and some SFE, SFE could be for example due to return currents in the supporting foil and not to direct laser interaction.

The integrated averaged lineout is obtained as follows: since all the FTC targets have different sizes (see Figure 5-43), the height of the box is chosen to be $\frac{1}{4}$ th larger than the top diameter (green arrow). The length of the box is such that the signal on both edges corresponds to the noise level. A lot of emission comes from the neck of the FTC, but since the profile is averaged, the value at the neck is artificially smaller, yielding to the drop in signal between TE and CWE.

Sections 5.4.3.4 and 5.4.4 (i.e. 5.4.4.1, 5.4.4.2, and 5.4.4.3) demonstrate that the Cu K α yield in the different sections of the cone can be correlated to proton energy.

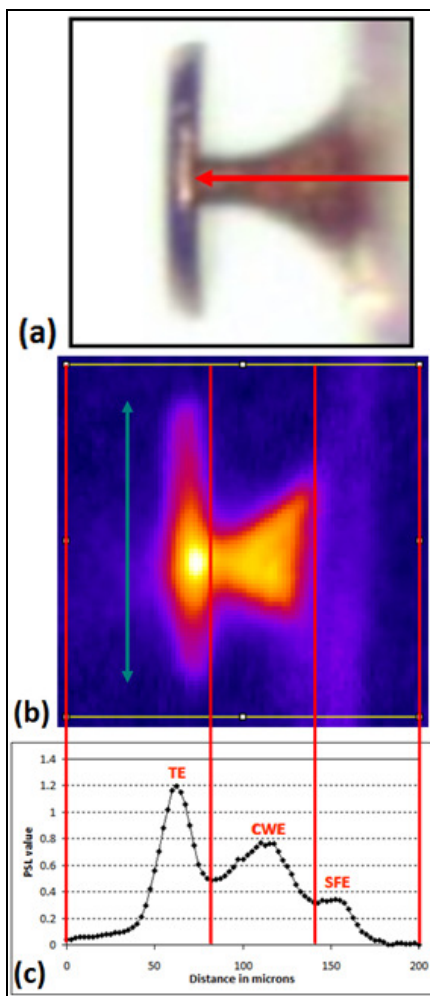


Figure 5-48: Definition of the various Cu K α emission zones; (a) Picture of an FTC target – the red arrow shows where the laser is focusing; (b) Cu K α image; since all the targets have different sizes, the height of the box is chosen to be 0.25 times larger than the top diameter (green arrow); (c) Integrated and averaged lineout across the Cu K α image, showing 3 distinctive bumps, referred to as top emission (TE) bump, cone wall emission (CWE) bump, and supporting foil emission (SFE) bump.

5.4.3.4 Proton Energies: Flat-foil targets, RMTs, and FTC targets

Making use of Cu K α imaging to correlate the proton energies with the Cu K α emission, we can conveniently summarize the data as illustrated in Figure 5-49, showing maximum proton energy as a function of how much emission is coming from the top of the FTC in

comparison to how much emission is coming from the other sections of the FTC: i.e. there can be emission from the supporting foil (SFE), the cone walls (CWE) and the top (TE), as we just saw in Section 5.4.3.3. The fraction of Cu K α emission from the top is given by the simple formula **CuK α (top) = TE / (SFE + CWE + TE)**:

- 1) **CuK α (top) = 1**: If there is no cone wall emission, nor any supporting foil emission, then $\text{CuK}\alpha(\text{top}) = 1/(0+0+1) = 1$, which corresponds to the case of an RMT or of a flat-foil target. Here, the proton energies go up to ~ 50 MeV for flat-foil targets (i.e. shot 21172, 77.8 J, 49 MeV and shot 21176, 83.7 J, 50 MeV) and up to ~ 59 MeV for the best RMT performer. The RMTs used here are pictured in Figure 5-44 and they are the best performers of another larger group of shots. These particular RMTs were all shot on the Si side (because that is the way the laser interacts with the flat top in an FTC target). They were 230 μm and 270 μm in diameter, yielding respectively ~ 59 MeV (shot 21166, 77.8 J) and ~ 55 MeV (shot 21156, 96.5 J); while the 400 μm diameter one yielded ~ 50 MeV (shot 21168, 76.3 J), acting just like a regular flat-foil target.
- 2) **CuK α (top) ~ 0.75** : If there is a lot of top emission, and only a little bit of cone wall emission and/or supporting foil emission, then $\text{CuK}\alpha(\text{top}) \sim 3/(0.25+0.75+3) \sim 0.75$. Here, the proton energies go up to ~ 55 MeV, close to the RMTs' best performer. The other three shots in this group performed worse, which is discussed in Section 5.4.4.2.
- 3) **CuK α (top) ~ 0.5** : If there is as much (or slightly more) top emission than there is cone wall emission and/or supporting foil emission, then $\text{CuK}\alpha(\text{top}) \sim 2/(0+1.75+2) \sim 0.5$. Here, the proton energies go up to 67.5 MeV, which corresponds to the highest energy seen so far for laser-accelerated protons

by any research institution in the world. Note that this group is the best performing group compared to the other groups. Three shots in this group did not perform particularly well; possible reasons why are given in Section 5.4.4.3.

- 4) **CuK α (top) ~ 0.25**: If there is a lot more cone wall emission and/or supporting foil emission than top emission, then $\text{CuK}\alpha(\text{top}) \sim 1/(1.5+2+1) \sim 0.25$. Here, the proton energies go up to ~ 45 MeV, just below the energy obtained for a flat foil.

This clearly shows the importance of how much emission there is from each section of the cone, and thus where and how the laser is interacting with the cone.

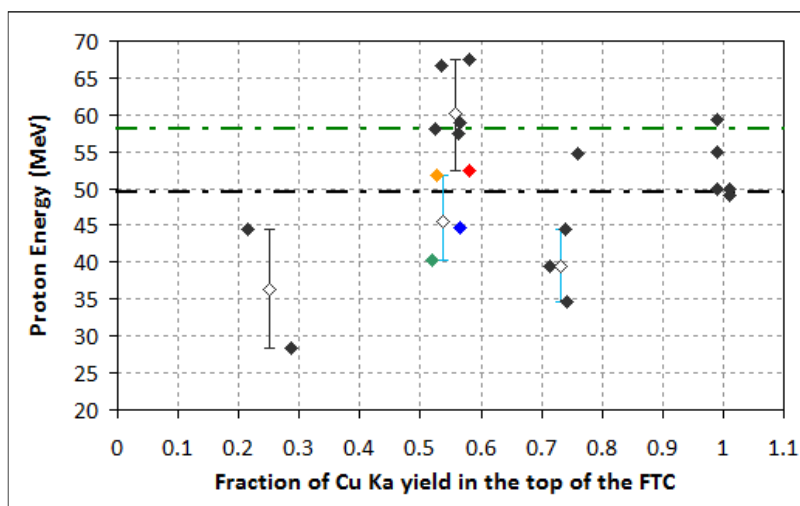


Figure 5-49: Maximum proton energy as a function of Cu K α yield fraction in the top versus in the cone walls and in the supporting foil; for each group (i.e. $\text{CuK}\alpha(\text{top}) \sim 0.25$, ~ 0.5 and ~ 0.75), the averaged value is represented (grey diamond) as well as the maximum and minimum values (grey error bars); in the case where some shots should have performed better, but did not for an understandable reason (i.e. green, blue and orange diamonds), they are isolated within the larger group, and their average as well as maximum and minimum values are also given (light blue error bars); note that the shot indicated by the red diamond (whose performance is low for a less obvious reason than the shots represented by the orange, blue and green diamonds) is included in the group of best performers, bringing the maximum proton energy average down. The horizontal black line at ~ 50 MeV represents the average of the flat-foil target results, while that at 58 MeV represents the previous Nova PW record [6].

As a side note, although well aligned, funnel cones always performed worse than flat foils, i.e. 34.7 MeV (shot 21161 and 76.3 J), 21.7 MeV (shot 21183 and 64.7 J), and 28.3 MeV (shot 21194 and 79.9 J).

5.4.4 Correlation between the Cu $K\alpha$ emission and the maximum proton energies – for all shots on FTC targets (80 J & 10^{-10} contrast)

5.4.4.1 Case CWE or SFE \gg TE and TE \sim 0, where there is much more cone wall emission (CWE) or supporting foil emission (SFE) than top emission (TE), as well as very little TE

We observe that, if all of the Cu $K\alpha$ is emitted from the cone walls or from the supporting foil, and very little Cu $K\alpha$ is emitted from the top (CWE \gg TE or SFE \gg TE, TE \sim 0), protons of very little energy are produced, meaning that the electrons did not propagate efficiently to the tip, which is very similar to the intrinsic contrast case described earlier (e.g. shot 20518, Figure 5-27). Indeed, as noted earlier, at intrinsic contrast, the results from August 2008 suggest that the proton beam from a flat-top cone or a funnel cone was never better than that of a flat foil, in both the aligned and the misaligned cases. This case (CWE \gg TE or SFE \gg TE, TE \sim 0) is illustrated by the two following shots at enhanced contrast (see Figure 5-50):

- Shot 21182: the laser could have been offset too much, hit the cone wall, bounced right off, and therefore did not make it through to the top; the laser energy was only \sim 72 J; the proton beam produced was \sim 28 MeV.
- Shot 21208: the laser was misaligned and hit the cone wall too low (leading to more SFE); the proton beam produced was \sim 45 MeV, slightly less than what was obtained for a flat foil (\sim 50 MeV).

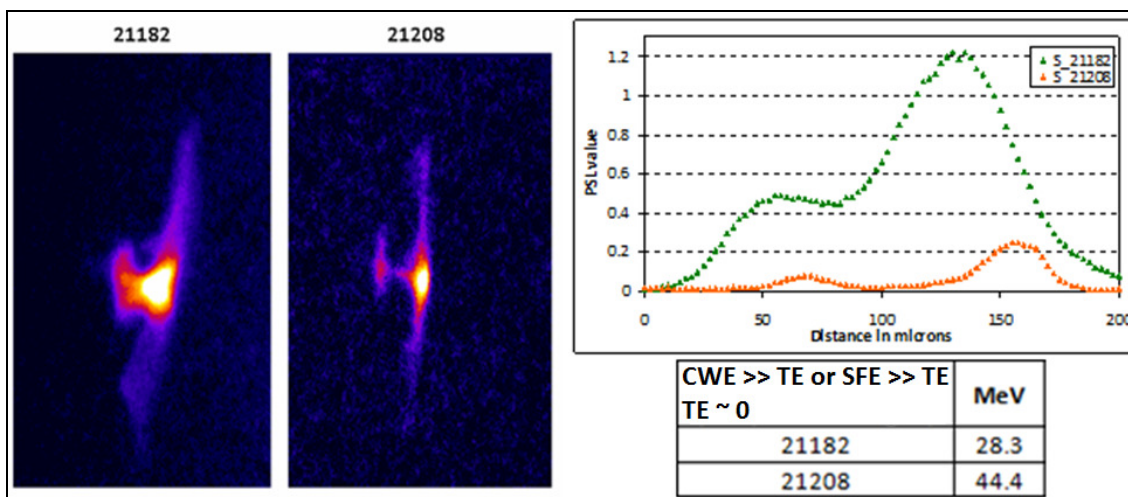


Figure 5-50: CWE >> TE or SFE >> TE and TE ~ 0; Shots 21182 and 21208; Cu K α images and integrated averaged lineouts.

CWE >> TE or SFE >> TE, TE ~ 0 (low proton energies)	MeV	J	fs	TE	CWE	SFE	Max(SFE,CWE) / TE	TE / (SFE+CWE+TE)
21182	28.3	71.9	699	0.487	1.219	/	2.503	0.285
21208	44.4	83.8	625	0.076	0.027	0.25	3.289	0.215

Table 7: CWE >> TE or SFE >> TE and TE ~ 0; Shots 21182 and 21208; Values of proton energy, laser energy, laser pulse duration, top, cone wall, and supporting foil emission values (TE, CWE and SFE), ratio Maximum(SFE,CWE)/TE, and ratio TE/(SFE+CWE+TE).

5.4.4.2 Case TE >> CWE or TE >> SFE, where there is much more top emission (TE) than cone wall emission (CWE) or than supporting foil emission (SFE)

When much more Cu K α is emitted from the top than from the cone walls or from the supporting foil (TE >> CWE or TE >> SFE), as for the shots illustrated in Figure 5-51, the proton energies would be expected to be as high as those observed with simple RMTs, i.e. up to ~ 59 MeV in the best case (Shot 21166, 230 μ m, Si side, 77.8 J, and 587 fs).

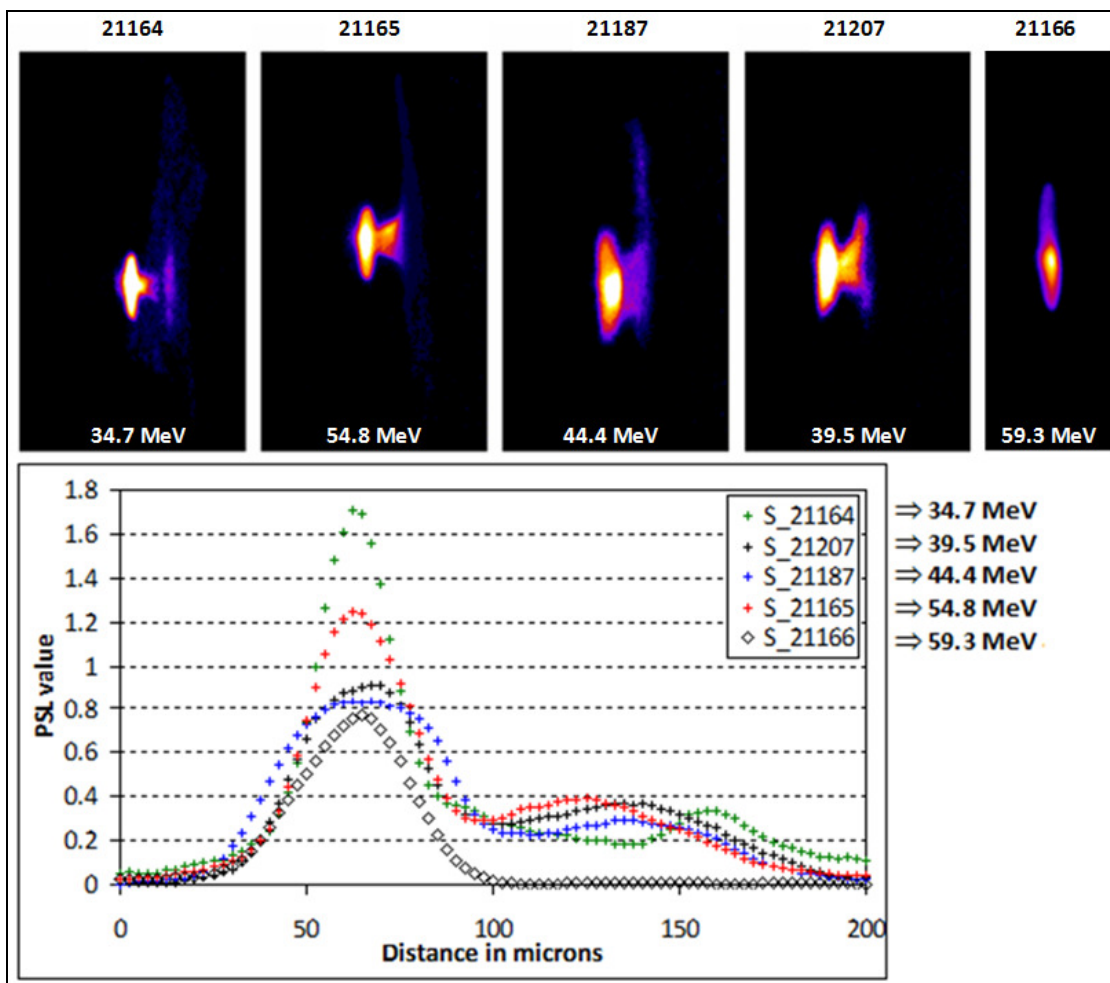


Figure 5-51: TE \gg CWE or TE \gg SFE and TE \sim 0; Shots 21164, 21165, 21187, 21207, and 21208; Cu K α images and integrated averaged lineouts.

TE \gg CWE	MeV	J	fs	TE	CWE	SFE	Max(SFE,CWE)/TE	TE / (SFE+CWE+TE)
21164	34.7	83.9	651	1.709	0.257	0.338	0.198	0.742
21165	54.8	80.6	572	1.243	0.391	/	0.314	0.761
21187	44.4	68	665	0.834	0.294	/	0.352	0.739
21207	39.5	72.1	572	0.913	0.367	/	0.402	0.713

Table 8: TE \gg CWE or TE \gg SFE and TE \sim 0; Shots 21164, 21165, 21187, 21207, and 21208; Values of proton energy, laser energy, laser pulse duration, top, cone wall and supporting foil emission values (TE, CWE and SFE), ratio Maximum(SFE,CWE)/TE, and ratio TE/(SFE+CWE+TE).

The only shot which performed about as well as the best RMT (i.e. shot 21166) is shot 21165. The interaction was asymmetric and yielded \sim 55 MeV. One can already see that

that the Cu K α emission is asymmetric; this already indicates that an asymmetric laser-target interaction is beneficial. This is shown in experimental results in Section 5.4.4.3, and confirmed in Sections 6.2.4 and 6.2.4.2 by PICLS simulations.

None of the others performed particularly well, even though, intuitively, they should have. Looking at each shot carefully, one can isolate a few plausible reasons, i.e. laser energy, supporting foil size and laser emission from the supporting foil justifying why the other 3 shots in this group did not perform well:

- Shot 21164: the laser interacted with the substrate (most probably the wings of the laser), leading to a hump in the supporting foil region and to only ~ 35 MeV.
- Shot 21187: the laser was very well aligned, made it to the top without interacting with the walls much; however, the laser energy was low, i.e. 68 J, and the resulting proton beam only ~ 45 MeV. Shot 21156 (RMT, 270 μm , Si side, 96.5 J and 738 fs) produced 55 MeV, with a laser energy of 96.5 J. So the laser energy could well be the reason for the ~ 45 MeV obtained (since the top size of 260 μm in 21187 is similar to the RMT diameter in 21156).
- Shot 21207: the interaction is asymmetric, very similar to that of shot 21165 (see Table 9), but the substrate size is much smaller (trimmed target) than in the case of shot 21165, and the laser energy is about 10 J lower, yielding to only ~ 40 MeV.

Shot #	fs	J	TW	Target Name	L1	L2	A	V	T	N	T/N	H	p+
21165	572	80.6	141	PTJ #3	490	690	338100	3796475	115	32	3.59	70	54.8
21207	572	72.1	126	PTJ trimmed #5	150	250	37500	947555	135	43	3.14	65	39.5

TE	CWE	CWE/TE	Area (75 \times 150 pix 2)	Mean	Standard Dev.	Min	Max	Int. Dens.	Median	Int. Dens. - backg round	Area \times Mean	Max - Min
1.24	0.39	0.31	11250	0.45	0.45	0.17	2.74	5094	0.259	3139	5096	2.56
0.91	0.37	0.40	11250	0.91	0.44	0.49	2.75	10299	0.747	4826	10294	2.26

Table 9: Comparison between shot 21165 and shot 21207: L1 and L2 are the dimensions of the supporting foil, A the area of the supporting foil, V the volume of the supporting foil, T

the FTC top diameter, N the FTC outer neck diameter, T/N the top-to-neck ratio, H the FTC height, p+ the maximum proton energy, TE and CWE the amount of top and cone wall emission (respectively), CWE/TE the ratio between CWE and TE, Area the area selected around the FTC, Mean the mean PSL value in that area, Min and Max the minimum and maximum PSL values in that area, Int. Density = Area × Mean PSL value, and Background = Area × Min PSL value.

5.4.4.3 Case TE >~ CWE, where there is slightly more top emission (TE) than cone wall emission (CWE)

5.4.4.3.1 Best Performers

When only slightly more Cu K α is emitted from the top than from the cone walls (TE >~ CWE), then the best proton energies are observed (see Figure 5-52), greater to or just slightly below the best case of RMT.

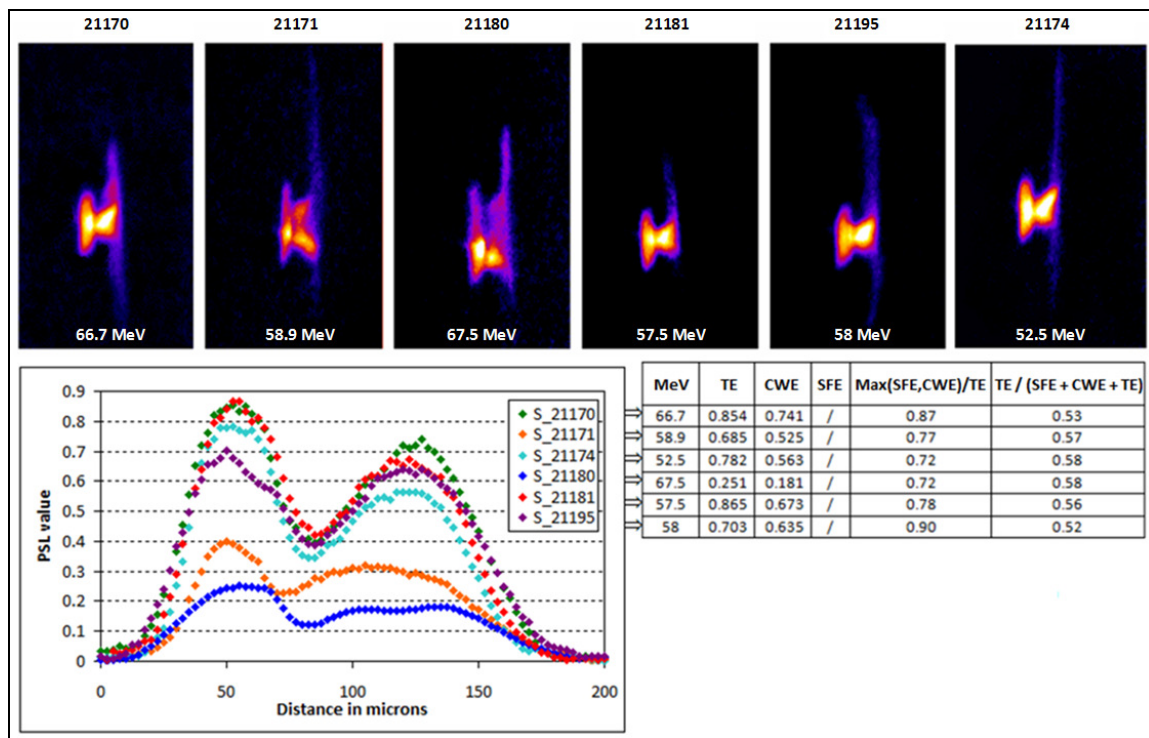


Figure 5-52: TE >~ CWE; Shots 21170, 21171, 21180, 21181, 21195, and 21174; Cu K α images and integrated averaged lineouts.

The highest proton energy to date from laser-accelerated proton beams was achieved from such an interaction: 67.5 MeV (see Figure 6-5). The next best performer reached 66.7 MeV (see Figure 6-4), another world record. These energies compared to the energy of 50 MeV from a flat foil represent an energy increase of 135 %.

TE >~ CWE (Best proton energies)	MeV	J	fs	TE	CWE	SFE	Max(SFE,CWE)/TE	TE / (SFE+CWE+TE)
21170	66.7	80.9	627	0.854	0.741	/	0.868	0.535
21171	58.9	81.3	653	0.685	0.525	/	0.766	0.566
21174	52.5	80	633	0.782	0.563	/	0.7199	0.581
21180	67.5	79.3	795	0.251	0.181	/	0.721	0.581
21181	57.5	74.5	641	0.865	0.673	/	0.778	0.562
21195	58	78	538	0.703	0.635	/	0.903	0.525

Table 10: TE >~ CWE; Shots 21170, 21171, 21180, 21181, 21195, and 21174; Values of proton energy, laser energy, laser pulse duration, top, cone wall, and supporting foil emission values (TE, CWE and SFE), ratio Maximum(SFE,CWE)/TE, and ratio TE/(SFE+CWE+TE).

From Table 10, one can see that all the laser energies are very similar (ranging from 74.5 MeV to 81.3 MeV). All of these shots, except for shot 21174, yielded very high energy protons. At first, it seems that shots 21170 and 21174 are very similar and should have performed the same (see Table 11); and unfortunately, there is no electron temperature measurement for shot 21170. However, if one isolates shots 21171 and 21180 since the target dimensions are different than in the other 4 cases (i.e. 21170, 21174, 21181, and 21195), shot 21174 is the one that has the smallest value for Maximum(SFE,CWE)/TE, i.e. ~ 0.72 (21174) especially compared to ~ 0.87 (21170), as well as to ~ 0.78 (21181) and ~ 0.90 (21195). This means that a little more cone wall emission, i.e. laser interaction path, would have been beneficial for maximizing the proton energy.

Shot #	fs	J	TW	Target Name	L	L	A	V	T	N	T/N	H	p+
21170	627	80.9	129	PTJ #5	375	590	221250	2572181	107	22	4.86	65	66.7
21174	633	80	126	PTJ #11	410	660	270600	2977716	93	25	3.72	65	52.5

TE	CWE	CWE / TE	Area (75 × 150 pix ²)	Mean	Standard Dev.	Min	Max	Int. Dens.	Median	Int. Dens. – background	Area × Mean	Max – Min
0.85	0.74	0.87	11250	0.84	0.45	0.42	2.64	9419	0.64	4680	9416	2.22
0.78	0.56	0.72	11250	0.83	0.45	0.45	2.64	9355	0.63	4351	9360	2.19

Table 11: Comparison between shot 21170 and shot 21174: L1 and L2 are the dimensions of the supporting foil, A the area of the supporting foil, V the volume of the supporting foil, T the FTC top diameter, N the FTC outer neck diameter, T/N the top-to-neck ratio, H the FTC height, p+ the maximum proton energy, TE and CWE the amount of top and cone wall emission (respectively), CWE/TE the ratio between CWE and TE, Area the area selected around the FTC, Mean the mean PSL value in that area, Min and Max the minimum and maximum PSL values in that area, Int. Density = Area × Mean PSL value, and Background = Area × Min PSL value.

5.4.4.3.2 Understandable exceptions (laser energy, supporting foil size, and supporting foil emission): shots 21169, 21184, and 21192

Looking only at the CWE/TE ratios of shots 21169, 21184, and 21192, one would expect their proton energies to have been higher.

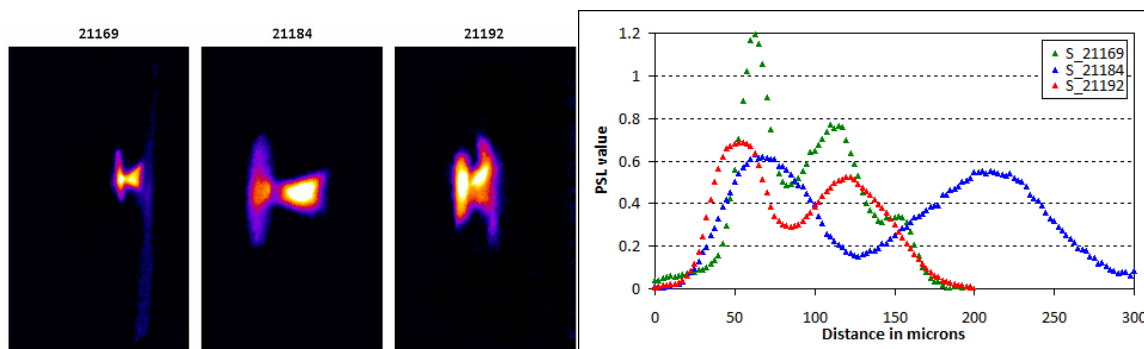


Figure 5-53: TE >~ CWE; Shots that did not perform so well for understandable reasons: 21169, 21184, and 21192; Cu Kα images and integrated averaged lineouts.

TE >~ CWE	MeV	J	fs	TE	CWE	SFE	Max(SFE,CWE)/TE	TE / (SFE+CWE+TE)
21192	44.6	77.2	708	0.685	0.524	0	0.765	0.567
21184	51.7	54.4	609	0.619	0.554	0	0.895	0.528
21169	40.3	83.4	687	1.193	0.765	0.342	0.641	0.519

Table 12: TE >~ CWE; Shots that did not perform so well for understandable reasons: 21169, 21184, and 21192; Values of proton energy, laser energy, laser pulse duration, top, cone wall and supporting foil emission values (TE, CWE and SFE), ratio Maximum(SFE,CWE)/TE, and ratio TE/(SFE+CWE+TE).

However, looking at these three shots carefully, one can isolate a few plausible reasons (i.e. laser energy, supporting foil size, and supporting foil emission) explaining why they did not perform well (note that these reasons are the same as the ones evoked in Section 5.4.4.2):

- Shot 21169: some emission comes from the supporting foil (which could be due to some interaction between the wings of the laser and the supporting foil, or to return currents...), yielding a proton beam of ~ 40 MeV.
- Shot 21184: the laser energy was 50 J, rather than 80 J, yielding a proton energy of ~ 52 MeV.
- Shot 21192: this shot, which yielded ~ 45 MeV, is very similar to shot 21171, which performed very well and yielded ~ 59 MeV (see Table 13 and Figure 5-54). The only clear difference between these two shots is the size of the supporting foil (much smaller for 21192 than that of 21171).

Shot #	fs	J	TW	Target Name	L	L	A	V	T	N	T/N	H	p+
21171	653	81.3	124	PTJ #6	500	900	450000	5355299	165	64	2.58	70	58.9
21192	708	77.2	109	PTJ Trimmed #3	175	250	43750	1010055	135	46	2.93	65	44.6

TE	CWE	CWE / TE	Area (75 × 150 pix ²)	Mean	Standard Dev.	Min	Max	Int. Dens.	Median	Int. Dens. – background	Area × Mean	Max – Min
0.69	0.52	0.76	11250	0.83	0.23	0.56	1.87	9387	0.74	3094	9383	1.31
0.69	0.53	0.76	11250	0.81	0.33	0.48	2.07	9063	0.659	3645	9068	1.587

Table 13: Comparison between shot 21171 and shot 21192: L1 and L2 are the dimensions of the supporting foil, A the area of the supporting foil, V the volume of the supporting foil, T the FTC top diameter, N the FTC outer neck diameter, T/N the top-to-neck ratio, H the FTC height, p+ the maximum proton energy, TE and CWE the amount of top and cone wall emission (respectively), CWE/TE the ratio between CWE and TE, Area the area selected around the FTC, Mean the mean PSL value in that area, Min and Max the minimum and maximum PSL values in that area, Int. Density = Area × Mean PSL value, and Background = Area × Min PSL value.

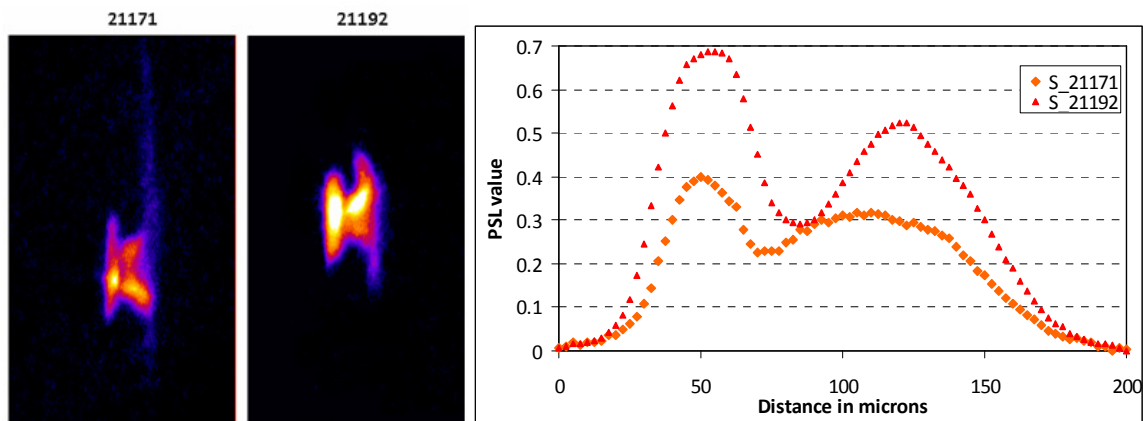


Figure 5-54: Comparison between shot 21171 and shot 21192; Cu K α images and integrated averaged lineouts.

5.4.4.4 Behavior of similar small neck size targets

The only occasions where a 3rd hump, due to SFE, is seen in the line-out, is with the smallest neck targets, lumping them with the more poorly performing targets. So it could have been that smaller neck targets would have performed better, if SFE had not been present, but all exhibited SFE. It is not clear if there is a direct correlation between smallest neck and SFE, or if it was merely coincidental.

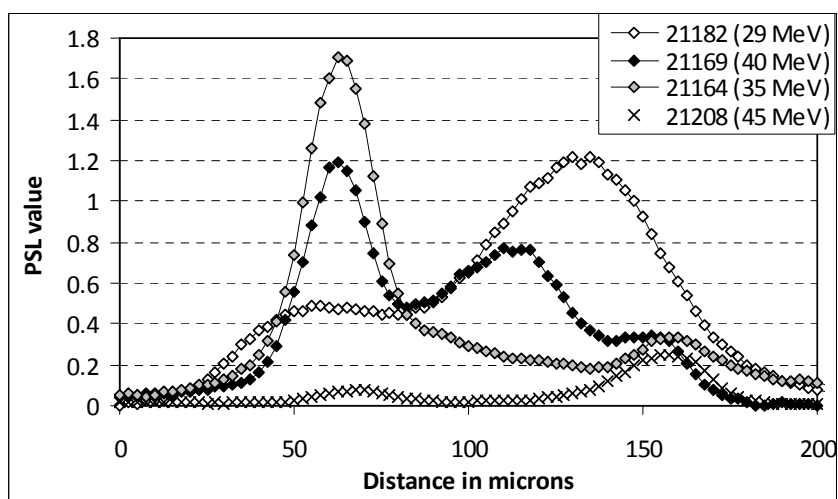


Figure 5-55: PSL value as a function of distance for all the shots with the smallest necks: 21182 (12 μm), 21169 (11 μm), 21164 (15 μm), and 21208 (15 μm).

In the case of shot 21164 (grey diamonds), the neck diameter is $\sim 15 \mu\text{m}$. Only TE and SFE are observed, while there is no CWE at all. The proton energy reaches 34.7 MeV.

In the case of shot 21169 (black diamonds), the neck diameter is $\sim 11 \mu\text{m}$. Emission from all 3 regions of the FTC is observed, i.e. TE, CWE, and SFE. The maximum proton energy is 40.3 MeV.

In the case of shot 21182 (white diamonds), the neck diameter is $\sim 12 \mu\text{m}$. The emission comes primarily from the cone walls (i.e. CWE), and the maximum proton energy is 28.3 MeV.

In the case of shot 21208 (crosses), the laser was misaligned. The neck diameter is $\sim 12 \mu\text{m}$, but the laser never made it down the throat. The maximum proton energy is 44.4 MeV, closer to the energy obtained from flat foil (i.e. 50 MeV).

5.4.5 Correlation between proton energies and supporting foil size

Empirically, just as in the case of RMTs, which shows a maximum proton energy for an “optimal” target diameter of $230 \mu\text{m}$, immediately followed by a target diameter of $270 \mu\text{m}$ diameter (see Figure 5-56), the FTC targets which belong to the group of best performers, perform better with an “optimally” sized supporting foil (see Figure 5-57). This is especially true in the case of a very small supporting foil as shot 21192 (blue diamond) compared to the well performing shot 21171.

This hypothesis of a supporting foil size being an impediment on proton acceleration when either too small or too large has been tested with 2-D PICLS simulations. The 2-D PICLS simulations do not agree with this experimental observation. The under-performance of shot 21174 (red diamond) was already described above (see Table 11 in Section 5.4.4.3.1). As far as shots 21169 and 21184, their rather poor performance has already been explained in Section 5.4.4.3.2.

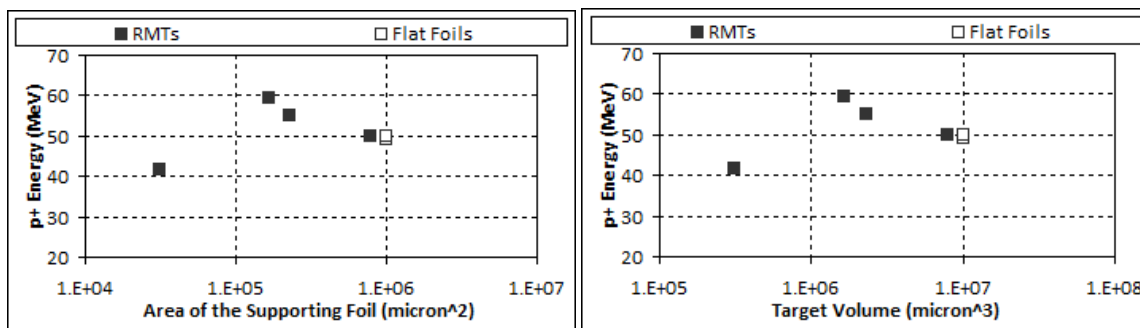


Figure 5-56: Correlation between proton energies and RMT area: Maximum proton energy as a function of (left) target area and (right) target volume for the best performing RMTs (black squares) and regular flat-foil targets (white squares).

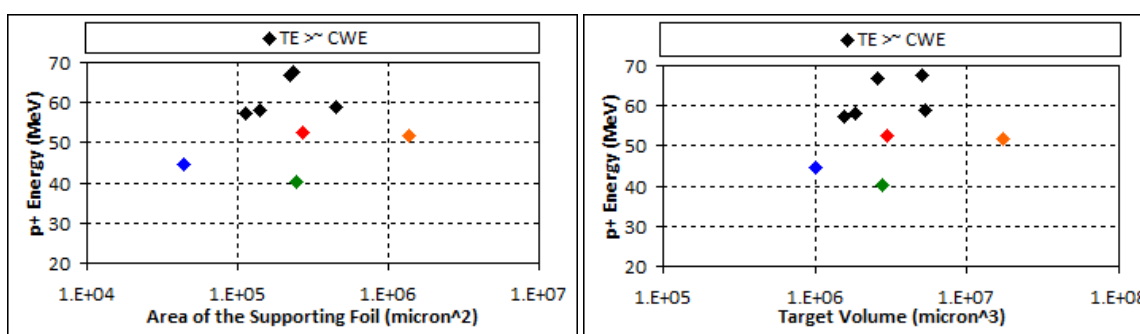


Figure 5-57: Correlation between proton energies and supporting foil size of an FTC target: Maximum proton energy as a function of (left) target area and (right) target volume for the best performing FTC targets (diamonds), i.e. for the case where $TE \gg CWE$; the blue diamond corresponds to shot 21192 (small supporting foil); the red diamond corresponds to shot 21174 (slightly smaller CWE/TE than the others); the green diamond corresponds to shot 21169 (presence of SFE); and the orange diamond corresponds to shot 21184 (low laser energy).

5.4.6 Correlation between electron temperature and proton energy

Figure 5-59 and Figure 5-58 show the electron temperatures T_1 and $(T_1+T_2)/2$ as a function of proton energy for flat-foil targets only (Figure 5-59), as well as for cone targets (Figure 5-58). Trendlines are added to each set of electron temperatures. Figure 5-59 even includes a few shots from a year earlier (i.e. August 2008), and the data fits well with the other set of data from June 2009, giving us confidence that both experiments can be directly compared, i.e. the variation in set-up of the electron spectrometer is small enough.

Just as it is described in Section 5.3.5, the lower electron temperature T_1 is taken between 4 and 20 MeV, and the higher electron temperature T_2 between 20 and 50 MeV (see Figure 4-23). Also, the meaning of $(T_1+T_2)/2$ might not be as significant as that of T_1 alone; indeed, one should probably consider a temperature average weighted by the number of electrons for each electron energy, requiring more data analysis. Again, the proton energies taken into account here are not necessarily the highest, but always the ones corresponding to the proton beam emitted from the top of the FTC or from the tip of the funnel cone, which is the beam co-linear with the electron spectrometer.

Just as in Section 5.3.5, three trendlines of the type $T_{e^-} = \alpha E_{\max_p^+}$, $T_{e^-} = \alpha E_{\max_p^+} + \beta$, and $T_{e^-} = \alpha E_{\max_p^+}^\gamma$ are added to each set of electron temperatures. As we said earlier, physically, the hot-electron temperature and the maximum proton energy should be linked by a simple linear relation, i.e. $T_{e^-} = \alpha E_{\max_p^+}$, which requires that when $T_{e^-} = 0$, $E_{\max_p^+} = 0$. This relation is the one presented in [98]. However, the data shown in Figure 5-58 and Figure 5-59 indicates that there is a better correlation between proton energy and electron temperature if an equation of the type $T_{e^-} = \alpha E_{\max_p^+} + \beta$ is used. Again, this may well be due to the fact that for the TNSA protons to be accelerated, a certain sheath field has to exist, i.e. a certain sheath electron temperature and sheath electron density. If those conditions are not met, the acceleration cannot turn on, and this could well be due to the fact that the TNSA mechanism is not simply an ion blow off process. Similarly, an equation of the type $T_{e^-} = \alpha E_{\max_p^+}^\gamma$ also would indicate a certain threshold above which the TNSA ions can be accelerated, and below which they cannot. Note that, in the case of the cone targets, the average $(T_1+T_2)/2$ of these temperatures yields a much better correlation with proton energy than T_1 alone (using $T_{e^-} = \alpha E_{\max_p^+} + \beta$).

In the case of the cones (Figure 5-58), the correlations are stronger in the enhanced contrast case than in the intrinsic contrast case; this is probably caused by a cleaner laser-cone interaction due to a smaller amount of preplasma. Unlike the intrinsic contrast case, and for all trendlines, the correlation is better with T1 than with $(T_1+T_2)/2$. In general, hotter temperatures are obtained for the case where $TE \gtrsim CWE$ – which yields the highest proton energies (see Section 5.4.4.3), than for the case where $TE \gg CWE$ (see Figure 5-58); the latter case being similar to the case of RMTs and flat-foil targets, both electron-temperature-wise (see Figure 5-60) and proton-energy-wise (see Section 5.4.4.2).

The purple data point (shot 21171) in Figure 5-58 represents a shot that yielded a strong enhancement or “electron bunch” at ~ 4 MeV; most of the electron production is concentrated around that energy, and therefore, less electrons are present at higher energies, explaining why a low electron temperature is obtained. Since the behavior of that shot is different than that of the others, i.e. non-Maxwellian, it is removed from the data set, and is not included in the trendlines.

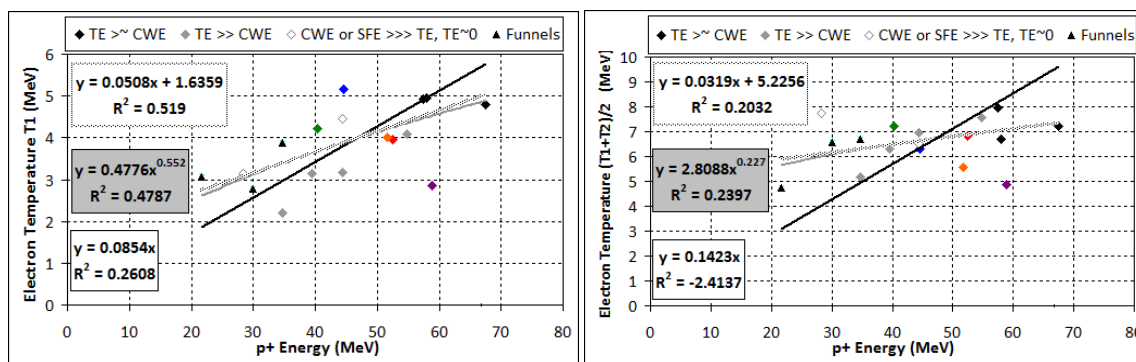


Figure 5-58: Funnel-cone targets, flat-top-cone targets, and reduced-mass targets: Electron temperatures at enhanced contrast as a function of the proton energy; (left) Lower electron temperature T₁; (right) Average of the lower and higher temperatures (T₁+T₂)/2; The trendline does not include the purple data point (shot 21171).

Unlike in the intrinsic contrast case, the flat foils at enhanced contrast (Figure 5-59) show a very good correlation between electron temperatures T1 (top) and $(T_1+T_2)/2$ (bottom) and

proton energy; again, this is probably due to a cleaner laser-cone interaction caused by a smaller amount of preplasma. Unlike in the intrinsic contrast case, the targets used here all have a similar thickness (except for the blue data points).

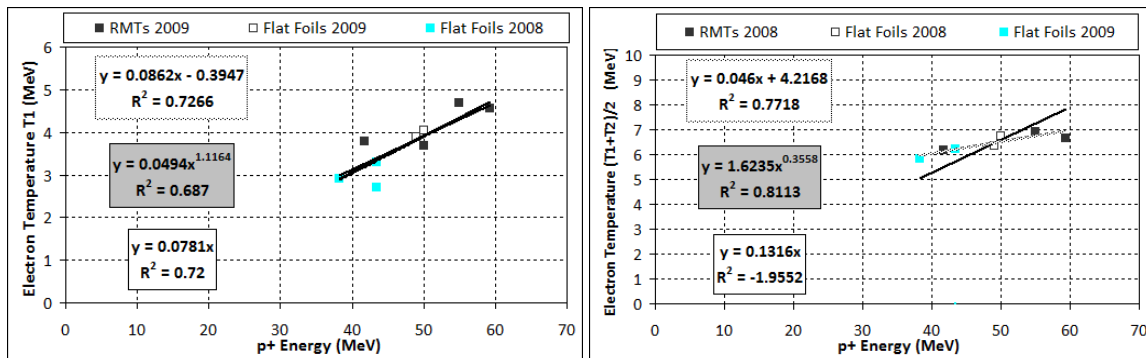


Figure 5-59: Flat-foil targets and reduced-mass targets: Electron temperatures at enhanced contrast as a function of the proton energy; (left) Lower electron temperature T_1 ; (right) Average of the lower and higher temperatures $(T_1+T_2)/2$. The 3 OPCPA shots obtained in 2008 at enhanced contrast are included. Only 2 shots out of 3 have a T_2 , due to bleeding in the last case.

Figure 5-60 shows the same data as Figure 5-59, but added to that data are the cases of the FTCs for which almost no CWE was seen, but a lot of TE ($TE \gg CWE$). These data points, i.e. $TE \gg CWE$, fit the trend of the flat-foil targets and reduced-mass targets well.

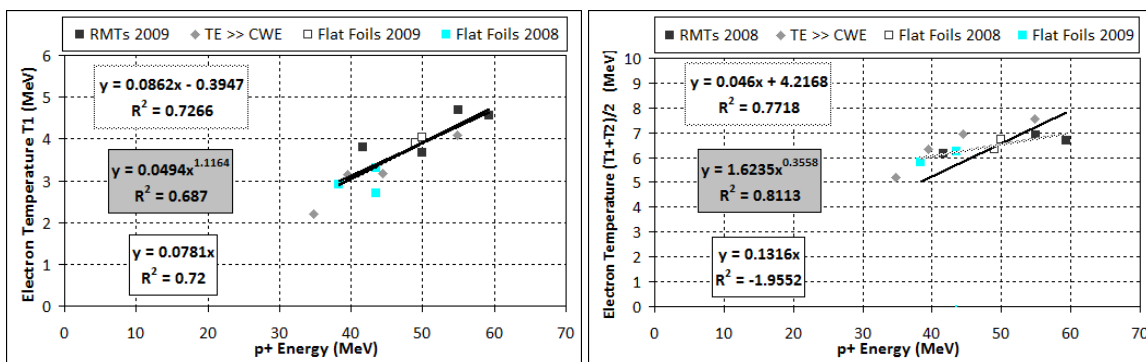


Figure 5-60: Reproduction of Figure 5-59; added to the data are the cases of the FTCs for which almost no CWE was seen, but a lot of TE ($TE \gg CWE$). This data seems to fit well with that of the flat-foil targets and reduced-mass targets.

6 DISCUSSIONS, SIMULATIONS & CONCLUSIONS

6.1 Overall comparison in terms of proton energy and electron temperature of all results: 20 J and 80 J, intrinsic and enhanced contrast, flat-foil, flat-top-cone, funnel-cone, and reduced-mass targets

This section compares the performance of all experimental runs (i.e. 20 J and 10^{-8} , 80 J and 10^{-8} , and 80 J and 10^{-10}) in terms of proton maximum energies and proton conversion efficiencies, and hot-electron temperatures.

6.1.1 Proton energies

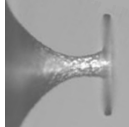

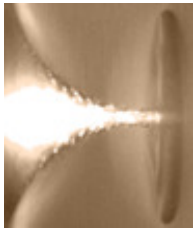
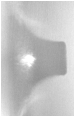
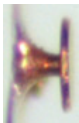
	20 J, 10 ⁸	80 J, 10 ⁸	50 J, 10 ¹⁰	80 J, 10 ¹⁰
Flat-foil target	19 MeV 19 J Compound angle	55 MeV 94 J 22.5 deg		48 MeV 78 J
RMT (Si-Cu or Cu-Si-Cu)		300 μm diameter 46 MeV 82 J		230 μm diameter 59 MeV 78 J
	> 30 MeV 19 J			
		27 μm neck OD 27 MeV 76 J <i>Nice round top beam</i>		24 μm neck OD 28 MeV 80 J <i>No significant top beam</i>
		39 μm neck OD 47 MeV 82 J		
		30 MeV 80 J	50 MeV 54 J	
		42 MeV 88 J		
				160 μm neck OD 67.5 MeV 79 J
				22 μm neck OD 66.7 MeV 81 J

Table 14: Summary for the best targets (~ 10 μm thick), represented to scale, of the maximum proton energies obtained for the 3 FTC campaigns on Trident: 2006, 2nd column; 2008, 3rd column; 2009, 4th and 5th columns.

6.1.2 Proton conversion efficiencies

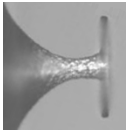

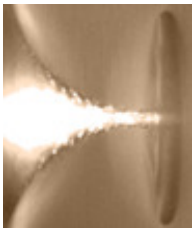
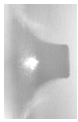

	20 J, 10 ⁸	80 J, 10 ⁸	50 J, 10 ¹⁰	80 J, 10 ¹⁰
Flat Foil	0.15 % (0.5 % scanner) 19 J Compound angle	1.5 % 94 J 22.5 deg		2.2 % 78 J
RMT (Si-Cu or Cu-Si-Cu)		300 μm diameter 2.1 % 82 J		230 μm diameter 2.5 % 78 J
	1.1 % (2.5 % scanner) 19 J			
		27 μm neck OD 0.79 % 76 J		24 μm neck OD ~ 0.1 % 80 J
		39 μm neck OD 0.58 % 82 J		
		1.62 % 80 J	1.56 % 54 J	
		1.8 % 88 J		
				160 μm neck OD 2.06 % 79 J
				22 μm neck OD 1.87 % 81 J

Table 15: Summary for the best targets (~ 10 μm thick), represented to scale, of the laser-to-proton conversion efficiencies for the best targets obtained for the 3 FTC campaigns on Trident: 2006, 2nd column; 2008, 3rd column; 2009, 4th and 5th columns.

6.1.3 Electron temperatures

As shown in Figure 6-1 and Figure 6-2, for flat-foil targets, RMTs, and cone targets, and for both electron temperatures T_1 (top) and $(T_1+T_2)/2$ (bottom), all the data and all the fits are shown again. The equations for the best fits (i.e. of the form $T_{e-} = \alpha E_{\max_p+} + \beta$) are given in Table 16 and Table 17. The intrinsic contrast case (left) always shows higher electron temperatures than the enhanced contrast case (right). This therefore means that the higher proton energies obtained at enhanced contrast did not require hotter electron temperatures. However, one needs to realize that the data reported here corresponds to the hot-electron population which escaped the target; the hot electrons that are responsible for the proton acceleration may have a similar behavior as those recorded, as these electrons were presumably born very early, and escaped the target before it had a chance to charge up and keep other electrons from leaving. Thus the two populations (escaped and confined to the target) should have similar temperatures, since they have been created in the same plasma. On the contrary, they may exhibit a completely different trend, as the confined electrons temperature may be modified by refluxing and thermalizing with the colder background electrons. With this in mind, although the temperature of the escaped hot electrons correlates well with proton energy, especially in the enhanced contrast case (because of less preplasma and a cleaner laser-target interaction), it cannot fully explain the proton energies in and of itself. There must be another variable, e.g. electron density, responsible for the enhanced proton energies. More work needs to be carried out, in order to establish whether that is the case.

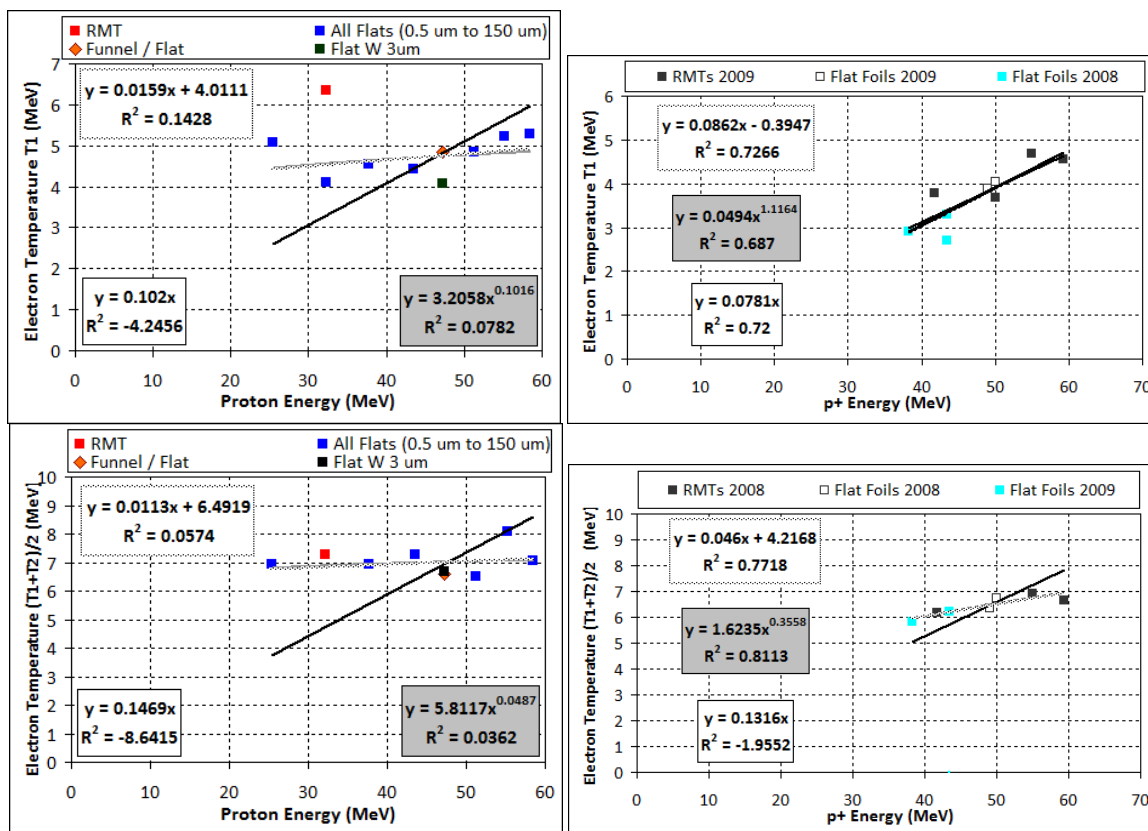


Figure 6-1: Flat-foil targets and RMTs: summary of the electron temperatures as a function of the proton energy, with trendlines for the intrinsic contrast case (left) and the enhanced contrast case (right); (top) Lower electron temperature T_1 ; (bottom) Average of the lower and higher temperatures $(T_1+T_2)/2$.

$T_{e-} = \alpha E_{\max_p+} + \beta$	T_1	$(T_1+T_1)/2$
Intrinsic Contrast FLATS	$T_1 = 0.0159 E_p + 4.011$ $E_p \sim 63 (T_1 - 4.011)$	$(T_1+T_2)/2 = 0.0113 E_p + 6.4919$ $E_p \sim 88 ((T_1+T_2)/2 - 6.4919)$
Enhanced Contrast FLATS & RMTS	$T_1 = 0.0862 E_p - 0.03947$ $E_p \sim 12 (T_1 + 0.03947)$	$(T_1+T_2)/2 = 0.0460 E_p + 4.2168$ $E_p \sim 22 ((T_1+T_2)/2 - 4.2168)$

Table 16: Flat-foil targets and RMTs, enhanced and intrinsic contrast; trendline equations giving $T_1 = f(E_p)$, $(T_1+T_2)/2 = f(E_p)$, $E_p = f(T_1)$, $E_p = f((T_1+T_2)/2)$.

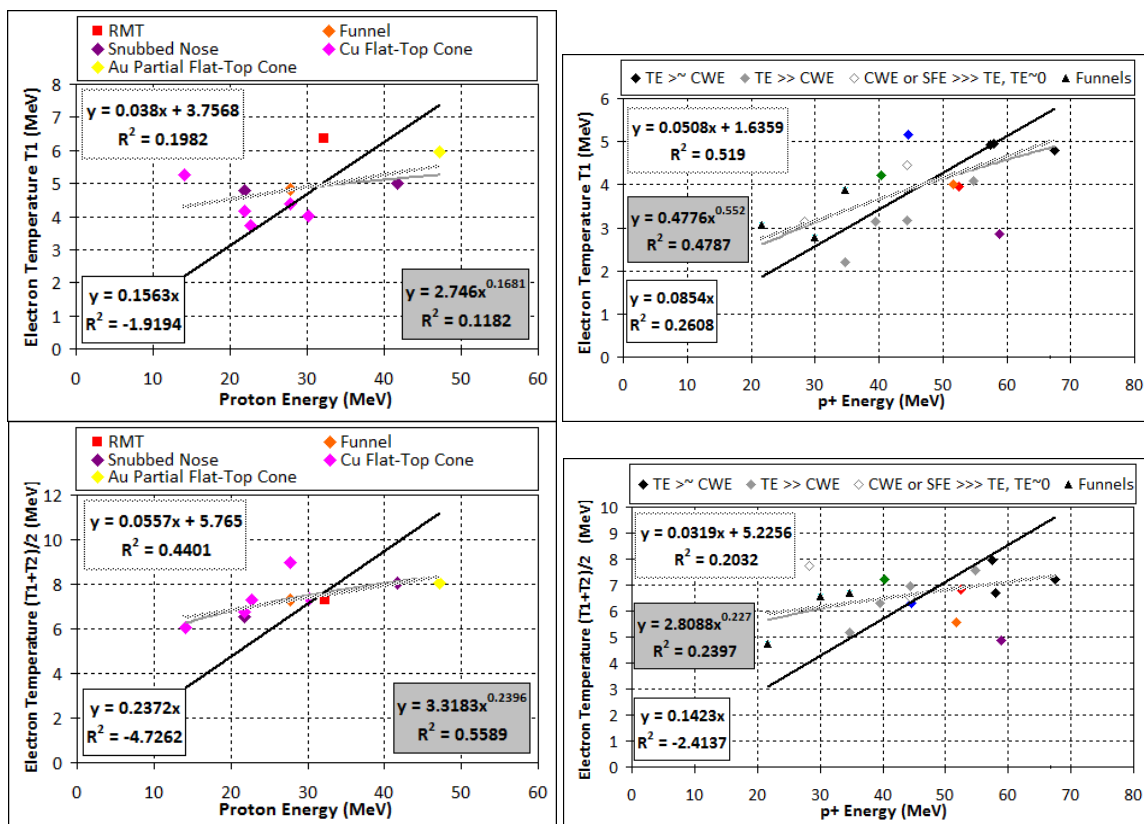


Figure 6-2: Cone targets (flat-top cones, funnel cones and snubbed-nose cones): summary of the electron temperatures as a function of the proton energy, with trendlines for the intrinsic contrast case (left) and the enhanced contrast case (right); (top) Lower electron temperature T_1 ; (bottom) Average of the lower and higher temperatures $(T_1+T_2)/2$.

$T_{e^-} = \alpha E_{\max_p^+} + \beta$	T_1	$(T_1+T_2)/2$
Intrinsic Contrast	$T_1 = 0.0278 E_p + 4.0892$	$(T_1+T_2)/2 = 0.0680 E_p + 5.3645$
VARIOUS CONES	$E_p \sim 36 (T_1 - 4.0892)$	$E_p \sim 15 ((T_1+T_2)/2 - 5.3645)$
Enhanced Contrast	$T_1 = 0.0508 E_p + 1.6359$	$(T_1+T_2)/2 = 0.0319 E_p + 5.2256$
VARIOUS CONES	$E_p \sim 20 (T_1 - 1.6359)$	$E_p \sim 31 ((T_1+T_2)/2 - 5.2256)$

Table 17: Various cones (i.e. Funnel cones, FTCs, Snubbed noses), enhanced and intrinsic contrast; trendline equations giving $T_1 = f(E_p)$, $(T_1+T_2)/2 = f(E_p)$, $E_p = f(T_1)$, $E_p = f((T_1+T_2)/2)$.

6.2 Discussions, simulations, and conclusions

6.2.1 Cu K α emission from the top region (TE) compared to emission from the cone region (CWE) and ratio TE / (SFE + CWE + TE): correlations with proton energy

6.2.1.1 80 J and 10⁻¹⁰ contrast

- 1) If there is a lot of top emission, and only a little bit of cone wall emission and/or supporting foil emission, the proton energies go up to ~ 55 MeV, close to the RMTs' best performer.
- 2) If there is as much (or slightly more) top emission than there is cone wall emission and/or supporting foil emission, the proton energies reach up to 67.5 MeV, which corresponds to the highest energy seen so far for laser-accelerated protons by any research institution in the world.
- 3) If there is much more cone wall emission and/or supporting foil emission than top emission, then the proton energies reach only ~ 45 MeV, just below the energy obtained for a flat foil.

6.2.1.2 80 J and 10⁻⁸ contrast

At intrinsic contrast, only the Case 3) described in Section 6.2.1.1 happens. It describes the case where there is a lot more cone wall emission and/or supporting foil emission than top emission, and where the proton energies only reach ~ 30 MeV, while a flat-foil target yields 55 MeV. This is attributed to preplasma filling the cone, hindering electron transport for strong TNSA sheath formation.

6.2.2 Effects of the FTC neck size as well as of the asymmetric laser-FTC interaction

6.2.2.1 20 J and 10^{-8} contrast

Although in [1] and in Section 5.2, we focused our attention on the best FTC performer which had a top diameter of $\sim 100 \mu\text{m}$, a neck OD of $\sim 25 \mu\text{m}$, and T/N ratio of ~ 4 , and which yielded more than 30 MeV (compared to 19 MeV obtained using a flat foil), Figure 6-3 shows that there are some good performers for large top and neck diameters: the second best performer with 24.2 MeV had a top diameter of $\sim 250 \mu\text{m}$ and a neck OD of $\sim 90 \mu\text{m}$. In hindsight, this indicates that regardless of the neck and top diameters, good proton energy performances can be expected, as long as the laser interacts in such a fashion so as to maximize the laser absorption and/or increase the effective laser intensity.

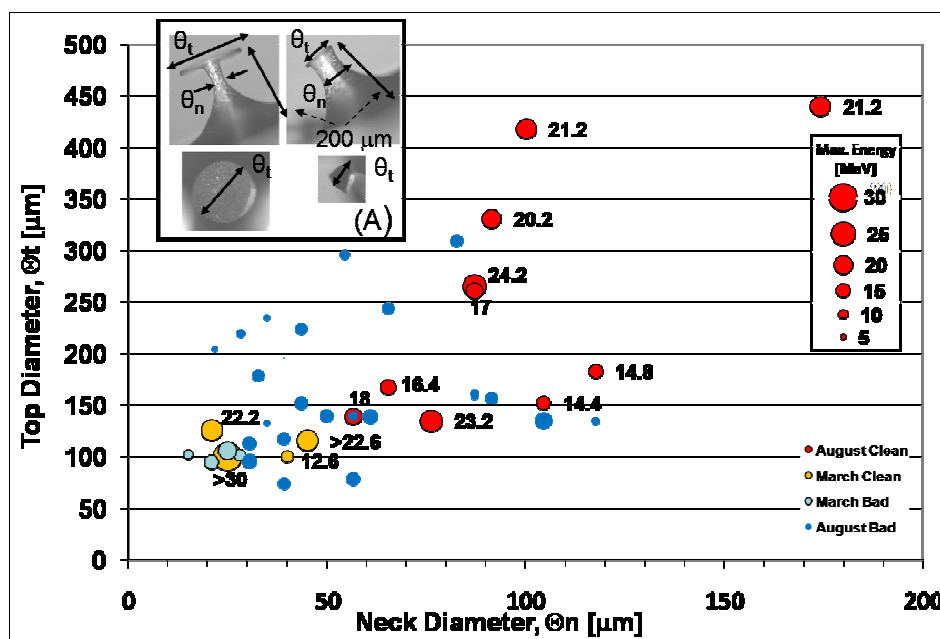


Figure 6-3: Reproduction of Figure 5-12: Proton energy performance as a function of both the top diameter and the neck outside diameter. The larger the circle is, the greater the proton energy. The yellow and the red circles represent aligned shots from the March and August 2006 campaigns respectively, and the light blue and dark blue circles represent the misaligned shots from the March and August campaign respectively. Inset (A): picture an FTC and a Football top (very close to a large diameter neck funnel cone).

6.2.2.2 80 J and 10^{-10} contrast

The best performers (see Figure 6-4 and Figure 6-5) are targets that have a neck size of $\sim 22 \mu\text{m}$ OD (shot 21170) and a neck size of $\sim 160 \mu\text{m}$ OD (shot 21180). They yielded very symmetric proton beams, even though the Cu $K\alpha$ image revealed a fairly asymmetric interaction with much more emission from one side of the wall than from the other. This tells us that the important factor is not the neck size, but rather how the laser interacted with respect to the cone walls and to the top.

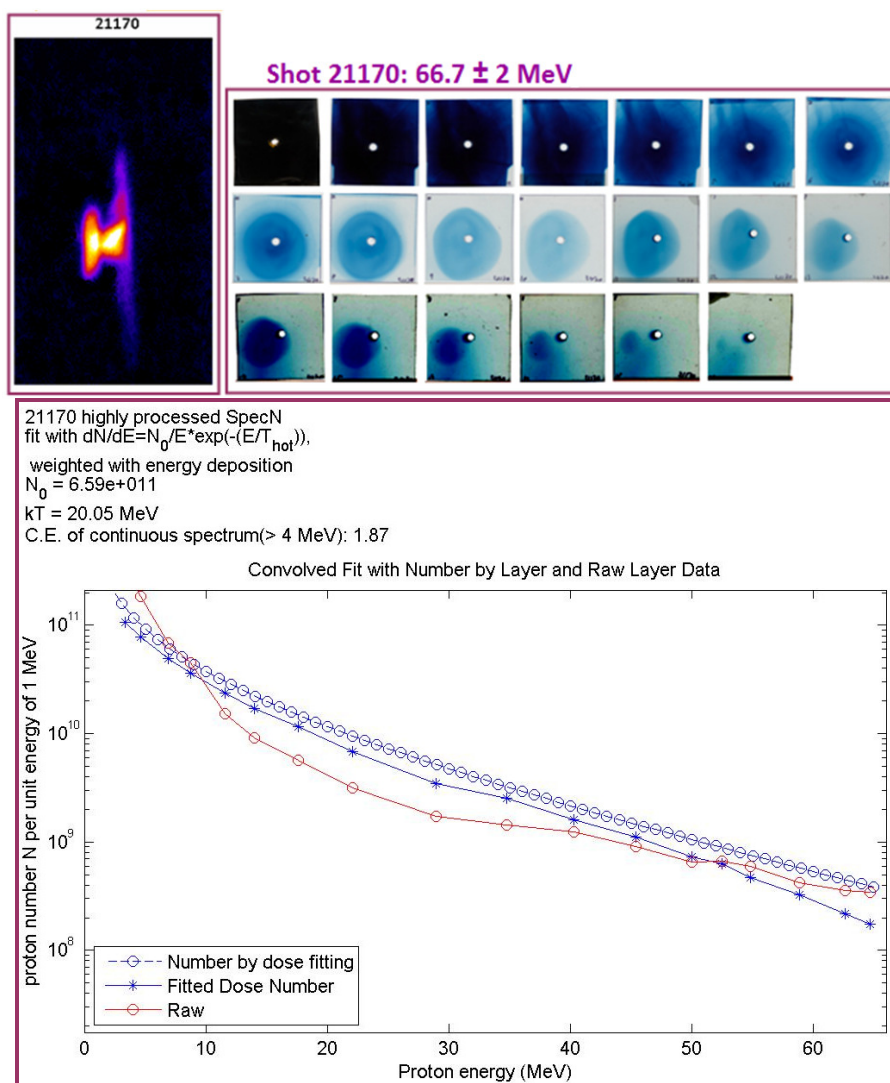


Figure 6-4: Shot 21170, Proton energy: 66.7 MeV, Conversion efficiency: 1.87 %; (top) Cu $K\alpha$ image and RCF stack (the last row of RCFs is contrast-enhanced to see the end of the beam more clearly); (bottom) Proton spectrum.

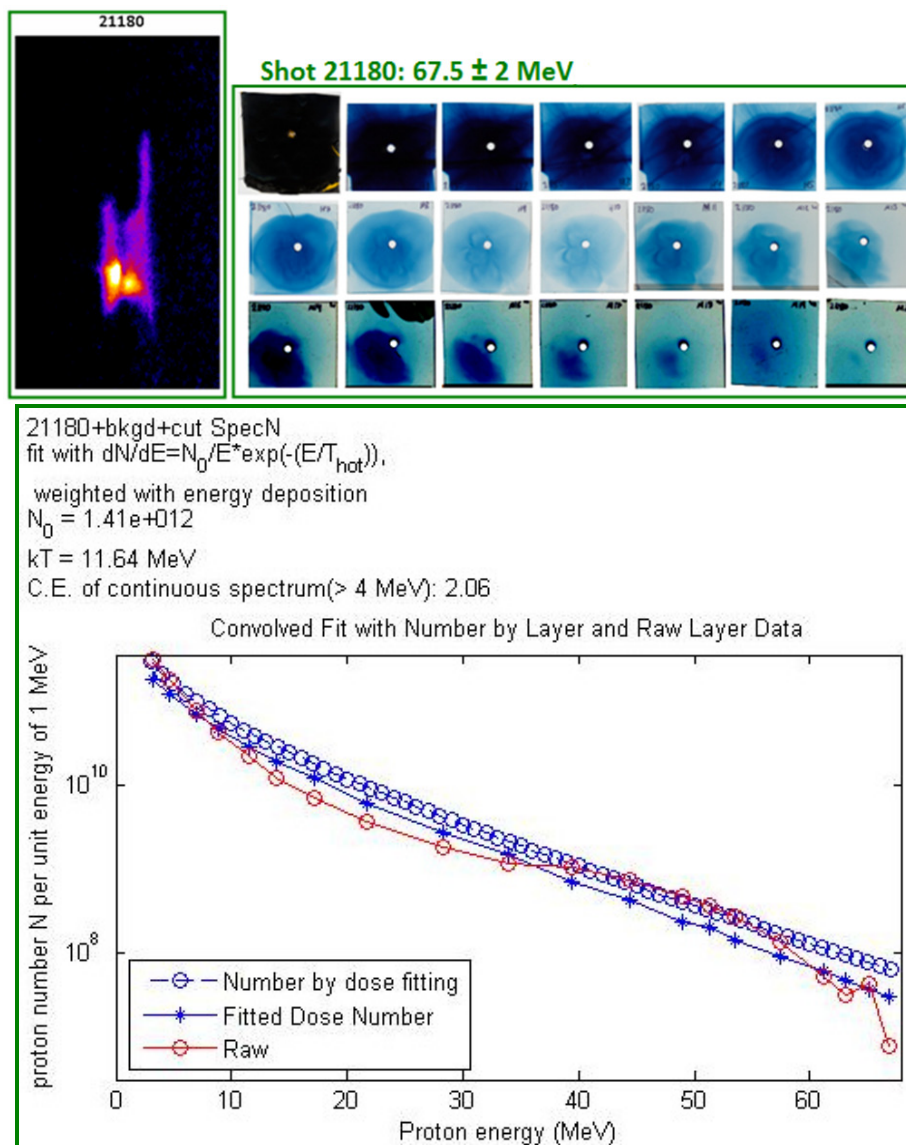


Figure 6-5: Shot 21180, Proton energy: 67.5 MeV, Conversion efficiency: 2.06 %; (top) Cu K α image and RCF stack (the last row of RCFs is contrast-enhanced to see the end of the beam more clearly); (bottom) Proton spectrum.

In the case of shot 21180 (see Figure 6-5), the fact that such a large neck worked so well was surprising to us. We had assumed that the thinner necks should help the laser light to be guided to the tip, because a conical target should concentrate light towards the top by reflections, as was described in [178]. In the case of a large neck, it is likely that the cone walls, or a cone wall, guides surface electrons towards the flat top. However, the large neck

size is not useful for laser guiding but does increase the interaction area and therefore the laser absorption, especially when the laser light comes in contact with the cone wall. This can happen either at an angle (see Section 6.2.3) or via an offset parallel to the horizontal axis (see Section 6.2.4.2). That portion of the cone wall may also act to shepherd the electrons to the sheath.

Finally, as shown in Figure 6-6, we can see that whether there is much more or slightly more emission from the top than from the cone wall, i.e. respectively $TE \gg CWE$ (see Section 5.4.4.2 and Figure 5-51) or $TE \gtrsim CWE$ (see Section 5.4.4.3 and Figure 5-52), an asymmetric interaction with more emission from one side of the cone than the other is always beneficial as far as maximum proton energy is concerned.

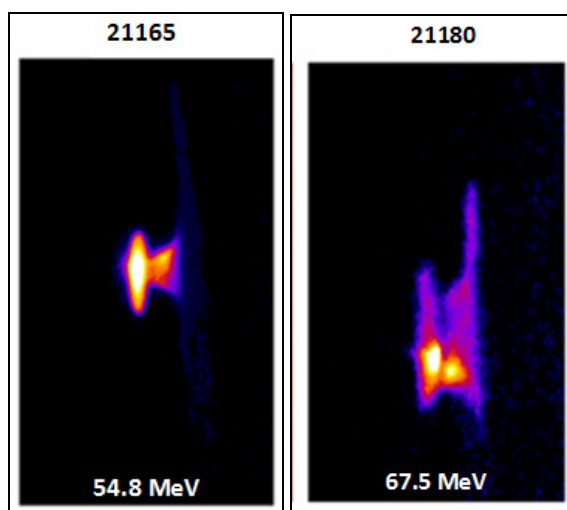


Figure 6-6: Asymmetric laser-FTC interaction for the case where (left) $TE \gg CWE$ and the case where (right) $TE \gtrsim CWE$.

6.2.3 *S*-polarization vs. *P*-polarization

Trident pre-enhancement, i.e. at 20 J, was *P*-polarized, which means that the electric field of the laser could interact most strongly with the viewed/opposing sides of the cone walls (see Figure 6-7) for a *k*-vector going down the throat horizontally. When the laser energy was upgraded to 80 J, the polarization changed to *S*, and the electric field could now most

strongly interact with the top/bottom sides of the cone walls (see Figure 6-7). The Cu $K\alpha$ imager sees the same view as that of Figure 6-7. This means that, in the *S*-polarized case, the 2-D Cu $K\alpha$ images are representative of the E-field interaction, and an asymmetric top/bottom interaction case can be diagnosed using the imager (as we have seen in Figure 5-52 for example, and especially in Figure 6-4 and Figure 6-5), while if the interaction was asymmetric on the viewed/opposing sides, the Cu $K\alpha$ emission would look much more symmetric and no conclusion could be drawn. However, purely from a polarization point of view, in the *S*-polarized case, the theoretical laser absorption should not increase when the interaction is with the viewed/opposing side of the cone walls, due to the fact that the E-field vector is not interacting with the surface much, since it stays mostly parallel to it. Therefore, one would not necessarily expect higher electron temperatures. For cases where the *k*-vector comes in at an angle, this could change, and only matters when the neck size is small enough (i.e. it would not make any difference in a wide-neck case). All these cases are currently under study in simulations.

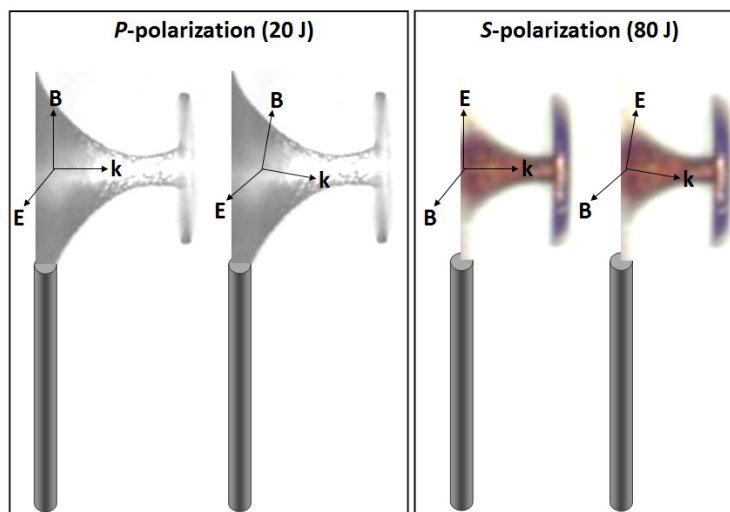


Figure 6-7: Comparison between the case of a *P*-polarized and an *S*-polarized laser, as it interacts with an FTC (mounted on a stalk) at normal and a slight angle (in the plane of the page) of incidence. In both cases, i.e. the *P*-polarization, 20 J case and in the *S*-polarization 80 J case, the *k* vector is always collinear to the plane of the ground. The picture on the left hand-side of each case corresponds to the nominal case where the stalk is perpendicular to the ground plane and to the *k* vector. The picture on the right-hand

side of each case represents, in the frame of the target, the case where the stalk and the target are tilted with respect to the ground plane and to the k vector, in such a way that the laser is at an angle with respect to the flat top of the target, creating a case that is similar to a combination of both a P -polarization and an S -polarization. This mixture of polarizations only matters for small inner-neck diameters, while it does not for the wide necks, because for wide necks, the E-field vector cannot reach the upper portion of the neck.

6.2.4 PICLS simulations

In the PICLS simulations, performed by Thomas Kluge, the target characteristics are the following: 10 μm thick, 30 μm neck (inner diameter), 180 μm top, and 80 μm radius curvature of the walls. This target is very close to the one used for shot 21171, and corresponds to a target half-way between the one used for shot 21180 (67.5 MeV) and the one used for shot 21170 (66.7 MeV). To be as close as possible to the experimental case, the simulations include ionizations and collisions (see [123] and Section 2.3.3.1.2). In the simulations described in Section 6.2.4.1 (6.2.4.2), the density is set to $370 n_c$ ($40 n_c$) for the target, with a resolution of the plasma skin depth of $10 n_c$ density. All other simulation conditions are as close as possible to the experimental conditions. Some preplasma is set along the cone walls (4 μm long with an exponential profile). The electron and proton spectra are smoothed using a Savitzky-Golay routine. For the electron spectra displayed in Figure 6-8 and Figure 6-13, the number of electrons per MeV (i.e. $\#e^-/\text{MeV}$ on the vertical axis) corresponds to a number of macroparticles per MeV, where each macroparticle contains 1911 electrons (in 3-D). The intensity is $2 \times 10^{20} \text{ W/cm}^2$. The focal spot is 7 μm FWHM. The pulse rises for 200 fs (with half of a Gaussian profile that has a FWHM/2 of 80 fs), then plateaus for 425 fs (flat top pulse), and finally drops for 200 fs, also with a half Gaussian profile. This helps having a reasonable time in the simulation with constant intensity. If the simulation were a 3-D simulation, then the total corresponding laser energy calculated from the spot size, the laser intensity and the pulse duration would be $\sim 67 \text{ J}$.

Each output time step corresponds to 106 fs. The time step t_6 corresponds to the time 492 fs after the laser plateau enters the simulation box and 140 fs after it hits the target, t_8 to 706 fs and 352 fs respectively, t_{11} to 1026 fs and 670 fs respectively, and t_{15} to 1452 fs and 1094 fs respectively.

6.2.4.1 Laser grazing in the throat

From the data at enhanced contrast shown in Figure 5-52 (i.e. best performing group, TE \sim CWE), and especially the 2 best performers (i.e. Figure 6-4 and Figure 6-5), it looks like, as long as the laser still makes it to the tip, a slight misalignment of the laser inside the cone does not seem to matter, and can even boost the interaction. We were able to verify this in PILCS simulations (see Figure 6-8). An asymmetric interaction allows more surface area to see the laser light and more light to be absorbed, producing more and hotter electrons. The hot electrons produced when the laser hits the cone at an angle while still reaching the top (obliquely incident laser, 22.5° , orange) have a characteristic spectrum with 3 temperatures, T_1 , T_2 , and T_3 . When the laser is perpendicular to the top (normally incident laser, blue), the hot electrons have a characteristic spectrum with 2 temperatures, T_1 and T_2 . 213 fs after the peak of the interaction, both proton spectra (blue and orange) are similar. The electron and proton densities after 320 fs have increased in the obliquely incident laser case. However, 640 fs after the peak of the interaction, the hot-electron population in the obliquely incident laser case have fallen while the 3 temperatures remain the same, but at the same time, the proton energy has increased over that of the normally incident laser case. These simulations were run for a laser incidence of 22.5° in order to test a case which maximizes the amount of laser grazing against the cone wall. More simulations are still currently running to determine which laser incidence angle maximizes the proton energy.

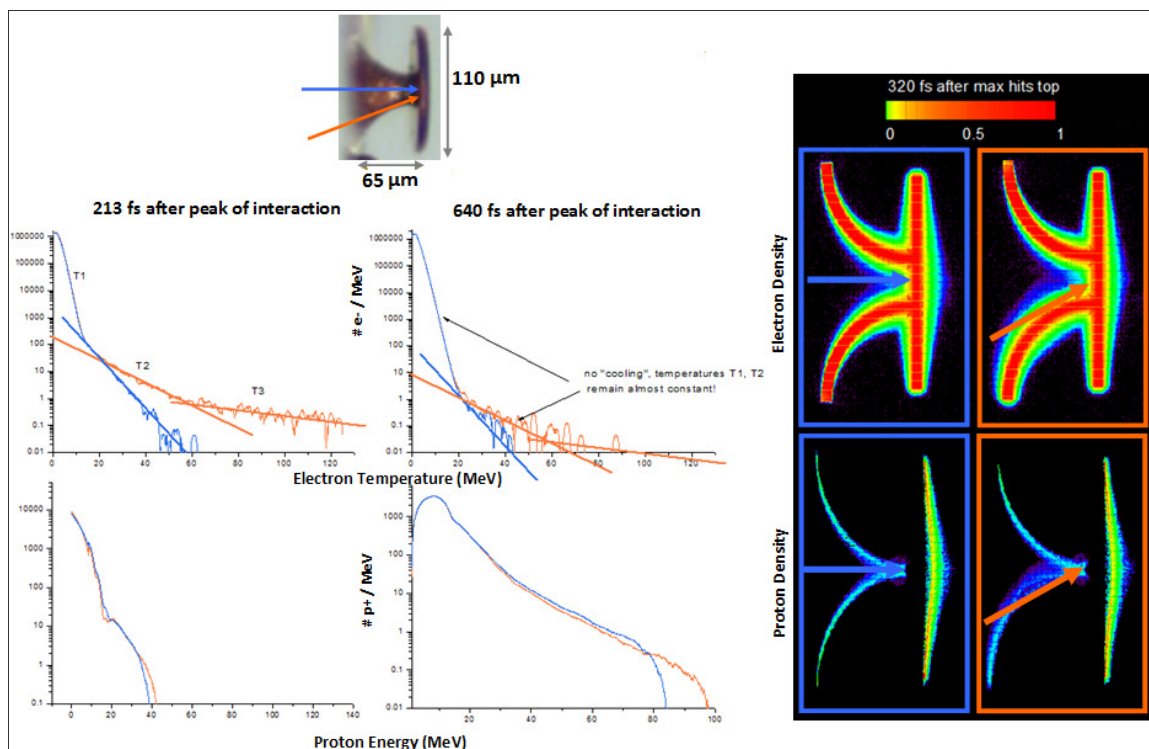
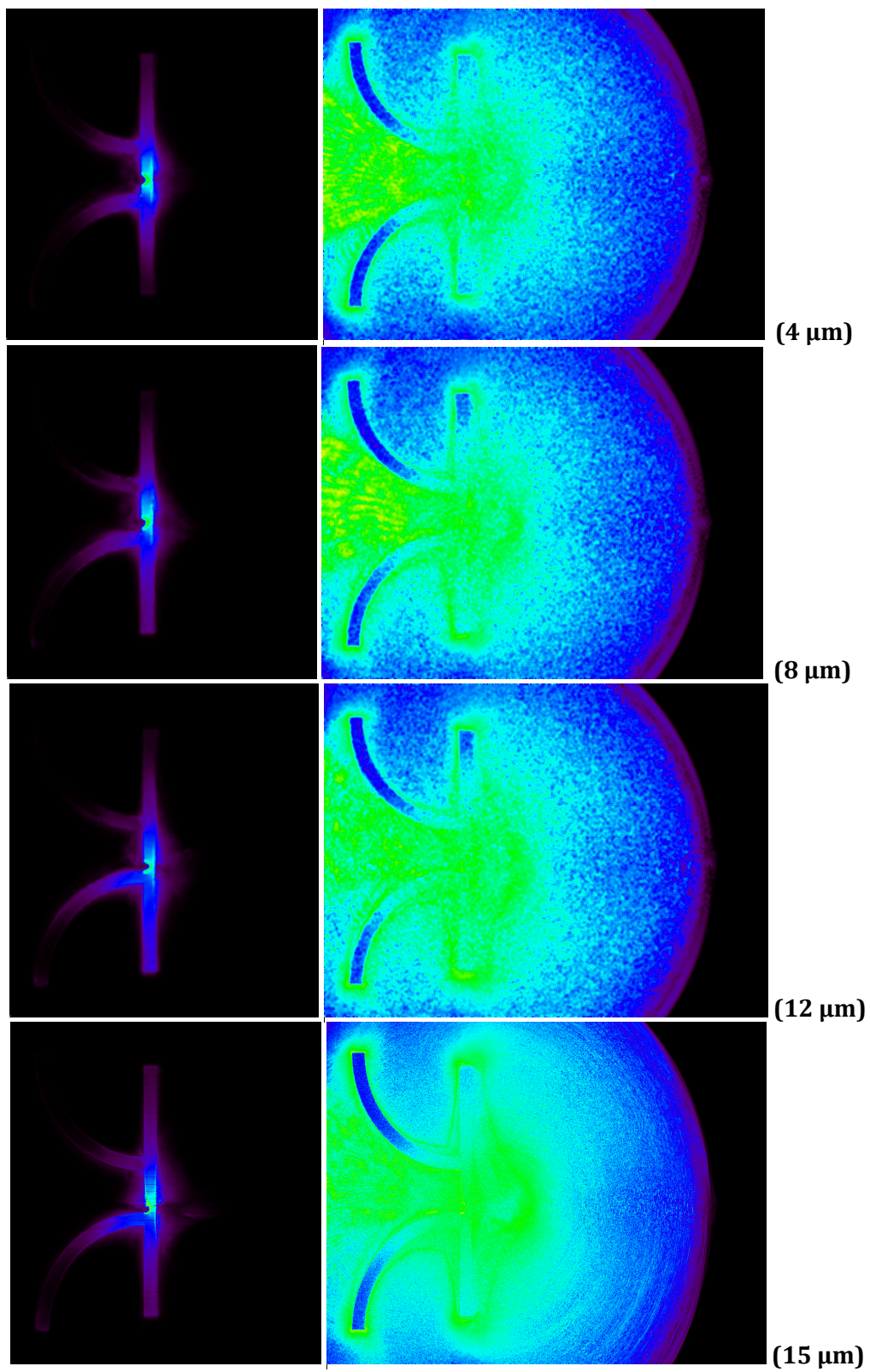
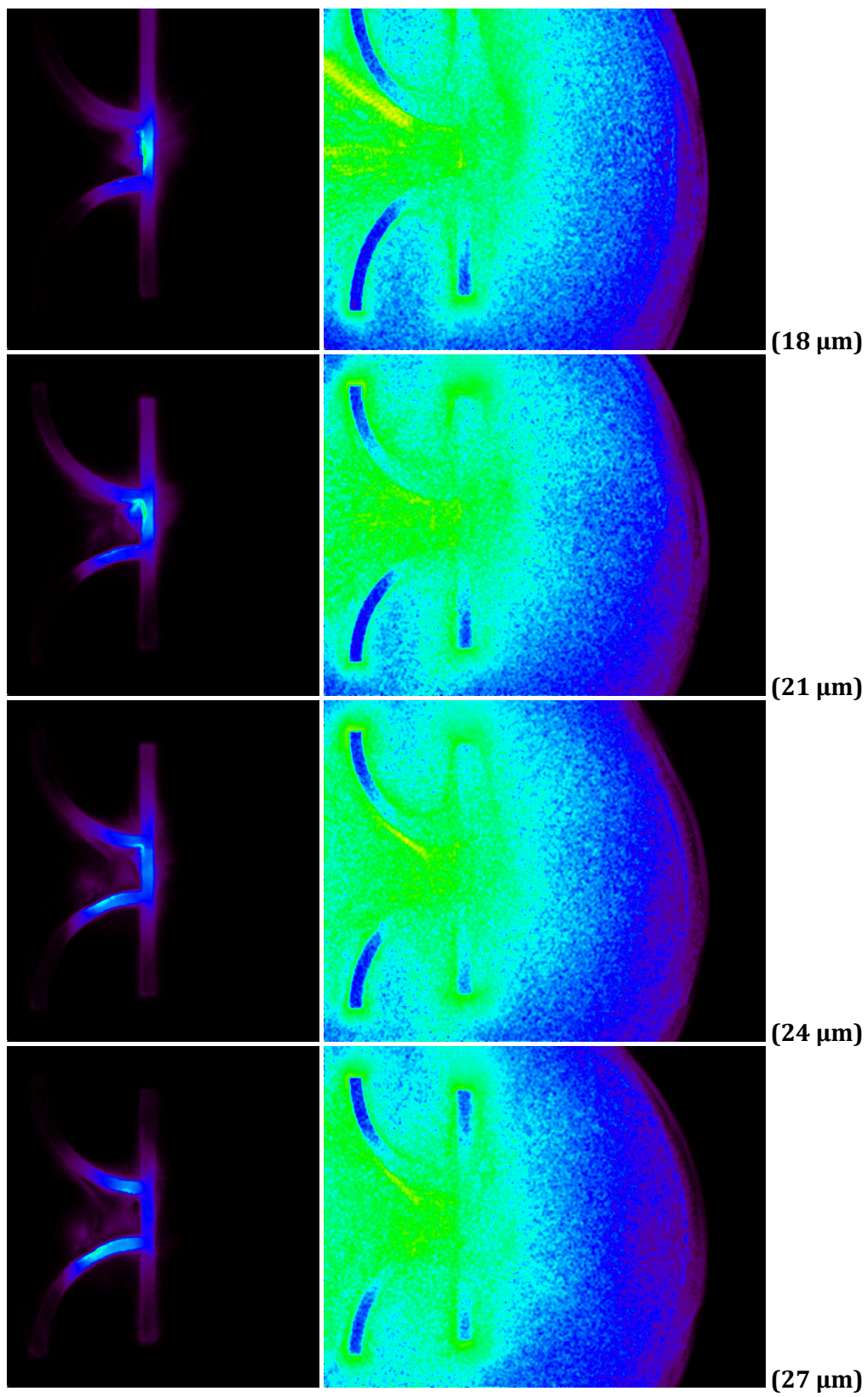


Figure 6-8: PICLS simulation: Comparison between the case where the laser is incident at an angle (orange) and horizontally (blue), but always makes it to the top. The electron and proton spectra obtained 213 and 640 fs after the peak of the interaction, and the electron and proton densities obtained 320 fs after the peak of the interaction are given.

6.2.4.2 PICLS simulations: detailed laser offset scan in the throat

Figure 6-9 shows a very detailed progression of the offset (which starts from the center and which is given in μm), for the time-step 11 (i.e. 670 fs after the laser hits the target), for the electron energy density (left) and the total electric field amplitude (right). At an offset of 15 μm, the laser grazes the cone wall horizontally and still hits the top. Past that value, the laser mostly interacts with the cone wall, unless some portion of light is reflected. For comparison, Figure 6-10 shows the electric field amplitude for a flat target.





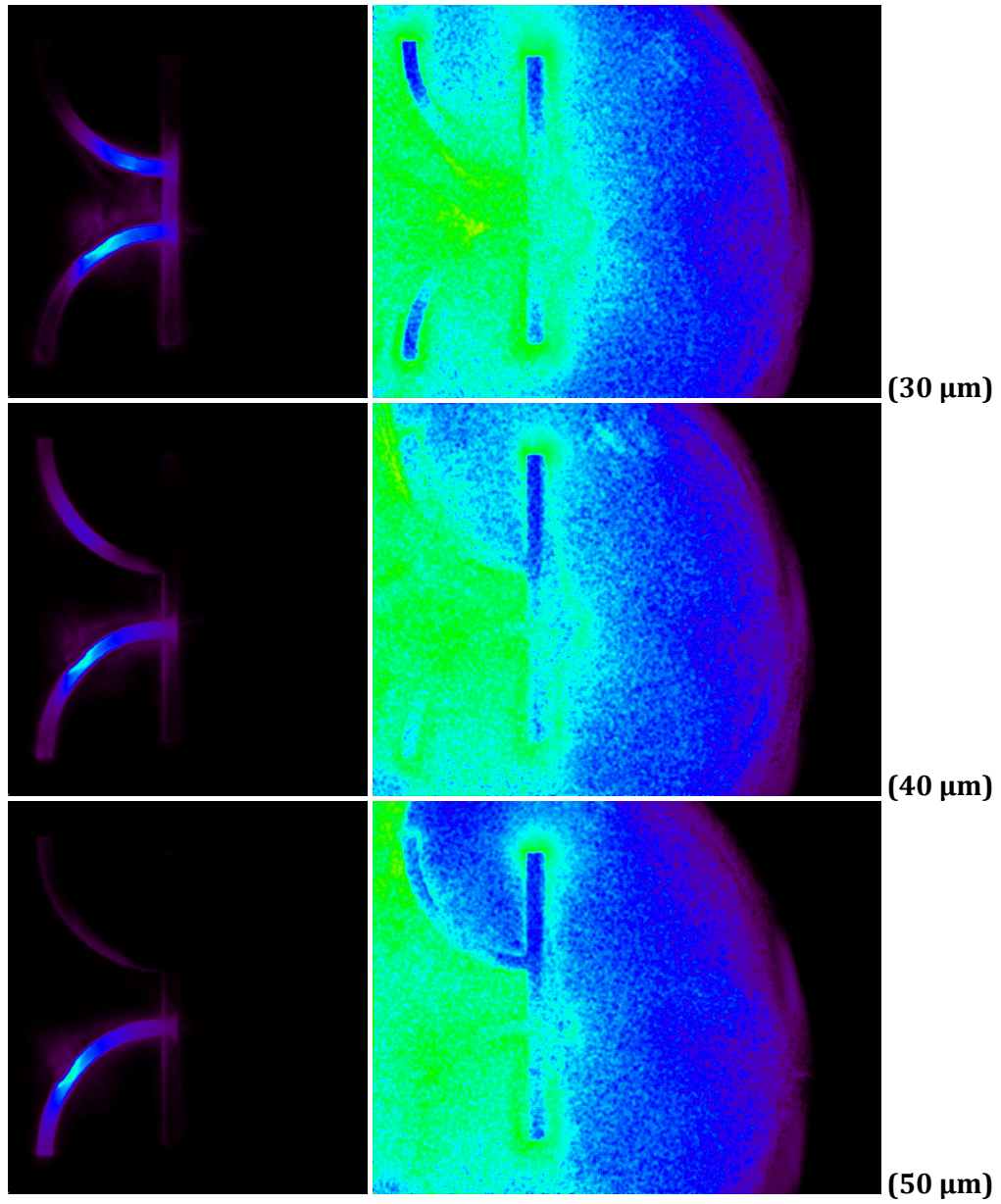


Figure 6-9: PICLS simulations of a cone target for different offsets for the time-step 11; (left) electron energy density; (right) electric field amplitude $(E_x^2 + E_y^2)^{1/2}$.

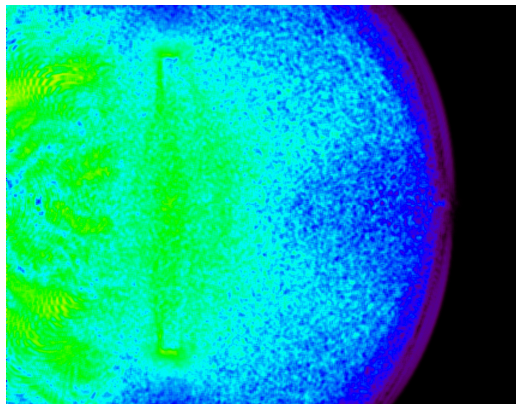


Figure 6-10: PICLS simulations of a flat target, i.e. of the flat-top of an FTC target, without the cone; electric field amplitude $(E_x^2 + E_y^2)^{1/2}$.

First, compared to the case of the flat top of the FTC only (RMT), the proton energy and carbon energy, as well as the total laser-to-proton and laser-to-electron conversion efficiencies, are always better from FTCs. Figure 6-11 (a) shows that the best proton energy is obtained with the offset of 15 μm , i.e. when the laser is tangential to the cone wall, but still hits the top. There is no offset which maximizes the heavier ions' energy (e.g. C^{6+}). When the offset varies from 0 to 12 μm , i.e. regardless of where the laser hits on the top, as long as it only hits the top, there is almost no difference in the proton energy. Figure 6-11 (b) shows that the best conversion of laser to protons is also obtained when the laser is tangential to the cone wall. As far as proton energy and laser-to-proton conversion efficiency are concerned (see Figure 6-11 (a) and (b)), a little less offset (12 μm , i.e. when the laser hits the top off-centered) performs the same way as a little more offset (18 μm , i.e. when the laser hits the beginning of the cone wall). As the offset increases, i.e. for an offset starting when the laser is on center and goes down towards the cone wall, both the proton energy and the laser-proton conversion efficiency increase. Figure 6-11 (b) shows that the best laser-electron conversion happens for a different offset than for protons, i.e. 24 μm , which corresponds to the case where the laser is reflected onto the opposing neck corner. This means that there is no correlation between the maximum electron energy and

maximum proton energy, as when the electrons peak, many of those electrons are not produced near the flat-top, and do not participate in the creation of the sheath (see offset 24 μm in Figure 6-9).

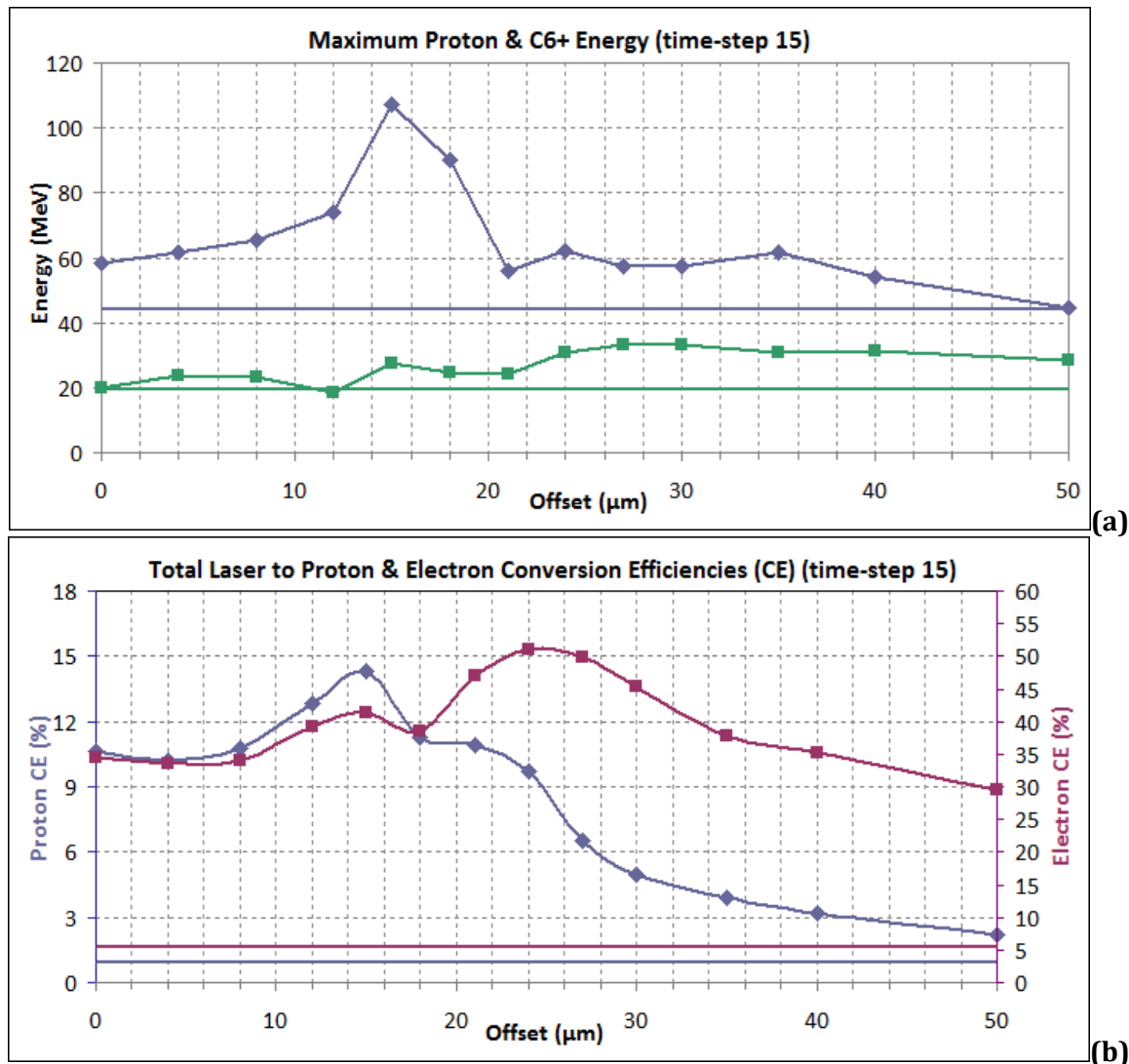


Figure 6-11: As a function of laser offset in the throat [μm] ~ 1.1 ps after the laser hits the targets, (a) Maximum proton (blue) and C6+ energy (green); (b) Laser-Proton (blue, left vertical axis) and Laser-Electron (purple, right vertical axis) conversion efficiencies; for (a) and (b), the horizontal lines represent the RMT comparison, i.e. the flat-top of the FTC without the cone.

Figure 6-12 shows the electron energy density (Gmns), the electric field in the vertical direction (E_y), the magnetic field perpendicular to simulation plane (B_z) and the electric

field amplitude (E , where $E=(E_x^2+ E_y^2)^{1/2}$) as a function of the offset in the throat [μm]. G_{mns} , B_z , E_y and E are normalized and compared to the normalized laser potential a_L . Figure 6-12 (a) and (b) both show, at two different time-steps, that G_{mns} , B_z , E_y and E are maximum for the offset of 15 μm , i.e. when the laser is tangential to the cone wall but still reaches the top.

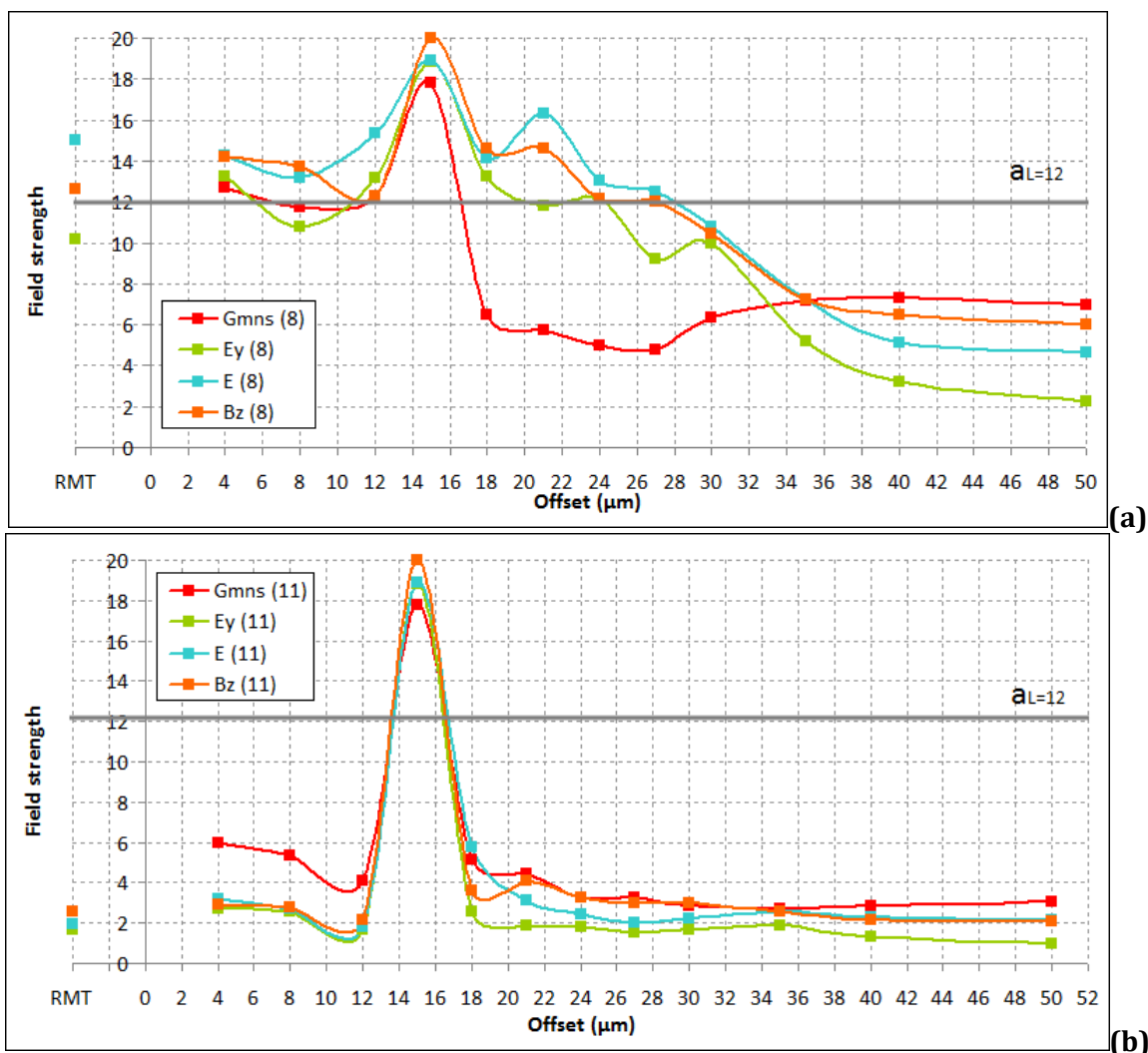


Figure 6-12: Field strengths as a function of offset in the throat [μm]: G_{mns} (red) is the electron energy density, E_y (light green) is the electric field in the vertical direction, E (turquoise) is the electric field amplitude $(E_x^2+ E_y^2)^{1/2}$ and B_z (orange) is the magnetic field perpendicular to the simulation plane; G_{mns} , E_y , E and B_z are normalized and compared to the normalized laser potential a_L (grey horizontal line); (a) at time-step 8 and (b) at time step 11; the data given to the left of the vertical axis (corresponds to the flat-top case, without cone (i.e. RMT)).

Figure 6-13 shows electron spectra at different time-steps, comparing the RMT (diamonds, left) with the best performing FTC target case in terms of proton energy and conversion efficiency, i.e. with 15 μm laser offset (squares, right). It demonstrates that the electron number, maximum energy and temperature are higher in the offset FTC case, for which the proton energy and conversion efficiency are higher, than in the RMT case.

Note that the pulse plateau ends at time-step 9 and is down to $\sim 5\%$ of the intensity (e^{-3}) at time-step 11. One can see from both these graphs that the electron number initially increases (from t8-t9) then holds steady (from t9-t10), and finally falls below the initial (t8) number (from t10-t11). Although, note that in the case of the RMT at lower electron energies (up to ~ 15 MeV) the number at t11 is still higher than the initial (t8) number, while past 15 MeV it is lower.

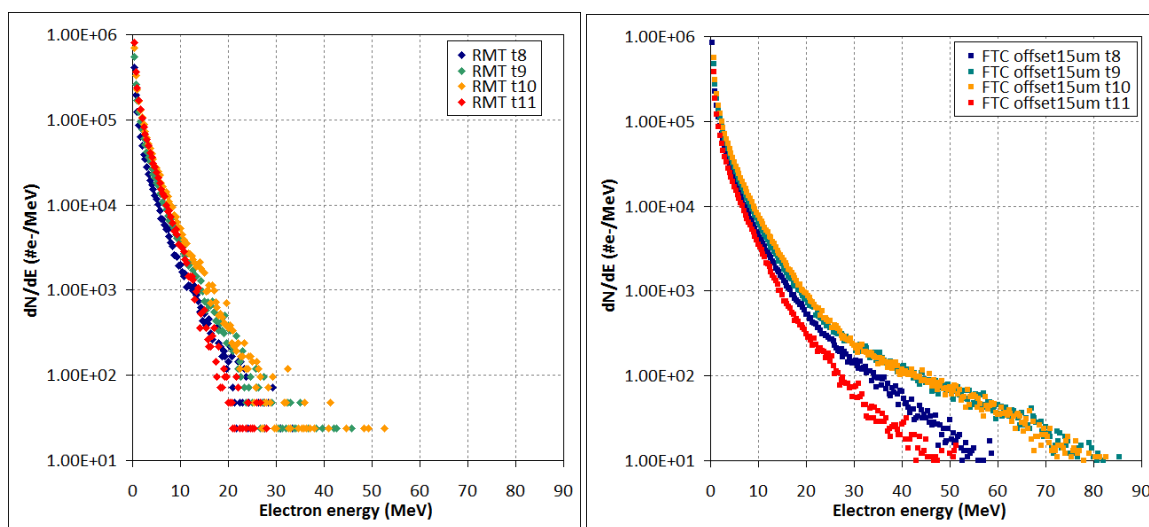


Figure 6-13: Electron spectra (left) of the RMT (diamonds), and (right) of the FTC target with 15 μm offset (squares), for different time-steps: time-step 8, dark blue; time-step 9, green; time-step 10, orange; time-step 11, red.

Figure 6-14 shows that the electron number, maximum energy and temperature are higher in the offset FTC case (red), for which the proton energy and conversion efficiency are higher, than in the FTC case with no offset (green), the latter behaving identically (in terms

of density and temperature) to the RMT case (black). In the case of the 1 μm FTC neck (blue), the temperature is similar to the 30 μm offset FTC case, but the total electron number is doubled, and especially increased in the electron energy range [~ 20 MeV; ~ 40 MeV], due to the fact that in the 1 μm neck case, the laser can now interact with both cone walls. This increased number of hot electrons in the 1 μm FTC neck case explains the increase in laser-to-proton conversion efficiency reported in Table 18.

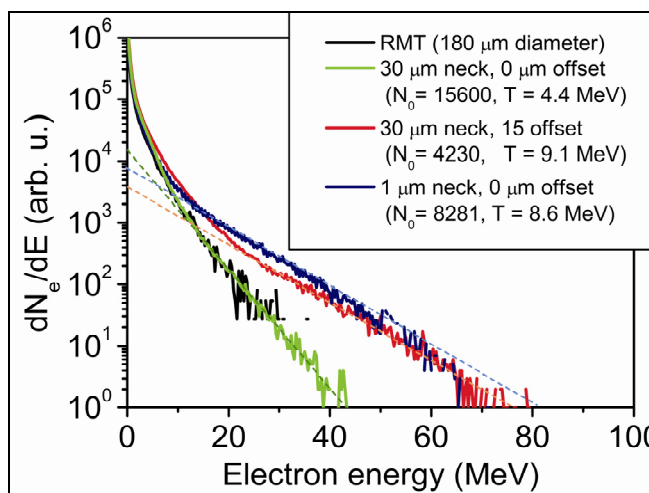


Figure 6-14: Electron spectra at t8 of the RMT (black), the 30 μm neck FTC target without offset (green) and with 15 μm offset (red), and the 1 μm FTC (without offset, blue).

Simulations of the magnetic field perpendicular to simulation plane (B_z) the electric field amplitude (E), and the electron current show (see Figure 6-15) that the laser grazing along the cone wall (due to the horizontal 15 μm offset) causes an electron current in the cone wall, implying more laser light absorption; as well, it causes some shallow laser light reflections off the cone wall, toward the flat-top, which enhances the laser intensity along the cone wall and at the flat-top of the FTC as seen in the E and B_z plots (shown in red). Figure 6-15 (bottom) shows the presence of a very sharp gradient (log scale) in the electron current and no evidence of surface current. Indeed, the surface guiding of electrons would be indicated at the cone wall inner surface by an inversion in the magnetic field amplitude,

but this is not seen in Figure 6-15 (top). But what is seen is a large gradient in the magnetic field (blue to white) across the cone wall, corresponding to the edge of the current, as seen in Figure 6-15 (bottom). An offset laser pulse allows for more target area interaction, as well as for more absorption, with hot electrons streaming through the cone wall toward the flat-top.

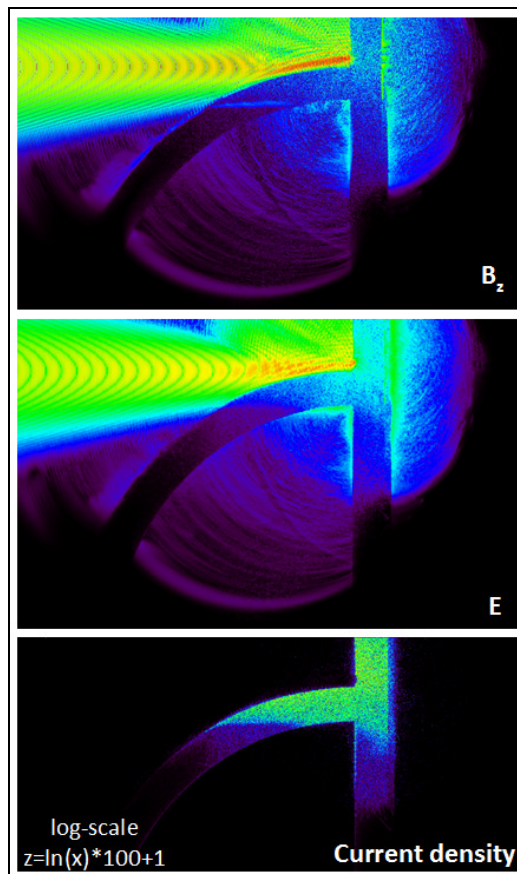


Figure 6-15: PICLS simulation, 140 fs after the laser hits the flat top (t6) for the 15 μm offset case (the laser is grazing the cone wall horizontally), showing (top) B_z , (middle) E and (bottom) current density (color scale is in log-scale).

Preliminary results from simulations with a 1 μm and a 0 μm inner neck diameter are summarized in Table 18. They show that for a laser coming in with no offset and at normal incidence to the top, the total proton energy and conversion efficiency obtained with a very narrow neck cone are larger than that obtained with a wider neck cone, i.e. 30 μm inner

diameter with a grazing offset (15 μm), although the maximum proton energy does not really improve. The proton energy improves significantly when, for a same size neck, the laser grazes along a cone wall (see Table 18 and Figure 6-11 (a)). The 1 μm neck is similar to an ideal case where the laser can skim both sides of the cone walls, and indeed shows that laser interaction and electron acceleration over a larger area or distance is beneficial for electron production and thus proton acceleration. In summary, although only the laser-to-proton conversion efficiency is increased when the laser interacts with the two sides of the cone walls, the maximum proton energy is the same whether the laser interacts with one or two cone walls.

	Total energy for all protons (arbitrary units, 2-D)	Laser-to-proton conversion efficiency (%)	Maximum proton energy (MeV)
1 μm neck case, no offset (laser centered)	0.43	17 %	111
30 μm neck, 15 μm offset (laser grazing the cone wall)	0.36	14 %	107
30 μm neck, no offset (laser centered)	0.27	11 %	58
RMT (laser centered)	0.20	8 %	44

Table 18: Summary of the total proton energy, conversion efficiency and maximum proton energy from PICLS simulations for the 1 μm neck FTC (no offset), for the 30 μm neck FTC with 15 μm offset and no offset, and for the RMT.

6.2.5 Validated and unverified hypotheses

After the first set of experiments in 2006 (see Section 5.2), and based on the understanding and simulations available at the time, the most likely hypothesis was that laser guiding, and/or a small-scale preformed plasma confined within the cone neck caused an enhancement in the laser absorption and an increase in the hot-electron temperature. The

more extensive list is given at the end of Section 5.2.4 (after Figure 5-16). After two more experimental runs (see Sections 5.3 and 5.4), some of the prior hypotheses used to explain the enhanced proton acceleration exhibited with FTC targets compared to flat-foil targets have been disproven, are unlikely or unconfirmed, and some are still plausible and believed to be true. New ones have also been identified (underlined). We present here an updated list of the various possible hypotheses (note that there still may be others), along with a ✓ mark if that hypothesis is still plausible, and a ✖ mark if it is unlikely or unconfirmed:

- **Increased laser absorption in the cone ✓**; this is a very general idea, which assumes that the better and the more efficient the laser light absorption in the target, the better the hot-electron production and the better the proton acceleration. However, we have no easy way of measuring the total laser absorption quantitatively in the cone. Cu K α emission tells us where the hot electrons are emitted from, but not necessarily how much absorption there is. In general increased absorption should lead to more and hotter electrons, which are the subject of more specific hypotheses below.
- **Better coupling efficiency to the responsible electron population ✓**; this the second very general idea: there is a particular population of hot electrons (i.e. with a certain temperature, between a certain energy range) that is mostly responsible for an efficient acceleration of protons. However, this responsible hot-electron population still remains to be observed experimentally. But making more of these electrons at the right place in the target would increase the accelerating field, making more energetic protons. More detailed and specific ways this may occur are also discussed below.

- **Enhanced hot-electron confinement on the flat-top region due to edge fields ✖**; if fields from the flat top itself helped confine electrons (i.e. keep the density high) then protons could gain more energy; though, if this were true, the size of the top and the size of the neck would matter, but at this point, the data does not show this (see Section 6.2.2).

- **Hotter electron temperature at the top of the FTC ✓**:

In light of the electron data, hotter electrons do not necessarily imply more energetic protons (see Section 6.1.3), as previously inferred (e.g. [95]); however, it is important that they reach the sheath efficiently. It seems that the experimental electron diagnostic (i.e. the electron spectrometer) is not a good enough diagnostic (i.e. it only samples a small portion of the electron beam, and it only measures the escaped electrons, which may or may not be representative of the hot electrons in the sheath), and more work needs to be done to implement a better one. The most responsible electron population for TNSA still remains to be determined. Simulations so far have shown that compared to flat foils, traditional cones or FTCs always yield higher electron temperatures, whether the laser is aligned or misaligned (see Figure 2-13 (right) and Figure 5-14 respectively). However, when the laser is grazing along the cone wall, the electron temperature is even higher (Figure 6-8 and Figure 6-13), and they are born near the flat-top. These hotter electrons can be:

- o **due to optical guiding via the cone geometry ✖**; if this were true, the thinner necks should have performed the best, and they did not (see Section 5.4.4.4); PICLS simulations also show that a thinner neck is not particularly beneficial (see Table 18).

- **due to a partial plasma prefill in the cone (i.e. better underdense coupling) ✖**; two levels of preplasma were used: at intrinsic contrast, the laser was absorbed too far away from the top, and the proton energies were reduced (as compared to a flat foil), even in the snubbed nose cases, which are shorter (i.e. $\sim 60 \mu\text{m}$) than the FTCs and for which the preplasma still seems too high for good absorption at the top; at enhanced contrast, where a small amount of preplasma was present, the best results were obtained; this shows that a plasma prefill of the cone is not beneficial for proton acceleration, likely due to the fact that preplasma moves the electron creation point away from the proton acceleration point (i.e. the sheath).
- **due to the enhanced intensity on the flat top due to some laser reflection (laser grazing) ✓**; this is a new hypothesis, and has been found in simulations (see Figure 6-15 (top) and (middle)), which have been carried out to understand why the best FTC performers for proton energy were the ones whose Cu $K\alpha$ emission was asymmetric; the laser can be grazing alongside a cone wall either horizontally or at an angle, and when this is true, it leads to more light absorption as well as an enhanced intensity on the flat top due to shallow reflections from the cone wall toward the flat top.
- **due to a direct acceleration of surface confined electrons by the laser light pressure ✓**; this is also a completely new hypothesis, and was discovered from simulations (just as this dissertation was being submitted). Higher-energy electrons are generated via this mechanism when the laser is grazing along a cone wall and the cone neck size is large compared to the

laser spot size (i.e. 30 μm), and also when the laser is centered and the cone neck is small (i.e. 1 μm) compared to the focal spot.

- **Higher electron sheath density at the top of the FTC ✓:**

An increase in the electron density of the particular responsible population is perhaps a more valid hypothesis to be looked at than simply the increase in electron temperature alone, or a combination of both. The higher sheath density can be:

- **due to surface electron guiding via the cone geometry ✓**; Figure 6-15 (top) does not show an enhanced current at the surface or an inversion of the magnetic field at the inner cone wall surface, which are characteristic of surface electron guiding. This is because one would need to look at the time-averaged fields (rather than at a snapshot in time), which are not readily available at this time, especially in the 1 μm neck FTC case. However, we believe that electron guiding is still a valid hypothesis.
- **due to concentration of more electrons in the flat-top region ✗**; this is not verified experimentally when the laser is aligned and centered down the cone neck, whether the neck be small or large (see Figure 5-51, TE \gg CWE, shots 22164 and 21187), nor is it verified in simulations; the laser-to-hot-electron conversion efficiency is the lowest when the offset is minimum, corresponding to a laser aligned and centered in the neck (see Figure 6-11 (b)).
- **due to concentration of more electrons near the flat-top region due to grazing ✓**; unlike the case where the laser is perfectly aligned, when the laser is grazing the cone wall, more electrons are concentrated at the top based on higher electric field seen in Figure 6-9. Experimentally, in the best

performers group, i.e. $TE \sim CWE$ (see Figure 5-52), the best proton energies are obtained when the interaction is asymmetric (see for example Figure 6-4 and Figure 6-5); in the group where $TE \gg CWE$ (see Figure 5-51), the best performer is again a case where the interaction is asymmetric (see Figure 6-6). Simulations show (see Figure 6-11 (b)) that the best laser-to-hot-electron conversion efficiency is not correlated with the best proton energy; however, when the proton energy is maximum (i.e. grazing along the cone wall), the laser-to-hot-electron conversion efficiency, although not maximized, is still higher than when the laser is centered in the neck, but more importantly localized near one point at the flat top.

- **due to guiding of laser light from the cone ✓**; this is an effect of the entire cone guiding light to the cone apex, not to be confused with the new hypothesis described in the next bullet. Unlike in Figure 2-13 (left) where an increase in laser intensity by a factor of 10 had been observed at the cone apex due to laser light guiding caused by the traditional cone geometry, the laser intensity increase in the recent PICLS simulations (described in Section 6.2.4) only see an increase in ~ 1.2 , whether the cone has a wide neck (i.e. $30 \mu\text{m}$) compared to the laser spot size and the light is grazing along the cone wall, or whether the cone has a very small neck (i.e. $1 \mu\text{m}$), much smaller than the spot size.
- **due to optical collection of laser light from the cone wall grazing ✓**; an increase in laser light intensity of about a factor of 1.2 is observed when the laser grazes against the cone wall (see Figure 6-15 (top) and (middle)) due to shallow reflections off the cone wall adding constructively at the flat-top

off of the cone axis. This happens for an asymmetric interaction, and does not correspond to the traditional guiding or focusing of the cone geometry at the cone apex, as described in the bullet above.

In conclusion, based on our present understanding and simulations, the most likely hypotheses for the measured enhancement in proton energies are the enhanced laser absorption; the increased laser intensity at the flat top due to the increased laser-wall interaction area and oblique reflections, i.e. the laser grazes along a larger cone wall surface area, either horizontally or at an angle, and reflects at a shallow angle, adding constructively at the flat top; as well as the generation of high-energy electrons due to a direct acceleration of surface confined electrons by the laser light pressure [5].

7 FUTURE WORK

This section describes shortly the future work needed to further our understanding of the laser-FTC target interaction. Some of the data from the 2008 campaign concerning the monoenergetic features found in the beam of a flat-top cone target, a funnel-cone target and a snubbed nose target require further analysis, and especially some modeling. As far as future experiments are concerned, the following sections give a list of improvements and variables with respect to the laser, the diagnostics, and the targets.

7.1 Laser

- For a simple flat foil, at enhanced contrast, vary the laser incidence angle between 0° (i.e. normal incidence) and 90° , to understand laser absorption, and verify the hypothesis that grazing the wall enhances the proton acceleration in the S-polarization.
- Vary the contrast for a given FTC, and find the best contrast for the best maximum proton energy performance. This could help proving that:
 - o A yet to be determined optimal pre-formed plasma (obtained using a to-be-determined laser contrast level) may allow for hotter, and more MeV electrons to accelerate the protons; it should also yield a higher conversion efficiency, and a higher electron density;
 - o if the contrast was too high, the hot-electron temperature would be somewhat lower and one would expect a lower proton energy, which has been disproven by the data; thus the enhanced contrast may be optimal for generating more electrons.

- Improve the laser beam pointing accuracy to control the laser offset in the cone: on Trident (LANL), the pointing accuracy is $\sim 10 \mu\text{m}$, while it is $\sim 3 \mu\text{m}$ on the Draco laser system (FZD).

7.2 Diagnostics

- Use Cu $K\alpha$ on both sides of the cone target to check whether the interaction is symmetric and to diagnose the interaction better.
- Use RCF all around the target, as well as in the back (which is what has been done so far), to capture the electron and proton beams from all target areas.
- Use proton radiography; this diagnostic requires the addition of another 20 J short-pulse beamline on Trident. Proton radiography would allow one to look at the sheath shape on the flat-top, and at the electric fields.
- Using temporally resolved Cu $K\alpha$ measurements (i.e. fs streak camera) would also help characterizing the laser interaction better.
- Through interferometric probing, we would obtain insight into the electron density at the sheath on the flat top of the FTC.

7.3 Target development

- Establish with certainty whether the size of the supporting foil matters for a given Cu FTC.
- Try an L-shaped target, in which the laser would graze the bottom foil and protons would be accelerated from the vertical foil.

- Vary the Cu thickness to thinner targets to make use of the enhanced TNSA phenomenon observed for flat-foil targets: going to thinner targets allows for increasing the conversion efficiency as well as the maximum proton energy.
- Develop a better target design for increasing conversion efficiency.
- Use an alloy of Cu and other near Z materials (i.e. Mo, Ag, Ni...) to spatially resolve the different hot-electron populations.
- Try the Ti-Cu, Ti-Cu-Ti funnel cones again at high contrast to determine whether the heating comes from the bulk or from the surface.
- Use platinum FTCs to produce quasi mono-energetic carbon beams: Pt, when heated to greater than 800°C, acts as a catalyst to form a thin C film on the target surface, thus providing the required C atoms for the beam.
- Use structured flat-top cones to determine the proton beam source size: this is developed in more detail in Section 7.4, since some preliminary work has already been done.
- Develop a new target design with a focusing hemisphere replacing the flat-top in order to focus proton and carbon beams.

7.4 Micro-structured Cu FTCs

Using microstructured tops will help us identify the proton beam source size [14]. Micro-structured targets are targets with micro-corrugations present on the foil rear side, which causes the generation of beamlets in laser-accelerated proton beam. These perturbations in the protons' momentum space are embedded in the beam expansion to a point where the divergence angles originating from different microgrooves are well separated from each

other. In that case, a contrast pattern or image forms in the RCF detector; this effect is called microfocusing [13, 183, 127] and is shown in Figure 7-1 (left).

Therefore, the proton beam is able to map the rear side structure of the foil onto the film detector. Energy dependent information about the transverse emittance and the source size of the proton beam can be extracted in each layer of the RCF stack, using the deviations of the mapped image in the detector from the ideal image of the inserted grooves in the target. The symmetry and the divergence can also be determined by the imprint in the film. The grooves have to follow a gentle sinusoid [13, 183]. The groove depth has to be between ~ 1 and $3 \mu\text{m}$ and the separation between grooves ~ 3 to $20 \mu\text{m}$. A variety of groove profiles can be thought of, i.e. cycloid, inverse cycloid and sine functions (as shown in Figure 7-1 (right)).

The energy resolved real source size S_{real} , i.e. the proton emission zone on the target rear surface, is obtained (as a function of proton energy) by counting the line pattern in each RCF layer and by multiplying with the original line space of the microstructured foil.

The virtual source size S_{virtual} , i.e. the point source where the protons appear to originate from, is best to obtain quantitative information about the quality of the laser-accelerated proton beams. The virtual source size can be determined by extrapolation of the proton trajectories to a region in front of the target, using the well-known microstructures of the target and the measured line pattern in the RCFs. The width of the virtual source size is a suitable parameter for comparison of beam quality between different proton beams.

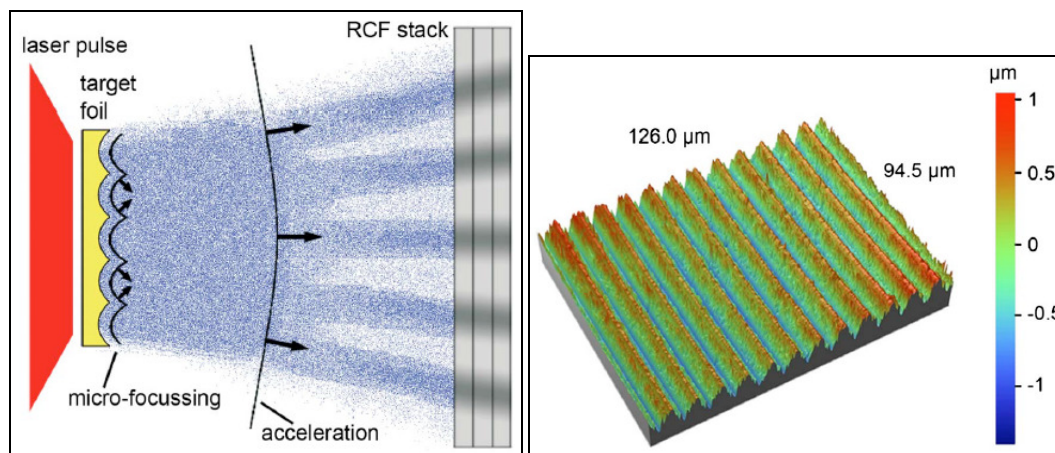


Figure 7-1: (left) Schematics of the foil-induced micro-focusing of the laser (red) accelerated proton beam (blue). The foil's grooved rear surface and the proton acceleration induced by the TNSA mechanism cause the micro-focusing of the protons when the acceleration starts. The separation of the beamlets can be seen in the RCF detectors as density modulations of the proton distribution. (right) Example of an interferometry image of the rear side of a micro-structured gold foil: sine structure with a ~ 10 μm period and ~ 1 μm amplitude.

A first generation of FTC with microstructured tops was released by Nanolabz before the June 2009 experimental run (see Figure 7-2 which shows the Si mold, and Figure 7-3 which shows a mounted Cu FTC). These targets have a heavier top due to the added structures, which makes them extremely fragile, hard to release, and hard to handle. A few targets were tested. In one case, the presence of some unetched Si in the throat prevented the laser interaction with the top, thereby yielding rather poor results. In a few other cases, and even the case where the top only was shot as an RMT, no imprint in the proton beam was visible/distinguishable in the RCF. In fact, finding the right structure profile for maximizing the contrast in the RCF images is not easy, and the grooves may have been too sharp, rather than being gently sinusoidal.

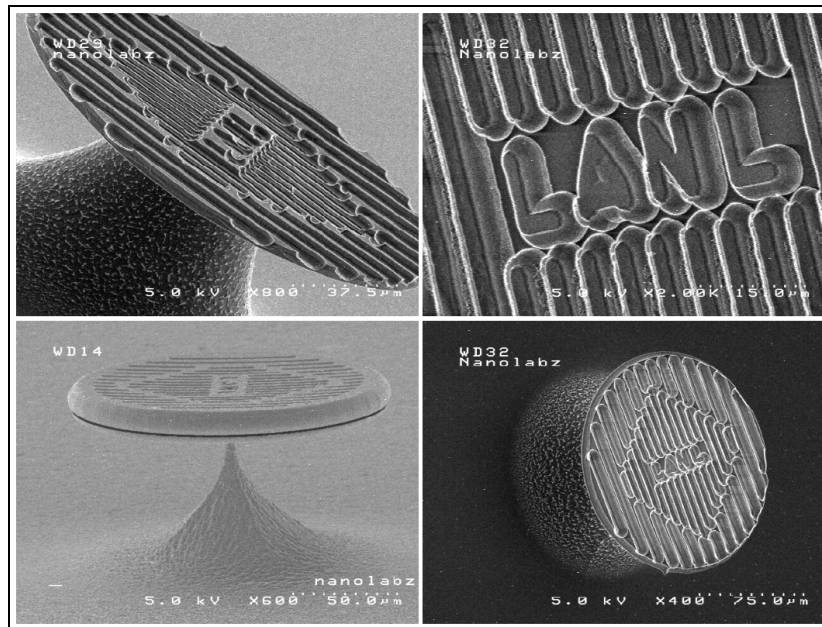


Figure 7-2: Mold of structured tops FTC targets.

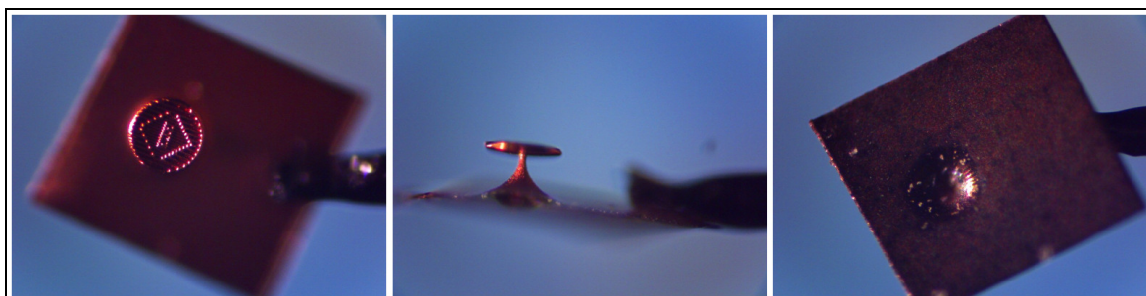


Figure 7-3: Cu targets made from the Si mold; FTC target g3, shot 21185.

8 VITA AND PUBLICATION LIST

MS in Physics, December 2005, University of Nevada, Reno

MS in Engineering, Specialty 'Energy & Environment', June 2003, EPF - Ecole Polytechnique Féminine, Engineering School in Sceaux, France

PAPERS IN PREPARATION

S. A. Gaillard, T. Kluge, K. A. Flippo, B. Gall, T. Lockard, M. Schollmeier, M. Geissel, D. T. Offermann, J. M. Rassuchine, D. C. Gautier, E. d'Humières, M. Bussmann, Y. Sentoku, T. E. Cowan, **Increased proton energies up to 67.5 MeV from high-contrast high-intensity short-pulse laser-interactions with micro-cone targets**, in preparation (2010).

S. A. Gaillard, J. S. Cowan, K. A. Flippo, D. C. Gautier, K. Harres, F. Nürnberg, M. Schollmeier, W. Leemans, M. Roth, T. E. Cowan, **Cross-Calibrations of RCF (MD-55 HD-810 and HS) from multiple proton sources from 4 to 25 MeV and using multiple scanning techniques (scanners and microdensitometer)**, in preparation for Review of Scientific Instruments (2010).

PAPERS SUBMITTED

T. Kluge, M. Bussmann, S. A. Gaillard, K. Flippo, D. C. Gautier, B. Gall, T. Lockard, M. E. Lowenstern, J. E. Mucino, Y. Sentoku, K. Zeil, S. Kraft, U. Schramm, T. E. Cowan and R. Sauerbrey, **Low-Divergent, Energetic Electron Beams from Ultra-Thin Foils**, submitted to AIP Conference proceedings (2009).

S. A. Gaillard, K. A. Flippo, M. E. Lowenstern, J. E. Mucino, J. M. Rassuchine, D. C. Gautier, J. Workman and T. E. Cowan, **Proton acceleration from ultra high-intensity short-pulse laser-matter interactions with Cu micro-cone targets at the intrinsic $\sim 10^{-8}$ contrast**, submitted to Journal of Physics Conference Series (JPCS) (2009).

Kirk Flippo, Teresa Bartal, Farhat Beg, Sugreev Chawla, Jim Cobble, Sandrine Gaillard, Daniel Hey, Andrew MacKinnon, Andrew MacPhee, Phillip Nilson, Dustin Offermann, Sébastien Le Pape and Mark J. Schmitt, **Omega EP, Laser Scalings and the 60 MeV Barrier: First Observations of Ion Acceleration Performance in the 10 Picosecond Kilojoule Short-Pulse Regime**, submitted to Journal of Physics Conference Series (JPCS) (2009).

E. d'Humières, J. L. Feugeas, P. Nicolai, S. Gaillard, T. Cowan, Y. Sentoku and V. Tikhonchuk, **Investigation of high intensity laser proton acceleration with underdense targets**, submitted to Journal of Physics Conference Series (JPCS) (2009).

B. J. Albright, L. Yin, B. M. Hegelich, K. J. Bowers, C. Huang, A. Henig, J. C. Fernandez, K. A. Flippo, S. Gaillard, T. J. T. Kwan, X. Q. Yan, T. Tajima and D. Habs, **Ultra-intense laser interaction with nanoscale targets: a simple model for layer expansion and ion acceleration**, submitted to Journal of Physics Conference Series (JPCS) (2009).

D. T. Offermann, K. A. Flippo, S. A. Gaillard, D.C. Gautier, S. Letzring, J. C. Cobble, G. Wurden, R.P. Johnson, T. Shimada, D. S. Montgomery, R. P. Gonzales, T. Hurry, M. J. Schmitt, S-M. Reid,

T. Bartal, M. S. Wei, D. P. Higginson and F. N. Beg, **Carbon ion beam focusing using laser irradiated, heated diamond hemispherical shells**, submitted to Journal of Physics Conference Series (JPCS) (2009).

PAPERS PUBLISHED

D. Kiefer, A. Henig, D. Jung, D. C. Gautier, K. A. Flippo, S. A. Gaillard, S. Letzring, R. P. Johnson, R. C. Shah, T. Shimada, J. C. Fernández, V. Kh. Liechtenstein, J. Schreiber, D. Habs and B. M. Hegelich, **First observation of quasi-monoenergetic electron bunches driven out of ultra-thin diamond-like carbon (DLC) foils**, European Physical Journal D, **55**, N°2 (2009).

J. Rassuchine, E. d'Humières, S. D. Baton, P. Guillou, M. Koenig, M. Chahid, F. Pérez, J. Fuchs, P. Audebert, R. Kodama, M. Nakatsutsumi, N. Ozaki, D. Batani, A. Morace, R. Redaelli, L. Grémillet, C. Rousseaux, F. Dorchie, C. Fourment, J. J. Santos, J. Adams, G. Korgan, S. Malekos, S. B. Hansen, R. Shepherd, K. Flippo, S. Gaillard, Y. Sentoku and T. E. Cowan, **Enhanced hot-electron localization and heating in high-contrast ultra-intense laser irradiation of sharp micro-cone targets**, Physical Review E, **79**, 0364408 (2009).

J. S. Cowan, K. A. Flippo and S. A. Gaillard, **Characterization of RadioChromic Film (RCF) Scanning Techniques used in Short-pulse-laser Ion Acceleration**, Review of Scientific Instruments, **79**, 10E535 (2008).

D. C. Gautier, K. A. Flippo, S. A. Letzring, J. Workman, T. Shimada, R. P. Johnson, T. R. Hurry, S. A. Gaillard and B. M. Hegelich, **A Novel Backscatter Focus Diagnostic for the TRIDENT 200 TW Laser**, Review of Scientific Instruments, **79**, 10F547 (2008).

D. C. Gautier, J. L. Kline, K. A. Flippo, S. A. Gaillard, S. A. Letzring and B. M. Hegelich, **A Simple Apparatus for Quick Qualitative Analysis of CR39 Nuclear Track Detectors**, Review of Scientific Instruments, **79**, 10E536 (2008).

M. Schollmeier, S. Becker, M. Geißel, K. Flippo, A. Blažević, S. A. Gaillard, D. C. Gautier, F. Grüner, K. Harres, M. Kimmel, F. Nürnberg, P. Rambo, U. Schramm, J. Schreiber, J. Schüttrumpf, J. Schwarz, N. Tahir, B. Atherton, D. Habs, B. M. Hegelich and M. Roth, **Controlled Transport and Focusing of Laser-Accelerated Protons with Miniature Magnetic Devices**, Physical Review Letters, **101**, 055004 (2008).

A. Mančić, J. Fuchs, P. Antici, S. A. Gaillard and P. Audebert, **Absolute calibration of photo-stimulable image plate detectors used as high-energy proton (0.5-20 MeV) detectors**, Review of Scientific Instruments, **79**, 073301 (2008).

K. Flippo, E. d'Humières, S. A. Gaillard, J. Rassuchine, D. C. Gautier, J. L. Kline, M. Schollmeier, F. Nürnberg, K. Harres, B. J. Albright, M. Bakeman, R. P. Johnson, G. Korgan, N. Renard - LeGalloudec, S. Malekos, M. Roth, Y. Sentoku, T. E. Cowan, J. C. Fernández and B. M. Hegelich, **Increased Efficiency and Energy of Laser-Accelerated Protons Using Novel Cone Targets**, Physics of Plasmas (Invited paper), **15**, 5 (2008).

R. Presura, V. V. Ivanov, Y. Sentoku, A. Esaulov, V. I. Sotnikov, S. Neff, C. Plechaty, S. Wright, P. J. Laca, A. Haboub, A. Morozov, M. Bakeman, S. Gaillard, P. Leblanc, R. Royle, J. Andersen and

T. E. Cowan, **Dynamics of laser-plasma expansion across strong magnetic field**, IEEE Pulsed Power Plasma Science Conferences, 1284-1287 (2007).

P. Antici, J. Fuchs, E. d'Humières, E. Lefebvre, M. Borghesi, E. Brambrink, C. A. Cecchetti, S. Gaillard, L. Romagnani, Y. Sentoku, T. Toncian, O. Willi, P. Audebert and H. Pépin, **Energetic protons generated by ultrahigh contrast laser pulses interacting with ultrathin targets**, Physics of Plasmas, **14**, 030701 (2007).

S. Gaillard, J. Fuchs, N. Renard-Le Galloudec and T. E. Cowan, **Study of saturation of CR39 nuclear track detectors at high ion fluence and of associated artifact patterns**, Review of Scientific Instruments, **78**, 1 (2007).

S. Gaillard, J. Fuchs, N. Renard-Le Galloudec and T. E. Cowan, **Comment on "Measurements of Energetic Proton Transport through Magnetized Plasma from Intense Laser Interactions with Solids"**, Physical Review Letters, **96**, 249201 (2006).

S. A. Gaillard, **Limitations of the use of CR39 Detectors, a particular type of Solid State Nuclear Track Detector, in High-energy, Short-pulse Laser Ion Acceleration Experiments**, Master's Thesis, University of Nevada, Reno (2005).

G. Dyer, B. Cho, D. R. Symes, T. Ditmire, T. Ohkubo, S. Gaillard, Y. Sentoku, N. Renard-LeGalloudec and T. E. Cowan, **Pyramidal targets as an advanced radiation source in laser-solid interactions**, IEEE-QELS (Quantum Electronics & Laser Science), **3**, 1804-6 (2005).

9 APPENDIX: LASER-PLASMA INTERACTIONS, AN INTRODUCTION

Unless otherwise specified, in this section, the equations are all given in S.I. units. First, we start with some basics on plasma physics [9.1]. Then, the interaction physics between an ultra-short high-intensity laser and a solid target is examined [9.2]. However, because such a laser has some level of prepulse, its interaction with a solid target creates some amount of preplasma – the amount depends on the contrast level, thereby interacting with an underdense plasma first [9.2.3], before reaching the solid density region [9.2.4]. Both collisional [9.2.4.3] and collisionless [9.2.4.4] laser absorption processes are described. The goal of this dissertation is to look simultaneously at protons, electrons, and X-rays, and to try to correlate to some extent their behavior. The generation of these radiations is discussed in Section 2: electrons [2.1], both thermal (< 100 keV), and hot (100 keV – tens of MeV), X-rays, especially $K\alpha$ [2.2], and ions, especially protons [2.3].

9.1 Basic plasma physics

In this sub-section, the basic and most important equations governing a plasma are briefly introduced and derived. For more detailed information, refer to [184] and [185].

9.1.1 Definitions

9.1.1.1 Plasma: introduction

Starting from basics, there are four common states of matter: solid, liquid, gas, and plasma (see Figure 9-1 (left) and (middle)). It is possible to transition between these states,

although some transitions are easier than others. The transitions between solids, liquids, and gases are fairly basic.

A plasma consists of a collection of free moving electrons and ions - atoms that have lost electrons. Energy is required to strip the electrons from the atoms to make a plasma. The energy can be of various origins, i.e. thermal, electrical, or light (ultraviolet light or intense visible light from a laser). The fourth state of matter was first identified in 1879 by Sir William Crookes (an English physicist), and an ionized gas was first named in 1929 by Dr. Irving Langmuir (an American chemist and physicist).

Plasma temperatures and densities range from relatively cool and tenuous (like aurora), to very hot and dense (like the central core of a star). Ordinary solids, liquids, and gases are both electrically neutral and too cool or dense to be in a plasma state (see Figure 9-1 (right)).

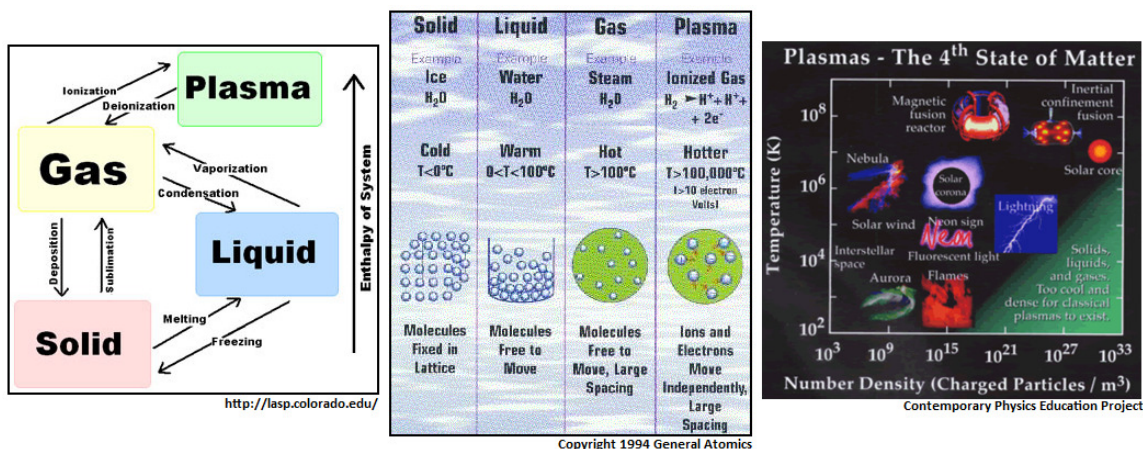


Figure 9-1: (left) Diagram showing the different states of matter (solid, liquid, gas, and plasma) when the enthalpy of the system goes up; (middle) Illustration of the different states of matter for the example of water; (right) Diagram of the different kinds of plasmas as a function of temperature (in K) and number density (in #charged particles per m³).

9.1.1.2 Plasma and Debye length

A plasma is a quasi-neutral collection of charged particles, which can screen out each other's fields. In a plasma, the screening distance is known as the Debye length,

$\lambda_{D_e} = \sqrt{\frac{\epsilon_0 k_B T_e}{n_e e^2}}$, where ϵ_0 is the permittivity of free space, k_B is the Boltzmann constant,

T_e is the electron temperature, n_e is the electron density, and e^2 is the square of the electron charge. It is obtained as follows:

- assuming that the likelihood of finding an electron is determined by a Boltzmann distribution, at a location where the potential to be screened is ϕ , the number of particles is

given by $n_e(\phi) = n_{e,0} \exp\left(\frac{e\phi}{k_B T_e}\right)$, where the energy of a particle with charge e is $e\phi$ and

$n_{e,0}$ is the number of particles with a zero potential;

- the Poisson equation yields $\nabla^2 \phi = -\frac{e(n_e(\phi) - n_{e,0})}{\epsilon_0}$;

- the thermal voltage is given by $V_{th} = \frac{k_B T_e}{e}$;

- the Poisson equation now reads as $\nabla^2 \left(\frac{\phi}{V_{th}}\right) = \left(\frac{1}{\lambda_{D_e}}\right)^2 \left(1 - \exp\left(-\frac{\phi}{V_{th}}\right)\right)$; after

identification, it yields $\lambda_{D_e} = \sqrt{\frac{\epsilon_0 k_B T_e}{n_{e,0} e^2}}$.

Thus, from this equation, one can see that in a plasma, when the temperature increases so does the screen distance, and when the density of charged particles is increased the screen distance decreases. This screening is one of the reasons a plasma can exhibit collective behavior.

9.1.1.3 Electromagnetism equations

To describe the properties of the electric (\vec{E}) and magnetic (\vec{B}) fields in the plasma, the Maxwell's equations are used, along with the Lorentz force:

- Gauss's law: $\vec{\nabla} \cdot \vec{D} = \rho_f$, where \vec{D} is the electric displacement field and ρ_f the free charge density. Assuming the medium is linear, isotropic, and homogeneous, $\vec{D} = \epsilon_0 \vec{E}$,

therefore $\vec{\nabla} \cdot \vec{E} = \frac{\rho}{\epsilon_0}$, where ρ is the charge density.

- Gauss's law for magnetism: $\vec{\nabla} \cdot \vec{B} = 0$.

- Maxwell-Faraday Equation: $\vec{\nabla} \times \vec{E} = -\frac{\partial \vec{B}}{\partial t}$.

- Ampère's law: $\vec{\nabla} \times \vec{H} = \vec{J}_f + \frac{\partial \vec{D}}{\partial t}$, where \vec{J}_f is the free current density, $\vec{H} = \frac{\vec{B}}{\mu_0}$ and

$\vec{D} = \epsilon_0 \vec{E}$ in free space, therefore $\vec{\nabla} \times \vec{B} = \mu_0 \vec{J} + \mu_0 \epsilon_0 \frac{\partial \vec{E}}{\partial t}$, where \vec{J} is the current density

and $\frac{1}{\mu_0 \epsilon_0} = c^2$.

- Lorentz force $\vec{F} = q(\vec{E} + \vec{v} \times \vec{B})$.

9.1.1.4 Equation of motion and continuity equation

The collection of charged particles in the plasma can also be seen as a fluid composed of positively charged and negatively charged species. The ions can be considered to be immobile because of their comparatively large mass. The electrons can be described using

their equation of motion $m_e n_e \left[\frac{\partial \vec{v}_e}{\partial t} + (\vec{v}_e \cdot \vec{\nabla}) \vec{v}_e \right] = -en_e \vec{E}$ and their continuity equation

$\frac{\partial n_e}{\partial t} + \vec{\nabla} \cdot (n_e \vec{v}_e) = 0$ where \vec{E} is the restoring electrostatic field from a displaced electron

bulk within the plasma, \vec{v}_e is the electron velocity, which for simplicity will be assumed to be only in the x direction, and m_e is the electron mass.

9.1.1.5 Plasma frequency

To obtain the plasma frequency, which plays a very important role in defining the interaction of light with a plasma, we use the continuity equation $\frac{\partial n_e}{\partial t} + \vec{\nabla} \cdot (n_e \vec{v}_e) = 0$,

Newton's second law $e\vec{E} = m_e \frac{\partial \vec{v}}{\partial t}$ and Gauss's law, $\epsilon_0 \vec{\nabla} \cdot \vec{E} = e(n_i - n_e)$.

The following assumptions are made:

- The plasma is uniform, neutral, and at rest before the electrons are displaced:

$$\begin{cases} \vec{\nabla} n_0 = \vec{v}_0 = \vec{E}_0 = 0 \\ \frac{\partial n_0}{\partial t} = \frac{\partial \vec{v}_0}{\partial t} = \frac{\partial \vec{E}_0}{\partial t} = 0 \end{cases}$$

Indeed, the neutrality of the plasma can be disrupted for example when an electron plasma wave, i.e. an electrostatic wave [9.1.2.1] separates the high and low electron density regions.

- $n_{i0} = n_{e0}$ in equilibrium, and $n_{i1} = 0$ because the ions are fixed.

- The density n_e , the velocity \vec{v}_e , and the electric field E_e are a sum of an equilibrium term ("0") and an oscillating term ("1").

$$\begin{cases} n_e = n_0 + n_1 & n_1 = n_1 e^{i(kx - \omega t)} \\ \vec{v}_e = \vec{v}_0 + \vec{v}_1 & \vec{v}_1 = v_1 e^{i(kx - \omega t)} \hat{x} \\ \vec{E} = \vec{E}_0 + \vec{E}_1 & \vec{E}_1 = E_1 e^{i(kx - \omega t)} \hat{x} \end{cases}$$

We know that $\frac{\partial}{\partial t} \rightarrow -i\omega$ and $\vec{\nabla} \rightarrow i\vec{k}$. By substitution, we obtain:

- The continuity equation which writes as $\frac{\partial n_1}{\partial t} + n_0 \vec{\nabla} \cdot \vec{v}_1 = 0$ and simplifies to $v_1 = \frac{n_1 \omega}{n_0 k}$.

- Newton's second law which writes as $-e\vec{E}_1 = m_e \frac{\partial \vec{v}_1}{\partial t}$ and simplifies to $v_1 = \frac{eE_1}{im_e \omega}$.

- Gauss's law which writes as $\epsilon_0 \vec{\nabla} \cdot \vec{E}_1 = -en_1$ and simplifies to $n_1 = -\frac{\epsilon_0 ikE_1}{e}$.

Therefore, combining the above three terms and eliminating v_1 , E_1 , and n_1 , we obtain

$$\omega^2 = \frac{e^2 n_0}{\epsilon_0 m_e}, \text{ which is known as the plasma frequency } \omega_p = \sqrt{\frac{e^2 n_0}{\epsilon_0 m_e}}.$$

If the plasma wave is relativistic, the plasma frequency becomes $\omega_p' = \sqrt{\frac{n_0 e^2}{\epsilon_0 m_e \gamma}} = \frac{\omega_p}{\sqrt{\gamma}}$, with

$$\gamma = \frac{1}{\sqrt{1 - \left(\frac{v}{c}\right)^2}}, \text{ the relativistic Lorentz factor.}$$

9.1.2 Electromagnetic waves

9.1.2.1 In vacuum

Let's assume a transverse electromagnetic plane wave propagating in vacuum, $\mu_0 \vec{J} = \vec{0}$.

Taking the curl of Ampère's law $\vec{\nabla} \times \vec{B} = \frac{1}{c^2} \frac{\partial \vec{E}}{\partial t}$ and substituting in the Maxwell-Faraday

$$\text{equation } \vec{\nabla} \times \vec{E} = -\frac{\partial \vec{B}}{\partial t}, \text{ we find } \vec{\nabla} \times (\vec{\nabla} \times \vec{B}) = \frac{1}{c^2} \vec{\nabla} \times \left(\frac{\partial \vec{E}}{\partial t} \right) = \frac{1}{c^2} \frac{\partial (\vec{\nabla} \times \vec{E})}{\partial t} = -\frac{1}{c^2} \frac{\partial^2 \vec{B}}{\partial t^2}.$$

Using the vector identity $\vec{\nabla} \times (\vec{\nabla} \times \vec{B}) = \vec{\nabla} (\vec{\nabla} \cdot \vec{B}) - \nabla^2 \vec{B}$ and the fact that $\vec{\nabla} \cdot \vec{B} = 0$, we

obtain $\nabla^2 \vec{B} = \frac{1}{c^2} \frac{\partial^2 \vec{B}}{\partial t^2}$. Substituting $\vec{B} = \vec{B}_0 + \vec{B}_1$ where $\vec{B}_1 = B_1 e^{i(kx - \omega t)} \hat{x}$, into the previous

plane wave equation, we find $k^2 = \frac{\omega^2}{c^2}$, which is the dispersion relation for light in vacuum.

9.1.2.2 In an unmagnetized plasma

We apply a similar treatment as in the previous section. Taking the curl of the Maxwell-

Faraday equation $\vec{\nabla} \times \vec{E} = -\frac{\partial \vec{B}}{\partial t}$, and substituting in for Ampere's law in a plasma

$\vec{\nabla} \times \vec{B} = \mu_0 \vec{J} + \mu_0 \epsilon_0 \frac{\partial \vec{E}}{\partial t}$, we find $\vec{\nabla} \times (\vec{\nabla} \times \vec{E}) = -\frac{\partial (\vec{\nabla} \times \vec{B})}{\partial t} = -\frac{\partial}{\partial t} \left(\mu_0 \vec{J} + \frac{1}{c^2} \frac{\partial \vec{E}}{\partial t} \right)$. Since

$\vec{\nabla} \times (\vec{\nabla} \times \vec{E}) = \vec{\nabla} (\vec{\nabla} \cdot \vec{E}) - \nabla^2 \vec{E}$ and $\vec{\nabla} (\vec{\nabla} \cdot \vec{E}) = \vec{\nabla} \left(\frac{\rho}{\epsilon_0} \right) = 0$, due to the plasma neutralizing on

scales larger than the Debye length, we obtain $\nabla^2 \vec{E} = \mu_0 \frac{\partial \vec{J}}{\partial t} + \frac{1}{c^2} \frac{\partial^2 \vec{E}}{\partial t^2}$.

Since $\vec{J} = -n_0 e \vec{v}_e$ and \vec{v}_e can be found using $m_e \frac{\partial \vec{v}_e}{\partial t} = -e \vec{E}$, we find

$\nabla^2 \vec{E} = -\frac{e^2 \mu_0 n_0}{m_e} \vec{E} + \frac{1}{c^2} \frac{\partial^2 \vec{E}}{\partial t^2}$. Substituting $\vec{E} = \vec{E}_0 + \vec{E}_1$ with $\vec{E}_1 = E_1 e^{i(kx - \omega t)} \hat{x}$, the

equation becomes $(ik)^2 \vec{E}_1 = -\frac{e^2 \mu_0 n_0}{m_e} \vec{E}_1 + \frac{1}{c^2} (-i\omega)^2 \vec{E}_1$. Using the definition of the

plasma frequency, $\omega_p = \sqrt{\frac{e^2 n_0}{\epsilon_0 m_e}}$, we obtain $\omega^2 = \omega_p^2 + c^2 k^2$, which is the fundamental

equation governing the behavior of an EM wave of frequency ω in a plasma. Dividing by

ω^2 , we find $1 = \frac{\omega_p^2}{\omega^2} + \frac{c^2 k^2}{\omega^2}$, and defining the plasma index of refraction to be $\eta = \frac{c^2 k^2}{\omega^2}$,

we get $\frac{\omega_p^2}{\omega^2} = 1 - \eta$.

Note that if the laser light field is relativistic, the equation becomes

$$\omega^{2'} = \omega_p^2 + c^2 k^2 = \frac{\omega_p^2}{\gamma} + c^2 k^2.$$

9.1.2.2.1 Critical density and Characteristic skin depth

For a fixed frequency ω of a light wave, as the plasma frequency ω_p increases and eventually surpasses ω , the wave number k must go through zero and become imaginary.

When k is imaginary, the wave is evanescent, and $k = 0$ corresponds to the wave cutoff.

The cutoff occurs when $\omega^2 = \omega_p^2 = \frac{e^2 n_{e,0}}{\epsilon_0 m_e}$, or solving for n_e as a function of the light

frequency, ω , when $n_e(\omega) = \frac{m_e \cdot \epsilon_0}{e^2} \omega^2$. This density is called the cutoff or critical density

and is denoted as n_c . The laser is able to propagate up to the characteristic skin depth δ

given by $\delta = \frac{1}{|k|} = \frac{c}{\sqrt{\omega_p^2 - \omega^2}}$, after which the light waves become evanescent. A simple

formula for the critical density in the non-relativistic case is, $n_c [m^{-3}] = \frac{1.1 \times 10^{27}}{\lambda^2 [\mu m]}$. For a

laser wavelength of $\sim 1 \mu m$ this expression yields a critical density of $\sim 10^{21} \text{ cm}^{-3}$.

9.1.2.2.2 Collisionless skin depth and Relativistic induced transparency

When $\omega_p^2 \gg \omega^2$, the skin depth is given by the collisionless skin depth $\delta = \frac{c}{\omega_p}$, which is

the quantity used to determine the laser penetration in an overdense plasma. At solid density, a typical collisionless skin depth ranges between 5 and 10 nm.

In the relativistic case, the critical density becomes $n_e'(\omega) = \gamma n_e'(\omega)$, or as a numerical

formula, $n_e' [m^{-3}] = \gamma \frac{1.1 \times 10^{27}}{\lambda^2 [\mu m]}$. The higher the γ , the deeper the laser can propagate into

the plasma - a condition known as relativistic induced transparency - and the greater the bulk heating of the plasma can become.

9.2 Laser interactions in underdense and dense plasmas

This section discusses the processes through which the laser interacts with and deposits its energy in a solid target. The target's front surface ionizes via tunnel and collisional ionization. So we start by looking at the ionization potentials and also at the effect of prepulses; the presence of prepulses is an inherent characteristic to any laser system. Because of these prepulses, the main compressed laser has to interact with an underdense plasma first before it can reach the solid dense target.

9.2.1 Electron motion, quiver velocity, and ponderomotive force

9.2.1.1 Definitions

9.2.1.1.1 Electron quiver velocity

An electron at rest, irradiated by a relativistic intense laser field, is quickly accelerated, up

to relativistic energies. The electron quiver velocity $v_e = \frac{eE_L}{m_e\omega}$ corresponds to the velocity

of the electron just after ionization. The velocity and position of the electron for a linearly

polarized laser $\vec{E} = \hat{x}E_L \cos(\omega t)$ are respectively given by $v = v_e \sin(\omega t) + v_i$ and

$$x = -\frac{v_e}{\omega} \cos(\omega t) + v_i t - x_i \quad [187, \text{page 29}].$$

9.2.1.1.2 Normalized vector potential

The Lorentz factor $\gamma = \frac{1}{\sqrt{1-\beta^2}}$ where $\beta = \frac{v}{c}$ describes how relativistic the electron is.

Since $\beta = \frac{p}{\gamma mc}$, then we can write $\gamma = \sqrt{1 + \frac{p^2}{m^2 c^2}}$ as a function of the electron momentum.

The normalized vector potential $a_0 = \frac{eA_0}{mc}$ or $a_0 = \frac{eE_0}{mc\omega} = \frac{v_{e-}}{c}$ ($\vec{E} = -\frac{\partial \vec{A}}{\partial t}$ and

$\vec{A} = A_0 \cos(kz - \omega t)\hat{z} \Rightarrow E_0 = \omega A_0$) determines how strong the laser field is. It is

proportional to the field driving the electron's acceleration and since $a_0^2 = \frac{2p^2}{m^2 c^2}$, we can

rewrite the Lorentz factor γ as the relation $\gamma = \sqrt{1 + \frac{a_0^2}{2}}$.

9.2.1.1.3 Intensity and electric field

The intensity of the laser light is defined as the energy density of the electric field

$$I = \frac{\mathcal{E}}{2} \|\vec{E}_L\|^2.$$

The normalized vector potential a_0 can also be expressed as a function of the laser intensity

$$\text{through the above relationship for } I \text{ and } E_L \text{ as the formula } a_0 = 0.85\lambda_0 [\mu\text{m}] \sqrt{I \left[10^{18} \frac{\text{W}}{\text{cm}^2} \right]}.$$

For a normally incident EM wave into an underdense plasma, the electrons can gain energy through either the transverse component of the electric field or ponderomotive potential, originating from the laser pulse, or from the longitudinal component of the electric field, originating from plasma waves. The electron plasma waves, i.e. plasma oscillations, are also known as Langmuir waves.

The amplitude of the transverse electric field of a linearly polarized laser is given by

$$E_L [\text{TV/m}] = \frac{m_e c^2 k}{e} a_0 \sim 3.21 \frac{a_0}{\lambda_0 [\mu\text{m}]} \sim 2.7 \sqrt{I \left[10^{18} \frac{\text{W}}{\text{cm}^2} \right]}.$$

For a 1 μm light, $a_0^2 = 1$, $\gamma \sim 1.2$, which is mildly relativistic, and the laser intensity is $I(a_0^2 = 1) = 1.38 \times 10^{18} \text{ W/cm}^2$. When $a_0 > 1$, significant relativistic effects may occur, for example, the mass of the laser-accelerated electrons increases by the factor γ .

In this dissertation, the experiments take place between the two following intensities:

- $I \sim 2 \times 10^{19} \text{ W/cm}^2$, $a_0 \sim 3.8$ and $\gamma \sim 2.9$. The critical density is $\sim 3 \times 10^{21} \text{ cm}^{-3}$, and the transverse electric field is $E_L [\text{TV/m}] \sim 12$.

- $I \sim 2 \times 10^{20}$ W/cm², $a_0 \sim 12$ and $\gamma \sim 8.5$. The critical density is $\sim 8.5 \times 10^{21}$ cm⁻³, and the transverse electric field is E_L [TV/m] ~ 38 .

9.2.1.2 Photon pressure

At the laser irradiated target interface, the laser light hits a higher density medium. Therefore, the photon cannot propagate any further. This leads to a sudden drop in the laser intensity, creating a laser intensity gradient, which creates photon or light pressure, defined as $P_L = \frac{2I}{c}$. At intensities of the order of 10^{19} W/cm², the light pressure can be $\sim 6 \times 10^3$ Mbar, and can exceed the plasma thermal pressure. This allows the laser to push against the expanding plasma, leading to effects like profile steepening and hole boring, described in Sections 9.2.3.5 and 9.2.4.1.

9.2.1.3 Ponderomotive force and Ponderomotive potential

The ponderomotive force $F_p = -\frac{1}{4} \frac{e^2}{m\omega^2} \nabla E^2$ is a “virtual force” due to the gradient of the light pressure $\nabla P_L \propto \nabla E^2$, which can also be formulated in the form of the gradient of the laser intensity $\nabla I \propto \nabla E^2$.

It may be derived in the following way [187, pages 36-39]. Assume a single non-relativistic electron oscillating near the center of a focused laser beam. If $\beta \ll 1$, the equation of motion of an electron is given by $\frac{\partial v_y}{\partial t} = -\frac{e}{m} E_y(r)$. The EM wave is assumed to propagate only in the x-direction, and the radial dependence in the potential $E_y(r)$ is assumed to correspond to the y-direction only. $E_y(r)$ is an oscillating potential, whose Taylor

expansion around $y = 0$ is given by: $E_y(r) \sim E_0(y)\cos\varphi + y\frac{\partial E_0(y)}{\partial y}\cos\varphi + \dots$. To the first

order, using Section 9.2.1.1.1, $v_y^{(1)} = v_e \sin(\omega t)$ and $y^{(1)} = -\frac{v_e}{\omega}\cos(\omega t)$, where v_e is the

quiver velocity. By substitution into the equation of motion, the second order yields

$\frac{\partial v_y^{(2)}}{\partial t} = -\frac{e^2}{m^2\omega^2}E_0\frac{\partial E_0(y)}{\partial y}\cos^2\varphi$. Taking the average over one cycle of the previous

expression, and multiplying by m , the electron mass, we find

$F_p = m\overline{\frac{\partial v_y^{(2)}}{\partial t}} = -\frac{1}{4}\frac{e^2}{m\omega^2}\frac{\partial(E_0(y))^2}{\partial y}$. The Ponderomotive potential is then simply

$$\Phi_p = \frac{e^2 E_L^2}{4m\omega_L^2}.$$

9.2.2 Target ionization

For intensities greater than 10^{10} W/cm², target ionization can occur. For the Trident laser, main pulses are of the order of 10^{19} W/cm² (20 J, no deformable mirror) or 2×10^{20} W/cm² (80 J, with deformable mirror). This means that the laser contrast has to be better than 10^{-9} or 10^{-10} respectively to avoid preionization of the target before the main pulse arrives.

In fact, experiments have even shown [186] that a prepulse as small as $\sim 10^8$ W/cm² can significantly affect and increase the absorption of laser light, and increase desorption of neutral gas, which would then be ionized by the foot of the main pulse. Therefore, even for an ultra-high contrast laser system (unless better than 10^{-12}), this phenomenon can be present, creating a very short scale-length preplasma.

9.2.2.1 Field ionization potential

To define “high” or “ultrahigh” laser intensity, one generally first looks at the hydrogen

atom, via the Bohr model. The Bohr radius is defined as $a_B = \frac{\hbar^2}{m_e e^2} = 5.3 \times 10^{-9} \text{ cm}$, the

electric field strength as $E_a = \frac{1}{4\pi\epsilon_0} \frac{e}{a_B^2} = 5.1 \times 10^9 \text{ V} \cdot \text{m}^{-1}$, and the atomic intensity as

$I_a = \frac{\epsilon_0 c}{2} E_a^2 = 3.5 \times 10^{16} \text{ W} \cdot \text{cm}^{-2}$, which is the intensity at which the laser field matches the

binding strength of the electrons to the atom. When the laser intensity is greater than the atomic intensity, any target material becomes ionized [187, pages 17-18] and these field strengths are referred to as “high”; when the field becomes relativistic as “ultrahigh”, see Section 9.2.1.1.3.

9.2.2.2 Tunneling ionization

If we assume a Coulomb potential modified by a stationary homogeneous electric field

$V(x) = -\frac{Ze^2}{x} - e\xi x$ (see Figure 9-2), electrons escape spontaneously when the barrier falls

below E_{ion} , the ionization potential for an atom or ion of charge of $Z-1$. This process is known as the “over-the-barrier ionization” (OTBI). The threshold field strength at which it takes place is obtained as follows. The position of the barrier is given by the solution of

$\frac{dV(x)}{dx} = \frac{Ze^2}{x^2} - e\xi = 0$, which is $x_{max} = \sqrt{\frac{Ze}{\xi}}$. The barrier’s height is set to $V(x_{max}) = E_{ion}$,

and also $V(x_{max}) = -2e\sqrt{Ze\xi}$ using the value of x_{max} . Therefore, the threshold field

strength for which the over the barrier ionization occurs is $\xi = \frac{E_{ion}^2}{4Ze^3}$. The corresponding

intensity is $I_{OTBI} = \frac{\epsilon_0 c}{2} \xi^2 = \frac{\epsilon_0 c E_{ion}^4}{32 e^6 Z^2}$. E_{ion} is the ionization potential; for hydrogen with

$Z=1$, $E_{ion} = E_H = \frac{e^2}{2a_B} = 13.61\text{eV}$. In that particular case, $\xi_{Z=1} = \frac{e}{16a_B^2} = \frac{E_a}{16}$, and

$$I_{OTBI,Z=1} = \frac{I_a}{256} \sim 1.4 \times 10^{14} \text{W} \cdot \text{cm}^{-2}.$$

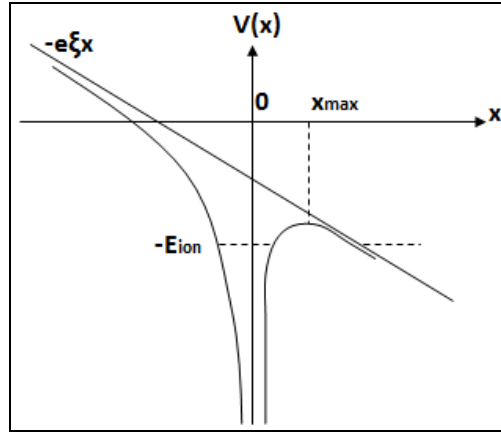


Figure 9-2: Picture of tunneling or barrier-suppression by a strong external electric field [187, page 21].

9.2.2.3 Multi-photon ionization

Target ionization can happen for even smaller intensities than the atomic intensity via multiphoton effects [187, pages 3, 18-19, 20-23]. When light hits a material, if the photon energy $\hbar\omega$ matches the height of the atomic potential barrier I_p which the electron experiences in the vicinity of the ion, i.e. $I_p = \hbar\omega$, this single photon can cause the ejection of an electron from the atom. This is known as the photoelectric effect [188]. For outer shells of the atom, this energy is of the order of eV, while for the inner shells, it is of the order of the keV. Multi-photon ionization, expressed by the condition $I_p = n\hbar\omega$, easily starts taking place for laser intensities $> 10^{10} \text{W/cm}^2$.

9.2.3 Laser interaction with underdense plasmas

Unless the laser contrast is extremely high, the laser interacts with the underdense preplasma first – the preplasma being caused, as we have discussed previously in Sections 9.2.2 and 3.3.1, by prepulse, or high-intensity pedestal.

Generally, ablation is responsible for the formation of this underdense plasma region from a solid target. The plasma pressure created during heating causes matter to blow off at

roughly the sound speed $c_s = \sqrt{\frac{Z^* k_B T_e}{M}}$, where $c_s \approx 3.1 \times 10^7 \sqrt{\frac{Z^* T_e [\text{keV}]}{A}}$ cm/s [187,

pages 128-129]. Assuming that the plasma expands isothermally [189], the density profile will assume an exponentially decreasing form with a definite scale-length $L = c_s \tau$, where

$$L \approx 3 \times \sqrt{\frac{Z^* T_e [\text{keV}]}{A}} \tau [\text{fs}] \text{ \AA} \text{ and } \tau \text{ is the expansion time.}$$

If the underdense region happens to be very long (10s or 100s of μm), then a very intense pulse could drive the electrons forward in a snow-plough manner before the pulse even reaches the target's critical surface (i.e. see 9.2.4.1 on hole boring); also in the underdense region, the laser pulse could undergo relativistic self-focusing, or suffer Raman forward back- and side-scatter instabilities [187, page 177], or other nonlinear phenomena discussed below.

9.2.3.1 Ionization-induced defocusing

The phenomenon of ionization-induced defocusing [187, pages 24-27] has been described in [190, 191, 192]. At the foot of an intense pulse, where the field is close to the ionization threshold, the gas at the center of the beam will be ionized more, giving rise to a steep radial

density gradient. This differential ionization rate also acts longitudinally in the time domain, which leads to spectral blue-shifting of a portion of the transmitted light [193].

The refractive index of the plasma created after ionization is given by $\eta(r,t) = \sqrt{1 - \frac{n_e(r,t)}{n_c}}$,

where $n_e(r,t)$ is the local electron density and n_c the critical density. If more electrons are created at the beam center, the refractive index will have a minimum there, forming a defocusing lens for the following portion of the beam, resulting in, for high gas pressures, the fact that the laser can be diffracted away before it can reach its nominal focus.

9.2.3.2 Laser self-focusing

Similar to ionization self-focusing, several other phenomena can lead to self-focusing in the plasma such as relativistic, ponderomotive, and thermal effects [194, 195]. Self-focusing in the plasma causes an increase in the laser intensity, which leads to high electron temperatures, and can change the nature of the laser-matter interaction.

9.2.3.2.1 Ponderomotive self-focusing

In an underdense plasma, the ponderomotive force on-axis can be high enough to push electrons off-axis, away from the region where the laser beam is more intense, which is known as plasma cavitation [196]. The cavitation condition is given by $I_{18} \lambda_\mu^2 > \frac{1}{20} n_{18} \sigma_\mu^2$,

where σ_μ and λ_μ are the laser spot size and wavelength, I_{18} and n_{18} are the laser intensity and plasma density in units of 10^{18} W/cm² and 10^{18} cm⁻³, respectively [187, page 107].

When this occurs, then similarly to the description in Section 9.2.3.2.2, the index of refraction becomes greater on-axis, acting like a positive lens, and causing the laser to self-focus. This phenomenon is called ponderomotive self-focusing [197].

9.2.3.2.2 Relativistic self-focusing

In Section 9.2.3.1, we have seen that in a plasma which is being ionized, transverse variations in the background density can lead to premature defocusing. In a uniform, fully ionized plasma, as the laser intensity increases, relativistic self-focusing can take place.

The plasma refractive index η is given by $\eta = cv_{phase} = \frac{ck}{\omega_0} = \sqrt{1 - \left(\frac{\omega_p}{\omega_0}\right)^2}$. In the

relativistic case, because the electrons' mass increase, the plasma index of refraction is

modified and is given by $\eta(\gamma) = \sqrt{1 - \frac{1}{\gamma} \left(\frac{\omega_p}{\omega_0}\right)^2}$. In that case, the plasma ends up having a

higher index of refraction on-axis than off-axis, and acts as a positive lens. As a result the laser wavefront will be bent back toward the axis, further increasing the intensity on-axis and decreasing it further off-axis: the initially planar wavefront is bent as illustrated in Figure 9-3. This phenomenon is known as relativistic self-focusing [198, 199, 200].

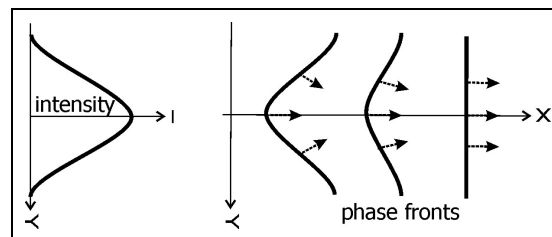


Figure 9-3: Relativistic self-focusing [200]

Above the relativistic critical power [187, pages 104-105] (power threshold),

$$P_{critical} = \frac{m_e c^5}{e^2} \left(\frac{\omega_0}{\omega_p}\right)^2 \sim 17.4 \times \left(\frac{\omega_0}{\omega_p}\right)^2 = 17.4 \times \frac{n_c}{n_e} \text{ GW, self-focusing always occurs [201,$$

202].

9.2.3.2.3 Thermal self-focusing

Thermal self-focusing [203] is due to collisional heating of a plasma exposed to electromagnetic radiation. The rise in temperature induces a hydrodynamic expansion which leads to an increase of the index of refraction and further heating.

9.2.3.2.4 Self-phase modulation

Because the intensity of the pulse varies in time, the index of refraction is also a function of time. The phase velocity of the laser can be expressed as a function of the index of

refraction, i.e. $v_{phase} = \frac{\eta}{c} = \frac{1}{c} \sqrt{1 - \left(\frac{\omega_p}{\omega_0}\right)^2}$. Thus, the temporal change in η causes a phase

modulation in the laser pulse, due to group velocity dispersion. This process is known as relativistic self-phase modulation [198]. It can result in a broadening of the laser pulse spectrum, as well as of its temporal profile, which can change the interaction at the critical surface, and may affect any optical diagnostics looking for reflected light.

9.2.3.2.5 Self-channeling, self-guiding, and sausinging

A combination of ponderomotive and relativistic self-focusing of a laser pulse, which has a duration greater than a few plasma periods, can balance the natural diffraction of the plasma and self-channel and/or self-guide the laser. When the laser power equals the critical power, the beam propagates in a self-made channel oscillating around some mean radius. Self-channeling has been observed experimentally in the early 90s [204, 205] and is the basis for the rather large field of electron laser wakefield accelerators.

9.2.3.2.6 Filamentation

Under extreme local ponderomotive forces, the laser beam can filament into several beams, each of which is self-focused and makes its own channel [206, 207, 208, 209]. Filamentation can occur due to, for example, density fluctuations or magnetic fields (Weibel instability [210, 211, 212]). This can have an effect on how the electrons propagate into and through a solid target, creating large internal fields, disrupting the energy transport. The filamentation can be imprinted on the resulting proton beam via the sheath, preventing a smooth uniform beam from being accelerated.

9.2.3.3 Parametric instabilities

Parametric excitation of waves is a result of energy transfer (coupling) from one wave to another. In an underdense plasma, in which waves are coupled, the following basic feedback interaction can occur. The ponderomotive force bunches the electrons in the plasma, which results in a plasma wave. This causes a local density increase, which decreases the group velocity of the light ($\partial\omega/\partial k$), which causes photons to bunch up, resulting in scattered light waves. This creates larger density gradients, and therefore a stronger ponderomotive force to propagate the mechanism. Ion acoustic waves are also created when the bunched electrons' large static fields force the ions to move, over longer periods of time.

9.2.3.3.1 Parametric decay instability

A laser light wave (ω_0, k_0) can decay into a plasma wave (ω_p, k_p) and an ion acoustic wave (ω_i, k_i) if $\omega_0 > \omega_p$ and if the resonant phase matching conditions of $\omega_0 = \omega_i + \omega_p$ and $k_0 = k_i + k_p$ are met. The light wave can be completely absorbed by the plasma in this case.

9.2.3.3.2 Stimulated Brillouin Scattering (SBS)

A laser light wave (ω_0, k_0) can decay into an ion acoustic wave (ω_i, k_i) and a scattered light wave (ω_s, k_s) provided $\omega_s = \omega_0 \pm \omega_i$ and $k_s = k_0 \pm k_i$.

9.2.3.3.3 Stimulated Raman Scattering (SRS)

A laser light wave (ω_0, k_0) can decay into a plasma wave (ω_p, k_p) and a scattered light wave (ω_s, k_s) provided $\omega_s = \omega_0 \pm \omega_p$ and $k_s = k_0 \pm k_p$. This happens when $\omega_0 > 2\omega_p$ or $n_e < \frac{n_c}{4}$.

When $n_e = \frac{n_c}{4}$, the light wave satisfies the special condition $\omega_0 = 2\omega_p$, and this is referred to as the 2 plasmon decay, or the $2\omega_p$ instability [213].

There are four particular cases of SRS:

- frequency downshifted, $k_- = k_p - k_0$, also called Stokes;
- frequency upshifted, $k_+ = k_p + k_0$, also called Anti-Stokes;
- stimulated Raman forward-scattered (SRFS) light, which is a four-wave interaction, with the phase matching conditions depicted in Figure 9-4 (a);
- stimulated Raman back-scattered (SRBS) light, is a three-wave interaction, with the phase matching conditions represented in Figure 9-4 (b).

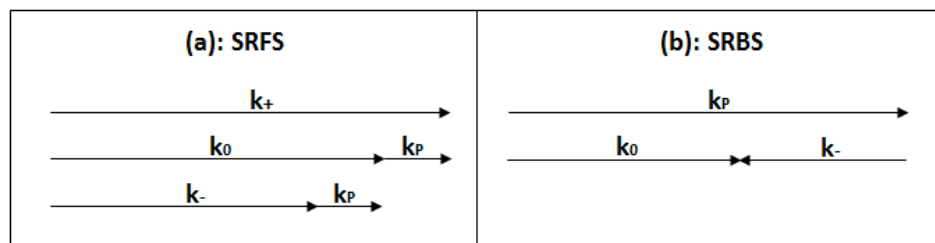


Figure 9-4: Phase matching conditions for Stimulated Raman Forward Scattering and Stimulated Raman Backward Scattering [187, page 86].

These types of instabilities create electron plasma waves which dampen in the plasma, therefore heating it and producing very energetic electrons. SRFS can drive a Self-Modulated Laser Wakefield (SMLWF, see Section 9.2.3.4.4), and accelerate electrons to MeV energies [214].

9.2.3.4 Plasma Wake-Field Accelerator

In [215], Tajima and Dawson proposed using laser beams to excite plasma waves for electron acceleration. In [216], a very thorough overview of the physics issues relevant to the plasma wake-field accelerator (PWFA), the plasma beat-wave accelerator (PBWA), the laser wake-field accelerator (LWFA), including the self-modulated regime (SMLWFA) is given, but here, we only describe them shortly, quoting [216]. Figure 9-5 [216] illustrates the different types of plasma-based accelerators.

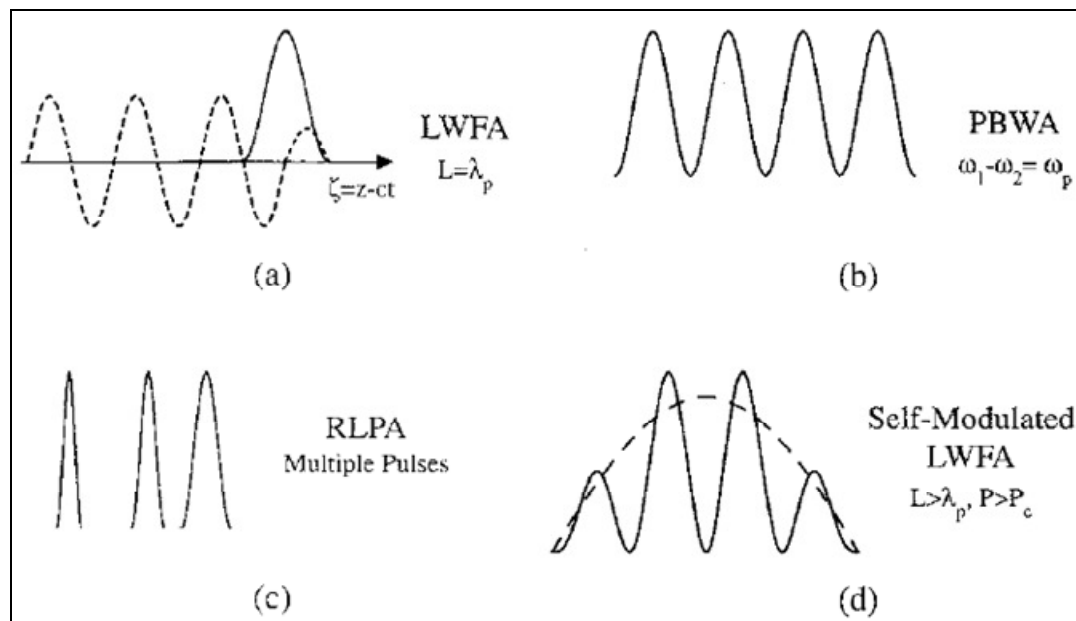


Figure 9-5: Schematic of the plasma-based accelerators [216] - the pulses are moving to the right: (a) LWFA (or PWFA) in which a short $L \sim \lambda_p$ laser pulse (or electron beam) drives a plasma wave (dashed curve); (b) PBWA in which two long pulse ($L > \lambda_p$) lasers with frequencies $\omega_1 - \omega_2 \sim \omega_p$ resonantly drive a plasma wave; (c) RLPA in which a train of short laser pulses resonantly drives a plasma wave; (d) SMLWFA in which an initially long pulse (dashed curve) breaks up into a series of short pulses and resonantly drives a plasma wave.

9.2.3.4.1 Plasma Wake-Field Acceleration (PWFA)

Plasma-based accelerators, in which the plasma wave is driven by one or more electron beams, are referred to as PWFAs. In the PWFA, plasma wake-fields can be excited by a relativistic electron beam provided that the electron beam terminates in a time shorter than the plasma period, $1/\omega_p$; if instead of an electron beam, a laser is used, one can then have the following four acceleration schemes

9.2.3.4.2 Plasma Beat-Wave Acceleration (PBWA)

In PBWA, two long pulse laser beams of frequencies ω_1 and ω_2 are used to resonantly excite a plasma wave. This is done by appropriately adjusting the laser frequencies and plasma density such that the resonance condition $\omega_1 - \omega_2 \sim \omega_p$ is satisfied.

9.2.3.4.3 Laser Wake-Field Acceleration (LWFA)

In LWFA, a single short (i.e. ≤ 1 ps) ultrahigh intensity (i.e. $\geq 10^{18}$ W/cm²) laser pulse drives a plasma wave. The wakefield is driven most efficiently when the laser pulse length $L = c\tau_L$ is approximately the plasma wavelength $\lambda_p = 2\pi c/\omega_p$ i.e. $L = \lambda_p$, implying the need for 10s of fs lasers, depending on the plasma conditions. A special case of the LWFA is when the laser wavelength is shorter than the plasma wavelength and is particularly intense (i.e. $> \sim 10^{20}$ W/cm²). It can then create a cavitation of the plasma. This results in a cavity, or bubble, forming behind the laser pulse, which can trap electrons and accelerate them to very high energies. This is called bubble acceleration [217, 218].

9.2.3.4.4 Self-modulated laser Wake-field Acceleration (SMLWFA)

The SMLWFA is the most important electron acceleration mechanism for these experiments, since an underdense plasma can form in front of a solid target, or inside a cone, and since these experiments use a laser of ~ 1 ps, a SMLWF can be produced.

SMLWFA, as in the standard LWFA, also uses a single short (i.e. ≤ 1 ps) ultrahigh intensity (i.e. $\geq 10^{18}$ W/cm²) laser pulse. The SMLWFA, however, operates at higher densities than the standard LWFA, such that the laser pulse length is long compared to the plasma wavelength, $L > \lambda_p$, and the laser power P is somewhat larger than the critical power P_C for relativistic guiding, $P \geq P_C$. In this high density regime, the laser pulse undergoes a self-modulation instability which causes the pulse to become axially modulated at the plasma period. Associated with the modulated pulse structure, is a large amplitude, resonantly driven plasma wave. The self-modulation instability resembles a highly 2-D version of a forward Raman instability. Forward Raman scattering occurs simultaneously, adding to the modulation, and in the 1-D limit, pulse modulation can occur via forward Raman scattering alone.

9.2.3.4.5 Resonant Laser-Plasma Acceleration (RLPA)

RLPA uses an optimized train of short laser pulses to drive a plasma wave, in which the width of each pulse and the spacing between pulses is independently controlled. By optimizing the pulse widths and inter-pulse spacings, resonance with the plasma wave can be maintained, and saturation of the plasma wave by resonant detuning can be eliminated.

9.2.3.5 Density profile steepening

For intensities greater than 10^{18} W/cm², the laser pressure can be strong enough to slow, stall or even reverse the plasma expansion. The plasma is pushed back into a steeper density profile, and this phenomenon is known as profile steepening.

As the laser ionizes the plasma the ponderomotive force pushes the electrons away from the laser and into the target up to the critical surface. For higher intensities, it can continue punching a hole into the plasma, and this is known as hole boring (see Section 9.2.4.1).

9.2.3.6 Laser envelope profile steepening

Another important effect is the steepening of pulse envelopes propagating with group velocity $v_{gr} = c\eta$. The peak region with high intensity runs faster than the regions with low intensity at the pulse front, and this leads to optical shock formation, as illustrated in Figure 9-6. Pulse shapes with steeply rising fronts are interesting for studying high intensity effects in matter, and are the theoretical basis for some staged acceleration mechanisms.

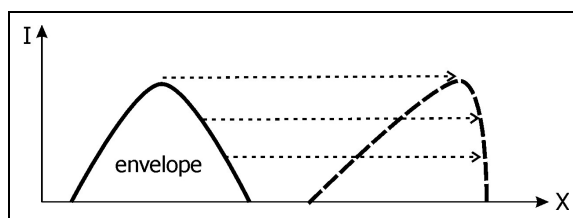


Figure 9-6: Schematic of a temporal profile steepening of the laser envelope [200].

9.2.4 Laser interactions with solids

After having made its way through the underdense plasma, the laser pulse finally reaches the critical surface, i.e. the solid target, or close to where the original target surface was (unless the preplasma is sufficiently large), producing a hot solid density plasma via collisional and collisionless absorption and heating mechanisms. As it interacts with the critical surface up to the skin depth, it couples into electrostatic and/or scattered light waves via both classical (e.g. resonance absorption and inverse Bremsstrahlung) and relativistic (e.g. vacuum and $\vec{J} \times \vec{B}$ heating) absorption processes. In this dissertation, the laser intensity is $> 10^{18}$ W/cm², therefore relativistic effects such as Brunel and $\vec{J} \times \vec{B}$ heating, are dominant.

Using the scale-length defined in the first paragraph of Section 9.2.3, one sees that, for the example of a 500-1000 ps long prepulse and a preplasma temperature of ~ 1 eV, the

preplasma can be expected to have a steep 5-10 μm scale-length; this of course requires that the laser contrast be high enough for the surface to remain unperturbed until the main pulse arrives (i.e. very good contrast). Thanks to this steep density gradient, the laser pulse can interact with a solid density plasma which has just formed: the laser energy can be deposited at much higher densities than in ns interactions (where the plasma scale-length is 100s of μm); the laser energy can then be absorbed at, or below, the critical density. In that case, an intense electromagnetic wave impinges on a highly overdense, mirror-like wall of plasma. In the simplified case where there is no absorption, a standing wave is formed in front of the target by the electromagnetic field, as well as an evanescent component penetrating into the overdense region to the collisionless skin depth $\delta = \frac{c}{\omega_p}$ [9.1.2.2.2]

[187, page 129].

9.2.4.1 Hole boring

2-D PIC simulations show [98] that a tightly focused (typically diffraction limited 2-10 μm) normally incident beam, with an intensity greater than 10^{18} W/cm^2 , can bore a hole several wavelengths deep through a moderately overdense plasma (i.e. $n_e \sim 10n_c$) on the sub-ps time-scale. At such light intensities, the pulses have a pressure greater than 10 Gbar, and drive the plasma relativistically. Hole boring results from a pressure imbalance: if the light pressure is much greater than the plasma pressure, i.e. $\frac{P_L}{P_e} \gg 1$, the plasma is pushed away

from the laser from highest intensity to lowest intensity; this results in an electrostatic bow shock, and a density discontinuity which travels into the target at constant velocity.

Any target surface deformation, such as hole boring for example, modifies the interaction geometry in such a way that the laser field may couple directly and usually more efficiently

to plasma oscillations parallel to the density gradient. If a hole or a channel is formed, Brunel-type absorption [9.2.4.4.2] may take place along the sides. The $\vec{J} \times \vec{B}$ mechanism [9.2.4.4.4] may be enhanced at the back of the hole because of additional self-focusing [9.2.3.2] of the laser light in the underdense plasma present in front of the target [187, pages 176-177].

9.2.4.2 Ion shocks

For sharp enough rise time of the laser pulse (i.e. for a steep laser envelope profile [9.2.3.6]), compared to the ion response time, the formation of an ion shock can take place. This ion shock can heat the electrons quickly. The non-oscillating component of the ponderomotive force accelerates the ions into the solid target at pressures $P_L [\text{Mbar}] = 330 \times 10^{-18} I \lambda^2$ for intensities greater than $10^{19} \text{ W} \mu\text{m}^2/\text{cm}^2$ [219]. For our laser conditions, when $I = 10^{19} \text{ W/cm}^2$, $P = 3.6 \text{ Gbar}$ and for $I = 2 \times 10^{20} \text{ W/cm}^2$, $P = 73 \text{ Gbar}$. A similar mechanism called short-pulse skin-layer laser-plasma interaction has been proposed by Badziak [220] to explain the observed ion energies from relatively low laser energies irradiating thin solid targets.

9.2.4.3 Collisional absorption: Helmholtz equations

To treat collisional absorption [187, pages 132-137], we need to use the equation of motion,

and add the collisional damping term $m \nu_{ei} \vec{v}$, i.e. $m \frac{\partial \vec{v}}{\partial t} = -e \left(\vec{E} + \frac{\vec{v}}{c} \times \vec{B} \right) - m \nu_{ei} \vec{v}$, where

ν_{ei} , the electron-ion collision frequency is given by $\nu_{ei} = \frac{4\sqrt{2\pi}}{3} \frac{n_e Z e^4}{m^2 \nu_{ie}^3} \ln \Lambda \text{ s}^{-1}$, i.e.

$\nu_{ei} \sim 2.91 \times 10^{-6} Z n_e T_e^{-3/2} \ln \Lambda \text{ Hz}$. Z is the number of free electrons per atom, n_e the electron density (in cm^{-3}), T_e is the temperature in eV and $\ln \Lambda$ is the Coulomb logarithm, accounting

for the limits b_{\min} and b_{\max} of the electron-ion scattering cross-section. These distances correspond respectively to the classical distance of closest approach and the Debye length,

in such a way that $\ln \Lambda = \frac{b_{\max}}{b_{\min}} = \lambda_D \frac{k_B T_e}{Z e^2} = \frac{9 N_D}{Z}$, with λ_D defined in Section 9.1.1.2, also

equal to $\lambda_D = \frac{v_{te}}{\omega_p}$, and N_D the number of particles contained in a Debye sphere, i.e.

$N_D = \frac{4\pi}{3} \lambda_D^3 n_e$. The binary collisions are responsible for a frictional drag on the electron

motion, which are taken into account by the collisional damping term $m \nu_{ei} \vec{v}$.

We now make use of Maxwell's equations.

Using the same method as in Section 9.1.2.1, and without assuming that $\mu_0 \vec{J} = \vec{0}$, we find

$$\nabla^2 \vec{B} = \frac{1}{c^2} \frac{\partial^2 \vec{B}}{\partial t^2} - \mu_0 \nabla \times \vec{J}.$$

Using the same method as in Section 9.1.2.2, and without assuming that $\vec{\nabla}(\vec{\nabla} \cdot \vec{E}) = 0$, we

obtain $\nabla^2 \vec{E} = \frac{1}{c^2} \frac{\partial^2 \vec{E}}{\partial t^2} + \mu_0 \frac{\partial \vec{J}}{\partial t} + \vec{\nabla}(\vec{\nabla} \cdot \vec{E})$.

As we have seen in Section 9.1.1.5, $\frac{\partial}{\partial t} \rightarrow -i\omega$ and $\vec{\nabla} \rightarrow i\vec{k}$. Also, $n_e = n_0 + n_1$,

$$\vec{J} = -n_0 e \vec{v}_e = -n_0 e \vec{v}_1, \text{ and } \vec{E}_1 = \vec{E} + \vec{v} \times \vec{B}.$$

By substitution in $m \frac{\partial \vec{v}}{\partial t} = -e \left(\vec{E} + \frac{\vec{v}}{c} \times \vec{B} \right) - m \nu_{ei} \vec{v}$, we obtain: $\vec{v}_1 = \frac{-i}{\omega + i \nu_{ei}} \frac{e}{m} \vec{E}_1$.

This immediately gives $\vec{J}_1 = \frac{i}{\omega + i \nu_{ei}} \frac{n_0 e^2}{m} \vec{E}_1 = \sigma_e \vec{E}_1$, where $\sigma_e = \epsilon_0 \frac{\omega_p^2}{\omega} \frac{i}{1 + i \tilde{\nu}_{ei}}$ is the

alternating current electrical conductivity of the plasma, and $\tilde{\nu}_{ei} = \frac{\nu_{ei}}{\omega}$.

For the electric field:

In $\nabla^2 \vec{E} = \frac{1}{c^2} \frac{\partial^2 \vec{E}}{\partial t^2} + \mu_0 \frac{\partial \vec{J}}{\partial t} + \vec{\nabla}(\vec{\nabla} \cdot \vec{E})$, replacing for the value \vec{J}_1 , and using $\frac{\partial}{\partial t} \rightarrow -i\omega$, we

$$\text{deduce } \nabla^2 \vec{E}_1 = -\frac{\omega^2}{c^2} \vec{E}_1 + \frac{\omega_p^2}{c^2} \frac{\vec{E}_1}{1+i\tilde{\nu}_{ei}} + \vec{\nabla}(\vec{\nabla} \cdot \vec{E}_1).$$

For a planar, transverse EM wave propagating in a uniform plasma, we can use $\vec{\nabla} = i\vec{k}$ and $\vec{E}_1 \perp \vec{k}$, so that $\vec{\nabla} \cdot \vec{E}_1 = 0$. In that case, the standard linear dispersion relation is obtained:

$$k^2 c^2 - \omega^2 + \omega_p^2 \frac{1}{1+i\tilde{\nu}_{ei}} = 0. \text{ The dielectric constant of the propagation medium is defined}$$

$$\text{as } \epsilon = \frac{k^2 c^2}{\omega^2} = 1 - \frac{\omega_p^2}{\omega^2} \frac{1}{1+i\tilde{\nu}_{ei}} = 1 + \frac{i\sigma_e}{\epsilon_0 \omega}. \text{ By defining a local permittivity and letting this}$$

dielectric constant vary in space, this can be generalized to a non-uniform plasma.

Now, for simplicity, consider a plasma density with a gradient in only one direction, i.e.

$$\epsilon(x) \equiv n^2(x) = 1 - \frac{n_0(x)}{n_c(x)} \frac{1}{1+i\tilde{\nu}_{ei}(x)}. \quad n(x) \text{ is the local refractive index, } n_0(x) \text{ the}$$

equilibrium electron density, and $n_c(x)$ the critical density of the EM wave.

The wave equation $\nabla^2 \vec{E} = \frac{1}{c^2} \frac{\partial^2 \vec{E}}{\partial t^2} + \mu_0 \frac{\partial \vec{J}}{\partial t} + \vec{\nabla}(\vec{\nabla} \cdot \vec{E})$ can still be simplified, even with an

inhomogeneous plasma, if one considers only a plane wave, incident at some fixed angle θ onto the plasma density gradient, as illustrated in Figure 9-7 [187, page 135]. Note that θ is *always* defined as the angle of incidence of the laser from the plasma or the target normal.

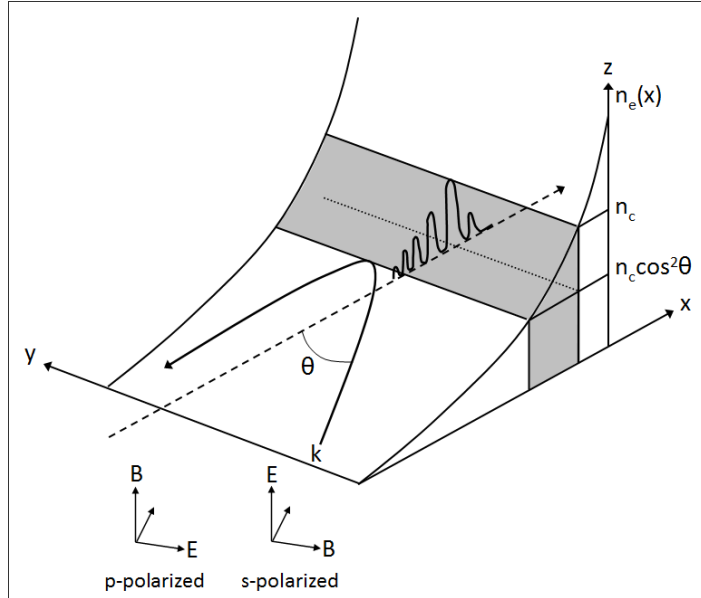


Figure 9-7: Geometry of a plane-wave, incident on a plasma density profile for both P-polarized (i.e. the E-field is in the plane of ∇n_e) and S-polarized light (i.e. the E-field is in the vertical (z) direction). When the plane wave is S-polarized, no resonance happens [187, page 135].

9.2.4.3.1 Case of an S-polarized wave

If the wave is polarized out of the propagation (x, y) plane, the plane wave has a *periodicity*

in y given by $\vec{E}_1 = (0, 0, E_z) e^{iky \sin \theta}$. The gradient operator writes as $\nabla = \left(\frac{\partial}{\partial x}, ik \sin \theta, 0 \right)$.

One can easily verify that $\vec{\nabla} \cdot \vec{E}_1 = 0$. Using the fact that $\epsilon = \epsilon(x)$, the wave equation

reduces to the Helmholtz equation for the electric field $\frac{\partial^2 E_z}{\partial x^2} + k^2(\epsilon - \sin^2 \theta)E_z = 0$. The

waves' modes are purely transverse: since $n_1 = \vec{\nabla} \cdot \vec{E}_1 = 0$, there is no coupling between an

S-polarized EM wave and electrostatic modes.

9.2.4.3.2 Case of a P-polarized wave

For a P-polarized plane wave, $\vec{E}_1 = (E_x, E_y, 0)$ and $\vec{\nabla} \cdot \vec{E}_1 \neq 0$. In that case, a component of the laser field lies along the density gradient, which is why plasma waves will be driven along the light path. To solve for B_z , we proceed as follows.

In the wave equation $\nabla^2 \vec{B} = \frac{1}{c^2} \frac{\partial^2 \vec{B}}{\partial t^2} - \mu_0 \nabla \times \vec{J}$, using $\vec{J}_1 = \sigma_e \vec{E}_1$ and $\frac{\partial}{\partial t} \rightarrow -i\omega$, we

$$\text{deduce } \nabla^2 \vec{B}_1 = \frac{(-i\omega)^2}{c^2} \vec{B}_1 - \mu_0 \nabla \times (\sigma_e \vec{E}_1), \text{ i.e. } \nabla^2 \vec{B}_1 = -\frac{\omega^2}{c^2} \vec{B}_1 - \mu_0 (\nabla \sigma_e \times \vec{E}_1 + \sigma_e \nabla \times \vec{E}_1).$$

Maxwell-Faraday equation reads $\vec{\nabla} \times \vec{E}_1 = i\omega \vec{B}_1$, and Ampere's law reads $\vec{\nabla} \times \vec{B}_1 = \mu_0 \vec{E}_1 (\sigma_e - i\omega \epsilon_0) = i\mu_0 \epsilon \vec{E}_1$, where the dielectric constant has already been introduced as $\epsilon = 1 + \frac{i\sigma_e}{\epsilon_0 \omega}$.

The wave equation becomes $\nabla^2 \vec{B}_1 + \frac{\omega^2}{c^2} \vec{B}_1 = i\nabla \sigma_e \times \left(\frac{1}{\epsilon} \vec{\nabla} \times \vec{B}_1 \right) - i\mu_0 \sigma_e \omega \vec{B}_1$, which yields to

$$\nabla^2 \vec{B}_1 + \frac{\omega^2}{c^2} \vec{B}_1 + \frac{\nabla \epsilon}{\epsilon} \times (\vec{\nabla} \times \vec{B}_1) = 0 \text{ after some developing and rearranging of the terms by}$$

Gibbon [187, page 136].

If the wave is polarized out of the propagation (x,y) plane, the plane wave has a *periodicity*

in y given by $\vec{B}_1 = (0, 0, B_z) e^{iky \sin \theta}$. The gradient operator writes as $\nabla = \left(\frac{\partial}{\partial x}, ik \sin \theta, 0 \right)$.

Using the fact that $\epsilon = \epsilon(x)$, the wave equation reduces to the Helmholtz equation for the

$$\text{magnetic field } \frac{\partial^2 B_z}{\partial x^2} - \frac{1}{\epsilon} \frac{\partial \epsilon}{\partial x} \frac{\partial B_z}{\partial x} + k^2 (\epsilon - \sin^2 \theta) B_z = 0.$$

9.2.4.3.3 Solutions of the Helmholtz equations

Three main parameters can be varied when working with collisions: the non-dimensional scale-length kL , the angle of incidence θ , and the collision frequency ν_{ei} .

Figure 9-8 [187, page 138] shows the absorption fraction for both S -polarized and P -polarized light for three different scale-lengths ($L/\lambda = 0.01, L/\lambda = 0.1$ and $L/\lambda = 1$).

The optimum absorption for P -polarized laser light occurs at an angle of incidence which increases as the density gradient steepens.

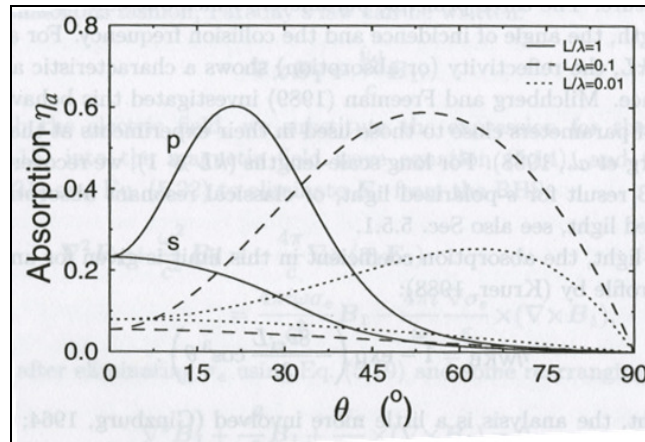


Figure 9-8: Angular absorption dependence for S -polarized and P -polarized light and for various density scale-lengths: $L/\lambda=1$ (continuous line), $L/\lambda=0.1$ (dashed line), and $L/\lambda=0.01$ (dotted line) [187, page 138].

9.2.4.3.3.1 Long non-dimensional scale-lengths: $kL \gg 1$

If the density gradient L is such that $\epsilon(x)$ varies slowly over one laser wavelength,

$$\frac{1}{L} \approx \frac{1}{\epsilon} \frac{\partial \epsilon}{\partial x} \ll k, \text{ or } kL \gg 1, \text{ then the Helmholtz equations for the electric and magnetic}$$

field can be solved in the Wentzel-Kramers-Brillouin (WKB) approximation is given, for which, for S -polarized light, yields a solution in the form of an Airy function. The absorption

$$\text{coefficient for an exponential profile is: } \eta_{WKB} = 1 - \exp\left(-\frac{8\nu_{ei}L}{3c} \cos^3 \theta\right) [189].$$

For P -polarized light, one recovers the classical resonant absorption result [9.2.4.4.1]. For moderate damping, the absorption is found to be of $\sim 60\%$ at the optimum incidence angle

given by $\theta_{opt} = \arcsin\left(0.8\left(\frac{1}{kL}\right)^{1/3}\right)$ [189].

9.2.4.3.3.2 Short non-dimensional scale-lengths: $kL \ll 1$

The Wentzel-Kramers-Brillouin (WKB) fails, and one needs to resort to solving the Helmholtz equations for the electric and magnetic field numerically, for example using a wave-solver code.

9.2.4.3.4 Inverse Bremsstrahlung absorption

In a plasma, light can be absorbed by the process of inverse Bremsstrahlung, or braking radiation. The process in which an electron interacts with a nucleus for example, decelerates, causing light to be emitted, is called Bremsstrahlung. The electron energy loss

$$-\frac{\partial\xi}{\partial x} \text{ scales with the electron energy } \xi, \text{ and the charge of the nucleus as } -\frac{\partial\xi}{\partial x} \propto \xi Z^2.$$

Inverse Bremsstrahlung on the other hand corresponds to the process in which a light wave is being absorbed by an electron, causing the electron to accelerate. The inverse Bremsstrahlung process is the main form of absorption when the plasma is dominated by collisions [221]. When absorption is resonant, a plasma wave is excited. This plasma wave can decay (or be damped), and as a result, the bulk temperature of the plasma increases.

9.2.4.3.5 Collisional damping

For a planar, transverse EM wave propagating in a uniform plasma, we obtained the

standard linear dispersion relation $k^2c^2 - \omega^2 + \omega_p^2 \frac{1}{1 + i \frac{v_{ei}}{\omega}} = 0$. Assuming that $\frac{v_{ei}}{\omega}$ is very

small, the dispersion relation approximates to $k^2c^2 - \omega^2 + \omega_p^2 \left(1 - i \frac{v_{ei}}{\omega}\right) = 0$, i.e.

$\omega^2 = k^2c^2 + \omega_p^2 \left(1 - i \frac{v_{ei}}{\omega}\right)$. To find the damping rate Δ_{col} , we assume that ω writes as a

real term and an imaginary term, i.e. $\omega = \omega_{\Re} - \frac{i\Delta_{col}}{2}$. After some calculations and

simplifications by Gibbon [189, page 48], this yields to $\omega_{\Re} = \sqrt{k^2c^2 + \omega_p^2}$ and

$\Delta_{col} = \left(\frac{\omega_p}{\omega_{\Re}}\right)^2 v_{ei}$. The rate of damping of the electromagnetic wave $\frac{\Delta_{col} E^2}{8\pi}$ (in CGS units)

is balanced by the increase of the plasma temperature, because of the collision rate.

Another method to find the damping rate Δ_{col} also consists of equating the damping of the

electrostatic wave with the energy dissipated by the electron-ion collision, i.e.

$\frac{\Delta_{col} E^2}{8\pi} = v_{ei} \frac{nmv_{\omega}}{2}$, where n is the plasma density, $v_{\omega} = \frac{eE}{m\omega}$ and ω is the electrostatic

field frequency. This yields $\Delta_{col} = \frac{\omega_p^2}{\omega^2} v_{ei}$, and if $\omega_p \approx \omega$ then we have simply $\Delta_{col} \approx v_{ei}$.

9.2.4.4 Collisionless absorption

There are many absorption mechanisms which do not rely on collisions between ions and

electrons. These collisionless processes couple laser energy directly to the plasma. In this

section, we are looking at the following mechanisms: resonance absorption, Brunel heating, relativistic $\vec{J} \times \vec{B}$ heating, anomalous skin effect, and sheath inverse Bremsstrahlung.

9.2.4.4.1 P-polarized obliquely incident light wave: Resonance absorption

Resonance absorption is probably the best known of these collisionless absorption mechanisms. It has been studied extensively in the 1970s and 1980s with 2-D PIC codes, to understand where the electrons originate from in nanosecond scale laser plasma interactions [189, 222, 223, 224, 225].

Resonance absorption occurs at a plasma-vacuum gradient boundary for an obliquely incident P-polarized laser beam. This P-polarized light wave tunnels through a monotonically increasing density profile (as illustrated in Figure 9-9, it is only a function of z) up to the critical surface ($n_e = n_c$), where it drives up a plasma wave, which grows over a few laser periods, but eventually is damped, either by collisions at low intensities, or by wave breaking as well as particle trapping at high intensities [189]. Resonance absorption is not efficient for very steep density gradients, as illustrated in Figure 9-8.

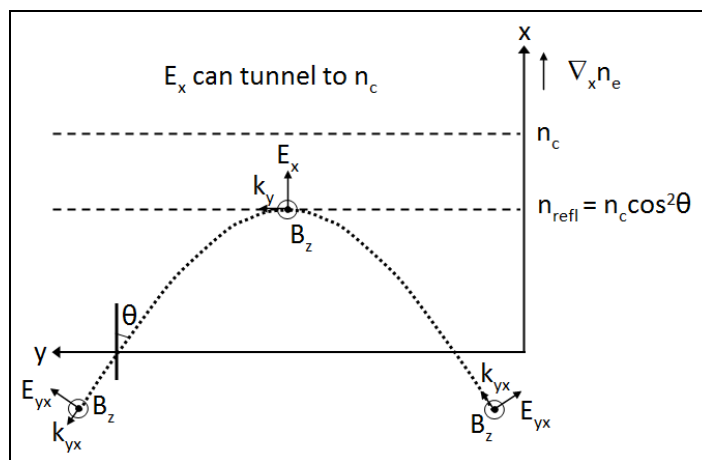


Figure 9-9: Diagram of the resonant absorption process: a P-polarized laser wave propagating at oblique incidence into a monotonically increasing inhomogeneous plasma, showing that the effective critical surface is reduced by a factor $\cos^2\theta$; the E_x field can tunnel to n_c [11].

In this process the beam is reflected from a density lower than the critical density. Since

$\omega_p = \omega_p(y, k_x)$, and k_x must be conserved, $k_x = \frac{\omega}{c} \sin \theta$, where θ is the angle of

incidence. At the reflection point, i.e. when the density is equal to n_{refl} ,

$\vec{k}(n_{refl}) = k_x \vec{x} = \vec{x} \frac{\omega_0}{c} \sin \theta$, i.e. $\omega_0 = \frac{k_x c}{\sin \theta}$. Using $\eta(n_{refl}) = \left(\frac{k_x c}{\omega_0} \right)^2$ and $1 - \eta = \frac{\omega_p^2}{\omega^2}$, we find

$\eta(n_{refl}) = \sin^2 \theta = 1 - \frac{\omega_p^2(n_{refl})}{\omega_0^2}$, i.e. $\cos^2 \theta = \frac{\omega_p^2(n_{refl})}{\omega_0^2}$. Since, $\omega_0 = \omega_p(n_c)$, we obtain

$\cos^2 \theta = \frac{\omega_p^2(n_{refl})}{\omega_p^2(n_c)}$. Finally, using the fact that $n(\omega) = \frac{m_e \cdot \epsilon_0}{e^2} \omega^2$, we obtain the

result $n_{refl} = n_c \cos^2 \theta$.

In Figure 9-9, one can see that at the apex of the laser's trajectory, i.e. for $n = n_{refl}$, the direction of the electric field of the laser is normal to the reflection surface and to the critical surface.

Even though the laser is reflected before the critical surface, the electric field is still able to drive a plasma wave resonantly at the critical surface, by tunneling from the reflected region to the critical region.

The energy absorption and angle for maximum energy absorption are calculated in [189].

The energy absorption is given by $\Xi_{abs_resonant} \approx \frac{\omega L E_d^2}{8}$, where L is the plasma density

scale-length, and $E_d = E_0 \sqrt{\frac{c}{2\pi\omega}} \phi(\vartheta)$ is the electric field of the laser evaluated at the

reflection point. $\vartheta = \left(\frac{\omega L}{c} \right)^{1/3} \sin \theta$ and $\phi(\vartheta) \approx 2.3 \vartheta \exp\left(-\frac{2\vartheta^3}{3}\right)$. In particular,

$$\begin{cases} \phi(\vartheta = 0) = 0 \\ \phi(\vartheta \approx 0.8) = 1.3. \text{ Assuming a linear density profile, the angle for peak absorption is given} \\ \phi(\vartheta > 2) = 0 \end{cases}$$

$$\text{by } \theta_{opt} = \arcsin\left(0.8\left(\frac{c}{\omega L}\right)^{1/3}\right).$$

Resonance absorption can be enhanced locally if the surface is rippled [226, 227] or hole boring takes place, since in those cases, more components of the E-field can participate in the effect. Resonance absorption is dominant when large scale-lengths, i.e. when poor contrast exist, and absorption can reach upwards to 60 % at optimum conditions. The high noise level on the Cu K α imager diagnostic caused by high energy Bremsstrahlung and crystal florescence, and occurring at intrinsic contrast is a direct evidence of these fast electrons. At enhanced contrast however, enhanced heating occurs while much less noise is detected: this suggests that other heating mechanisms most likely dominate for the cone targets at enhanced contrast irradiation.

9.2.4.4.2 S-polarized obliquely incident light wave

Resonance absorption does not occur for obliquely incident S-polarized light because the electric field is always parallel to the critical surface. However, the reflections conditions are the same as in the case of the P-polarized obliquely incident light wave, i.e.

$$n_e = n_c \cos^2 \theta.$$

Although, Gaussian beam focusing effects will allow for some component of the electric field along the gradient even for S-polarization. A rippled surface or hole boring would have a similar effect for S-polarization as for P-polarization, since now components of the S-polarized field could be normal to the plasma's critical surface, and this could look very

much like the *P*-polarized resonance case. Also, for high intensity pulses, the ponderomotive force can accelerate electrons directly as well.

9.2.4.4.3 “Not-so-resonant”, Resonant absorption, Brunel heating or Vacuum heating

As indicated in Figure 9-8 [11], in sharp-edge gradient profiles, due to ultra-high contrast, or profile steepening and hole boring, resonance absorption ceases to work in its usual form.

Considering a resonantly driven plasma wave, at the critical density, with a field amplitude E_p , in a very steep gradient, E_p will end up being roughly the same as the incident laser field E_L . Thus, electrons will undergo oscillations along the density gradient with an amplitude

$$x_p \approx \frac{eE_L}{m_e \omega^2} = \frac{v_{osc}}{\omega} \quad (\text{note that } v_{\perp} \approx 2v_{osc} \sin \theta). \quad \text{The resonance breaks down if this}$$

amplitude is greater than the density scale-length L , i.e. if $\frac{v_{osc}}{\omega} > L$, because the plasma

wave length is longer than the plasma scale-length [187, page 156]. So in summary, when

the excursion length of the electron $v_{osc} = \frac{eE_L}{m_e \omega_L}$ is smaller than L , i.e. $\frac{v_{osc}}{L} < 1$, the

absorption mainly happens at the resonant surface, and when $\frac{v_{osc}}{L} > 1$, Brunel heating is

predominant. Also, the electrons that are present near the edge of an abrupt change in the

plasma-vacuum interface are directly exposed to the laser field: a thermal electron reaching the edge at the appropriate time in the laser cycle may be dragged out strongly into the

vacuum well beyond the thermal Debye sheath $\lambda_D = \frac{v_{te}}{\omega_p}$. As the field changes direction,

the same electron will be turned around and accelerated back into the plasma. Because the

plasma is highly overdense, the electric field only penetrates up to the skin depth

$\sim \lambda_D = \frac{c}{\omega_p}$, such that the electron can travel virtually unimpeded into the target, in which

it is eventually absorbed via collisions.

First described by Brunel [228], for two counter propagating lasers, the “not-so-resonant, resonant absorption” process can be extended for a single pulse, and is illustrated in Figure 9-10 [11]. The Brunel heating mechanism can absorb energy into a plasma via a surface which is non-resonant with the laser frequency. It is most efficient at a sharp gradient or a discontinuity, which is at the critical density or higher. Just like resonant absorption, it depends on the polarization of the incoming light, namely it only takes place for obliquely incident *P*-polarized light propagating onto an overdense plasma surface from the vacuum, but as in other absorption cases, hole boring or plasma rippling can allow this process for *S*-polarized light as well. In each half-cycle, or for every half-period, the plasma surface normal component of laser electric field pointing into the plasma switches to pointing away from it. Thus, the electrons present on the plasma surface see an E-field which changes sign at a frequency $2\omega_{\perp}$ modified by the incident angle θ to give $2\omega_{\perp} = 2\omega_0 \cos \theta$ (and $E_x = E_L \cos \theta$; in Figure 9-10, $E_L = E_{xy}$). Every $T_{\perp} = \frac{1}{\omega_{\perp}}$, the surface electrons are pulled into the vacuum (during the first-half of the cycle) and then accelerated back into the plasma (during the second-half of the cycle). Near the vertical *y*-axis, i.e. against the plasma surface, \vec{k} is only in the *x* direction, the electric field is indicated by the E_x and $-E_x$ arrows, and the magnetic field is null (because, for simplicity, the assumption [228] is made that the two *P*-polarized light waves are incident on the target at opposite and equal angles, θ and $\pi/2 + \theta$, cancelling out the effect of the B-field).

The electron trajectories are color coded: the darker trajectories (red) correspond to the first generation of electrons, and the lighter trajectories (light purple) correspond to the second generation of electrons. The yellow trajectory shows the electrons which are trapped on the vacuum side. Each cycle, $N = \frac{\epsilon E_x}{e}$ is the maximum number of electrons that can be pulled out into the vacuum.

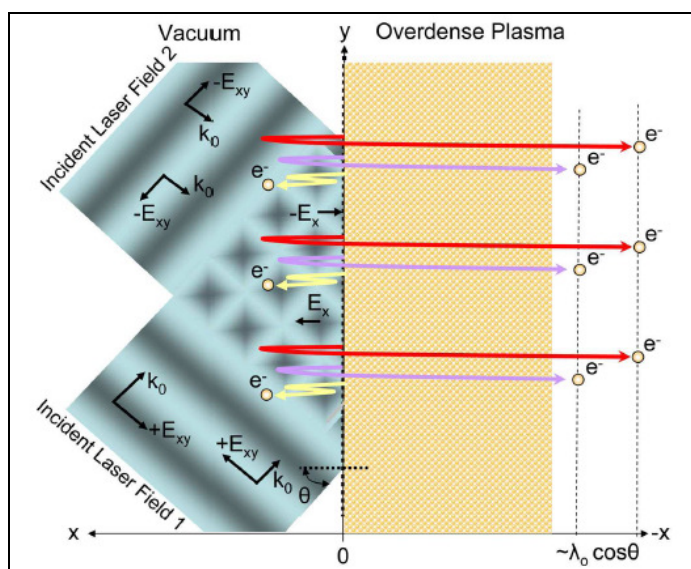


Figure 9-10: Brunel absorption process; the incident laser field E_L corresponds to E_{xy} . [11].

In simulations [228], it is shown that up to 66 % of the electrons accelerated into the vacuum each cycle can penetrate back into the overdense plasma, and escape the laser's influence taking laser energy with them, which is then available to heat the plasma. In the extreme case, the laser can accelerate a skin depth worth of electrons into the plasma. This process could also cause a recession of the electron-plasma interface and expose ions to a charge separation induced electric field at the vacuum interface, accelerating the ions into the target.

The energy absorbed is given by $\Xi_{abs_Brunel} = \frac{\eta}{2\pi} \frac{v_{\perp}}{8\pi} E_x^2 \approx \frac{\eta}{2\pi} \frac{v_{osc}}{4\pi} \frac{\sin \theta}{4\pi} E_x^2$ in CGS units,

where $\frac{\eta}{2\pi} \approx 0.25$ is obtained via numerical integration [228].

In [187, pages 158-159], the fractional absorption η_B (from the simplified capacitive Brunel model) is given by $\eta_B = \frac{4a_0}{\pi} \tan \theta \sin^2 \theta$, where $a_0 = \frac{v_{osc}}{c}$, which shows that the fractional absorption becomes greater at higher intensities and larger angles of incidence.

The Brunel absorption [228] with relativistic correction η_a is given by

$$\eta_a = \frac{f}{\pi a_0} \left(\sqrt{1 + (f a_0 \sin \theta)^2} - 1 \right) \tan \theta, \text{ where } f = 1 + \sqrt{1 - \eta_a}$$

is the laser electric field amplification factor. From these two equations which both depend on η_a and f , we obtain

$$1 - (f - 1)^2 = \frac{f}{\pi a_0} \left(\sqrt{1 + (f a_0 \sin \theta)^2} - 1 \right) \tan \theta.$$

It can be rewritten as $f = 2 - \alpha \left(\sqrt{1 + \beta f^2} - 1 \right)$, where $\alpha = \frac{1}{\pi a_0} \tan \theta$ and $\beta = (a_0 \sin \theta)^2$.

Solving for f , we find $f = \frac{-\alpha - 2 \pm \sqrt{(\alpha + 2)^2 + 4(\alpha^2 \beta - 1)(\alpha + 1)}}{\alpha^2 \beta - 1}$. The physically

meaningful solution is $f = \frac{-\alpha - 2 + \sqrt{(\alpha + 2)^2 + 4(\alpha^2 \beta - 1)(\alpha + 1)}}{\alpha^2 \beta - 1}$, which takes values

between 1 and 2 [229].

In [97], PIC simulations show that there is a complex transition between resonant absorption and Brunel heating, depending on the laser intensity and the plasma scale-length ($L/\lambda=0.1$ and $L/\lambda=0.04$), as illustrated in Figure 9-11 (left) [187, Figure 5-14, pages 161-162]. For high intensities (10^{18} W/cm²) and short scale-lengths ($L/\lambda=0.1$ and $L/\lambda=0.04$), the

absorption saturates at ~ 10-15 %. For intermediate values of intensities (10^{16} W/cm²) and the $L/\lambda=0.1$ scale-length, the absorption reaches up to 70 %. For low values of intensities (10^{15} W/cm²) and the $L/\lambda=0.04$ scale-length, the absorption reaches up to 60 %. Figure 9-11 (left, solid black line and right, all curves) shows plots of the function

$$\eta_a = \frac{f}{\pi\alpha_0} \left(\sqrt{1 + (fa_0 \sin \theta)^2} - 1 \right) \tan \theta, \text{ where } f = \frac{-\alpha - 2 + \sqrt{(\alpha + 2)^2 + 4(\alpha^2 \beta - 1)(\alpha + 1)}}{\alpha^2 \beta - 1},$$

which gives the amount of absorption as a function of the incidence angle. The Brunel model suggests very high absorption for strongly relativistic intensities, but it should be applied cautiously because of the over-simplifications mentioned in the next paragraph [230].

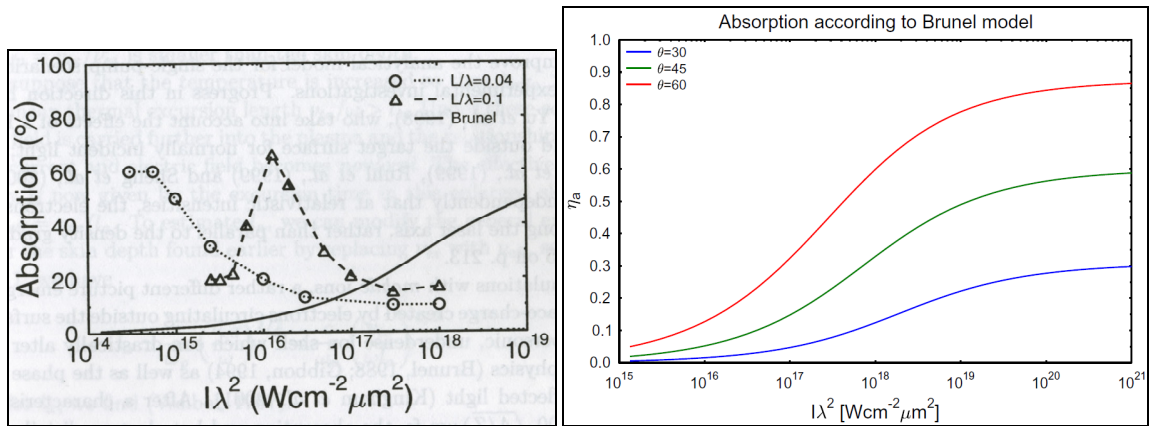


Figure 9-11: Percentage of absorption as a function of laser intensity for the Brunel heating case (left) for $\theta = 45^\circ$ [187, Figure 5-14, pages 161-162] (right) for $\theta = 30^\circ, 45^\circ,$ and 60° [229].

Figure 9-11 (left) therefore implicates that the PIC simulations show that absorption is enhanced for a higher contrast laser when the intensity goes down. In the low-intensity regime, one goes through different absorption regimes depending on the preplasma scale-length, and the peaks in the absorption correspond somehow to transitions between resonance absorption and vacuum heating (i.e. Brunel mechanism) [229]. Still looking at Figure 9-11 (left), there are probably several factors contributing to the discrepancy between the Brunel model and the PIC simulations [229]. First, the PIC simulations contain

more physics than the Brunel model. The latter is a simple electrostatic 'capacitor' approximation, which also assumes that the charge distribution in the target 'resets' itself each laser cycle. By contrast, the PIC simulations were fully electromagnetic, containing both the laser electric and magnetic fields and induced 'DC' fields in the target. These 'DC' fields are produced when charges and currents are circulating on the target surface, and can influence the behavior of the charge dynamics ultimately responsible for the absorption. Second, the parameters in those particular PIC simulations are not appropriate for modeling solid-density plasmas - the density used was just a few times critical instead of the more realistic 100–200 n_c . One would expect a better agreement for high-density, step-profile targets for intensity above 10^{18} W/cm² (this would require re-examining).

9.2.4.4.4 Relativistic $J \times B$ (or $v \times B$) heating

Since $\vec{J} = -n_0 e \vec{v}_e$, the result of the $\vec{J} \times \vec{B}$ heating can be described identically as the result of the $\vec{v} \times \vec{B}$ heating. The $\vec{J} \times \vec{B}$ heating mechanism is illustrated in Figure 9-12 [11]. A P -polarized laser normally incident onto an overdense plasma surface accelerates the electrons in the y -direction. They then experience a $\vec{v} \times \vec{B}$ force which attracts them back into the plasma. This takes place twice during each laser cycle ω . The white arrows inside the red loops of one of the electron trajectories point in the direction of the $\vec{v} \times \vec{B}$ force. Again, the electron trajectories are color coded: the first generation of electrons is represented in red (dark) and the second generation in lavender (light). The red trajectory at the very bottom shows an electron trapped inside the vacuum, and which cannot make it back into the plasma.

Whether the electrons are accelerated by the laser field in the y direction or have an initial thermal velocity in the x direction, once they leave the vacuum plasma interface, most of them will be forced back into the plasma due to the $\vec{J} \times \vec{B}$ force.

The $\vec{J} \times \vec{B}$ heating mechanism is physically very similar to the Brunel mechanism, because the electrons are directly accelerated by a laser field incident on a step-like density profile; the main difference between these two mechanisms is the fact that the driving term is the high frequency $\vec{v} \times \vec{B}$ component of the Lorentz force which oscillates at twice the laser frequency [187, page 166].

Brunel and $\vec{J} \times \vec{B}$ heating occur simultaneously when a laser is obliquely incident, and are sometimes indistinctively called “vacuum heating”, since they both require a sharp vacuum plasma interface.

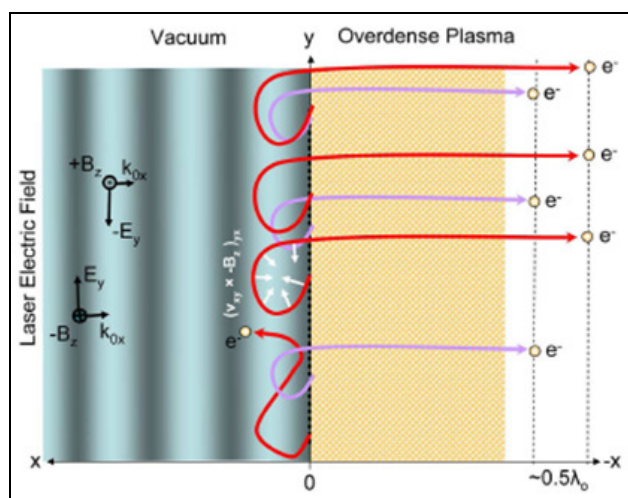


Figure 9-12: $J \times B$ heating mechanism [11].

The $\vec{J} \times \vec{B}$ heating mechanism happens at any polarization except circular. It dominates the absorption physics at relativistic intensities, becomes larger for larger laser intensities [231], and originates from the oscillating component of the ponderomotive force at normal incidence, which are derived in [231] using a sinusoidal electric field of the form

$\vec{E} = E_L(x)\sin(\omega_0 t)\hat{y}$. Using $v_L = \frac{eE_L}{m\omega_0}$, the ponderomotive force reads

$f = -\frac{m}{4} \frac{\partial}{\partial x} v_L^2(x)(1 - \cos(2\omega_0 t))\hat{x}$, which can be seen as a time averaged force causing

profile steepening [9.2.3.5] and an oscillatory part causing electron heating, this expression can be rewritten as an electrostatic potential yielding an equivalent electric field of the form

$$\frac{eE_d}{m} = \frac{1}{4} \frac{\partial}{\partial x} v_L^2(x)(1 - \cos(2\omega_0 t)), \text{ which is estimated to be } \frac{eE_d}{m} \approx 0.6 \frac{(v_{osc})^{1.8}}{(v_{th})^{0.2}} \frac{\omega_0}{c}, \text{ and}$$

simulations at 10^{18} W/cm², 100 n_c, and at an initial temperature of 4 keV show 11 % laser energy absorption into the plasma. Another simulation in [232] finds the maximum energy absorption to take place for an angle of incidence of 35°, which clearly shows that this cannot be only one mechanism, since the maximum absorption for the $\vec{J} \times \vec{B}$ mechanism should be at 0° (i.e. normal laser incidence); therefore, it must be a combination of heating mechanisms.

9.2.4.4.5 Anomalous skin effect and Sheath inverse Bremsstrahlung

The absorption from both these mechanisms becomes larger when switching from normal incidence to oblique incidence, and is more prominent for *P*-polarized light.

Both the anomalous skin effect and the sheath inverse Bremsstrahlung mechanisms are complementary to the Brunel's vacuum heating effect discussed in [9.2.4.4.3], in that they

are important for steep gradients $\frac{L}{\lambda} \ll 1$, when the light pressure P_L is less than the

plasma pressure P_e . Quantitatively, this implies that $\left(\frac{v_{osc}}{v_{te}}\right)^2 < \frac{n_e}{n_c}$, or that $\frac{P_L}{P_e} = \frac{2I_0}{cn_e k_B T_e}$,

i.e. $\frac{P_L}{P_e} \approx \frac{660I_{18}}{160n_{23}T_{keV}} < 1$. As this threshold is crossed, a transition from *sheath inverse*

Bremsstrahlung / Anomalous skin effect to resonance absorption / vacuum heating can be expected [187, page 165].

9.2.4.4.5.1 *Anomalous skin effect*

The anomalous skin effect mechanism is closely related to vacuum heating. It occurs when

$\omega_p^2 v^2 \approx \omega^2 c^2$ [233, 234]. The electrons present within the skin layer $l_s = \frac{c}{\omega_p}$ oscillate in

the laser field and dissipate energy through collisions with ions (via inverse Bremsstrahlung [9.2.4.3.4]). The oscillation energy is thus locally thermalized, at the condition that the

electron mean free path $\lambda_{MFP} = \frac{v_{te}}{v_{ei}}$ be smaller than the skin depth.

The absorption rate is given by $\eta_{anomalous_skin_effect} = \frac{8\omega l_a}{3\sqrt{3}c} \approx \left(\sqrt{\frac{T_e}{511\text{keV}}} \frac{n_c}{n_e} \right)^{1/3}$, where

$l_a = \left(\sqrt{\frac{2}{\pi}} \frac{c^2 v_{te}}{\omega \omega_p^2} \right)^{1/3}$ is the anomalous skin depth and v_{te} the thermal collision rate [187,

pages 163-164, 233, 235].

The maximum absorption for *P*-polarized light is nominally $\eta_{anomalous_skin_effect} \approx \frac{2}{3}$ at

grazing incident angles independent of density and temperature, but can be enhanced further if the distribution function is anisotropic.

9.2.4.4.5.2 **Sheath inverse Bremsstrahlung**

When $\omega_p^2 v^2 \ll \omega^2 c^2$, sheath inverse Bremsstrahlung occurs. Unlike in the anomalous skin effect regime, the electron transit time through the skin depth is *longer* than a plasma period. The energy transfer happens through a series of irreversible kicks received by the

electrons from the laser field, as they are turned around at the plasma-vacuum interface, which is where the analogy with inverse Bremsstrahlung [9.2.4.3.4] for small $\frac{v_{osc}}{c}$ comes from [187, page 164].

9.2.4.4.6 Landau damping

Collisional damping, also known as Landau damping, is a process in which the electron plasma wave (EPW) can exchange energy with resonant electrons that are not part of the EPW. Resonant electrons are electrons which happen to travel at a velocity near the EPW's phase velocity. The hot background electrons can surf on the EPW's electrostatic potential and either give energy to the wave, or gain energy from it. This energy exchange between the near-resonant or resonant electrons and the EPW turns the electrostatic wave energy into thermal energy, due to the fact that the Maxwellian distribution of all electrons has more particles with low energy than high energy. This is why in fact, the EPW loses more energy accelerating low energy electrons than it gains energy when high energy electrons decelerate. In the end, the EPW is damped, and the damping rate is given in [189] as

$$\Gamma_{Landau} = -\sqrt{\frac{\pi}{8}} \frac{(\omega_p \omega)^2}{(|k|v_e)^3} \exp\left(-\frac{\omega^3}{2(|k|v_e)^2}\right) \text{ in CGS units.}$$

10 REFERENCES

-
- 1 K. A. Flippo, E. d'Humières, S. A. Gaillard, J. Rassuchine, D. C. Gautier, M. Schollmeier, F. Nürnberg, J. L. Kline, J. Adams, B. Albright, M. Bakeman, K. Harres, R. P. Johnson, G. Korgan, S. Letzring, S. Malekos, N. Renard-Le Galloudec, Y. Sentoku, T. Shimada, M. Roth, T. E. Cowan, J. C. Fernández, and B. M. Hegelich, **Increased Efficiency of Short-Pulse Laser Generated Proton Beams from Novel Flat-Top Cone Targets**, *Physics of Plasmas* (Invited) **15**, 5 (2008).
- 2 S. A. Gaillard, K. A. Flippo, M. E. Lowenstern, J. E. Mucino, J. M. Rassuchine, D. C. Gautier, J. Workman, and T. E. Cowan, **Proton acceleration from ultra high-intensity short-pulse laser-matter interactions with Cu micro-cone targets at the intrinsic $\sim 10^{-8}$ contrast**, submitted to *Journal of Physics Conference Series* (JPCS) (2009).
- 3 J. Rassuchine, E. d'Humières, S. D. Baton, P. Guillou, M. Koenig, M. Chahid, F. Pérez, J. Fuchs, P. Audebert, R. Kodama, M. Nakatsutsumi, N. Ozaki, D. Batani, A. Morace, R. Redaelli, L. Grémillet, C. Rousseaux, F. Dorchies, C. Fourment, J. J. Santos, J. Adams, G. Korgan, S. Malekos, S. B. Hansen, R. Shepherd, K. Flippo, S. Gaillard, Y. Sentoku, and T. E. Cowan, **Enhanced hot electron localization and heating in high-contrast ultra-intense laser irradiation of sharp micro-cone targets**, *Physical Review E* **79**, 0364408 (2009).
- 4 S. D. Baton, M. Koenig, J. Fuchs, A. Benuzzi-Mounaix, P. Guillou, B. Loupiau, T. Vinci, L. Grémillet, C. Rousseaux, M. Drouin, E. Lefebvre, F. Dorchies, C. Fourment, J. J. Santos, D. Batani, A. Morace, R. Redaelli, M. Nakatsutsumi, R. Kodama, A. Nishida, N. Ozaki, T. Norimatsu, Y. Aglitskiy, S. Atzeni, and A. Schiavi, **Inhibition of fast electron energy deposition due to preplasma filling of cone-attached targets**, *Physics of Plasmas* **15**, 042706 (2008).
- 5 S. A. Gaillard, T. Kluge, K. A. Flippo, B. Gall, T. Lockard, M. Schollmeier, M. Geissel, D. T. Offermann, J. M. Rassuchine, D. C. Gautier, E. d'Humières, M. Bussmann, Y. Sentoku, and T. E. Cowan, **Increased proton energies up to 67.5 MeV from high-contrast high-intensity short-pulse laser-interactions with micro-cone targets**, in preparation (2010).
- 6 (a) R. Snavely, M. Key, S. Hatchett, T. Cowan, M. Roth, T. Phillips, M. Stoyer, E. Henry, T. Sangser, M. Singh, S. Wilks, A. Mackinnon, A. Offenberger, D. Pennington, K. Yasuike, A. Langdon, B. Lasinski, J. Johnson, M. Perry, and E. Campbell, **Intense high-energy proton beams from petawatt-laser irradiation of solids**, *Physical Review Letters* **85**, 2945 (2000).
- (b) S. P. Hatchett, C. G. Brown, T. E. Cowan, E. A. Henry, J. S. Johnson, M. H. Key, J. A. Koch, A. B. Langdon, B. F. Lasinski, R. W. Lee, A. J. Mackinnon, D. M. Pennington, M. D. Perry, T. W. Phillips, M. Roth, T. C. Sangster, M. S. Singh, R. A. Snavely, M. A. Stoyer, S. C. Wilks, and K. Yasuike, **Electron, photon, and ion beams from the relativistic interaction of petawatt laser pulses with solid targets**, *Physics of Plasmas* **7**, 2076 (2000).
- 7 E. L. Clark, M. Zepf, M. Tatarakis, C. Escoda, M. Norrefeldt, A. E. Dangor, K. Krushelnick, R. J. Clarke, P. A. Norreys, I. Spencer, and K. W. D. Ledingham, **Energetic proton generation and plasma jet formation from ultra-intense laser plasma interactions with solids**, *Central Laser Facility Annual Report* (1999/2000).
- E. L. Clark, K. Krushelnick, J. R. Davies, M. Zepf, M. Tatarakis, F. Beg, A. Machacek, P. A. Norreys, M. I. K. Santala, I. Watts, and A. E. Dangor, **Measurement of energetic proton transport through magnetized plasma from intense laser interactions with solids**, *Physical Review Letters* **84**, pp. 670-674 (2000).

8 A. Maksimchuk, S. Gu, K. Flippo, and D. Umstadter, **Forward ion acceleration in thin films driven by a high-intensity laser**, *Physical Review Letters* **84**, 4108 (2000).

K. Flippo, A. Maksimchuk, S. Banerjee, V. Wong, K. Nemoto, V. Y. Bychenkov, G. Mourou, and D. Umstadter, **Multi-MeV ion beams from terawatt laser thin-foil interactions**, Proceedings of the 2001 *Particle Accelerator Conference*, P. Lucas and S. Webber, eds. (IEEE, Piscataway,NJ) **3**, pp. 2081–2083 (2001).

A. Maksimchuk, K. Flippo, H. Krause, G. Mourou, K. Nemoto, D. Shultz, D. Umstadter, R. Vane, V. Yu. Bychenkov, G. I. Dudnikova, V. F. Kovalev, K. Mima, V. N. Novikov, Y. Sentoku, and S. V. Tolokonnikov, **High-energy ion generation by short laser pulses**, *Plasma Physics Reports* **30**, 473 (2004).

9 Kirk Flippo, Teresa Bartal, Farhat Beg, Sugreev Chawla, Jim Cobble, Sandrine Gaillard, Daniel Hey, Andrew MacKinnon, Andrew MacPhee, Phillip Nilson, Dustin Offermann, Sébastien Le Pape, and Mark J. Schmitt, **Omega EP, Laser Scalings and the 60 MeV Barrier: First Observations of Ion Acceleration Performance in the 10 Picosecond Kilojoule Short-Pulse Regime**, submitted to *Journal of Physics Conference Series (JPCS)* (2009).

10 J. Fuchs, Y. Sentoku, S. Karsch, J. Cobble, P. Audebert, A. Kemp, A. Nikroo, P. Antici, E. Brambrink, A. Blažević, E.M. Campbell, J.C. Fernández, J.-C. Gauthier, M. Geissel, M. Hegelich, H. Pépin, H. Popescu, N. Renard-Le Galloudec, M. Roth, J. Schreiber, R. Stephens, and T.E. Cowan, **Comparison of laser ion acceleration from the front and rear surfaces of thin foils**, *Physical Review Letters* **94** (2005).

11 Kirk Flippo, **Ion beam generation from high-intensity-laser dense-plasma interactions and applications**, *PhD Dissertation, University of Michigan* (2004).

12 S. Wilks, A. Langdon, T. Cowan, M. Roth, M. Singh, S. Hatchett, M. Key, D. Pennington, A. MacKinnon, and R. Snavely, **Energetic proton generation in ultra-intense laser-solid interactions**, *Physics of Plasmas* **8**, 542 (2001).

13 T.E. Cowan, J. Fuchs, H. Ruhl, A. Kemp, P. Audebert, M. Roth, R. Stephens, I. Barton, A. Blažević, E. Brambrink, J. Cobble, J. Fernández, J.-C. Gauthier, M. Geissel, M. Hegelich, J. Kaæ, S. Karsch, G.P. Le Sage, S. Letzring, M. Manclossi, S. Meyroneinc, A. Newkirk, H. Pépin, and N. Renard-Le Galloudec **Ultralow emittance, multi-MeV proton beams from a laser virtual-cathode plasma accelerator**, *Physical Review Letters* **92** (2004).

14 F. Nürnberg, M. Schollmeier, K. Harres, A. Blažević, P. Audebert, E. Brambrink, D. C. Carroll, K. Flippo, D. C. Gautier, B. M. Hegelich, O. Lundh, K. Markey, P. McKenna, D. Neely, and M. Roth, **RadioChromic film imaging spectroscopy**, *Review of Scientific Instruments* **80**, 033301 (2007).

15 M. Roth, T. Cowan, M. Key, S. Hatchett, C. Brown, W. Fountain, J. Johnson, D. Pennington, R. Snavely, S. Wilks, K. Yasuike, H. Ruhl, F. Pegoraro, S. Bulanov, E. Campbell, M. D. Perry, and H. Powell, **Fast ignition by intense laser-accelerated proton beams**, *Physical Review Letters* **86**, 436 (2001).

16 M. Temporal, J. J. Honrubia, and S. Atzeni, **Numerical study of fast ignition of ablatively imploded deuterium-tritium fusion capsules by ultra-intense proton beams**, *Physics of Plasmas* **9**, 3098 (2002).

17 K. A. Flippo, J. Workman, D. C. Gautier, R. P. Johnson, and T. Shimada, **Scaling Laws for energetic ions from the commissioning of the new LANL 200 TW Trident Laser**, *Review of Scientific Instruments* **79**, 10E534 (2008).

18 <http://www.extreme-light-infrastructure.eu/Hadron-therapy-for-cancer-treatment>

<http://www.proton-therapy.org/patientdemand.htm>

19 <http://www.nupec.org/iai2001/report/B32.pdf> : Report by U. Amaldi, **Hadron-therapy in the world**.

-
- U. Amaldi and G. Kraft, **Hadrontherapy: cancer treatment with proton and carbon beams**, Springer Science + business Media B.V. (2009).
- G. Kraft, **Heavy ion tumor therapy: from the scientific principles to the clinical routine**, *Nuclear Physics News* **17**, 29 (2007).
- 20 U. Linz and J. Alonso, **What will it take for laser driven proton accelerators to be applied to tumor therapy?**, *Physics Review Special Topics – Accelerator and Beams*, **10** 094801 (2007).
- 21 R. R. Wilson, **Radiological Use of Fast Protons**, *Radiology* **47**, 487 (1946).
- 22 http://www.gsi.de/portrait/Broschueren/Therapie/Krebstherapie_e.html
- 23 http://www.nirs.go.jp/ENG/research/charged_particle/index.shtml
- 24 <http://www.protons.com/>
- 25 http://www.nirs.go.jp/ENG/research/charged_particle/index.shtml
- 26 J. O. Archambeau, G. W. Bennett, G. S. Levine, R. Cowen, and A. Akanuma, **Proton Radiation Therapy**, *Radiology* **110**, 445 (1974).
- 27 M. R. Raju, **Proton Radiobiology, Radiosurgery and Radiotherapy**, *International Journal of Radiation and Biology* **67**, 237 (1995).
- 28 S. V. Bulanov and V. S. Khoroshkov, **Feasibility of using laser ion accelerators in proton therapy**, *Plasma Physics Reports* **28**, 453, pp. 493-496 (2002).
- 29 R. Becker, **Modern options for hadron therapy of tumors**, *Review of Scientific Instruments* **77**, 03A903 (2006).
- 30 K. W. D. Ledingham, W. Galster, and R. Sauerbrey, **Laser-driven proton oncology – a unique new cancer therapy?**, *British Journal of Radiology* **80**, pp. 855-858 (2007).
- 31 **Cancer Research**, *Forschungszentrum Dresden Rossendorf, Biennial Scientific Report 2007-2008*, Volume 2, Wissenschaftlich-Technische Berichte, FZD-508 2009 – ISSN 1437-322X.
- 32 E. M. Syresin, **Centers of hadron therapy on the basis of cyclotrons**, *Proceedings of RuPAC*, Zvenigorod, Russia (2008).
- 33 E. Fourkal, J. S. Li, M. Ding, T. Tajima, and C. M. Ma, **Particle selection for laser-accelerated proton therapy feasibility study**, *Medical Physics* **30**, 7, p. 1660 (2003).
- 34 Toma Toncian, Marco Borghesi, Julien Fuchs, Emmanuel d’Humières, Patrizio Antici, Patrick Audebert, Erik Brambrink, Carlo Alberto Cecchetti, Ariane Pipahl, Lorenzo Romagnani, and Oswald Willi, **Ultrafast Laser-Driven Microlens to Focus and Energy-Select Mega-Electron Volt Protons**, *Science* **312**, 410 (2006).
- 35 M. Schollmeier, S. Becker, M. Geißel, K. Flippo, A. Blažević, S. A. Gaillard, D. C. Gautier, F. Grüner, K. Harres, M. Kimmel, F. Nürnberg, P. Rambo, U. Schramm, J. Schreiber, J. Schüttrumpf, J. Schwarz, N. Tahir, B. Atherton, D. Habs, B. M. Hegelich, and M. Roth, **Controlled Transport and Focusing of Laser-Accelerated Protons with Miniature Magnetic Devices**, *Physical Review Letters* **101**, 055004 (2008).
- 36 J. D. Lindl, **Development of the indirect-drive approach to inertial confinement fusion and the target physics basis for ignition and gain**, *Physics of Plasmas* **2**, pp. 3933-4024 (1995).
- 37 M. Tabak, J. Hammer, M. E. Glinsky, W. L. Kruer, S. C. Wilks, J. Woodworth, E. M. Campbell, M. D. Perry and R. J. Mason, **Ignition and high gain with ultrapowerful lasers**, *Physics of Plasmas* **1**, 1626 (1994).
- 38 <https://lasers.llnl.gov/science-technology/fusion-science/fast-ignition.php>

-
- 39 K. Eidmann, U. Andiel, F. Pisani, P. Hakel, R.C. Mancini, G.C. Junkel-Vives, J. Abdallah, and K. Witte, **K-shell spectra from hot dense aluminum layers buried in carbon and heated by ultrashort laser pulses**, *Journal of Quantitative Spectroscopy & Radiative Transfer* **81**, pp. 133–146 (2003).
- 40 A. Saemann, K. Eidmann, I.E. Golovkin, R. C. Mancini, E. Andersson, E. Förster, and K. Witte, **Isochoric heating of solid aluminum by ultrashort laser pulses focused on a tamped target**, *Physical Review Letters* **82**, pp. 4843–4846 (1999).
- 41 P. Audebert, R. Shepherd, K. B. Fournier, O. Peyrusse, D. Price, R. Lee, P. Springer, J.-C. Gauthier, and L. Klein, **Heating of Thin Foils with a Relativistic-Intensity Short-Pulse Laser**, *Physical Review Letters* **89**, 265001 (2002).
- 42 J. Myatt, W. Theobald, J. A. Delettrez, C. Stoeckl, M. Storm, T. C. Sangster, A. V. Maximov, and R. W. Short, **High-intensity laser interactions with mass-limited solid targets and implications for fast-ignition experiments on OMEGA EP**, *Physics of Plasmas* **14**, 056301 (2007).
- 43 Y. Sentoku, A. Kemp, M. Bakeman, R. Presura, and T. E. Cowan, **Isochoric heating of hot dense matter by ultra-intense short pulse irradiation**, *Journal de Physique IV France* **133**, 521 (2006).
- 44 Y. Sentoku, K. Mima, H. Ruhl, Y. Toyama, R. Kodama, and T. E. Cowan, **Laser light and hot electron micro focusing using a conical target**, *Physics of Plasmas* **11**, 3083 (2004).
- 45 R. Kodama, Y. Sentoku, Z. L. Chen, G. R. Kumar, S. P. Hatchett, Y. Toyama, T. E. Cowan, R. R. Freeman, J. Fuchs, Y. Izawa, M. H. Key, Y. Kitagawa, K. Kondo, T. Matsuoka, H. Nakamura, M. Nakatsutsumi, P. A. Norreys, T. Norimatsu, R. A. Snavely, R. B. Stephens, M. Tampo, K. A. Tanaka, and T. Yabuuchi, **Plasma devices to guide and collimate a high density of MeV electrons**, *Nature* **432**, 1005 (2004).
- 46 http://www.clf.rl.ac.uk/news/clf_news/apsaward06.htm
- 47 <http://www.hiper-laser.org/fusion/storyboard.asp>
- 48 M. Temporal, **Fast ignition of a compressed inertial confinement fusion hemispherical capsule by two proton beams**, *Physics of Plasmas* **13**, 122704 (2006).
- 49 J. C. Fernández, J.J. Honrubia, B. J. Albright, K. A. Flippo, D. C. Gautier, B. M. Hegelich, M. J. Schmitt, M. Temporal, and L. Yin, **Progress and prospects of ion-driven fast ignition**, *Nuclear Fusion* **49**, 065004 (2009).
- 50 B. M. Hegelich, B. J. Albright, J. Cobble, K. Flippo, R. Johnson, S. Letzring, M. Paffett, H. Ruhl, J. Schreiber, R. Schulze, and J. C. Fernandez, **Mono-energetic multi-MeV/nucleon ion beams accelerated by ultrahigh intensity lasers**, *Nature* **439**, pp. 441-444 (2006).
- 51 Y. Fukuda, A. Ya. Faenov, M. Tampo, T. A. Pikuz, T. Nakamura, M. Kando, Y. Hayashi, A. Yogo, H. Sakaki, T. Kameshima, A. S. Pirozhkov, K. Ogura, M. Mori, T. Zh. Esirkepov, J. Koga, A. S. Boldarev, V. A. Gasilov, A. I. Magunov, T. Yamauchi, R. Kodama, P. R. Bolton, Y. Kato, T. Tajima, H. Daido, and S. V. Bulanov, **Energy Increase in Multi-MeV Ion Acceleration in the Interaction of a Short Pulse Laser with a Cluster-Gas Target**, *Physical Review Letters* **103**, 165002 (2009).
- 52 B. M. Hegelich *et al.*, in preparation (2009).
- 53 T. Esirkepov, M. Borghesi, S. V. Bulanov, G. Mourou, and T. Tajima, **Highly Efficient Relativistic-Ion Generation in the Laser-Piston Regime**, *Physical Review Letters* **92**, Issue 17, 175003 (2004).
- 54 Tatiana V. Liseykina, Marco Borghesi, Andrea Macchi, and Sara Tuveri, **Radiation pressure acceleration by ultraintense laser pulses**, *Plasma Physics and Controlled Fusion* **50**, 124033 (2008).
- 55 A. P. L. Robinson, M. Zepf, S. Kar, R. G. Evans, and C. Bellei, **Radiation pressure acceleration of thin foils with circularly polarized laser pulses**, *New Journal of Physics* **10**, 013021 (2008).

-
- 56 L. Yin, B. J. Albright, B. M. Hegelich, K. J. Bowers, K. A. Flippo, T. J. T. Kwan, and J. C. Fernández, **Monoenergetic and GeV ion acceleration from the laser break-out afterburner using ultrathin targets**, *Physics of Plasmas* **14**, 056706 (Invited) (2007).
- 57 K. Flippo, B. M. Hegelich, B. J. Albright, L. Yin, D. C. Gautier, S. Letzring, M. Schollmeier, J. Schreiber, R. Schulze, and J. C. Fernández, **Laser-Driven Ion Accelerators: Spectral Control, Monoenergetic Ions And New Acceleration Mechanisms**, *Laser and Particle Beams* **25**, 3-8 (Invited) (2007).
- 58 K. W. D. Ledingham, J. Magill, P. McKenna, J. Yang, J. Galy, R. Schenkel, J. Rebizant, T. McCanny, S. Shimizu, L. Robson, R. P. Singhal, M. S. Wei, S. P. D. Mangles, P. Nilson, K. Krushelnick, R. J. Clarke, and P. A. Norreys, **Laser-driven photo-transmutation of I-129 – a long-lived nuclear waste product**, *Journal of Physics D: Applied Physics* **36** (2003).
- 59 K. Nemoto, A. Maksimchuk, S. Banerjee, K. Flippo, G. Mourou, D. Umstadter, and V. Y. Bychenkov, **Laser-triggered ion acceleration and table-top isotope production**, *Applied Physics Letters* **78**, 596 (2001).
- 60 P. Patel, A. Mackinnon, M. Key, T. Cowan, M. Foord, M. Allen, D. Price, H. Ruhl, P. Springer, and R. Stephens, **Isochoric heating of solid-density matter with an ultrafast proton beam**, *Physical Review Letters* **91**, 125004 (2003).
- 61 D. S. Hey, **Laser-Accelerated Proton Beams: Isochoric Heating and Conversion Efficiency**, *PhD dissertation, University of California, Davis* (2007).
- 62 M. Borghesi, A. Mackinnon, D. Campbell, D. Hicks, S. Kar, P. Patel, D. Price, L. Romagnani, A. Schiavi, and O. Willi, **Multi-Mev proton source investigations in ultra-intense laser-foil interactions**, *Physical Review Letters* **92**, 055003 (2004).
- 63 M. Borghesi, D. H. Campbell, A. Schiavi, M. G. Haines, O. Willi, A. J. MacKinnon, P. Patel, L. A. Gizzi, M. Galimberti, R. J. Clarke, F. Pegoraro, H. Ruhl, and S. Bulanov, **Electric field detection in laser-plasma interaction experiments via the proton imaging technique**, *Physics of Plasmas* **9**, 2214 (2002).
- 64 J. A. Cobble, R. P. Johnson, T. E. Cowan, N. Renard-Le Galloudec, and M. Allen, **High resolution laser-driven proton radiography**, *Journal of Applied Physics* **92**, 1775 (2002).
- 65 C. Colin, Y. Durand, F. Floux, D. Guyot, P. Langer, and P. Veyrie, **Laser produced plasmas from solid deuterium targets**, *Journal of Applied Physics* **39**, 2991 (1968).
- 66 S. Gitomer, R. Jones, F. Begay, A.W.Ehler, J. F. Kephart, and R. Kristal, **Fast ions and hot electrons in the laser-plasma interaction**, *Physics of Fluids* **29**, 2679 (1986).
- 67 Juan C. Fernández, B. Manuel Hegelich, James A. Cobble, Kirk A. Flippo, Samuel A. Letzring, Randall P. Johnson, D. Cort Gautier, Tsutomu Shimada, George A. Kyrala, Yongqiang Wang, Chris J. Wetteland, and Jörg Schreiber, **Laser-ablation treatment of short-pulse laser targets: Toward an experimental program on energetic-ion interactions with dense plasmas**, *Laser and Particle Beams* **23**, pp. 267-273 (2005).
- 68 K. A. Flippo, B. M. Hegelich, M. J. Schmitt, C. A. Meserole, G. L. Fisher, D. C. Gautier, J. A. Cobble, R. Johnson, S. Letzring, J. Schreiber, M. Schollmeier, and J. C. Fernandez, **Ultrashort-laser-produced heavy ion generation via target laser-ablation cleaning**, *Journal de Physique IV France* **133**, pp. 1117-1122 (2006).
- 69 M. Hegelich, S. Karsch, G. Pretzler, D. Habs, K. Witte, W. Guenther, M. Allen, A. Blažević, J. Fuchs, J. Gauthier, M. Geissel, P. Audebert, T. Cowan, and M. Roth, **MeV ion jets from short-pulse-laser interaction with thin foils**, *Physical Review Letters* **89**, 085002 (2002).

70 M. Allen, P. K. Patel, A. Mackinnon, D. Price, S. Wilks, and E. Morse, **Direct experimental evidence of back-surface ion acceleration from laser-irradiated gold foils**, *Physical Review Letters* **93**, 265004 (2004).

71 Y. Sentoku, V. Y. Bychenkov, K. Flippo, A. Maksimchuk, K. Mima, G. Mourou, Z. M. Sheng, and D. Umstadter, **High-energy ion generation in interaction of short laser pulse with high-density plasma**, *Applied Physics B* **74**, 207 (2002).

72 H. Alfvén, **On the motion of cosmic rays in interstellar space**, *Physical Review Letters* **55**, pp. 425-429 (1939).

73 B. Bezzerides, S. J. Gitomer, and D. W. Forslund, **Randomness maxwellian distribution and resonance absorption**, *Physical Review Letters* **44**, pp. 651-654 (1980).

74 S. C. Wilks and W. L. Kruer, **Absorption of ultrashort, ultra-intense laser light by solids and overdense plasmas**, *IEEE Journal Quantum Electronics* **33**, pp. 1954-1968 (1997).

75 D. Salzmann, Ch. Reich, I. Uschmann, E. Forster, and P. Gibbon, **Theory of $K\alpha$ generation by femtosecond laser produced hot electrons in thin foils**, *Physical Review E* **65**, 036402 (2002).

76 R. G. Evans, **Modeling electron transport for fast ignition**, *Plasma Physics and Controlled Fusion* **49**, B87 (2007).

77 Th. Schlegel, S. Bastiani, L. Grémillet, J.-P. Geindre, P. Audebert, J.-C. Gauthier, E. Lefebvre, G. Bonnaud, and J. Delettrez, **Comparison of measured and calculated x-ray and hot-electron production in short-pulse laser-solid interactions at moderate intensities**, *Physical Review E* **60**, pp. 2209-2217 (1999).

78 M. Honda, J. Meyer-Ter-Vehn, and A. Pukhov, **Two-dimensional particle-in-cell simulation for magnetized transport of ultra-high relativistic currents in plasma**, *Physics of Plasmas* **7**, Issue 4, pp. 1302-1308 (2000).

79 Y. Sentoku, K. Mima, P. Kaw, and K. Nishikawa, **Anomalous Resistivity Resulting from MeV-Electron Transport in Overdense Plasma**, *Physical Review Letters* **90**, 155001 (2003).

80 J. R. Davies, **Electric and magnetic field generation and target heating by laser-generated fast electrons**, *Physical Review E* **68**, 056404 (2003).

81 R. J. Mason, E. S. Dodd, and B. J. Albright, **Hot-electron surface retention in intense short-pulse laser-matter interactions**, *Physical Review E* **72**, 015401 (2005).

82 A. J. Kemp, Y. Sentoku, V. Sotnikov, and S. C. Wilks, **Collisional relaxation of super thermal electrons generated by relativistic laser pulses in dense plasma**, *Physical Review Letters* **97** (2006).

83 A. R. Bell, J. R. Davies, S. Guerin, and H. Ruhl, **Fast-electron transport in high-intensity short-pulse laser - solid experiments**, *Plasma Physics and Controlled Fusion* **39**, pp. 653-659 (1997).

84 Ondrej Klimo, V. T. Tikhonchuk, and A. Debayle, **High-current fast electron beam propagation in a dielectric target**, *Physical Review E* **75**, 016403 (2007).

85 M. S. Wei, F. N. Beg, E. L. Clark, A. E. Dangor, R. G. Evans, A. Gopal, K. W. D. Ledingham, P. McKenna, P. A. Norreys, M. Tatarakis, M. Zepf, and K. Krushelnick, **Observations of the filamentation of high-intensity laser-produced electron beams**, *Physical Review E* **70**, 056412 (2004).

86 L. Labate, M. Galimberti, A. Giuliotti, D. Giuliotti, P. Köster, P. Tomassini, and L. A. Gizzi, **Study of forward accelerated fast electrons in ultrashort Ti $K\alpha$ sources**, *Applied Physics B* **86**, 229 (2007).

-
- 87 P. A. Norreys, J. S. Green, J. R. Davies, M. Tatarakis, E. L. Clark, F. N. Beg, A. E. Dangor, K. L. Lancaster, M. S. Wei, M. Zepf, and K. Krushelnick, **Observation of annular electron beam transport in multi-Terawatt laser-solid interactions**, *Plasma Physics and Controlled Fusion* **48**, L11 (2006).
- 88 K. L. Lancaster, J. S. Green, D. S. Hey, K. U. Akli, J. R. Davies, R. J. Clarke, R. R. Freeman, H. Habara, M. H. Key, R. Kodama, K. Krushelnick, C. D. Murphy, M. Nakatsutsumi, P. Simpson, R. Stephens, C. Stoeckl, T. Yabuuchi, M. Zepf, and P. A. Norreys, **Measurements of Energy Transport Patterns in Solid Density Laser Plasma Interactions at Intensities of 5×10^{20} W cm⁻²**, *Physical Review Letters* **98**, 125002 (2007).
- 89 J. J. Santos, F. Amiranoff, S. D. Baton, L. Grémillet, M. Koenig, E. Martinolli, M. Rabec Le Gloahec, C. Rousseaux, D. Batani, A. Bernardinello, G. Greison, and T. Hall, **Fast Electron Transport in Ultraintense Laser Pulse Interaction with Solid Targets by Rear-Side Self-Radiation Diagnostics**, *Physical Review Letters* **89**, 025001 (2002).
- 90 M. Manclossi, J. J. Santos, D. Batani, J. Faure, A. Debayle, V. T. Tikhonchuk, and V. Malka, **Study of Ultraintense Laser-Produced Fast-Electron Propagation and Filamentation in Insulator and Metal Foil Targets by Optical Emission Diagnostics**, *Physical Review Letters* **96**, 125002 (2006).
- 91 S. J. Rose, **New experimental possibilities for measuring radiative opacity under conditions in the Sun's interior**, *Plasma Physics and Controlled Fusion* **47**, B735-B741 (2005).
- 92 K. B. Wharton, S. P. Hatchett, S. C. Wilks, M. H. Key, J. D. Moody, V. Yanovsky, A. A. Offenberger, B. A. Hammel, M. D. Perry, and C. Joshi, **Experimental Measurements of Hot Electrons Generated by Ultraintense ($> 10^{19}$ W/cm²) Laser-Plasma Interactions on Solid-Density Targets**, *Physical Review Letters* **81**, pp. 822-825 (1998).
- 93 M. H. Key, **Status of and prospects for the fast ignition inertial fusion concept**, *Physics of Plasmas* **14**, 055502 (2007).
- 94 K. G. Estabrook and W. L. Kruer, **Properties of resonantly heated electron distributions**, *Physical Review Letters* **40**, pp. 42-45 (1978).
- 95 F. N. Beg, A. R. Bell, A. E. Dangor, C. N. Danson, A. P. Fews, M. E. Glinsky, B. A. Hammel, P. Lee, P. A. Norreys, and M. Tatarakis, **A study of picosecond laser-solid interactions up to 10^{19} W/cm²**, *Physics of Plasmas* **4**, 447 (1997).
- 96 F. Brunel, **Anomalous absorption of high intensity subpicosecond laser pulses**, *Physics of Fluids* **31**, 9, 2714 (1988).
- 97 P. Gibbon and A. R. Bell, **Collisionless absorption in sharp edged plasmas**, *Physical Review Letters* **68**, pp. 1535-1538 (1992).
- 98 S. Wilks, W. Kruer, M. Tabak, and A. Langdon, **Absorption of ultra-intense laser pulses**, *Physical Review Letters* **69**, 1383 (1992).
- 99 W. L. Kruer and K. Estabrook, **$\mathbf{J} \times \mathbf{B}$ heating by very intense laser**, *Physics of Fluids* **28**, pp. 430-432 (1985).
- 100 Thomas Kluge, private communication, December 2009.
- 101 J. D. Kmetec, C. L. Gordon, III, J. J. Macklin, B. E. Lemoff, G. S. Brown, and S. E. Harris, **MeV X-ray generation with a femtosecond laser**, *Physical Review Letters* **68**, pp. 1527-1530 (1992).
- 102 M. Schnürer, M. P. Kalashnikov, P. V. Nickles, Th. Schlegel, W. Sandner, N. Demchenko, R. Nolte, and P. Ambrosi, **Hard X-ray emission from intense short pulse laser plasmas**, *Physics of Plasmas* **2**, 3106 (1995).

-
- 103 H. Schwoerer, P. Gibbon, S. Düsterer, R. Behrens, C. Ziener, C. Reich, and R. Sauerbrey, **MeV X-rays and photo-neutrons from femtosecond laser-produced plasmas**, *Physical Review Letters* **86**, pp. 2317-2320 (2001).
- 104 B. Soom, H. Chen, Y. Fisher, and D. D. Meyerhofer, **Strong K α emission from picosecond laser plasma interactions**, *Journal of Applied Physics* **74** (1993).
- 105 A. Rousse, P. Audebert, J. P. Geindre, F. Falliès, J. C. Gauthier, A. Mysyrowicz, G. Grillon, and A. Antonetti, **An Efficient K α X-ray Source from Femtosecond Laser-Produced Plasmas**, *Physical Review E* **50**, 3, 2200 (1994).
- 106 Z. Jiang, J. C. Kieffer, J. P. Matte, M. Chaker, O. Peyrusse, D. Gilles, G. Korn, A. Maksimchuk, S. Coe, and G. Mourou. **X-ray spectroscopy of hot solid density plasmas produced by subpicosecond high contrast laser pulses at 10^{18} – 10^{19} W/cm 2** , *Physics of Plasmas* **2**, pp. 1702-1711 (1995).
- 107 <http://physics.nist.gov/cgi-bin/XrayTrans/search.pl?element=Cu&trans=All&lower=&upper=&units=A>
- 108 Ch. Reich, P. Gibbon, I. Uschmann, and E. Förster, **Yield Optimization and Time Structure of Femtosecond Laser Plasma K α Sources**, *Physical Review Letters* **84**, 4846 (2000).
- 109 P. Köster, K. Akli, D. Batani, S. Baton, R. G. Evans, A. Giuliatti, D. Giuliatti, L. A. Gizzi, J. S. Green, M. Koenig, L. Labate, A. Morace, P. Norreys, F. Perez, J. Waugh, N. Woolsey, and K. L. Lancaster, **Experimental investigation of fast electron transport through K α imaging and spectroscopy in relativistic laser-solid interaction**, *Plasma Physics and Controlled Fusion* **51**, 014007 (2009).
- 110 S. D. Baton, D. Batani, M. Manclossi, A. Morace, D. Piazza, A. Benuzzi-Mounaix, M. Koenig, P. Guillou, B. Loupias, J. Fuchs, F. Amiranoff, M. Rabec Le Gloahec, H. Popescu, C. Rousseaux, M. Borghesi, C. Cecchetti, R. Kodama, T. Norimatsu, M. Nakatsutsumi, and Y. Aglitskiy, **Recent experiments on electron transport in high intensity laser matter interactions**, *Plasma Physics and Controlled Fusion* **47**, B777-B789 (2005).
- 111 C. A. Quarles, **Semi-empirical analysis of electron-induced K-shell ionization**, *Physical Review A* **13**, pp. 1278-1280 (1976).
- 112 Michal Gryziński, **Classical Theory of Atomic Collisions. I. Theory of Inelastic Collisions**, *Physical Review* **138**, A336-A358 (1965).
- 113 M. Liu, Z. A. C. Tang, Z. Luo, X. Peng, and X. Long, *Atomic Data Nuclear Data Tables* **76**, 213 (2000).
- 114 M. A. Uddin and A. K. Basak, **K-shell ionization of atoms**, *Physica Scripta* **67**, pp. 37-43 (2003).
- 115 S. C. Wilks, A. B. Langdon, T. E. Cowan, M. Roth, M. Singh, S. Hatchett, M. H. Key, D. Pennington, A. Mackinnon, and R. A. Snavely, **Energetic proton generation in ultra-intense laser-solid interactions**, *Physics of Plasmas* **8**, 542 (2001).
- 116 J. Denavit, **Collisionless plasma expansion into a vacuum**, *Physics of Fluids* **22**, 1384 (1979).
- 117 P. Mora, **Plasma expansion into a vacuum**, *Physical Review Letters* **90**, 185002 (2003).
- 118 Patrick Mora, **Thin-foil expansion into a vacuum**, *Physical Review E* **72**, 056401 (2005).
- 119 L. Robson, P.T. Simpson, R.J. Clarke, K. W. D. Ledingham, F. Lindau, O. Lundh, T. McCanny, P. Mora, D. Neely, C.-G. Wahlström, M. Zepf, and P. McKenna, **Scaling of proton acceleration driven by petawatt-laser-plasma interactions**, *Nature Physics* **3**, pp. 58-62 (2007).
- 120 J. M. Dawson, **Particle simulation of plasmas**, *Reviews of Modern Physics* **55**, 403 (1983).
- 121 Hideo Okuda, **Nonphysical noises and instabilities in plasma simulation due to a spatial grid**, *Journal of Computational Physics* **10**, 475 (1972).

-
- 122 Y. Sentoku and A. J. Kemp, **Numerical methods for particle simulations at extreme densities and temperatures: Weighted particles, relativistic collisions and reduced currents**, *Journal of Computational Physics* **227**, pp. 6846–6861 (2008).
- 123 A. J. Kemp, Y. Sentoku, V. Sotnikov, and S. C. Wilks, **Collisional relaxation of super thermal electrons generated by relativistic laser pulses in dense plasma**, *Physical Review Letters* **97**, 235001 (2006).
- 124 Y. Sentoku, T.E. Cowan, A. Kemp, and H. Ruhl, **High-energy proton acceleration in interaction of short-pulse with dense plasma target**, *Physics of Plasmas* **10**, 5, pp. 2009-2015 (2003).
- 125 A. J. Mackinnon, Y. Sentoku, P. K. Patel, D. W. Price, S. Hatchett, M. H. Key, C. Andersen, R. Snavely, and R. R. Freeman, **Enhancement of proton acceleration by hot-electron recirculation in thin foils irradiated by ultra-intense laser pulses** *Physical Review Letters* **88**, 21, 15006 (2002).
- 126 J. Fuchs, P. Antici, E. d’Humières, E. Lefebvre, M. Borghesi, E. Brambrink, C. Cecchetti, M. Kaluza, V. Malka, M. Manclossi, S. Meyroneinc, P. Mora, J. Schreiber, T. Toncian, H. Pepin, and P. Audebert, **Laser-driven proton scaling laws and new paths towards energy increase**, *Nature Physics* **2**, 48 (2006).
- 127 M. Roth, A. Blažević, M. Geissel, T. Schlegel, T. E. Cowan, M. Allen, J.-C. Gauthier, P. Audebert, J. Fuchs, J. Meyer-ter-Vehn, M. Hegelich, S. Karsch, and A. Pukhov, **Energetic ions generated by laser pulses: A detailed study on target properties**, *Physical Review special topics – Accelerators and Beams* **5**, 061301 (2002).
- 128 A. Yogo, H. Daido, A. Fukumi, Z. Li, K. Ogura, A. Sagisaka, A. S. Pirozhkov, S. Nakamura, Y. Iwashita, T. Shirai, A. Noda, Y. Oishi, T. Nayuki, T. Fujii, K. Nemoto, I. W. Choi, J. H. Sung, D.-K. Ko, and J. Lee, **Laser prepulse dependency of proton-energy distributions in ultraintense laser-foil interactions with an online time-of-flight technique**, *Physics of Plasmas* **14**, 043104 (2007).
- 129 Peter Pronko and Xiaoqing Pan, **Ultrafast-laser ablation creates new thin films**, *Laser Focus World* (2006).
- 130 B.N. Chichkov, C. Momma, S. Nolte, F. von Alvensleben, and A. Tünnermann, **Femtosecond, picosecond and nanosecond laser ablation of solids**, *Applied Physics A* **63**, pp. 109-115 (1996).
- 131 P. P. Pronko, S. K. Dutta, D. Du, and R. K. Singh, **Thermo-physical effects in laser processing of materials with picosecond and femtosecond pulses**, *Journal of Applied Physics* **78**, pp. 6233-6240 (1995).
- 132 Sophie D. Baton, Michel Koenig, Perceval Guillou, Bérénice Loupiau, Alessandra Benuzzi-Mounaix, Julien Fuchs, Christophe Rousseaux, Laurent Grémillet, Dimitri Batani, Alessio Morace, Motoaki Nakatsutsumi, Ryosuke Kodama, and Yefim Aglitskiy, **Relativistic electron transport and confinement within charge-insulated, mass-limited targets**, *High Energy Density Physics* **3**, pp. 358-364 (2007).
- 133 M. Schnürer, S. Ter-Avetisyan, S. Busch, E. Risse, M. P. Kalachnikov, W. Sandner, and P. V. Nickles, **Ion acceleration with ultrafast laser driven water droplets**, *Laser and Particle Beams* **23**, pp. 337-343 (2005).
- 134 T. Sokollik, M. Schnürer, S. Steinke, P.V. Nickles, W. Sandner, M. Amin, T. Toncian, O. Willi, and A. A. Andreev, **Directional laser-driven ion acceleration from microspheres**, *Physical Review Letters* **103**, 135003 (2009).
- 135 J. Schreiber, F. Bell, F. Grüner, U. Schramm, M. Geissler, M. Schnürer, S. Ter-Avetisyan, B. M. Hegelich, J. Cobble, E. Brambrink, J. Fuchs, P. Audebert and D. Habs, **Analytical Model for Ion Acceleration by High-Intensity Laser Pulses**, *Physical Review Letters* **97**, 045005 (2006).

136 M. Zepf, E.L. Clark, K. Krushelnick, *et al.*, *Phys. Plasmas*, 8, 2323 (2001); A.J. Mackinnon, M. Borghesi, S. Hatchett, *et al.*, *Phys. Rev. Lett.*, 86, 1769 (2001); J. Badziak, P. Parys, A.B. Vankov, *et al.*, *Phys. Rev. Lett.*, 87, 215001 (2001); T.E. Cowan, M. Roth, J. Johnson, *et al.*, *Nuc. Inst. & Meth. Phys. Res. Sec. A*, 455, 130-139 (2000); P.K. Patel, M.H. Key, A.J. Mackinnon, *et al.*, *Plasma Phys. Cont. Fus.*, 47, B833-B840 (2005); K.W.D. Ledingham, P. McKenna, T. McCanny, *et al.*, *J. Phys. D. App. Phys.*, 37, 2341-2345 (2004); K. Krushelnick, E.L. Clark, M. Zepf, *et al.*, *Phys. of Plasmas*, 7, 2055 (2000).

137 N. K. Moncur, R. P. Johnson, R. G. Watt, and R. B. Gibson, **Trident: a versatile high-power Nd:Glass laser facility for inertial confinement fusion experiments**, *Applied Optics* **34**, 4274 (1995).

http://www.lanl.gov/orgs/tt/partnering/user_facility/facilities/trident_laser.shtml

138 S. H. Batha, R. Aragonez, F. L. Archuleta, T. N. Archuleta, J. F. Benage, J. A. Cobble, J. S. Cowan, V. E. Fatherley, K. A. Flippo, D. C. Gautier, R. P. Gonzales, S. R. Greenfield, B. M. Hegelich, T. R. Hurry, R. P. Johnson, J. L. Kline, S. A. Letzring, E. N. Loomis, F. E. Lopez, S. N. Lou, D. S. Montgomery, J. A. Oertel, D. L. Paisely, S. M. Reid, P. G. Sanchez, A. Seifter, T. Shimada, and J. B. Workman, **TRIDENT high-energy-density facility experimental capabilities and diagnostics**, *Review of Scientific Instruments* **79**, 10F305 (2008).

<http://trident.lanl.gov/>

139 D. Strickland and G. Mourou, **Compression of amplified chirped optical pulses**, *Optics Communications* **56**, 219 (1985).

140 Antonio Ting, Daniel F. Gordon, Eldridge Briscoe, Joseph R. Peñano, and Phillip Sprangle, **Direct characterization of self-guided femtosecond laser filaments in air**, *Applied Optics* **44**, 8, pp. 1474-1479 (2005).

141 A. E. Siegman, **Lasers**, *University science books* (1986).

142 http://www.mellesgriot.com/products/optics/gb_2_3.htm

143 R. A. Ganeev, F. Sh. Ganikhanov, I. G. Gorelik, A. A. Dakhin, D. G. Kunin, T. Usmanov, and A. V. Zinoviev, **Laser pulse duration measurements in the range of 0.2 to 50 picosecond**, *Optics Communications* **114**, Issues 5-6 (1995).

144 Rekha Tambay, D. Victor Suvishesha Muthu, V. Kumar and R. K. Thareja, **Laser induced air breakdown using 0.355, 0.532, and 1.06 μm radiation**, *Pramana – Journal of Physics* **37**, 2, pp. 163-166 (1991).

145 N. V. Didenko, A. V. Konyashchenko, A. P. Lutsenko, and S. Yu. Tenyakov, **Contrast degradation in a chirped-pulse amplifier due to generation of prepulses by postpulses**, *Optics Express* **16**, 5, 3178 (2008).

146 C. Dorrer, I. A. Begishev, A. V. Okishev, and J. D. Zuegel, **High-contrast optical-parametric amplifier as a front-end of high-power laser systems**, *Optics Letters* **32**, 2143 (2007).

147 Rahul C. Shah, Randall P. Johnson, Tsutomu Shimada, Kirk A. Flippo, Juan C. Fernandez, and B. M. Hegelich, **High-temporal contrast using low-gain optical parametric amplification**, *Optics Express* **34**, 2273 (2008).

148 Jim Schwiegerling and Daniel R. Neal, **Historical Development of the Shack-Hartmann Wavefront Sensor**, SPIE (2004).

Daniel R. Neal, **Shack-Hartmann sensor engineered for commercial measurement applications**, SPIE AM100-20 (2004).

149 D. C. Gautier, K. A. Flippo, S. A. Letzring, J. Workman, T. Shimada, R. P. Johnson, T. R. Hurry, S. A. Gaillard, and B. M. Hegelich, **A Novel Backscatter Focus Diagnostic for the TRIDENT 200 TW Laser**, *Review of Scientific Instruments* **79**, 10F547 (2008).

150 S.A. Durrani and R.K. Bull, **Solid state nuclear track detection: Principles, Methods and Applications**, *Pergamon Press* (1987).

151 S. A. Gaillard, **Limitations of the use of CR39 Detectors, a particular type of Solid State Nuclear Track Detector, in High-energy, Short-pulse Laser Ion Acceleration Experiments**, *Master's thesis, University of Nevada Reno* (2005).

152 S. Gaillard, J. Fuchs, N. Renard-Le Galloudec, and T. E. Cowan, **Study of saturation of CR39 nuclear track detectors at high ion fluence and of associated artifact patterns**, *Review of Scientific Instruments* **78**, 1 (2007).

153 S. Gaillard, J. Fuchs, N. Renard-Le Galloudec, and T. E. Cowan, **Comment on "Measurements of Energetic Proton Transport through Magnetized Plasma from Intense Laser Interactions with Solids"**, *Physical Review Letters* **96**, 249201 (2006).

154 www.gafchromic.com

155 A. Niroomand-Rad, C. R. Blackwell, B. M. Coursey, K. P. Gall, J. M. Galvin, W. L. McLaughlin, A. S. Meigooni, R. Nath, J. E. Rodgers, and C. G. Soares, **RadioChromic film dosimetry: Recommendations of AAPM Radiation, Therapy Committee Task Group 55**, *Medical Physics* **25**, 11 (1998).

156 F. Nürnberg, **Reconstruction and 3-D-transport-simulations of laser-accelerated ion beams using structured targets**, *Master's thesis, Technische Universität Darmstadt* (2006).

157 J. S. Cowan, K. A. Flippo, and S. A. Gaillard, **Characterization of RadioChromic Film (RCF) Scanning Techniques used in Short-pulse-laser Ion Acceleration**, *Review of Scientific Instruments* **79**, 10E535 (2008).

158 W. L. McLaughlin, Chen Yun-Dong, C. G. Soares, A. Miller, G. van Dyk, and D. F. Lewis, **Sensitometry of the response of a new RadioChromic film dosimeter to gamma radiation and electron beams**, *Nuclear Instruments and Methods in Physics Research Section A* **302**, 1, pp. 165-176 (1991).

159 Philip James Muench, Ali S. Meigooni, Ravinder Nath, and William L. McLaughlin, **Photon energy dependence of the sensitivity of RadioChromic Film and comparison with silver halide film and LiF TLDs used for brachy-therapy dosimetry**, *Medical Physics* **18**, pp. 769-775 (1994).

160 S. A. Gaillard, J. S. Cowan, K. A. Flippo, D. C. Gautier, K. Harres, F. Nürnberg, M. Schollmeier, W. Leemans, M. Roth, and T. E. Cowan, **Cross-Calibrations of RCF (MD-55 HD-810 and HS) from multiple proton sources from 4 to 25 MeV and using multiple scanning techniques (scanners and microdensitometer)**, in preparation for *Review of Scientific Instruments* (2010).

161 M. Schollmeier and M. Geißel, private communication (June 2009).

162 J. Fuchs, C. A. Cecchetti, M. Borghesi, T. Grismayer, E. d'Humières, P. Antici, S. Atzeni, P. Mora, A. Pipahl, L. Romagnani, A. Schiavi, Y. Sentoku, T. Toncian, P. Audebert, and O. Willi, **Laser-acceleration of high-energy protons in small-scale gradients**, *Physical Review Letters* **99**, 015002 (2007).

163 http://www.fujifilm.com/products/life_science/si_imgplate/img_plate.html

164 http://www.fujifilm.com/products/life_science_systems/science_imaging/imaging_plate/faq/

165 John Pizzonia (Director, Applications, Fujifilm – Life science – USA) and Toshio Yamada (Fuji Photo Film Co., Ltd. – Japan), private communication (September 2009).

166 Kazuo A. Tanaka, Toshinori Yabuuchi, Takashi Sato, Ryosuke Kodama, Yoneyoshi Kitagawa, Teruyoshi Takahashi, Toshiji Ikeda, Yoshihide Honda, and Shuuichi Okuda, **Calibration of imaging plate of high energy electron spectrometer**, *Review of Scientific Instruments* **76**, 013507 (2005).

167 T.E. Cowan, M. Roth, J. Johnson, C. Brown, M. Christl, W. Fountain, S. Hatchett, E.A. Henry, A.W. Hunt, M.H. Key, A. MacKinnon, T. Parnell, D.M. Pennington, M.D. Perry, T.W. Phillips, T.C. Sangster, M. Singh, R. Snavely, M. Stoyer, Y. Takahashi, S.C. Wilks, and K. Yasuike, **Intense electron and proton beams from Petawatt laser-matter interactions**, *Nuclear Instruments and Methods in Physics Research A*, **455**, pp. 130-139 (2000).

168 Jeffrey A. Koch, Otto L. Landen, Troy W. Barbee, Jr., Peter Celliers, Luiz B. Da Silva, Sharon G. Glendinning, Bruce A. Hammel, Dan H. Kalantar, Charles Brown, John Seely, Guy R. Bennett, and Warren Hsing, **High-energy x-ray microscopy techniques for laser-fusion plasma research at the National Ignition Facility**, *Applied Optics* **37**, 10 (1998).

169 J. A. Koch, Y. Aglitskiy, C. Brown, T. Cowan, R. Freeman, S. Hatchett, G. Holland, M. Key, A. Mackinnon, J. Seely, R. Snavely, and R. Stephens, **4.5- and 8-keV emission and absorption X-ray imaging using spherically bent quartz 203 and 211 crystals**, *Review of Scientific Instruments* **74**, pp. 2130-2135 (Invited) (2003).

170 Daniel B. Sinars, Guy R. Bennett, David F. Wenger, Michael E. Cuneo, and John L. Porter, **Evaluation of bent-crystal X-ray backlighting and microscopy techniques for the Sandia Z machine**, *Applied Optics* **42**, 19 (2003).

171 E. Förster, K. Gäbel, and I. Uschmann, **X-ray microscopy of laser-produced plasmas with the use of bent crystals**, *Laser and Particle Beams* **9**, pp. 135-148 (1991).

172 Jeffrey A. Koch, Otto L. Landen, Troy W. Barbee, Peter Celliers, Luiz B. Da Silva, Sharon G. Glendinning, Bruce A. Hammel, Dan H. Kalantar, Charles Brown, John Seely, Guy R. Bennett, and Warren Hsing, **High-Energy X-ray Microscopy Techniques for Laser-Fusion Plasma Research at the National Ignition Facility**, *Applied Optics* **37**, pp. 1784-1795 (1998).

H. Nishimura, T. Kiso, H. Shiraga, T. Endo, K. Fujita, A. Sunahara, H. Takabe, Y. Kato, and S. Nakai, **Study of indirectly driven implosion by x-ray spectroscopic measurements**, *Physics of Plasmas* **2**, 2063 (1995).

173 Yefim Aglitskiy, Thomas Lehecka, Stephen Obenschain, Stephen Bodner, Carl Pawley, Kent Gerber, John Sethian, Charles M. Brown, John Seely, Uri Feldman, and Glenn Holland, **High-resolution monochromatic x-ray imaging system based on spherically bent crystals**, *Applied Optics* **37**, 22, pp. 5253-5261 (1998).

S. Pikuz, T. Shelkovenko, V. Romanova, D. Hammer, A. Faenov, V. Dyakin, and T. Pikuz, **High-luminosity monochromatic x-ray backlighting using an incoherent plasma source to study extremely dense plasmas**, *Review of Scientific Instruments* **68**, 740 (Invited) (1997).

T. A. Pikuz, A. Y. Faenov, and A. Zigler, **Shadow monochromatic backlighting: Large-field high resolution X-ray shadowgraphy with improved spectral tenability**, *Laser and Particle Beams* **19**, 2, pp. 285-293 (2001).

I. Uschmann, E. Förster, H. Nishimura, K. Fujita, Y. Kato, and S. Nakai, **Temperature mapping of compressed fusion pellets obtained by monochromatic imaging**, *Review of Scientific Instruments* **66**, 734 (1995).

174 F. Blasco, C. Stenz, F. Salin, A. Y. Faenov, A. I. Magunov, T. A. Pikuz, and I. Y. Skobelev, **Portable, tunable, high-luminosity spherical crystal spectrometer with an x-ray charge coupled device, for high-resolution x-ray spectro-microscopy of clusters heated by femtosecond laser pulses**, *Review of Scientific Instruments* **72**, 1956 (2001).

Ingo Uschmann, Kazuhiza Fujita, Izam Niki, Randolph Butzbach, Hiroaki Nishimura, Jiro Funakura, Mitsuo Nakai, Eckhart Förster, and Kunioki Mima, **Time-Resolved Ten-Channel Monochromatic Imaging of Inertial Confinement Fusion Plasmas**, *Applied Optics* **39**, pp. 5865-5871 (2000).

175 I. Uschmann, P. Gibbon, D. Klöpffel, T. Feurer, E. Förster, P. Audebert, J. P. Geindre, J. C. Gauthier, A. Rousse, and C. Rischel, **X-ray emission produced by hot electrons from fs-laser produced plasma - diagnostic and application**, *Laser and Particle Beams* **17**, 671 (1999).

176 K. U. Akli, M. D. Key, H. K. Chung, S. B. Hansen, R. R. Freeman, M. H. Chen, G. Gregori, S. Hatchett, D. Hey, N. Izumi, J. King, J. Kuba, P. Norreys, A. J. Mackinnon, C. D. Murphy, R. Snavely, R. B. Stephens, C. Stoeckel, W. Theobald, and B. T. Zhang, **Temperature sensitivity of Cu K α imaging efficiency using a spherical Bragg reflecting crystal**, *Physics of Plasmas* **14**, 023102 (2007).

177 T. Ma, Presentation at 36th International Conference on Plasma Science – San Diego, 2009: http://maeresearch.ucsd.edu/beg/Conferences/Ma_ICOPSSOFE09.pdf

178 M. Nakatsutsumi, R. Kodama, P. A. Norreys, S. Awano, H. Nakamura, T. Norimatsu, A. Ooya, M. Tampo, K. A. Tanaka, T. Tanimoto, T. Tsutsumi, and Y. Yabuuchi, **Reentrant cone angle dependence of the energetic electron slope temperature in high-intensity laser-plasma interactions**, *Physics of Plasmas* **14**, 050701 (2007).

179 M. Nakatsutsumi, R. Kodama, Y. Aglitskiy, K. Akli, D. Batani, S. Baton, F. Beg, A. Benuzzi-Mounaix, S. Chen, D. Clark, J. Davies, R. Freeman, J. Fuchs, J. Green, C. Gregory, P. Guillou, H. Habara, R. Heathcote, D. Hey, K. Highbarger, P. Jaanimagi, M. H. Key, M. Koenig, K. Krushelnick, K. Lancaster, B. Loupais, T. Ma, A. MacPhee, A. MacKinnon, K. Mima, A. Morace, H. Nakamura, P. Norreys, D. Piazza, C. Rousseaux, R. Stephens, M. Storm, M. Tampo, W. Theobald, L. V. Woerkom, R. Weber, M. S. Wei, and N. Woolsey, **Heating of solid target in electron refluxing dominated regime with ultra-intense laser**, *Journal of Physics: Conference Series* **112**, 022063 (2008).

180 J. Rassuchine, **Enhanced Hot Electron Confinement and Isochoric Heating in High Contrast Ultra-Intense Laser Produced Plasmas via Novel Conical Micro-Target Design**, *PHD dissertation, University of Nevada, Reno* (2007).

181 J. Rassuchine, E. d'Humières, S. Baton, J. Fuchs, P. Guillou, M. Koenig, R. Kodama, M. Nakatsutsumi, T. Norimatsu, D. Batani, A. Morace, R. Redaelli, L. Grémillet, C. Rousseaux, F. Dorchie, C. Fourment, J. J. Santos, J. Adams, G. Korgan, S. Malekos, Y. Sentoku, and T. E. Cowan, **Enhanced energy localization and heating in high contrast ultra-intense laser produced plasmas via novel conical micro-target design**, *Journal of Physics: Conference Series* **112**, 022050 (2008).

182 T. Kluge, M. Bussmann, S. A. Gaillard, K. Flippo, D. C. Gautier, B. Gall, T. Lockard, M. E. Lowenstern, J. E. Mucino, Y. Sentoku, K. Zeil, S. Kraft, U. Schramm, T. E. Cowan and R. Sauerbrey, **Low-Divergent, Energetic Electron Beams from Ultra-Thin Foils**, submitted to *AIP Conference proceedings* (2009).

183 H. Ruhl, T. E. Cowan, and J. Fuchs, **The generation of micro-fiducials in laser-accelerated proton flows, their imaging property of surface structures and application for the characterization of the flow**, *Physics of Plasmas* **11**, L17 (2004).

184 F. F. Chen, **Introduction to Plasma Physics and Controlled Fusion**, Vol.1, 2nd Edition, *Plenum Press, New York* (1990).

185 D.R. Nicholson, **Introduction to plasma theory**, *Krieger Publishing Company* (1992).

186 K. B. Wharton, C. D. Boley, A. M. Komashko, A. M. Rubenchik, J. Zweibeck, J. Crane, G. Hays, T. Cowan, and T. Ditmire, **Effects of non-ionizing prepulses in high-intensity laser-solid interactions**, *Physical Review E* **64**, 025402(R) (2001).

187 Paul Gibbon, **Short Pulse Laser Interactions with Matter – An introduction**, *Imperial College Press* (2005).

-
- 188 A. Einstein, **Über einen die Erzeugung und Verwandlung des Lichtes betreffenden heuristischen Gesichtspunkt**, *Annalen der Physik* **17**, pp. 132-148 (1905).
- 189 W. L. Kruer, **The Physics of Laser Plasma Interaction**, *Addiso-Wesley, Redwood City, CA* (1988).
- 190 T. Auguste, P. Monot, L.-A. Lompré, G. Mainfray, and C. Manus, **Defocusing effects of a picosecond terawatt laser pulse in an underdense plasma**, *Optics Communications* **89**, 2-4, pp. 145-148. (1992).
- 191 W. P. Leemans, C. E. Clayton, W. B. Mori, K. A. Marsh, P. K. Kaw, T. A. Dyson, C. Joshi, and J. M. Wallace, **Experiments and simulations of tunnel-ionized plasmas**, *Physical Review A* **46**, pp. 1091-1105 (1992).
- 192 S. C. Rae, **Ionization-induced defocusing of intense laser pulses in high-pressure gases**, *Optics Communications* **97**, 1-2, pp. 25-28 (1993).
- 193 S. P. Le Blanc, R. A. Sauerbrey, S. C. Rae, and K. Burnett, **Spectral blue shifting of a femtosecond laser pulse propagating through a high-pressure gas**, *Journal of the Optical Society of America B: Optical Physics* **10**, pp. 1801-1809 (1993).
- 194 W. B. Mori, C. Joshi, J. M. Dawson, D. W. Forslung, and J. M. Kindel, **Evolution of self-focusing of intense electromagnetic waves in plasma**, *Physical Review Letters* **60**, 1298 (1988).
- 195 J. Faure, V. Malka, J.-R. Marquès, P.-G. David, F. Amiranoff, K. Ta Phuoc, and A. Rousse, **Effects of pulse duration on self-focusing of ultra-short lasers in underdense plasmas**, *Physics of Plasmas* **9**, 756 (2002).
- 196 G. S. Sarkisov, V. Y. Bychenkov, V. N. Novikov, V. T. Tikhonchuk, A. Maksimchuck, S.-Y. Chen, R. Wagner, G. Mourou, and D. Umstadter, **Self-focusing, channel formation, and high-energy ion generation in interaction of an intense short laser pulse with a He jet**, *Physical Review E* **59**, 7042 (1999).
- 197 P. Kaw, G. Schmidt, and T. Wilcox, **Filamentation and trapping of electromagnetic radiation in plasmas**, *Physics of Fluids* **16**, 1522 (1973).
- 198 Claire Ellen Max, Jonathan Arons, and A. Bruce Langdon, **Self-modulation and self-focusing of electromagnetic waves in plasmas**, *Physical Review Letters* **33**, 209 (1974).
- 199 A. Pukhov, **Strong field interaction of laser radiation**, *Rep. Prog. Phys.* **66**, 47 (2003).
- 200 <http://www.mpg.de/lpg/research/RelLasPlas/Rel-Las-Plas.html>
- 201 G. Z. Sun, E. Ott, Y. C. Lee, and P. Gudzdard, **Self-focusing of short intense pulses in plasmas**, *Physics of Fluids* **30**, pp. 526-532 (1987).
- 202 P. Chessa, P. Mora, and T. M. Antonsen, **Numerical simulations of short laser pulse relativistic self-focusing in underdense plasma**, *Physics of Plasmas* **5**, pp. 3452-3458 (1998).
- 203 F. W. Perkins and E. J. Valeo, **Thermal self-focusing of electromagnetic waves in plasmas**, *Physical Review Letters* **32**, 1234 (1974).
- 204 A. B. Borisov, A. V. Borovskiy, V. V. Korobkin, A. M. Prokhorov, O. B. Shiryayev, X. M. Shi, T. S. Luk, A. McPherson, J. C. Solem, K. Boyer, and C. K. Rhodes, **Observation of relativistic and charge-displacement self-channeling of intense subpicosecond ultraviolet (248 nm) radiation in plasmas**, *Physical Review Letters* **68**, 2309 (1992).
- 205 P. Monot, T. Auguste, P. Gibbon, F. Jakober, G. Mainfray, A. Dulieu, M. Louis-Jacquet, G. Malka, and J. L. Miquel, **Experimental demonstration of relativistic self-channeling of a multi-terawatt laser pulse in an underdense plasma**, *Physical Review Letters* **74**, pp. 2953-2956 (1995).

-
- 206 Burke Ritchie, **Relativistic self-focusing and channel formation in laser-plasma interactions**, *Physical Review E* **50**, R687-R689 (1994).
- 207 P. E. Young, S. C. Wilks, W. L. Kruer, J. H. Hammer, G. Guethlein, and M. E. Foord, **Laser beam propagation, filamentation and channel formation in laser-produced plasmas**, *Conference Proceedings for the 10th APS topical conference on atomic processes in plasmas* (1996).
- 208 R. Wagner, S.-Y. Chen, A. Maksimchuk, and D. Umstadter, **Electron Acceleration by a Laser Wakefield in a Relativistically Self-Guided Channel**, *Physical Review Letters* **78**, pp. 3125-3128 (1997).
- 209 C. E. Clayton, K.-C. Tzeng, D. Gordon, P. Muggli, W. B. Mori, C. Joshi, V. Malka, Z. Najmudin, A. Modena, D. Neely, and A. E. Dangor, **Plasma Wave Generation in a Self-Focused Channel of a Relativistically Intense Laser Pulse**, *Physical Review Letters* **81**, pp. 100-103 (1998).
- 210 Erich S. Weibel, **Spontaneously Growing Transverse Waves in a Plasma Due to an Anisotropic Velocity Distribution**, *Physical Review Letters* **2**, pp. 83-84 (1959).
- 211 Y. Sentoku, K. Mima, S. Kojima, and H. Ruhl, **Magnetic instability by the relativistic laser pulses in overdense plasmas**, *Physics of Plasmas* **7**, 689 (2000).
- 212 F. Califano, F. Pegoraro, S. V. Bulanov, and A. Mangeney, **Kinetic saturation of the Weibel instability in a collisionless plasma**, *Physical Review E* **57**, 7048 (1998).
- 213 N. Ebrahim, H. Baldis, C. Joshi, and R. Benesch, **Hot electron generation by the two-plasmon decay instability in the laser-plasma interaction at 10.6 μm** , *Physical Review Letters* **45**, 1179 (1980).
- 214 S.-Y. Chen, M. Krishnan, A. Maksimchuk, R. Wagner, and D. Umstadter, **Detailed dynamics of electron beams self-trapped and accelerated in a self-modulated laser wakefield**, *Physics of Plasmas* **6**, 4739 (1999).
- 215 T. Tajima and J. M. Dawson, **Laser electron accelerator**, *Physical Review Letters* **43**, pp. 267-270 (1979).
- 216 Eric Esarey, Phillip Sprangle, Jonathan Krall, and Antonio Ting, **Overview of Plasma-Based Accelerator Concepts**, *IEEE Transactions on Plasma Science* **24**, 2 (1996).
- 217 A. Pukhov and J. Meyer-ter-Vehn, **Laser wake field acceleration: The highly non-linear broken-wave regime**, *Applied Physics B* **74**, pp. 355-361 (2002).
- 218 A. Pukhov, S. Gordienko, S. Kiselev, and I. Kostyukov, **The bubble regime of laser-plasma acceleration: monoenergetic electrons and the scalability**, *Plasma Physics and Controlled Fusion* **46**, B179-B186 (2004).
- 219 D. A. Tidman and N. A. Krall, **Shock Waves in Collisionless Plasmas**, *Wiley-Interscience New York* (1971).
- 220 J. Badziak, S. Glowacz, S. Jablonski, P. Parys, J. Wolowski, and H. Hora, **Production of ultrahigh-current-density ion beams by short-pulse skin-layer laser-plasma interaction**, *Applied Physics Letters* **85**, 15 (2004).
- 221 A. Langdon, **Nonlinear inverse bremsstrahlung and heated-electron distributions**, *Physical Review Letters* **44**, 575 (1980).
- 222 K. G. Estabrook, E. J. Valeo, and W. L. Kruer, **Two-dimensional relativistic simulations of resonance absorption**, *Physics of Fluids* **18**, pp. 1151-1159 (1975).
- 223 D. W. Forslund, J. M. Kindel, and K. Lee, **Theory of hot-electron spectra at high intensity**, *Physical Review Letters* **39**, pp. 284-288 (1977).

-
- 224 K. G. Estabrook and W. L. Kruer, **Properties of resonantly heated electron distributions**, *Physical Review Letters* **40**, pp. 42-45 (1978).
- 225 J.-C. Adam and A. Héron, **Parametric instabilities in resonant absorption**, *Physics of Fluids* **31** pp. 2602-2614 (1988).
- 226 K. Estabrook, **Critical surface bubbles and corrugations and their implications to laser fusion**, *Physics of Fluids* **19**, pp. 1733-1739 (1976).
- 227 W. W. Woo, J. S. DeGroot, and C. Barnes, **Rippling of the critical surface by four-wave processes in a laser-irradiated plasma**, *Physics of Fluids* **23**, pp. 2291-2295 (1980).
- 228 F. Brunel, **Not-so-resonant, resonant absorption**, *Physical Review Letters* **59**, 52 (1987).
- 229 P. Gibbon, Private communication, November 2009.
- 230 Jonathan R. Davies, **Laser absorption by overdense plasmas in the relativistic regime**, *Plasma Physics and Controlled Fusion* **51**, 014006 (2009).
- 231 W. Kruer and K. Estabrook, **$J \times B$ heating by very intense laser light**, *Physics of Fluids* **28**, 430 (1985).
- 232 S. Bulanov, N. M. Naumova, and F. Pegoraro, **Interaction of an ultrashort, relativistically strong laser pulse with an overdense plasma**, *Physics of Plasmas* **1**, 745 (1994).
- 233 W. Rozmus and V. T. Tikhonchuk, **Heating of solid targets by sub-picosecond laser-pulses**, *Physical Review A* **46**, pp. 7810-7814 (1992).
- 234 T.-Y. B. Yang, W. L. Kruer, R. M. More, and A. B. Langdon, **Absorption of laser-light in overdense plasmas by sheath inverse Bremsstrahlung**, *Physics of Plasmas* **2**, pp. 3146-3154 (1995).
- 235 A. A. Andreev, E. G. Gamaliy, V. N. Novikov, A. N. Semakhin, and V. T. Tikhonchuk, **Heating of a dense plasma by an ultrashort laser pulse in the anomalous skin-effect regime**, *Soviet Journal JETP* **74**, pp. 963-973 (1992).